

LLE 2010 Annual Report



October 2009 – September 2010

**UR
LLE** **40**
YEARS OF EXCELLENCE
1970 - 2010

MOSHE J. LUBIN
LLE FOUNDING DIRECTOR
1970-1981

ROBERT L. SPROULL
UNIVERSITY OF ROCHESTER
PRESIDENT EMERITUS

ROBERT L. MCCRORY
LLE DIRECTOR, 1983-PRESENT

DONALD K. HESS
UNIVERSITY OF ROCHESTER
VICE PRESIDENT EMERITUS

JAY M. EASTMAN
LLE DIRECTOR, 1981-1982

ZETA LASER
1978

OMEGA EP LASER
2008

OMEGA LASER FACILITY
2008

OMEGA 60-BEAM LASER
1995

OMEGA 24-BEAM LASER
1980

Cover Photos

Top (left to right): Moshe J. Lubin, the founding director of the Laboratory; Robert L. Sproull, University of Rochester President at the time of the Laboratory's founding; Robert L. McCrory, present LLE CEO and Director; Donald K. Hess, University of Rochester Vice President at the time of the Laboratory founding, and along with Sproull, key to its successful implementation; Jay M. Eastman, LLE Director 1981–82 and project manager for the original OMEGA 24-beam Laser System.

The photographs on the bottom show (left to right): photograph of the ZETA target chamber used to conduct experiments with the first six beams of the OMEGA system; the OMEGA EP laser (LLE's latest laser facility) activated in 2008; the OMEGA 60-beam target chamber area during a target shot taken in 2008; the OMEGA 60-beam UV laser amplifiers during a shot taken during the system activation in 1995; and the original 24-beam OMEGA laser activated in 1980. In the background is a photograph taken of a target shot inside the target chamber of the OMEGA 60-beam laser facility.

Prepared for
U.S. Department of Energy
Albuquerque Service Center
DOE/NA/28302-985

Distribution Category
October 2009–September 2010

Printed in the United States of America
Available from
National Technical Information Services
U.S. Department of Commerce
5285 Port Royal Road
Springfield, VA 22161
www.ntis.gov

This report was prepared as an account of work conducted by the Laboratory for Laser Energetics and sponsored by New York State Energy Research and Development Authority, the University of Rochester, the U.S. Department of Energy, and other agencies. Neither the above named sponsors, nor any of their employees, makes any warranty, expressed or implied, or assumes any legal liability or responsibility for the accuracy, completeness, or usefulness of any information, apparatus, product, or process disclosed, or represents that its use would not infringe privately owned rights. Reference herein to any specific commercial product, process, or service by trade name, mark, manufacturer, or otherwise, does not necessarily constitute or imply its endorsement, recommendation, or favoring by the United States Government or any agency thereof or any other sponsor. Results reported in the LLE Review should not be taken as necessarily final results as they represent active research. The views and opinions of authors expressed herein do not necessarily state or reflect those of any of the above sponsoring entities.

The work described in this volume includes current research at the Laboratory for Laser Energetics, which is supported by New York State Energy Research and Development Authority, the University of Rochester, the U.S. Department of Energy Office of Inertial Confinement Fusion under Cooperative Agreement No. DE-FC52-08NA28302, and other agencies.

For questions or comments, Laboratory for Laser Energetics,
250 East River Road, Rochester, NY 14623-1299, (585) 275-5286.
www.lle.rochester.edu

LLE 2010 Annual Report

October 2009 – September 2010



**Inertial Fusion Program and
National Laser Users' Facility Program**

Contents

Executive Summary	v
Demonstration of the Highest Deuterium–Tritium Areal Density Using Triple-Picket Cryogenic Designs on OMEGA	1
High-Precision Measurements of the Equation of State of Hydrocarbons at 1 to 10 Mbar Using Laser-Driven Shock Waves	6
A Generalized Measurable Ignition Condition for Inertial Confinement Fusion	22
<i>In-Situ</i> Detection and Analysis of Laser-Induced Damage on a 1.5-m Multilayer-Dielectric Grating Compressor for High-Energy, Petawatt-Class Laser Systems	27
Probing High-Areal-Density (ρR) Cryogenic-DT Implosions Using Down-Scattered Neutron Spectra Measured by the Magnetic Recoil Spectrometer	33
Strong Coupling and Degeneracy Effects in Inertial Confinement Fusion Implosions	44
Neutron-Induced Nucleation Inside Bubble Chambers Using Freon 115 as the Active Medium	50
Photoswitchable Gas Permeation Membranes Based on Liquid Crystals	63
High-Intensity Laser–Plasma Interaction with Wedge-Shaped–Cavity Targets	72
Crossed-Beam Energy Transfer in Inertial Confinement Fusion Implosions on OMEGA	79
Characterization of Highly Stable, Mid-IR, GaSb-Based Laser Diodes	85
A Reduced Particle-in-Cell Model for Two-Plasmon-Decay Instability	88
Two-Dimensional Simulations of the Neutron Yield in Cryogenic-DT Implosions on OMEGA	111
X-Ray Radiography of Cryogenic Implosions on OMEGA	128
A Gated Liquid-Scintillator–Based Neutron Detector for Fast-Ignitor Experiments and Down-Scattered Neutron Measurements	145
On-Chip Double Emulsion Droplet Assembly for Laser-Target Fabrication	149
Charge-Injection-Device Performance in the High-Energy-Neutron Environment of Laser-Fusion Experiments	159
Grating Inspection System for Large-Scale Multilayer-Dielectric Gratings for High-Energy Laser Systems	165
Scaling Hot-Electron Generation to High-Power, Kilojoule-Class Laser–Solid Interactions	174
Measurement of the Self-Phase Modulation on OMEGA	179

Large-Aperture, Plasma-Assisted Deposition of Inertial Confinement Fusion Laser Coatings	184
Improved On-Shot Focal-Spot Measurement on OMEGA EP Using Phase-Retrieval-Enhanced Wavefront Measurements	192
The Second Omega Laser Facility Users Group Workshop	205
LLE's Summer High School Research Program	224
FY10 Laser Facility Report	226
National Laser Users' Facility and External Users' Programs	229
Publications and Conference Presentations	297

Executive Summary

The fiscal year ending September 2010 (FY10) concluded the third year of the third five-year renewal of Cooperative Agreement DE-FC52-08NA28302 with the U.S. Department of Energy (DOE). This annual report summarizes progress in inertial fusion research at the Laboratory for Laser Energetics (LLE) during the past fiscal year including work on the National Ignition Campaign (NIC). It also reports on LLE's progress on laboratory basic science research; laser, optical materials, and advanced technology development; operation of OMEGA and OMEGA EP for the NIC and high-energy-density (HED) campaigns, the National Laser Users' Facility (NLUF), and for other external users; and programs focusing on the education of high school, undergraduate, and graduate students during the year.

Progress in Inertial Confinement Fusion Research

One of the principal missions of the University of Rochester's Laboratory for Laser Energetics (LLE) is to conduct research in inertial confinement fusion (ICF) with particular emphasis on supporting the goal of achieving ignition on the National Ignition Facility (NIF). This program relies on the full use of the OMEGA 60-beam UV laser as well as the OMEGA EP high-energy, short-pulse laser system. During FY10, a record total of 1823 target shots were taken on the Omega Laser Facility. Within the NIC, LLE plays a lead role in the validation of the performance of cryogenic target implosions, essential to all forms of ICF ignition. LLE is responsible for a number of critical elements within the Integrated Experimental Teams (IET's) supporting the demonstration of indirect-drive ignition on the NIF and is the lead laboratory for the validation of the polar-drive approach to ignition on the NIF. LLE has also developed, tested, and constructed a large number of diagnostics that are being used on the NIF for the NIC. During this past year, progress in the inertial fusion research program continued to be made in three principal areas: NIC experiments; development of diagnostics for experiments on OMEGA, OMEGA EP, and the NIF; and theoretical analysis and design efforts aimed at improving direct-drive-ignition capsule designs and advanced ignition concepts such as fast ignition and shock ignition.

1. National Ignition Campaign Experiments

LLE achieved a fuel areal density of 0.3 g/cm^2 on an OMEGA cryogenic-DT direct-drive capsule driven with a picket pulse at a shell adiabat $\alpha \sim 2$. This represents the highest DT-fuel areal density achieved to date in direct-drive implosions, and the results are a crucial step in validating predictive capabilities of hydrodynamic codes used to design ignition capsules to be used on the NIF. The first article (p. 1) of this Annual Report discusses in detail the achievement of this high-areal-density milestone. A critical challenge of hot-spot-implosion design is controlling the generation of strong shocks while simultaneously accelerating the fuel shell to a high velocity ($\sim 3 \times 10^7 \text{ cm/s}$). To avoid preheating the fuel, only shocks with shock strength less than a few million atmospheres (Mbar) can be launched into the cryogenic fuel at the start of an implosion. To avoid, however, break up of the shell caused by Rayleigh-Taylor instabilities, the shell must be driven at pressures exceeding 100 Mbar. The targets that successfully demonstrated high fuel areal density on OMEGA were driven with multiple picket pulses that launched a sequence of shocks of increasing strength in the fuel [multiple-shock (MS) designs].

Understanding the equation of state (EOS) of the materials used in ignition targets is critical to optimizing target performance. Beginning on p. 6, we report on high-precision measurements of the EOS of hydrocarbons at pressures ranging from 1 to 10 Mbar. Precision data resulting from the use of α quartz as an impedance-matching (IM) standard were used to tightly constrain the EOS of polystyrene and polypropylene. Both hydrocarbons were observed to reach similar compressions and temperatures as a function of temperature. The materials were observed to transition from transparent insulators to reflecting conductors at pressures of 1 to 2 Mbar.

The results of experiments on the interaction of high-intensity, short-pulse laser irradiation of small-mass-copper (Cu), wedge-shaped-cavity targets are presented (p. 72). Experimental diagnostics provided spatially and spectrally resolved measurements of the Cu K_α line emission at 8 keV.

The coupling efficiency of short-pulse laser energy into fast electrons was inferred from the x-ray yield for wedge opening angles between 30° and 60° and for *s*- and *p*-polarized laser irradiation. Up to $36\pm 7\%$ coupling efficiency was measured for the narrowest wedge with *p*-polarization. The results are compared with predictions from two-dimensional particle-in-cell simulations.

A report on the scaling of hot-electron generation in high-power, kilojoule-class laser–solid interactions is presented on p. 174. Thin-foil targets were irradiated with high-power (~ 210 -TW), 10-ps pulses focused to intensities of $I > 10^{18}$ W/cm² and studied with K-photon spectroscopy. Comparing the energy emitted in K photons to target-heating calculations shows a laser-energy–coupling efficiency to hot electrons of $\eta_{L\rightarrow e} = 20\pm 10\%$. Time-resolved x-ray–emission measurements suggest that laser energy is coupled to hot electrons over the entire duration of the incident laser drive. Comparison of the K-photon emission data to previous data at similar laser intensities shows that $\eta_{L\rightarrow e}$ is independent of laser-pulse duration from $1 \text{ ps} \leq \tau_p \leq 10 \text{ ps}$.

2. Cryogenic Target Fabrication

Beginning on p. 149 we report on the development of a microfluidics-based, on-chip, electric-field–actuated technique to fabricate cryogenic-foam ICF targets. The electrowetting-on-dielectric and dielectrophoresis effects make it possible to manipulate both conductive and dielectric droplets simultaneously on a substrate. Aqueous and non-aqueous liquid droplets precisely dispensed from two reservoirs on a microfluidic chip are transported and combined to form oil-in-water-in-air or water-in oil-in-air double-emulsion droplets. The dispensing reproducibility is studied as a function of a set of operation parameters. Conditions for spontaneous emulsification for double-emulsion formation are developed in terms of droplet surface energies. This technique has the potential of meeting the high-precision, high-rate, low-cost, compact, low-tritium inventory requirements of future inertial fusion energy reactor systems.

3. Target Diagnostics for OMEGA, OMEGA EP, and the NIF

A critical instrument used to measure compressed fuel areal density (ρR) in highly compressed DT targets is the magnetic recoil spectrometer (MRS). The MRS was developed and implemented on OMEGA as well on NIF by a collaborative team comprised of MIT, LLE, and LLNL scientists and engineers. The fundamental principles and design parameters of this instrument are described in detail beginning on p. 33. The MRS measures the absolute neutron spectrum in the range of

5 to 30 MeV. In high-density target implosions, the fusion neutrons scatter on the deuteron and triton ions of the compressed core and the resulting downshift in the neutron energy can be used to directly infer the core areal density. The OMEGA MRS was used to measure the fuel ρR of cryogenic-DT implosions demonstrating $\rho R \sim 0.3 \text{ g/cm}^2$. A version of the OMEGA MRS was installed on the NIF in FY10.

Another important diagnostic to characterize the density of highly compressed targets is x-ray radiography. The first radiographs of cryogenic implosions on OMEGA were obtained using short-pulse, K-shell emission-line backlighters driven by the OMEGA EP laser (see p. 128). Simulations show that radiography near peak compression is feasible. The backlighter composition in this set of experiments was chosen so that the emission lines occurred at energies where the opacity profiles of the imploded cores provide a measurable range of optical depth and the specific intensity of the backlighter is capable of overcoming the core self-emission. Simulations of the first measured implosion radiographs were used to assess the implosion performance at times in advance of peak compression. Radial mass distributions were obtained from the radiographs using Abel inversion and the known temperature and density dependence of the free–free opacity of the hydrogen shell. Radiography based on Compton scattering of hard backlight x rays is also being investigated on the Omega Facility as an alternative approach. The relative advantages of both methods of radiography are compared in this article.

An LLE team partnered with Physikalisch Technische Bundesanstalt, Braunschweig, Germany, to develop a gated liquid-scintillator–based neutron detector to be used for fast-ignitor experiments and down-scattered neutron measurements (p. 145). The detection of neutrons in such experiments is very challenging since it requires the neutron-detection system to recover within 50 to 500 ns from a high background signal many orders of magnitude stronger than the signal of interest. The liquid-scintillator–based detector uses a gated microchannel photomultiplier that suppresses the high background signal and an oxygen-enriched liquid scintillation material that eliminates the afterglow present in conventional plastic scintillators.

The performance of a charge-injection device in the high-energy–neutron environment of laser-fusion experiments has been studied (p. 159). Charge-injection devices (CID's) are being used to image x rays in laser-fusion experiments on the OMEGA Laser System, up to the maximum neutron yields generated ($\sim 10^{14}$ DT). The detectors are deployed in x-ray pin-hole cameras and Kirkpatrick–Baez microscopes. The neutron

fluences ranged from $\sim 10^7$ to $\sim 10^9$ neutrons/cm², and useful x-ray images were obtained even at the highest fluences. At the NIF, CID cameras are intended for use as a supporting means of recording x-ray images. The results of this work predict that x-ray images should be obtainable on the NIF at yields up to $\sim 10^{15}$, depending on distance and shielding.

Neutron imaging is used in ICF experiments to measure the core symmetry of imploded targets. Liquid bubble chambers have the potential to obtain higher-resolution images of the targets for a shorter source-to-target distance than typical scintillator arrays. A theoretical model that describes the mechanism of bubble formation for Freon 115 as the active medium in a liquid bubble chamber is presented (p. 50). The bubble-formation model shows that the size of the critical radius for the nucleation process determines the mechanism of bubble formation and the sensitivity of the active medium for the 14.1-MeV incident neutrons resulting from ICF implosions. The bubble-growth mechanism is driven by the excitation of the medium electronic levels and not by electrons ejected from the medium's atoms as occurs in the bubble chambers used to detect charged particles. The model accurately predicts the neutron-induced bubble density measured on OMEGA with liquid bubble chambers and gel detectors.

4. Theoretical Design and Analysis

In ICF, a shell of cryogenic DT is accelerated inward by either direct laser irradiation or by x rays produced by heating a high-Z enclosure (a hohlraum). At the stagnation of this implosion, the compressed fuel is ignited by a central hot spot surrounded by a cold, dense shell. Ignition occurs when the alpha-particle heating of the hot spot exceeds all the energy losses. To measure progress toward ignition, we developed the metric described beginning on p. 22. This ignition condition is derived in terms of measurable parameters: the areal density, the ion temperature, and the ratio of measured neutron yield to the calculated clean, perfect implosion yield (YOC).

Beginning on p. 111 we report on the use of 2-D *DRACO* simulations to systematically investigate the impact of nonuniformities seeded by target and laser perturbations on neutron yield in cryogenic-DT implosions. Two sources of nonuniformity accounted for the observed neutron-yield reduction according to the *DRACO* simulations: target offset from the target chamber center and laser imprinting. The integrated simulations for individual shots reproduce the experimental YOC ratio to within a factor of ~ 2 . Typically, the YOC in OMEGA cryogenic experiments is $\sim 5\%$. The simulations suggest that YOC can be increased to the ignition hydro-equivalent level of

15% to 20% (with neutron-averaged ρR in the range of 0.2 to 0.3 g/cm²) by maintaining a target offset of less than 10 μm and employing beam smoothing by spectral dispersion (SSD).

Crossed-beam energy transfer in ICF implosions on OMEGA is discussed in an article beginning on p. 79. Radiative-hydrodynamic simulations of implosion experiments on the OMEGA Laser System show that energy transfer between crossing laser beams can significantly reduce laser absorption. A new quantitative model for crossed-beam energy transfer has been developed, allowing one to simulate the coupling of multiple beams in the expanding corona of implosion targets. Scattered-light and bang-time measurements show good agreement with predictions of this model when nonlocal thermal transport is used. The laser absorption can be increased by employing two-color light, which reduces the crossed-beam energy transfer.

An extension of the fully kinetic, reduced-description, particle-in-cell (RPIC) methodology to model two-plasmon-decay (TPD) instability is presented in an article beginning on p. 88. This work was motivated by the recent resurgent interest in suprathermal electron generation by TPD instability in direct-drive laser fusion. RPIC provides a computationally efficient, fully kinetic simulation tool, especially in nonlinear regimes where Langmuir decay instability (LDI) is a dominant saturation mechanism. This RPIC methodology is an extension of the modeling of laser-plasma instabilities in underdense plasmas reported previously. The relationship between RPIC and the extended Zakharov model previously used for TPD instability is explored theoretically and tested in simulations. The modification of electron-velocity distribution—in particular, the generation of hot electrons—as calculated in RPIC leads to weakening of the wave turbulence excited by TPD instability compared to the Zakharov model predictions. However, the locations in wave vector space of important spectral features, e.g., arising from the LDI, of the nonlinear wave fluctuations are exactly the same in the two approaches. New results involving two oblique, overlapping laser beams, a common geometrical feature in direct-drive schemes, are presented. The two laser beams can cooperatively excite common primary Langmuir waves, which initiate the LDI process.

An article beginning on p. 44 presents the results of a collaboration between scientists from LLE and the University of California, Berkeley, on the development of a first-principles equation-of-state (FPEOS) table for deuterium using the path-integral Monte Carlo method. Accurate knowledge about the equation of state (EOS) of deuterium is critical to ICF. Low-

adiabat ICF implosions routinely access strongly coupled and degenerate plasma conditions. The FPEOS table covers typical ICF fuel conditions at densities ranging from 0.002 g/cm³ to +1600 g/cm³ and temperatures of 1.35 eV to 5.5 keV. Discrepancies in internal energy and pressure have been found in strongly coupled and degenerate regimes with respect to *SESAME* EOS. Hydrodynamics simulations of cryogenic ICF implosions using the FPEOS table have indicated significant differences in peak density, areal density (ρR), and neutron yield relative to *SESAME* simulations. The FPEOS simulations result in better agreement of compression ρR with experiments.

Lasers, Optical Materials, and Advanced Technology

We report on a grating-inspection system and a damage-analysis method developed to measure *in-situ* laser-induced damage on the 1.4-m-long tiled-grating assembly of the OMEGA EP pulse compressor during a 15-ps, 2.2-kJ energy ramp (p. 27). The beam fluence at which significant damage growth occurred was determined. This is the first report on beam fluence versus laser-induced-damage growth of meter-sized multilayer-dielectric-diffraction gratings. This result was correlated to the damage-probability measurement conducted on a small grating sample and is consistent with the fluence corresponding to 100% damage probability.

An article on p. 165 reports on the development and implementation of a grating inspection system for large-scale (1.4-m aperture) multilayer-dielectric gratings on the OMEGA EP short-pulse laser system. The grating inspection system (GIS) is fully integrated within the vacuum grating compressor and enables one to carry out inspections while the compressor chamber is under vacuum. Damage is detected by imaging scattered light from damage sites on the grating surface. Features as small as 250 μm can be identified with this system.

Switchable gas permeation membranes have been fabricated (p. 63) in which a photoswitchable, low-molecular-weight liquid crystalline (LC) material acts as the active element. Liquid crystal mixtures are doped with mesogenic azo dyes and infused into commercially available track-etched membranes with regular cylindrical pores (0.40 to 10.0 μm). Tunability of mass transfer can be achieved through a combination of (1) LC/mesogenic dye composition, (2) surface-induced alignment, and (3) reversible photoinduced LC-isotropic transitions. Photoinduced isothermal phase changes in the imbibed material afford large and fully reversible changes in the permeability of the membrane to nitrogen. Both the LC and photogenerated isotropic states demonstrate a linear permeability/pressure relationship, but they show significant differences in their permeability

coefficients. Liquid crystal compositions can be chosen such that the LC phase is more permeable than the isotropic—or vice versa—and can be further tuned by surface alignment. Permeability switching response times are 5 s, with alternating UV and >420-nm radiation at an intensity of 2 mW/cm² being sufficient for complete and reversible switching. Thermal and kinetic properties of the confined LC materials are evaluated and correlated with the observed permeation properties. This is the first demonstration of reversible permeation control of a membrane with light irradiation.

Scientists from LLE, the State University of New York (SUNY) at Stony Brook, and Power Photonic Corp. co-authored a report on highly stable, room-temperature, mid-IR, GaSb-based laser diodes (p. 85). Such laser diodes have been characterized at various temperatures and driver currents. Up to 54 mW of output laser power was demonstrated in a 3150- to 3180-nm-wavelength range with <20-nm FWHM spectral width.

We report on a measurement of the self-phase-modulation-induced bandwidth in a 30-kJ-class laser-amplifier chain (p. 179). Self-phase modulation (SPM) in a multikilojoule laser system was detected spectroscopically and correlated with the time derivative of the intensity measured at the output of the system. This correlation provides an empirical relationship that makes it possible to rapidly determine the magnitude of the SPM being generated using measured experimental data. This empirical relationship was verified by modeling the propagation of an optical pulse in the laser-amplifier chain to predict both pulse shape and the SPM.

Work on large-aperture plasma-assisted deposition of ICF laser coatings is presented beginning on p. 184. Plasma-assisted electron-beam evaporation leads to changes in the crystallinity, density, and stresses of thin films. A dual-source plasma system was developed that provides stress control of large-aperture, high-fluence coatings used in vacuum for substrates 1 m in aperture.

A system was developed (p. 192) to conduct on-shot focal-spot measurements on OMEGA EP using phase-retrieval-enhanced wavefront measurements. Target-plane intensities of the short-pulse beamlines of OMEGA EP were characterized using the focal-spot diagnostic (FSD), an indirect wavefront-based measurement. Phase-retrieval methods were employed using on-shot and off-line far-field measurements to improve the on-shot wavefront measurements and yield more-accurate, repeatable focal-spot predictions. Incorporation of these

techniques has resulted in consistently high (>90%) correlation between the FSD focal-spot predictions and direct far-field fluence measurements in the target chamber in low-energy testing.

National Laser Users' Facility and External Users' Programs

Under the facility governance plan that was implemented in FY08 to formalize the scheduling of the Omega Facility as a National Nuclear Security Agency (NNSA) facility, Omega Facility shots are allocated by campaign. The majority (~65%) of the FY10 target shots were allocated to the NIC conducted by integrated teams from the national laboratories and LLE and to the high-energy-density campaigns conducted by teams led by scientists from the national laboratories.

During FY10 30% of the facility shots in were allocated to basic science experiments. Half of these shots were conducted for university basic science under the National Laser Users' Facility (NLUF) Program, and the remaining shots were allotted to the Laboratory Basic Science (LBS) Program comprising peer-reviewed basic science experiments conducted by the national laboratories and LLE/FSC.

The Omega Facility is also being used for several campaigns by teams from the Commissariat à l'énergie atomique (CEA) of France, and the Atomic Weapons Establishment (AWE) of the United Kingdom. These programs are conducted on the facility on the basis of special agreements put in place by the DOE/NNSA and the participating institutions.

During FY10 facility users included 11 collaborative teams participating in the NLUF Program; 12 teams led by LLNL and LLE scientists participating in the LBS program; many collaborative teams from the national laboratories conducting experiments for the NIC; investigators from LLNL and LANL conducting experiments for high-energy-density-physics programs; and scientists and engineers from CEA and AWE.

1. NLUF Programs

In FY10, DOE issued a solicitation for NLUF grants for the period of FY11–FY12. A total of 15 proposals were submitted to DOE for the NLUF FY11/12 program. An independent DOE Technical Evaluation Panel reviewed the proposals and recommended that 11 proposals receive DOE funding and 31 days of shot time be allocated on OMEGA in each of FY11 and FY12. Table I lists the successful NLUF proposals.

Table I: Approved FY11 and FY12 NLUF proposals.

Principal Investigator	Institution	Project Title
F. N. Beg	University of California, Berkeley	Systematic Study of Fast-Electron Transport in Imploded Plasmas
R. P. Drake	University of Michigan	Experimental Astrophysics on the OMEGA Laser
T. Duffy	Princeton University	Ramp Compression for Studying Equations of State, Phase Transitions, and Kinetics on OMEGA
R. Falcone	University of California, Berkeley	Detailed <i>In-Situ</i> Diagnostics of High-Z Shocks
P. Hartigan	Rice University	Clumpy Environments and Interacting Shock Waves: Realistic Laboratory Analogs of Astrophysical Flows
R. Jeanloz	University of California, Berkeley	Recreating Planetary Core Conditions on OMEGA
K. Krushelnick	University of Michigan	Intense Laser Interactions with Low-Density Plasma Using OMEGA EP
R. Mancini	University of Nevada, Reno	Investigation of Hydrodynamic Stability and Shock Dynamics in OMEGA Direct-Drive Implosions Using Spectrally Resolved Imaging
R. D. Petrasso	Massachusetts Institute of Technology	Charged-Particle Probing of Inertial Confinement Fusion Implosions and High-Energy-Density Plasmas
A. Spitkovsky	Princeton University	Collisionless Shocks in Laboratory High-Energy-Density Plasmas
R. Stephens	General Atomics	Investigation of Laser to Electron Energy Coupling Dependence on Laser Pulse Duration and Material Composition

FY10 was the second of a two-year period of performance for the NLUF projects approved for the FY09–FY10 funding and OMEGA shots. Eleven NLUF projects were allotted Omega Facility shot time and conducted a total of 197 target shots on the facility. Brief summaries of this work may be found beginning on p. 229.

2. Laboratory Basic Science Programs

In FY10, LLE issued a solicitation for LBS proposals to be conducted in FY11. A total of 23 proposals were submitted. An independent review committee reviewed the proposals and recommended that 16 proposals receive 29 shot days on the Omega Laser Facility in FY11. Table II lists the successful LBS proposals.

Eleven LBS projects were allotted Omega Facility shot time and conducted a total of 303 target shots on the facility in FY10. Brief summaries of the FY10 LBS work may be found beginning on p. 245 of this report.

3. FY10 LLNL Omega Facility Programs

In FY10, LLNL conducted several campaigns on the OMEGA and OMEGA EP Laser Systems. LLNL-led teams

conducted 301 target shots on the OMEGA laser and 96 target shots on OMEGA EP. Approximately 40% of all the shots supported the NIC. The remainder of the shots were conducted for the high-energy-density–physics (HEDP) program.

The objectives of the LLNL-led NIC campaigns on the Omega Facility included the following:

- *Reactivation of the 4ω Thomson-scattering diagnostics*
- *Study of bremsstrahlung backlighters for Compton radiography of ICF implosions*
- *Characterization of shell adiabat of spherically imploded inertial fusion targets using x-ray Thomson scattering*
- *High-resolution measurements of velocity nonuniformities created by microscopic perturbations in NIF ablator materials*
- *Equation-of-state measurements of Ge-doped CH*
- *Validation of the Compton radiography diagnostic platform for ICF experiments*
- *Experiments to study the physical properties (thermal conductivity) of shocked fusion fuels*
- *Characterization of hard x-ray sensitivity of MCP-based gated imagers*

Table II: Approved FY10 LBS proposals.

Principal Investigator	Institution	Project Title
H. Chen	LLNL	Exploring Pair Plasma and its Applications Using OMEGA EP
S. X. Hu	LLE	Charge-Particle Stopping Power in Warm Dense Plasmas
R. Betti	LLE/FSC	Shock-Ignition Experiments on OMEGA
I. V. Igumenshchev	LLE	Investigation of Self-Generated Electromagnetic Fields in Directly Driven ICF Implosions Using Proton Radiography
D. G. Hicks	LLNL	Multi-Megabar Ramp Compression: Studies Using X-Ray Absorption Fine Structure
R. A. Kritcher	LLNL	Capsule Adiabat Measurements with X-Ray Thomson Scattering
P. K. Patel	LLNL	Electron Source Characterization for Cone-Guided Fast Ignition
S. P. Regan	LLE	Diagnosing P , ρ , n_e , T_e , Z of H/He, CH ₄ , and NH ₃ Warm Dense Matter
G. Fiksel	LLE	Laser-Driven Magnetic-Flux Compression Experiments on OMEGA
V. A. Smalyuk	LLNL	Measurement of Ablative Rayleigh–Taylor Instability in Deeply Nonlinear Regime
R. Smith	LLNL	Measurement of Nucleation and Growth of the Fe α -to- ϵ Phase Transformation
B. Maddox	LLNL	Ultrahigh Pressure Lattice Dynamics in High-Z Metals
H. S. Park	LLNL	Astrophysical Collisionless Shock Generation in Laser-Driven Experiments
O. Hurricane	LLNL	Measurements of Linear, Nonlinear, and Turbulent-Mixing Regimes in Kelvin–Helmholtz Instability in the Subsonic Regime
C. Stoeckl	LLE	Fast-Electron Transport in Solid Density Matter
J. M. McNaney	LLNL	Short-Pulse-Laser-Based Neutron Resonance Spectrometry

- *Characterization of plasma conditions at the laser entrance hole (LEH) of a gas-filled hohlraum using Thomson scattering*
- *Validation of the modeling of multibeam scattering occurring in NIC targets*
- *Measurements of the plasma conductivity by means of collective x-ray Thomson scattering*

The LLNL-led HED campaigns covered five main areas of research:

1. *Material dynamics and equation of state*
 - a. *Quasi-isentropic compression experiments (ICE) for material properties such as strength, equation of state, phase, and phase-transition kinetics under high pressure*
 - b. *Platform development using radiographic measurements of instability growth in Ta to infer material strength using the joint OMEGA–OMEGA EP configuration*
 - c. *Properties of shocked CH and Si aerogel foams used in HED experiments*
 - d. *The equation of state of a CO₂ mixture along the Hugoniot*
 - e. *Initial experiments to develop an experimental platform to measure the melt and resolidation of Sn*
2. *Opacity*
 - a. *Opacity studies of high-temperature plasmas under LTE conditions*
 - b. *Initial experiments to compare short- and long-pulse techniques to heat materials to high temperature for opacity data*
3. *Hydrodynamics*
 - a. *Measurements of the Kelvin–Helmholtz instability in laser-driven shock tubes*
 - b. *The hydrodynamic evolutions of high-Mach-number copper-foam jets*
4. *X-ray sources applications*
 - a. *Development of multi-keV x-ray sources for radiography and for the study of material response in samples*
5. *Diagnostic technique development*
 - a. *Development of a target-mounted turning mirror for use with the VISAR diagnostic*
 - b. *Demonstration of ultrafast temperature and density measurements with x-ray Thomson scattering from short-pulse-laser-heated matter*
 - c. *Comparison of short- and long-pulse-generated x-ray backlights*
 - d. *Development of diffraction (white light Laue and powder) to measure the structure of solids (Ta, Fe, Sn)*

Brief summaries of the LLNL-led experiments may be found beginning on p. 255 of this report.

4. FY10 LANL Omega Facility Programs

In FY10, Los Alamos National Laboratory (LANL) executed 131 shots on the OMEGA Laser and 32 shots on the OMEGA EP Laser. LANL had three instruments qualified for use on OMEGA EP. They are the NIF 5 spectrometer, the target-heating Verdi laser (THVL), and the Thomson parabola ion energy (TPIE) diagnostic.

LANL experiments contributed to the NIC in the following areas:

- *Studies of the EOS of plastic ablators*
- *New experimental methods for determining the areal density of imploded ICF capsules using 4.44-MeV ¹²C(n,n') γ rays*
- *Demonstration of NIF components of the neutron imaging system*

HED campaigns included the following:

1. *Measurement of a supersonic radiation wave*
2. *Measurement of capsule yield in the presence of high-Z dopants*
3. *DT reaction product branching ratio measurements*
4. *Energetic ion generation from hemispherical targets*
5. *Development of x-ray sources for phase-contrast imaging*

The LANL-led experiments are summarized beginning on p. 278.

5. FY10 CEA Omega Facility Experiments

CEA-led teams conducted 62 target shots on OMEGA during FY10. The experiments included ablator-preheat characterization, Rayleigh–Taylor (RT) growth measurements, and rugby hohlraum characterization. The CEA work is summarized beginning on p. 288.

This year marked the tenth year of continuous collaborations between CEA and LLE on experiments conducted on the Omega Facility. During this period, more than 500 Omega Facility target shots have been conducted in collaborations involving the two institutions. The results of this past decade of collaboration have been very successful and will contribute significantly to demonstrating ICF ignition.

6. FY10 AWE Omega Facility Programs

AWE teams led experiments on three shot days of the OMEGA laser. The work included an investigation of asymmetrically driven hohlraums (two days) and a Laue-diffraction study of the dynamics of shocked Ta crystals (one day). A total

of 37 shots were taken for AWE in FY10. The AWE experiments are summarized beginning on p. 291.

FY10 Facility Report

During FY10, the Omega Laser Facility conducted a record total of 1823 target shots on the OMEGA (1343 target shots) and OMEGA EP (480 target shots) lasers (see Tables 124.III and 124.IV on p. 226). Nearly 46% of the total shots were taken for or in support of NIC. External users accounted for ~63% of the total Omega Facility target shots in FY10 (64.4% of OMEGA and 60.4% of OMEGA EP target shots).

Many modifications were made to the OMEGA laser to improve low-adiabat direct-drive cryogenic implosion performance. OMEGA conducted 38 DT spherical cryogenic target shots and 40 planar cryogenic target shots in support of shock-timing experiments. The OMEGA Availability and Experimental Effectiveness averages for FY10 were 93% and 94%, respectively.

OMEGA EP was operated extensively in FY10 for a variety of users. A total of 308 short-pulse IR shots were conducted. Of these, 232 target shots were taken into the OMEGA EP target chamber and 76 joint shots were taken into the OMEGA target chamber. The Availability and Experimental Effectiveness for OMEGA EP averaged 86% and 94%, respectively.

Several major modifications were implemented on the Omega Facility during FY10:

1. Three-color-cycle (3CC) beam smoothing was implemented on the OMEGA laser to improve the picket-pulse pointing performance.
2. The OMEGA pulse-shaping system was augmented with facility modifications in the temperature and humidity controls of the Driver Electronics Room to improve the temporal shape stability.
3. A new short-pulse timing diagnostic was implemented and calibrated on OMEGA EP. The pulse-shape measurement diagnostic (PSM) uses high-bandwidth oscilloscopes and photodiodes to measure short-pulse timing at the output of the grating compressor chamber (GCC).
4. A full complement of 12 multilayer dielectric gratings was acquired from a commercial vendor to improve short-pulse energy performance on one of the OMEGA EP beamlines. It is expected that the operational energy envelope of this

beamline will be increased by ~50% to over 1.5 kJ at 10 ps in the coming year.

5. An OMEGA EP focal-spot diagnostic system was implemented. As a result, on-shot target-plane, focal-spot fluence data are now provided for short-pulse shots on OMEGA EP.
6. A temporal contrast diagnostic system was implemented on OMEGA EP.
7. The first two distributed phase plates were deployed on OMEGA EP.
8. Vacuum antechambers for the backlighter and sidelighter off-axis parabolas (OAP's) were deployed on the OMEGA EP target chamber to facilitate storage of these focusing optics when they are not in use.
9. Two new ten-inch manipulators were installed on the OMEGA EP target chamber, increasing the non-fixed diagnostic capability of the system by 40%.

Education

As the only major university participant in the National ICF Program, education continues to be an important mission for the Laboratory. Laboratory education programs span the range of high school (p. 297) to graduate education.

1. High School Student Program

During the summer of 2010, 16 students from Rochester-area high schools participated in the Laboratory for Laser Energetics' Summer High School Research Program. The goal of this program is to excite a group of high school students about careers in the areas of science and technology by exposing them to research in a state-of-the-art environment. Too often, students are exposed to "research" only through classroom laboratories, which have prescribed procedures and predictable results. In LLE's summer program, the students experience many of the trials, tribulations, and rewards of scientific research. By participating in research in a real environment, the students often become more excited about careers in science and technology. In addition, LLE gains from the contributions of the many highly talented students who are attracted to the program.

The students spent most of their time working on their individual research projects with members of LLE's technical staff. The projects were related to current research activities at LLE and covered a broad range of areas of interest including experimental diagnostic development, computational modeling

of implosion physics, laser physics, experimental and theoretical chemistry, materials science, cryogenic target characterization, target vibration analysis, and computer control systems (see Table 124.II on p. 224).

The program culminated on 25 August with the “High School Student Summer Research Symposium,” at which the 16 students presented the results of their research to an audience including parents, teachers, and LLE staff. The students’ written reports will be made available on the LLE Web site.

Two hundred and sixty-five high school students have now participated in the program since it began in 1989. This year’s students were selected from a record 80 applicants.

At the symposium, LLE presented its 14th annual William D. Ryan Inspirational Teacher Award to Mr. Bradley Allen, AP Physics teacher at Brighton Senior High School. This award is presented to a teacher who motivated one of the participants in LLE’s Summer High School Research Program to study science, mathematics, or technology and includes a \$1000 cash prize.

Teachers are nominated by alumni of the summer program. Mr. Allen was nominated by Nicholas Harvest Zhang and Aaron Van Dyne, participants in the 2009 Summer Program.

2. Undergraduate Student Programs

Approximately 31 undergraduate students participated in work or research projects at LLE this past year. Student projects

include operational maintenance of the OMEGA Laser Facility; work in laser development, materials, and optical-thin-film-coating laboratories; computer programming; image processing; and diagnostics development. This is a unique opportunity for students, many of whom will go on to pursue a higher degree in the area in which they gained experience at the Laboratory.

3. Graduate Student Programs

Graduate students are using the OMEGA Facility as well as other LLE facilities for fusion and high-energy-density physics research and technology development activities. These students are making significant contributions to LLE’s research program. Twenty-five faculty from the five University academic departments collaborate with LLE scientists and engineers. Presently, 82 graduate students are involved in research projects at LLE, and LLE directly sponsors 38 students pursuing Ph.D. degrees via the NNSA-supported Frank Horton Fellowship Program in Laser Energetics. Their research includes theoretical and experimental plasma physics, high-energy-density physics, x-ray and atomic physics, nuclear fusion, ultrafast optoelectronics, high-power-laser development and applications, nonlinear optics, optical materials and optical fabrication technology, and target fabrication.

In addition, LLE directly funds research programs within the MIT Plasma Science and Fusion Center, the State University of New York (SUNY) at Geneseo, and the University of Wisconsin. These programs involve a total of approximately 6 graduate students, 25 to 30 undergraduate students, and 10 faculty members.

Robert L. McCrory

Director, Laboratory for Laser Energetics
Vice Provost, University of Rochester

Demonstration of the Highest Deuterium–Tritium Areal Density Using Triple-Picket Cryogenic Designs on OMEGA

In inertial confinement fusion (ICF) implosions, a cryogenic shell of deuterium–tritium (DT) fuel is driven inward by means of direct or indirect laser illumination to achieve high compression and burn.¹ Fuel burn proceeds in two stages: First, a lower-density, higher-temperature (~ 10 -keV) hot spot is formed by PdV work of converging higher-density, lower-temperature shells. Calculations show that to initiate burn, the shell kinetic energy must exceed the threshold value,² which depends on the shell implosion velocity V_{imp} (peak mass-averaged shell velocity), the in-flight shell adiabat α_{if} (ratio of shell pressure to the Fermi-degenerate pressure at the position in peak shell density), and the drive pressure p_{d} . Second, as burn propagates through the fuel, shell inertia provides sufficient confinement time to burn a significant fraction of the assembled fuel. This requires fuel areal densities (ρR) at peak compression in excess of ~ 0.9 g/cm² (Ref. 1). The peak areal density in a direct-drive implosion depends mainly on α_{if} and laser energy E_{L} (Ref. 3):

$$\max(\rho R)_{\text{g/cm}^2} = \frac{2.6 E_{\text{L,MJ}}^{1/3}}{\alpha_{\text{if}}^{0.54}}. \quad (1)$$

Therefore, to burn a sufficient fraction of the fuel, the shell adiabat must be $\alpha_{\text{if}} \leq 7 E_{\text{L,MJ}}^{0.6}$. While hot-spot formation and burn-initiation physics require laser energy in excess of ~ 300 kJ, which will be available on the National Ignition Facility (NIF),⁴ implosions on the OMEGA laser⁵ validate the ability of ignition designs to assemble cryogenic fuel with ignition-relevant implosion velocities ($V_{\text{imp}} > 3 \times 10^7$ cm/s), maintaining the required fuel adiabat. A deviation of the adiabat from the designed value in an implosion can be inferred by comparing the measured and predicted values of ρR . The areal density is determined by measuring spectral shapes of reaction products as they interact with the fuel.^{6,7} This gives a value $\langle \rho R \rangle_{\text{n}}$ averaged over reaction time history. The theoretical value of $\langle \rho R \rangle_{\text{n}}$ has a similar dependence on α_{if} and E_{L} as in Eq. (1) with a numerical factor of 1.7 instead of 2.6 (Ref. 3). Using this scaling, an OMEGA cryogenic-DT design, hydrodynamically equivalent to an $\alpha_{\text{if}} = 2$ ignition design on the NIF, is predicted to achieve $\langle \rho R \rangle_{\text{n}} \sim 300$ mg/cm² at a laser

energy ~ 25 to 30 kJ and a laser absorption fraction of 60% to 70%, typical for OMEGA-scale targets. Reaching these areal densities on OMEGA, therefore, is a crucial step in validating predictive capabilities of hydrodynamic codes used to design ignition targets on the NIF.

The shell adiabat is determined by heating sources, including shock waves, radiation, and suprathermal electrons. Because of inaccuracies in the models used to design targets, experimental tuning is required to ensure that preheat is at an acceptable level. This article describes direct-drive target designs optimized for experimental shock timing to prevent adiabat degradation caused by excessive shock heating. This is accomplished by combining three intensity pickets with the main drive pulse [triple-picket (TP) design]. The main pulse in this case requires minimal shaping (an intensity step is introduced to control the strength of the main shock). Areal densities up to 300 mg/cm² are observed in cryogenic-DT implosions on OMEGA using the TP designs driven at peak intensities $\sim 8 \times 10^{14}$ W/cm².

One of the main challenges in designing hot-spot ignition implosions is to control the generation of strong shocks while accelerating the fuel shell to high implosion velocities. To avoid excessive shock heating, only few-Mbar shocks can be launched into cryogenic fuel at the beginning of an implosion. On the other hand, reaching $V_{\text{imp}} > 3 \times 10^7$ cm/s without the Rayleigh–Taylor instability⁸ disrupting the shell requires drive pressures p_{d} in excess of 100 Mbar since the shell’s in-flight aspect ratio A_{in} (ratio of shell radius R to shell thickness) is proportional to $p_{\text{d}}^{-2/5}$ (Ref. 3) and shells with higher A_{in} are more susceptible to perturbation growth during the acceleration phase. Such a pressure increase from a few Mbar to 100 Mbar can be achieved either adiabatically [continuous-pulse (CP) design]^{9,10} or by launching a sequence of shocks of increasing strength [multiple-shock (MS) designs].^{1,11}

Early cryogenic spherical implosions on OMEGA used the CP designs.^{12–15} Both 5- and 10- μm -thick CD shells with cryogenic 95- μm -thick D₂ and 80- μm -thick DT layers were

used in these experiments. Areal densities close to the predicted values ($\langle \rho R \rangle_n \sim 100$ to 120 mg/cm²) were achieved in implosions with 5- μ m shells driven at peak intensities below $I_{\text{limit}} = 3 \times 10^{14}$ W/cm² ($p_d \sim 50$ Mbar) and a laser pulse contrast ratio (CR) of less than 3.5. When 10- μ m shells were used, $\langle \rho R \rangle_n$ values up to 200 mg/cm² (80% to 90% of the predicted areal densities) were measured for designs with $I_{\text{limit}} = 5 \times 10^{14}$ W/cm² ($p_d \sim 75$ Mbar) and a CR < 30 (Ref. 15). The implosion velocity was $V_{\text{imp}} \simeq 2.2 \times 10^7$ cm/s. Increasing drive intensities above I_{limit} resulted in significant deviations of measured and predicted $\langle \rho R \rangle_n$ (Ref. 14). Shock velocity measured in the CP designs using a velocity interferometry system for any reflector (VISAR)¹⁶ revealed difficulty in reproducing an adiabatic compression wave predicted in simulations.^{14,17} Since the effect of steepening a compression wave into a shock, not predicted in simulations, is exacerbated by increasing either peak drive intensity or laser pulse CR, it is impractical to experimentally tune the adiabat in the CP designs to ignition-relevant values.

Initial fuel compression prior to reaching peak drive intensity can be accurately controlled in the MS designs by launching a sequence of shocks using intensity pickets. Here we describe the main features of such designs. First, we assume that N shocks are launched by narrow pickets (picket duration is much shorter than shock transit time across the shell), and the main shock is launched and supported by the main pulse. Since pressure of an unsupported shock decays in time, the fuel adiabat decreases from the front to the back of the shell. Equation (1) needs to be modified in this case to reflect spatial variation in α_{if} . The following supports using only the adiabat at the inner shell surface (“inner adiabat” α_{inn}) to determine areal density.³ The maximum shell convergence during an implosion is limited by a rarefaction wave, created at the main shock-breakout time, with a tail propagating from the inner part of the shell toward the target center. Since material in a rarefaction moves at the local sound speed with respect to position of the peak shell density, the low-density tail is larger if the inner adiabat is higher. Later, as the main shock reflects from the center and begins interacting with the rarefaction, pressure at the target center starts to build up, initiating shell deceleration. Therefore, the larger the inner adiabat, the larger the rarefaction region, causing the main shell to decelerate farther from the center, thereby reducing the final shell convergence and areal density.

Since the adiabat is proportional to pressure over density to the 5/3rd power, shocks launched by the pickets must raise the inner shell density to a value sufficient to keep the main

shock with $p_d \sim 100$ Mbar from increasing the inner adiabat above the required value. To maximize this compression, all shocks must coalesce nearly simultaneously in the vapor region, soon after they break out of the shell. This relates the picket amplitudes and timing. Using the adiabat relation with pressure and density ρ in DT fuel, $\alpha \simeq p(\text{Mbar})/2.16 \rho^{5/3}$, the required inner shell compression after the main shock can be written as $\rho_{\text{main}}/\rho_0 \simeq 40[(p_d/100 \text{ Mbar})/\alpha_{\text{inn}}]^{3/5}$, where $\rho_0 = 0.25$ g/cm³ is the initial shell density. The density at the first shock front is compressed by a factor of ~ 4 if shock pressure p_1 stays above ~ 1 Mbar. Maximizing the density compression by the remaining N shocks ($N-1$ shocks from pickets and the main shock) leads, with the help of Hugoniot relations,¹⁸ to a condition on shock-pressure ratio as the shocks reach the inner surface, $p_{i+1} = p_i(p_d/p_1)^{1/N}$, where $i = 1, \dots, N$. The inner adiabat in this case is

$$\alpha_{\text{inn}} = 46.3 \left(\frac{p_d}{100 \text{ Mbar}} \right) \left[\frac{(p_d/p_1)^{1/N} + 4}{4(p_d/p_1)^{1/N} + 1} \right]^{5N/3}. \quad (2)$$

Because of radiation preheat and additional heating caused by a secondary compression wave formed at the beginning of shell acceleration, the in-flight adiabat used in Eq. (1) is higher than α_{inn} predicted by Eq. (1). In general, for an optimized multiple-picket design, an effective α_{inn} is larger by a factor of 2 to 2.5. Therefore, a high-yield, direct-drive NIF design requires that the number N of pickets be determined by setting $\alpha_{\text{inn}} \simeq 1$ (which is equivalent to an $\alpha \simeq 2.5$ CP design) in Eq. (2). This gives a relation between N and p_d , which can be approximated by $p_d(\text{Mbar}) \simeq 6.5 N e^{0.78 N}$. For $p_d \sim 100$ Mbar, this gives $N = 3$, and pressures of the first three shocks as they break out of the shell are 1, 4.6, and 21 Mbar, respectively.

Next, a simple model is used to gain insight into the shock evolution in a multiple-picket design. A shock wave traveling along the x axis with a velocity U_{sh} is assumed to be strong enough that the flow velocity ahead of the shock can be neglected with respect to post-shock velocity in the laboratory frame of reference. Using the ideal-gas equation-of-state model, the mass density in this case increases by a factor of 4 across the shock front. Gradients in the flow created by unsupported shocks lead to PdV work on a fluid element, $d_t p \equiv \partial_t p + v \partial_x p = -(5/3)p \partial_x v$. The spatial gradient in velocity can be expressed in terms of pressure gradient and acceleration in the shock-front frame using Bernoulli’s relation $v \partial_x v + \partial_x p / \rho = -d_t U_{\text{sh}} - \partial_t v$. In the strong-shock limit, $v = -U_{\text{sh}}/4$ and $U_{\text{sh}} = \sqrt{(4/3)p_{\text{sh}}/\rho_0}$, leading to $d_t(p_{\text{sh}} U_{\text{sh}}^5) = -U_{\text{sh}}^6 (\partial_x p)_{\text{sh}}$, where p_{sh} is shock pressure and ρ_0 is density ahead of the shock. This equation can

be simplified by introducing a mass coordinate, $dm = \rho dx$, and replacing time with the mass m_{sh} overtaken by the shock, $dm_{\text{sh}} = \rho U_{\text{sh}} dt$. At the shock front, this gives

$$\frac{d \ln(p_{\text{sh}} U_{\text{sh}}^5)}{dm_{\text{sh}}} = -4 \left(\frac{\partial \ln p}{\partial m} \right)_{\text{sh}}. \quad (3)$$

According to a self-similar solution¹⁹ and simulation results, the pressure behind the unsupported shock changes nearly linearly with mass, $p \sim m$. In this case, Eq. (3) gives $p_{\text{sh}} \sim m_{\text{sh}}^{-1.14} \rho_0^{0.71}$. The first shock travels through uniform density; therefore, the shock pressure decays as $p_1 \sim m_{\text{sh}}^{-1.14}$ and the post-shock adiabat varies as $\alpha_1 \sim m^{-1.14}$. Compared to the results of a self-similar solution,¹⁹ the error in the power index predicted by this model is within 10%. The density after the shock evolves as $\rho \sim (p/\alpha_1)^{3/5}$. Therefore, as the second shock is launched, the density ahead of its front grows as $\rho_0 \sim m_{\text{sh}}^{1.29}$ and shock pressure decays as $p_2 \sim m_{\text{sh}}^{-0.22}$. To generalize, if an $i + 1$ shock with $p_{i+1} \sim m_{\text{sh}}^{\delta_{i+1}}$ travels through the flow with an adiabat profile $\alpha_i \sim m^{-\omega_i}$, the model gives $\delta_{i+1} = 0.57 \delta_i + 0.43$ and $\omega_{i+1} = 0.57 \omega_i + 1.71$ with $\delta_1 = -\omega_1 = -1.14$. Therefore, starting with the third shock, the pressure at the unsupported shock front increases as the shock travels through the shell. For the main shock launched after N decaying shocks and supported by pressure p_d , Eq. (3) gives (assuming that pressure changes linearly with the mass coordinate)

$$p_{\text{main}} = p_d \left[3(\omega_N + 1) \left(m_{\text{sh}} / m^* \right)^{\delta_{N+1}} - 8 \right] / (3\omega_N - 5),$$

where m^* is a normalization constant that depends on picket duration.

The model shows that the main shock pressure increases as the shock propagates through the shell, significantly exceeding the ablation pressure. To avoid an increase in the inner adiabat caused by this pressure amplification, it is necessary to either increase the number of pickets to 4 or reduce the strength of the main shock by introducing an intensity step at the beginning of the main drive. Since incorporating the fourth picket in the design is very challenging because of the short time separation between the last picket and the main drive, a combination of three pickets and a step pulse is chosen as a baseline for the multiple-picket, low-adiabat designs.

As mentioned earlier, all shocks launched by the pickets and the main drive must coalesce nearly simultaneously in the vapor region of the target, in close proximity to the inner shell surface.

A VISAR measurement in an optimized design should produce, therefore, a decaying velocity of the first shock, followed by a rapid velocity increase, at the coalescence time, up to a value above $\sim 120 \mu\text{m/ns}$ (see the dotted line in Fig. 121.1). Because of the radiative precursor, the VISAR signal is absorbed in a region ahead of the shock front if $V_{\text{sh}} > 75 \mu\text{m/ns}$ (Ref. 20). As a result, only the first shock velocity and time of shock coalescence can be measured by the VISAR. Deviations from the predicted strength of any shock can be inferred by observing multiple jumps in the velocity of the leading shock wave. For example, if the third picket is too high, the third shock will prematurely overtake the second and first shocks, resulting in an early velocity jump, as shown in Fig. 121.1. The measurement presented in Fig. 121.1 was performed on OMEGA with a 900- μm -diam, 10- μm -thick CD shell filled with liquid D_2 and fitted with a VISAR cone.¹⁷ As seen in Fig. 121.1, the two coalescence events, separated by ~ 300 ps, are a signature of mistimed shocks that can be corrected by reducing the intensity of the third picket.

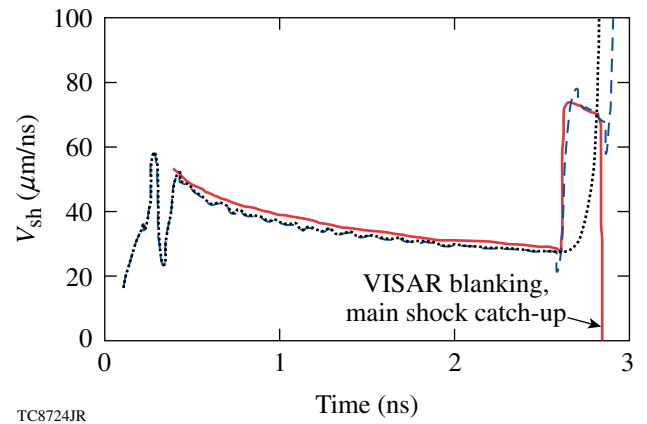


Figure 121.1

Example of leading shock-velocity history measured (red line) and predicted (dashed line) in the TP design with a mistimed third shock. The calculated velocity history for an optimized design is shown by the dotted line.

To verify the shock optimization procedure and validate control of the main shock strength with an intensity step, the TP designs with both square and step main pulses were used on OMEGA to drive targets with a 65- μm -thick cryogenic-DT layer overcoated with a 10- μm CD shell. The pulse shapes shown in Fig. 121.2 had a peak intensity of $\sim 8 \times 10^{14} \text{ W/cm}^2$. The laser energy varied from 23 kJ for the square main pulse to 25 kJ for the step main pulse, respectively. The predicted implosion velocity in these designs reached $V_{\text{imp}} = 3 \times 10^7 \text{ cm/s}$. A magnetic recoil spectrometer (MRS)⁶ was used to infer $\langle \rho R \rangle_n$. Two charged-particle spectrometers (CPS's) were also used to

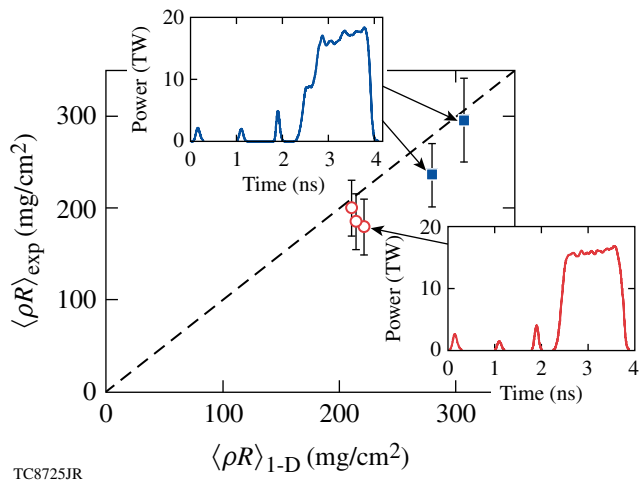


Figure 121.2

Predicted and measured areal densities for triple-picket square (circles) and step (squares) OMEGA designs. The inserts show the pulse shapes used to drive the implosions.

measure the spectral shape of the knock-on deuterons (KOD's), elastically scattered by primary DT neutrons. The shape in the KOD spectrum is insensitive, however, to areal densities above $\langle \rho R \rangle_n > 180 \text{ mg/cm}^2$ (Ref. 6). These measurements were used to infer the lower limit on $\langle \rho R \rangle_n$ as well as assess asymmetries developed at different views of an implosion. In Fig. 121.2 the measured areal densities are compared to those calculated using the one-dimensional hydrocode *LILAC*.²¹ Good agreement between measurements and calculations validates the accuracy of shock tuning in the TP designs. Also, the observed increase in $\langle \rho R \rangle_n$ in the step design confirms that the inner adiabat can be accurately controlled by changing step amplitude in the main drive.

Based on the good performance of the TP designs on OMEGA, a new triple-picket, direct-drive-ignition design is proposed for the NIF (Fig. 121.3). Driven at a peak intensity of $8 \times 10^{14} \text{ W/cm}^2$, the shell reaches $V_{\text{imp}} = 3.5$ to $4 \times 10^7 \text{ cm/s}$, depending on the thickness of the fuel layer. At a laser energy of 1.5 MJ, this design is predicted to ignite with a gain $G = 48$. A stability assessment of the NIF TP design is currently in progress.

In summary, triple-picket designs were used in cryogenic-DT implosions on OMEGA. The highest areal densities ever measured in cryogenic-DT implosions (up to 300 mg/cm^2) were inferred with $V_{\text{imp}} \sim 3 \times 10^7 \text{ cm/s}$ driven at a peak laser intensity of $8 \times 10^{14} \text{ W/cm}^2$. Scaled to the NIF, the TP design is predicted to ignite with a gain $G = 48$.

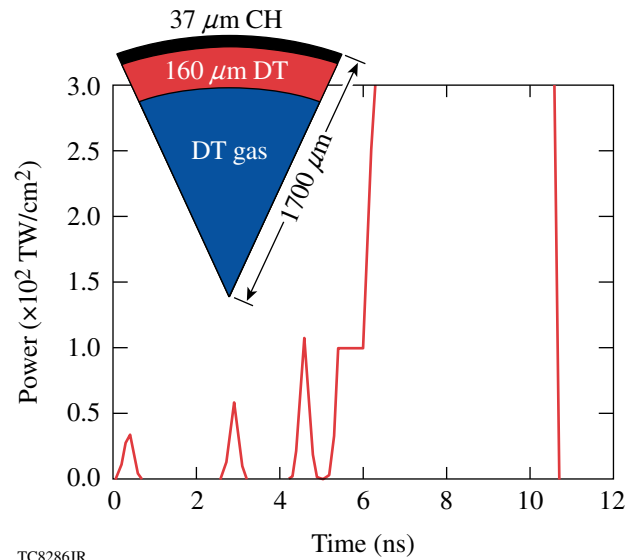


Figure 121.3

Triple-picket, direct-drive design for the NIF.

ACKNOWLEDGMENT

This work was supported by the U.S. Department of Energy Office (DOE) of Inertial Confinement Fusion under Cooperative Agreement No. DE-FC52-08NA28302, the University of Rochester, and the New York State Energy Research and Development Authority. The support of DOE does not constitute an endorsement by DOE of the views expressed in this article.

REFERENCES

1. J. D. Lindl, *Inertial Confinement Fusion: The Quest for Ignition and Energy Gain Using Indirect Drive* (Springer-Verlag, New York, 1998).
2. M. C. Herrmann, M. Tabak, and J. D. Lindl, *Phys. Plasmas* **8**, 2296 (2001).
3. C. D. Zhou and R. Betti, *Phys. Plasmas* **14**, 072703 (2007).
4. J. Paisner *et al.*, *Laser Focus World* **30**, 75 (1994).
5. T. R. Boehly, D. L. Brown, R. S. Craxton, R. L. Keck, J. P. Knauer, J. H. Kelly, T. J. Kessler, S. A. Kumpan, S. J. Loucks, S. A. Letzring, F. J. Marshall, R. L. McCrory, S. F. B. Morse, W. Seka, J. M. Soures, and C. P. Verdon, *Opt. Commun.* **133**, 495 (1997).
6. J. A. Frenje, C. K. Li, F. H. Séguin, D. T. Casey, R. D. Petrasso, T. C. Sangster, R. Betti, V. Yu. Glebov, and D. D. Meyerhofer, *Phys. Plasmas* **16**, 042704 (2009).
7. F. H. Séguin, C. K. Li, J. A. Frenje, D. G. Hicks, K. M. Green, S. Kurebayashi, R. D. Petrasso, J. M. Soures, D. D. Meyerhofer, V. Yu. Glebov, P. B. Radha, C. Stoeckl, S. Roberts, C. Sorce, T. C. Sangster, M. D. Cable, K. Fletcher, and S. Padalino, *Phys. Plasmas* **9**, 2725 (2002).
8. S. Chandrasekhar, in *Hydrodynamic and Hydromagnetic Stability*, International Series of Monographs on Physics (Clarendon Press, Oxford, 1961), p. 428.

9. P. W. McKenty, V. N. Goncharov, R. P. J. Town, S. Skupsky, R. Betti, and R. L. McCrory, *Phys. Plasmas* **8**, 2315 (2001).
10. V. N. Goncharov, J. P. Knauer, P. W. McKenty, P. B. Radha, T. C. Sangster, S. Skupsky, R. Betti, R. L. McCrory, and D. D. Meyerhofer, *Phys. Plasmas* **10**, 1906 (2003).
11. J. D. Lindl and W. C. Mead, *Phys. Rev. Lett.* **34**, 1273 (1975).
12. F. J. Marshall, R. S. Craxton, J. A. Delettrez, D. H. Edgell, L. M. Elasky, R. Epstein, V. Yu. Glebov, V. N. Goncharov, D. R. Harding, R. Janezic, R. L. Keck, J. D. Kilkenny, J. P. Knauer, S. J. Loucks, L. D. Lund, R. L. McCrory, P. W. McKenty, D. D. Meyerhofer, P. B. Radha, S. P. Regan, T. C. Sangster, W. Seka, V. A. Smalyuk, J. M. Soures, C. Stoeckl, S. Skupsky, J. A. Frenje, C. K. Li, R. D. Petrasso, and F. H. Séguin, *Phys. Plasmas* **12**, 056302 (2005).
13. T. C. Sangster, R. Betti, R. S. Craxton, J. A. Delettrez, D. H. Edgell, L. M. Elasky, V. Yu. Glebov, V. N. Goncharov, D. R. Harding, D. Jacobs-Perkins, R. Janezic, R. L. Keck, J. P. Knauer, S. J. Loucks, L. D. Lund, F. J. Marshall, R. L. McCrory, P. W. McKenty, D. D. Meyerhofer, P. B. Radha, S. P. Regan, W. Seka, W. T. Shmayda, S. Skupsky, V. A. Smalyuk, J. M. Soures, C. Stoeckl, B. Yaakobi, J. A. Frenje, C. K. Li, R. D. Petrasso, F. H. Séguin, J. D. Moody, J. A. Atherton, B. D. MacGowan, J. D. Kilkenny, T. P. Bernat, and D. S. Montgomery, *Phys. Plasmas* **14**, 058101 (2007).
14. V. A. Smalyuk, R. Betti, T. R. Boehly, R. S. Craxton, J. A. Delettrez, D. H. Edgell, V. Yu. Glebov, V. N. Goncharov, D. R. Harding, S. X. Hu, J. P. Knauer, F. J. Marshall, R. L. McCrory, P. W. McKenty, D. D. Meyerhofer, P. B. Radha, S. P. Regan, T. C. Sangster, W. Seka, R. W. Short, D. Shvarts, S. Skupsky, J. M. Soures, C. Stoeckl, B. Yaakobi, J. A. Frenje, C. K. Li, R. D. Petrasso, and F. H. Séguin, *Phys. Plasmas* **16**, 056301 (2009).
15. T. C. Sangster, V. N. Goncharov, P. B. Radha, V. A. Smalyuk, R. Betti, R. S. Craxton, J. A. Delettrez, D. H. Edgell, V. Yu. Glebov, D. R. Harding, D. Jacobs-Perkins, J. P. Knauer, F. J. Marshall, R. L. McCrory, P. W. McKenty, D. D. Meyerhofer, S. P. Regan, W. Seka, R. W. Short, S. Skupsky, J. M. Soures, C. Stoeckl, B. Yaakobi, D. Shvarts, J. A. Frenje, C. K. Li, R. D. Petrasso, and F. H. Séguin, *Phys. Rev. Lett.* **100**, 185006 (2008).
16. L. M. Barker and R. E. Hollenbach, *J. Appl. Phys.* **43**, 4669 (1972).
17. T. R. Boehly, D. H. Munro, P. M. Celliers, R. E. Olson, D. G. Hicks, V. N. Goncharov, G. W. Collins, H. F. Robey, S. X. Hu, J. A. Marozas, T. C. Sangster, O. L. Landen, and D. D. Meyerhofer, *Phys. Plasmas* **16**, 056302 (2009).
18. L. D. Landau and E. M. Lifshitz, *Fluid Mechanics*, 2nd ed., Course of Theoretical Physics, Vol. 6 (Butterworth-Heinemann, Newton, MA, 1987).
19. Ya. B. Zel'dovich and Yu. P. Raizer, in *Physics of Shock Waves and High-Temperature Hydrodynamic Phenomena*, edited by W. D. Hayes and R. F. Probstein (Dover Publications, Mineola, NY, 2002), Vol. II, Chap. XII, pp. 820–848.
20. D. H. Munro *et al.*, *Phys. Plasmas* **8**, 2245 (2001).
21. J. Delettrez, R. Epstein, M. C. Richardson, P. A. Jaanimagi, and B. L. Henke, *Phys. Rev. A* **36**, 3926 (1987).

High-Precision Measurements of the Equation of State of Hydrocarbons at 1 to 10 Mbar Using Laser-Driven Shock Waves

Introduction

Shock waves are routinely used to study the behavior of materials at high pressure. Recently, laser-driven shock waves provided equation-of-state (EOS) data for a variety of materials used in high-energy-density ($E/V \geq 10^{11} \text{ J/m}^3$) physics experiments at pressures above 1 Mbar (Refs. 1–3). Such data are relevant to inertial confinement fusion (ICF) targets for the National Ignition Facility (NIF), where multiple shock waves are used to provide an approximate isentropic compression of the fusion fuel.^{4,5} Understanding how polymer ablators respond to several-Mbar shock waves is critical to optimizing target performance.

Some of the NIF indirect-drive ablators will be made of glow-discharge polymer (GDP) ($\text{C}_{43}\text{H}_{56}\text{O}$) with various levels of germanium doping (Ge-GDP).^{6,7} No high-pressure data exist for these materials. Polystyrene (CH) is closest in structure and was considered a coarse indicator for shock-timing simulations of NIF targets involving such ablators. Shocked polystyrene has been studied using gas-gun drivers up to ~ 0.5 Mbar and laser-driven shock waves between ~ 7 to 41 Mbar (Refs. 8–10). Experiments above 1 Mbar (Refs. 8 and 9) had large error bars and appeared to behave noticeably stiffer than the models used to match the low-pressure data. Moreover, there was no verification of material behavior in the pressure range relevant to the NIF multiple-shock compression scheme, where successive shocks produce pressures of around 1 to 10 Mbar.¹¹ The use of these limited, low-precision data for polystyrene to predict the behavior of NIF Ge-doped ablator materials provides an unacceptable uncertainty.

Ultimately, the goal is to verify and understand the behavior of Ge-GDP at pressures of 1 to 10 Mbar. EOS models for this material will likely be based on existing models for polymers. To this end, we first address the behavior of polystyrene to determine whether this material indeed behaves stiffer than predicted, as suggested by Refs. 8 and 9. Next, the effect of stoichiometry (C-to-H ratio) is studied by measuring the EOS of polypropylene. Having quality EOS data on these two materials will provide a basis on which models of more-complicated

polymers (Ge-GDP) can be based. This article reports the results of precise EOS measurements on polystyrene and polypropylene and compares them to existing data.

Polystyrene and polypropylene (CH_2) are relatively simple organic compounds, composed solely of hydrogen and carbon. Atoms in each polymer molecule are covalently bonded, while attraction between molecules can include Van der Waals forces, dipole interactions, and hydrogen bonds.¹² These hydrocarbons are thought to experience chemical decomposition into phases of diamond-like C and H (Ref. 13) at sufficiently high pressures and temperatures. Several studies have demonstrated this using principal Hugoniot data in the 0.01- to 1-Mbar regime.^{13,14} Electrical conductivity measurements¹⁵ in a similar pressure range showed a predictable dependency on the C-to-H ratio in the hydrocarbons. Studying CH and CH_2 in the high-energy-density regime opens the possibility of observing high-pressure chemistry.

In the present study, laser-driven shock waves were used to produce high-precision impedance-matching (IM) measurements using quartz as a reference material.^{1,16–18} This provided $\sim 1\%$ precision in shock-velocity measurements. Single-shock measurements were performed on CH and CH_2 , showing that both materials undergo similar compressions between 1 to 10 Mbar, although their behavior in the P – ρ plane is distinctly different. Measurements of reflectance and brightness temperatures show that these two hydrocarbons behave similarly at high pressures. Additionally, polystyrene's behavior under double-shock compression was measured, and those results were consistent with single-shock results. All measurements are compared with available models and previous works.

In the following sections, experimental conditions including diagnostics and targets are described; the IM technique, including single- and double-shock states, is discussed, with emphasis on improvements that enable one to acquire high-precision data; high-precision velocity measurements and error analysis are discussed in more detail; and, finally, results are presented, followed by concluding remarks.

Experiment

Experiments were performed on LLE's OMEGA Laser System.¹⁹ Shock pressures of 1 to 10 Mbar were produced by laser energies between 200 J and 1130 J delivered in 2-ns temporally square pulses of 351-nm light. The laser's focal spot was smoothed using distributed phase plates,²⁰ resulting in nearly uniform irradiation spots with diameters of either 600 or 800 μm . The average laser intensity was between 0.3 and 1.1×10^{14} W/cm².

The targets for the single-shock measurements consisted of 90- μm pushers made of z -cut α -quartz with the samples mounted on the rear side. The samples were 50- μm -thick CH and/or CH₂ foils. Impedance measurements were performed at the interface between the quartz and the sample.^{21,22} A second set of targets for CH EOS consisted of "anvil" targets, having a second piece of z -cut α -quartz glued onto the back of the 50- μm CH sample. For these targets, single-shock measurements were obtained at the first interface (quartz-to-sample), and re-shock measurements were obtained at the second interface (sample-to-quartz), where the shock in the sample reflected off the denser quartz. The glue layers were kept below a few microns. The use of 90- μm -thick pushers minimized preheating of the sample. The laser-produced plasmas that drove these shock waves had temperatures of 1 to 2 keV. The soft- and mid-energy x rays from such plasmas were absorbed in the first half (laser side) of the quartz pusher.

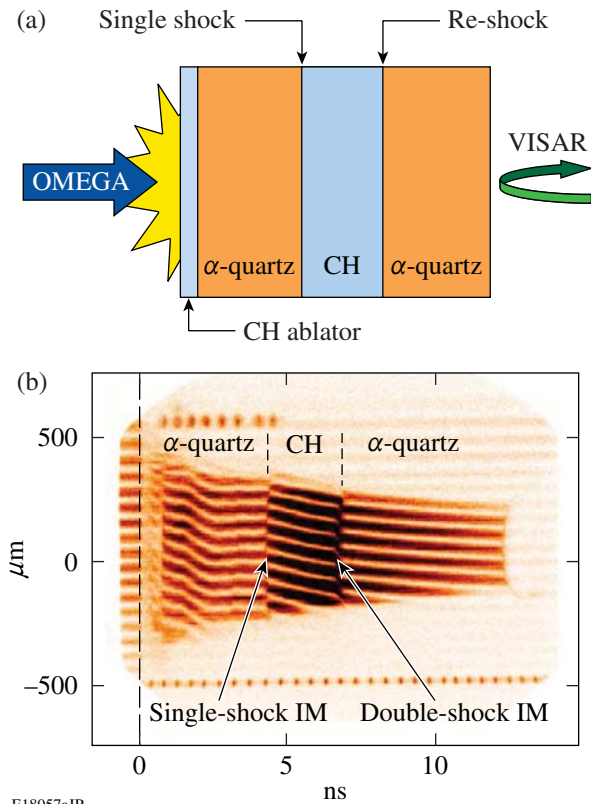
All targets had a 20- μm CH ablator (on the laser side) to absorb the incident laser and reduce the production of x rays that might preheat the samples. To minimize ghost reflections, the free surface of the samples and the quartz anvils had antireflection coatings. Material densities were 2.65 g/cm³ for quartz, 1.05 g/cm³ for CH, and 0.90 g/cm³ for CH₂. The index of refraction for these materials at the 532-nm probe-laser wavelength was 1.55, 1.59, and 1.49 for quartz, CH, and CH₂, respectively.

A line-imaging velocity interferometer system for any reflector (VISAR)^{23–26} measured shock velocities in the samples. The drive pressures were sufficient to produce optically reflective shock fronts in both the quartz and the polymer samples (see **Optical and Thermal Measurements**, p. 16). This resulted in direct, time-resolved measurements of the shock velocity in both the pusher and the samples. Two VISAR's with different velocity sensitivities were used to discern the 2π phase-shift ambiguity that occurs when the shock velocity instantaneously jumps at material interfaces. Etalons of 18-mm and 7-mm thickness were used to produce uncorrected velocity

sensitivities of 2.732 and 6.906 $\mu\text{m}/\text{ns}/\text{fringe}$, respectively. The indices of refraction determined the VISAR sensitivity in each material. The VISAR data were analyzed with a fast Fourier transform (FFT) method that determines fringe position to $\sim 5\%$ of a fringe. Since the shock speeds used in these experiments typically cause approximately five fringe shifts, velocities are measured to $\sim 1\%$ precision (lower shock speeds produce slightly larger velocity errors). Shock-front reflectivity information is encoded in the fringe pattern and can be obtained by measuring its amplitude after applying the FFT. Since the drive pressures are high enough to cause metallic-like states in the materials, the probe-laser reflection occurs within the skin depth (~ 100 nm or less)²³ of the metalized fluid; this, along with the steep shock front, produces a highly reflective surface. The probe laser for VISAR was a Q -switched, injection-seeded Nd:YAG laser operating at 532 nm with a pulse length of ~ 50 ns at full width at half maximum (FWHM). The reflected probe signal was detected by a ROSS²⁷ streak camera, one for each VISAR, having either 15- or 9-ns temporal windows. The response time of the diagnostic was dominated by the delay time associated with the etalons—90 or 40 ps.

An absolutely calibrated streaked optical pyrometer (SOP)²⁸ was used simultaneously with VISAR. The SOP measured the visible and near-infrared self-emission from the shock front as it propagated through the target. Its wavelength-dependent spectral responsivity was determined by the relay optics, diagnostic filtration (long pass filter with a cutoff wavelength of 590 nm), and streak camera photocathode response, defining a red channel from 590 to 900 nm. The device was absolutely calibrated using a NIST-traceable tungsten lamp and power supply.²⁸ The temporal window of the diagnostic was set to 10 or 20 ns, depending on expected irradiances on target. Using a 500- μm slit and a 10-ns temporal window led to an ~ 170 -ps temporal response time.²⁸ The SOP provides a temporal history of shock-front temperature. The VISAR and SOP are temporally calibrated so that combining the data provides temperature as a function of velocity and, consequently, temperature as a function of pressure.

The experimental configuration is shown in Fig. 121.4(a). The OMEGA Laser System irradiates the CH ablator on the front of the EOS targets, producing a shock wave that traverses the quartz pusher, sample, and quartz anvil (the quartz anvil was not used for all experiments). The VISAR and SOP view the rear side of the target, and since each of these layers is transparent, they measure the shock velocity and self-emission inside each layer. Figure 121.4(b) shows VISAR data for an anvil target. The horizontal lines are the VISAR fringes whose vertical



E18057aJR

Figure 121.4

(a) Schematic of planar anvil targets used in the experiments. The laser drive irradiates the target from the left, while the VISAR probe beam reflects off the shock from the rear side of the target (right). (b) VISAR streak image, showing continuous track of shock front within standard and sample.

position is proportional to the shock velocity. Before $t = 0$, the fringes are horizontal and constant because no shock wave is present. The x rays from the laser-driven plasma (which start at $t = 0$) caused the CH ablator to become opaque. As a result, the VISAR fringes disappear from $t = 0$ to ~ 0.7 ns. At 0.7 ns the shock wave enters the quartz, where the VISAR detects it. The shock-wave strength decays as it transits the quartz but soon stabilizes as the rarefactions equilibrate the pressure between the target layers and the ablation front driven by the laser. This produces a relatively steady shock from 2 to 4.3 ns.

At 4.3 ns, the shock wave transits the quartz–CH interface and enters the CH, where its velocity changes. This is seen as a jump in the position of the VISAR fringes and an abrupt change in their intensity. The latter is a result of the difference in the reflectivities of the shock waves in quartz and CH. The single-shock IM measurement is made across this interface. At 6.7 ns the shock wave reaches the quartz anvil and the fringe position and intensity change again. The double-shock (re-shock) IM measurements are made at this interface.

Note in Fig. 121.4(b) that the observed quartz–CH interface has a finite temporal width; this is the region where the shock transits the thin glue layer. In addition, the VISAR response time (given by the etalon thickness) is 40 ps and 90 ps. The shock velocities are, therefore, not measured directly at the contact interface between materials. This is accounted for by linearly fitting the shock velocities at least 0.3 ns before and after the interface transition region and extrapolating to the “ideal” interface. This also accounts for any slope present in these velocity profiles.

Compared to previous studies on hydrocarbons in the Mbar range, this study is novel in both the precision (1%) of the velocity measurements and the treatment of the errors in the IM technique: both random and systematic errors are evaluated. The next section describes the IM technique and the error analysis used for this study.

Impedance-Matching Analysis

1. Single-Shock Experiments

The jump conditions for shock waves are described by the Rankine–Hugoniot relations derived from the conservation of mass, momentum, and energy; they relate pre- and post-shock conditions via particle velocity (U_p) and shock velocity (U_s),^{21,22} as

$$P_1 - P_0 = \rho_0 U_s U_p, \quad (1)$$

$$\rho_1 (U_s - U_p) = \rho_0 U_s, \quad (2)$$

$$E_1 - E_0 = \frac{1}{2} (P_1 + P_0) \left(\frac{1}{\rho_0} - \frac{1}{\rho_1} \right), \quad (3)$$

where subscripts 0 and 1 denote initial and shock conditions in terms of pressure P , density ρ , and internal energy E . The first two equations have four unknowns (given that the initial pressure and density are known) and can be solved by measuring two variables. This solution constitutes a kinematic equation of state and is often defined as U_s as a function of U_p . High-pressure shock waves are typically reflecting, allowing one to optically measure the shock velocity, but usually preventing direct optical measurement of the particle velocity. The IM technique is used to infer the particle velocity by referencing the sample under study to a standard material whose equation of state is known.^{21,22}

The conservation equations dictate that the pressure and particle velocity are conserved across the contact interface between the standard and the sample. This makes it possible to infer the common particle velocity from the shock velocities in the standard and the sample, as the shock wave enters and exits the contact interface between the materials. This is shown in Fig. 121.5(a) in the pressure–particle velocity ($P-U_p$) plane. A measurement of the shock velocity in the standard provides the initial condition of the shock wave before it interacts with the sample. This state (A) is the intersection of the Rayleigh line ($P = \rho_0 U_s U_p$) and the known Hugoniot for the standard. If the sample has lower impedance than the standard, the standard will undergo isentropic release until its impedance “matches” that of the sample, when the continuity equations are satisfied across the interface between the standard and the sample. This determines the shocked state of the sample [state (B) in Fig. 121.5(a)]. This shocked state is the intersection between the release curve for the standard and the Rayleigh line defined by the measurement of the shock velocity in the sample. By measuring two shock velocities (one in the standard and one in the sample), the particle velocity in the sample can be inferred. The U_s and U_p for the sample define the equation of state of the sample. Care must be taken to ensure that the measured shock velocities are those just before and just after the shock wave crosses the interface between the two materials. The shock-wave jump conditions are a consequence of conservation of mass and momentum, which are always satisfied regardless of shock stability. Therefore, shock steadiness is not a requirement for IM with transparent standards since jump conditions for a shock hold for decaying (and increasing) shock waves. If the measurement has sufficient time resolution, the requirement for shock steadiness can be relaxed as long as the variation in velocity can be measured.

The IM technique requires knowledge of the Hugoniot and release behavior of the standard. The precision of the data obtained through the IM technique depends on the accuracy with which the states in the standard are known. The quartz principal Hugoniot was studied in the high-pressure fluid regime (2 to 15 Mbar) using laser-driven shock waves.¹ That study bridged the gap in data between existing gas-gun,^{29,30} explosively driven,³¹ and nuclear-driven³² experiments. The laser-driven data were consistent with previous studies having longer characteristic time scales. This indicates that the shock waves equilibrate on time scales shorter than the measurement times in laser experiments. The data show that shocked quartz is solid up to about 1 Mbar; above 1 Mbar shocked quartz melts and becomes reflective. The EOS of quartz is characterized by a piecewise linear U_s-U_p relationship of the general form $U_s = a_0 + a_1(U_p - \beta)$ as

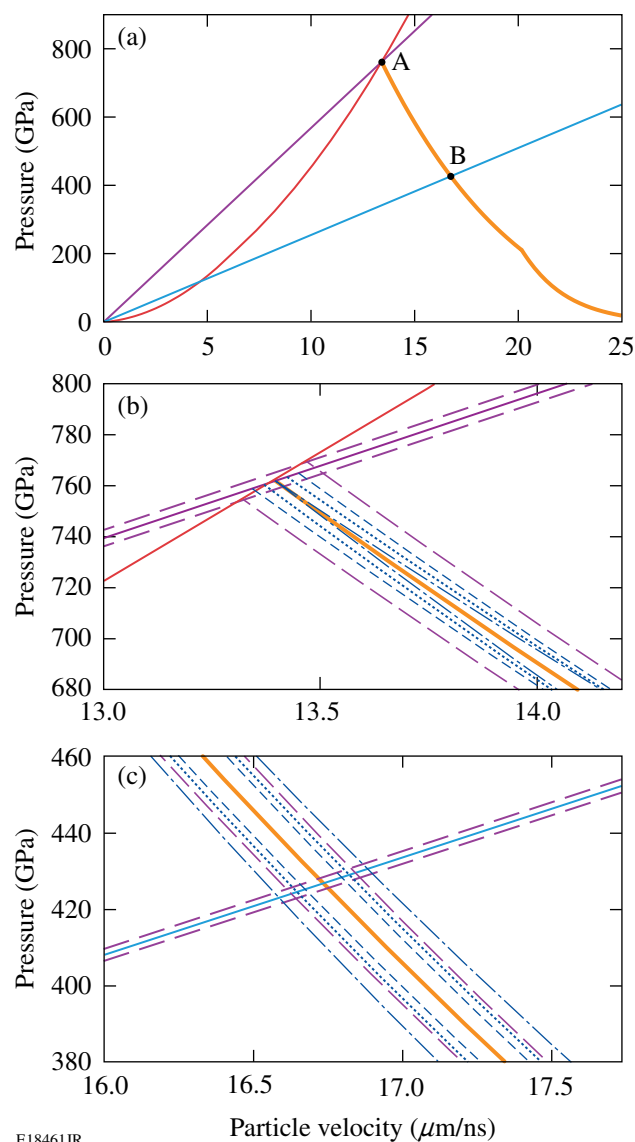


Figure 121.5 Sample IM construct with inclusion of errors for a 7.6-Mbar shock propagating from quartz to CH. Total errors are found by taking the quadrature sum of random and systematic uncertainties. (a) General IM diagram. Rayleigh lines for quartz and CH are shown as purple and light blue lines, respectively, while red and orange solid curves correspond to the principal Hugoniot and release of quartz. (b) Errors associated with quartz’s initial shock state and release variation from nominal. Systematic contributions are shown in dark blue and random contributions are shown in purple. Error in quartz’s Rayleigh line is shown by purple dashed lines. This causes a random variation propagated as an offset release curve, shown as purple dashed lines. Systematic variations from nominal release are shown as dark blue dashed–dotted, dashed, and small dashed curves, corresponding to $\delta\Gamma$, δa_0 , and δa_1 , respectively. (c) Final variations from a nominal (U_p, P) state are depicted by intersections between the nominal CH Rayleigh line and previously mentioned releases caused by random and systematic error contributions. A second random error contribution is found through the intersection between nominal quartz release and the CH Rayleigh line with $\delta U_{s,CH}$ contribution, shown as a purple dashed line.

$$U_s = (6.914 \pm 0.028) + (1.667 \pm 0.038)(U_p - 3.0244), \quad (4)$$

for $U_p < 6.358 \mu\text{m/ns}$,

$$U_s = (19.501 \pm 0.068) + (1.276 \pm 0.022)(U_p - 11.865), \quad (5)$$

for $U_p \geq 6.358 \mu\text{m/ns}$,

where an orthonormal basis is used so that the resulting errors are uncorrelated.¹⁸ This U_s - U_p relation was used in this work.³³ The quartz was shocked to 1 to 15 Mbar, producing reflective shock waves that allowed for VISAR measurements of the shock velocity, thereby providing the initial state of the standard for IM.

The quartz's impedance was matched to the sample when its release isentrope intersected the Rayleigh line in the sample. Quartz's release isentropes were calculated using the Mie-Grüneisen formalism as described in previous works.^{18,34} In this work's analysis, the reflected experimental Hugoniot was used, resulting in isentropes that follow a piecewise behavior stemming from the description of quartz's principal Hugoniot EOS, as described by Eqs. (4) and (5) [Fig. 121.5(a)]. For strongly shocked quartz in the dense fluid regime, calculations of the Mie-Grüneisen parameter based on solid and porous silica Hugoniot measurements^{1,32,35} showed Γ to be nearly constant with a value $\Gamma = 0.66 \pm 0.1$ (Ref. 18). Inspection of various EOS models for silica in the high-pressure fluid regime led to a constant value $\Gamma = 0.64 \pm 0.11$ (Ref. 2), consistent with the experimentally derived value. This latter model-based value for Γ and its associated error were used in this work. The value of Γ is the only model-dependent parameter used here.

The total error in the measured U_p , P , and ρ is the quadrature sum of the random and systematic errors inherent in the IM technique. Random errors originate in the shock-velocity measurements in both the quartz and samples. Systematic uncertainties arise from errors in the EOS of the standard, i.e., the a_0 and a_1 coefficient of quartz's experimentally derived principal Hugoniot, and from the Mie-Grüneisen parameter Γ . The relative contributions of these errors varied over the range of pressures studied.

2. Double-Shock Experiments

The above discussion of the IM technique applies to single-shock measurements, i.e., the standard and sample both experience a single shock wave. Multiple shock waves

produce off-Hugoniot states that are pertinent to ICF target designs that employ multiple shock waves to approximate isentropic compression. Double-shock measurements can validate models since they amplify small differences in the principal Hugoniot.³⁶

A double-shock measurement was created in these experiments by placing a second slab of quartz behind the samples, creating an "anvil" target. The shock wave traveled through the first layer of quartz into the polymer (where single-shock Hugoniot data were obtained). When the shock wave in the sample reached the second layer of quartz, it was reflected back into the sample. The conservation equations applied at this sample-quartz interface and a second IM measurement provided the U_p and P for the double-shocked sample. The important measurements were the shock velocity in the sample just before it impacted the quartz and the velocity of the shock wave just after it entered the quartz. The former provided the initial single-shock state of the CH, and the quartz's shock velocity provided the pressure of the second shock wave (which was conserved between the sample and the quartz).

High-Precision Velocity Measurements

Since quartz is transparent, its use as a standard^{1,16-18} provides high-precision EOS data because instantaneous velocities can be measured before and after the IM point (provided the sample is transparent). Several other studies have demonstrated precise IM measurements using quartz as a standard.^{2,37}

The continuity equations are central to the IM technique. As the shock traverses the interface, the materials accelerate, expand, and experience shock, reshock, or release, to equilibrate and satisfy those conditions. The use of a quartz standard and VISAR with high temporal resolution significantly reduces the inaccuracies by providing "instantaneous" measurements. In this study, shock velocities were measured to ~1% precision. Trends in the temporal profile of the observed velocities were linearized over the ~300 ps before and after the quartz-sample interface and extrapolated to that interface. This accounted for both the unsteadiness of the shock and the response time of VISAR (i.e., the etalon delays).

The usefulness of EOS data is determined by the size and validity of the error bars. As the precision of the velocity measurements increases, the effects of systematic errors become increasingly important. The random and systematic errors are rigorously accounted for in this study, and the total uncertainties are found by calculating the quadrature sum of random and systematic errors.

The total uncertainties for U_p , P , and ρ , each obtained through the IM technique, depend on seven error contributions: δU_{sQ} , δU_{sCH_x} , δa_{0L} , δa_{0H} , δa_{1L} , δa_{1H} , and $\delta \Gamma$. The first two are random errors, associated with the two shock-velocity measurements. The last five are systematic errors, of which the first four are fitting parameters for the quartz experimental Hugoniot $U_s = a_0 + a_1(U_p - \beta)$, where subscripts L and H correspond to fitting parameters to the low ($U_p < 6.358 \mu\text{m/ns}$) and high ($U_p \geq 6.358 \mu\text{m/ns}$) linear fits. The last ($\delta \Gamma$) is used to approximate quartz's release isentrope by assuming a Mie–Grüneisen EOS and having knowledge of quartz's principal Hugoniot.

Figures 121.5(a)–121.5(c) show a graphical description of the IM analysis and the errors encountered. Measurement errors δU_{sQ} produce a random uncertainty in the quartz's initial shocked state, producing multiple possible Rayleigh lines that can intersect the quartz Hugoniot at different points. Systematic errors in the quartz Hugoniot produce uncertainty in this initial state. These are shown as the 1σ variation in quartz Hugoniot. Continuing with this formalism, each of these possible states can be the initial condition for the isentropic release of quartz, which has errors associated with a_0 , a_1 , and Γ . These release curves form a cascade of possible release curves that the standard could follow. Figures 121.5(b) and 121.5(c) indicate the quantitative bounds on the release curves that can be used for an IM solution.

The state of the shocked sample and therefore the final state of the quartz release were determined by the measured shock velocity in the sample. Errors in this measurement, δU_{sCH_x} , produced multiple Rayleigh lines that intersect with the various release curves. Rigorous propagation of these errors provides confidence in the error bars that were assigned to the pressure and particle velocity inferred from the IM technique.

The total uncertainty for the derived IM variables is found by taking the quadrature sum of the error contributions. The predominance of random or systematic uncertainties varies with pressure. At low pressures (lower velocities), random uncertainties dominate because the phase excursion results in fewer fringes and the 5% error in fringe location is more significant. Shock-front reflectivities are lower, resulting in lower VISAR signal levels. At higher pressures, the random uncertainties become smaller. At pressures of ~ 9 Mbar in CH, corresponding to quartz pressures of ~ 15 Mbar, systematic uncertainties are around $3\times$ larger than random uncertainties. This results from the lower accuracy of the quartz Hugoniot at these higher pressures, making it increasingly difficult to perform precision measurements.

Kinematic Results

1. Polystyrene (CH)

The single-shock results for polystyrene (see Table 121.I) are shown as orange squares in Fig. 121.6, a U_s-U_p plot that also contains previous results and various models.³⁸ This study's data were fit with the line $U_s = (21.029 \pm 0.057) + (1.305 \pm 0.015)(U_p - 14.038)$, derived using a least-squares fit of the data set with their total error over an orthogonal polynomial basis; this produced uncorrelated errors in the coefficients of the fit. The total error bars for this study are smaller than the random-only errors of other works. The benefit of these smaller errors is demonstrated in Fig. 121.7 showing the various data and models in the P - ρ plane. The error derived in density scales as $(\eta-1)$ times the errors in shock velocity, where η is the compression (ρ/ρ_0) (Ref. 39). Here the difference in results and models is more apparent.

The data are compared to three *SESAME* models (refer to Figs. 121.6 and 121.7). *SESAME* 7591 and 7592 are similar in the method used to calculate the electronic, nuclear, and 0 K isotherm contributions to the total EOS, where differences arise from certain input parameters used to carry out these calculations. The electronic contribution for both models is calculated via a temperature-dependent Thomas–Fermi–Dirac (TFD) model, with assumption of an average atom, where the exchange parameter is equal to $2/3$. The cold curve is obtained from principal Hugoniot measurements and the assumption of a Mie–Grüneisen EOS. At low densities the solution is matched to the Lennard–Jones formula, and at high densities it is matched to calculations obtained through TFD. In addition to the atomic weight (6.510), atomic number (3.5), and initial density, a reference Grüneisen parameter and Debye temperature are required for the cold curve construct. The reference Grüneisen parameter is calculated from experimental values of the specific heat at constant pressure, the isentropic bulk modulus, the thermal expansion coefficient, and the initial density. *SESAME* 7591 adjusts the value of the reference Grüneisen parameter from 0.565 (value used for *SESAME* 7592) to 0.5 in order to reproduce shock EOS data for porous polystyrene. *SESAME* 7591 has higher values for the reference Debye temperature and temperature of melt by $\sim 16\%$ compared to *SESAME* 7592. The available low-pressure shock data are better predicted by *SESAME* 7592, which closely follows the change in slope in the U_s-U_p plane between 2 to 4 $\mu\text{m/ns}$ in U_p . Cohesive energies used in the cold curve calculations are also different between these models: *SESAME* 7591 uses a higher cohesive energy calculated from the heat of vaporization of carbon and the dissociation energy of hydrogen, while for *SESAME* 7592 the cohesive energy was set at

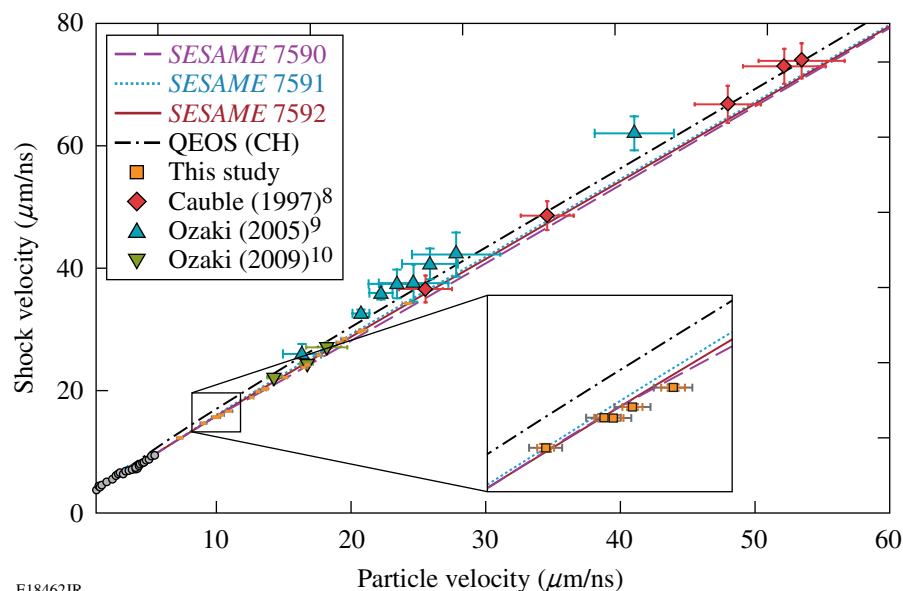


Figure 121.6

Principal Hugoniot data and models for CH in the U_s-U_p plane. Data for this study were taken on polystyrene (C_8H_8)_n, with initial density $\rho_0 = 1.05$ g/cc, using IM with quartz reference. Random uncertainties are shown as orange error bars and total uncertainty (quadrature sum of random and systematic errors) are shown as gray error bars. Previous gas-gun experiments (gray circles);^{30,40-43} absolute measurements on NOVA (red diamonds);⁸ and IM experiments on GEKKO using aluminum⁹ and quartz¹⁰ reference (cyan and green triangles, respectively). Various SESAME³⁸ models are shown along with a QEOS model.

E18462JR

Table 121.I: Polystyrene principal Hugoniot results from impedance matching with quartz reference. Measured shock velocity in the quartz and polystyrene, U_{sQ} and U_{sCH} , is given with associated random error, arising from measurement limitations. U_{pCH} (ran,sys), P_{CH} (ran,sys), and ρ_{CH} (ran,sys) are the resulting particle velocity, pressure, and density of shocked polystyrene obtained through the IM construct. Random errors enter the analysis through measurement uncertainties in U_{sQ} and U_{sCH} , while systematic errors emerge from uncertainties in the principal Hugoniot and release states of quartz.

Shot No.	U_{sQ} ($\mu\text{m/ns}$)	U_{sCH} ($\mu\text{m/ns}$)	U_{pCH} (ran,sys) ($\mu\text{m/ns}$)	P_{CH} (ran,sys) (Mbar)	ρ_{CH} (ran,sys) (g/cc)
52795	11.73±0.19	12.36±0.11	7.26 (0.16, 0.13)	0.94 (0.02, 0.02)	2.54 (0.09, 0.06)
52800	13.68±0.1	14.76±0.12	9.01 (0.12, 0.21)	1.4 (0.02, 0.03)	2.7 (0.07, 0.1)
52793	14.47±0.11	15.74±0.12	9.86 (0.14, 0.22)	1.63 (0.02, 0.04)	2.81 (0.08, 0.1)
52124	14.59±0.12	15.73±0.09	10.01 (0.15, 0.22)	1.65 (0.03, 0.04)	2.89 (0.08, 0.11)
52464	14.85±0.12	16.09±0.09	10.29 (0.15, 0.22)	1.74 (0.03, 0.04)	2.91 (0.08, 0.11)
52628	15.38±0.14	16.72±0.1	10.89 (0.18, 0.22)	1.91 (0.03, 0.04)	3.01 (0.1, 0.11)
52792	17.09±0.09	18.95±0.12	12.6 (0.1, 0.1)	2.51 (0.02, 0.02)	3.13 (0.07, 0.05)
52463	17.63±0.1	19.92±0.1	13.06 (0.11, 0.1)	2.73 (0.03, 0.02)	3.05 (0.06, 0.05)
52631	18.08±0.12	20.27±0.12	13.51 (0.14, 0.11)	2.88 (0.03, 0.02)	3.15 (0.08, 0.05)
52799	18.23±0.12	20.41±0.12	13.66 (0.14, 0.11)	2.93 (0.03, 0.02)	3.18 (0.08, 0.05)
52791	19.72±0.12	22.26±0.1	15.08 (0.14, 0.14)	3.52 (0.03, 0.03)	3.25 (0.07, 0.06)
52634	21.16±0.1	23.87±0.13	16.46 (0.11, 0.17)	4.13 (0.03, 0.04)	3.38 (0.07, 0.08)
52122	21.46±0.09	24.3±0.09	16.73 (0.11, 0.17)	4.27 (0.03, 0.04)	3.37 (0.06, 0.08)
52118	22.45±0.1	25.92±0.12	17.6 (0.12, 0.19)	4.79 (0.04, 0.05)	3.27 (0.06, 0.08)
52121	24.1±0.13	27.98±0.1	19.16 (0.15, 0.23)	5.63 (0.05, 0.07)	3.33 (0.07, 0.09)
52117	24.49±0.11	28.58±0.1	19.51 (0.12, 0.24)	5.86 (0.04, 0.07)	3.31 (0.05, 0.09)
52113	25.64±0.11	29.73±0.16	20.64 (0.13, 0.27)	6.44 (0.05, 0.08)	3.43 (0.07, 0.1)
52633	25.89±0.12	29.94±0.14	20.89 (0.14, 0.27)	6.57 (0.05, 0.09)	3.47 (0.07, 0.11)
52119	29.42±0.18	34.36±0.11	24.22 (0.21, 0.37)	8.74 (0.08, 0.13)	3.56 (0.08, 0.13)

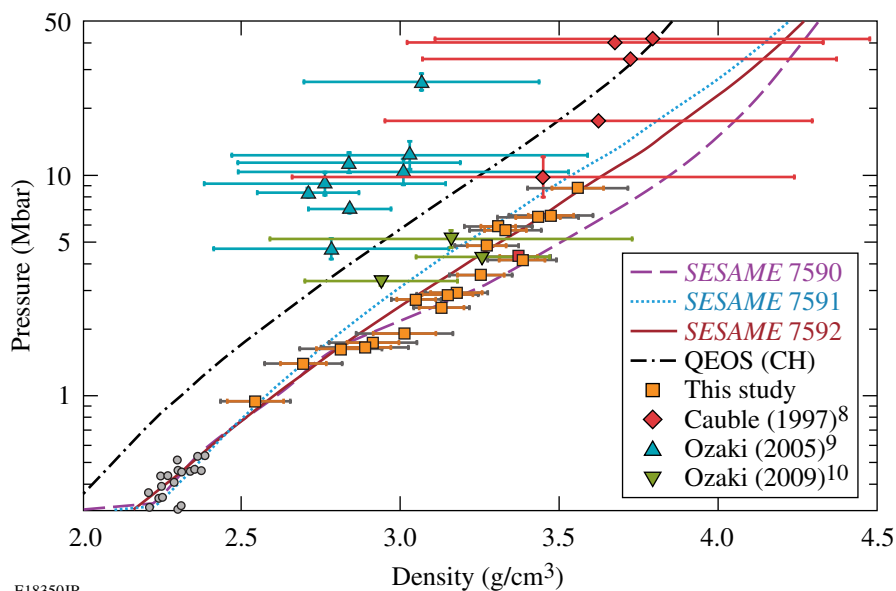


Figure 121.7

Principal Hugoniot data and models for CH in the P - ρ plane. Data for this study were taken on polystyrene (C_8H_8)_n, with initial density $\rho_0 = 1.05$ g/cc, using IM with quartz reference. Random uncertainties are shown as orange error bars and total uncertainty (quadrature sum of random and systematic errors) are shown as gray error bars. Previous gas-gun experiments (gray circles);^{30,40–43} absolute measurements on NOVA (red diamonds);⁸ and IM experiments on GEKKO using aluminum⁹ and quartz reference¹⁰ (cyan and green triangles, respectively). Various *SESAME*³⁸ models are shown along with a QEOS model.

E18350JR

15 kcal/mole (~ 4.8 MJ/kg) in order to reproduce the critical point. The nuclear models calculate the kinetic contribution of atoms and ions in both solid and gas. Lattice vibrational contributions are carried out assuming a Debye–Grüneisen solid; therefore, the reference Grüneisen parameter and Debye temperature are also used in these calculations. At high temperatures or low densities, this nuclear term describes an ideal gas, where ideal mixing is used. These limiting theories are joined by means of interpolation functions.^{38,44,45} No detailed information of the construction of *SESAME* 7590 was available.

SESAME 7592 appears to best model the present data for polystyrene, although a slight softening with respect to this model is observed between 2 and 4 Mbar. It is thought that at intermediate pressures, the C–H bonds in these polymers undergo chemical decomposition, favoring C–C and H–H bonds. It is possible that the softening at 2 to 4 Mbar indicates these bonds are breaking. This represents an energy sink that could explain the softening.

Previous results by Cauble *et al.*⁸ (absolute data) and Ozaki *et al.*⁹ (IM with an aluminum standard) show distinctly stiffer behavior than these data and most of the models, as shown in Fig. 121.7. These authors have stated, post publication, that their results likely suffered from x-ray preheating of the samples.⁴⁶ The newest data from Ozaki *et al.*¹⁰ used thicker pushers and low- Z ablaters to reduce preheat of the samples. Those experiments also used IM with a quartz standard and show results (green triangles in Fig. 121.7) that are much closer to this work.

In the anvil targets the shocks that reflect off the rear quartz layer produced double-shocked states in CH; these states were measured using the IM at that reflection point (see Table 121.II). The pressure reached in double-shock experiments is highly dependent on the initial state from which it launches, being particularly sensitive to the single-shock density. Because of this dependence, double-shock measurements provide a valuable tool to assess single-shock densities reached in CH. It is difficult to deconvolve measured quantities and model-dependent effects originating from the use of a standard material in the impedance-matching technique; in this aspect, double-shock measurements provide another advantage, where it is possible to separate models and observables, presenting a

Table 121.II: Double-shock states in polystyrene (CH) were probed by using reflected shock waves from anvil targets. Observables, listed below, were used for direct comparison with model behavior.

Shot No.	U_{sQ} ($\mu\text{m/ns}$)	U_{sCH} ($\mu\text{m/ns}$)
52464	11.45 ± 0.16	12.25 ± 0.09
52792	13.27 ± 0.31	14.60 ± 0.09
52463	14.14 ± 0.11	15.80 ± 0.11
52791	15.51 ± 0.10	17.45 ± 0.10
52122	17.25 ± 0.11	19.77 ± 0.09
52118	18.77 ± 0.11	21.71 ± 0.09
52117	20.96 ± 0.11	24.65 ± 0.13
52113	23.22 ± 0.09	27.66 ± 0.11
52119	26.25 ± 0.10	31.59 ± 0.14

sensitive platform for model comparison. Re-shock results are plotted in Fig. 121.8, showing the experimental observables: U_{sQ} versus incident U_{sCH} . Here the associated measurement error bars are quite small. These are compared with double-shock states as predicted by each model. The curves representing each model were produced by performing the IM analysis with each model (using its principal Hugoniot and re-shock curves) and the experimental quartz Hugoniot. The errors produced in this analysis were about the thickness of the lines and stemmed from the experimental errors associated with the quartz fit. The CH shock velocity (U_{sCH}) represents the single-shocked state of the CH, and, based on conservation equations, the re-shocked state of CH is derived from quartz's shock velocity U_{sQ} . Plotting the data in this manner removes any model dependence from the data. Despite the apparent similarity among the models, the small error bars in the data allow one to discriminate between them. This is shown in the inset in Fig. 121.8, an expanded region of the plot near $26 \mu\text{m/ns}$. In this type of plot, a model that assumes the material to be more compressible (softer) will display a higher quartz shock velocity for a given CH shock velocity. These re-shock data show behavior similar to the single-shock data, where a slight softening is observed at single-shock pressures from ~ 2 to 4 Mbar. For single-shock pressures outside this range, double-shock data are in agreement with *SESAME 7592*. Such behavior

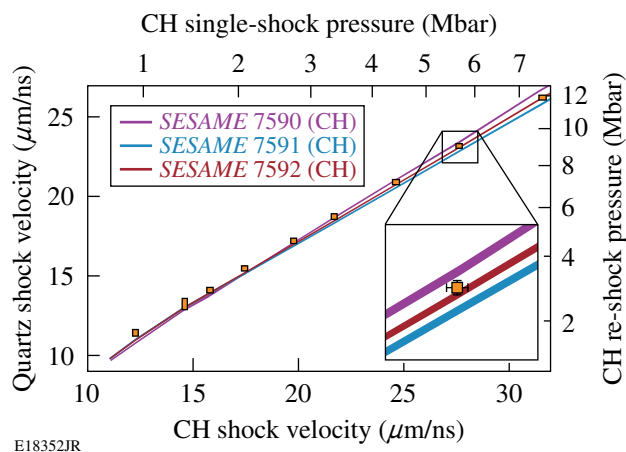


Figure 121.8

Double-shock (re-shock) data for CH using quartz anvil targets. Measured observables are plotted against *SESAME* models,³⁸ displayed as two quasi-parallel lines, resulting from errors associated with quartz experimental EOS fitting parameters. In this plot, softer models will display higher shock velocities in quartz for a given shock velocity in CH. The data are shown as orange rectangles, where the height and width of each are determined by the associated errors in shock-velocity measurements in CH and quartz, respectively. The data are consistent with the *SESAME 7592* model³⁸ at high and low pressures, where there is an evident softening of the data from around 2 to 4 Mbar. This shows agreement between single- and double-shock experiments.

is consistent to that observed in single-shock measurements. The measured quantities for CH re-shock experiments can be found in Table 121.II.

Double-shock results can be directly compared to single-shock data by transforming double-shock observables into single-shock quantities in the P - ρ plane via an inversion method as described by Hicks *et al.* (Ref. 3). This analysis is based on the concept that the double-shock compressibility is better known than the single-shock compressibility—often justified since dissociation along the Hugoniot is the largest source of uncertainty in the models. Such an inversion method uses the Hugoniot equations for the single- and double-shock states and an average of several models (in this case *SESAME* models for polystyrene) to predict the re-shock state through calculation of a model-based averaged adiabatic exponent. By using the double-shock pressure and particle velocity obtained from the measured shock velocity in quartz and quartz's experimental fit, and the shock velocity in the single-shock state, one arrives at a single-shock pressure and density. The results of this analysis (yellow diamonds) are shown in Fig. 121.9, along with the single-shock data. The total uncertainty associated with the inferred single-shock results is represented by black error bars. The total uncertainty is the quadrature sum of systematic uncertainties stemming from the 1σ variation in the averaged model-based adiabatic exponent and the errors in the experimental quartz Hugoniot, and random uncertainties stemming from measurement errors in the CH and quartz shock velocity. The inferred principal Hugoniot results are consistent with the single-shock data, also showing a change in compressibility around 4 Mbar. It is important to note that the systematic effects involved in each of these data sets are different, making their agreement significant. In the impedance-matching technique, systematic uncertainties arise from uncertainties in quartz's experimental principal Hugoniot and its release behavior, whereas in the inversion method, systematic effects enter through the experimental quartz Hugoniot and the model-based prediction of the CH re-shock density.

The accuracy of the inversion method was tested by using the model-based-averaged adiabatic exponent and the measurable quantities U_{sCH} and U_{sQ} , as predicted by each model. The CH shock velocities used in the analysis spanned a range equivalent to those measured experimentally in the double-shock experiments. The inferred single-shock pressure and density were compared to the pressure and density on the principal Hugoniot, as predicted by each model. Inferred single-shock states were shown to be consistent for all models. For a given pressure, percent differences between density predicted

by models and inferred single-shock density fell between 1%–3%, 1%–2%, and 0.2%–0.3% for *SESAME* 7590, 7591, and 7592, respectively, where differences in density decreased as a function of increasing pressure. This gives confidence that the inversion method leads to accurate results for inferred single-shock conditions.

Quartz is thought to transition from a conducting liquid to a dense plasma at around 4 Mbar. Pressures from 2 to 4 Mbar in

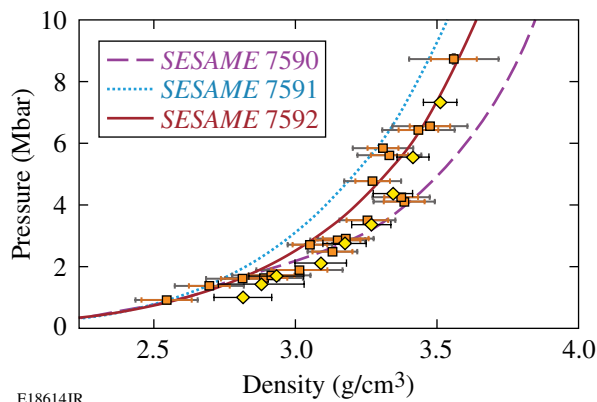


Figure 121.9 Single-shock Hugoniot data for polystyrene as inferred from re-shock (double-shock) data via the inversion method described by Hicks *et al.*³ are shown as yellow diamonds. Uncertainties are shown as black error bars, which represent the total error (quadrature sum of random and systematic uncertainties). Single-shock IM measurements are also shown (orange squares) along with *SESAME* models.³⁸ Inferred single-shock data are consistent with single-shock measurements, where both data sets show stiffening of the material starting at 4 Mbar.

CH correspond to pressure from 3.5 to 7 Mbar in quartz. There was concern that the softening in CH was not its true behavior but rather a manifestation of quartz’s rheology. The fact that the double-shock measurements and the inferred single-shock states display similar behavior to that observed in the single-shock data indicates that the softening is not due to a systematic problem with the quartz release. Moreover, results for CH₂ (see **Polypropylene** below), which encounter similar quartz pressures, show no softening. Again, this indicates that the softening observed in CH is its intrinsic high-pressure behavior.

2. Polypropylene (CH₂)

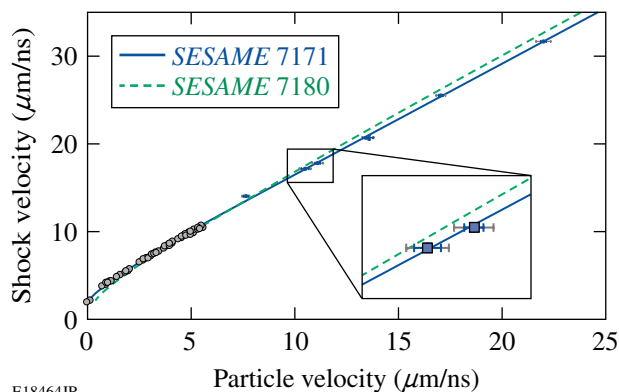
Principal Hugoniot measurements for polypropylene (see Table 121.III) were obtained from 1 to 6 Mbar—the highest published pressure results for this material studied to date. These data have a linear U_s-U_p relation, shown in Fig. 121.10, described by $U_s = (20.025 \pm 0.102) + (1.228 \pm 0.025)(U_p - 12.715)$. A least-squares fitting of the data over an orthogonal polynomial basis was used (using total error) such that the associated errors in the fitting coefficients were uncorrelated. The total uncertainty in the density was between 2.9% and 4.4%. Unlike CH, CH₂ followed a smooth concave trend in the $P-\rho$ plane, with no pressure-induced softening, as shown in Fig. 121.11. On this plane CH₂ was observed to reach lower density for a given pressure, compared to CH. Compression of both CH and CH₂ (see Fig. 121.12) behaved in a similar manner with increasing pressure; therefore, differences in the $P-\rho$ plane were mostly due to density variations in their initial states. *SESAME* 7171 and *SESAME* 7180 are models for branched (polymer has other chains or branches stemming from the main chain backbone) and linear (polymer has atoms arranged in a chain-like struc-

Table 121.III: Polypropylene principal Hugoniot results from impedance matching with quartz reference. Measured shock velocity in the quartz and polypropylene, U_{sQ} and U_{sCH_2} is given with associated random error arising from measurement limitations. U_{pCH_2} (ran,sys), P_{CH_2} (ran,sys), and ρ_{CH_2} (ran,sys) are the resulting particle velocity, pressure, and density of shocked polypropylene obtained through the IM construct. Random errors enter the analysis through measurement uncertainties in U_{sQ} and U_{sCH_2} , while systematic errors emerge from uncertainties in the principal Hugoniot and release states of quartz.

Shot No.	U_{sQ} ($\mu\text{m/ns}$)	U_{sCH_2} ($\mu\text{m/ns}$)	U_{pCH_2} (ran,sys) ($\mu\text{m/ns}$)	P_{CH_2} (ran,sys) (Mbar)	ρ_{CH_2} (ran,sys) (g/cc)
52798	12.14±0.14	14.07±0.11	7.64 (0.12, 0.14)	0.97 (0.02, 0.02)	1.97 (0.04, 0.04)
52797	14.89±0.14	17.2±0.13	10.5 (0.18, 0.22)	1.63 (0.03, 0.03)	2.31 (0.07, 0.08)
52628	15.42±0.1	17.83±0.12	11.11 (0.13, 0.23)	1.78 (0.02, 0.04)	2.38 (0.05, 0.08)
52796	17.65±0.13	20.72±0.1	13.44 (0.16, 0.12)	2.51 (0.03, 0.02)	2.56 (0.06, 0.04)
52631	17.78±0.16	20.74±0.25	13.59 (0.19, 0.12)	2.54 (0.04, 0.02)	2.61 (0.1, 0.05)
52634	21.38±0.1	25.55±0.11	17.05 (0.11, 0.2)	3.92 (0.03, 0.04)	2.71 (0.05, 0.06)
52633	26.42±0.11	31.69±0.12	22 (0.13, 0.33)	6.28 (0.04, 0.09)	2.94 (0.05, 0.1)

ture with no branches) polyethylene (same C-to-H ratio as polypropylene); these models were evaluated at polypropylene's initial density and compared with results.

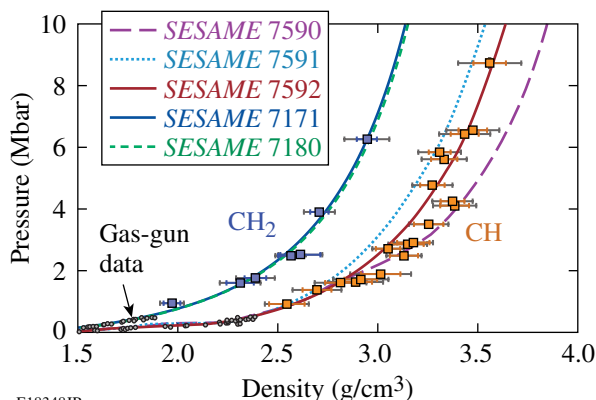
As shown in Figs. 121.10 and 121.11, the CH₂ data are in good agreement with both *SESAME* 7171 and *SESAME* 7180, which predict almost identical behavior in the P - ρ plane. This



E18464JR

Figure 121.10

Principal Hugoniot data and models for CH₂ in the U_s - U_p plane. Data for this study were taken on biaxially oriented polypropylene (C_3H_6)_n with initial density $\rho_0 = 0.9$ g/cc, using IM with quartz reference. Random uncertainties are shown as blue error bars and total uncertainties (quadrature sum of random and systematic errors) are shown as gray error bars. Previous gas-gun experiments from Marsh³⁰ are shown. Data are compared with *SESAME*³⁸ models for polyethylene (C_2H_4)_n evaluated with initial density $\rho_0 = 0.9$ g/cc.

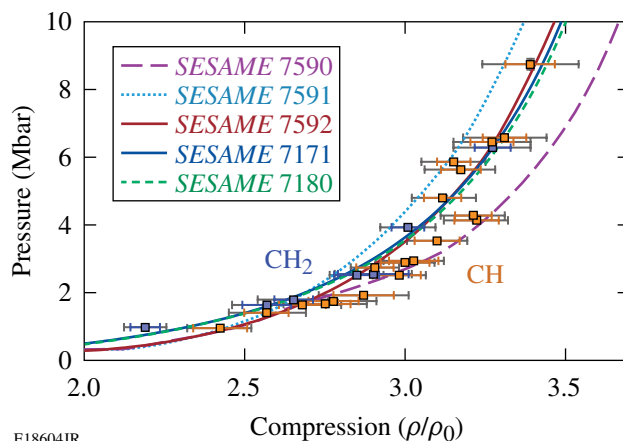


E18348JR

Figure 121.11

Principal Hugoniot data and models for CH₂ and CH in the P - ρ plane (CH models and error bars as in previous figures). Data for CH₂ were taken on biaxially oriented polypropylene (C_3H_6)_n with initial density $\rho_0 = 0.9$ g/cc, using IM with quartz reference. Random uncertainties are shown as blue error bars and total uncertainties (quadrature sum of random and systematic errors) are shown as gray error bars. Previous gas-gun experiments from Marsh³⁰ are shown. Data for CH₂ are compared with *SESAME*³⁸ models for polyethylene (C_2H_4)_n, evaluated with initial density $\rho_0 = 0.9$ g/cc.

is not entirely surprising since both models make similar physical assumptions with only slightly varying inputs. The electronic contribution was modeled the same way as the *SESAME* models for CH TFD with an exchange constant equal to 2/3. The ground electronic contribution (cold curve) was calculated from shock data and an assumption of a Mie-Grüneisen EOS, where the reference Grüneisen parameter was calculated in the same manner as in the CH *SESAME* models, leading to values 0.561 and 0.739 for *SESAME* 7171 and 7180, respectively. The reference Debye temperature was calculated from the U_s - U_p intercept, average atomic weight, initial density, and a Poisson ratio of 1/3. The nuclear contribution was obtained via a solid-gas interpolation formula, which is in agreement with the Debye formula at low temperatures or high densities and approaches the ideal gas at high temperatures or low densities. Differences in the models arise from experimental Hugoniot data used to construct the cold curve and parameters derived from other experimental measurements, such as the reference Grüneisen coefficient and Debye temperature, used to compute the lattice vibrational contribution. The cohesive energies were set at 3.35 and 4 MJ/kg for *SESAME* 7171 and 7180, and binding energies resulting from cold-curve calculations differed by ~3%. The atomic number and atomic weight were assumed to be 8/3 and 4.6757, respectively.^{47,48}



E18604JR

Figure 121.12

Principal Hugoniot measurements for CH and CH₂ in the P - η plane using quartz as IM reference. Models and error bars as described in previous figures.

Optical and Thermal Measurements

1. Reflectivity

The reflectivity of the observed shocks was determined by the signal level of the probe beam detected by the VISAR streak camera. The incident probe intensity was essentially constant over its pulse duration. That intensity was normalized using the detected levels produced by the α -quartz pusher, whose

reflectivity as a function of shock velocity is known.¹⁸ This leads to continuous records of reflectivity as a function of time for materials under study. However, the intensity profiles in CH showed an anomalous behavior: the detected intensity increased as the decaying shock transited the sample. This behavior was amplified with increasing pressure. This was the result of a “fogging” in the CH that attenuated the VISAR probe beam. X rays from the laser plasma were absorbed in the sample material, producing free electrons that can absorb light, although insufficient to produce noticeable preheat.⁴⁹ As the shock front (which was decaying in strength) moved through the CH, the VISAR probe beam passed through less-absorbing material, causing the streak cameras to register an increase in intensity signal levels, even though the shock was decaying. The anomalous behavior was observed in CH but not observed in CH₂ at low pressures, where the intensity decreased as a function of time, as expected. Anomalous behavior of CH₂ was observed only at the highest-pressure experiment. To account for this, reflectivity data were calculated only at the quartz–CH (CH₂) interface. Here the quartz signal was attenuated by the same amount as the CH signal, and the normalization to the known quartz reflectivity held. To do this, the intensity returned from the shocked pusher (quartz) and polymer was linearly fit and extrapolated to the contact interface. The reflected intensities and the known reflectivity of quartz (as a function of shock velocity) provided reflectance measurements for the hydrocarbons. For CH, this led to one data point $R(U_s)$, translated to $R(P)$, having knowledge of the pressure obtained from a corresponding CH shock/velocity value via IM. Continuous $R(U_s)$ measurements were obtained for CH₂ at low pressures, but for precaution, only reflectivities at the contact interface were used, resulting in one $R(P)$ data point; this also translates to temperature measurements since they are dependent on measured reflectance. The reflectivity of CH and CH₂ as a function of pressure is shown in Fig. 121.13. Errors in reflectivity varied from 31% at the lowest pressure to 9% at the highest pressure for CH and from 25% to 15% from lowest to highest pressure for CH₂. At higher pressures, there was a better signal-to-noise ratio since the shocked hydrocarbons became better reflectors. Low-pressure measurements in the hydrocarbons corresponded to pressures of 1 to 2 Mbar in quartz, close to its melt onset. At these pressures, quartz is barely reflective and the reflected intensity measurements are less accurate.

Both CH and CH₂ underwent a drastic increase in reflectivity at around 1 Mbar and saturated at ~40%. This occurred at 2.5 to 3 Mbar for both materials. This behavior—steep reflectivity increase and saturation—is often seen in materials undergoing an insulator–conductor transition.^{50–52}

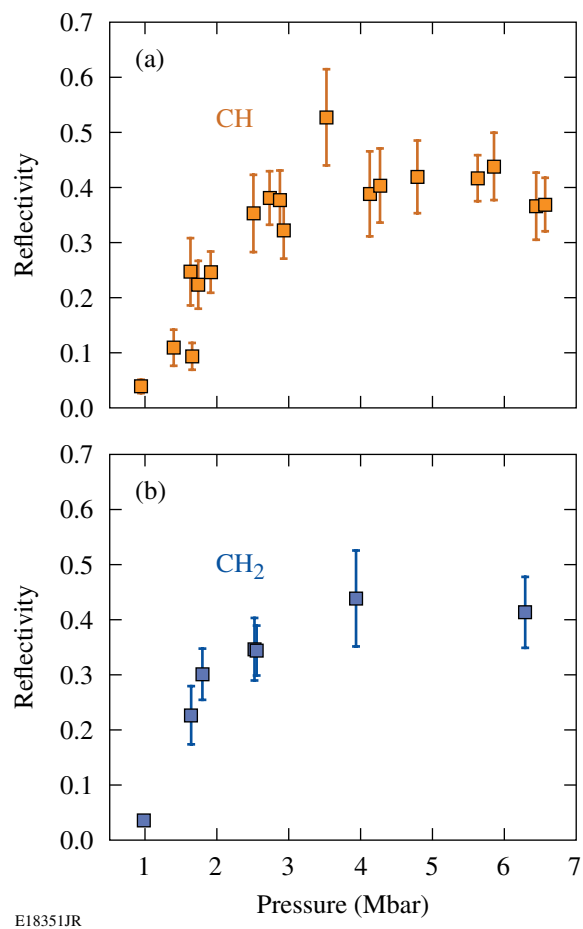


Figure 121.13 Reflectivity measurements from VISAR signal and quartz known reflectivity for (a) polystyrene and (b) polypropylene, where saturation occurs at 40% for both materials.

Polystyrene’s optical properties have been previously studied by Koenig *et al.*⁵³ with CH shock velocities of 11 to 16 $\mu\text{m}/\text{ns}$ (~0.8 to 1.7 Mbar), where they observed steadily increasing reflectivities reaching values up to 50%, well above our measurements. In that same pressure range, we observed smaller reflectivities, <25%. The reflectivity of shocked CH was also measured by Ozaki *et al.*¹⁰ who found reflectivities from 16% to 42% in the CH shock-velocity range of ~22 to 27 $\mu\text{m}/\text{ns}$ (~3 to 5 Mbar), in better agreement with our findings.

Discrepancies in reflectivities between studies could arise from differences in diagnostic configurations or from probe-beam stability. Reflectivity measurements in these studies are relative measurements since reflected intensities between a standard material and sample are compared and “normalized” with known reflectivities of the unshocked or shocked standard. If the probe-beam stability is compromised either temporally

or spatially and the analysis does not correct for it, this could yield biased reference reflectivities. In these experiments a reference image of the returned probe intensity is acquired on each shot. These were used to monitor deviations in the incident probe-beam intensity, which were quite small.

2. Temperature

The brightness temperatures of the shocks were determined from spectral radiance intensities detected by the SOP with a wavelength range of 590 to 900 nm, with a centroid wavelength of 682 nm (Ref. 28). Recorded SOP intensities were modeled assuming a gray-body Planckian spectrum given by

$$L(\lambda, T) = \varepsilon(\lambda) \frac{2hc^2}{\lambda^5} \frac{1}{e^{hc/\lambda T} - 1},$$

where ε is the emissivity, h is Planck's constant, c is the speed of light, λ is the radiation wavelength, and T is the temperature of a Planckian radiator.

The emissivity is given by $1-R(\lambda)$, where $R(\lambda)$ is the reflectivity that is assumed to vary only slightly as a function of wavelength in the optical spectral range, such that $R(\lambda)$ is the same optical reflectivity measured by VISAR at 532 nm. As described in **Reflectivity** (p. 16), reflectivity values were obtained by linearly fitting the VISAR intensities and extrapolating to the contact interface, avoiding attenuation effects of the VISAR probe beam in polystyrene. Consequently the recorded SOP spectral intensities emitted by the shocked polymer were linearly fit over a time interval of ~ 500 to 600 ps and extrapolated to a time corresponding to that of the contact interface, such that obtained reflectivity measurements could be used for emissivity calculations. This implies that SOP measurements were taken close to the quartz–glue–CH boundary. SOP has a temporal resolution of ~ 170 ps; therefore, the self-emission from the shock front is integrated over this time interval. At material boundaries, the recorded SOP intensity could be the integrated signal from different materials. Large time intervals were chosen to linearly fit the SOP data with this in mind. Material boundaries on SOP records are not easily identified (as on VISAR records); therefore, care was taken to choose/define the beginning of a material region, containing a signal for such material, only after the SOP signal had recovered from observable spectral-intensity changes.

Having observed absorption of the VISAR probe beam in CH (at all pressures) and CH₂ (at the highest pressure only), there was concern that spectral intensities as recorded by SOP

were affected as well. To account for this, the sample temperatures were normalized to the quartz. Quartz reflectivity and temperature as functions of pressure (shock velocity) have been previously studied.¹⁶ Since the quartz and polymer signal in the SOP diagnostic are subject to the same conditions (optical path, camera sensitivity, and resulting spectral response of the diagnostic), one can re-derive the equation for the temperatures in the sample by substituting diagnostic constants with the quartz's observed temperature and emissivity. The resulting sample temperatures are relative temperatures since they are referenced, or normalized, to the quartz's known shock Hugoniot thermal and optical behavior.

Tables 121.IV and 121.V list the brightness and normalized temperatures for CH and CH₂, respectively. The brightness temperatures are those derived simply from the measured spectral intensity and the SOP calibration. The normalized temperatures use the observed brightness of the quartz shock plus its velocity to provide a normalization that is applied to the CH and CH₂ results. On average, normalized temperatures for CH were $\sim 1.3\times$ larger than those measured using CH SOP intensities only; for CH₂ that factor was ~ 1.1 . [It should be noted that two shots (52628 and 52631), each simultaneously studying both CH and CH₂, showed brightness temperatures that were higher than shots at similar conditions. When normalized to quartz, those temperatures had negligible changes. This suggests that for some reason these two shots did not experience fogging in the samples.]

Table 121.IV: Hugoniot temperatures for polystyrene as obtained using reflectivity and SOP spectral intensities for each shot. Relative temperatures, normalized to quartz, show that polystyrene's behavior also affects SOP spectral intensities.

Shot No.	T (eV)	$T_{\text{normalized}}$ (eV)
52795	0.43±0.05	0.51±0.05
52800	0.59±0.03	1.06±0.07
52793	0.70±0.06	0.88±0.10
52464	0.63±0.07	1.01±0.13
52628	1.22±0.06	1.19±0.06
52792	1.05±0.08	1.39±0.17
52631	1.97±0.21	1.95±0.18
52799	1.38±0.09	1.79±0.17
52791	1.75±0.32	2.50±0.57
52634	2.25±0.35	2.84±0.43
52633	4.29±0.52	5.57±0.62

Table 121.V: Hugoniot temperatures for polypropylene as obtained using the reflectivity and SOP spectral intensities for each shot. Relative temperatures, normalized to quartz, were also obtained.

Shot No.	T (eV)	$T_{\text{normalized}}$ (eV)
52798	0.46 ± 0.06	0.53 ± 0.05
52797	0.70 ± 0.05	0.81 ± 0.08
52628	1.02 ± 0.06	1.05 ± 0.08
52796	0.95 ± 0.06	1.15 ± 0.11
52631	1.44 ± 0.09	1.42 ± 0.13
52634	2.18 ± 0.40	2.42 ± 0.43
52633	3.86 ± 0.59	5.01 ± 0.81

Figure 121.14 shows normalized temperatures for polystyrene [orange points in (a)] and polypropylene [blue points in (b)]. Temperature errors were between 5% and 22% for CH and 8% and 18% for CH₂; these errors stemmed from system calibration and measurements of self-emission and reflectivity in each hydrocarbon. Quartz parameters for normalization were taken from a fit to the data in Ref. 16. The various *SESAME* models available for CH and CH₂ predict similar thermal behavior for both materials: both materials reach comparable temperatures from ~1 to 7 Mbar. The models predict similar shock temperatures that all agree fairly well with measurements over that range. The models are similar enough to each other that the data, with their moderate precision, do not favor any one of the models. CH temperatures at 3 to 5 Mbar by Ozaki *et al.*¹⁰ [green points in Fig. 121.14(a)] are consistent with these data.

Conclusions

The equation of state was measured for two hydrocarbons at shock pressures of 1 to 10 Mbar. A time-resolved VISAR diagnostic provided precise (~1%) measurement of shock velocity in the transparent standard and sample materials. The use of experimental data for the Hugoniot of the quartz pusher made it possible to determine the systematic errors in the IM technique for the derived quantities. These data are the most-precise measurements of the EOS of hydrocarbons performed at these high pressures (≥ 1 Mbar).

Polystyrene (CH) was observed to compress by 2.5 \times to ~3.5 \times at pressures of 1 to 10 Mbar. This behavior was predicted by the *SESAME* 7592 model. Polystyrene exhibits slightly greater compressibility (compared to *SESAME* 7592) in the 2- to 4-Mbar range. Previous results from other researchers showed much stiffer behavior, most likely due to preheating of those samples.

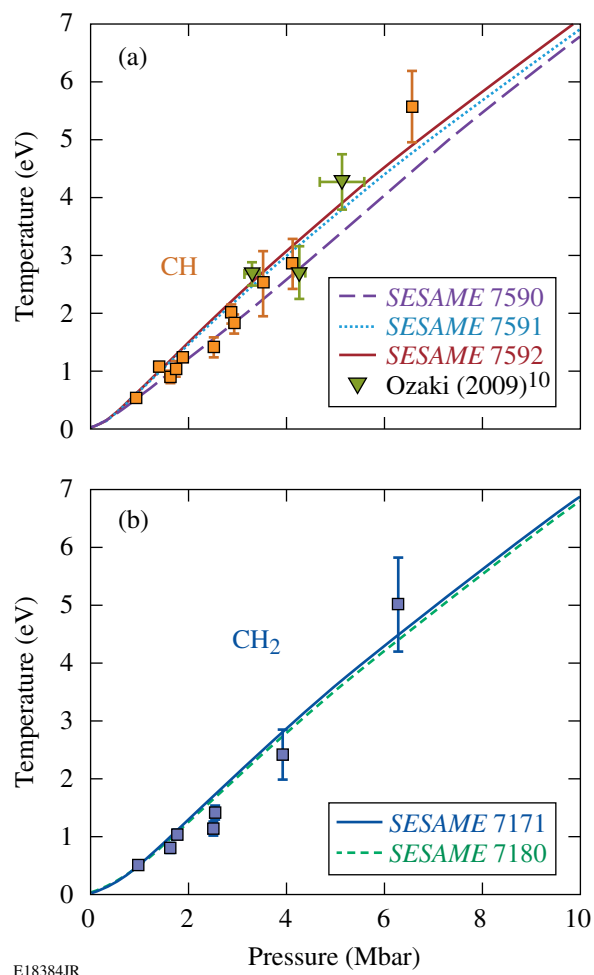


Figure 121.14 Temperature measurements were calculated from SOP self-emission records, fitted to a gray-body Planckian radiator, where emissivity was obtained from reflectivity measurements from VISAR, and normalized using the known quartz temperature and reflectivity. Both (a) polystyrene and (b) polypropylene reach similar temperatures with increasing pressure.

Polypropylene (CH₂) was observed to compress by similar amounts over a similar range of pressures. Two *SESAME* models (7171 and 7180) reproduced the behavior well (in this pressure range, the two models for polypropylene were nearly indistinguishable). This agreement for both materials suggests that the effect of the C-to-H ratio is properly accounted for in these models for polystyrene and polypropylene.

Reflectivity measurements indicated that both polystyrene and polypropylene become reflective when shocked to 1 to 2 Mbar. Above 3 Mbar, shock waves in both materials have a reflectivity of ~40%. This behavior is typical of materials that undergo a shock-induced transition from an insulator to a conductor.

The measured intensity of the self-emission from these shocks, normalized to known temperatures in quartz, was used to infer the brightness temperature of shocks in the two materials. Reflectivity measurements were used to infer gray-body brightness temperatures of the shock waves. The results show that both polystyrene and polypropylene are heated to 0.5 to 5 eV by shock pressures of ~ 1 to 6 Mbar. The shock temperatures in each material are well predicted by the *SESAME* models, but the models are so similar that no model is favored. Normalized temperatures showed consistent differences from brightness temperatures, and it was concluded that partial blanking of the SOP diagnostic occurred. This was evident in the CH at all pressures and only at the highest pressure for CH₂.

These results are significant in that they provide high-precision kinematic and thermal data for two hydrocarbons shocked to 1 to 10 Mbar, providing a complete EOS of those materials. The polystyrene data indicate that this material does not stiffen at high pressures (as suggested by earlier experiments), and the polypropylene data show that the effect of the C-to-H ratio is reasonably predicted by the models. These results are particularly important to the design of ICF targets for the NIF, which will use similar hydrocarbon ablaters that are compressed by multiple shocks in this pressure region. Similarly, the behavior of hydrocarbons shocked to ~ 10 Mbar is important to general studies of high-energy-density physics.

ACKNOWLEDGMENT

This work was supported by the U.S. Department of Energy Office of Inertial Confinement Fusion under Cooperative Agreement No. DE-FC52-08NA28302, the University of Rochester, and the New York State Energy Research and Development Authority. The support of DOE does not constitute an endorsement by DOE of the views expressed in this article.

REFERENCES

1. D. G. Hicks, T. R. Boehly, P. M. Celliers, J. H. Eggert, E. Vianello, D. D. Meyerhofer, and G. W. Collins, *Phys. Plasmas* **12**, 082702 (2005).
2. D. G. Hicks, T. R. Boehly, P. M. Celliers, D. K. Bradley, J. H. Eggert, R. S. McWilliams, R. Jeanloz, and G. W. Collins, *Phys. Rev. B* **78**, 174102 (2008).
3. D. G. Hicks, T. R. Boehly, P. M. Celliers, J. H. Eggert, S. J. Moon, D. D. Meyerhofer, and G. W. Collins, *Phys. Rev. B* **79**, 014112 (2009).
4. J. D. Lindl *et al.*, *Phys. Plasmas* **11**, 339 (2004).
5. S. W. Haan *et al.*, *Phys. Plasmas* **2**, 2480 (1995).
6. S. W. Haan *et al.*, *Phys. Plasmas* **12**, 056316 (2005).
7. S. W. Haan *et al.*, *Eur. Phys. J. D* **44**, 249 (2007).
8. R. Cauble *et al.*, *Phys. Plasmas* **4**, 1857 (1997).
9. N. Ozaki *et al.*, *Phys. Plasmas* **12**, 124503 (2005).
10. N. Ozaki *et al.*, *Phys. Plasmas* **16**, 062702 (2009).
11. T. R. Boehly, D. H. Munro, P. M. Celliers, R. E. Olson, D. G. Hicks, V. N. Goncharov, G. W. Collins, H. F. Robey, S. X. Hu, J. A. Marozas, T. C. Sangster, O. L. Landen, and D. D. Meyerhofer, *Phys. Plasmas* **16**, 056302 (2009).
12. G. R. Moore and D. E. Kline, *Properties and Processing of Polymers for Engineers* (Prentice-Hall, Englewood Cliffs, NJ, 1984).
13. F. H. Ree, *J. Chem. Phys.* **70**, 974 (1979).
14. W. J. Nellis *et al.*, *J. Chem. Phys.* **80**, 2789 (1984).
15. W. J. Nellis, D. C. Hamilton, and A. C. Mitchell, *J. Chem. Phys.* **115**, 1015 (2001).
16. D. G. Hicks, T. R. Boehly, J. H. Eggert, J. E. Miller, P. M. Celliers, and G. W. Collins, *Phys. Rev. Lett.* **97**, 025502 (2006).
17. T. R. Boehly, J. E. Miller, D. D. Meyerhofer, J. G. Eggert, P. M. Celliers, D. G. Hicks, and G. W. Collins, in *Shock Compression of Conducted Matter—2007*, edited by M. Elert *et al.* (American Institute of Physics, Melville, NY, 2007), Vol. 955, pp. 19–22.
18. S. Brygoo, D. G. Hicks, P. Loubeyre, J. H. Eggert, S. McWilliams, P. M. Celliers, T. R. Boehly, R. Jeanloz, and G. W. Collins, “Development of Melted Quartz as an Impedance-Matching Standard for Strong Laser Shock Measurements,” to be published in the *Journal of Applied Physics*.
19. T. R. Boehly, R. S. Craxton, T. H. Hinterman, J. H. Kelly, T. J. Kessler, S. A. Kumpan, S. A. Letzring, R. L. McCrory, S. F. B. Morse, W. Seka, S. Skupsky, J. M. Soures, and C. P. Verdon, *Rev. Sci. Instrum.* **66**, 508 (1995).
20. Y. Lin, T. J. Kessler, and G. N. Lawrence, *Opt. Lett.* **20**, 764 (1995).
21. Ya. B. Zel’dovich and Yu. P. Raizer, in *Physics of Shock Waves and High-Temperature Hydrodynamic Phenomena*, edited by W. D. Hayes and R. F. Probstein (Dover Publications, Mineola, NY, 2002), Vol. I, Chap. I, pp. 1–104.
22. R. P. Drake, *High-Energy-Density Physics: Fundamentals, Inertial Fusion, and Experimental Astrophysics*, Shock Wave and High Pressure Phenomena (Springer, Berlin, 2006).
23. P. M. Celliers, D. K. Bradley, G. W. Collins, D. G. Hicks, T. R. Boehly, and W. J. Armstrong, *Rev. Sci. Instrum.* **75**, 4916 (2004).
24. P. M. Celliers *et al.*, *Appl. Phys. Lett.* **73**, 1320 (1998).
25. L. M. Barker and R. E. Hollenbach, *J. Appl. Phys.* **43**, 4669 (1972).
26. L. M. Barker and K. W. Schuler, *J. Appl. Phys.* **45**, 3692 (1974).

27. P. A. Jaanimagi, R. Boni, D. Butler, S. Ghosh, W. R. Donaldson, and R. L. Keck, in *26th International Congress on High-Speed Photography and Photonics*, edited by D. L. Paisley *et al.* (SPIE, Bellingham, WA, 2005), Vol. 5580, pp. 408–415.
28. J. E. Miller, T. R. Boehly, A. Melchior, D. D. Meyerhofer, P. M. Celliers, J. H. Eggert, D. G. Hicks, C. M. Sorce, J. A. Oertel, and P. M. Emmel, *Rev. Sci. Instrum.* **78**, 034903 (2007).
29. G. A. Lyzenga, T. J. Ahrens, and A. C. Mitchell, *J. Geophys. Res. B* **88**, 2431 (1983).
30. S. P. Marsh, ed. *LASL Shock Hugoniot Data*, Los Alamos Series on Dynamic Material Properties (University of California Press, Berkeley, CA, 1980).
31. R. F. Trunin *et al.*, *Izv. Acad. Sci. USSR Phys. Solid Earth*, **8** (1971).
32. R. F. Trunin, *Phys.-Usp.* **37**, 1123 (1994).
33. Recent work on the Sandia Z Machine by Knudson, first presented at 16th Topical Conference on Shock Compression of Condensed Matter, measured Hugoniot and sound speed of α -quartz in the 1- to 16-Mbar regime, observing some curvature in $U_s(U_p)$. [M. Knudson and M. Desjarlais, presented at the 16th APS Topical Conference on Shock Compression of Condensed Matter, Nashville, TN, 28 June–3 July 2009 (Paper V2.00001); M. Knudson, *Bull. Am. Phys. Soc.* **54**, 134 (2009).] If real, this can cause shifts in the data obtained using α -quartz as an IM standard, although it does not compromise the precision of the data presented in this article. To resolve this, measurement of the Mie–Grüneisen parameter using laser-driven shock waves is currently underway. The data presented here will be reanalyzed with this new data in a future publication. The percent difference in density between the fit found by Knudson and that used in this study varies with quartz shock velocity, peaking around 19 to 20 km/s (6 to 7 Mbar) at ~6% and decreasing with increasing shock velocity and pressure. This implies that values would be most compromised only in these ranges, and data obtained at higher pressures would be less affected.
34. R. G. McQueen, Los Alamos National Laboratory, Los Alamos, NM, LA-UR-90-1996 (1989).
35. R. F. Trunin, *Shock Compression of Condensed Materials* (Cambridge University Press, Cambridge, England, 1998).
36. A. N. Mostovych *et al.*, *Phys. Plasmas* **8**, 2281 (2001).
37. T. R. Boehly, D. G. Hicks, P. M. Celliers, T. J. B. Collins, R. Earley, J. H. Eggert, D. Jacobs-Perkins, S. J. Moon, E. Vianello, D. D. Meyerhofer, and G. W. Collins, *Phys. Plasmas* **11**, L49 (2004).
38. S. P. Lyon and J. D. Johnson, Los Alamos National Laboratory, Los Alamos, NM, Report LA-CP-98-100 (1998).
39. N. C. Holmes, *Rev. Sci. Instrum.* **62**, 1990 (1991).
40. I. P. Dudoladov *et al.*, *Prikl. Mekh. Tekh. Fiz.* **4**, 148 (1969).
41. R. G. McQueen *et al.*, in *High-Velocity Impact Phenomena*, edited by R. Kinslow (Academic Press, New York, 1970), Chap. VII, Sec. II, pp. 293–417.
42. M. Van Thiel, J. Shaner, and E. Salinas, Lawrence Livermore National Laboratory, Livermore, CA, Report UCRL-50108, Rev. 1 (1977).
43. A. V. Bushman *et al.*, *JETP Lett.* **82**, 895 (1996).
44. J. Abdallah, Jr., Los Alamos National Laboratory, Los Alamos, NM, Report LA-10244-M, NTIS Order No. DE85001405 (1984). (Copies may be obtained from the National Technical Information Service, Springfield, VA 22161.)
45. G. I. Kerley, Sandia National Laboratory, Albuquerque, NM, Report SAND-88-2291, NTIS Order No. DE91017717 (1991). (Copies may be obtained from the National Technical Information Service, Springfield, VA 22161.)
46. R. Cauble (Lawrence Livermore National Laboratory) and N. Ozaki (Osaka University), private communication (2009).
47. F. Dowell, Los Alamos National Laboratory, Los Alamos, NM, Report LA-9559-MS, NTIS Order No. DE83003896 (1982). (Copies may be obtained from the National Technical Information Service, Springfield, VA 22161.)
48. F. Dowell, Los Alamos National Laboratory, Los Alamos, NM, Report LA-9564-MS, NTIS Order No. DE83004996 (1982). (Copies may be obtained from the National Technical Information Service, Springfield, VA 22161.)
49. W. Theobald, J. E. Miller, T. R. Boehly, E. Vianello, D. D. Meyerhofer, T. C. Sangster, J. Eggert, and P. M. Celliers, *Phys. Plasmas* **13**, 122702 (2006).
50. D. K. Bradley *et al.*, *Phys. Rev. Lett.* **93**, 195506 (2004).
51. P. M. Celliers *et al.*, *Phys. Rev. Lett.* **84**, 5564 (2000).
52. P. M. Celliers *et al.*, *Phys. Plasmas* **11**, L41 (2004).
53. M. Koenig *et al.*, *Phys. Plasmas* **10**, 3026 (2003).

A Generalized Measurable Ignition Condition for Inertial Confinement Fusion

In inertial confinement fusion (ICF),¹ a shell of cryogenic deuterium and tritium (DT) thermonuclear fuel is accelerated inward by direct laser irradiation or by the x rays produced by heating a high-Z enclosure (hohlraum). At stagnation, the compressed fuel is ignited by a central hot spot surrounded by a cold, dense shell. Ignition occurs when the alpha-particle heating of the hot spot exceeds all the energy losses. To measure progress toward ignition, a metric is needed to assess how an implosion experiment performs with respect to the ignition condition. In a stationary plasma, the ignition condition is given by the Lawson criterion.² In ICF, the same ignition condition must be derived in terms of measurable parameters. Different forms of the 1-D ignition condition have been derived,^{1,3,4} but none of them can be accurately measured. Measurable parameters of the ICF fuel assembly are the areal density, the ion temperature, and the neutron yield. This article demonstrates that the ICF ignition condition can be written in terms of these measurable parameters. We start from the 1-D ignition model of Ref. 5 and generalize it to multidimensions through a single parameter: the yield-over-clean (YOC). The YOC is the ratio of the measured neutron yield to the predicted 1-D yield. The latter must be calculated consistently with the measured ρR and T_i . The generalized ignition criterion depends on the areal density, the ion temperature, and the YOC. Alternatively, the ignition condition can be written in terms of the areal density, the neutron yield, and the target mass.

This article first deals with the 3-D extension of the dynamic ignition model^{5,6} and an analytic ignition condition. The results of hydrodynamic simulations of imploding capsules forming the database used to generate a more-accurate ignition condition will also be shown. A measurable criterion requires the solution of a dynamic ignition model. The analysis starts by modifying the 1-D ignition model [Eq. (15) of Ref. 5] and the following considerations about multidimensional effects: The hot spot is enclosed by a surrounding shell that can be highly distorted by hydrodynamic instabilities. The hot-spot volume V_{hs} is bounded by Rayleigh–Taylor (RT) bubbles and spikes from the shell. The plasma in the bubbles is cold and does not contribute to the fusion yield. Following the analysis of Ref. 7,

we assume that only the “clean” hot-spot volume V_{clean} within the RT spikes (Fig. 121.15) is hot enough to induce fusion reactions, and the central temperature is unchanged by the RT evolution as long as the RT spikes do not reach the hot spot’s center. The 1-D ignition model can be extended to 3-D by integrating the alpha-particle energy deposition over the clean hot-spot volume, leading to

$$\frac{d}{d\tau}(\hat{P}\hat{R}^3) = -2\hat{P}\hat{R}^2 \frac{d\hat{R}}{d\tau} + \gamma_\alpha \hat{P}^2 \hat{T} \hat{R}_{clean}^3, \quad (1)$$

$$\frac{d}{d\tau} \left(\frac{\hat{P}\hat{R}^3}{\hat{T}} \right) = \hat{R} \hat{T}^{5/2}, \quad (2)$$

$$\frac{d^2 \hat{R}}{d\tau^2} = \hat{P} \hat{R}^2. \quad (3)$$

With respect to the 1-D case, the alpha heating is reduced by the clean volume fraction R_{clean}^3/R^3 , where R_{clean} and R are

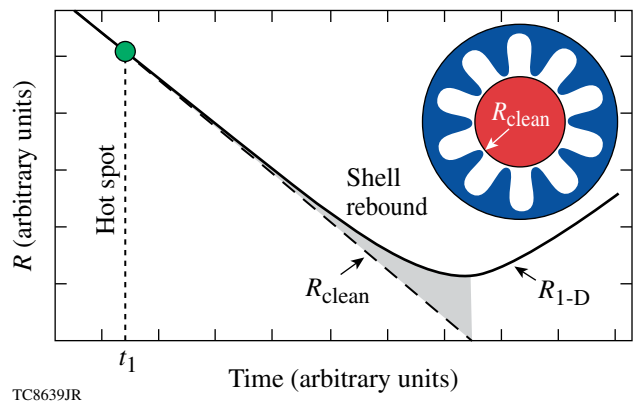


Figure 121.15 Schematic of the free-fall model. Fusion reactions occur only in the clean volume within the Rayleigh–Taylor spikes. The spikes “free-fall” after saturation of the linear growth.

the clean and 1-D radii, respectively. We assume this to be the main effect of the implosion nonuniformities. In Eqs. (1)–(3), the hot-spot radius R , pressure P , and central temperature T are normalized with their stagnation values calculated without including the alpha-particle energy deposition $R_{\text{stag}}^{\text{no } \alpha}$, $P_{\text{stag}}^{\text{no } \alpha}$, and $T_*^{\text{no } \alpha}$ defined later. The dimensionless time $\tau = tV_i/R_{\text{stag}}^{\text{no } \alpha}$ is a function of the implosion velocity V_i . Equations (1)–(3) represent the hot-spot energy balance, the temperature equation from the hot-spot mass conservation, and the thin-shell Newton's law, respectively. For simplicity, we have neglected the radiation losses (included in Ref. 5) in the derivation but retained in the simulation. The expansion [first term on the right-hand side of Eq. (1)] and the heat-conduction losses [right-hand side of Eq. (2)] are retained. This article focuses on the 3-D effects included in the term R_{clean} in Eq. (1). The term γ_α governs the ignition conditions and can be written as

$$\gamma_\alpha = \left(\varepsilon_\alpha C_0 P_{\text{stag}}^{\text{no } \alpha} R_{\text{stag}}^{\text{no } \alpha} T_*^{\text{no } \alpha} \right) / (8 V_i), \quad (4)$$

where ε_α is the alpha-particle energy (3.5 MeV) and $C_0 \simeq 2.5 \times 10^{-26} \text{ m}^3 \text{ keV}^{-3} \text{ s}^{-1}$ comes from approximating the volume integral of the fusion rate around a 4- to 15-keV central temperature with a power law $\sim T^3$. The initial conditions are defined at the time of peak implosion velocity V_i : $P(0) = P_0$, $R(0) = R_0$, $\dot{R}(0) = -V_i$, and $T(0) = T_0$. The stagnation values $R_{\text{stag}}^{\text{no } \alpha}$, $P_{\text{stag}}^{\text{no } \alpha}$, and $T_{\text{stag}}^{\text{no } \alpha}$ are obtained by solving the dimensional form of Eqs. (1)–(3) without alpha-particle–energy deposition ($\gamma_\alpha = 0$) and in the limit of large initial kinetic energy $\epsilon_0 = (M_{\text{shell}} V_i^2 / 4\pi P_0 R_0^3) \gg 1$. This leads to the following stagnation values without alphas:

$$P_{\text{stag}}^{\text{no } \alpha} \simeq P_0 \epsilon_0^{5/2}, \quad R_{\text{stag}}^{\text{no } \alpha} \simeq R_0 \epsilon_0^{-1/2}, \quad (5)$$

$$T_*^{\text{no } \alpha} \simeq \left(1.2 P_{\text{stag}}^{\text{no } \alpha} R_{\text{stag}}^{\text{no } \alpha} V_i / \kappa_0 \right)^{2/7}, \quad (6)$$

where $T_*^{\text{no } \alpha} \simeq 1.3 T_{\text{stag}}^{\text{no } \alpha}$ and $\kappa_0 \simeq 3.7 \times 10^{69} \text{ m}^{-1} \text{ s}^{-1} \text{ J}^{-5/2}$ is the coefficient of Spitzer thermal conductivity $\kappa_{\text{Sp}} \simeq \kappa_0 T^{5/2}$ for $\ln \Lambda \approx 5$. Using the no- α stagnation values, the initial conditions of the dimensionless model are rewritten in the simple form $\hat{P}(0) = \epsilon_0^{-5/2}$, $\hat{T}(0) = \epsilon_0^{-1/2}$, $\hat{R}(0) = \epsilon_0^{-1/2}$, and $\hat{\dot{R}}(0) = -1$. The ignition model comprises Eqs. (1)–(3) and the initial conditions. Ignition is defined by the critical value of the parameter γ_α in Eq. (1), yielding an explosive singular solution. In the limit of $\epsilon_0 \rightarrow \infty$, the critical value of γ_α depends solely on the effect of nonuniformities entering through the clean radius R_{clean} . In the absence of nonuniformities (1-D), $R_{\text{clean}} = R$ and the critical value of γ_α is γ_α (1-D) $\simeq 1.1$. As the alpha heating raises the

hot-spot temperature, the RT spikes are ablated by the enhanced heat flux as well as by the alpha particles leaking from the hot spot and depositing their energy onto the spikes.⁸ This causes the ablative stabilization of the RT and an enhancement of the clean volume. This effect can be heuristically included by letting the clean radius increase up to the 1-D radius as the hot-spot temperature rises above the no- α value.

The aim of the new ignition model is to identify a measurable parameter describing the effects of hot-spot nonuniformities entering through the time history of the clean radius $R_{\text{clean}}(\tau)$. The RT spikes first grow exponentially until reaching a saturation amplitude. After saturation, the spikes free-fall into the hot spot as shown in Fig. 12.15; the acceleration $g(t) = R''(t)$ determines the linear growth rates $\gamma_{\text{RT}} = \sqrt{k g(t)}$, where $k \sim \ell/R(t)$ is the perturbation wave number. The number of e foldings of linear growth is

$$n_e = \sqrt{\ell} \hat{n}_e = \int_0^{t_{\text{lin}}} \gamma_{\text{RT}}(t) dt,$$

where t_{lin} is the interval of linear growth up to saturation. In the nonlinear free-fall stage, the spikes' amplitude grows as

$$\Delta R \approx \eta(t_{\text{lin}}) + \int_{t_{\text{lin}}}^t dt' \int_{t_{\text{lin}}}^{t'} g(t'') dt'',$$

where $\eta(t_{\text{lin}})$ is the linear amplitude at saturation. For simplicity, we assume that the linear growth can be neglected [small $\eta(t_{\text{lin}})$] with respect to the nonlinear growth so that the spike amplitude ΔR depends only on t_{lin} and t . This leads to a clean radius $R_{\text{clean}} = R - \Delta R = R(t_{\text{lin}}) + R'(t_{\text{lin}})(t - t_{\text{lin}})$ for $t > t_{\text{lin}}$. Before t_{lin} , the clean radius equals the 1-D radius, $R_{\text{clean}} \approx R$. The time t_{lin} depends on the amplitude of the inner DT-ice roughness at the end of the acceleration phase. The larger the initial nonuniformity level, the smaller the time t_{lin} . We first solve Eqs. (1)–(3) without alpha-particle–energy deposition and compute $\hat{R}^{\text{no } \alpha}(\tau)$. Then we use $\hat{R}^{\text{no } \alpha}$ to determine \hat{R}_{clean} using the free-fall model. The most-severe reduction of the clean volume corresponds to $\tau_{\text{lin}} = 0$, when the nonlinear RT growth starts from the beginning of the deceleration phase. The number of e foldings of linear growth is directly proportional to

$$\hat{n}_e^{\text{no } \alpha} \approx \frac{\pi}{2} + \arctan \left(\sqrt{\epsilon_0} - \frac{\epsilon_0}{\tau_{\text{lin}}} \right). \quad (7)$$

For a given τ_{lin} , we compute $\hat{n}_e^{\text{no } \alpha}$, $R_{\text{clean}}(\tau, \tau_{\text{lin}})$, and the yield-over-clean without alphas (YOC^{no } \alpha}):

$$\text{YOC}^{\text{no } \alpha} = \frac{\int_0^\infty \hat{p}^2 \hat{T} \hat{R}_{\text{clean}}^3 d\tau}{\int_0^\infty \hat{p}^2 \hat{T} \hat{R}^3 d\tau}, \quad (8)$$

where \hat{p} , \hat{T} , and \hat{R} are the solutions of Eqs. (1)–(3) without alpha-particle–energy deposition (i.e., $\gamma_\alpha = 0$). The $\text{YOC}^{\text{no } \alpha}$ is the ratio of the neutron yield for a reduced clean volume to the 1-D neutron yield for the case without alphas. Both $\text{YOC}^{\text{no } \alpha}$ and $\hat{n}_e^{\text{no } \alpha}$ depend on τ_{lin} , and a relation can be numerically derived, yielding the functional relation $\hat{n}_e^{\text{no } \alpha} = \hat{n}_e^{\text{no } \alpha}(\text{YOC}^{\text{no } \alpha})$. Since $\hat{n}_e^{\text{no } \alpha}$ is a measure of the initial nonuniformities, $\text{YOC}^{\text{no } \alpha}$ can also be used to define the initial nonuniformities' level. For a given value of $\text{YOC}^{\text{no } \alpha}$, it is possible to determine the ignition condition, including the effects of nonuniformities, by solving Eqs. (1)–(3) with alpha deposition for the corresponding clean radius \hat{R}_{clean} and by varying γ_α to find the critical value for a singular solution. We start by determining the transition time τ_{lin} from linear to nonlinear growth by solving Eqs. (1)–(3) with $\hat{R}_{\text{clean}} \approx \hat{R}$ (valid in the linear regime) and a given value of γ_α . The resulting radius $R^\alpha(\tau)$ is used to compute the linear e foldings:

$$\hat{n}_e^\alpha(\tau_{\text{lin}}) = \int_0^{\tau_{\text{lin}}} \sqrt{R^{\alpha''}/R^\alpha} d\tau. \quad (9)$$

This is used to determine the time τ_{lin} by setting

$$\hat{n}_e^\alpha(\tau_{\text{lin}}) = \hat{n}_e^{\text{no } \alpha}(\text{YOC}^{\text{no } \alpha}),$$

leading to a functional relation $\tau_{\text{lin}} = \tau_{\text{lin}}(\text{YOC}^{\text{no } \alpha})$. Using τ_{lin} , the clean radius history follows from

$$\hat{R}_{\text{clean}}^\alpha = \hat{R}^\alpha(\tau_{\text{lin}}) + \hat{R}^{\alpha'}(\tau_{\text{lin}})(\tau - \tau_{\text{lin}}). \quad (10)$$

The effect of nonuniformities on ignition is studied by varying the initial level of nonuniformities through $\text{YOC}^{\text{no } \alpha}$, computing τ_{lin} , and finding the critical γ_α in Eq. (1), yielding a singular explosive solution. This leads to the 3-D ignition condition shown in Fig. 121.16, which can be approximated by $\gamma_\alpha(\text{YOC}^{\text{no } \alpha})^{4/5} > 1.2$. Using the definition γ_α in Eq. (4) and substituting the energy conservation and the shell mass at stagnation (modified to include the finite shell-thickness effects⁵), one finds that $\gamma_\alpha \sim (\rho R)^{3/4} T_*^{15/8}$, leading to the following analytic ignition condition:

$$\chi^{\text{an}} \approx \rho R_{\text{tot}}^{\text{no } \alpha} (T^{\text{no } \alpha} / 4.5)^{5/2} (\text{YOC}^{\text{no } \alpha})^\mu \approx 1, \quad (11)$$

where $\rho R_{\text{tot}}^{\text{no } \alpha}$ is the total areal density (approximately equal to the shell areal density) in g/cm^2 , $T^{\text{no } \alpha}$ is the peak hot-spot

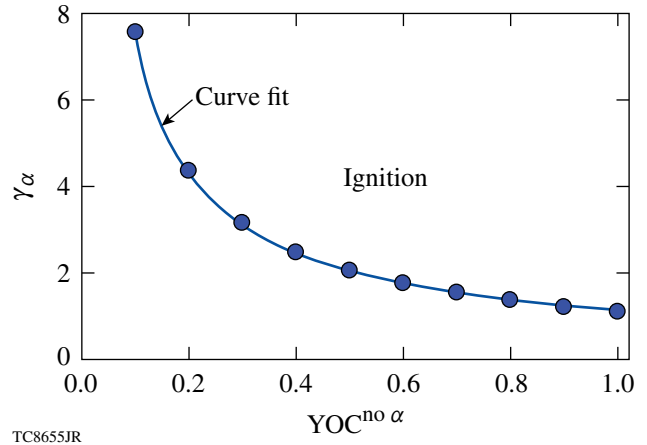
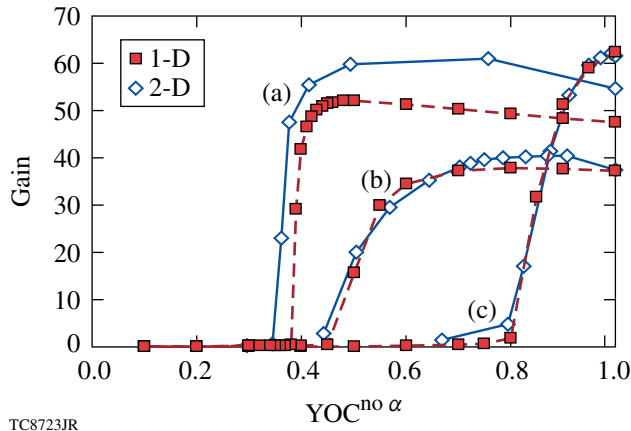


Figure 121.16

The critical parameter γ_α required for a singular solution of Eqs. (1)–(3) versus the YOC. The numerical solution can be fitted by a simple power law $\gamma_\alpha \approx 1.2/(\text{YOC}^{\text{no } \alpha})^{4/5}$.

temperature in keV, and $\mu \approx 1$. Equation (11) represents a measurable criterion that can be used to assess the 3-D implosion performance, provided the alpha particles do not significantly change the hydrodynamics. This is the case with surrogate deuterium D_2 and tritium–hydrogen–deuterium (THD) [with a few % of D (Ref. 9)] as well as low-gain (<10%) DT capsules. Obviously, ignited DT capsules do not require an ignition criterion. The effect of nonuniformities enters the ignition condition through a single parameter: the YOC. The accuracy of the generalized ignition condition can be improved by including the effect of the ablative stabilization of the deceleration RT and by tuning the power indices in Eq. (11) through a set of numerical simulations. We have carried out a set of 2-D simulations of ignition targets with varying inner-ice-surface roughness using the code *DRACO*.¹⁰ The initial ice roughness is increased until ignition fails. Each run is repeated without the alpha-particle–energy deposition to determine the no- α neutron yield and the $\text{YOC}^{\text{no } \alpha}$. A gain curve is generated by plotting the energy gain (fusion energy yield/laser energy on target) versus the $\text{YOC}^{\text{no } \alpha}$. Figure 121.17 shows the gain curves for (a) a 420-kJ direct-drive–ignition target designed to simulate the 1-MJ indirect-drive point design¹¹ for the National Ignition Facility (NIF),¹² (b) the 1.5-MJ, all-DT direct-drive point design,¹³ and (c) the 1-MJ direct-drive wetted-foam design.¹⁴

To validate the clean volume analysis used in the analytic ignition model, we compare the result of 2-D simulations with the same gain curve obtained from 1-D simulations, where the fusion rate $\langle \sigma v \rangle$ is reduced by a factor ξ equal to the $\text{YOC}^{\text{no } \alpha}$. Since the alpha-energy deposition depends on the product



TC8723JR

Figure 121.17

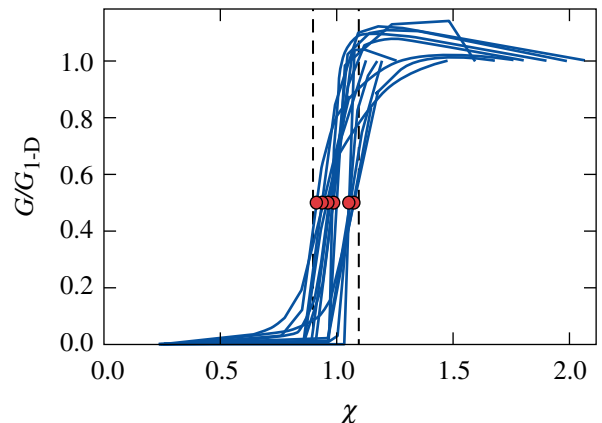
Energy gain versus $YOC^{no \alpha}$ computed with 1-D (squares) and 2-D (diamonds) simulations. The 2-D simulations use a varying initial ice roughness. The 1-D simulations use a fusion rate reduced by the YOC to mimic the reduction of the clean hot-spot volume. The gain curves are for (a) a 420-kJ direct-drive surrogate of the 1-MJ indirect-drive NIF point design, (b) the 1.5-MJ, all-DT direct-drive point design, and (c) the 1-MJ direct-drive wetted-foam design.

$\langle \sigma v \rangle V_{\text{clean}}$, reducing $\langle \sigma v \rangle$ in the 1-D code by the factor $\xi = YOC^{no \alpha}$ is approximately equivalent to reducing the hot-spot volume by the clean volume fraction. In the 1-D code, the reduction of $\langle \sigma v \rangle$ takes effect as long as the central hot-spot temperature is below 10 keV. For temperatures above 10 keV, the hot spot is robustly ignited, the RT becomes ablatively stabilized, and ξ is increased linearly with the temperature until $\xi = 1$ for $T > 15$ keV. This effect can also be included in the analytic model by letting R_{clean} approach R_{1-D} [in Eq. (1)] as the temperature exceeds its no- α value. This leads to a reduction of the YOC exponent in Eq. (11) ($\mu \approx 0.8$) and an analytic ignition condition $\chi^{\text{an}} \approx \rho R_{\text{tot}}^{no \alpha} (T_n^{no \alpha} / 4.5)^{5/2} (YOC^{no \alpha})^{0.8} \approx 1$. Phasing out the reduction factor ξ after ignition makes it possible for the 1-D code to correctly predict the burn-wave propagation through the cold shell and the final gain. The results from the modified 1-D code are compared with the 2-D simulations for the three targets above. As shown in Fig. 121.17, the modified 1-D code predicts the “ignition cliff” for critical values of the $YOC^{no \alpha}$ in agreement with the 2-D simulations. The ignition cliff represents the sharp decrease in gain occurring for a critical value of the YOC. After validating the modified 1-D code with the 2-D simulations, we used the fast 1-D code to generate a database of $\rho R_n^{no \alpha}$, $T_n^{no \alpha}$, and $YOC^{no \alpha}$ for marginally ignited capsules with the ignition YOC varying between 0.3 and 0.8. Marginal ignition is defined as the gain corresponding to the middle point of the ignition cliff (\sim half the 1-D gain). This is a physical definition of ignition describing the onset of the burn-wave propagation. The 3-D ignition criterion based on a

power law of the three measurable parameters has been derived through the best fit of the simulation results. Figure 121.18 shows the normalized gain curves ($G/G_{1-D} = \text{gain}/1\text{-D gain}$) from the database versus the ignition parameter χ representing the “best fit.” The best fit of the ignition criterion $\chi \approx 1$ yields

$$\chi^{\text{fit}} \equiv \rho R_{\text{tot}(n)}^{no \alpha} (T_n^{no \alpha} / 4.7)^{2.1} (YOC^{no \alpha})^{\mu} \quad (12)$$

with $\mu \approx 0.63$. This fit predicts the ignition cliff with a $\pm 10\%$ error. The subscript n indicates the spatial and temporal average with the fusion rate (i.e., neutron average) used to approximate the experimental observables. Note that $T_n^{no \alpha}$ in Eq. (12) is the 1-D temperature. Since the central temperature decreases slightly with increasing nonuniformities (lower YOC), one would expect a weaker dependence on the YOC in Eq. (12) when the 2-D (or the measured) temperature is used. This is shown by the fit from a LASNEX¹⁵ 2-D simulation database of DT and surrogate THD⁹ NIF-point-design targets. A fit of the gain curves using the LASNEX database yields an ignition condition like Eq. (12) with $\mu \approx 0.47$. The best-performing DT cryogenic implosion on OMEGA¹⁶ to date has achieved an areal density of ≈ 0.2 g/cm² and a temperature of ≈ 2 keV with a YOC of $\approx 10\%$ (Ref. 17), leading to an ignition parameter $\chi \sim 10^{-2}$. Notice that the $YOC^{no \alpha} \equiv (Y^{\text{ex}} / Y^{1-D})$ requires the 1-D yield (Y^{1-D}) as normalization of the experimental yield (Y^{ex}). Since the 1-D yield is a strong function of the temperature, one expects a severe reduction of the temperature dependence in Eq. (12). A fit of the simulation database used in Fig. 121.18



TC8658JR

Figure 121.18

Gain curves from the simulation database. The normalized gain G/G_{1-D} is plotted versus the ignition parameter χ . The ignition cliff is predicted by $\chi = 1$ with a $\pm 10\%$ error.

shows that an approximate ignition condition ($\pm 20\%$ error) for DT targets can be written without the temperature as

$$\rho R_{\text{tot}(n)}^{\text{no } \alpha} \left[0.1 Y_{16(\text{no } \alpha)}^{\text{ex}} / M_{\text{sh}}^{\text{mg}} \right]^{0.58} \approx 1, \quad (13)$$

where Y_{16}^{ex} is in units of 10^{16} neutrons and M_{sh} (in mg) is the portion of the shell mass stagnating at the time of peak neutron rate (bang time). For typical ICF implosions, M_{sh} is about half of the unablated shell mass. The latter can be measured or estimated from the simulations with reasonable accuracy. This result is in reasonable agreement with the analysis of Spears *et al.*⁹ of the simulated down-scattered neutron spectrum database for the NIF point-design target (fixed M_{sh}). An ignition condition similar to Eq. (12) can be recovered from Eq. (13) by setting $Y^{\text{ex}} = \text{YOC} \cdot Y^{1\text{-D}}$ and by using the following fit for $Y^{1\text{-D}}$ of DT targets from a 1-D simulation database:

$$Y_{16(\text{no } \alpha)}^{1\text{-D}} \approx \left(\frac{T_n^{\text{no } \alpha}}{4.7} \right)^{4.7} \left[\rho R_{\text{tot}(n)}^{\text{no } \alpha} \right]^{0.6} \left(\frac{M_{\text{sh}}^{\text{mg}}}{0.1} \right). \quad (14)$$

The criteria of Eqs. (12) or (13) can be used to assess the performance of cryogenic implosions on the NIF and OMEGA.

ACKNOWLEDGMENT

This work has been supported by the U.S. Department of Energy under Cooperative Agreement DE-FC02-04ER54789 and DE-FC52-08NA28302, the University of Rochester, and the New York State Energy Research and Development Authority. The support of DOE does not constitute an endorsement by DOE of the views expressed in this article.

REFERENCES

1. S. Atzeni and J. Meyer-ter-Vehn, *The Physics of Inertial Fusion: Beam Plasma Interaction, Hydrodynamics, Hot Dense Matter*, International Series of Monographs on Physics (Clarendon Press, Oxford, 2004); J. D. Lindl, *Phys. Plasmas* **2**, 3933 (1995).
2. J. D. Lawson, *Proc. Phys. Soc. Lond.* **B70**, 6 (1957).
3. M. C. Herrmann, M. Tabak, and J. D. Lindl, *Nucl. Fusion* **41**, 99 (2001).
4. A. Kemp, J. Meyer-ter-Vehn, and S. Atzeni, *Phys. Rev. Lett.* **86**, 3336 (2001).
5. C. D. Zhou and R. Betti, *Phys. Plasmas* **15**, 102707 (2008).
6. J. Garnier and C. Cherfils-Cl  rouin, *Phys. Plasmas* **15**, 102702 (2008).
7. R. Kishony and D. Shvarts, *Phys. Plasmas* **8**, 4925 (2001).
8. A. Schiavi and S. Atzeni, *Phys. Plasmas* **14**, 070701 (2007).
9. B. K. Spears *et al.*, "Prediction of Ignition Implosion Performance Using Measurements of Low-Deuterium Surrogates," to be published in *Physics of Plasmas*.
10. P. B. Radha, T. J. B. Collins, J. A. Delettrez, Y. Elbaz, R. Epstein, V. Yu. Glebov, V. N. Goncharov, R. L. Keck, J. P. Knauer, J. A. Marozas, F. J. Marshall, R. L. McCrory, P. W. McKenty, D. D. Meyerhofer, S. P. Regan, T. C. Sangster, W. Seka, D. Shvarts, S. Skupsky, Y. Srebro, and C. Stoeckl, *Phys. Plasmas* **12**, 056307 (2005).
11. S. W. Haan *et al.*, *Phys. Plasmas* **12**, 056316 (2005).
12. E. I. Moses, *J. Phys., Conf. Ser.* **112**, 012003 (2008).
13. P. W. McKenty, V. N. Goncharov, R. P. J. Town, S. Skupsky, R. Betti, and R. L. McCrory, *Phys. Plasmas* **8**, 2315 (2001).
14. T. J. B. Collins, J. A. Marozas, R. Betti, D. R. Harding, P. W. McKenty, P. B. Radha, S. Skupsky, V. N. Goncharov, J. P. Knauer, and R. L. McCrory, *Phys. Plasmas* **14**, 056308 (2007).
15. G. B. Zimmerman and W. L. Kruer, *Comments Plasma Phys. Control. Fusion* **2**, 51 (1975).
16. T. R. Boehly, D. L. Brown, R. S. Craxton, R. L. Keck, J. P. Knauer, J. H. Kelly, T. J. Kessler, S. A. Kumpan, S. J. Loucks, S. A. Letzring, F. J. Marshall, R. L. McCrory, S. F. B. Morse, W. Seka, J. M. Soures, and C. P. Verdon, *Opt. Commun.* **133**, 495 (1997).
17. T. C. Sangster, V. N. Goncharov, P. B. Radha, V. A. Smalyuk, R. Betti, R. S. Craxton, J. A. Delettrez, D. H. Edgell, V. Yu. Glebov, D. R. Harding, D. Jacobs-Perkins, J. P. Knauer, F. J. Marshall, R. L. McCrory, P. W. McKenty, D. D. Meyerhofer, S. P. Regan, W. Seka, R. W. Short, S. Skupsky, J. M. Soures, C. Stoeckl, B. Yaakobi, D. Shvarts, J. A. Frenje, C. K. Li, R. D. Petrasso, and F. H. S  guin, *Phys. Rev. Lett.* **100**, 185006 (2008).

In-Situ Detection and Analysis of Laser-Induced Damage on a 1.5-m Multilayer-Dielectric Grating Compressor for High-Energy, Petawatt-Class Laser Systems

Introduction

Understanding the *in-situ* laser-induced-damage threshold of large-aperture multilayer-dielectric-diffraction (MLD) gratings is paramount for petawatt-class laser facilities to reach design energies.^{1–8} Until now, short-pulse damage testing has been performed only on small-scale samples.^{9–15} No vacuum-damage test data are available on large-scale MLD gratings, and it has not been proven that one can simply transfer the results of the small samples to full-aperture MLD gratings. This article reports on the performance and findings of a vacuum-compatible grating-inspection system (GIS) that was deployed to detect *in-situ* damages of large-aperture gratings between high-energy shots. The deployment of a GIS makes it possible to operate OMEGA EP¹ safely and effectively because the morphological change of the compressor-grating-surface feature can be monitored in real-time without breaking the vacuum. The following sections (1) describe the mechanism and characterization of the inspection system; (2) introduce the methodology for detecting grating damage and the analysis method for determining the laser-beam fluence causing damage growth; (3) discuss the accuracy of the determined laser-beam fluence; (4) compare the damage-test result of a large-aperture MLD grating to the damage-probability measurement conducted on a small-grating witness sample; and (5) present conclusions.

Grating-Damage Inspection System

The grating-based pulse compressor of the petawatt-class, short-pulse OMEGA EP laser consists of four sets of tiled-grating assemblies, each measuring 141 cm × 43 cm (Refs. 1 and 16). The line density of the gratings is 1740 lines/mm. The incident and diffraction angles of the laser beam on grating 4 are 61.4° and 72.5°, respectively. During a recent 15-ps, 2.2-kJ energy ramp, it was imperative to monitor the damage growth of the final grating (grating 4) between shots to ensure that damage did not grow to a size that would damage downstream optics. A GIS, illustrated in Fig. 121.19(a), was deployed in the compressor vacuum chamber to detect damage growth on grating 4 during the energy ramp.

The GIS consists of a line-shape illumination generator and an imaging system. The optical layout of the line generator is illustrated in Fig. 121.19(b). A point source from a fiber-based, 1053-nm continuous-wave laser is projected to form a line-shape illumination pattern on the surface of grating 4 using a multi-element lens assembly. An aspheric singlet collimates the light from the fiber and is followed by a half-wave plate used to adjust polarization of the illumination beam. Two spherical lenses focus the light onto a grating surface ~2 m away. The lens pair was designed to provide a $1/e^2$ spot width of approximately 1 mm at the grating. A negative cylindrical lens located after

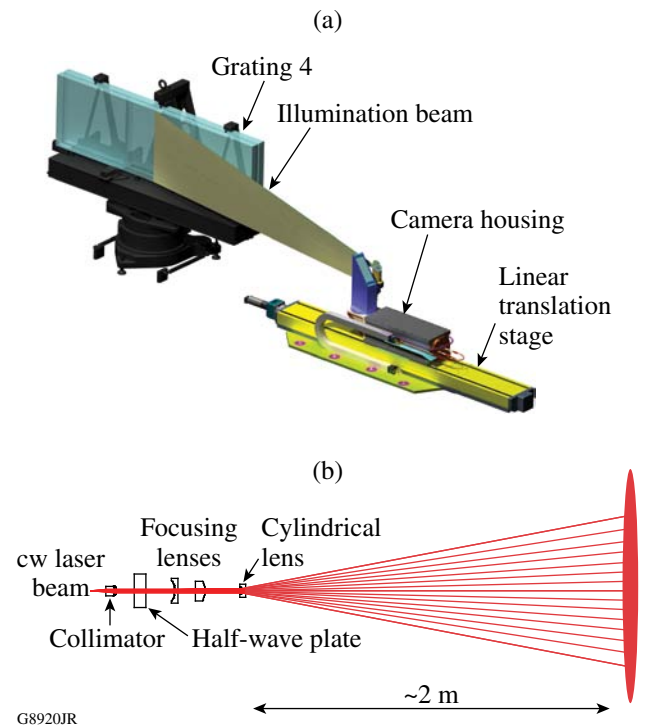


Figure 121.19 (a) The grating-inspection system scans through a 1.5 × 0.43-m large-aperture tiled-grating assembly. (b) Optical layout of the line-shape illumination generator of the grating-damage inspection system.

the spherical lens pair spreads the light in a direction parallel to the grating grooves, perpendicular to the scanning direction. The line length and associated illumination falloff along that direction are determined by the focal length of the cylindrical lens. Successive iterations of the design resulted in a trade-off between illumination uniformity and energy loss from light dispersed past the grating edges. The realized illumination pattern is shown in Fig. 121.20. The line length at 50% and the $1/e^2$ intensity are 243 mm and 450 mm, respectively. The angle between the illumination beam and grating normal is 80° . This line-shape illumination is scanned across the grating, and light scattered from any features on the surface is imaged to a 10-bit

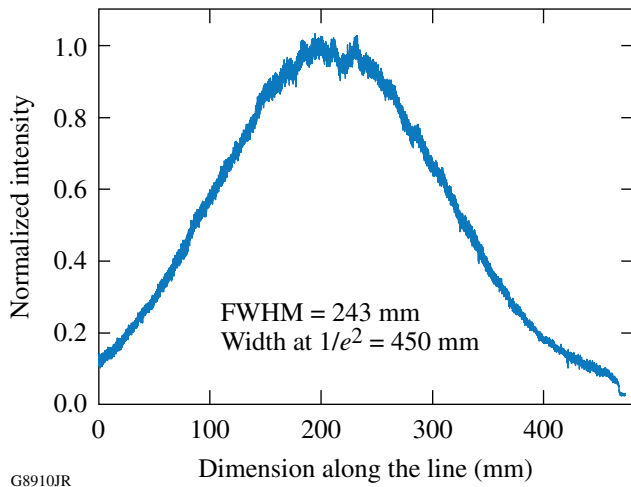


Figure 121.20
Illumination on the surface of grating 4 exhibits a Gaussian pattern along the groove direction.

charge-coupled device (CCD), having 8192×1 pixels with $7\text{-}\mu\text{m} \times 7\text{-}\mu\text{m}$ pixel size. The CCD is scanned across the grating along with the line-shape generator. The scanned images are then combined to generate a composite two-dimensional (2-D) image of the grating surface. The spatial resolution of a GIS image is limited by the modulation transfer function (MTF) of the imaging system, which was measured to be 0.4 cycle/mm and 1 cycle/mm in horizontal and vertical directions, respectively, at a modulation level of 20%.

In-Situ Grating-Damage Detection and Damage Analysis

Before the energy ramp, a reference scan of grating 4 was taken to record any existing features on the grating surface. An on-shot near-field fluence map was measured for each high-energy shot, and a GIS image was obtained after each shot. Six shots delivered the following energies to grating 4: 1.12 kJ, 1.33 kJ, 1.58 kJ, 1.82 kJ, 1.95 kJ, and 2.20 kJ. The corresponding laser-beam peak fluences were 2.5 J/cm^2 , 2.7 J/cm^2 , 3.3 J/cm^2 , 3.6 J/cm^2 , 4.0 J/cm^2 , and 4.6 J/cm^2 . The nominal pulse width was 15 ps. The near-field imaging system measuring the laser-beam fluence map resides downstream of the grating compressor, as shown in Fig. 121.21(a). During each high-energy shot, 0.7% of the main laser beam was delivered to the short-pulse-diagnostics path (SPDP) through a diagnostic mirror. This sample beam was then down-collimated, further attenuated, and sent to a near-field CCD, imaged to grating 4 for energy and fluence measurement. Figure 121.21(b) shows the scanned image of grating 4 after the 2.2-kJ shot. A majority of the damage features reside in areas ROI 1 and ROI 2 (ROI: region of interest); these two ROI's were chosen for damage analysis. Some of the features on this image were intrinsic to

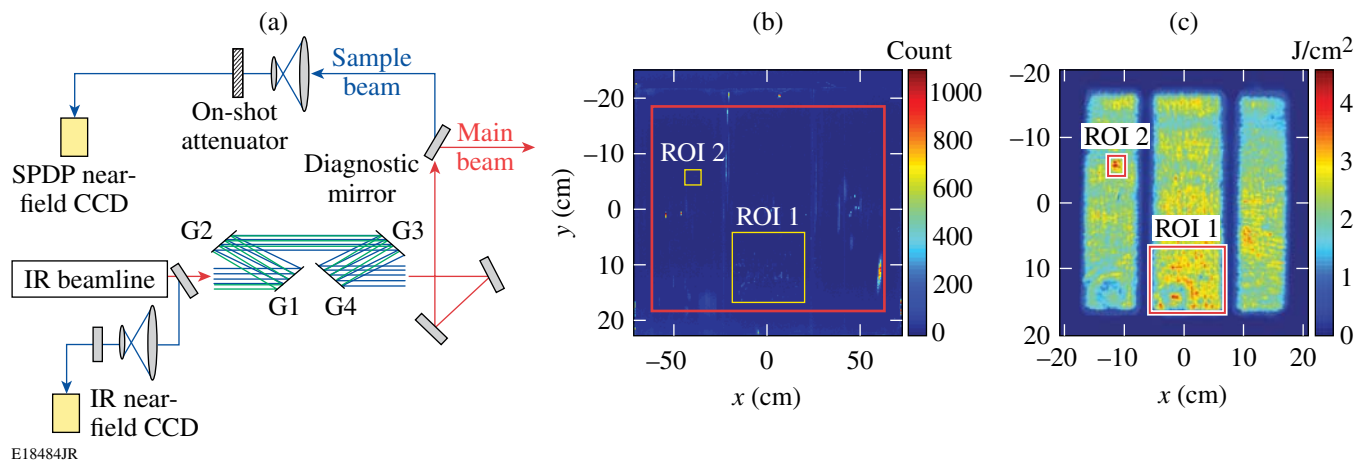


Figure 121.21
(a) The on-shot laser-fluence measurement path in relation to the grating compressor and the main-beam path; (b) a GIS image after the 2.2-kJ laser shot; (c) a beam-fluence map of the 2.2-kJ laser shot.

the holographic patterning of the gratings, and some existed prior to the energy ramp. Figure 121.21(c) shows the corresponding beam fluence measured on the 2.2-kJ shot. The main beam was shadowed along the gaps of the three individual tiles of grating 4. There is a factor of 0.3 scaling reduction in the x direction between Figs. 121.21(b) and 121.21(c). This is due to the 72.5° angle between the diagnostic beam and the normal of grating 4. Comparative analysis of the scanned images before and after each shot was used to assess any damage initiation and growth. By spatially registering the scanned image of the grating surface to the fluence map and by correlating the identified feature size and peak beam fluence within a specified ROI for each subsequent shot, the upper fluence limit below which damage growth occurred can be determined.

A scanned image of grating 4 was taken after each high-energy shot. Features in the image were identified using various image-processing techniques: A raw image was filtered

and properly down-sampled based on the MTF limitation of the imaging system of the GIS. For each specified ROI in the image [shown in Fig. 121.21(b)], the corresponding portion of the down-sampled image was binarized for subsequent feature identification. The portion of the image within an ROI having intensity higher than the binarization threshold was identified as a feature. The binarization threshold was determined using the statistical intensity information of the background and the scattering patterns within an ROI. The location and area size of each identified feature were calculated. Although the identified features exhibit various shapes, for ease of comparison between shots, the equivalent diameter of an identified feature was defined as the diameter of a circle that has the same area size as the identified feature. The histogram of the identified features was defined as the number of features at various equivalent diameters. This property was calculated for each ROI after each high-energy shot. The identified features in ROI 1 prior to the energy ramp are illustrated in Fig. 121.22(a). (Note that

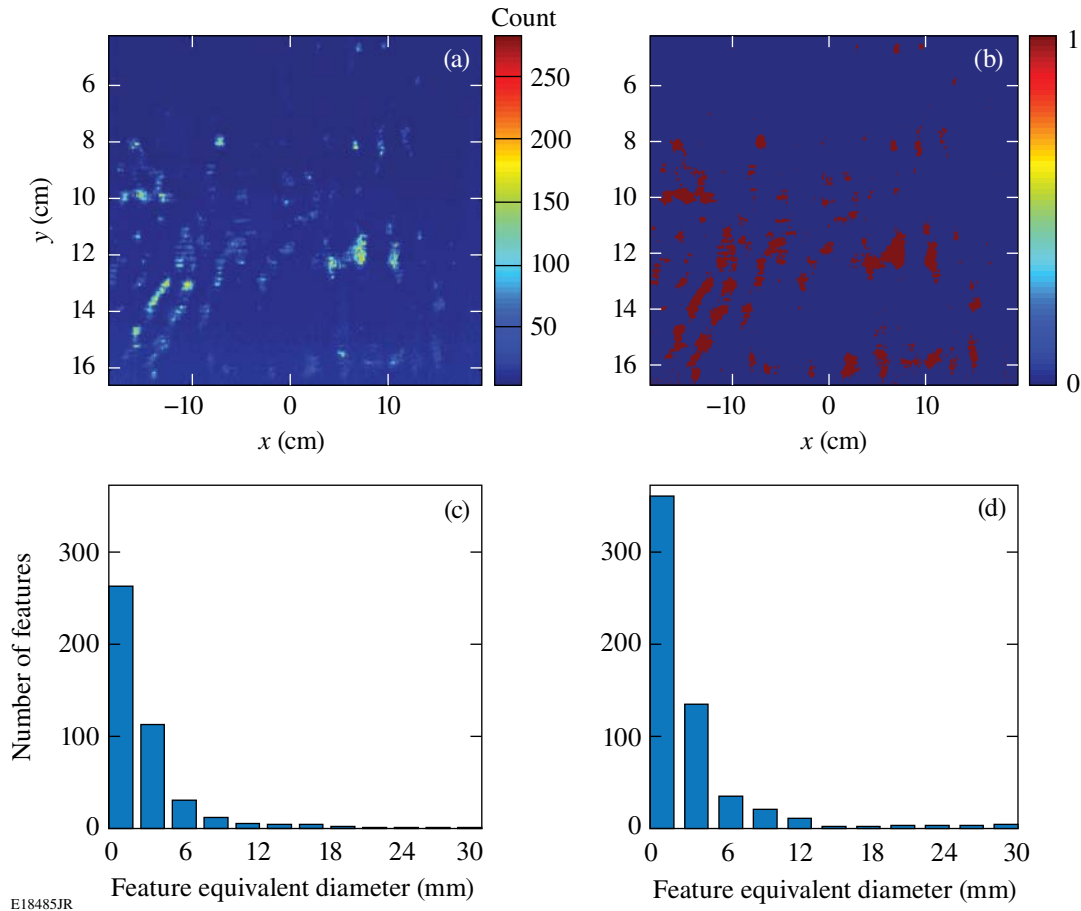


Figure 121.22
 (a) Detected features in ROI 1 prior to the energy ramp; (b) binarized image of the detected features in ROI 1 prior to the energy ramp; (c) histogram of the detected features after the 1120-J shot; (d) histogram of the detected features after the 2210-J shot.

there are already a significant number of features in this ROI.) Figure 121.22(b) shows the corresponding binarized image of Fig. 121.22(a). Figures 121.22(c) and 121.22(d) illustrate the histograms of the detected features within ROI 1 prior to and after the energy ramp, respectively. Comparing histograms of damage sites of two consecutive shots, one can determine the shot energy that caused significant amounts of damage growth.

Owing to the fact that it is very challenging to register the grating-damage map and the beam-fluence map within high precision, the peak fluence within a ROI was used to estimate the upper limit of the fluence causing damage growth within that area. ROI 2 [also shown in Fig. 121.21(b)], measuring $23 \text{ mm} \times 24 \text{ mm}$ of grating 4, had no GIS-detectable features before the energy ramp and exhibited significant change after the completion of the energy ramp. This region was chosen to determine the upper limit of the incident fluence causing damage initiation and growth. The binarized scanning image, dimensions scaled to the laser-beam space, and the corresponding fluence map within ROI 2 for 2.2-kJ shot energy are shown in Figs. 121.23(a) and 121.23(b). The growth in damage versus peak fluence in ROI 2 is shown in Fig. 121.23(c). The fluence at which significant growth in damage occurred was determined to be 3.3 J/cm^2 . This fluence was measured normal to the laser beam (72.5° relative to the grating normal). The corresponding shot energy was 1.58 kJ. The signal on the streak camera used for pulse measurement was saturated on this shot; therefore, no valid pulse measurement was obtained. Our on-shot pulse-prediction model predicted a narrowed, 12.9-ps (FWHM intensity) pulse due to dispersion induced by nonlinear phase accumulations in the glass amplifiers.¹⁷ A similar analysis performed for ROI 1 showed a consistent result.

Accuracy of Peak-Fluence Measurement

The spatial resolution of the fluence measurement [Fig. 121.21(c)] was limited by the coherent transfer function (CTF) of the imaging system. The CTF cutoff frequency of the near-field imaging system was measured to be 0.25 cycles/mm. In addition, this imaging system is downstream of grating 4; therefore, the measurement of the beam fluence at a given location could have been affected by damage that existed prior to a particular shot. It is worth verifying that the peak-fluence measurement was not distorted by any damage on the optics of the diagnostics chain. To estimate the accuracy of peak fluence determined for a given ROI, the image from a different on-shot near-field imaging system was used. This system is located just upstream of the grating compressor [illustrated as IR near-field CCD in Fig. 121.21(a)], and its spatial resolution was measured to be $3\times$ better than the one used to measure

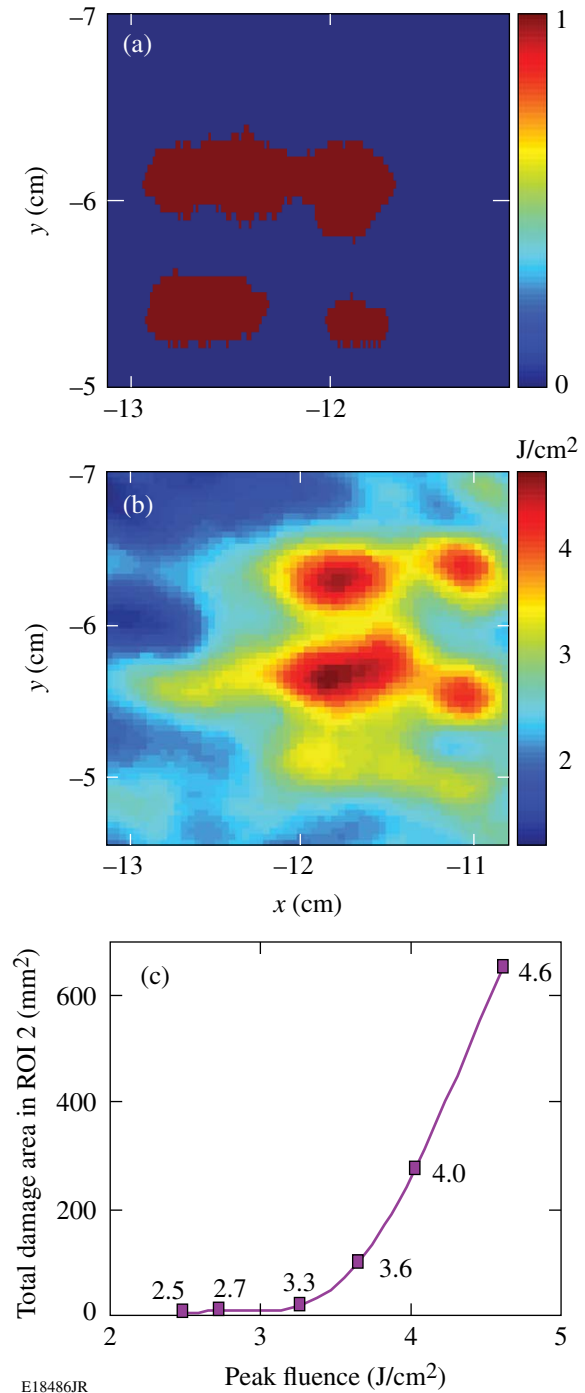


Figure 121.23

(a) Detected features in ROI 2 after the energy ramp; (b) fluence map of ROI 2 of the 2.2-kJ shot; (c) damage size versus beam fluence.

fluence. We then used a propagation model of the compressor, which includes the estimated phase of the beam at the input to the compressor and the phase and intensity effects caused by the compressor, to propagate the fluence map measured at the

input to the compressor to the grating-4 plane. Figure 121.24(a) shows the modeled fluence map for the 2.2-kJ shot. Comparing this fluence map to the measured beam fluence [for ease of comparison, Fig. 121.21(c) is repeated as Fig. 121.24(b)], the measured on-shot peak fluence agrees with the modeled result within 3% and represents the accurate on-shot fluence at grating 4.

Correlation to the Damage-Test Results Obtained on Small Grating Samples

Damage probability versus beam fluence was measured in vacuum on a small-scale, 100-mm-diam MLD-grating sample. This piece was the fabrication witness sample of the large-scale gratings deployed on OMEGA EP. Figure 121.25(a) shows the layout of the damage-test setup for sample gratings.

An excitation beam with a pulse width of 11.5 ps (FWHM) for inducing damage and a 1053-nm continuous-wave illumination beam for detecting damage were co-aligned and co-focused to a 420- μm (width at FWHM) focal spot on the grating surface. The incidence angle of the two beams was 61.4° relative to grating normal. The illumination beam was shuttered during the damage excitation process and was turned on afterward for damage detection. The illumination light was scattered by the induced-damage sites and was imaged to a CCD. The resolution of the CCD was 10 μm /pixel. Change in the scattered image was used to determine the initiation of damage. The sample grating was translated along and across the grating-groove directions for damage tests at various locations. For each fluence, ten sites across the grating sample were chosen, and the percentage of sites damaged was used to determine

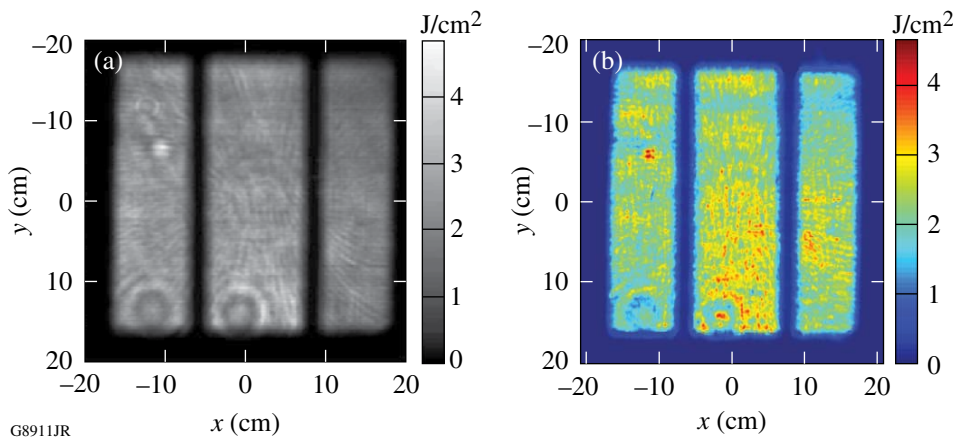


Figure 121.24
(a) The modeled fluence map using the measured fluence at the input of the compressor; (b) measured-beam-fluence map of the 2.2-kJ laser shot.

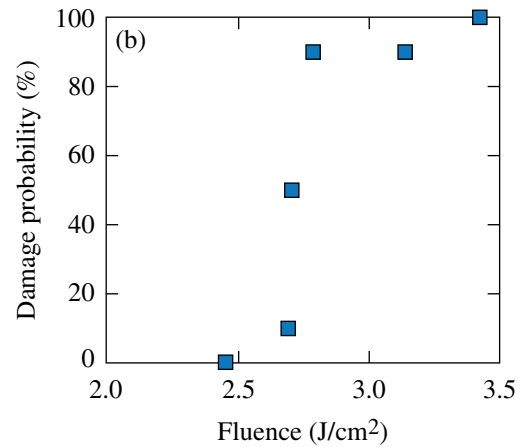
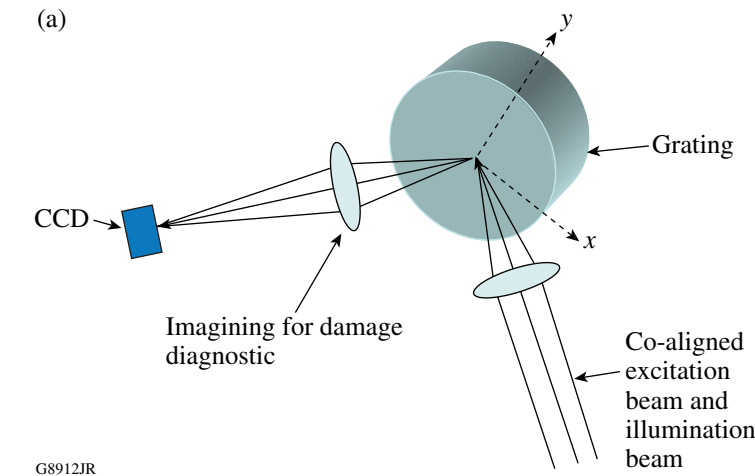


Figure 121.25
(a) Damage-test setup for damage probability at various beam fluences; (b) damage probability versus beam fluence measured on a 100-mm MLD-grating sample in vacuum.

damage probability. Figure 121.25(b) shows damage probability versus peak beam fluence. To compare with damage-test results of the large-aperture grating, the fluence was scaled to the beam space 72.5° relative to grating normal. As shown in Fig. 121.25(b), all ten sites under test were damaged at a fluence of 3.4 J/cm^2 . This result is consistent with the determined fluence, where significant growth in damage occurred for a 12.9-ps pulse on large-scale gratings, taking into account that damage threshold scales approximately with the square root of the pulse length.¹⁸ This is the first damage test comparison between a small-sized witness sample and a large-scale grating. More tests will be conducted and results will be reported in a subsequent publication.

Conclusions

A vacuum-compatible grating-inspection system has been developed to measure the *in-situ* laser-induced damage of a 1.5-m tiled-grating assembly of the OMEGA EP pulse compressor during a 15-ps, 2.2-kJ energy ramp. The grating surface scanning image after each high-energy shot was correlated to the on-shot laser-beam fluence map to determine the relation between damage growth and beam fluence. The upper limit of the fluence at which significant grating-damage growth occurred was determined to be 3.3 J/cm^2 . This result is consistent with damage-probability measurement conducted on a 100-mm-diam witness-grating sample: the measured peak fluence at which 100% selected sites on the small sample were damaged was 3.4 J/cm^2 . The deployment of a GIS makes it possible to operate OMEGA EP safely and effectively because the morphological change of the compressor-grating-surface feature can be monitored in real-time without breaking the vacuum. For future work, the damage-probability measurement on a large-scale grating can be conducted using the damage-detection analysis technique described here. The correlation between grating-damage growth, morphological change, and grating diffraction efficiency degradation should be investigated.

ACKNOWLEDGMENT

We thank Dr. J. H. Kelly for his support on characterizing the coherent transfer functions of the imaging systems for measuring on-shot laser-beam fluence. This work was supported by the U.S. Department of Energy Office of Inertial Confinement Fusion under Cooperative Agreement No. DE-FC52-08NA28302, the University of Rochester, and the New York State Energy Research and Development Authority. The support of DOE does not constitute an endorsement by DOE of the views expressed in this article.

REFERENCES

1. J. H. Kelly, L. J. Waxer, V. Bagnoud, I. A. Begishev, J. Bromage, B. E. Kruschwitz, T. J. Kessler, S. J. Loucks, D. N. Maywar, R. L. McCrory, D. D. Meyerhofer, S. F. B. Morse, J. B. Oliver, A. L. Rigatti, A. W. Schmid, C. Stoeckl, S. Dalton, L. Folsnsbee, M. J. Guardalben, R. Jungquist, J. Puth, M. J. Shoup III, D. Weiner, and J. D. Zuegel, *J. Phys. IV France* **133**, 75 (2006).
2. C. P. J. Barty *et al.*, *Nucl. Fusion* **44**, S266 (2004).
3. N. Blanchot *et al.*, in *Topical Problems of Nonlinear Wave Physics*, edited by A. M. Sergeev (SPIE, Bellingham, WA, 2006), Vol. 5975, p. 59750C.
4. C. Le Blanc *et al.*, in *Inertial Fusion Sciences and Applications 2003*, edited by B. A. Hammel, D. D. Meyerhofer, J. Meyer-ter-Vehn, and H. Azechi (American Nuclear Society, La Grange Park, IL, 2004), pp. 608–611.
5. C. N. Danson *et al.*, *Nucl. Fusion* **44**, S239 (2004).
6. K. Mima *et al.*, *Fusion Sci. Technol.* **47**, 662 (2005).
7. V. Yanovsky *et al.*, *Opt. Express* **16**, 2109 (2008).
8. M. Martinez *et al.*, in *Laser-Induced Damage in Optical Materials: 2005*, edited by G. J. Exarhos *et al.* (SPIE, Bellingham, WA, 2006), Vol. 5991, p. 59911N.
9. J. A. Britten *et al.*, in *Laser-Induced Damage in Optical Materials: 2003*, edited by G. J. Exarhos *et al.* (SPIE, Bellingham, WA, 2004), Vol. 5273, pp. 1–7.
10. J. A. Britten *et al.*, in *Laser-Induced Damage in Optical Materials: 1995*, edited by H. E. Bennett *et al.* (SPIE, Bellingham, WA, 1996), Vol. 2714, pp. 511–520.
11. A. Reichart *et al.*, in *Laser-Induced Damage in Optical Materials: 2000*, edited by G. J. Exarhos *et al.* (SPIE, Bellingham, WA, 2001), Vol. 4347, pp. 521–527.
12. F. Canova *et al.*, *Opt. Express* **15**, 15324 (2007).
13. W.-J. Kong *et al.*, *Chin. Opt. Lett.* **3**, 181 (2005).
14. A. Cotel *et al.*, presented at the Conference on Lasers and Electro-Optics (CLEO 2005), Baltimore, MD, 22–27 May 2005 (Paper JFB6).
15. J. Neauport *et al.*, *Opt. Express* **15**, 12508 (2007).
16. J. Qiao, A. Kalb, T. Nguyen, J. Bunkenburg, D. Canning, and J. H. Kelly, *Opt. Lett.* **33**, 1684 (2008).
17. Y.-H. Chuang, L. Zheng, and D. D. Meyerhofer, *IEEE J. Quantum Electron.* **29**, 270 (1993).
18. LLE grating-sample test result provided by A. W. Schmid, University of Rochester.

Probing High-Areal-Density (ρR) Cryogenic-DT Implosions Using Down-Scattered Neutron Spectra Measured by the Magnetic Recoil Spectrometer

Introduction

Proper assembly of capsule mass, as manifested through the evolution of fuel areal density (ρR),¹⁻³ is essential for achieving hot-spot ignition planned at the National Ignition Facility (NIF).⁴ Experimental information about ρR and ρR asymmetries, ion temperature (T_i), and neutron yield (Y_n) is therefore critical to understanding how the fuel is assembled. To obtain this information, a neutron spectrometer—the magnetic recoil spectrometer (MRS)—is being implemented to measure the absolute neutron spectrum in the range of 5 to 30 MeV (Ref. 5). This range covers all essential details of the spectrum, making it possible to determine ρR , Y_n , T_i , and possible nonthermal features in the neutron spectrum, as discussed in Ref. 5. Another MRS has been built and activated on the OMEGA laser⁶ for diagnosing energy-scaled, low-adiabat cryogenic deuterium-tritium (DT) implosions.⁷ This enables one to experimentally validate the direct-drive-ignition capsule design prior to any experiments at the NIF. Since there are currently no other ways to diagnose ρR values larger than ~ 200 mg/cm² (Ref. 8), the MRS is now playing an important role on OMEGA.^{9,10} The MRS will also play a critical role in guiding the National Ignition Campaign¹¹ toward the demonstration of thermonuclear ignition and net energy gain.

This article will (1) discuss the principle and design of the MRS on OMEGA and the NIF; (2) present the results from the first measurements of the down-scattered neutron spectrum on OMEGA, from which ρR in plastic-capsule implosions and low-adiabat cryogenic-DT implosions have been inferred; (3) discuss the *ab initio* (first-principle) characterization of the MRS and its performance of probing high- ρR implosions at the NIF; and, finally, (4) present conclusions.

The Magnetic Recoil Spectrometer (MRS) on OMEGA and the NIF

1. MRS Principle

The MRS consists of three main components, as shown in Fig. 121.26: a CH (or CD) foil positioned 10 and 26 cm from the implosion on OMEGA and the NIF, respectively, for producing recoil protons (or deuterons) from incident neutrons; a

focusing magnet, located outside the target chamber on both OMEGA and the NIF, for energy dispersion and focusing of forward-scattered recoil particles onto the focal plane of the spectrometer; and an array of CR-39 detectors, positioned at the focal plane, which records the position of each recoil particle with a detection efficiency of 100% (Ref. 12). The spectrum of the recoil protons (or deuterons) is determined by position at the detector plane and used to infer the absolute neutron spectrum, as discussed in Refs. 5 and 13.

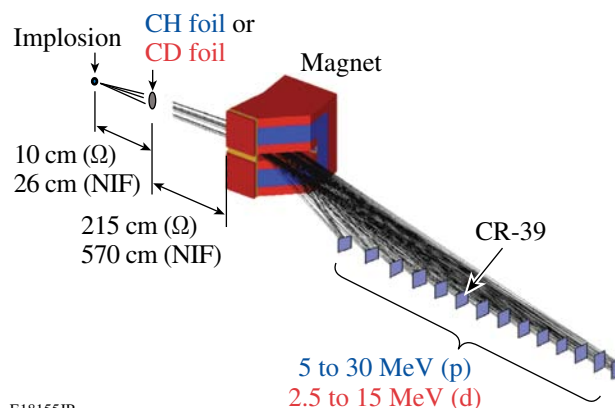


Figure 121.26

A schematic drawing of the MRS, including the CH (or CD) foil, magnet, and CR-39 detector array. The foil is positioned 10 cm and 26 cm from the implosion on OMEGA or the NIF, respectively; the magnet is positioned outside the target chamber on both facilities, i.e., 215 cm from the foil on OMEGA and 570 cm from the foil on the NIF. It is important to the overall design that the same magnet design is used in both the OMEGA MRS and NIF MRS. To detect the forward-scattered recoil protons (or deuterons) when using a CH foil (or CD foil), eleven and nine 7×5 -cm² CR-39 detectors are positioned at the focal plane in the OMEGA MRS and NIF MRS, respectively. The trajectories shown are for proton energies from 5 to 30 MeV, corresponding to deuteron energies from 2.5 to 15 MeV. The length of the detector plane is 166 cm or 84 cm for the OMEGA MRS or NIF MRS, respectively.

An important strength of the MRS is that the technique can be accurately characterized from first principles (*ab initio*), allowing one to perform quantitative signal and background calculations before the system has been built. An *in-situ* calibration, however, is required to check that the system has been

built and installed according to specification. Since the *ab initio* characterization and *in-situ* calibration of the MRS on OMEGA have been described elsewhere,⁵ these efforts will be addressed only briefly in this article. An *ab initio* characterization of the MRS on the NIF is, on the other hand, discussed in detail herein because the system has undergone significant redesign since Ref. 5 was published.

2. MRS Design Considerations

For the MRS to be useful for a wide range of applications on OMEGA and the NIF, it has been designed with the highest-possible detection efficiency (ϵ_{MRS}) for a given energy resolution (ΔE_{MRS}), the largest-possible single-shot dynamic range, and an insensitivity to different types of background. Built-in flexibility has also been included to increase the dynamic range and to more effectively use the MRS for different applications. This is important because a tradeoff between ϵ_{MRS} and ΔE_{MRS} must be applied depending on yield. For instance, for practical implementation of low-yield applications, such as measurements of down-scattered neutrons from cryogenic-DT implosions on OMEGA and low-yield tritium–hydrogen–deuterium (THD)¹⁴ implosions on the NIF, it is necessary to degrade ΔE_{MRS} to increase ϵ_{MRS} . For high-yield applications, on the other hand, such as measurements of down-scattered

neutrons from DT implosions on the NIF, the MRS can be configured to operate in a high-resolution/low- ϵ_{MRS} mode. Several options are available for configuring the MRS: Either a CH or CD foil can be selected to produce recoil protons or deuterons and, therefore, whether the energy range covered for neutrons is 5.0 to 30 MeV or 3.1 to 16.9 MeV. The foil area and foil thickness can be adjusted to change the ϵ_{MRS} and ΔE_{MRS} . Table 121.VI illustrates the MRS configurations that will be used on the NIF and OMEGA, depending on application. Geant4 (Ref. 15) and a Monte Carlo code were used for the *ab initio* modeling of the MRS (and for assessing its performance when probing high- ρR implosions at the NIF), when operated in the different configurations shown in Table 121.VI. The results from that modeling at 14 MeV are also shown in Table 121.VI.

The principal sources of background are primary neutrons and neutrons scattered by the chamber wall, diagnostics, and other structures surrounding the MRS. Soft and hard x rays, as well as γ rays, are not an issue since the CR-39 is immune to these types of radiation. Although the CR-39 efficiency for detecting primary neutrons is small¹⁶ ($\epsilon_{\text{CR-39}} \approx 6 \times 10^{-5}$), measures are required to reduce the neutron fluence to the required level for successful implementation of the MRS down-scattered

Table 121.VI: Configurations for the MRS on the NIF and OMEGA. Different configurations will be used, depending on application. The OMEGA MRS settings are shown in the parentheses. The low-resolution/high-efficiency mode (Low-Res) will be used when yields are expected to be below 10^{14} (the values in parentheses are for the MRS on OMEGA when diagnosing cryogenic-DT implosions), the medium-resolution/medium-efficiency mode (Med-Res) will be used when yields are expected to be in the range 10^{14} to 10^{18} (the values in the parentheses are for the MRS on OMEGA when diagnosing plastic-capsule implosions), and the high-resolution/low-efficiency mode (High-Res) can be used when yields are expected to be above $\sim 10^{15}$. The computed ϵ_{MRS} and ΔE_{MRS} values at 14 MeV are shown as well. Similar performance is obtained with a CD foil that is about a factor of 2 thinner than the CH foil specified in the table.

	NIF High-Res	NIF (OMEGA) Med-Res	NIF (OMEGA) Low-Res
Yield range	10^{15} to 10^{19}	10^{14} to 10^{18} ($>10^{13}$)	$<10^{14}$ ($>10^{12}$)
Magnet distance to foil (cm)	570	570 (215)	570 (215)
Magnet aperture area (cm ²)	20	20 (22)	20 (22)
Foil distance to TCC* (cm)	26	26 (10)	26 (10)
Foil area (cm ²)	13	13 (10)	13 (10)
CH-foil thickness (μm)	100	250 (250)	550 (550)
ΔE_{MRS} (FWHM) at 14 MeV (keV)	480	820 (850)	1810 (1830)
ϵ_{MRS} at 14 MeV	2×10^{-11}	5×10^{-11} (2×10^{-9})	10^{-10} (4×10^{-9})

*TCC: Target chamber center.

neutron measurements on the NIF (and also on OMEGA as discussed in detail in Ref. 5). This is achieved by adding polyethylene shielding to the MRS as a first step and positioning the CR-39 detector array in the shadow of the NIF target chamber. As the CR-39 detector array is positioned on an off-axis detection plane that is well outside the target chamber, enough space exists to position ~6000 lbs of polyethylene shielding around the MRS [see Figs. 121.27(a) and 121.27(b)]. Through neutron-transport simulations using the MCNP code,¹⁷ it was established that the shielding reduces the neutron fluence from $\sim 10^{-7} \text{ cm}^{-2}$ to $\sim 3 \times 10^{-9} \text{ cm}^{-2}$ ($E_n > 100 \text{ keV}$) per produced neutron at the CR-39 detector array.¹⁸ Additional reduction of the background (neutron-induced and intrinsic background¹⁹) is required for successful implementation of the down-scattered neutron measurements for low-yield THD implosions on the NIF (and for cryogenic-DT and plastic-capsule implosions on OMEGA). This is accomplished by the coincidence-counting technique (CCT),¹⁹ which uses the fact that incident signal particles (protons or deuterons) pass straight through the CR-39 material, resulting in front and backside tracks that are correlated. Signal tracks can therefore be distinguished relatively easily from background tracks (neutron-induced and intrinsic tracks) using the CCT since the latter tracks are

generated mainly on one of the surfaces. Applying the CCT to OMEGA MRS data demonstrated orders-of-magnitude signal-to-background (S/B) improvement.¹⁹ For high-yield scenarios, such as an ignited case, the standard counting technique (SCT) must instead be applied to the data because the CCT is not effective at high track densities.¹⁹ As a consequence, the S/B ratio is reduced but compensated by a high signal-to-noise ratio.

Probing Plastic and Cryogenic-DT Implosions on OMEGA Using Down-Scattered Neutrons

The ρR in DT-filled-plastic-capsule implosions on OMEGA has been routinely diagnosed for more than a decade. In these experiments, two magnet-based charged-particle spectrometers (CPS's),¹² shown in Fig. 121.28, have been used to measure the spectrum of knock-on deuterons (KO-D's), elastically scattered by primary DT neutrons, from which fuel ρR can be inferred.²⁰⁻²² With the implementation of the MRS (Fig. 121.28), spectral measurements of the complementary particle, i.e., the down-scattered neutron, are now possible. From the measured neutron spectrum, the yield ratio between down-scattered neutrons and primary neutrons is determined. This yield ratio, called down-scattered fraction (dsf), is to the first order proportional to the fuel ρR and probes the com-

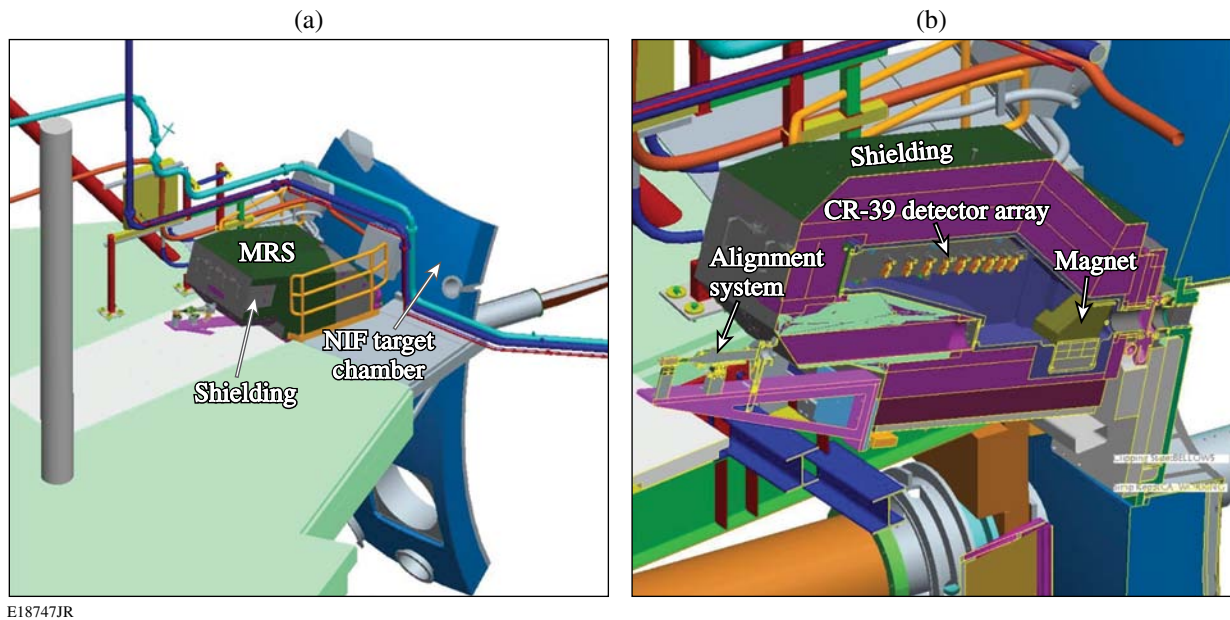
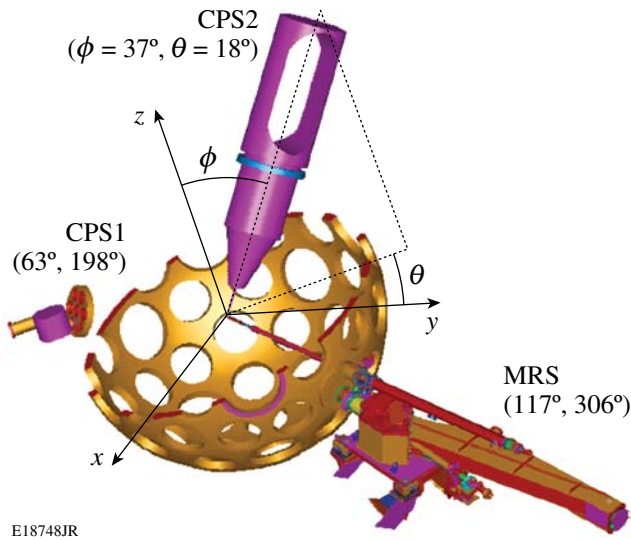


Figure 121.27 (a) An engineering drawing of the MRS positioned onto the NIF target chamber at a 77° to 324° line of sight. For maximum suppression of the neutron-induced background, the CR-39 detector array is fully enclosed by ~6000 lbs of polyethylene shielding (gray and green) and positioned in the shadow of the 60-cm-thick NIF target chamber (50 cm of concrete and 10 cm of aluminum). (b) A vertical cross cut through the MRS illustrating the various components in the system, i.e., the magnet, CR-39 detector array, alignment system, and shielding. The diagnostic insertion manipulator (DIM) (90° to 315°), not shown in these figures, will be used to insert the foil to a distance of 26 cm from the implosion.

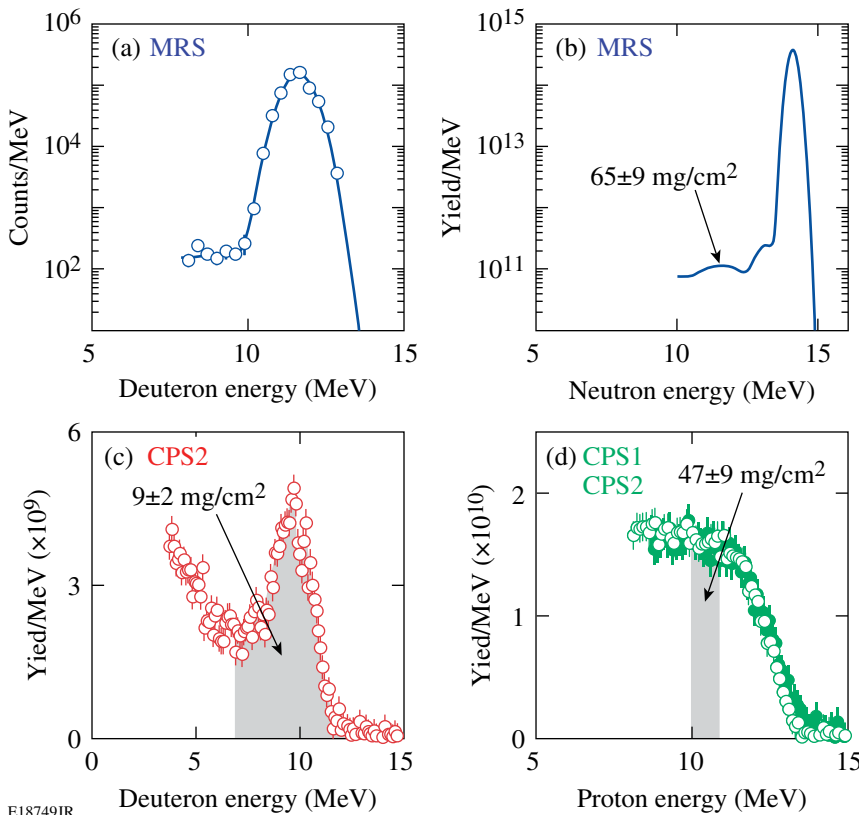


E18748JR

Figure 121.28
MRS, CPS1, and CPS2 on the OMEGA chamber. The MRS is shown here without the 2000-lb shielding that surrounds the diagnostic. The line of sight for each diagnostic is illustrated in terms of the polar angle ϕ and azimuthal angle θ . These spectrometers measure the spectra of KO-D's (CPS1 and CPS2) and down-scattered neutrons (MRS), from which fuel ρR and ρR asymmetries in cryogenic-DT implosions are inferred.

pression performance of an implosion.⁵ To more accurately establish the relationship between ρR and the measured dsf , second-order effects, caused by implosion geometry (profiles of primary source and fuel density), were considered as well by using 1-D Monte Carlo and hydro modeling of an implosion. Any geometrical 3-D effects have, on the other hand, not been considered in the modeling. This is a topic for future work.

Measurements of the down-scattered neutron spectrum have been conducted for the first time using the MRS on OMEGA. From the measured dsf (in the neutron-energy range of 10 to 12 MeV, which corresponds to the deuteron-energy range of about 8 to 10 MeV and ~ 7 to 9 MeV when the MRS is operated in Med-Res and Low-Res modes, respectively), ρR values have been inferred for both low- ρR plastic-capsule implosions and low-adiabat, high- ρR cryogenic-DT implosions. Data points at neutron energies below 10 MeV were excluded in the analysis since it is comprised primarily by T-T (triton-on-triton) neutrons. The ρR data obtained by well-established CPS techniques were used to authenticate the MRS data for these low- ρR plastic-capsule implosions. This authentication is shown in Figs. 121.29 and 121.30, which illustrate integrated MRS and CPS data for a series of eight CH-capsule implosions



E18749JR

Figure 121.29

Integrated MRS and CPS data obtained for a series of eight CH-capsule implosions producing 1.6×10^{14} primary neutrons (neutron-averaged T_i was 5.3 keV). In each shot, a capsule with a 15- μm -thick CH shell filled with 15 atm of DT gas was imploded with a 1-ns square pulse delivering ~ 23 kJ of laser energy. (a) The MRS-measured deuteron spectrum and fit to the measured spectrum, which are convolutions of the neutron spectrum and MRS-response function. In these measurements, the MRS was operated with a CD foil in Med-Res mode (see Table 121.VI). From the dsf value determined from the modeled neutron spectrum, shown in (b), a total ρR (fuel + shell) of $65 \pm 9 \text{ mg/cm}^2$ was inferred. Data points at neutron energies below 10 MeV were excluded in the analysis since they are comprised primarily of T-T neutrons. (c) CPS2 measured spectrum of KO-D's produced in the fuel. From the yield in the high-energy peak²⁰ (gray), a fuel ρR of $9 \pm 2 \text{ mg/cm}^2$ was inferred. (d) CPS1 and CPS2 measured spectra of knock-on protons (KO-P's) produced in the shell. From the yield in the plateau²⁰ (gray), a shell ρR of $47 \pm 9 \text{ mg/cm}^2$ was inferred. A total ρR of $56 \pm 10 \text{ mg/cm}^2$ was therefore determined from the CPS1 and CPS2 data. Given that $\pm 15\%$ ρR asymmetries are typically observed for this type of implosion, the ρR values determined from the MRS and CPS data are in good agreement.

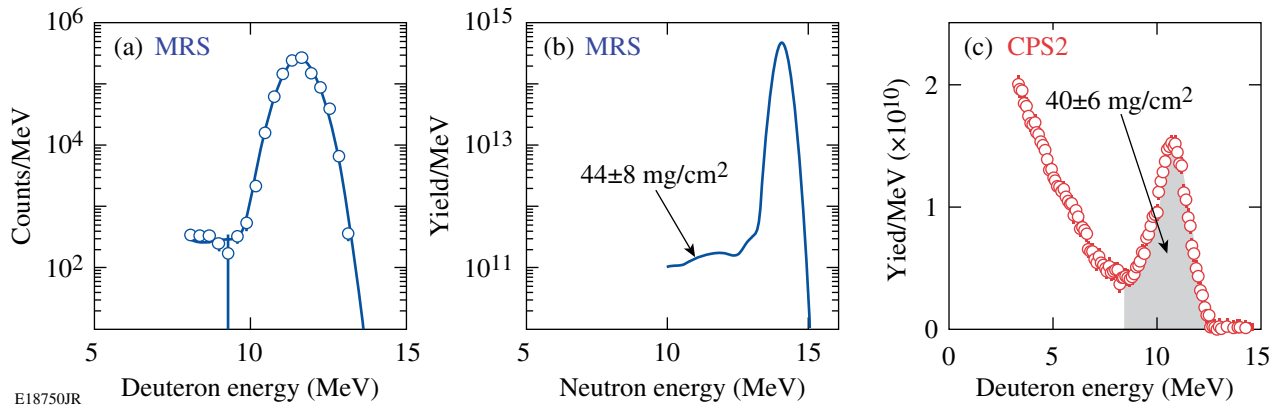


Figure 121.30

Integrated MRS and CPS data obtained for a series of five CD-capsule implosions producing 2.6×10^{14} primary neutrons (neutron-averaged T_i was 8.0 keV). In each shot, a capsule with a 10- μm -thick CD shell filled with 10 atm of DT gas was imploded with a 1-ns square pulse delivering ~ 23 kJ of laser energy. (a) The MRS-measured deuteron spectrum and fit to the measured spectrum, which are convolutions of the neutron spectrum and MRS-response function. In these measurements, the MRS was operated with a CD foil in Med-Res mode (see Table 121.VI). From the dsf value determined from the modeled neutron spectrum, shown in (b), a total ρR (fuel + shell) of 44 ± 8 mg/cm² was inferred. Data points at neutron energies below 10 MeV were excluded in the analysis since they are primarily comprised of T-T neutrons. (c) CPS2 measured spectrum of KO-D's produced in the fuel and shell. From the yield in the high-energy peak²⁰ (gray), a total ρR of 40 ± 6 mg/cm² was inferred, which is in excellent agreement with the ρR value determined from the MRS.

and a series of five CD-capsule implosions, respectively. As shown by the data, the ρR values inferred from the two different techniques are in good agreement, considering the error bars and that $\pm 15\%$ ρR asymmetries are typically observed for these types of implosions. These results indicate that the MRS technique provides high-fidelity ρR data.

An essential step in achieving high fuel compression and high ρR in direct-drive cryogenic-DT implosions on OMEGA is to minimize the shock preheating of the main fuel and therefore maintain the fuel adiabat at the lowest-possible value throughout the pulse. This is achieved by using a multiple-picket laser-drive design,¹⁰ in which the individual picket energies and temporal spacing have been tuned to generate a series of decaying shocks that are designed to coalesce simultaneously with the main drive at the inner surface of the main fuel. Areal density data obtained with the MRS, CPS1, and CPS2 were used to find the multiple-picket laser-drive design that provides maximum compression. From the shape of the CPS-measured KO-D spectrum, the ρR is determined for moderate- ρR cryogenic-DT implosions (up to ~ 180 mg/cm²) (Ref. 8). For ρR values higher than ~ 180 mg/cm², assessment of the implosion performance relies on the MRS data. Examples of MRS data obtained for three low-adiabat cryogenic-DT implosions are shown in Fig. 121.31. The MRS-measured deuteron spectra and fits to the measured data, which are convolutions of the neutron spectra and MRS-response function, are shown in Fig. 121.31(a). The modeled neutron spectra that give the best fits to the measured data are shown in Fig. 121.31(b). From the

modeled neutron spectra, dsf values and therefore ρR values were determined for these implosions. A ρR of 83 ± 13 mg/cm² was determined for shot 54926 (imploded with an alpha-3 laser pulse), which is $\sim 40\%$ of the 1-D value—a result caused by incorrectly tuned pickets in front of the main drive. A ρR of 179 ± 34 mg/cm² was determined for shot 55231 (imploded with an alpha-3 laser pulse). In this case, the multiple pickets were tuned correctly, resulting in a ρR value closer to the 1-D value of 220 mg/cm². For shot 55723, a ρR of 295 ± 47 mg/cm² was determined (imploded with an alpha-2 laser pulse), which is $\sim 95\%$ of the 1-D value. Proper shock timing was applied in this case as well. All ρR data to date inferred from the CPS systems are shown in Fig. 121.32 as a function of ρR data inferred from the MRS. The open data points were obtained when the imploding capsule was centered close to target chamber center (TCC) and had a high-quality ice layer. As expected, these data points are close to the symmetric-implosion line (dashed line). At ρR values higher than ~ 180 mg/cm² these data points follow the horizontal line at which the CPS technique has saturated (this upper limit depends somewhat on the density and temperature profiles at bang time). In these high- ρR cases, assessment of the compression performance relies on the MRS data, ice-layer data, and offset data. In addition, the solid data points shown in Fig. 121.32 were obtained when the imploding capsule had a poor ice layer and was significantly offset from TCC. As illustrated by these data points, the poor ice layer and large offset have a detrimental impact on the ρR symmetry of an implosion. This is also generally the case when the offset is larger than the hot-spot radius at peak compression.⁹

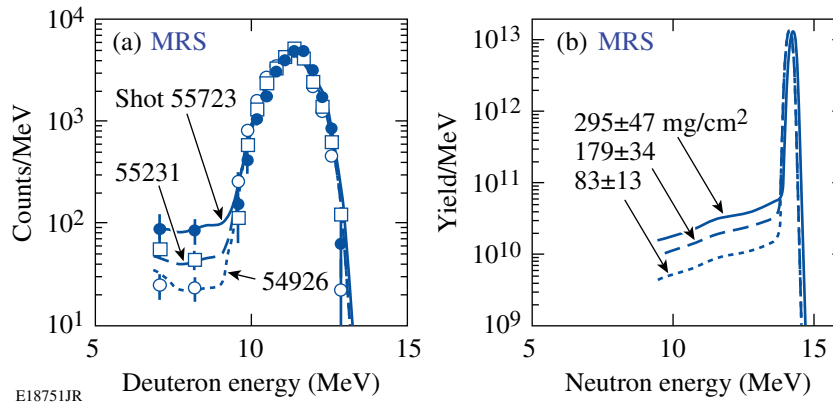


Figure 121.31

MRS data obtained for three low-adiabat cryogenic-DT implosions producing neutron yields in the range of 2×10^{12} to 4×10^{12} (neutron-averaged T_i was ~ 2 keV for these implosions). (a) MRS-measured deuteron spectra for the three implosions and fits to the measured spectra, which are convolutions of the underlying neutron spectra and the MRS-response function. In these measurements, the MRS was operated with a CD foil in Low-Res mode (see Table 121.VI). From the modeled neutron spectra, shown in (b), dsf values and, therefore, ρR 's were determined for the three implosions. A ρR of 83 ± 13 mg/cm² was determined for shot 54926 (imploded with an alpha-3 laser pulse), which is $\sim 40\%$ of the 1-D value—a result of a poorly designed laser drive. A ρR of 179 ± 34 mg/cm² was determined for shot 55231 (imploded with an alpha-3 laser pulse). In this case, the picket pulses in front of the main laser drive were tuned correctly, resulting in a ρR value closer to the 1-D value of 220 mg/cm². For shot 55723, a ρR of 295 ± 47 mg/cm² was determined (imploded with an alpha-2 laser pulse), which is in agreement with the 1-D ρR value considering the error bar. An optimal multiple-picket laser drive was applied in this case as well.

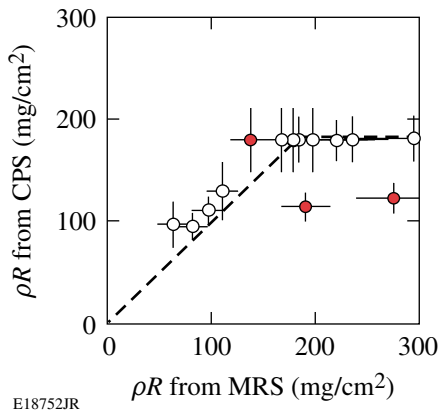


Figure 121.32

The ρR inferred from CPS data as a function of ρR inferred from MRS data. The open data points were obtained when the imploding capsule had a high-quality ice layer and was centered close to TCC, while the solid points were obtained when the imploding capsule had a poor ice layer and was significantly offset from TCC. As expected, the open data points are close to the symmetric-implosion line (dashed line). At ρR values higher than ~ 180 mg/cm², the assessment of the compression performance must rely on MRS data, ice-layer data, and offset data since the CPS technique has saturated. As shown by the solid data points, the poor ice layer and large offset have a detrimental impact on the ρR symmetry of an implosion. This is also generally the case when the offset is larger than the hot-spot radius at peak compression.

Ab initio Characterization of the MRS at the NIF

The performance of a low-yield THD or a high-yield DT implosion at the NIF can be expressed in terms of the ignition threshold factor (ITF),²³ which is a strong function of the

total ρR , T_i , and ρR of the hot spot. Although the ITF is not an accurate representation describing the implosion performance, it provides guidance for how accurately these implosion parameters should be determined at the NIF. From 1-D and 2-D LASNEX²⁴ simulations it has been concluded that the ITF should be determined to an accuracy better than $\pm 30\%$, which puts strong requirements on the ρR and T_i determination. Table 121.VII illustrates one set of requirements that is consistent with the $\pm 30\%$ -ITF-accuracy requirement for determining dsf , T_i , and Y_n in THD and DT implosions (in the yield range of 10^{14} to 10^{19}). Also shown in the table are the expected absolute and relative measurement uncertainties that the MRS will provide for these implosion parameters. These numbers were determined from MRS spectra simulated by a Monte Carlo code that used LASNEX-simulated neutron spectra as input (see Fig. 121.33). From the MRS signal and background levels, the relative uncertainties were computed, as discussed in **Appendix A** (p. 40), where the systematic uncertainties are also derived. As shown by the numbers in Table 121.VII, it is clear that the MRS will meet the requirements for diagnosing both low-yield THD and high-yield DT implosions.

To accurately determine dsf values from measured MRS spectra, different proton-energy, or deuteron-energy, ranges must be used depending on MRS configuration and type of implosion diagnosed. Table 121.VIII illustrates the proton-energy ranges used for the MRS configured with a CH foil and operated in High-Res, Med-Res, and Low-Res modes.

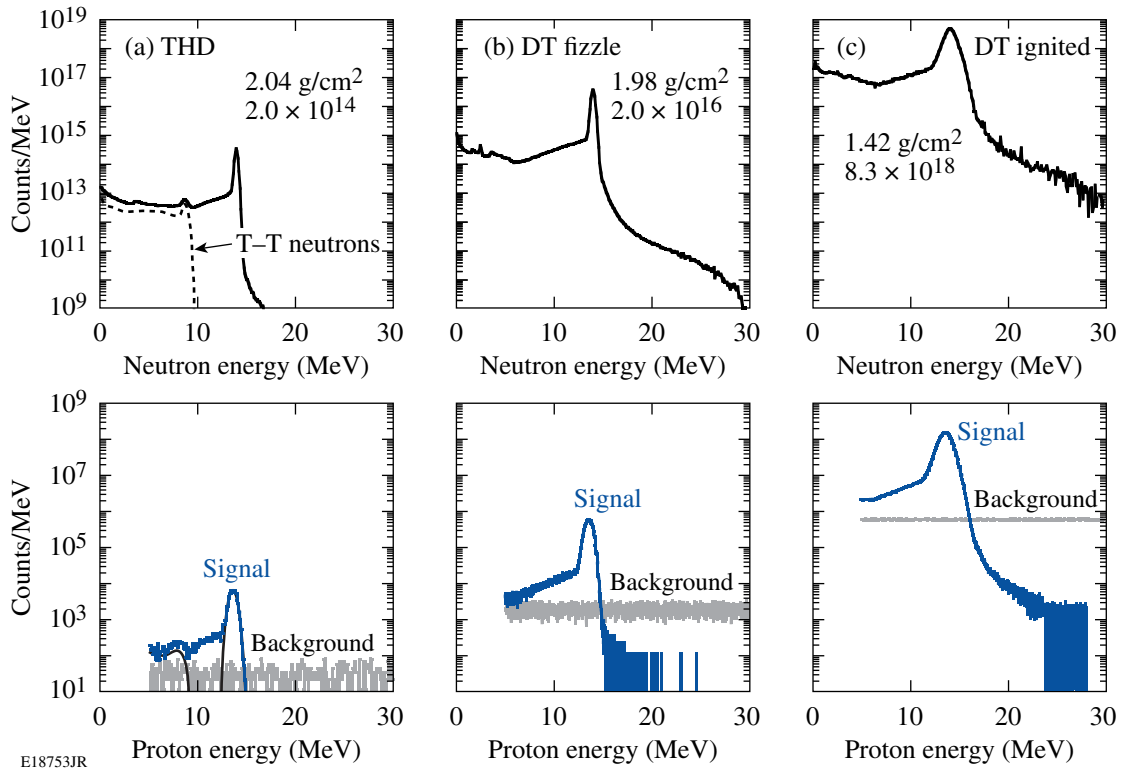


Figure 121.33

A set of LASNEX-simulated neutron spectra and associated MRS signal and background spectra for three NIF implosions: (a) a low-yield THD implosion (the dashed line indicates the T-T neutron spectrum), (b) a fizzle DT implosion, and (c) an ignited DT implosion. The T-T neutron component in the two DT cases is insignificant and, therefore, not shown. The total ρR and Y_n for each implosion are shown in each figure. These spectra were simulated for the MRS configured with a CH foil (Med-Res mode). The CCT, recently developed and now routinely used to analyze OMEGA MRS data, was applied to determine the MRS signal and background spectra for the low-yield THD and fizzle DT implosions. For the ignited case, a standard counting technique (SCT) was applied to the data since the CCT is not effective at high track densities.¹⁹ As shown by the spectra, excellent S/B is achieved for the dsf , T_i , and Y_n measurements.

Table 121.VII: Requirements and expected uncertainties for the MRS measuring the down-scattered fraction (dsf) (which to the first order depends on ρR), T_i , and Y_n produced in THD and DT implosions at the NIF.

		Physics requirements		Expected measurement uncertainties*	
Campaign	Parameter	Absolute	Relative	Absolute (Fig. 121.34; Table 121.IX)	Relative (Fig. 121.34)
THD (2×10^{14})	dsf	$\pm 7\%$	$\pm 5\%$	$\pm 6\%$	$\pm 4\%$
	T_i	$\pm 3\%$	$\pm 3\%$	$\pm 16\%$	$\pm 15\%$
	Y_n	$\pm 8\%$	$\pm 2\%$	$\pm 5\%$	$\pm 2\%$
DT (2×10^{16})	dsf	$\pm 7\%$	$\pm 5\%$	$\pm 3\%$	$\pm 0.5\%$
	T_i	$\pm 3\%$	$\pm 3\%$	$\pm 3\%$	$\pm 1\%$
	Y_n	$\pm 8\%$	$\pm 2\%$	$\pm 4\%$	$\pm 0.2\%$
DT 10^{17} to 10^{19}	dsf	$\pm 7\%$	$\pm 5\%$	$\pm 3\%$	$\pm 0.2\%$
	T_i	$\pm 3\%$	$\pm 3\%$	$\pm 3\%$	$\pm 0.3\%$
	Y_n	$\pm 8\%$	$\pm 2\%$	$\pm 4\%$	$\pm 0.1\%$

*The absolute measurement uncertainties are due to both systematic and statistical uncertainties. The relative uncertainties are due only to statistical uncertainties.

Table 121.VIII: Proton-energy ranges for determining the dsf value from the measured MRS spectra. In the THD case, the T-T neutron spectrum sets a lower limit for the dsf determination. The primary peak, broadened by the MRS-response function, sets an upper limit for both the THD and DT cases.

	High-Res*	Med-Res*	Low-Res
THD	9.5 to 13.0 MeV	9.4 to 12.5 MeV	9.3 to 11.3 MeV
DT	5.0 to 13.0 MeV	5.0 to 12.5 MeV	5.0 to 11.3 MeV

*The useful proton-energy range for the dsf determination is narrower if the implosion ignites. In this case, the energy range is 5 to 11.5 MeV.

These energy ranges were also used to determine the statistical uncertainties for the dsf values shown in Table 121.VII.

Summary

For the first time, down-scattered neutron spectra have been measured using the MRS, recently installed and commissioned on OMEGA. From the measured down-scattered neutron spectrum, a dsf value has been measured from which ρR has been inferred for both low- ρR plastic-capsule implosions and low-adiabat, high- ρR cryogenic-DT implosions. The ρR data obtained from the well-established CPS technique were used to authenticate the MRS data for these low- ρR plastic-capsule implosions, and results illustrate good agreement between the two techniques. In addition, the ρR data obtained from the MRS for the low-adiabat, high- ρR cryogenic-DT implosions have been essential for understanding how the fuel is assembled and for guiding the cryogenic program at LLE to ρR values up to ~ 300 mg/cm².

Recent OMEGA MRS data and Monte Carlo simulations indicate that the MRS on the NIF will meet most of the absolute and relative requirements for determining ρR , T_i , and Y_n in both low-yield THD and high-yield DT implosions.

ACKNOWLEDGMENT

The work described here was supported in part by the U.S. Department of Energy (Grant No. DE-FG03-03SF22691), LLE (No. 412160-001G), LLNL (No. B504974), and GA under DOE (DE-AC52-06NA27279). This work was also supported by the U.S. Department of Energy Office of Inertial Confinement Fusion under Cooperative Agreement No. DE-FC52-08NA28302, the University of Rochester, and the New York State Energy Research and Development Authority. The support of DOE does not constitute an endorsement by DOE of the views expressed in this article.

Appendix A: Statistical and Systematic Uncertainties for the MRS at the NIF

From the simulated MRS signal and background spectra (three example spectra are shown in Fig. 121.33), it is readily straightforward to calculate the statistical uncertainties for the measured dsf , T_i , and Y_n . Equation (A1) represents the statisti-

cal uncertainty associated with the dsf value; Eq. (A2) represents the statistical uncertainty associated with T_i (Ref. 25); and Eq. (A3) represents the statistical uncertainty associated with Y_n :

$$\frac{\Delta(dsf)}{dsf} = \frac{\sqrt{S_{ds} + 2B}}{S_{ds}}, \quad (A1)$$

$$\frac{\Delta T_i}{T_i} = \left[1 + \left(\frac{\Delta E_{MRS}}{\Delta E_D} \right)^2 \right] \frac{1}{\sqrt{S_p}}, \quad (A2)$$

$$\frac{\Delta Y_n}{Y_n} = \frac{1}{\sqrt{S_p}}. \quad (A3)$$

Here, S_{ds} is the integrated down-scattered neutron signal in the selected energy range shown in Table 121.VIII, B is the total background in this energy range, ΔE_D is the width of the Doppler-broadened neutron spectrum, which is to the first order equal to $177\sqrt{T_i}$ for the DT reaction (T_i given in keV) (Ref. 26), and S_p is the integrated primary neutron signal. As shown by Eq. (A3), the yield uncertainty can be expressed in terms of only S_p because the primary signal is orders of magnitude higher than the background. These equations were applied to simulated MRS spectra for 13 different implosions, which resulted in the statistical uncertainties shown in Fig. 121.34.

For illustration purposes, as well as for calculating systematic uncertainties involved with the MRS, it is useful to express ϵ_{MRS} and ΔE_{MRS} as⁵

$$\epsilon_{MRS}(E_n) = \frac{\Omega_n}{4\pi} \cdot n_i \cdot t_f \int \frac{d\sigma(E_n)}{d\Omega_{lab}} d\Omega \quad (A4)$$

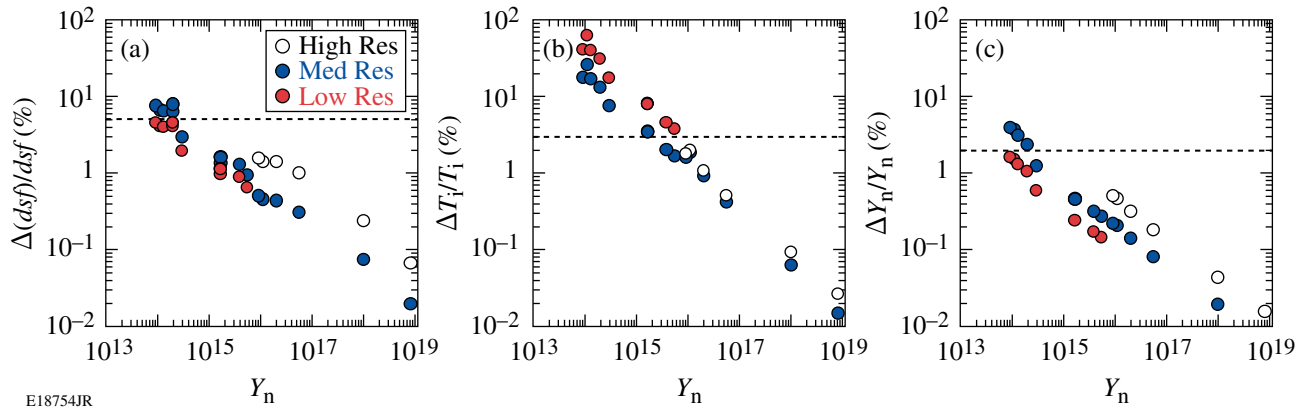


Figure 121.34

Statistical measurement uncertainty for (a) dsf , (b) T_i , and (c) Y_n as a function of neutron yield when the MRS is operating in High-Res, Med-Res, and Low-Res modes. Thirteen implsions were used in these calculations. The relative requirements, illustrated in Table 121.VII, are indicated by the dashed lines.

and

$$\Delta E_{\text{MRS}}(E_n) \approx \sqrt{\Delta E_f^2(E_n) + \Delta E_k^2(E_n) + \Delta E_m^2(E_n)}, \quad (\text{A5})$$

respectively. Here, Ω_n is the solid angle subtended by the foil, n_i is the hydrogen (or deuterium) number density in the foil, t_f is the thickness of the foil, $d\sigma(E_n)/d\Omega_{\text{lab}}$ is the differential elastic-scattering cross section in the laboratory frame, “ Ω_a ” is the solid angle subtended by the aperture in front of the magnet, ΔE_f is the energy broadening in the conversion foil, ΔE_k is the kinematic energy broadening, and ΔE_s is the ion-optical broadening. Since the solid angle subtended by the foil can be expressed in terms of foil area (A_f) and foil distance (R_f), and the differential elastic cross section integrated over the solid angle subtended by the magnet aperture can be approximated by $d\sigma/d\Omega_{\text{lab}}(E_n, 0^\circ) \cdot (A_a/R_a^2)$ (where A_a is the magnet aperture area and R_a is the magnet-aperture distance to the foil), Eq. (A4) can be rewritten as

$$\varepsilon_{\text{MRS}}(E_n) \approx \frac{A_f}{4\pi R_f^2} \cdot n_i \cdot t_f \cdot \frac{d\sigma(E_n, 0^\circ)}{d\Omega_{\text{lab}}} \cdot \frac{A_a}{R_a^2}. \quad (\text{A6})$$

Using Eq. (A6) and the Brysk formula,²⁶ Y_n , dsf , and T_i can now be expressed as

$$Y_n \approx \frac{S_p}{\frac{A_f}{4\pi R_f^2} \cdot n_i \cdot t_f \cdot \frac{d\sigma(E_n, 0^\circ)}{d\Omega_{\text{lab}}} \cdot \frac{A_a}{R_a^2}}, \quad (\text{A7})$$

$$dsf \approx \frac{\frac{d\sigma(p, 0^\circ)}{d\Omega_{\text{lab}}} S_{\text{ds}}}{\frac{d\sigma(ds, 0^\circ)}{d\Omega_{\text{lab}}} S_p}, \quad (\text{A8})$$

and

$$T_i = \frac{1}{177^2} [\Delta E_{\text{meas}}^2 - \Delta E_{\text{MRS}}^2], \quad (\text{A9})$$

respectively. Here, p and ds in Eq. (A8) represent the average energy of primary and down-scattered neutrons, respectively, and ΔE_{meas} is the width of the measured primary spectrum. An expression for the systematic uncertainty involved with the dsf , Y_n , and T_i measurements can now be derived from Eqs. (A7)–(A9), i.e.,

$$\frac{\sigma_{Y_n}}{Y_n} \approx \sqrt{\left(\frac{\sigma_{A_f}}{A_f}\right)^2 + \left(\frac{\sigma_{R_f}}{R_f}\right)^2 + \left(\frac{\sigma_{n_i}}{n_i}\right)^2 + \left(\frac{\sigma_{t_f}}{t_f}\right)^2 + \left[\frac{\sigma_{d\sigma(p, 0^\circ)}}{d\Omega_{\text{lab}}}\right]^2 + \left(\frac{\sigma_{A_a}}{A_a}\right)^2 + 4\left(\frac{\sigma_{R_a}}{R_a}\right)^2}, \quad (\text{A10})$$

Table 121.IX: Systematic uncertainties for the different parameters expressed in Eqs. (A9) and (A10) and their combined contribution to the total error for the different MRS configurations shown in Table 121.VII. These numbers are valid only for the CH foils. The cross-section uncertainties involved with the CD foil are about a factor of 2 higher than the ones involved with the CH foil.

	Absolute	High-Res (%)	Med-Res (%)	Low-Res (%)
Foil area uncertainty	$\pm 0.3 \text{ cm}^2$	± 2.3	± 2.3	± 2.3
Foil distance uncertainty	$\pm 0.1 \text{ cm}$	± 0.4	± 0.4	± 0.4
Number density uncertainty	$\pm 10^{21} \text{ cm}^3$	± 1.3	± 1.3	± 1.3
Foil thickness uncertainty	$\pm 2.0 \text{ mm}$	± 2.0	± 0.8	± 0.4
Cross section uncertainty (p)	$\pm 3 \text{ mb/sr}$	± 1.4	± 1.4	± 1.4
Cross section uncertainty (ds)	$\pm 0.9 \text{ mb/sr}$	± 2.5	± 2.5	± 2.5
Magnet-aperture area uncertainty	$\pm 0.2 \text{ cm}^2$	± 1.0	± 1.0	± 1.0
Response function uncertainty	$\pm 10 \text{ keV}$	± 2.1	± 1.1	± 0.6
Magnet-aperture distance uncertainty	$\pm 0.1 \text{ cm}$	± 0.02	± 0.02	± 0.02
Total uncertainty for Y_n		± 4.5	± 4.1	± 4.0
Total uncertainty for dsf		± 2.9	± 2.9	± 2.9
Total uncertainty for T_i (at 5 keV)		± 2.9	± 6.4	± 13.4

$$\frac{\sigma_{dsf}}{dsf} \approx \sqrt{\left(\frac{\sigma_{d\sigma(p,0^\circ)}}{d\Omega_{\text{lab}}} \right)^2 + \left(\frac{\sigma_{d\sigma(ds,0^\circ)}}{d\Omega_{\text{lab}}} \right)^2}, \quad (\text{A11})$$

and

$$\frac{\sigma_{T_i}}{T_i} \simeq \frac{2}{\left(\frac{\Delta E_{\text{meas}}}{\Delta E_{\text{MRS}}} \right)^2 - 1} \frac{\sigma_{\Delta E_{\text{MRS}}}}{\Delta E_{\text{MRS}}}, \quad (\text{A12})$$

respectively. As shown by Eq. (A11), the systematic uncertainty for the dsf value depends only on the uncertainties in the differential elastic-scattering cross sections at the different energies. This is an important feature of the MRS that can be explained by the fact that the systematic uncertainties associated with the MRS geometry are canceled out, i.e., simultaneous measurements of the down-scattered and primary neutrons are exposed to identical geometry-related uncertainties. Table 121.IX illustrates the actual systematic uncertainties for the different parameters expressed in Eqs. (A9)–(A11) and their combined contribution to the total error for the different MRS configurations shown in Table 121.VII.

REFERENCES

1. S. W. Haan *et al.*, Phys. Plasmas **2**, 2480 (1995).
2. J. D. Lindl, R. L. McCrory, and E. M. Campbell, Phys. Today **45**, 32 (1992).
3. M. D. Rosen, Phys. Plasmas **3**, 1803 (1996).
4. G. H. Miller, E. I. Moses, and C. R. Wuest, Nucl. Fusion **44**, S228 (2004).
5. J. A. Frenje, D. T. Casey, C. K. Li, J. R. Rygg, F. H. Séguin, R. D. Petrasso, V. Yu. Glebov, D. D. Meyerhofer, T. C. Sangster, S. Hatchett, S. Haan, C. Cerjan, O. Landen, M. Moran, P. Song, D. C. Wilson, and R. J. Leeper, Rev. Sci. Instrum. **79**, 10E502 (2008).
6. T. R. Boehly, D. L. Brown, R. S. Craxton, R. L. Keck, J. P. Knauer, J. H. Kelly, T. J. Kessler, S. A. Kumpan, S. J. Loucks, S. A. Letzring, F. J. Marshall, R. L. McCrory, S. F. B. Morse, W. Seka, J. M. Soures, and C. P. Verdon, Opt. Commun. **133**, 495 (1997).
7. R. L. McCrory, D. D. Meyerhofer, R. Betti, R. S. Craxton, J. A. Delettrez, D. H. Edgell, V. Yu. Glebov, V. N. Goncharov, D. R. Harding, D. W. Jacobs-Perkins, J. P. Knauer, F. J. Marshall, P. W. McKenty, P. B. Radha, S. P. Regan, T. C. Sangster, W. Seka, R. W. Short, S. Skupsky, V. A. Smalyuk, J. M. Soures, C. Stoeckl, B. Yaakobi, D. Shvarts, J. A. Frenje, C. K. Li, R. D. Petrasso, and F. H. Séguin, Phys. Plasmas **15**, 055503 (2008).
8. J. A. Frenje, C. K. Li, F. H. Séguin, D. T. Casey, R. D. Petrasso, T. C. Sangster, R. Betti, V. Yu. Glebov, and D. D. Meyerhofer, Phys. Plasmas **16**, 042704 (2009).

9. T. C. Sangster, V. N. Goncharov, R. Betti, T. R. Boehly, D. T. Casey, T. J. B. Collins, R. S. Craxton, J. A. Delettrez, D. H. Edgell, R. Epstein, K. A. Fletcher, J. A. Frenje, V. Yu. Glebov, D. R. Harding, S. X. Hu, I. V. Igumenshchev, J. P. Knauer, S. J. Loucks, C. K. Li, J. A. Marozas, F. J. Marshall, R. L. McCrory, P. W. McKenty, D. D. Meyerhofer, P. M. Nilson, S. P. Padalino, R. D. Petrasso, P. B. Radha, S. P. Regan, F. H. Séguin, W. Seka, R. W. Short, D. Shvarts, S. Skupsky, V. A. Smalyuk, J. M. Soures, C. Stoeckl, W. Theobald, and B. Yaakobi, "Shock-Tuned Cryogenic DT-Implsion Performance on OMEGA," to be published in *Physics of Plasmas*.
10. V. N. Goncharov, T. C. Sangster, T. R. Boehly, S. X. Hu, I. V. Igumenshchev, F. J. Marshall, R. L. McCrory, D. D. Meyerhofer, P. B. Radha, W. Seka, S. Skupsky, C. Stoeckl, D. T. Casey, J. A. Frenje, and R. D. Petrasso, "Multiple-Picket Cryogenic Designs for OMEGA and the NIF," submitted to *Physical Review Letters*.
11. E. I. Moses, in *Current Trends in International Fusion Research: Proceedings of the 7th Symposium Selected Presentations*, edited by E. Panarella and R. Raman (American Institute of Physics, New York, 2009), Vol. 1154, pp. 53–59.
12. F. H. Séguin, J. A. Frenje, C. K. Li, D. G. Hicks, S. Kurebayashi, J. R. Rygg, B.-E. Schwartz, R. D. Petrasso, S. Roberts, J. M. Soures, D. D. Meyerhofer, T. C. Sangster, J. P. Knauer, C. Sorce, V. Yu. Glebov, C. Stoeckl, T. W. Phillips, R. J. Leeper, K. Fletcher, and S. Padalino, *Rev. Sci. Instrum.* **74**, 975 (2003).
13. J. A. Frenje, K. M. Green, D. G. Hicks, C. K. Li, F. H. Séguin, R. D. Petrasso, T. C. Sangster, T. W. Phillips, V. Yu. Glebov, D. D. Meyerhofer, S. Roberts, J. M. Soures, C. Stoeckl, K. Fletcher, S. Padalino, and R. J. Leeper, *Rev. Sci. Instrum.* **72**, 854 (2001).
14. A THD capsule is filled with more deuterium-lean fuel mixtures and H-dopant levels up to 25% (by atom).
15. S. Agostinelli *et al.*, *Nucl. Instrum. Methods Phys. Res. A* **506**, 250 (2003).
16. J. A. Frenje, C. K. Li, F. H. Séguin, S. Kurebayashi, R. D. Petrasso, J. M. Soures, J. Delettrez, V. Yu. Glebov, D. D. Meyerhofer, P. B. Radha, S. Roberts, T. C. Sangster, S. Skupsky, and C. Stoeckl, *Phys. Plasmas* **9**, 4719 (2002).
17. X-5 Monte Carlo Team, *Version 5*, Los Alamos National Laboratory, Los Alamos, NM, Report LA-R-03-1987 (24 April 2003).
18. D. T. Casey, J. A. Frenje, C. K. Li, F. H. Séguin, R. D. Petrasso, V. Yu. Glebov, D. D. Meyerhofer, and T. C. Sangster, "Minimizing Neutron Background for the Magnetic Recoil Spectrometer at OMEGA and the NIF," to be submitted to *Review of Scientific Instruments*.
19. D. T. Casey, J. A. Frenje, C. K. Li, F. H. Séguin, R. D. Petrasso, V. Yu. Glebov, D. D. Meyerhofer, and T. C. Sangster, "The Coincidence Counting Technique for Enhanced Background Rejection in the MRS Data," to be submitted to *Review of Scientific Instruments*.
20. C. K. Li, F. H. Séguin, D. G. Hicks, J. A. Frenje, K. M. Green, S. Kurebayashi, R. D. Petrasso, D. D. Meyerhofer, J. M. Soures, V. Yu. Glebov, R. L. Keck, P. B. Radha, S. Roberts, W. Seka, S. Skupsky, C. Stoeckl, and T. C. Sangster, *Phys. Plasmas* **8**, 4902 (2001).
21. S. Skupsky, R. W. Short, T. Kessler, R. S. Craxton, S. Letzring, and J. M. Soures, *J. Appl. Phys.* **66**, 3456 (1989).
22. S. Kacenjar, S. Skupsky, A. Entenberg, L. Goldman, and M. Richardson, *Phys. Rev. Lett.* **49**, 463 (1982).
23. B. K. Spears *et al.*, "Prediction of Ignition Implosion Performance Using Measurements of Low-Deuterium Surrogates," to be published in *Physics of Plasmas*.
24. G. B. Zimmerman and W. L. Kruer, *Comments Plasma Phys. Control. Fusion* **2**, 51 (1975).
25. O. N. Jarvis *et al.*, *Rev. Sci. Instrum.* **57**, 1717 (1986).
26. H. Brysk, *Plasma Phys.* **15**, 611 (1973).

Strong-Coupling and Degeneracy Effects in Inertial Confinement Fusion Implosions

As one of the potentially viable ways to generate clean energy, inertial confinement fusion (ICF) has been pursued for decades.¹ In “hot-spot” ICF designs, a cryogenic DT capsule is driven to implode either directly by intense laser pulses² or indirectly by x rays in a hohlraum.³ At the stagnation stage, a high-density shell ($>1000\times$ solid-DT density) is assembled around the hot spot for the fusion burn to propagate, thereby generating a net energy gain. To reach such high compression, the imploding shell must stay on a low adiabat, which is conventionally characterized as α (the ratio of the fuel pressure to the Fermi-degenerate pressure). Accurate knowledge of the equation of state (EOS) of the DT fuel is essential to ICF designs¹ because the compressibility is determined by the EOS.⁴

Dynamically compressed by shocks and/or adiabatic compression waves driven by laser ablation,⁵ the imploding DT

shell undergoes a wide range of plasma conditions at densities from $\sim 0.1 \text{ g/cm}^3$ up to 1000 g/cm^3 and temperatures varying from a few electron volts to several hundred electron volts.¹ One may expect such plasmas to enter the strongly coupled and degenerate regimes, where many-body effects become important. Strongly coupled and degenerate plasma conditions are indeed accessed in low-adiabat cryogenic implosions on the OMEGA Laser System⁶ as well as at the National Ignition Facility (NIF).⁷ Examples from hydrosimulations are shown in Figs. 121.35(a)–121.35(c) for a low-adiabat ($\alpha \simeq 2.5$) cryo-DT implosion on OMEGA and in Figs. 121.35(d)–121.35(f) for a direct-drive-ignition design for the NIF. The laser pulse shapes in panels (a) and (d) are plotted. Our hydrocode simulations show that the predicted density (ρ) and temperature (T) “paths” of the driven DT shell, which are plotted in the middle panels [(b) and (e)], undergo a variety of drive stages, includ-

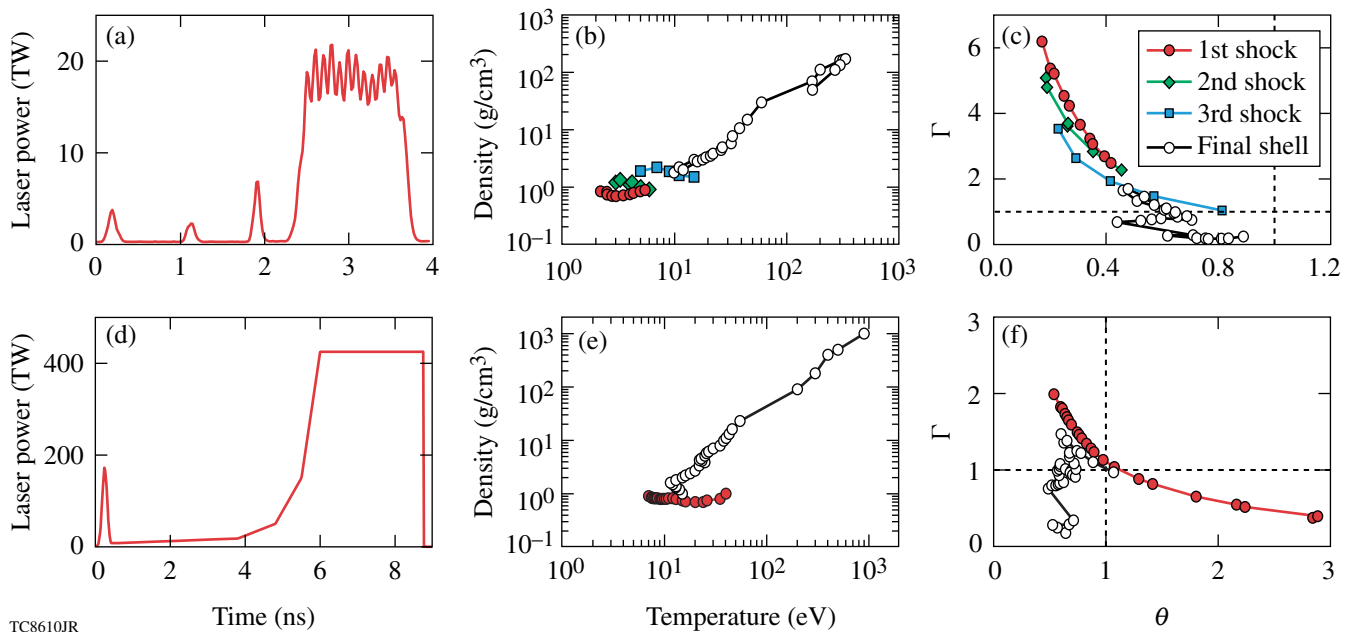


Figure 121.35

[(a)–(c)] A cryogenic-DT implosion on OMEGA; [(d)–(f)] a direct-drive-ignition design for the NIF. In both cases, strongly coupled and degenerate plasma conditions are *indeed* accessed.

ing several shocks and the final push by the main pulse. If we cast the ρ - T history of the imploding DT shell onto the plane spanned by the coupling parameter $\Gamma = 1/akT$ (where a is the Wigner-Seitz radius and k is the Boltzman constant) and the degeneracy parameter $\theta = T/T_F$ (where T_F is the Fermi temperature), we find that the imploding shell indeed undergoes the coupled ($\Gamma > 1$) and degenerate ($\theta < 1$) regimes. It is therefore expected that the effects of strong coupling and degeneracy in such plasmas would affect the compression and fusion yield in low-adiabat ICF implusions.

The effects of strong coupling and degeneracy in ICF plasmas have recently attracted much attention since they may redefine the so-called “1-D physics” of ICF implusions. For example, the essential pieces of physics models used in ICF hydrosimulations, such as the electron-ion energy relaxation rate,⁸ the thermal conductivity,⁹ and the fusion-reaction rate¹⁰ in coupled and degenerate plasmas, were recently re-examined. In recent experiments, the EOS of liquid deuterium along the principal Hugoniot around 100 to 200 GPa was measured using laser-driven shock waves,^{11–16} magnetically driven flyers,^{17,18} and convergent explosives.^{19,20} Over the years, enormous theoretical efforts have been put forth to better understand the properties of deuterium under high pressure. The widely used *SESAME* EOS table of deuterium was based on the “chemical model” of matter,^{21,22} which has adopted the liquid perturbation theory in the molecular/atomic fluid phase for ICF plasma conditions. The first-order expansion was originally used in the *SESAME* model²¹ to take only the nearest-neighbor interactions into account, which did not fully account for the effects of strong coupling and many-body degeneracy in nonideal plasmas. *Ab initio* calculations for the deuterium EOS have been performed by using the method of density functional theory-based molecular dynamics (DFT-MD)^{23–30} and the path-integral Monte Carlo (PIMC) method.^{31–35} The first-principle methods take the strong-coupling and degeneracy effects fully into account, in contrast to using chemical models.^{21,22,36–39}

For ICF applications, we are especially concerned about the EOS accuracy along the implosion path in the density-temperature plane, i.e., in the range of $\rho \sim 0.1$ to 1000 g/cm³ and $T \sim 1.0$ to 1000 eV. For these plasma conditions, the DFT-based methods become very expensive because of the large number of electronic orbitals required,⁴⁰ while the EOS can be derived efficiently with the PIMC method. This article presents a first-principles equation-of-state (FPEOS) table of deuterium from restricted PIMC calculations.⁴¹ The same method has been successfully applied to compute the deuterium EOS up to a density of $\rho = 5.388$ g/cm³ (Refs. 33 and 42) and has been

favorably compared with DFT-MD calculations.³⁴ We have used free-particle nodes to construct the many-body trial density matrix. The Coulomb interactions enter via a high- T pair-density matrix⁴³ $\rho(R, R'; \delta\beta)$. Using its convolution property, the density matrix $\rho(R, R'; \beta)$ can be expressed by

$$\rho(R, R'; \beta) = \int dR_1 dR_2 \dots dR_{M-1} \rho(R, R_1; \delta\beta) \times \rho(R_1, R_2; \delta\beta) \dots \rho(R_{M-1}, R'; \delta\beta) \quad (1)$$

with $\beta = 1/kT$ and $\delta\beta = \beta/M$, where M is the number of steps along the path in imaginary “time.” Monte Carlo methods are used to efficiently evaluate the multidimensional integration. Thermodynamic properties (associated with operator \hat{O}) of plasmas are derived from

$$\langle \hat{O} \rangle = \frac{\int dR dR' \langle R | \hat{O} | R' \rangle \langle R' | \rho(R, R'; \beta) | R \rangle}{\int dR \langle R' | \rho(R, R'; \beta) | R \rangle}. \quad (2)$$

We have performed our PIMC calculations with various numbers of atoms in periodic cubic simulation cells depending on the deuterium-density ranges: 64 atoms for $\rho < 2.5$ g/cm³, 128 atoms for $2.5 < \rho < 10.5$ g/cm³, and 256 atoms for $\rho > 10.5$ g/cm³. The time step $\delta\beta$ was chosen small enough, $1/\delta\beta \geq 75 \times kT_F$ to accurately account for interactions and degeneracy effects. Convergence tests have been done for each density range.

In Fig. 121.36(a), we compare the principal Hugoniot between our FPEOS table and the *SESAME* (5263) EOS for different temperatures marked on the curve. It is noted that this version of *SESAME* EOS is still used in ICF designs, although improvements have recently been made by Kerley.²² We have also plotted the previous Hugoniot calculated using the same PIMC method with 32 atoms and a time step of $1/\delta\beta = 8 \times 10^6$ K (Refs. 33 and 42). Good agreement is found with these previous PIMC calculations. Current PIMC simulations used 64 atoms and a smaller time step of $1/\delta\beta = 1.6 \times 10^7$ K. We found that, according to our PIMC calculations, deuterium is slightly softer than the *SESAME* prediction for pressures below ~ 2 Mbar, while it is stiffer in the pressure range of $\sim 2 < P < 100$ Mbar (the dynamic compression range in ICF). The PIMC-predicted compression of $\rho/\rho_0 \simeq 4.3$ below ~ 2 Mbar agrees better with DFT-MD calculations^{26,28} and EOS measurements using magnetically driven flyers.^{17,18} It may also agree with the laser-shock results^{15,16} after the quartz standard used in experiments is corrected.⁴⁴ To give an interpretation of these discrepancies, in Figs. 121.36(b) and 121.36(c) we have plotted the percentage differences in pressure and energy versus

density, for two temperatures $T = 344.47$ eV and $T = 21.54$ eV. The statistical error bars of our PIMC results are also marked. At $T = 344.47$ eV, both the pressure and energy from PIMC and *SESAME* are within $\sim 1\%$. This is expected because plasmas at such high temperatures are classical ($\Gamma \ll 1$, $\theta \gg 1$), where both PIMC and *SESAME* should agree. The PIMC and *SESAME* Hugoniot curves above 344 eV are identical, as shown in

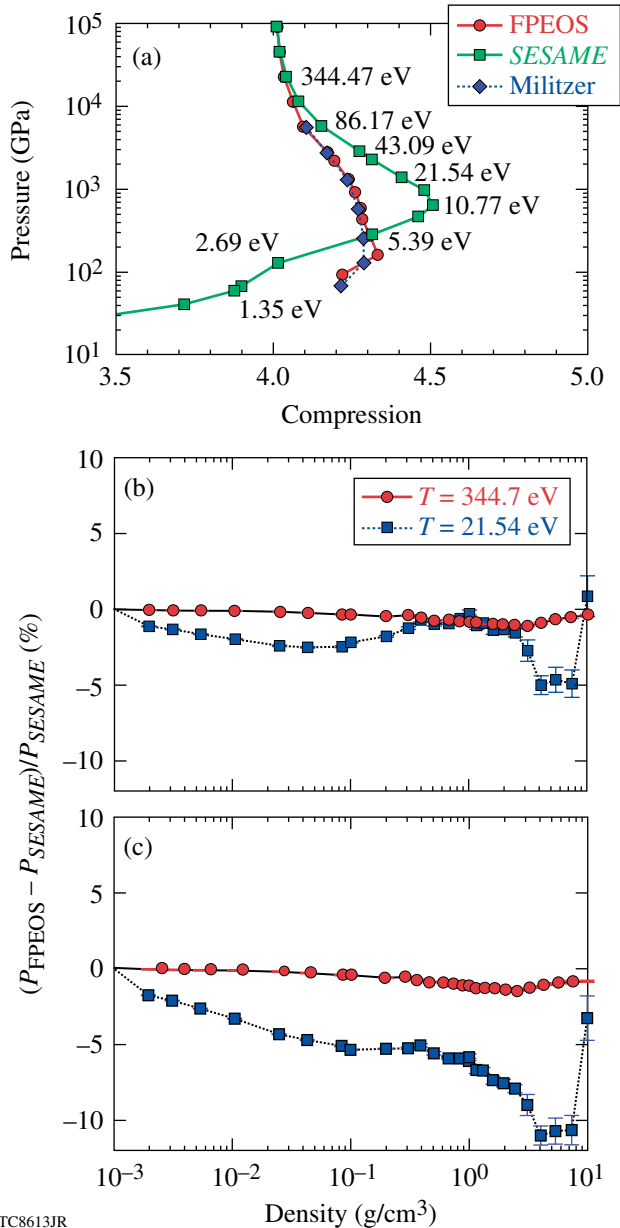
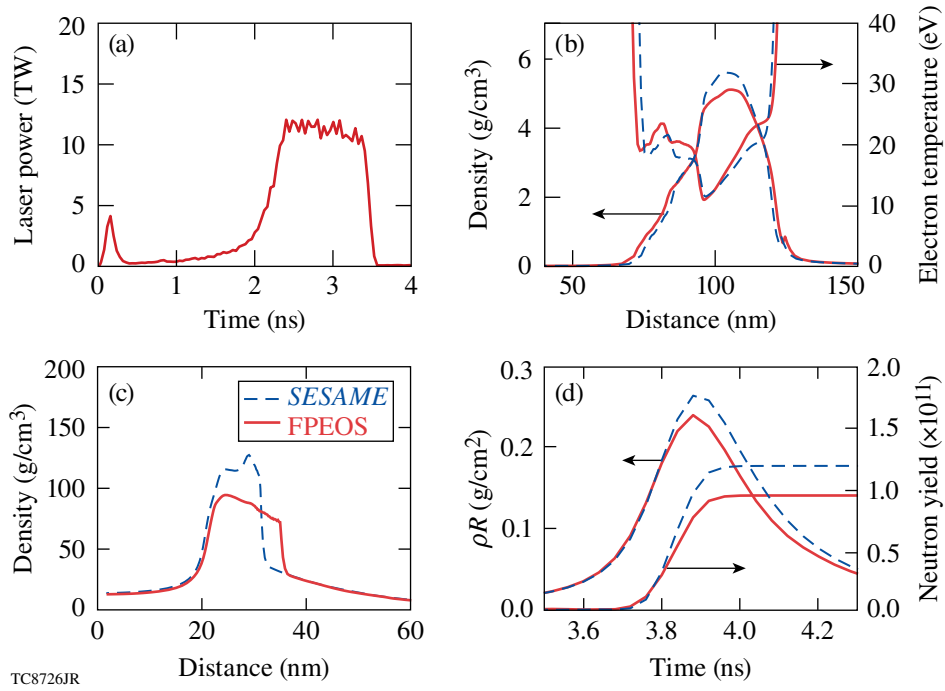


Figure 121.36 (a) The principal Hugoniot for liquid deuterium. The relative deviation in (b) pressure and (c) energy between the FPEOS and *SESAME* as a function of density, for temperatures $T = 344.7$ eV (red circles) and $T = 21.54$ eV (blue squares).

Fig. 121.36(a). For a lower temperature of 21.54 eV, however, the energy difference is larger, as indicated in Fig. 121.36(c). For the principal Hugoniot, in the density range of $\rho = 0.6$ to 0.8 g/cm^3 , the internal energy in FPEOS is $\sim 6\%$ lower than that of *SESAME* (for this comparison, the zero energy has been set to the ground state of an isolated molecule, $E_0 = -15.886$ eV), even though the pressure is comparable in both within $\sim 1\%$. According to the Hugoniot equation [$E_f - E_0 + (1/2)(P_f + P_0) \times (V_f - V_0) = 0$], the final state can be expressed as $E_f + (1/2) \times P_f V_f \simeq E_0 + (1/2) P_f V_0$ because of $P_f \gg P_0$, where (P_0, E_0, V_0) and (P_f, E_f, V_f) are the initial and final pressure, energy, and volume of deuterium. Therefore, with the similar value of P_f , the smaller E_f predicted by the FPEOS requires larger V_f to satisfy the Hugoniot equation.⁴⁵ Larger V_f relative to the *SESAME* case means a smaller final density and compression, as seen in Fig. 121.36(a). Such discrepancy was noticed by Kerley²² in 2003; with some improvements to the ionization equilibrium model adopted in *SESAME*, he succeeded in decreasing the *SESAME* compression to better agree with the first-principle calculations in this high-pressure (~ 10 -Mbar) regime.²² The lower internal energy in FPEOS, for $T < 100$ eV, is attributed to many-body interactions. Figure 121.36(c) indicates that as the density increases, the relative deviation in energy reaches a maximum of $\sim 11\%$ around $\rho \sim 4$ to 5 g/cm^3 ($\Gamma \simeq 1.3$ and $\theta \simeq 0.4$) for this isothermal curve at $T = 21.54$ eV. The *SESAME* model again agrees with PIMC calculations at very high densities (e.g., $\rho = 10$ g/cm^3), as local screening was correctly accounted for in chemical models.^{21,22}

From PIMC calculations, we have derived a first-principles EOS table for deuterium, which covers the typical ICF fuel conditions of $\rho = 0.002$ to 1596 g/cm^3 and $T = 1.35$ eV to 5.5 keV. For each density point, we have performed PIMC calculations including low temperature corresponding to $\theta = T/T_F \simeq 0.1$. To comply with the *SESAME* format used in our hydrocodes, we have added the experimentally benchmarked low- T (< 1.35 -eV) *SESAME* points to our FPEOS table, although those points are not actually used in ICF hydrocodes (except for defining the initial state). The high-temperature limit of $T > 5.5$ keV is obtained by linearly extrapolating (in T) the highest PIMC point since ideal plasma conditions are expected at high temperatures.

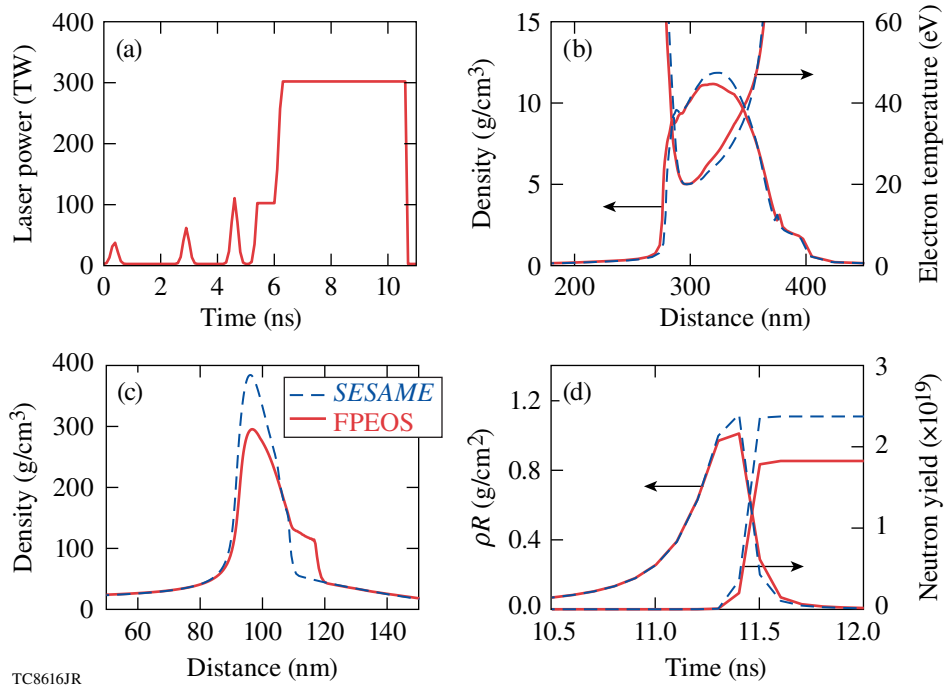
With our FPEOS table, we can now explore the implications of strong-coupling and degeneracy effects in ICF implosions using hydrocodes. Results are shown in Figs. 121.37 and 121.38, respectively, for a cryogenic D_2 implosion ($\alpha \simeq 2.5$) on the OMEGA Laser System and a direct-drive DT design on the NIF. We have used the 1-D radiative hydrocode *LILAC*⁴⁶ to



TC8726JR

Figure 121.37

The hydrocode simulations of a cryogenic D₂ implosion on OMEGA using the FPEOS table (solid red line) and the *SESAME* EOS table (dashed blue line): (a) the laser pulse shape; (b) the density and temperature profiles of the imploding D₂ shell at the end of laser pulse ($t = 3.6$ ns); (c) the density profile at peak compression; and (d) the areal density (ρR) and neutron yield as functions of time.



TC8616JR

Figure 121.38

Similar to Fig. 121.37 but for a NIF direct-drive-ignition design.

perform these simulations. In Fig. 121.37(a), we plot the pulse shape used to implode a cryogenic D_2 target (877- μm diameter) with a 10- μm CD ablator and 95 μm of D_2 ice. Figure 121.37(b) shows the density and temperature profiles at the end of the laser pulse ($t = 3.6$ ns) from both the FPEOS and *SESAME* simulations. The shell's peak density and average temperature were $\rho_p \sim 5$ g/cm³ and $T \sim 15$ eV, which correspond to the strongly coupled and degenerate regime with $\Gamma \simeq 1.7$ and $\theta \simeq 0.3$. It is shown that the FPEOS simulation predicted $\sim 10\%$ -lower ρ_p but higher temperature relative to the *SESAME* prediction. As the Hugoniot comparison indicated in Fig. 121.36(a), the FPEOS is slightly stiffer than *SESAME* in this temperature range, which explains the lower ρ_p . The slightly higher temperature in the FPEOS case originated from the lower internal energy [see Fig. 121.36(c)]. Since the laser ablation does the work/energy to the shell compression and its kinetic motion, a lower internal energy in FPEOS means more energy is partitioned to heat the shell, thereby resulting in a slightly higher temperature. Such a temperature increase and density drop can have consequences in the implosion performance. At the stagnation stage (peak compression), Fig. 121.37(c) shows that the peak density is $\sim 30\%$ lower according to FPEOS ($\rho_p \simeq 90$ g/cm³) compared to *SESAME* ($\rho_p \simeq 130$ g/cm³). The peak areal density $(\rho R)_{\text{peak}}$ and neutron yield were also reduced by $\sim 10\%$ to 20% as shown in Fig. 121.37(d). The neutron-averaged areal density $\langle \rho R \rangle_n$ predicted with FPEOS was ~ 198 mg/cm², which is in better agreement with the experimental measured $\langle \rho R \rangle_n = 202 \pm 7$ mg/cm² (Ref. 47), in contrast to the *SESAME* prediction of $\langle \rho R \rangle_n = 247$ mg/cm². Nonuniformities cannot account for the large discrepancy between measurements and *SESAME* predictions, as we have noted that certain perturbations in experiments can reduce the neutron yield⁴⁸ but hardly affect the compression ρR .

A similar effect was seen for the NIF designs. Figure 121.38 shows an example for a NIF target ($\phi = 3.37$ mm) having a 37- μm CH ablator and 150 μm of DT ice. At the end of the laser pulse [$t = 10.7$ ns in Fig. 121.38(b)], we also found a decrease in ρ_p and a temperature increase for the FPEOS relative to *SESAME* simulations. The peak density near the stagnation dropped from $\rho_p = 383$ g/cm³ (*SESAME*) to $\rho_p = 294$ g/cm³ (FPEOS), as is indicated by Fig. 121.38(c). The resulting ρR and neutron yield as a function of time are plotted in Fig. 121.38(d). The peak ρR dropped from 1.1 g/cm² (*SESAME*) to 1.0 g/cm² (FPEOS), while the yield dropped from the *SESAME*-predicted value of $Y = 2.4 \times 10^{19}$ to 1.8×10^{19} for the FPEOS simulation. Consequently, the energy gain dramatically decreased from 45 (*SESAME*) to 34 (FPEOS).

In summary, we have derived a first-principles equation-of-state table of deuterium for ICF applications from PIMC calculations. The FPEOS table covers the typical fuel density and temperature conditions in ICF implosions. In comparison with the *SESAME* table, the FPEOS predicts $\sim 10\%$ -lower internal energy but comparable pressure (within few percent) for strongly coupled and degenerate plasma conditions. Hydrosimulations using the FPEOS table indicate significant decreases in the predicted peak density ($\sim 30\%$ to 40%). The results also show a reduction in the peak areal density ρR ($\sim 10\%$) and the neutron yield (energy gain) by $\sim 20\%$ with respect to the corresponding *SESAME* simulations. The compression (ρR) predicted from FPEOS agrees better with experiments. The FPEOS table will become more important for even lower adiabat ($\alpha \simeq 1$ to 2) ICF target designs since one expects strong coupling and degeneracy effects to increase in such plasmas.

ACKNOWLEDGMENT

This work was supported by U.S. Department of Energy Office of Inertial Confinement Fusion under Cooperative Agreement No. DE-FC52-08NA28302, the University of Rochester, and New York State Energy Research and Development Authority. S. X. Hu thanks the National Science Foundation for its support under the NSF-TeraGrid grant PHY090093. A portion of this research was carried out on the NICS' Kraken Supercomputer. B. Militzer acknowledges support from UC's laboratory research program, NSF, and NASA.

REFERENCES

1. S. Atzeni and J. Meyer-ter-Vehn, *The Physics of Inertial Fusion: Beam Plasma Interaction, Hydrodynamics, Hot Dense Matter*, International Series of Monographs on Physics (Clarendon Press, Oxford, 2004).
2. R. L. McCrory, D. D. Meyerhofer, R. Betti, R. S. Craxton, J. A. Delettrez, D. H. Edgell, V. Yu Glebov, V. N. Goncharov, D. R. Harding, D. W. Jacobs-Perkins, J. P. Knauer, F. J. Marshall, P. W. McKenty, P. B. Radha, S. P. Regan, T. C. Sangster, W. Seka, R. W. Short, S. Skupsky, V. A. Smalyuk, J. M. Soares, C. Stoeckl, B. Yaakobi, D. Shvarts, J. A. Frenje, C. K. Li, R. D. Petrasso, and F. H. Séguin, *Phys. Plasmas* **15**, 055503 (2008).
3. J. D. Lindl, *Phys. Plasmas* **2**, 3933 (1995).
4. S. X. Hu, V. A. Smalyuk, V. N. Goncharov, J. P. Knauer, P. B. Radha, I. V. Igumenshchev, J. A. Marozas, C. Stoeckl, B. Yaakobi, D. Shvarts, T. C. Sangster, P. W. McKenty, D. D. Meyerhofer, S. Skupsky, and R. L. McCrory, *Phys. Rev. Lett.* **100**, 185003 (2008).
5. S. X. Hu, V. A. Smalyuk, V. N. Goncharov, S. Skupsky, T. C. Sangster, D. D. Meyerhofer, and D. Shvarts, *Phys. Rev. Lett.* **101**, 055002 (2008).
6. T. R. Boehly, D. L. Brown, R. S. Craxton, R. L. Keck, J. P. Knauer, J. H. Kelly, T. J. Kessler, S. A. Kumpan, S. J. Loucks, S. A. Letzring, F. J. Marshall, R. L. McCrory, S. F. B. Morse, W. Seka, J. M. Soares, and C. P. Verdon, *Opt. Commun.* **133**, 495 (1997).

7. J. Paisner *et al.*, *Laser Focus World* **30**, 75 (1994).
8. M. S. Murillo and M. W. C. Dharma-wardana, *Phys. Rev. Lett.* **100**, 205005 (2008); M. W. C. Dharma-wardana, *Phys. Rev. Lett.* **101**, 035002 (2008); B. Jeon *et al.*, *Phys. Rev. E* **78**, 036403 (2008); G. Dimonte and J. Daligault, *Phys. Rev. Lett.* **101**, 135001 (2008); J. N. Glosli *et al.*, *Phys. Rev. E* **78**, 025401 (R) (2008); L. X. Benedict *et al.*, *Phys. Rev. Lett.* **102**, 205004 (2009).
9. V. Recoules *et al.*, *Phys. Rev. Lett.* **102**, 075002 (2009).
10. E. L. Pollock and B. Militzer, *Phys. Rev. Lett.* **92**, 021101 (2004).
11. L. B. Da Silva *et al.*, *Phys. Rev. Lett.* **78**, 483 (1997).
12. G. W. Collins *et al.*, *Science* **281**, 1178 (1998).
13. G. W. Collins *et al.*, *Phys. Plasmas* **5**, 1864 (1998).
14. A. N. Mostovych *et al.*, *Phys. Rev. Lett.* **85**, 3870 (2000); A. N. Mostovych *et al.*, *Phys. Plasmas* **8**, 2281 (2001).
15. T. R. Boehly, D. G. Hicks, P. M. Celliers, T. J. B. Collins, R. Earley, J. H. Eggert, D. Jacobs-Perkins, S. J. Moon, E. Vianello, D. D. Meyerhofer, and G. W. Collins, *Phys. Plasmas* **11**, L49 (2004).
16. D. G. Hicks, T. R. Boehly, P. M. Celliers, J. H. Eggert, S. J. Moon, D. D. Meyerhofer, and G. W. Collins, *Phys. Rev. B* **79**, 014112 (2009).
17. M. D. Knudson *et al.*, *Phys. Rev. Lett.* **87**, 225501 (2001); M. D. Knudson *et al.*, *Phys. Rev. Lett.* **90**, 035505 (2003).
18. M. D. Knudson *et al.*, *Phys. Rev. B* **69**, 144209 (2004).
19. S. I. Belov *et al.*, *JETP Lett.* **76**, 433 (2002).
20. V. E. Fortov *et al.*, *Phys. Rev. Lett.* **99**, 185001 (2007).
21. G. I. Kerley, *Phys. Earth Planet. Inter.* **6**, 78 (1972).
22. G. I. Kerley, Sandia National Laboratory, Albuquerque, NM, Report SAND2003-3613 (2003).
23. L. Collins *et al.*, *Phys. Rev. E* **52**, 6202 (1995).
24. T. J. Lenosky *et al.*, *Phys. Rev. B* **61**, 1 (2000).
25. G. Galli *et al.*, *Phys. Rev. B* **61**, 909 (2000).
26. L. A. Collins *et al.*, *Phys. Rev. B* **63**, 184110 (2001).
27. J. Cl rouin and J.-F. Dufr che, *Phys. Rev. E* **64**, 066406 (2001).
28. M. P. Desjarlais, *Phys. Rev. B* **68**, 064204 (2003).
29. S. A. Bonev, B. Militzer, and G. Galli, *Phys. Rev. B* **69**, 014101 (2004).
30. S. A. Bonev *et al.*, *Nature* **431**, 669 (2004).
31. C. Pierleoni *et al.*, *Phys. Rev. Lett.* **73**, 2145 (1994).
32. W. R. Magro *et al.*, *Phys. Rev. Lett.* **76**, 1240 (1996).
33. B. Militzer and D. M. Ceperley, *Phys. Rev. Lett.* **85**, 1890 (2000).
34. B. Militzer *et al.*, *Phys. Rev. Lett.* **87**, 275502 (2001).
35. V. Bezukrovnyy *et al.*, *Phys. Rev. E* **70**, 057401 (2004); V. S. Filinov *et al.*, *Plasma Phys. Rep.* **31**, 700 (2005).
36. D. Saumon and G. Chabrier, *Phys. Rev. A* **46**, 2084 (1992).
37. M. Ross, *Phys. Rev. B* **58**, 669 (1998).
38. F. J. Rogers, *Contrib. Plasma Phys.* **41**, 179 (2001).
39. H. Juranek, R. Redmer, and Y. Rosenfeld, *J. Chem. Phys.* **117**, 1768 (2002).
40. L. A. Collins, Los Alamos National Laboratory, private communication (2009).
41. D. M. Ceperley, *Rev. Mod. Phys.* **67**, 279 (1995).
42. B. Militzer, "Path Integral Monte Carlo Simulations of Hot Dense Hydrogen," Ph.D. thesis, University of Illinois at Urbana-Champaign, 2000.
43. B. Militzer, "Computation of the High Temperature Coulomb Density Matrix in Periodic Boundary Conditions," to be published in *Physical Review E*.
44. M. D. Knudson and M. P. Desjarlais, *Phys. Rev. Lett.* **103**, 225501 (2009).
45. B. Militzer, *Phys. Rev. Lett.* **97**, 175501 (2006).
46. J. Delettrez, R. Epstein, M. C. Richardson, P. A. Jaanimagi, and B. L. Henke, *Phys. Rev. A* **36**, 3926 (1987).
47. T. C. Sangster, V. N. Goncharov, P. B. Radha, V. A. Smalyuk, R. Betti, R. S. Craxton, J. A. Delettrez, D. H. Edgell, V. Yu. Glebov, D. R. Harding, D. Jacobs-Perkins, J. P. Knauer, F. J. Marshall, R. L. McCrory, P. W. McKenty, D. D. Meyerhofer, S. P. Regan, W. Seka, R. W. Short, S. Skupsky, J. M. Soures, C. Stoeckl, B. Yaakobi, D. Shvarts, J. A. Frenje, C. K. Li, R. D. Petrasso, and F. H. S guin, *Phys. Rev. Lett.* **100**, 185006 (2008).
48. S. X. Hu, P. B. Radha, J. A. Marozas, R. Betti, T. J. B. Collins, R. S. Craxton, J. A. Delettrez, D. H. Edgell, R. Epstein, V. N. Goncharov, I. V. Igumenshchev, F. J. Marshall, R. L. McCrory, D. D. Meyerhofer, S. P. Regan, T. C. Sangster, S. Skupsky, V. A. Smalyuk, Y. Elbaz, and D. Shvarts, *Phys. Plasmas* **16**, 112706 (2009).

Neutron-Induced Nucleation Inside Bubble Chambers Using Freon 115 as the Active Medium

Introduction

The vast majority of controlled fusion experiments worldwide involve deuterium–tritium (DT) or deuterium–deuterium (DD) mixtures.¹ Nuclear diagnostics provide a direct measurement of the DD or DT fusion burn within a compressed inertial confinement fusion (ICF) target.² These diagnostics are used to infer the fuel areal density, neutron yield, fuel-ion temperature, and bang time.² Neutrons are a primary fusion-reaction product that can provide an image of the fusion burn region. Neutron imaging (NI) can be used to determine failure modes of ICF ignition capsules, such as poor implosion symmetry or improper laser pulse shaping.^{3,4} NI has been used on OMEGA⁵ to measure the core symmetry of gas-filled plastic shells and cryogenic target implosions.⁶ NI systems use extended pinholes or penumbral apertures (with annular apertures as a particular case) to capture images on a neutron-sensitive detector.⁴ They are sensitive to both alignment and fabrication errors of the apertures used.⁷

A neutron image provides a direct measurement of the spatial extent of the fusion burn area for an ICF implosion, drawn from the physical characteristics of the neutrons that exit the plasma core as primary or secondary products of the fusion reactions.⁴ The core image is obtained by placing an appropriate aperture in front of a spatially sensitive neutron detector. The apertures are typically coded.⁴ The neutrons are detected by a plastic scintillator⁶ array or a bubble chamber.⁸

In NI systems, the coded image must be deconvolved to produce an accurate representation of the neutron source. This process requires precise knowledge of the aperture point-spread function (PSF) and the flat-field response of the imaging detector.³ Both pinhole and penumbral apertures are used.⁷ For both pinholes and penumbral apertures, uncertainties in the exact shape (caused by finite fabrication tolerances) lead to errors in the reconstructed image because of uncertainties in the calculated PSF. A computational study⁷ previously investigated the influences of various parameters from the NI system on the quality of the reconstructed image.

The required spatial resolution for an imaging system can be determined from numerical simulations.² A resolution of about $10\ \mu\text{m}$ appears to provide sufficient information to validate implosion models, but a resolution of $5\ \mu\text{m}$ may be necessary to see details in the implosion structure.² Previous studies⁸ have already shown that bubble chambers have the potential to obtain higher-resolution images of the targets for a shorter source–target distance than typical scintillator arrays and could be used for the very high neutron yields ($\geq 10^{16}$) expected to be measured at the National Ignition Facility (NIF).

This article discusses the mechanism of neutron-induced bubble formation inside Freon 115 and the influence of the critical radius size on the neutron detection sensitivity. Two forthcoming publications will focus on the design of the liquid Freon bubble chamber used on OMEGA and the data recorded with the detector, respectively.^{9,10}

Interactions of Neutrons with Freon 115— A Simplified Model

Freon 115 (chloropentafluoroethane, $\text{C}_2\text{F}_5\text{Cl}$) has been used as the active medium in bubble chambers for high-energy-physics experiments at the European Organization for Nuclear Research (CERN) since the early 1980s.¹¹ It is nonflammable, inexpensive, safe to operate, and easy to store in compressed gas tanks. A Freon 115 bubble chamber does not need cryogenic cooling and can be operated at around 50°C .

1. Thermodynamic Conditions for Bubble Formation

A bubble chamber is initially pressurized with its active medium in a liquid state. Several milliseconds before the incident particles enter the chamber, the pressure is quickly decreased and the liquid enters a superheated, metastable phase. The temperature becomes higher than its standard boiling point, without actually boiling. Deposition of small quantities of energy by incident particles or by any heterogeneous nucleation sites such as gas pockets or impurities disturbs the energy balance in the liquid and locally vaporizes the liquid. Because the vapor pressure is higher than the surrounding liquid pressure, the

newly formed bubble tends to expand, but the expansion force is counterbalanced by the surface tension force at the gas–liquid boundary.¹² Other factors influencing the bubble growth are the viscosity force that slows down the bubble expansion and the force transmitted to the bubble growth from the bubble/wall interaction. If the radius of the generated bubble is greater than a certain critical value R_c , the force balance is dominated by the vapor pressure and the bubble continues to grow (otherwise the bubble is reabsorbed into the liquid). As a fraction of the chamber volume vaporizes through the nucleation process, the liquid pressure inside the active medium increases until a balance is reached for a bubble radius of macroscopic size. After a short interval of time (usually a few tens of milliseconds), the bubbles fill the chamber and the boiling spreads to the whole liquid volume.¹² The chamber has to be repressurized to clean the gas pockets resulting from boiling and then decompressed again to take a new set of data. For the particular case of a gel detector, the active medium is represented by tiny pressurized liquid drops suspended in a transparent gel. Due to the higher pressure, these drops are in a superheated state and each of them behaves as a miniature bubble chamber.¹² The mechanism of bubble formation works in the same way as a liquid bubble chamber.⁸

The minimum energy E_b necessary for the formation of a bubble of critical radius R_c is described by^{13,14}

$$E_b = W_b + H + E_{\text{wall}} + E_{\text{visc}}, \quad (1)$$

where W_b is the minimum reversible work required for bubble formation, H is the vaporization energy, E_{wall} is the kinetic energy transmitted to the liquid during the growth process, and E_{visc} is the energy lost during the bubble growth by viscous forces.¹⁵ E_{wall} and E_{visc} can be neglected in this work.^{16,17} During the nucleation process, the bubble forms so rapidly that there is no time for energy exchange to take place between the bubble and the surrounding liquid.¹⁴ Once the bubble is initiated, the energy required to maintain it is given by the minimal reversible work W_b expressed as

$$W_b = 4\pi r^2 \gamma(T) - \frac{4}{3}\pi r^3 (p_v - p_0), \quad (2)$$

where $\gamma(T)$ is the liquid–vapor interfacial tension (temperature dependent), p_v is the vapor pressure of the superheated liquid, and p_0 is the ambient liquid pressure. The difference $p_v - p_0$ is called the degree of superheat of a given liquid. W_b is minimized for a critical radius

$$R_c = \frac{2\gamma(T)}{p_v - p_0}. \quad (3)$$

When a bubble reaches its critical radius, its vapor pressure is greater than its surface tension force. It becomes thermodynamically unstable and grows quickly. Once the liquid has vaporized locally, the minimum amount of energy W_b needed to form a vapor bubble of critical size R_c , as given by Gibbs (1875)¹³ from reversible thermodynamics, is

$$W_b = \frac{16\pi\gamma^3(T)}{3(p_v - p_0)^2}. \quad (4)$$

The vaporization energy can be expressed as^{14,18}

$$H = \frac{4}{3}\pi R_c^3 \rho_v H_v \quad (5)$$

with ρ the vapor density and H_v the latent heat of vaporization. Replacing Eqs. (4) and (5) in Eq. (1) and neglecting the kinetic and viscous energies, the minimum energy necessary to produce a bubble can be expressed as

$$E_b = \frac{16\pi\gamma^3(T)}{3(p_v - p_0)^2} + \frac{4}{3}\pi R_c^3 \rho_v H_v. \quad (6)$$

Equation (6) can be rewritten as

$$E_b = W_b \left(1 + \frac{\rho_v H_v}{p_v - p_0} \right). \quad (7)$$

Equation (7) accounts for the conversion efficiency (η) of heat to work, described by the relation

$$\eta = \frac{W_b}{E_b}. \quad (8)$$

For typical superheated liquids (Freon 12, Freon 115, Freon 134a), the value of η ranges from 2% to 6%.¹⁹ The energy necessary to create a bubble, E_b , is supplied through the energy deposition per unit length dE/dx by the electrons ejected by the recoil nuclei.¹⁸ The bubble nucleation requirements for a superheated medium are satisfied if the incident particle deposits enough energy to create a bubble within a specified length L , given by

$$L = k_b \cdot R_c, \quad (9)$$

where k_b is a constant that may vary between 2 and 13, in most cases being approximated as 2 (Refs. 16 and 19). The nucleation requirement is satisfied if [cf. Eq. (8) and (9)]

$$\frac{dE}{dx} \geq \frac{E_b}{k_b \cdot R_c} = \frac{W_b}{\eta \cdot k_b \cdot R_c}. \quad (10)$$

The condition necessary to create a bubble can be expressed as a minimum energy density ρ_E deposited over a sphere of radius R_c :

$$\rho_E \geq \frac{3E_b}{4\pi R_c^3}. \quad (11)$$

Replacing the values for the Freon 115 bubble chamber at 50°C (Ref. 20) (the operating temperature of the OMEGA bubble detector^{9,10}) in Eq. (6), the critical radius is $R_c = 7.5 \times 10^{-9}$ m and the minimum energy necessary to generate a bubble is $E_b = 107$ eV.

Bubble chambers operate at a quasi-constant temperature and therefore behave as isothermal systems. W_b can be obtained from the difference between the liquid pressure in the superheated state and the pressure of the foam limit.^{21,22} A bubble chamber is sensitive to particle detection only in its superheated state. The conditions necessary to reach this state depend on the thermodynamic-phase diagram of the liquid used as the active medium. Figure 121.39 shows the phase diagram for Freon 115.²² The medium is in the liquid state above the vapor pressure line, gaseous below the foam limit line, and in a metastable coexistence state in the middle. During the bubble chamber operation the temperature is held constant while the pressure decreases quickly from a point on the upper curve (start/stable) to a value close to the lower curve (working unstable), where it is ready to record any interactions with the incident particles. The detector sensitivity and the bubble growth speed depend on temperature. Measurements made at CERN in the 1980s found that the bubble density for Freon 115 reaches maximum at 48°C (Ref. 22). For the bubble detector used on OMEGA,^{9,10} the position of the piston during the decompression and the quantity of the Freon inside the chamber suggested that an operating temperature of 50°C was optimal.

The lines of constant bubble density come closer to the foam limit at higher temperatures. For a different active medium, the nominal values described in Fig. 121.39 may vary widely, but all liquid bubble chambers operate with the same principle. The foam limit is reached at the pressure $p^*(T)$, which is estimated, according to Bugg,²³ to be

$$p^*(T) = P_v - K \sqrt{\frac{k_L T}{\gamma^3}}, \quad (12)$$

where p_v and γ are the vapor pressure and surface tension, respectively, at the temperature T , k_L is the thermal conductivity of the liquid, and K is a numerical proportionality constant determined experimentally (in most cases close to 1).

The bubble growth rate can be estimated from the formula deduced by Plesset and Zwick:²⁴

$$r = A \sqrt{t} \quad (13)$$

with

$$A = 2 \sqrt{\frac{3}{\pi}} \sqrt{k_L \rho c_l (T_\infty - T_b)} / H_v \rho', \quad (14)$$

where k_L is the thermal conductivity of the liquid, ρ is its density, c_l is the specific heat, H_v is the heat of vaporization, ρ' is the density of the gas, T_∞ is the temperature of the liquid, and T_b is the temperature of the bubble (at the same pressure). The difference, $T_\infty - T_b$, decreases as the temperature increases. Equation (14) shows that the bubble growth rate decreases with increasing temperature. The effect of bubble movement caused by buoyancy forces and the effect of the spatial variation of the pressure during the bubble chamber cycle have been neglected during the bubble growth process.²² Table 121.X, adapted from Ref. 22, shows the change of A as a function of temperature.

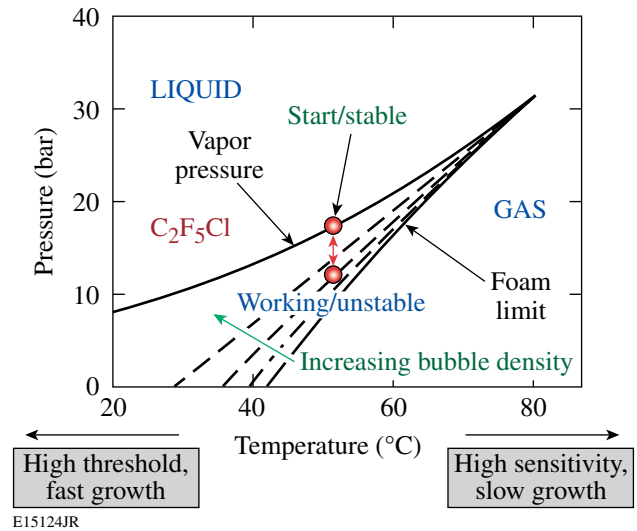


Figure 121.39

Bubble production as a function of pressure and temperature in a Freon 115 bubble chamber. The working region is the area between the vapor pressure line and the foam limit line. The dashed lines represent lines of constant bubble density (adapted from Ref. 20).

Table 121.X: Heat content and bubble growth rate for Freon 115 and hydrogen as functions of temperature (from Ref. 19).

Liquid	Temperature	$A(\text{cm}/\sqrt{\text{s}})$	Heat content (cal)
$\text{C}_2\text{F}_5\text{Cl}$	48°C	0.35	1.2×10^{-5}
	55°C	0.10	5.0×10^{-7}
	60°C	0.046	5.9×10^{-8}
	65°C	0.023	8.6×10^{-9}
H_2	29 K	0.095	9.3×10^{-8}

Equations (13) and (14) show that the development of an average bubble radius depends on both the temperature and time after initiation as shown in Fig. 121.40. From the temperature fluctuations inside the chamber, an active medium (Freon 115) variation range for parameter A was estimated. A temperature difference of 0.2°C between two Freon regions inside the chamber induces a 2% difference in the bubble-growth speed.

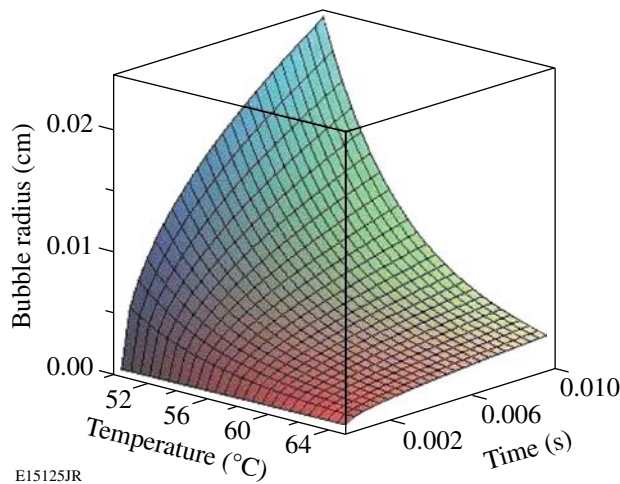


Figure 121.40
The average bubble radius as a function of temperature and time for Freon 115.

2. The Thermodynamic Mechanism of Bubble Formation in Freon 115

The mechanism of bubble generation inside a bubble chamber depends on the production of highly localized regions where heat is released (“temperature spikes”) within the active medium. These areas quickly expand into bubbles larger than the critical radius R_c [described by Eq. (3)] and grow through the evaporation of the superheated liquid.¹⁸

An incident neutron will interact with the sensitive medium inside a bubble chamber as follows:¹⁸

1. A percentage of the neutrons that reach the liquid scatter elastically off the nuclei of the constituent molecules. During this interaction, the neutrons eject charged nuclei from these molecules (C, F, Cl for Freon 115).
2. The ejected nuclei interact with molecules of the active medium, freeing nuclei or electrons from the medium atoms or moving the bound electrons to excited states.
3. The ejected electrons lose their energy inside the medium over a distance proportional to their initial velocity, ejecting more electrons. The recombination of the free electrons and ions/nuclei or the return of the electrons from their excited states to stable energy levels release energy that behaves as a “temperature spike.” When these processes occur in a quasi-spherical zone of volume $\sim R_c^3$, a bubble is generated.

The number of bubbles produced inside a neutron detector depends on the neutron path inside the active medium (directly related to the bubble chamber’s size), the neutron yield, the geometry of the experiment (the distance from the neutron source to the detector influences the solid angle), and the efficiency of the bubble creation mechanism by the incident neutrons. From previous experimental measurements, the total neutron-scattering cross sections are known to be $S_C = 1.30$ barn for carbon, $S_{Cl} = 2.0$ barn for chlorine, and $S_F = 0.053$ barn for fluorine.²⁵ The total cross section is $S_t = 4.865$ barn for a Freon molecule (8 atoms) that has a mass of $M = 154.5$ atomic units. The total cross section of the medium can be estimated from the detector volume. By taking the ratio between the total cross section and the detector cross section, the fraction of the incident neutrons interacting with the medium is determined.

To create a bubble, the energy released by the neutron has to reach the value E_b described in Eq. (5). Elastic collisions are described by a set of equations describing the conservation of momentum and energy:

$$m_n v_n + m_i v_i = m_n v'_n + m_i v'_i \tag{15}$$

$$\frac{m_n v_n^2}{2} + \frac{m_i v_i^2}{2} = \frac{m_n v'^2_n}{2} + \frac{m_i v'^2_i}{2},$$

where m and v represent the mass and velocity, with the indices “n” and “i” standing for the neutron and the recoil ion, respectively, and the prime annotation indicating the particles after interaction. The Freon molecules are at rest compared with the

high velocity of the incident neutrons, $v_i = 0$, and the maximum velocity of the recoil ion is (for a 180° scattering angle)

$$v_i' = \frac{2m_n v_n}{m_n + m_i}. \quad (16)$$

A fraction of the incident neutrons will interact with the Freon and eject nuclei from its molecules. Based on the 14.1-MeV initial energy of the neutrons and the dynamics of the elastic scattering, the final kinetic energy of the ejected nuclei can range from 0 MeV to ~ 4 MeV for the carbon ions (the lightest components from the Freon molecule). It takes 2 keV to 5 keV to completely ionize an atom of C, Cl, or F (only 11 to 17 eV to singly ionize it, depending on the atom species), so, for a first approximation, the ionization energies can be neglected.

The stopping power for heavy-charged particles in the classical regime (with $E \ll m_0 c^2$) is described by the Bethe–Bloch equation^{26,27}

$$S_i = \frac{Zz^2 e^4 N_A m_i}{8\pi \epsilon_0^2 m_e E_{kin} M_A} \cdot \rho \cdot \ln \left(\frac{3m_e E_{kin}}{2\bar{T}m_i} \right), \quad (17)$$

where the stopping power is expressed in MeV/cm, Z is the atomic number of target atoms, z is the atomic number of the charged particle, N_A is Avogadro's constant (mol^{-1}), m_e is the rest mass of the electron (kg), ϵ_0 is the electric permittivity of free space ($C \cdot V^{-1} \cdot m^{-1}$), E_{kin} is the kinetic energy of the particle (J), M_A is the molar mass of the target (g/mol), \bar{T} is the mean ionization energy (J), ρ is the medium density (kg/m^3), and e is the electron charge.

Using the SRIM software designed by James Ziegler (<http://www.srim.org>, based on the Bethe–Bloch equation and experimental data from many sources), the scattered ion range was found to be between $\sim 0 \mu\text{m}$ and $9 \mu\text{m}$, depending on the atom type and recoil ion energy. Each bubble produced inside the active medium expands from a very small volume associated with the transfer of the threshold energy E_b to either an electron or a nucleus from the incident particle as a result of Rutherford scattering.

The case where a recoil ion ejects further nuclei from the active medium molecules deserves a quick analysis. The cross section σ_p for ejecting a nucleus varies with $1/E_c$ in the Rutherford range, where E_c is the kinetic energy of the incident particle.¹⁸ For a given energy $E \geq E_b$, a simple calculation of

the ratio of the cross sections necessary to eject a nucleus and an electron is given by¹⁸

$$\frac{\sigma_p}{\sigma_e} = \frac{n_m m_e}{Z_e M_n}, \quad (18)$$

where n_m is the number of nuclei per molecule, m_e is the electron mass, Z_e is the number of electrons per molecule (the sum of the component atomic numbers), and M_n is the mass of the nucleus. The average mass for the nucleus of a Freon 115 molecule is $M_n = 19.3$ and $Z_e = 74$. Replacing all the values in Eq. (6), the obtained interaction cross-section ratio is $\sigma_p/\sigma_e \cong 3 \times 10^{-6}$. The fraction of the ejected nuclei that produce bubbles is only 3×10^{-6} of the number of electrons creating bubbles, so it can be neglected. Essentially all the bubbles generated by incident neutrons originate from free electrons ejected by recoil ions.

To measure the energy transferred to electrons by an ejected nucleus, one has to know the stopping power for a particle moving inside a medium. This is defined as the differential energy loss dE along the path element dx :²⁷

$$S = -\frac{dE}{dx}. \quad (19)$$

Using data obtained from simulations with the SRIM software, the stopping power's dependence on the ion energy has been plotted in Fig. 121.41.

To satisfy the minimum nucleation conditions, Eq. (9) must be true for the ion energy loss inside the superheated medium. If minimum energy loss/distance to create a bubble is written as L_b and the energy loss/distance for the recoil ion as L_i , the nucleation condition is satisfied for $L_i \geq L_b$. When this is satisfied, it does not mean that a bubble is created since bubble formation requires the electrons resulting from the recoil ion collision with the medium molecule electronic layers to have both the minimum nucleation energy and the minimum range, while the nucleation centers are too close to each other and will fuse quickly into a single visible bubble. In most cases, however, $L_i \leq L_b$ and the nucleation occurs with a probability depending on the energy loss per volume since Eq. (10) also needs to be satisfied. For the case of ions with low energies (valid for the case of 14-MeV neutron detection inside Freon 115), the number of bubbles generated by a recoil ion moving over a distance equal to the critical diameter can be expressed as

$$N_i = \alpha \cdot \left(\frac{L_i}{L_b} \right)^3, \quad (20)$$

where the third power is due to the volumes' ratio and α is a proportionality coefficient representing the energy conversion efficiency from the free electrons to the medium. Based on previous literature,^{12,14} this conversion efficiency is close to 1 and the bubbles' density depends on the energy loss of the ejected ions inside the superheated medium.

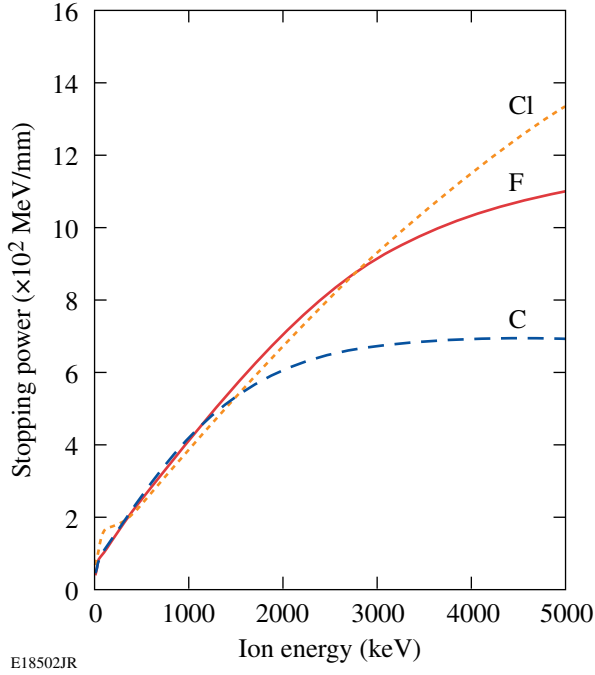


Figure 121.41
The total stopping power derived from SRIM simulations for ions of carbon, fluorine, and chlorine inside Freon 115.

3. The Stopping Power for Electrons Inside Freon 115

For electrons, the stopping power is calculated using the adapted Bethe–Bloch formula and expressed in MeV/mm (Ref. 27):

$$S_e = \frac{Ze^4 N_A}{8\pi\epsilon_0^2 m_e v^2 M_A} \cdot \rho \cdot \ln \left[\frac{m_e v^2 E_{kin}}{\bar{I}^2 (1 - \beta^2)} \right] + f(\beta), \quad (21)$$

where Z is the atomic number of the target atom, N_A is the Avogadro's constant (mol^{-1}), m_e is the rest mass of the electron (kg), ϵ_0 is the electric permittivity of free space ($C \cdot V^{-1} \cdot m^{-1}$), E_{kin} is the kinetic energy of the electron (J), M_A is the molar mass of the target (g/mol), \bar{I} is the mean ionization

energy (J), v is the electron velocity (m/s), ρ is the medium density (kg/m^3), e is the electron charge, $\beta = v/c$ with c the speed of light, and $f(\beta)$ is a relativistic correction function.

Using the ESTAR program designed by the National Institute of Standards and Technology (NIST) (<http://physics.nist.gov>), based on Eq. (21) and experimental measurements, the electron range r_e is multiplied by the density to give an areal density and is calculated by ESTAR in a similar way and displayed in Fig. 121.42(a). This value can be misleading since the electrons interact with the medium and do not move on straight trajectories. The actual range is about 30% less than that calculated by ESTAR. The electron stopping power inside Freon 115, normalized to the medium density, was calculated as shown in Fig. 121.42(b).

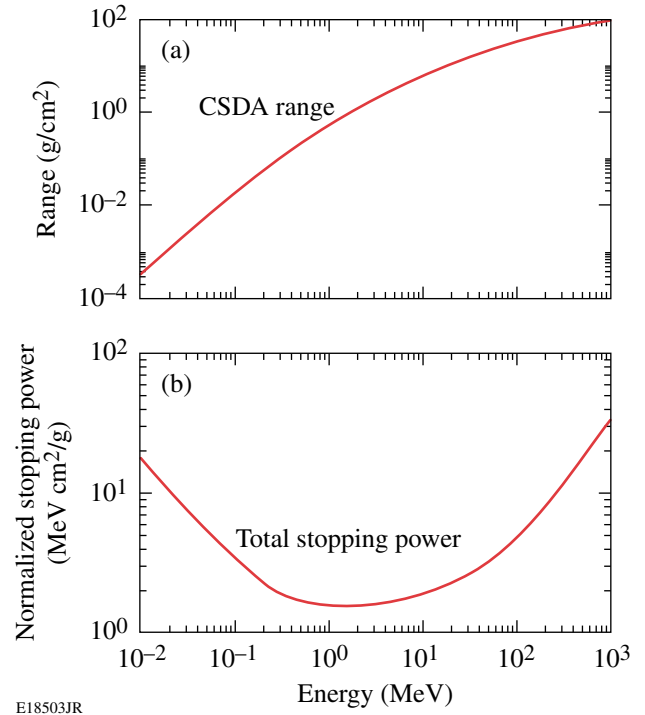


Figure 121.42
(a) The electron range multiplied by density inside Freon 115 and (b) the total stopping power for electrons inside Freon 115, normalized to the medium density.

The expression for the cross section (in cm^2) for an interaction between a nucleus and an electron (derived from the Rutherford formula) is (adapted from Ref. 18)

$$\sigma_{e,m} = 18.74 \times 10^{21} \frac{Z_e R_h}{E_b \beta^2} (\text{cm}^2), \quad (22)$$

where Z_e is the number of electrons/molecule, R_h is the Rydberg energy (13.6 eV), E_b is the threshold energy to create a bubble, and β is the ratio between the velocity of the incident particle (recoil ion) v and the speed of light c . As expressed by Eq. (22), $\sigma_{e,m}$ decreases with the recoil ion velocity.

Cross section, molecule concentration, and average molecular radius can be calculated from the medium density and molar mass. The fraction of electrons with energies high enough to cross a distance equal to the critical bubble diameter can be then expressed as

$$\alpha = \frac{\sigma_{e,m}}{\sigma_{\text{mol}}} \cdot \frac{r_d}{2R_c}, \quad (23)$$

where σ_{mol} is the molecule cross section, r_d is the ion recoil distance, and R_c is the bubble's critical radius. Combining Eqs. (20) and (23), the number of bubbles generated by a recoil ion becomes

$$N_i = \frac{\sigma_{e,m}}{\sigma_{\text{mol}}} \cdot \frac{r_d}{2R_c} \cdot \left(\frac{L_i}{\beta L_b} \right)^3. \quad (24)$$

Extending the calculations for a neutron detector, the sensitivity of a bubble chamber to neutrons can be expressed as

$$\begin{aligned} \frac{N_{\text{bubbles}}}{n_{\text{source}}} &= F_n \cdot N_i \cdot d\Omega \\ &= F_n \cdot \frac{\sigma_{e,m}}{\sigma_{\text{mol}}} \cdot \frac{r_d}{2R_c} \cdot \left(\frac{L_i}{\beta L_b} \right)^3 d\Omega, \end{aligned} \quad (25)$$

where F_n is the fraction of the incident neutrons interacting with the active medium and $d\Omega$ is the detector's solid angle. If this mechanism of bubble formation is valid, the value of $N_{\text{bubbles}}/N_{\text{source}}$ can range between 10^{-5} for a gel detector and 10^{-3} for a liquid detector. Unfortunately, as shown below, Eqs. (24) and (25) work only for a gel detector and for some liquid detectors. Freon 115 has a very small critical radius so the energy density required to generate a bubble cannot be reached based on the stopping power of the electrons ejected by the recoil ions.

The Mechanism of Bubble Formation for a Small Critical Radius

For nucleation to occur, the operating conditions must be in the thermodynamic limit, with critical radii in the range of

20 nm or larger and bubble threshold energies in the range of 1 keV or higher. An electron ejected by an incident particle ejects other electrons with relatively low energies. The incoming electron interacts with the orbital electrons in the medium, producing multiple new electrons (and ions) with lesser energy; each of these then interacts in the same way—a process that continues until many low-energy particles are produced. These are then stopped in the medium and absorbed. This process is known as a particle shower.

For very small critical radii, the volume of the critical bubble encloses only a few tens of molecules and the thermodynamic equations of bubble formation do not describe the nucleation process accurately. For example, for the case of Freon 115 at 50°C, the critical radius for bubble formation is 7 nm. Although the threshold energy for bubble generation decreases to ~100 eV for this volume, an electron with such a low energy has a range that is much less than the critical diameter. Its energy is transmitted to the medium over a range much smaller than the critical radius, and the bubble will collapse before it can nucleate. Even though an electron with a higher energy (500 eV) has a recoil range comparable to a critical bubble diameter, most of its energy will be lost while ejecting a small number of low-energy electrons that are immediately absorbed.

The software package CASINO (Monte Carlo simulation of electrons in solids, available for download at <http://www.srim.org/SREM.htm>), designed by Raynald Gauvin (Université de Sherbrooke, Québec, Canada), was used to calculate the electron ranges in Freon 115 at low energies. The average range of the electrons is ~14 nm (i.e., twice the critical radius). Electrons with energies higher than 500 eV will dissipate their energies over radii larger than the critical radius, while electrons with energies lower than 500 eV will not have enough energy to generate a shower of secondary particles that could fill the volume of a critical-radius bubble. For this reason, any generated micro bubble will quickly collapse before it can be observed. The mechanism of bubble formation based on the ejected electrons' stopping power does not work for media with a small critical radius, such as Freon 115.

For high-energy recoil ions, the dominant process that generates bubbles consists in the excitation of active medium molecules' electronic levels. This happens for energy values in excess of¹⁸

$$E_{\text{ex}} = \frac{M_i Z_i E_e}{m_e}, \quad (26)$$

where M_i is the mass of the incident particle (recoil ion), Z_i is the particle charge, and E_e is the first electronic excitation energy (13.6 eV). The excitation of the electronic levels releases energy quite uniformly inside a volume of a sphere of critical radius, and the distance between successive excited molecules will be less than the molecular mean free path. The nucleation process can be affected by the thermal motion since the growing bubble can break apart and collapse because of the random movement of molecules over the nucleation region. As shown in Eq. (22), the probability that a particle will eject a high-energy electron decreases with its energy. For very high energy particles, the probability of ejecting an electron drops to practically zero while the excitation of the electronic levels becomes the main mechanism for energy loss.¹⁸ Consequently, even for small critical radii, nucleation is possible for energies of the incident particles within the MeV range.

The probability of bubble generation for a recoil nucleus can be estimated from the ratio of the cross section for the first electronic-level excitation energy to the cross section of a critical radius bubble (as in this case where the energy is transmitted through the excitation of the electronic levels) and the nuclear recoil distance. The cross section for the first electronic-level excitation energy is difficult to estimate. It can be approximated using Eq. (26) to calculate the cross section to generate energies higher than the excitation level and subtracting from it the cross section for energies close to the E_b value (the energy necessary to create a bubble), which will generate more-energetic electrons that produce ionization in the medium and induce nucleation. Based on this approximation, the following equation provides a general estimate for the number of bubbles created by a recoil ion rather than an exact value:

$$N_{\text{ieex}} = \eta \left(\frac{\sigma_{\text{ex}} - \sigma_{\text{eject}}}{\pi R_c^2} \cdot n_{i,n} \right)^{\frac{E_b}{E_e}} \cdot \frac{r_d}{2R_c}, \quad (27)$$

where η is a correction coefficient that depends on the thermal influence for the bubble formation and must be determined experimentally, σ_{ex} is the cross section for a recoil ion to transmit the excitation energy E_e to an electron, σ_{eject} is the cross section for a recoil ion to eject an electron, R_c is the critical radius, E_e is the first electronic excitation energy, $n_{i,n}$ is the average number of interactions for which an electron of energy E_e is generated, E_b is the energy necessary to create a bubble, and r_d is the recoil ion range.

Adapting the calculations to a neutron detector, the bubble chamber's sensitivity to neutrons can be expressed as

$$\begin{aligned} \frac{N_{\text{bubbles}}}{n_{\text{source}}} &= F_n F_{\text{ex}} N_{\text{ieex}} d\Omega \\ &= F_n F_{\text{ex}} \eta \left(\frac{\sigma_{\text{ex}} - \sigma_{\text{eject}}}{\sigma R_c} \cdot n_{i,n} \right)^{\frac{E_b}{E_e}} \cdot \frac{r_d}{2R_c} d\Omega, \end{aligned} \quad (28)$$

where F_n is the fraction of the incident neutrons interacting with the active medium, F_{ex} is the fraction of carbon nuclei that can generate bubbles by exciting the electronic systems of the active medium, η is a thermal coefficient that must be determined experimentally, and $d\Omega$ is the detector's solid angle. With the exception of η , all of the factors can be estimated from theoretical calculations.

Calculation of the Thermal Coefficient η Based on Data from a Freon 115 Bubble Chamber Used at CERN

Bubble tracks were recorded by a Freon 115 detector designed and built at CERN in 1981.²⁸ The nucleations were generated by incident 360-GeV/c protons inside an externally induced magnetic field. The recorded bubble density along the charged-particle tracks was in the range of 160 bubbles/cm at 50°C, decreasing with temperature. Based on the SRIM simulations, the stopping power for charged particles decreases with increasing energy. For protons, it reaches a minimum of 0.2 MeV/mm at 2.75 GeV and increases slowly, reaching 0.3 MeV/mm at energies over 100 GeV/c (Ref. 29). For the operating conditions of the CERN bubble chamber, the pressure difference was in the range of 10 bar, with a critical bubble radius $R_c = 4.3$ nm at 50°C and $R_c = 2.6$ nm at 60°C. At high energies, the only possible interactions are those that excite the electronic levels (the interaction time is very short), and the interaction efficiency is close to 1. Equation (21) for the number of bubbles generated by a recoil ion can be rewritten as

$$N_i = \frac{r_d}{2R_c} \cdot \left(\frac{L_i}{L_b} \right)^3, \quad (29)$$

where r_d is the ion recoil distance, R_c is the critical bubble radius, L_b is the minimum energy loss/distance to create a bubble, and L_i is the energy loss/distance for the recoil ion. Using Eq. (29) the linear bubble density should be 429 bubbles/cm at 50°C and 155 bubbles/cm at 60°C.

The qualitative explanation is that the very small bubble radius and the thermal motion inside the liquid may disrupt and prevent the bubbles from nucleating. Using the data provided by Okada *et al.*,²⁰ describing the dependence of the Freon surface tension for Freon 115 as a function of temperature and

knowing the pressure drop during the chamber decompression, the critical radius for the bubble formation can be calculated using Eq. (3). Correlating the bubble's critical radius with the observed number of bubbles, a linear dependence of η with critical bubble radius was determined, as shown in Fig. 121.43. The η factor explains the discrepancies between the calculated and experimentally measured values.

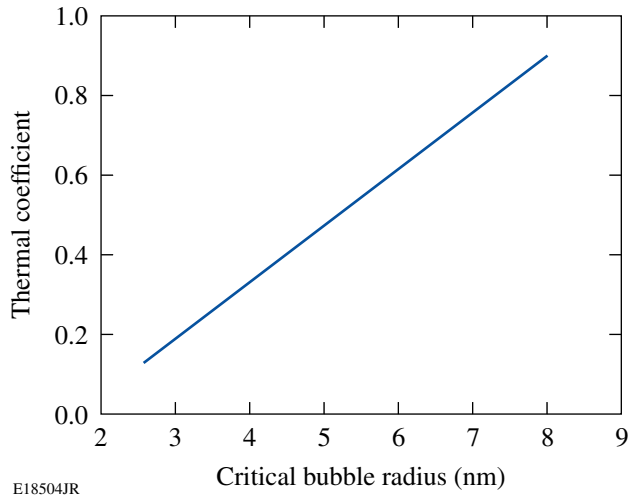


Figure 121.43
The thermal coefficient as a function of the critical bubble radius inside Freon 115.

For the experimental conditions encountered on OMEGA, the critical radius was in the range of 7 nm, so the thermal coefficient has a value of $\eta = 0.75$. In conclusion, the thermal motion affects bubble formation even for the mechanism of bubble formation involving the excitation of the electronic levels, and the bubble density decreases linearly with the increasing temperature.

Numerical Estimate for the Number of Nucleations Generated by 14.1-MeV Incident Neutrons Inside Freon 115

For Freon 115, the value of E_{ex} is 1.8 MeV for carbon, 4.2 MeV for fluorine, and 15.9 MeV for chlorine. Based on the recoil ion energies achieved from the elastic interactions with the incident 14.1-MeV neutrons, the maximum recoil energy is 4 MeV for carbon, 2.7 MeV for fluorine, and 1.5 MeV for chlorine. Equation (26) indicates that only the carbon recoil nuclei (ions) may have enough energy to generate nucleation inside Freon 115 by exciting the electronic system of the active medium molecules. The carbon recoil nuclei have an energy of 1.8 MeV or greater at a scattering angle of 50° .

Using the differential cross section for 14.1-MeV neutron elastic scattering on carbon shown in Fig. 121.44,³⁰ the fraction of carbon nuclei that can generate bubbles, F_{ex} , through the mechanism of exciting the electronic systems of the active medium can be estimated to be about 10% of the nuclei with which the incident 14.1-MeV neutrons interact.

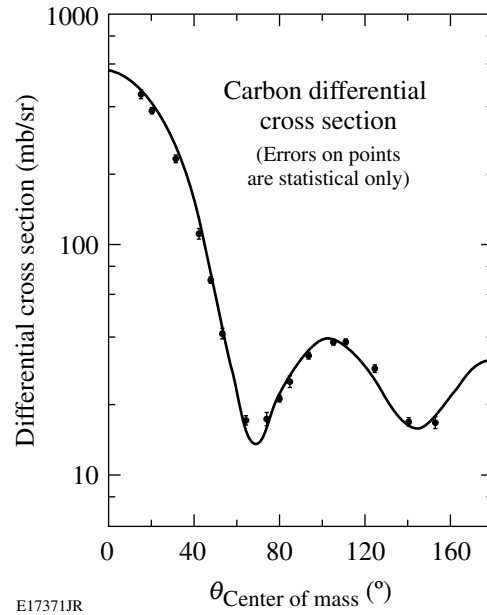


Figure 121.44
The differential cross section for 14-MeV neutron elastic scattering on carbon. About 98% of the recoil ions have energies greater than the threshold energy E_b necessary to generate a bubble (from Ref. 27).

The neutron-carbon cross section F_C represents 53% of the total cross section of Freon 115. Multiplying this value by F_n , one obtains the fraction of the incident neutrons interacting with the active medium that can theoretically generate bubbles inside Freon 115.

Based on Freon 115's density (1.15 g/cm^3) and molecular mass ($M = 154.5$ atomic units), the concentration of Freon molecules per cm^3 is $N_f = 4.99 \times 10^{21}$. This gives an average distance between molecules of $d_{\text{mol}} = 5.8 \times 10^{-8} \text{ cm}$ and a cross section for the volume occupied by a molecule of $\sigma_{\text{mol}} = 2.689 \times 10^{-15} \text{ cm}^2$ from Eq. (29).

The value of d_{mol} is used to estimate the factor

$$\left(\frac{\sigma_{\text{ex}} - \sigma_{\text{eject}}}{\sigma R_c} \cdot n_{i,n} \right)^{\frac{E_b}{E_e}} \approx 6.4 \times 10^{-8}.$$

The average recoil distance for carbon at energies between 1.8 MeV and 4 MeV is around $7 \mu\text{m}$ and $r_d/2R_c \approx 500$. With the thermal coefficient $\eta = 0.75$, the number of bubbles generated by a neutron that interacts with the medium and shape equivalent to that of the prototype detector used for neutron detection on OMEGA is

$$\frac{N_{\text{bubbles}}}{n_{\text{interact}}} = F_C F_{\text{ex}} N_{\text{icx}} = 5.8 \times 10^{-6}. \quad (30)$$

The detector is a 3.5-cm-diam, 10-cm-long cylinder. As specified in the previous section, the total cross section for the 14-MeV neutrons scattering on Freon is $S_t = 4.8$ barn (the Freon molecular mass is $M_{\text{Fr}} = 154.5$ atm). By knowing the active medium density, one can calculate the total cross section of the liquid. Freon has a density of 1.15 g/cm^3 at 50°C , so the corresponding mass for the volume is $m_f = 110$ g. As already shown, the fraction of the neutrons interacting with the Freon inside the detector is ≈ 0.22 and the solid angle of the detector is $d\Omega = 1.2 \times 10^{-6}$.

Substituting these values in Eq. (28), one obtains the estimated number of bubbles per source neutron $N_{\text{bubbles}}/n_{\text{source}} = 1.5 \times 10^{-12}$ or for the number of bubbles expected to be observed inside the detector, $N_{\text{det}} \approx 15$ for a neutron yield of 10^{13} . This low value for the number of bubbles created inside Freon 115 indicates that the Freon bubble chamber is not sensitive enough for neutron imaging for the yields achieved on OMEGA but may be appropriate for the higher yields produced at the NIF, where the neutron yield is expected to approach 10^{19} . These calculations were tested against experimental measurements with a Freon 115 bubble chamber. The experimentally observed values of $N_{\text{meas}} \approx 11$ to 14 bubbles agreed with these theoretically calculated values.¹⁰ If it were possible to use a liquid bubble chamber with Freon 115 at room temperature, the critical radius described by Eq. (4) would increase to ~ 20 nm and the ejected electrons would become dominant for bubble formation, as described previously. The number of observed bubbles should reach much higher values when calculated by Eq. (30) ($\sim 10^6$ bubbles). Unfortunately, for temperatures lower than 48°C , foaming occurs inside Freon 115 before any useful data can be recorded.¹¹

Numerical Estimate for the Number of Nucleations Generated by 14.1-MeV Incident Neutrons Inside a Gel Detector

Freon gel detectors were used to record 14.1-MeV neutrons on OMEGA in 2001.⁸ Disk-shaped gel bubble detectors,

8.5 cm in diameter and 1 cm thick, were installed behind the penumbral neutron aperture and close to the outside edge of the OMEGA target chamber. The detectors consisted of 10^5 droplets, approximately $3 \mu\text{m}$ in diameter, of a superheated liquid (Freon) suspended in an elastic polymer matrix support gel.⁸ The gel material has no effect on bubble generation.³¹ The neutron-imaging system's aperture was biconical, with a 0.75-mm inner diameter. The target-to-detector distance was 362 cm and the target-to-aperture distance was 8 cm, with a system magnification $M \approx 45$ (Ref. 8). The neutron yield was 6×10^{13} (Ref. 8).

Depending on the Freon type used, the calculated critical radius R_c at 22°C to 23°C can range from 20 nm to 40 nm with the energy necessary to create a bubble in the range of 1 keV to 5 keV. At these energies, the mean free path of the electrons ejected by the recoil nuclei inside the gas is about 20 nm to 40 nm, and the distance between two consecutive ejected electrons is shorter than the molecular mean free path of 1 nm to 3 nm, filling the critical bubble volume continuously with heat spikes resulting from the subsequent recombination of ions and electrons. As a result, the heat is released in a volume comparable to the volume of the critical radius for bubble formation R_c , the mechanism of bubble creation is valid, and Eq. (24) can be used.

The stopping power calculated for the recoil ions generated by incident 14.1-MeV neutrons inside Freon using the SRIM software is in the range of 400 MeV/mm, while the energy necessary to create a bubble along the particle trajectory is significantly lower, at 50 to 90 MeV/mm. On the molecular scale, most of the recoil ions (nuclei) will generate many electrons that can fill a critical bubble volume with enough energy to induce nucleation along its path. Since the ions have recoil ranges up to $9 \mu\text{m}$ (with an average value of $2 \mu\text{m}$), they will create a continuous track of bubbles that will grow rapidly and fuse into larger bubbles. These bubbles will fill the $3\text{-}\mu\text{m}$ superheated droplets and can be recorded.

The neutron-Freon interaction cross section is in the range of 4.2 barn for both Freon 12 and Freon 22. Using a similar calculation as for Freon 115, the neutron-detection efficiency per source neutron is estimated to be 0.021 for the 1-cm-thick gel detector, assuming it is filled entirely with Freon. Since only 0.1% of the detector's volume is actually filled with Freon, the detection efficiency is

$$\frac{N_{\text{bubbles}}}{n_{\text{source}}} = 2.1 \times 10^{-5} d\Omega. \quad (31)$$

Based on the geometry of the imaging system, the radius of the central maximum at the detector is $r \approx 3$ cm. The number of neutrons reaching the detector can be calculated using the formula

$$N_i = \frac{y \cdot r^2}{4 \cdot R^2}, \quad (32)$$

where y is the neutron yield, r is the radius of the detector, and R is the distance between the neutron source and detector. Inserting the numerical values into Eq. (32), the number of the neutrons entering the Freon medium is $N_i = 2.6 \times 10^8$. The solid angle of the detector is $d\Omega = 4.3 \times 10^{-6}$. Multiplying N_i by the neutron-detection efficiency per source neutron, the estimated number of bubbles inside the central maximum area is

$$N_{\text{bubbles}} = N_i \cdot \frac{N_{\text{bubbles}}}{n_{\text{source}}} = 5.4 \times 10^3. \quad (33)$$

The testing of gel detectors on OMEGA in 2001 measured 5.3×10^3 bubbles.⁸

Conclusions

Based on the classical mechanism of bubble formation, the interaction between an incident neutron and the sensitive medium inside a bubble takes place in three steps: first, the medium nuclei are elastically scattered; second, the scattered nuclei generate free electrons; and, third, the free electrons recombine with the ions over a quasi-spherical volume to generate bubbles.

The efficiency of nucleation depends on both the size of the critical radius and the medium temperature. For some particular cases, as in the use of Freon 115 on OMEGA, the critical radius is shown to be too small for bubble generation through the mechanism of free electron-ion recombination. Some bubbles are generated, however, through the excitation of electronic levels by charged incident particles at relatively high energies (MeV range).

For a bubble chamber used on OMEGA, the estimated number of bubbles per source neutron is calculated to be $N_{\text{bubbles}}/n_{\text{source}} = 1.5 \times 10^{-12}$, or for the number of bubbles observed inside the detector (after subtracting the turbulence area), the expected value is $N_{\text{det}} \approx 15$. These values agree with the experimentally recorded $N_{\text{meas}} \approx 11$ to 14 bubbles on OMEGA.¹⁰ The expected number of bubbles for the experi-

mental conditions encountered on OMEGA is insufficient for neutron imaging, but the higher yields from the NIF will be able to create a high-enough bubble density for a useful diagnostic tool, provided a similar but improved system is used.

Because of the lower temperature and larger (20-nm) critical radius, a simplified model of bubble formation that does not take into account the size of the critical radius gives accurate results for gel detectors. The numerical predictions of this model agree with the results obtained on OMEGA in 2001.⁸

ACKNOWLEDGMENT

This work was supported by the U.S. Department of Energy Office of Inertial Confinement Fusion under Cooperative Agreement No. DE-FC52-08NA28302, the University of Rochester, and the New York State Energy Research and Development Authority. The support of DOE does not constitute an endorsement by DOE of the views expressed in this article.

REFERENCES

1. S. Pfalzner, *An Introduction to Inertial Confinement Fusion* (Taylor & Francis, New York, 2006).
2. T. J. Murphy, C. W. Barnes, R. R. Berggren, P. Bradley, S. E. Caldwell, R. E. Chrien, J. R. Faulkner, P. L. Gobby, N. M. Hoffman, J. L. Jimerson, K. A. Klare, C. L. Lee, J. M. Mack, G. L. Morgan, J. A. Oertel, F. J. Swenson, P. J. Walsh, R. B. Walton, R. G. Watt, M. D. Wilke, D. C. Wilson, C. S. Young, S. W. Haan, R. A. Lerche, M. J. Moran, T. W. Phillips, T. C. Sangster, R. J. Leeper, C. L. Ruiz, G. W. Cooper, L. Disdier, A. Rouyer, A. Fedotoff, V. Yu. Glebov, D. D. Meyerhofer, J. M. Soares, C. Stockl, J. A. Frenje, D. G. Hicks, C. K. Li, R. D. Petrasso, F. H. Séguin, K. Fletcher, S. Padalino, and R. K. Fisher, *Rev. Sci. Instrum.* **72**, 773 (2001).
3. D. Ress *et al.*, *Science* **241**, 956 (1988).
4. L. Disdier, A. Rouyer, I. Lantuéjoul, O. Landoas, J. L. Bourgade, T. C. Sangster, V. Yu. Glebov, and R. A. Lerche, *Phys. Plasmas* **13**, 056317 (2006).
5. T. R. Boehly, D. L. Brown, R. S. Craxton, R. L. Keck, J. P. Knauer, J. H. Kelly, T. J. Kessler, S. A. Kumpan, S. J. Loucks, S. A. Letzring, F. J. Marshall, R. L. McCrory, S. F. B. Morse, W. Seka, J. M. Soares, and C. P. Verdon, *Opt. Commun.* **133**, 495 (1997).
6. L. Disdier, A. Rouyer, A. Fedotoff, J.-L. Bourgade, F. J. Marshall, V. Yu. Glebov, and C. Stoeckl, *Rev. Sci. Instrum.* **74**, 1832 (2003).
7. M. C. Ghilea, T. C. Sangster, D. D. Meyerhofer, R. A. Lerche, and L. Disdier, *Rev. Sci. Instrum.* **79**, 023501 (2008).
8. R. K. Fisher, R. B. Stephens, L. Disdier, J. L. Bourgade, A. Rouyer, P. A. Jaanimagi, T. C. Sangster, R. A. Lerche, and N. Izumi, *Phys. Plasmas* **9**, 2182 (2002).
9. M. C. Ghilea, D. D. Meyerhofer, and T. C. Sangster, "A Freon-Filled Bubble Chamber for Neutron Detection in Inertial Confinement Fusion Experiments," to be submitted to *Review of Scientific Instruments*.

10. M. C. Ghilea, D. D. Meyerhofer, and T. C. Sangster, "Neutron Detection with Bubble Chambers for Inertial Confinement Fusion on OMEGA," to be submitted to Review of Scientific Instruments.
11. A. Herve *et al.*, Nucl. Instrum. Methods Phys. Res. **202**, 417 (1982).
12. M. Das *et al.*, Radiat. Meas. **30**, 35 (1999).
13. J. W. Gibbs, Connecticut Academy Transactions **3**, 108 (1875-7).
14. L. K. Pan, J. Radioanal. Nucl. Chem. **240**, 707 (1999).
15. C. R. Bell *et al.*, Nucl. Sci. Eng. **53**, 458 (1974).
16. A. Norman and P. Spiegler, Nucl. Sci. Eng. **16**, 213 (1963).
17. C. R. Bell, "Radiation Induced Nucleation of the Vapor Phase," Ph.D. thesis, Massachusetts Institute of Technology, 1970.
18. F. Seitz, Phys. Fluids **1**, 2 (1958).
19. R. E. Apfel and S. C. Roy, Radiat. Prot. Dosim. **10**, 327 (1985).
20. M. Okada *et al.*, J. Chem. Eng. Data **33**, 399 (1988).
21. R. K. Fisher *et al.*, Rev. Sci. Instrum. **72**, 796 (2001).
22. J. Benichou *et al.*, Nucl. Instrum. Methods Phys. Res. **214**, 245 (1983).
23. D. V. Bugg, in *Progress in Nuclear Physics* (Butterworths-Springer, London, 1959), Vol. 7, pp. 1-52.
24. M. S. Plesset and S. A. Zwick, J. Appl. Phys. **25**, 493 (1954).
25. D. Hughes and R. Schwartz, *Neutron Cross Sections*, 2nd. ed (Brookhaven National Laboratory, Upton, NY, 1958).
26. H. A. Bethe and J. Ashkin, in *Experimental Nuclear Physics*, edited by E. Sergrè (Wiley, New York, 1953), Vol. I, pp. 166-357.
27. W. Benenson *et al.*, eds. *Handbook of Physics* (Springer, New York, 2002).
28. M. Dykes *et al.*, Nucl. Instrum. Methods **179**, 487 (1981).
29. H. Tai, *Comparison of Stopping Power and Range Databases for Radiation Transport Study*, NASA Technical Paper (National Aeronautics and Space Administration, Langley Research Center, Hampton, VA, 1997).
30. A. J. Frasca *et al.*, Phys. Rev. **144**, 854 (1966).
31. T. P. Pandya, A. K. Saxena, and B. C. Srivastava, Rev. Sci. Instrum. **47**, 1299 (1976).

Photoswitchable Gas Permeation Membranes Based on Liquid Crystals

Introduction

Research in the field of high-performance gas permeation membranes has, to date, focused on maximizing both mass transfer and selectivity. Although gateable interconnect membranes for liquids have evolved to a mature level, the development of gas membranes whose permeability can be controlled during operation or tuned to respond to changes in their environment is an important goal that has yet to be realized.^{1,2} Such “smart” materials are in high demand for smaller-scale membrane applications such as microanalysis, reactor devices, and also larger batch processes.² Our goal was to create a novel and scaleable membrane system to achieve complex chemical and fluidic manipulations controllable by external stimuli.

Our inspiration for employing liquid crystal materials as the “active” element for switchable and tunable gas separation membranes comes from two sources: (1) biological membranes composed of various types of lyotropic liquid crystal phospholipids, which, because of their enhanced ordering, make it possible to control reversible structural modifications and corresponding permeation changes, and (2) synthetic polymer-based membranes, where the sorption–diffusion process is controlled by segmental mobility and the free volume of the material. Primary relaxation processes of polymers, such as the glass transition, correspond to large changes in sorption–diffusion characteristics.³

Mesogenic materials offer a range of thermotropic secondary transitions that can potentially afford unique and tunable materials for permeation membranes. In the early 1980s Kajiyama and co-workers were the first to exploit these properties of mesogenic materials in a series of polymer-dispersed liquid crystal (PDLC) membranes. Such a system has many of the advantages of a liquid-diffusing phase, such as high mobility of permeants, yet retains the mechanical properties of a polymeric material. LC–polymer composites have been exploited for light-controlled active transport of metal ions; however, the majority of efforts have focused on harnessing thermotropic control. These PDLC systems demonstrated significant deviations in their permeation properties at both

the crystalline–nematic and the nematic–isotropic transition temperatures.⁴ An obvious caveat is that using changes in temperature to vary the permeability of the membrane material is intrinsically coupled to the kinetics of the permeant. Employing thermal events to tune permeability can be not only energy intensive but for many applications may also have an unacceptably long response time because of unfavorable thermal transport characteristics of polymer materials. Although thermally induced LC phase changes have been successful for controlling permeation in drug delivery applications,⁵ the primary aim of this work was to avoid the complications mentioned above by evaluating the permeation characteristics of LC materials under isothermal conditions.

To generate phase changes isothermally, a technique was adopted that is well established in LC photonics—using photochromic dyes that demonstrate a photomechanical effect. Azobenzene derivatives are among the most-studied and frequently employed photochromic dyes that convert incident light to mechanical energy through the process of *trans-cis* isomerization. Appropriate substitution at the *para* positions affords azobenzene derivatives, where the *trans* form is mesogenic because of its rod-like shape. In contrast, the *cis* isomer’s bent shape substantially perturbs LC ordering. This effect is illustrated in Fig. 122.1.

Several demonstrations of bulk nematic- to isotropic-phase changes induced by *trans-cis* photoisomerization in azobenzenes have been conducted in both low-molar-mass and polymeric systems. This “photomechanical” effect has been exploited to generate numerous types of reversible changes when azobenzene materials are added as “guest” dopants to both fluid and polymer “hosts.” Several extensive reviews document the azobenzene photomechanical effect in bulk materials.⁶

For efficient photoswitching in LC-based permeation membranes, the concentration of azobenzene absorbers in the LC host must be carefully selected to be large enough to effectively induce an isothermal phase shift but not large enough to pre-

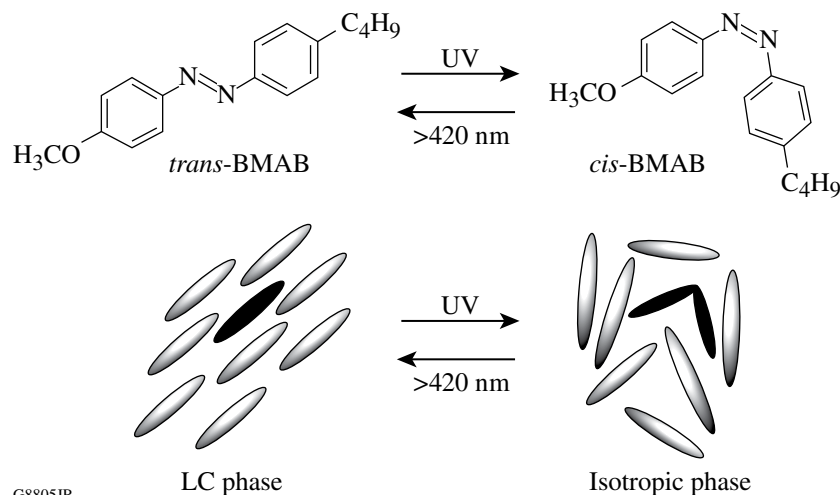


Figure 122.1

Photomechanical effect of 4-butyl-4'-methoxyazobenzene (BMAB) utilized to afford reversible isothermal LC-isotropic phase transitions.

vent penetration of the activating optical radiation throughout the bulk of the film. The particularly high molar extinction coefficient of azobenzenes makes it especially important to limit their content in the membranes to ensure that the entire depth of the film is actuated. Two azo-containing eutectic LC mixtures were prepared (Fig. 122.2). The azobenzene dye 4-butyl-4'-methoxyazobenzene (BMAB) has been used extensively as a photoresponsive mesogenic chromophore to generate refractive-index changes in thin polymer films⁷ and for optical data storage;⁸ it has also been incorporated at 15 wt% in a eutectic mixture with Merck E7 for photoswitching between the nematic and isotropic phases.⁸

To study the influence of chemical composition on permeation, a second eutectic mixture (Eutectic 2) based on the

phenyl benzoate LC materials 4-pentyl-4'-methoxybenzoate (PPMeOB) and 4-pentyl-4'-pentoxybenzoate (PPPOB) was used along with 4-ethoxy-4'-hexanoylazobenzene (EHAB) as the azobenzene dopant. Because both Eutectic 1 and Eutectic 2 have similar nematic ranges, viscosities, and dye content, these systems represented a nearly ideal “matched set” for evaluating the relationship of chemical composition of the LC phase on gas permeability in the confined membrane environment.

Photoswitchable membranes were fabricated either by dispersing the azobenzene-doped LC eutectic mixture into a host polymer solution and casting as a PDLC membrane as described by Kajiyama *et al.*⁷ or by imbibing the LC material directly into the cylindrical “track-etched” micropores of a commercial polycarbonate (Isopore) membrane. Isopore mem-

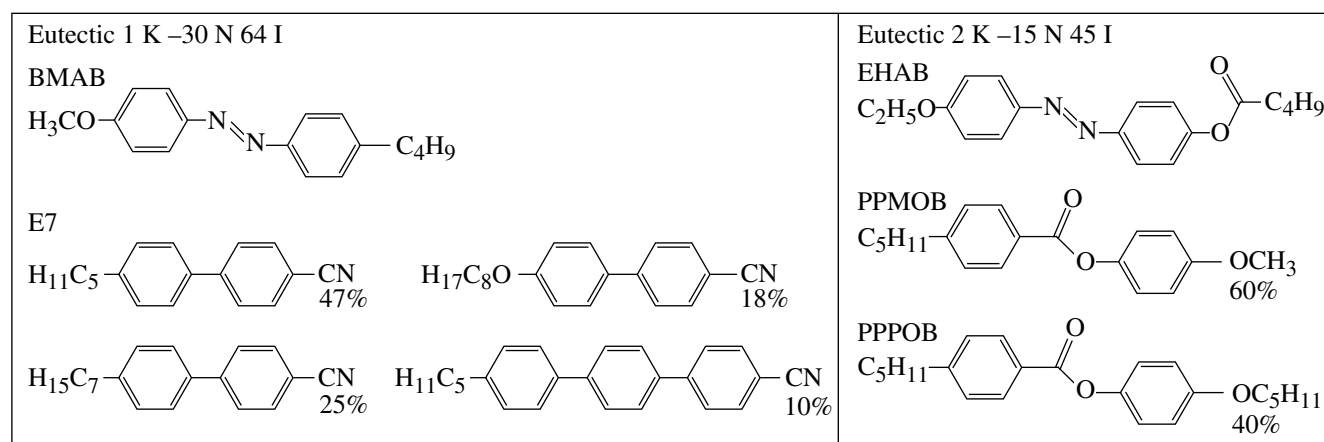


Figure 122.2

Molecular compositions and thermal properties of the two LC mixtures used.

branes are formed by bombardment with high-speed alpha particles, followed by chemically etching the damaged radiation tracks to produce cylindrical pores with remarkably smooth cavity surfaces. Previous studies of nematic LC materials confined in such a micropore environment have shown that the pore walls function as a homogenous alignment surface, resulting in the nematic director field configuration being uniaxial and parallel with respect to the pore wall.⁹ To test the effect of the LC alignment state (parallel or perpendicular to the pore walls) on permeation, the pore walls were treated with the reactive silane n-octyltriethoxysilane (OTS). Figure 122.3 shows a schematic diagram of how a photoswitchable LC material imbedded into a porous polymer membrane could be used for gas-phase switching and tuning applications. Using the well-defined, cylindrically symmetrical, preformed porous structure of the

membrane makes it possible to directly and conveniently probe the permeation properties of the photoswitchable LC host in the membrane as a function of LC orientation and irradiation. Porous membranes imbued with LC proved to be much better candidates than PDLC materials. We characterized the optical, thermal, and orientational properties of the confined LC eutectics and evaluated their permeation qualities, along with demonstrating reversible permeation control of nitrogen gas.

Results and Discussion

1. Photocontrollable PDLC Membranes

Our initial attempts focused on creating PDLC's for functional gas permeation membranes in a manner similar to that reported by Kajiyama *et al.*³ The major challenge in fabricating PDLC membranes for permeation applications is that the

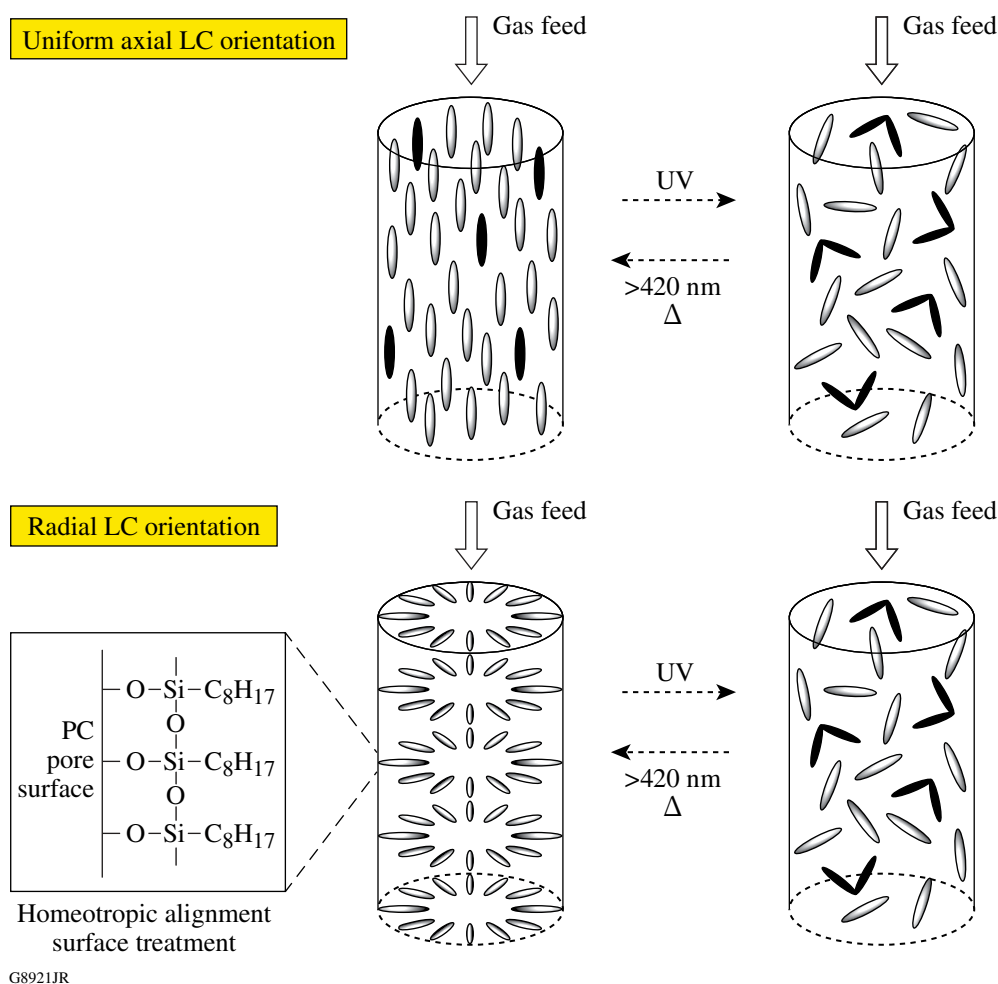


Figure 122.3

Photoswitchable operation of LC/mesogenic dye confined in track-etched pores based on reversible nematic–isotropic phase changes. Both homogeneous and homeotropic (radial) alignments with respect to the confining pore wall are evaluated in this article.

confined LC material will often heavily plasticize the polymer host, producing membranes without the necessary mechanical robustness. The PDLC's reported by Kajiyama overcame this difficulty by using a large thickness (several hundred microns), which precludes efficient photoactuation through the depth of the film because of the high extinction coefficient of azobenzene in the LC mixture. Although we successfully fabricated poly(vinyl chloride) (PVC)-based freestanding membranes that were only a few microns thick, they proved to be insufficiently mechanically robust and were ruptured by pressures >1 psi. Attempts to improve the membrane strength by using poly(methyl methacrylate) (PMMA) crosslinked with ethylene glycol dimethacrylate as the host polymer produced membranes that were extremely mechanically robust. The LC, however, still plasticized the host, resulting in membranes that stretched and "ballooned out" under pressure, but did not break because of the strength of the crosslinked PMMA. Based on these results, it became immediately apparent that, even with a great deal of additional materials research activities, freestanding PDLC membranes would not be practical candidates for photocontrolled membranes in the short term.

2. Photocontrollable Track-Etched Membranes with Imbided LC Material

a. Photoswitching and kinetics. The relatively thin membrane cross section of the photoswitchable LC-imbided Isopore polycarbonate membranes ($\approx 10 \mu\text{m}$), along with their high transparency in the long-wavelength-range UV, makes revers-

ible photoswitching possible by irradiation through alternating bandpass filters (365 nm or 420 nm).

To demonstrate that photoisomerization was indeed solely responsible for the observed phase changes, UV-Vis spectra were obtained for Isopore films imbided with Eutectic 1 and Eutectic 2 both before and after irradiation under the same conditions (Fig. 122.4). Ten seconds of irradiation time (which corresponds to a fluence of $2 \text{ mW}/\text{cm}^2$) is sufficient to nearly eliminate the absorbance band from the *trans* isomer at ≈ 360 nm. The accompanying rise of absorption at 420 nm from the photogenerated *cis* isomer appears as a small peak because of the low molar extinction coefficient of the *cis* isomer relative to the *trans* isomer. The 360-nm peak that appears as a shoulder in the spectrum of the Eutectic 1-imbided membranes is due to the absorbance of the cyanobiphenyl components of the E7 host LC. Irradiation with light >420 nm regenerates the *trans* form and affords the complete return to the original pre-irradiation spectrum for both eutectic mixtures. As is well known from PDLC research, the refractive-index mismatch between micrometer-sized nematic droplets and the polymer host results in a highly scattering film,¹⁰ and this refractive-index mismatch can be changed by inducing the LC material to undergo a phase change to the isotropic state either thermally or photochemically. In the case of an LC host containing azobenzene dyes imbided in a porous polycarbonate membrane, a similar photochemically induced phase change can be expected. The inset in Fig. 122.4 shows an image viewed through a stack of

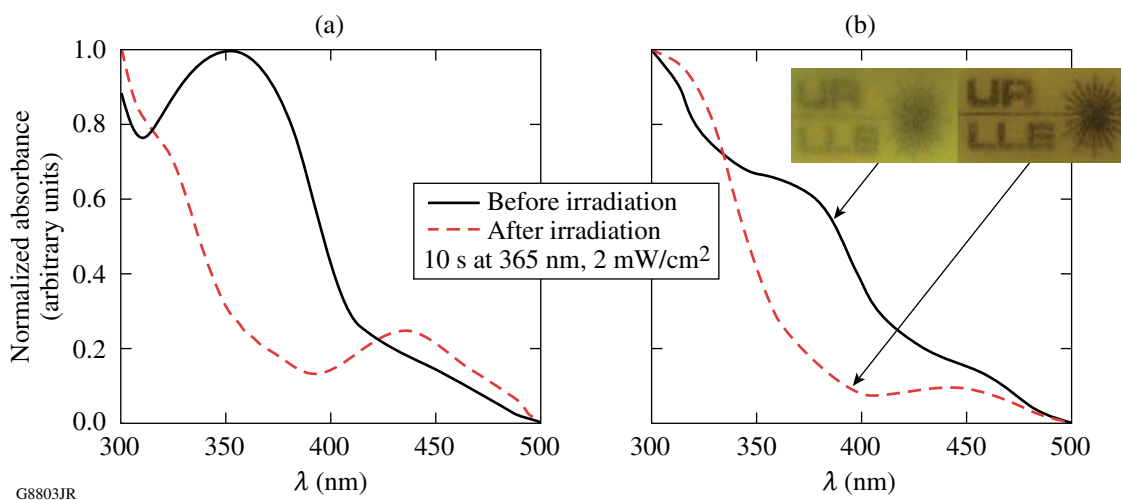


Figure 122.4

UV-Vis spectra of imbedded Isopore membranes before and after irradiation with UV light. Plot (a) shows Eutectic 2, plot (b) Eutectic 1. The inset in the upper right shows three stacked Eutectic 1-imbided membranes before and after irradiation, demonstrating the narrowing of refractive-index mismatch between host polycarbonate and confined Eutectic 1.

three photoswitchable LC-imbibed polycarbonate membranes containing Eutectic 1 (total path length = 30 μm) before and after irradiation with 365-nm UV. Although the contrast ratio between irradiated and non-irradiated membranes was relatively low because of the small LC domain size (400-nm LC-containing pores) in these membranes, they nevertheless clearly demonstrate that an LC-to-isotropic phase change is indeed occurring under the selected irradiation conditions. The isothermal nematic–isotropic phase changes were also verified by polarized optical microscopy (POM) (see **Dispersion State of Imbibed LC Materials** below).

The kinetics of thermal relaxation of the azobenzene dyes from the photogenerated *cis* state back to the original *trans* state in the confined environment are a parameter of interest. After irradiating a membrane for 10 s at 2 mW/cm^2 , the change in absorbance (A_t/A_0) at 365 nm was monitored as a function of time. The recovery of the *trans* isomer π - π^* absorption band with time obeys first-order kinetics for azobenzene dyes dissolved in solution. Azobenzene chromophores in the solid state, such as in thin films, are known to follow a more-complex behavior. This behavior is due to the fact that steric effects of the host environment on the azo dye affect the thermodynamics of thermal *cis*-*trans* isomerization. Figure 122.5 shows a logarithmic plot of A_t/A_0 as a function of time. The steep initial rise in the curve followed by a more-gradual leveling off and linear behavior is attributed to a first-order process with two rate constants, with the greater rate constant corresponding to azobenzene *cis* isomers that are in a more-strained environment. Because of the alignment effect of the confining surface,¹¹ we hypothesize that azobenzene mesogens close to the pore wall isomerize faster than those in the bulk. We found that the thermal relaxation of confined azobenzene mesogens resembled that of azobenzenes in the solid state¹¹ and could be modeled using the biexponential expression

$$[\text{trans}]_t/[\text{trans}]_0 = \alpha \exp[-k_1 t] + (1 - \alpha) \exp[-k_2 t]. \quad (1)$$

The calculated rate constants are an order of magnitude greater than typical azobenzenes in solution in an isotropic solvent.¹² The OTS-aligned Eutectic 1 proved to be anomalous to the other confined materials in that photoinduced isomerization occurred more slowly, and only after 10 min in the dark did the *cis*-isomer population begin to decline. We are currently conducting experiments to explain this observation.

b. Dispersion state of imbibed LC materials. Understanding the ordering of mesogenic molecules in the porous membrane structure is requisite to interpreting the permeation character-

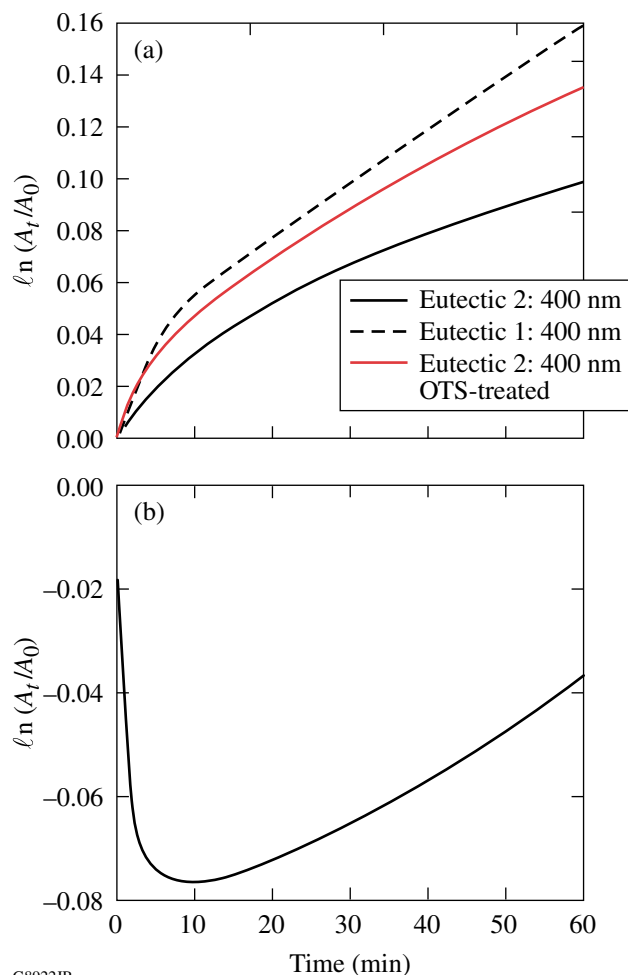


Figure 122.5 Normalized absorbance (A_t/A_0) over time for the two eutectic mixtures at 360 nm following 10 s of irradiation (2 mW/cm^2). Measurements were taken in the dark over 1 h, every 10 s. (a) Unaligned Eutectic 1: $k_1 = 0.72 \times 10^{-2} \text{ min}^{-1}$, $k_2 = 0.20 \times 10^{-2} \text{ min}^{-1}$. Eutectic 2: $k_1 = 0.61 \times 10^{-2} \text{ min}^{-1}$, $k_2 = 0.19 \times 10^{-2} \text{ min}^{-1}$. OTS-aligned Eutectic 2: $k_1 = 0.73 \times 10^{-2} \text{ min}^{-1}$, $k_2 = 0.20 \times 10^{-2} \text{ min}^{-1}$. Graph (b) shows the anomalous behavior of OTS-aligned Eutectic 1 in 400-nm pores.

istics of such materials. We evaluated the nematic range of the eutectic materials both in the bulk state and imbibed into the pores using both POM and differential scanning calorimetry (DSC). For DSC evaluation, the membranes were carefully chopped into pieces and then packed into a DSC pan for measurement. Although the quantity of mesogenic material in the pores was very small, definite phase-transition endotherms were visible with good signal-to-noise ratio at scan rates $\geq 40^\circ\text{C}/\text{min}$ on both heating and cooling. Repeated cycling produced no noticeable changes in the DSC thermograms for all samples evaluated. Thermograms for the eutectic materials in both the free-bulk and confined geometries were normalized to bal-

ance out the large disparity in sample quantity. Figure 122.6 compares the nematic–isotropic phase-transition temperatures for the two photoswitchable eutectic mixtures in the free-bulk versus the confined environment of the membrane pores, with and without treatment with OTS. For Eutectic 1 (biphenyl host), the nematic–isotropic transition temperature T_{cl} decreased only slightly in the confined state, while in Eutectic 2 (phenylbenzoate host) T_{cl} increased relative to the bulk material, which indicates the confined environment increases the LC bulk order and stabilizes the LC phase. For the biphenyl host (Eutectic 1), the observed reduction in T_{cl} may be caused by extraction of trace unreacted monomers from the porous polycarbonate membrane since biphenyl materials such as E7 are well known to plasticize many different polymer systems. Studies of E7 (Ref. 13) and other cyanobiphenyl LC materials¹² in PDLC's have also shown very small drops in T_{cl} of dispersed nematic droplets. OTS treatment increased the T_{cl} for both confined eutectics, suggesting the effectiveness of this treatment in supporting LC alignment.

Direct observation by POM of the texture of the LC photoswitchable host confined in the 400-nm pores of the Isopore membrane was not possible because of (1) the regions of highly crystalline polycarbonate domains of the order of several microns that extensively scatter light in the membrane and (2) the high birefringence of the membrane imparted by the

extrusion process used in its fabrication. For Isopore membranes with 10- μm pores, we were able to easily image the LC orientation in the pores by keeping the optical axis of the film fixed so that it was always aligned parallel to the incident polarizer. Rotating the analyzer so that it was oriented either parallel or perpendicular to the incident polarizer allowed one to see the confined LC at 1000 \times total magnification using combinations of transmitted and reflective illumination. Prior to imaging the membrane, any remaining traces of free LC material were removed from the surface by spinning the membranes at 3000 rpm and washing with several drops of hexane. Figure 122.7 shows a series of photomicrographs of the two photoswitchable LC eutectics imbibed into 10- μm pores of Isopore membranes. When viewed under crossed polarizers in reflection and transmission, the pores appeared as brighter areas while the surrounding polymer matrix appeared dark. The smeared birefringent areas around some of the pores are most likely caused by leaching of the LC eutectic into defect voids that extend laterally out from any pore walls that have been over-etched during membrane manufacture. Viewing under crossed polarizers with both transmitted and reflected illumination while rotating the sample stage establishes that the LC molecules are uniaxially arranged in the 10- μm pores and parallel to the pore axis. These findings are consistent with the ²H NMR studies of Crawford *et al.*¹¹ for nematogens in Isopore membrane pores, as well as for inorganic porous photonic

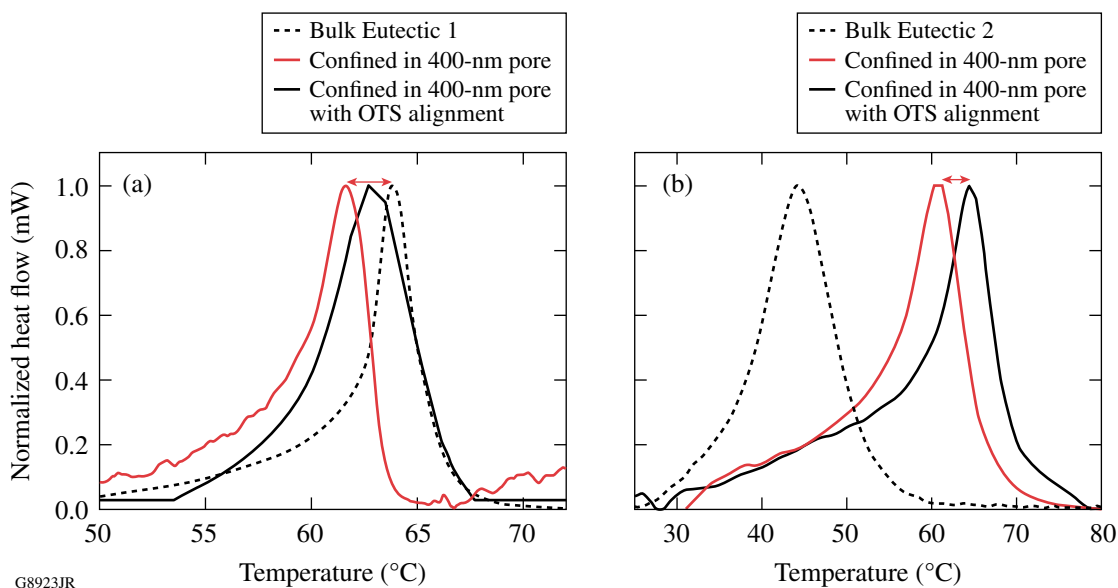


Figure 122.6

DSC heating scans for (a) Eutectic 1 and (b) Eutectic 2. Note that the signals are normalized to compensate for large disparity in sample quantity.

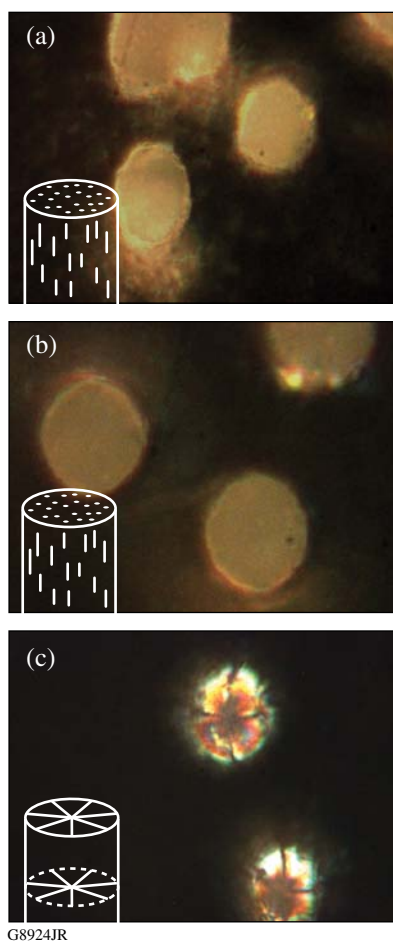


Figure 122.7
POM images of LC material confined in 10- μm pores. (a) Eutectic 1 without alignment, (b) Eutectic 2 without alignment, and (c) Eutectic 1 in a pore treated with 2% OTS solution. The inset drawings illustrate the orientation of the nematic director fields.

crystals (200- to 600-nm pores) imbibed with LC materials.¹⁴ Membranes treated with OTS demonstrated the Maltese-cross optical texture that is characteristic of radial alignment.

c. Permeation properties. Permeation tests are carried out using a traditional volume/time method to determine the steady-state permeation coefficient P (Ref. 15). The coefficient P is defined as the Fickian flux (J) times the value of membrane thickness (l) divided by the pressure difference (Δp) across the membrane, where the flux J equals the concentration gradient (concentration ϕ divided by length x) multiplied by a diffusion coefficient D :

$$J = -D \frac{d\phi}{dx} \quad (2)$$

$$P = \frac{J \cdot l}{\Delta p}. \quad (3)$$

After the membranes equilibrate at a given pressure, the volume of nitrogen diffused over time is measured. The membrane is then irradiated with 365-nm light for 5 s (2 mW/cm^2) to switch it into the isotropic state and subsequently reach equilibrium, after which the permeability is re-measured. Irradiation is then conducted using $>420 \text{ nm}$ for the same time and intensity as the UV irradiation to photoswitch the membrane back to the LC state. This test cycle is repeated to check for reversibility, which we define as four cycles between the alternately photogenerated states without measurable deviations from steady-state permeation behavior of the respective states. From our initial tests, a clear relationship emerged between confining pore size and the capacity to withstand incident pressure. Membranes with larger pores do not display sufficient stability with respect to sustained irradiation–permeation cycles. Neither 5- μm nor 10- μm pore sizes provided sufficient confinement strength to retain the LC eutectics in the pores. We did find that 400-nm pores perform very well over consecutive test cycles. Imbibed 400-nm pore membranes were 6 to 7 orders of magnitude less permeable than empty membranes. When filled with LC eutectics, they exhibited permeability of the same range as highly permeable rubbery polymeric materials, such as poly(dimethyl siloxane).¹ Both LC materials display good reversibility below 500 mmHg. Figure 122.8 shows permeability versus pressure (P/p) data for Isopore membranes with 400-nm pores imbibed with both Eutectic 1 and Eutectic 2. Both materials appear to follow ideal linear P/p behavior in both the LC and the isotropic states.

The isotropic state provides greatly increased permeation in photoswitched imbibed Eutectic 1. Treatment with OTS slightly lowers the permeability of the photogenerated isotropic state, although that of the LC state is unchanged. We conclude that uniaxial versus radial alignment has no effect on the permeability of Eutectic 1. In the case of Eutectic 2, the photogenerated isotropic state is less permeable than the initial LC state, and overall permeability values are an order of magnitude lower than Eutectic 1. The effect of the OTS alignment is significantly more pronounced. The increased T_{cl} shown by DSC and the faster *cis-trans* thermal isomerization suggest that enhanced LC ordering is responsible for lower permeation. Eutectic 1 shows permeation overall an order of magnitude greater than Eutectic 2, for both LC and isotropic states, with or without OTS treatment. This finding leads us to conclude that the intrinsic sorption–diffusion–desorption properties (with respect to nitrogen) of the imbibed material are what change upon photoirradiation. Increasing the permeation difference

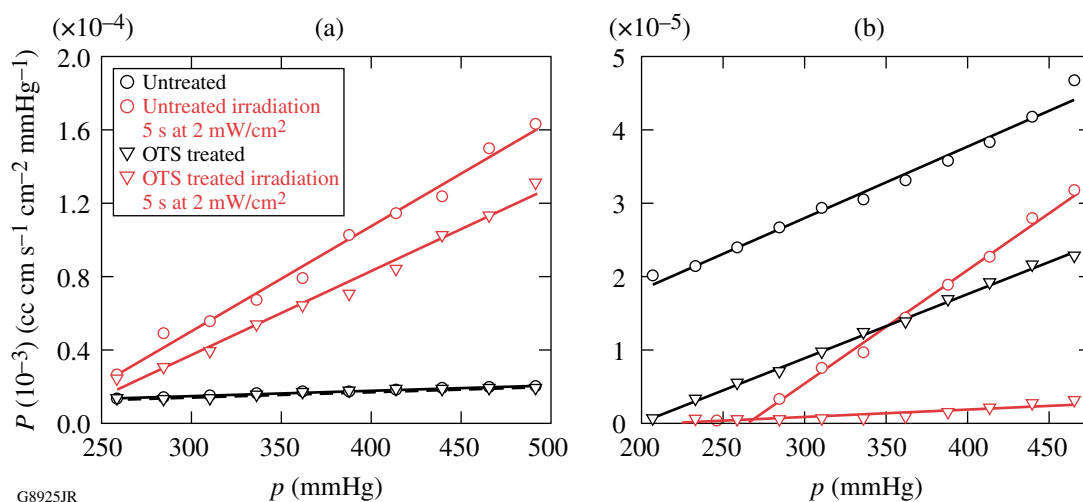


Figure 122.8

Permeability/pressure relationships for imbibed LC materials in 400-nm pores: (a) Eutectic 1 and (b) Eutectic 2. Photoswitching causes a reversible change in the permeation coefficient P .

between photogenerated states and achieving potential tunable selectivity are the subjects of our ongoing investigations.

Conclusions

The results of this effort have shown that photoswitchable LC materials based on azobenzene derivatives as the active element have potential for application to reversible photocontrollable gas permeation membranes. The imbibed mesogenic materials offer several tunable variables based on exploiting LC composition and alignment effects. For all imbibed materials, linear sorption–diffusion behavior was observed. Isothermal permeability switching response times between the LC and isotropic state of 5 s were demonstrated at an intensity of 2 mW/cm² using alternating UV and >420-nm radiation. Our goal now is to increase the overall differences in permeability that can be achieved through photoswitching, as well as explore possibilities for tunable selective permeation. These goals lead us to focus on exploiting the multitude of LC phases that are regularly used for various electro-optical applications (smectic phases, chiral phases, etc.). These materials potentially offer many types of tunable-ordered media that can be applied to separation technology and gateable interconnects in “smart” photocontrollable membranes.

Experimental

1. Preparation of Photoswitchable LC Mixtures

Photoswitchable eutectic mixtures were prepared by adding an azobenzene LC material to an existing eutectic LC mixture and mixing above the isotropic temperature of the

mixture. The phase transition of the mixtures was verified by hot-stage polarizing microscopy (POM). The composition of the two mixtures studied is given in Fig. 122.2. Eutectic 1 was prepared by doping 14% w/w of the azobenzene 4-butyl-4'-methoxyazobenzene (BMAB) into the biphenyl host Merck E7 at an elevated temperature. This azobenzene compound was synthesized, as previously reported.¹⁶ Eutectic 2 was prepared by doping 15% w/w of 4-ethoxy-4'-hexanoylazobenzene (EHAB) obtained from Eastman Chemical into a 60:40 w/w eutectic mixture of 4-pentylphenyl-4'-methoxybenzoate (PPMeOB) and 4-pentylphenyl-4'-pentoxybenzoate (PPPOB) at an elevated temperature. These two phenylbenzoate materials had been previously synthesized and purified in-house using well-known preparation and purification techniques.

2. Preparation of LC-Imbibed Track-Etched Membranes

Track-etched, 10- μ m-thick Isopore polycarbonate films (Millipore Corp.) with pore sizes of 0.4 μ m, 5 μ m, and 10 μ m were heated to 100°C in vacuum (200 mtorr) overnight to remove water and other volatile components. The membranes were imbibed with LC through capillary action by completely immersing them into the LC eutectic at a temperature above the LC isotropic transition (80°C) for 1 h. Excess LC on the surfaces of the membrane was removed by carefully rubbing the membranes between two sheets of filter paper. To achieve homeotropic alignment, reactive silane octyl triethoxysilane (OTS) was used. Membranes were immersed in a solution of 2-wt% OTS in ethanol with a few drops of acetic acid catalyst for 5 min, then dried in a vacuum oven. For POM imaging,

all residual LC material was removed from the surface by spinning the membranes at 3000 rpm and washing with a few drops of hexane. Photoswitching experiments were conducted using a Rolence Technologies Q-Lux handheld UV curing unit (365 nm at 70 mW/cm²). The output wavelength bandwidth was narrowed to 365 nm and 420 nm, as required, using optical bandpass filters (Edmund Optics).

3. Characterization

Differential scanning calorimetry (DSC) measurements were conducted using a Perkin-Elmer DSC 7 with a CCA-7 liquid nitrogen subambient accessory. The sample and reference compartments were purged with nitrogen at a flow rate of 20 ml/min. Optical spectroscopy (UV-VIS) was accomplished using a Perkin-Elmer Lambda 900 spectrophotometer, while visualization of the LC confined in the porous membrane structure was carried out using either a Leitz Orthoplan POL polarizing microscope or a Leica DMRX polarizing microscope at up to 1000× total magnification with reflected and transmitted illumination.

4. Permeability Measurements

The permeability of the photoswitchable LC membranes to nitrogen was measured according to the volume/time method using an apparatus that was constructed in-house. The membrane being tested was clamped between two rubber gaskets in an aluminum manifold and equilibrated with a given upstream pressure (200 to 500 mmHg). The permeation cell was designed in such a way that the membrane was irradiated directly. The permeation area was 0.5 cm².

ACKNOWLEDGMENT

This work was supported by the U.S. Department of Energy Office of Inertial Confinement Fusion under Cooperative Agreement No. DE-FC52-08NA28302, the University of Rochester, and the New York State Energy Research and Development Authority. The support of DOE does not constitute an endorsement by DOE of the views expressed in this article.

REFERENCES

1. D. R. Paul and Y. P. Yampol'skii, in *Polymeric Gas Separation Membranes*, edited by D. R. Paul and Y. P. Yampol'skii (CRC Press, Boca Raton, FL, 1994), Chap. 1, pp. 1–17.
2. M. Ulbricht, *Polymer* **47**, 2217 (2006).
3. T. Kajiyama, in *Polymers for Gas Separation*, edited by N. Toshima (VCH Publishers, New York, 1992), Chap. 3.
4. T. Kajiyama, A. Takahara, and H. Kikuchi, *Polym. J.* **23**, 347 (1991).
5. R. Dinarvand and M. Ansari, *J. Membr. Sci.* **223**, 217 (2003).
6. R. H. El Halabieh, O. Mermut, and C. J. Barrett, *Pure Appl. Chem.* **76**, 1445 (2004); C. J. Barrett *et al.*, *Soft Mat.* **3**, 1249 (2007); G. S. Kumar and D. C. Neckers, *Chem. Rev.* **89**, 1915 (1989).
7. H. Kurihara, A. Shishido, and T. Ikeda, *J. Appl. Phys.* **98**, 083510 (2005).
8. T. Ikeda and O. Tsutsumi, *Science* **268**, 1873 (1995).
9. G. P. Crawford *et al.*, *J. Chem. Phys.* **96**, 7788 (1992).
10. M. R. LaPointe and G. M. Sottile, in *Solar and Switching Materials*, edited by C. M. Lampert, C.-G. Granqvist, and K. L. Lewis (SPIE, Bellingham, WA, 2001), Vol. 4458, pp. 112–119.
11. I. Suzuki *et al.*, *Macromolecules* **35**, 577 (2002); I. Mancheva, I. Zhivakov, and S. Nespurek, *J. Optoelectron. Adv. M.* **7**, 253 (2005).
12. W. Ahn *et al.*, *Macromolecules* **25**, 5002 (1992).
13. S. R. Challa, S. Q. Wang, and J. L. Koenig, *J. Therm. Anal.* **45**, 1297 (1995).
14. P. El-Kallassi *et al.*, *J. Opt. Soc. Am. B* **24**, 2165 (2007).
15. D. W. Brubaker and K. Kammermeyer, *Anal. Chem.* **25**, 424 (1953).
16. E. Głowacki, K. L. Marshall, and C. W. Tang, in *Liquid Crystals XIII*, edited by I. C. Khoo (SPIE, Bellingham, WA, 2009), Vol. 7414, p. 74140H.

High-Intensity Laser–Plasma Interaction with Wedge-Shaped–Cavity Targets

Introduction

The interaction of intense, picosecond laser pulses with cone- and wedge-shaped–cavity targets is an important topic for applications such as fast ignition,¹ proton^{2,3} and electron⁴ acceleration, x-ray generation,⁵ and isochoric heating⁶ of solid matter. The primary coupling mechanism of high-intensity laser pulses ($\geq 10^{18}$ W/cm²) interacting with solids is the acceleration of electrons to kinetic energies of up to several MeV. A significant portion of the laser energy is converted into these suprathermal electrons. Maximizing this conversion efficiency for the various applications is a major challenge.

A number of factors that affect the conversion efficiency include the laser contrast (which is defined as the ratio of peak power to the power of a pedestal at a certain time before the main pulse), the laser polarization, and the target geometry. Several studies have shown that a high contrast ratio is critically important for cone-in-shell fast ignition.^{7–9} A better coupling efficiency has been demonstrated with second-harmonic irradiation of microcones.¹⁰ It has also been shown that pre-plasma formation in the hollow cone substantially affects the conversion process.^{8,9} Large-scale-length plasmas inside the cone significantly influence the relativistic laser–plasma interaction, the laser-energy deposition, and the generation and transport of hot electrons toward the compressed fuel core.¹¹

The coupling efficiency in wedge and cone targets is not completely understood, and more studies are required to fully quantify how the shape of the target affects the fast-electron production for the various applications. Particle-in-cell (PIC) simulations by Nakamura *et al.*³ predicted that higher-energy fast electrons and protons would be produced using cones having a narrower (30°) cone angle and irradiated with a laser intensity of $\sim 10^{19}$ W/cm². The simulations predict that laser energy is more efficiently absorbed and funneled into the tip of the cone through surface-field effects. Similar studies were performed by Lasinski *et al.* with 2-D PIC simulations for fast-ignition targets.¹² The cone geometry was studied to maximize the laser energy that is absorbed into fast electrons and to optimize the conditions for achieving a collimated fast-

electron beam at the tip. Other theoretical studies predict some benefit of using cone-shaped targets over flat foils in terms of increased laser absorption and enhanced energy transfer into fast electrons¹³ and surface-guided fast electrons into the cone tip.¹⁴

This article presents experimental studies of fast-electron generation in hollow wedge-shaped–cavity targets, which consist of two square copper metal foils that are seamlessly joined together at one side to form a cavity. A laser beam with a contrast ratio higher than 10^8 was focused into the cavity to the target’s corner with intensities of $\sim 1 \times 10^{19}$ W/cm² using either *s*- or *p*-polarization irradiation.^{15,16} The small-mass targets were in the refluxing regime,¹⁷ meaning that strong Debye sheath fields were created at the target boundaries that confined the majority of the fast electrons in the target.¹⁸ This made it possible to infer the laser-to-fast-electron conversion efficiency by measuring the absolute K_{α} -line emission produced in the target.¹⁹ The following sections describe the targets and the experimental setup; present and analyze the experimental results; discuss the results and compare them to 2-D PIC simulations; and present conclusions of this work.

Targets and Experimental Setup

General Atomics fabricated the targets by micromachining small wedges from ~ 100 - μm -wide aluminum (Al) bars to form an extremely sharp edge (edge radius of curvature of less than ~ 1 μm); the bars were electroplated with a thin (~ 20 - μm) Cu layer on both sides and cut into separate pieces. The inner Al material was etched away, leaving hollow Cu wedges comprising two ~ 100 - μm squares of ~ 20 - μm thickness joined seamlessly together. Figure 122.9 shows photos of (a) 30°- and (b) 45°-opening-angle wedges mounted on a target stalk.

Targets with 30°, 45°, and 60° full opening angles were fabricated. The laser propagated along the *y* direction (see Fig. 122.9 for the definition of the coordinate system) into the cavity with its focal plane located at the inside wedge seam. The inside corner radius was estimated to be ~ 1 μm , smaller than the focal-spot diameter of ~ 5 μm . The wedge-shaped–cavity

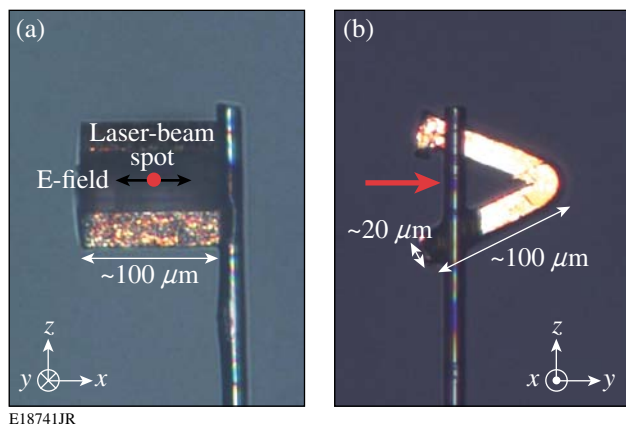


Figure 122.9

(a) A mounted 30°-opening-angle wedge looking along the laser propagation direction and (b) a mounted 45°-opening-angle wedge orthogonal to the laser propagation direction. Both targets were mounted for *s*-polarization irradiation.

targets' orientation set the laser polarization with respect to the target surface. With the electric field vector of the laser beam along the *x* direction, both targets in Fig. 122.9 were mounted for *s*-polarization irradiation. Rotating the target by 90° around the laser axis made it possible to investigate the interaction with a *p*-polarized beam. The targets were mounted onto 17- μm -diam SiC fibers. The accuracy of the target mounting with respect to beam polarization was estimated to be 5°. The targets were aligned with a precision of $\sim 5 \mu\text{m}$ and $\sim 2^\circ$ with a target-positioning station comprising three translational and one rotational axes; a target-viewing system made two orthogonal views of the target possible. Approximately 40 targets were used in this campaign with about half for each polarization.

The Multi-Terawatt (MTW) Laser System consists of an optical parametric chirped-pulse amplification (OPCPA) front end,¹⁵ which delivered pulses with $\sim 250\text{-mJ}$ energy and 0.5-ps duration at $\lambda = 1.053 \mu\text{m}$; these pulses were subsequently amplified in a Nd:glass amplifier chain up to 10 J (Ref. 20). For this experiment, pulse energies of around 5 J with 1-ps duration were used. The beam was focused with an off-axis parabolic mirror with an effective *f* number of ~ 4 to a nearly diffraction limited spot of $\sim 5\text{-}\mu\text{m}$ diameter, defined by the full width at half maximum (FWHM) of a peak intensity of $\sim 1 \times 10^{19} \text{ W/cm}^2$. The high temporal contrast was measured with a scanning third-order cross correlator. The ratio of the peak power to the power of a pedestal 100 ps before the main pulse was $>10^8$ (Ref. 16).

Laser-produced fast electrons generated an 8-keV line emission by knocking out K-shell electrons. Both x rays and

energetic electrons may produce inner-shell vacancies, assuming that the radiation has sufficient energy to excite above the K edge (for Cu, $h\nu > 9 \text{ keV}$), but energetic electrons are the main contributors to K_α and K_β production in a high-intensity, ultrashort, laser–solid interaction with low- and mid-*Z* materials.²¹ Three different single-shot x-ray diagnostics measured the 8-keV K_α fluorescence emission from the Cu targets. A single-photon-counting x-ray spectrograph (XCCD),²² a crystal spectrograph equipped with two highly oriented pyrolytic graphite (HOPG) crystals, and a crystal imager (IMAGER)²³ were used. The IMAGER was a spherically curved α -quartz (2131) crystal with a 38-cm bending radius that imaged the $K_{\alpha 1}$ emission in a narrow spectral bandwidth of $E/\Delta E = 1340$ and $8.57\times$ magnification onto a front-illuminated, 16-bit charge-coupled-device (CCD) camera.²⁴ A 13.5- μm , 1024 \times 1024-pixel chip provided a field of view of $\sim 1.6 \text{ mm} \times 1.6 \text{ mm}$. A 1.6-cm-diam aperture in front of the crystal reduced the astigmatism, resulting in a spatial resolution of $\sim 15 \mu\text{m}$. A thin, 35- μm Cu foil was mounted in front of the CCD camera to block stray laser light and provide bandpass filtering in the x-ray range from 8 to 9 keV. Additional lead apertures were introduced in the beam path to block the direct line of sight.

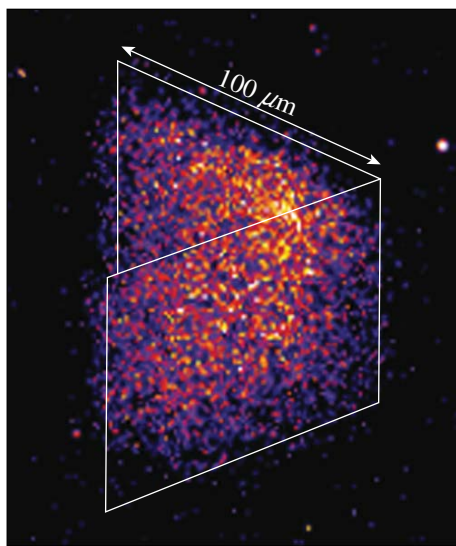
The HOPG consisted of two grade-ZYA (low-mosaic-spread) crystals,²⁵ 10 mm \times 50 mm and 2-mm thickness mounted 49 cm away from the target. The crystals covered photon-energy ranges of ~ 7.7 to $\sim 8.7 \text{ keV}$ and ~ 8.2 to $\sim 9.2 \text{ keV}$, respectively. A 16-bit, back-illuminated SI-800 CCD²⁴ with 2048 \times 2048, 13.5- μm -wide pixels was mounted 49 cm from the crystals to use mosaic focusing for best spectral resolution.²⁶ A spectral resolution of $E/\Delta E \approx 700$ was sufficient to resolve the $K_{\alpha 1}$ (8048-eV) and $K_{\alpha 2}$ (8028-eV) transitions. The integrated reflectivity of the HOPG crystal dispersing the K_α signal was measured with $2.82 \pm 0.1 \text{ mrad}$ at two different locations on the crystal. A 10- μm Cu foil filter mounted in front of the HOPG crystal blocked visible and soft x-ray radiation from the target while providing $>60\%$ transmission in the region of interest. Both the HOPG crystal and the XCCD used SI-800 CCD models equipped with back-illuminated chips from e2v Technologies,²⁷ comprising a 16- μm -thick depletion layer.²⁸ The XCCD's spectral resolution of $E/\Delta E \approx 45$ at 8 keV was insufficient to resolve the fine transitions. An absolute calibration was performed in Ref. 28 for single-photon-counting applications of the same camera model and chip used in this experiment. Assuming this calibration for the XCCD, an efficiency of $3.1 \pm 0.5\%$ was inferred for 8-keV x-ray photons when using the standard histogram analysis method.²⁸ This is lower than the $5 \pm 2.5\%$ that was previously measured for that camera model, but it is still in agreement with the recent calibration

within the measurement uncertainties.^{22,29} The current calibration error of the XCCD was $\sim 20\%$. An absolute calibration of the HOPG was obtained by taking into account the quantum efficiency of a $16\text{-}\mu\text{m}$ -thick Si slab at $\sim 8\text{ keV}$, the measured crystal reflectivity, the dispersion curve, and the transmission of the $10\text{-}\mu\text{m}$ Cu foil in front of the spectrograph. The HOPG calibration error was $\sim 10\%$.

The simultaneously operating diagnostics had different viewing directions: the azimuthal (θ) and polar (ϕ) diagnostic angles were $\theta = 135.0^\circ, 90.0^\circ, 62.4^\circ$ and $\phi = 0^\circ, 355.0^\circ, 59.7^\circ$ for the IMAGER, HOPG, and XCCD, with respect to the coordinate system shown in Fig. 122.9 with the polar axis along the z direction and the laser propagation along the y direction.

Experimental Results and Analysis

Figure 122.10 shows a spatially resolved K_α image of a 60° wedge. A nearly homogeneous emission was observed over the target although the laser interacted with only a small target region in the seam. The measurement indicated that the laser-generated fast electrons homogeneously filled the target. Only a small percentage of the fast electrons were energetic enough to escape the target. The resulting net charge set up strong electrostatic sheath fields at the target boundaries. Most of the fast electrons were confined in the target and were reflected back into the target upon reaching the boundary. The refluxing fast electrons eventually filled the target, provided that their mean-

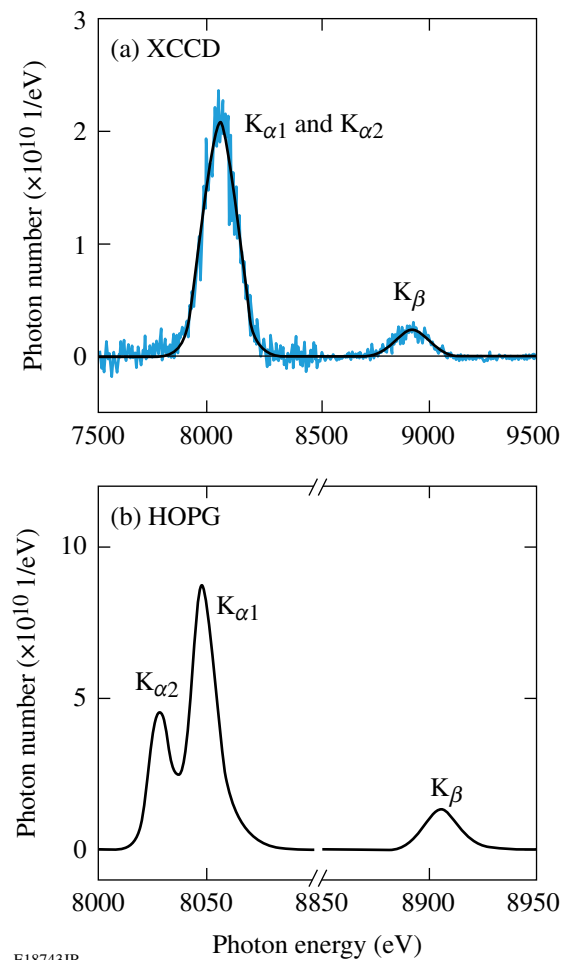


E18742JR

Figure 122.10 X-ray image of an s -polarized 60° -opening-angle wedge target (shot 2117). A nearly spatially homogenous 8-keV x-ray emission was observed. The pre-shot target boundaries are indicated by white lines for comparison.

free-path length was about the same as the target dimension or larger. The electron range in Cu is ~ 1 to $\sim 700\ \mu\text{m}$ for energies between 10 keV to 1 MeV (Ref. 30). Since fast electrons generate most of the K_α emission, this explains the observation of a spatially homogeneous fluorescence emission. Similar x-ray images were recorded with flat-foil targets.

Figure 122.11 shows measured x-ray spectra from (a) XCCD and (b) HOPG. The HOPG spectral resolution was high enough to resolve the $K_{\alpha 1}$ and $K_{\alpha 2}$ lines and the K_β line. Spectral integration yielded 4.38×10^{12} and 5.10×10^{11} photons into 4π steradians for K_α and K_β , respectively, for the XCCD spectrum. The HOPG spectrum yielded 4.39×10^{12} and 5.26×10^{11} photons for K_α and K_β . Both detectors were in very good agreement with respect to the total number of detected K_α and K_β photons.



E18743JR

Figure 122.11 Measured x-ray spectra from XCCD (a) and HOPG (b) from a 30° -wedge target irradiated with p -polarization (shot 2164). HOPG resolved the $K_{\alpha 1}$ and $K_{\alpha 2}$ lines because of a higher spectral resolution. The abscissa is broken in (b) to show the K_α and K_β lines with reasonable resolution.

The diagnostics measured the x-ray emission from different angles with respect to the target. The line emission generated in deeper layers of the target was affected by reabsorption. This was taken into account by calculating the opacity effect for each diagnostic depending on the diagnostic view angle. The $1/e$ absorption lengths³¹ of K_α and K_β photons were $22.2 \mu\text{m}$ and $29.7 \mu\text{m}$, respectively, for the solid-state Cu material, and there was a significant direction-dependent reabsorption of that emission in the $\sim 100 \times 100 \times 40\text{-}\mu\text{m}^3$ target volume. The opacity was taken into account by describing the wedges as two rectangular prisms. $N = 2.7 \times 10^4$ grid points were placed in each prism. The average transmitted radiation

$$1/N \sum_{i=1}^N \exp(-\alpha_x d_i)$$

was calculated, where α_x was the corresponding absorption length and d_i was the distance that the radiation had to propagate through the target into the solid angle of the diagnostic. The distances depend on each grid point, the target orientation, and the diagnostic angle. The average emission from each prism was calculated, and the total emission was calculated by taking into account the partial obscuration of the radiation of one prism by the other.

Five to six laser shots were performed for each target species and polarization, and the average K_α signal was calculated. Figure 122.12 shows the measured K_α signal normalized to the laser energy as a function of the wedge angle for the different diagnostics. All three diagnostics were in good agree-

ment, showing that the Cu K_α emission was isotropic within the probed line of sights and the measurement accuracy. The open symbols represent the HOPG measurement while the solid symbols show the XCCD yields in Fig. 122.12(a) and the IMAGER yields in Fig. 122.12(b). The error bars indicate the statistical error of each measurement. The HOPG and XCCD diagnostics were absolutely calibrated, while the IMAGER was cross calibrated against the HOPG diagnostic. The data point at 180° marks the reference measurement with flat foils irradiated under normal incidence. The measured average yield of ~ 20 planar-foil targets of about the same mass was $(7.07 \pm 0.3) \times 10^{-4}$ (XCCD) and $(7.14 \pm 0.5) \times 10^{-4}$ (HOPG). The yield was a factor of 2 higher for the wedges reaching $(1.38 \pm 0.10) \times 10^{-3}$ (XCCD) and $(1.34 \pm 0.09) \times 10^{-3}$ (HOPG) for p -polarization. The data may indicate a slight increase in signal for smaller wedge angles.

Using targets that were in the refluxing regime made it possible to infer the fast-electron coupling efficiency (CE) from an absolute measurement of the K_α emission.^{18,19,22} Reference 18 describes the model that was used to infer CE from the K_α yield. The data from the three diagnostics were averaged and used to infer CE using a fixed laser intensity of $1 \times 10^{19} \text{ W/cm}^2$. The Cu inner-shell line emission depended weakly on the laser intensity in the range of 1×10^{18} to 10^{20} W/cm^2 (Refs. 19 and 22), so that intensity variations were not significant. Figure 122.13(a) shows the experimental CE for the wedge-shaped-cavity targets and for flat foils. The square symbols refer to p -polarization and the triangles show the efficiency of s -polarization. A p -polarized laser beam interacting with a narrow cavity converted significantly more short-pulse

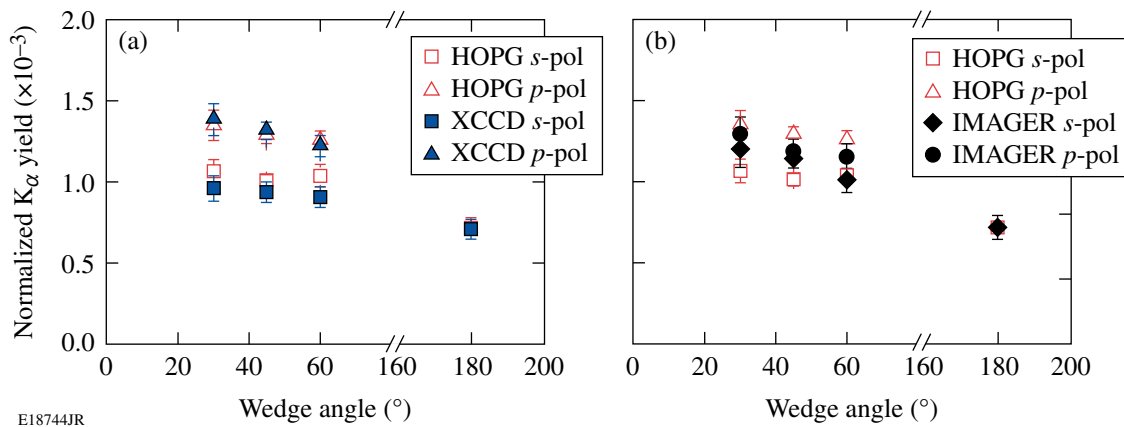


Figure 122.12 Measured K_α yield normalized to the laser energy on target from different diagnostics: (a) HOPG (open) and XCCD (solid) and (b) HOPG (open) and IMAGER (solid).

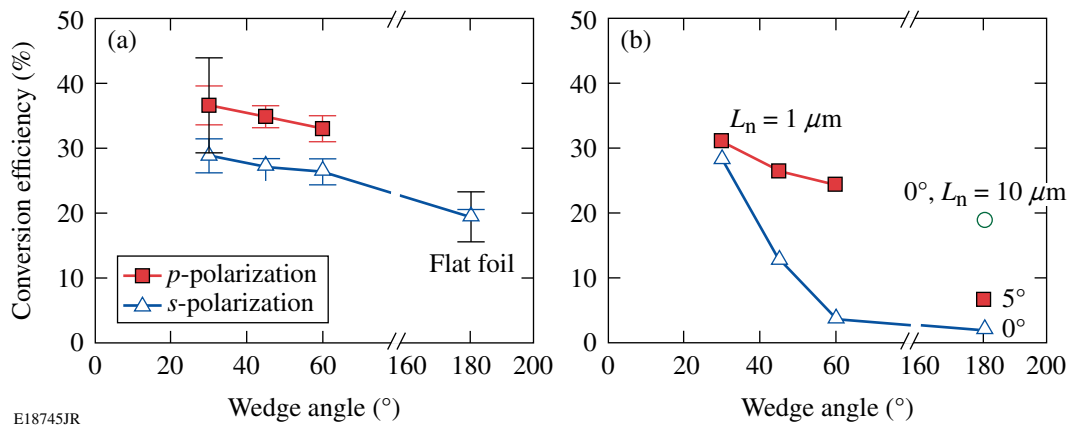


Figure 122.13

(a) Experimental and (b) theoretical conversion efficiency of short-pulse laser energy into fast electrons. The two error bars at 30° and 180° in (a) are representative absolute error bars of the measured conversion efficiency. The green circle in (b) represents a planar target with an overall target tilt of 5° relative to the beam axis. The red square at 180° in (b) was calculated using $L_n = 10 \mu\text{m}$, rather than $1 \mu\text{m}$.

energy (up to ~36%) into fast electrons than a flat foil of similar mass (20%). The absolute uncertainty of the conversion efficiency, ΔCE , was estimated at 20% relative to the CE, which gave an absolute ΔCE between $\pm 4\%$ and $\pm 7\%$ based on the calibration errors of the diagnostics. Two representative absolute error bars at 30° and 180° are included in Fig. 122.13(a).

2-D PIC Simulations and Discussion

To elucidate on the absorption mechanism, 2-D PIC simulations were performed with the code OSIRIS.³² The theoretical CE is defined as the fraction of the calculated total kinetic energy of all the electrons above 9 keV to the total laser energy. Only electrons with kinetic energy above 9 keV can contribute to the K_α production in the Cu target since the binding energy for K-shell electrons is approximately 9 keV. The calculated absorption fraction taking all the electrons into account was significantly higher. Wedge-shaped-cavity targets of 30°, 45°, and 60° full opening angle were used in the calculations, assuming a fully ionized Cu target with an electron density of $10\times$ the nonrelativistic critical electron density n_c . The initial target temperature was set to room temperature (~ 0.1 eV). The plasma density ramped linearly from zero to peak density over a $1\text{-}\mu\text{m}$ distance at the target boundary. Some simulations were performed for different density scale lengths. The simulation box of $\sim 10 \times 14 \mu\text{m}$ was divided into 600×900 cells giving a spatial resolution of $0.1 c/\omega_1 = 0.016 \mu\text{m}$, where ω_1 is the laser frequency and c is the speed of light in vacuum. There were 49 particles of each species per cell. The boundary condition in the longitudinal direction that coincides with the laser propagation direction was thermal for particles and open for the electromagnetic field. Periodic boundary conditions for

both particles and fields were chosen in the transverse direction. The $1\text{-}\mu\text{m}$ -wavelength laser pulse propagated along the symmetry axis of the cavity and was focused into the vertex to an intensity of $1 \times 10^{19} \text{ W/cm}^2$. Gaussian profiles were assumed both in time and space with a 0.5-ps (FWHM) pulse duration and a $4\text{-}\mu\text{m}$ (FWHM) focal spot.

The square and triangle symbols in Fig. 122.13(b) represent the calculations for p - and s -polarization, respectively. The calculated conversion efficiency for p -polarization slightly increased with narrower angle and reached up to 30%. Within the calibration error, simulations and experiments were in agreement for p -polarization. The PIC code showed reasonable agreement with experiment for 30° and s -polarization but calculated significantly less absorption for larger angles. The calculated strong dependence on opening angle for s -polarization was not observed in the measurement. This discrepancy may be due to imperfect polarization in the experiment. Target-alignment errors were of the order of $\sim 5^\circ$, and microstructures observed on the target surface under a light microscope might have affected the interaction. Both effects probably contributed partially p -polarized laser light. The PIC simulations calculated only 2% absorption for flat foils under normal incidence, which is much lower than measured in the experiment ($\sim 20\%$). The theoretical CE increased to 7% when the foil was tilted by 5° in the plane of incidence [see the red square at 180° in Fig. 122.13(b)]. The plasma density scale length also has a strong effect on the absorption fraction. The calculated absorption increased to 20% assuming a $10\text{-}\mu\text{m}$ density ramp on the boundary of a flat target for normal incidence [see the green circle in Fig. 122.13(b)]. Target alignment

errors, target microstructures, and density scale length have a significant effect on CE, which could explain the discrepancy of the calculated and measured absorption for flat foils.

The principal laser-absorption mechanisms responsible for the production of suprathermal electrons in this experiment are the Brunel effect,³³ resonance absorption,³⁴ and $\mathbf{j} \times \mathbf{B}$ heating.³⁵ The Brunel mechanism, or vacuum heating, describes the process when electrons are dragged out of the target surface into the vacuum by strong p -polarized fields and accelerated back into the overdense plasma, where the electrons deposit their kinetic energy. This mechanism probably explains the measured increased absorption for p -polarization. It does not, however, explain why for s -polarization the absorption in narrow cavities was larger than for flat foils that were irradiated under normal incidence. This effect was probably due to the target geometry. Despite the tight focus, the majority of the laser beam interacted with a flat target surface at a large angle of incidence. The laser absorption of obliquely irradiated flat foils generally decreases with larger angle of incidence,³⁶ while here maximum absorption was measured for the narrowest wedge cavity with a corresponding angle of incidence of 75° . The light that is reflected from one surface reaches the opposite target surface where it has another chance to be absorbed. The narrower the cavity, the more reflections the light undergoes so that the overall absorption increases, although the absorption per reflection is small due to the shallow interaction angle. A narrow wedge with reflecting walls forms a cavity where the laser field reflects multiple times between opposite walls before reaching the tip. Interference of the electromagnetic field in the vicinity of the tip then leads to a standing wave pattern that might result in higher laser intensities than for comparable laser irradiation onto a flat target at normal incidence.

Lasinski *et al.* reported 2-D PIC simulations with flat-top cones and wedge-shaped-cavity targets¹² under similar conditions ($1\text{-}\mu\text{m}$ wavelength, intensity of 1×10^{19} W/cm²). Compared to simple slab interactions, cone targets resulted in increased laser light absorption and higher temperatures of the fast-electron population, which is in general agreement with the PIC simulations shown in this article. Higher absorption was calculated for p -polarized laser light in agreement with the results presented here. The absorption reached up to 75%, which was defined in Ref. 12 as the total kinetic energy in all the electrons divided by the total light energy that had entered the simulation. The absorption fraction in this work reached $\sim 70\%$ when all the electrons were taken into account.

The ions were kept immobile in most of the simulation runs, but some runs were performed with mobile ions. No significant difference in absorption and fast-electron energy distribution was observed between fixed- and mobile-ion runs. This is similar to simulations in Ref. 12 with mobile and fixed ions that produced no significant difference in absorption and heated-electron-density distribution for a 26° full opening angle wedge cavity. In contrast, mobile ion runs for flat foils and flattop cones calculated significantly more absorption than with immobile ions. In these target geometries, the deformation of the relativistic critical-density surface by ponderomotive effects is important, especially for flat foils irradiated under normal incidence and for cones with a central flattop portion. Rippling of the plasma surface leads to an enhanced absorption through the Brunel effect³³ and resonance absorption.³⁴ The relativistic critical surface deformation is less important for wedge cavities (or cones with pointed tips) since the laser is very efficiently absorbed along the upper side walls of the target, showing insignificant difference in mobile- and fixed-ion runs.

Conclusions

High-intensity laser-plasma interaction experiments were performed with wedge-shaped-cavity Cu targets with various opening angles at a laser intensity of 1×10^{19} W/cm². Absolute measurements with three independent diagnostics viewing the target from different observation locations provided spatially and spectrally resolved measurements of the $\sim 8\text{-keV}$ K_α emission from these targets. The diagnostics measured an isotropic emission. The coupling efficiency of short-pulse laser energy into fast electrons with kinetic energy >9 keV was inferred for wedge opening angles between 30° and 60° and for s - and p -polarized laser light irradiation. An increased coupling efficiency of up to 36% was measured for the narrowest wedge and for p -polarization compared to 20% for flat foils. The experimental results are in reasonable agreement with predictions from 2-D PIC simulations for p -polarized laser light and for the narrowest cavity for s -polarization. For s -polarization and wider cavities, the calculated absorption is significantly lower than in the experiment.

ACKNOWLEDGMENT

The authors are indebted to the Target Fabrication Groups at General Atomics and LLE and to C. Mileham for experimental support. This work was supported by the U.S. Department of Energy Office of Inertial Confinement Fusion under Cooperative Agreement No. DE-FC52-08NA28302, the OFES Fusion Science Center grant No. DE-FC02-04ER54789, the OFES ACE grant No. DE-FG02-05ER54839, the University of Rochester, and the New York State Energy Research and Development Authority. The support of DOE does not constitute an endorsement by DOE of the views expressed in this article.

REFERENCES

1. M. Tabak *et al.*, *Phys. Plasmas* **1**, 1626 (1994).
2. K. A. Flippo *et al.*, *Phys. Plasmas* **15**, 056709 (2008).
3. T. Nakamura *et al.*, *Phys. Plasmas* **14**, 103105 (2007).
4. N. Renard-Le Galloudec *et al.*, *Phys. Rev. Lett.* **102**, 205003 (2009).
5. B. I. Cho *et al.*, *Phys. Plasmas* **15**, 052701 (2008).
6. P. M. Nilson, W. Theobald, J. F. Myatt, C. Stoeckl, M. Storm, J. D. Zuegel, R. Betti, D. D. Meyerhofer, and T. C. Sangster, *Phys. Rev. E* **79**, 016406 (2009).
7. L. Van Woerkom *et al.*, *Phys. Plasmas* **15**, 056304 (2008).
8. J. A. King, K. U. Akli, R. R. Freeman, J. Green, S. P. Hatchett, D. Hey, P. Jaanimagi, M. H. Key, J. Koch, K. L. Lancaster, T. Ma, A. J. MacKinnon, A. MacPhee, P. A. Norreys, P. K. Patel, T. Phillips, R. B. Stephens, W. Theobald, R. P. J. Town, L. Van Woerkom, B. Zhang, and F. N. Beg, *Phys. Plasmas* **16**, 020701 (2009).
9. S. D. Baton *et al.*, *Phys. Plasmas* **15**, 042706 (2008).
10. J. Rassuchine *et al.*, *Phys. Rev. E* **79**, 036408 (2009).
11. F. Beg, *Bull. Am. Phys. Soc.* **54**, 299 (2009); A. G. MacPhee *et al.*, *Phys. Rev. Lett.* **104**, 055002 (2010).
12. B. F. Lasinski, *Phys. Plasmas* **16**, 012705 (2009).
13. Y. Sentoku *et al.*, *Phys. Plasmas* **11**, 3083 (2004).
14. T. Nakamura *et al.*, *Phys. Rev. Lett.* **93**, 265002 (2004).
15. V. Bagnoud, I. A. Begishev, M. J. Guardalben, J. Puth, and J. D. Zuegel, *Opt. Lett.* **30**, 1843 (2005).
16. C. Dorrer, A. V. Okishev, I. A. Begishev, J. D. Zuegel, V. I. Smirnov, and L. B. Glebov, *Opt. Lett.* **32**, 2378 (2007).
17. A. J. MacKinnon *et al.*, *Phys. Rev. Lett.* **88**, 215006 (2002).
18. J. Myatt, W. Theobald, J. A. Delettrez, C. Stoeckl, M. Storm, T. C. Sangster, A. V. Maximov, and R. W. Short, *Phys. Plasmas* **14**, 056301 (2007).
19. P. M. Nilson, W. Theobald, J. Myatt, C. Stoeckl, M. Storm, O. V. Gotchev, J. D. Zuegel, R. Betti, D. D. Meyerhofer, and T. C. Sangster, *Phys. Plasmas* **15**, 056308 (2008).
20. J. D. Zuegel, V. Bagnoud, I. A. Begishev, M. J. Guardalben, J. Keegan, J. Puth, and L. J. Waxer, presented at the Conference on Lasers and Electro Optics (CLEO 2003), Baltimore, MD, 1–6 June 2003 (Paper CME3).
21. H. Chen, B. Soom, B. Yaakobi, S. Uchida, and D. D. Meyerhofer, *Phys. Rev. Lett.* **70**, 3431 (1993).
22. W. Theobald, K. Akli, R. Clarke, J. Delettrez, R. R. Freeman, S. Glenzer, J. Green, G. Gregori, R. Heathcote, N. Izumi, J. A. King, J. A. Koch, J. Kuba, K. Lancaster, A. J. MacKinnon, M. Key, C. Mileham, J. Myatt, D. Neely, P. A. Norreys, H.-S. Park, J. Pasley, P. Patel, S. P. Regan, H. Sawada, R. Shepherd, R. Snavely, R. B. Stephens, C. Stoeckl, M. Storm, B. Zhang, and T. C. Sangster, *Phys. Plasmas* **13**, 043102 (2006).
23. K. U. Akli, M. H. Key, H. K. Chung, S. B. Hansen, R. R. Freeman, M. H. Chen, G. Gregori, S. Hatchett, D. Hey, N. Izumi, J. King, J. Kuba, P. Norreys, A. J. MacKinnon, C. D. Murphy, R. Snavely, R. B. Stephens, C. Stoeckl, W. Theobald, and B. Zhang, *Phys. Plasmas* **14**, 023102 (2007).
24. Spectral Instruments, Tucson, AZ 85745 (http://www.specinst.com/Products/800s_datasheet.pdf).
25. Momentive Performance Materials, Albany, NY 12211 (<http://www.momentive.com/momentiveInternetDoc/Internet/Static%20Files/Documents/4%20Color%20Brochures/85508.pdf>).
26. B. Yaakobi and A. J. Burek, *IEEE J. Quantum Electron.* **QE-19**, 1841 (1983).
27. CCD42–40 Ceramic AIMO Back Illuminated Compact Package High Performance CCD Sensor, e2v technologies (uk) limited, Chelmsford, Essex CM1 2QU, UK.
28. B. R. Maddox *et al.*, *Rev. Sci. Instrum.* **79**, 10E924 (2008).
29. H.-S. Park, D. M. Chambers, H.-K. Chung, R. J. Clarke, R. Eagleton, E. Giraldez, T. Goldsack, R. Heathcote, N. Izumi, M. H. Key, J. A. King, J. A. Koch, O. L. Landen, A. Nikroo, P. K. Patel, D. F. Price, B. A. Remington, H. F. Robey, R. A. Snavely, D. A. Steinman, R. B. Stephens, C. Stoeckl, M. Storm, M. Tabak, W. Theobald, R. P. J. Town, J. E. Wicksham, and B. B. Zhang, *Phys. Plasmas* **13**, 056309 (2006).
30. M. J. Berger, in *Methods in Computational Physics: Advances in Research and Applications*, edited by B. Alder, S. Fernbach, and M. Rotenberg, Volume 1: Statistical Physics (Academic Press, New York, 1963), pp. 135–215.
31. B. L. Henke, E. M. Gullikson, and J. C. Davis, *At. Data Nucl. Data Tables* **54**, 181 (1993).
32. R. A. Fonseca *et al.*, in *Computational Science—ICCS 2002*, edited by P. M. A. Sloot *et al.*, Lecture Notes in Computer Science (Springer, Berlin, 2002), Vol. 2331, pp. 342–351.
33. F. Brunel, *Phys. Rev. Lett.* **59**, 52 (1987).
34. P. Gibbon and A. R. Bell, *Phys. Rev. Lett.* **68**, 1535 (1992).
35. S. C. Wilks and W. L. Kruer, *IEEE J. Quantum Electron.* **33**, 1954 (1997).
36. T. Feurer, W. Theobald, R. Sauerbrey, I. Uschmann, D. Altenbernd, U. Teubner, P. Gibbon, E. Förster, G. Malka, and J. L. Miquel, *Phys. Rev. E* **56**, 4608 (1997).

Crossed-Beam Energy Transfer in Inertial Confinement Fusion Implosions on OMEGA

Inertial confinement fusion (ICF) uses the energy of multiple laser beams to implode a millimeter-scale capsule containing nuclear fuel.¹ Direct-drive implosions are driven by heat that is generated by the absorption of laser light ($I \sim 10^{14}$ to 10^{15} W/cm²) in a plasma corona surrounding the capsule.² The crossed-beam energy transfer (CBET) caused by stimulated Brillouin scattering (SBS)³ reduces the laser absorption, making it possible for incoming light to bypass the highest absorption region near the critical radius, at which the electron number density n_e equals the critical density $n_{cr} = \pi c^2 m_e / \lambda_L^2 e^2$, where λ_L is the laser wavelength in vacuum. Under certain conditions, the CBET may be large and significantly reduce the performance of ICF implosions.⁴⁻⁶

In this article, the effect of SBS in implosion experiments on the OMEGA Laser System,⁷ operating at $\lambda_L = 351$ nm, is investigated. The results of a new CBET model coupled to the one-dimensional radiative hydrodynamic code *LILAC*⁸ are presented and quantitatively compared with experimental results. It is shown that the best agreement between simulations and scattered-light⁹ and bang-time¹⁰ measurements can be obtained by simultaneously employing the CBET and non-local thermal transport.^{11,12} *LILAC* simulations show that using two-color laser light with a wavelength separation $\Delta\lambda \sim 5$ to 8 Å can reduce the CBET and increase the absorption, thereby improving the implosion efficiency.

The CBET model considers the propagation of two crossing laser beams (probe and pump) in a moving plasma and the interaction of these beams with an ion-acoustic wave (IAW) that they excite.^{4,13,14} Assuming *s*-polarized light and steady state, the probe beam intensity $I^{(1)}$ along the path ℓ can be calculated as follows:

$$I^{(1)} = I_0^{(1)} \exp \left\{ \int \left[\eta L_{CBET}^{-1} - L_{IB}^{-1} \right] d\ell \right\}, \quad (1)$$

where L_{IB} is the inverse bremsstrahlung absorption scale length,³ L_{CBET} is the scale length of energy loss or gain caused by CBET, and η is an adjustment parameter $0 \leq \eta \leq 1$. The scale length L_{CBET} is defined by

$$L_{CBET}^{-1} = 0.0585 \frac{n_e/n_{cr}}{\sqrt{1-n_e/n_{cr}}} \times \frac{\lambda_{L,\mu m} I_{14}^{(2)}}{(1+3T_i/ZT_e) T_{e,keV}} \frac{P(\chi)}{\tilde{\nu}_a} \mu m^{-1}, \quad (2)$$

where $\lambda_{L,\mu m}$ is the laser wavelength in microns, $I_{14}^{(2)}$ is the pump-beam intensity in units of 10^{14} W/cm², T_e and T_i are the electron and ion temperatures ($T_{e,keV}$ in keV), Z is the average ionization, ν_a is the damping coefficient for IAW's, $\tilde{\nu}_a = \nu_a/k_a c_a$ is the dimensionless damping,

$$P(\chi) = \frac{\tilde{\nu}_a^2 \chi}{\tilde{\nu}_a^2 \chi^2 - (1 - \chi^2)} \quad (3)$$

is the resonance function,⁴ $\chi = -\omega_a/k_a c_a + (\mathbf{k}_a \cdot \mathbf{u})/k_a c_a$, \mathbf{u} is the velocity vector, c_a is the ion-acoustic velocity, $\omega_a = \omega_1 - \omega_2$ and $\mathbf{k}_a = \mathbf{k}_1 - \mathbf{k}_2$ are the IAW frequency and wave vector, respectively, and ω and \mathbf{k} with the lower indexes 1 and 2 are the frequencies and wave vectors of the probe and pump light, respectively.

The CBET model has been incorporated into the laser absorption algorithm in *LILAC*. The algorithm calculates the integral in Eq. (1) along various light-ray paths, accounting for all possible beam crossings in three dimensions. Doppler shift of the light frequencies is calculated using the equation $\Delta\omega = \omega_L (\partial\tau/\partial t)$ (Ref. 15), where τ is the light-wave flight time and $\omega_L = 2\pi c/\lambda_L$. The damping is approximately $\tilde{\nu}_a \approx 0.2$ for CH plasma under the considered conditions.¹⁶ Simulations, however, showed a weak dependence on $\tilde{\nu}_a$ over the interval $0.1 < \tilde{\nu}_a < 0.5$.

The energy is not conserved exactly in Eq. (1) because pump-light depletion is neglected. To enforce this conservation, the algorithm normalizes the total energy gain (or loss) for outgoing light to the total energy loss (or gain) for incoming

light at each radius. Calculations were significantly simplified assuming a uniform illumination of implosion capsules (but the intensity profile inside the beams is retained). Test simulations using this simplified assumption and the illumination by all 60 OMEGA beams showed good agreement between the two approaches. The random polarization of light on OMEGA is accounted for by reducing the numerical factor in Eq. (2) by 0.5.

Typical implosion targets on OMEGA are room-temperature-D₂- or DT-gas-filled plastic shells and cryogenic D₂- or DT-ice shells with a thin plastic overcoat. The outer diameter is about 840 to 880 μm. Laser pulses can have various shapes with pickets and pedestals, have durations from 0.1 to 4 ns, and deliver on target up to 30 kJ. LILAC simulations of OMEGA implosions have revealed the importance of CBET at laser intensities $I \gtrsim 10^{14}$ W/cm². At $I > 5 \times 10^{14}$ W/cm², the energy transfer can reach a significant level $\gtrsim 30\%$ of the incident energy. The CBET is most efficient in a radially extended plasma corona, which develops after the first 100 to 200 ps of a pulse. The transfer occurs in a relatively wide radial interval ~ 50 μm, in which n_e is in the range of 0.2 to 0.3 n_{cr} (see Fig. 122.14). As a result, the absorption is spatially redistributed, shifting outward, and its integrated value can be changed [see black and blue lines in Fig. 122.14(a)]. The most-energetic transfers involve the incoming light with small impact parameters (at the beam center) and outgoing light, which is inclined at $\sim 20^\circ$ to 30° with respect to the radial direction. The former light

loses some energy and the latter gains the energy. The nonzero angles between interacting light rays explain our finding that the energy transfer is maximized at the supersonic region of the corona, at $u_r/c_a \approx 1.4$ [see the red line in Fig. 122.14(a) and the blue dashed line in Fig. 122.14(b)], instead of at the transonic point, $u_r/c_a = 1$, if the angles were close to zero.⁵ Here, u_r is the radial component of the velocity. Fortunately, most CBET interaction occurs at moderate angles ($\lesssim 25^\circ$), where the paraxial approximation used in Eq. (2) is valid.

The CBET redistributes the energy inside the laser beams from light rays with small impact parameters to light rays with larger ones. This redistribution and corresponding modification of the absorption can be emulated using the effective profile in which the beam's central intensity is decreased and the beam's edge intensity is increased (see Fig. 122.15). Such effective profiles may be useful in multidimensional simulations in which the direct employment of the CBET model is highly impractical.¹⁷

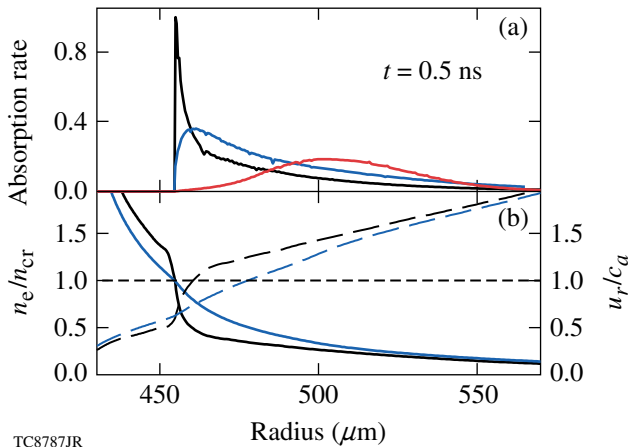


Figure 122.14 Simulated (a) absorption rate per unit volume (in relative units, black and blue lines) and (b) relative electron density n_e/n_{cr} (solid lines) and Mach number u_r/c_a (dashed lines), at $t = 0.5$ ns for an 880-μm-diam plastic shell (20-μm CH wall) imploded with a 1-ns square pulse at $I \sim 10^{15}$ W/cm². The simulations with flux-limited transport ($f = 0.06$) are shown in black and nonlocal transport and CBET ($\eta = 0.75$) in blue. The CBET rate (in relative units) from incoming to outgoing light is shown in (a) in red.

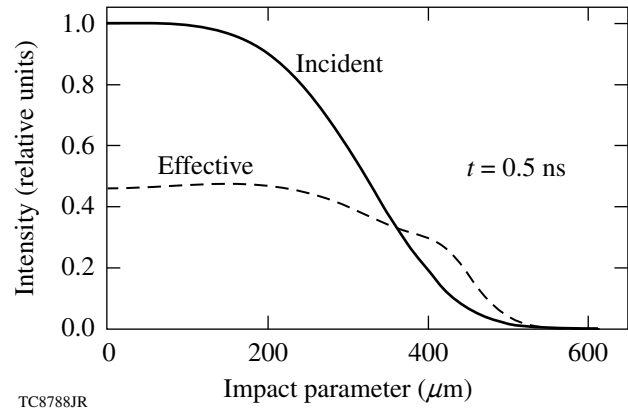


Figure 122.15 Incident (super-Gaussian with an index $n = 4$) and effective beam profiles at $t = 0.5$ ns for the same simulation with nonlocal transport and CBET as shown in Fig. 122.14. The effective profile emulates the loss ($\approx 26\%$) and redistribution of the energy inside the beam caused by CBET.

OMEGA planar and implosion experiments are typically simulated by employing the Spitzer thermal transport¹⁸ with flux limitation, in which the phenomenological constant-value flux-limiting parameter f is used.¹⁹ Assuming $f = 0.06$, the model can explain reasonably well planar shock-timing experiments²⁰ and implosion experiments with short (≤ 1 ns), square pulses.¹¹ In the case of long, shaped pulses, however, the flux-limited transport experiences difficulties in consistently explaining the whole range of experimental data, including

bang-time and scattered-light measurements.¹¹ The inaccuracy of the flux-limited transport becomes especially apparent in adiabat-shaped designs^{21,22} in which a time-dependent flux limiting was proposed.^{11,23}

A step-up from the Spitzer transport is the nonlocal transport model,^{11,12} which calculates heat fluxes by solving the simplified Boltzmann equation and employing the Krook approximation.²⁴ This transport introduces two major improvements. First, the flux in regions with steep temperature gradients is reduced from the Spitzer value, eliminating the need for flux limitation. Second, the heating by long-range hot electrons is accounted for. The latter introduces changes in the density scale length near n_{cr} , making this length longer by a factor of ~ 10 [Fig. 122.14(b)]. The longer scale length significantly reduces the prediction for resonance absorption²⁵ and reduces the strong bremsstrahlung absorption peak near critical density [Fig. 122.14(a)]. Simulations using the nonlocal transport predict well the shock-timing experiments with short picket pulses (~ 100 to 200 ps), but they over-predict the laser drive in implosions with long pulses.⁹

The agreement between simulations and experiments is significantly improved when the nonlocal transport and CBET are used simultaneously. As an example, Fig. 122.16 compares

the measurement and various simulations of time-resolved scattered-light power for a plastic-shell implosion (OMEGA shot 56830). The simulated power, using nonlocal transport and CBET (green line), shows very good agreement with the scattered-light measured power (thick black line) for $\eta = 0.75$. The models without CBET, which use flux-limited or nonlocal transport (red and blue lines, respectively), clearly underestimate the scattered power. Similar results were found in simulations of different warm and cryogenic implosions.

Figure 122.17 shows the neutron-production history for the implosion in Fig. 122.16. Again, the bang time inferred from the neutron data predicted in the model with CBET (thin solid line) shows very good agreement with the bang time inferred from the measured neutron data (thick solid line). In contrast, the bang times inferred from the results of the models without CBET (dashed and dotted lines in Fig. 122.17) are about 150 ps earlier. The reduction of the measured neutron rate with respect to the predicted rates in Fig. 122.17 is due to the growth of perturbations from laser imprint, which affects the implosion performance¹ and is not considered in *LILAC* simulations.

Based on simulations of warm and cryogenic implosions with different laser energies and pulses, one concludes that bang-time and scattered-light measurements can typically

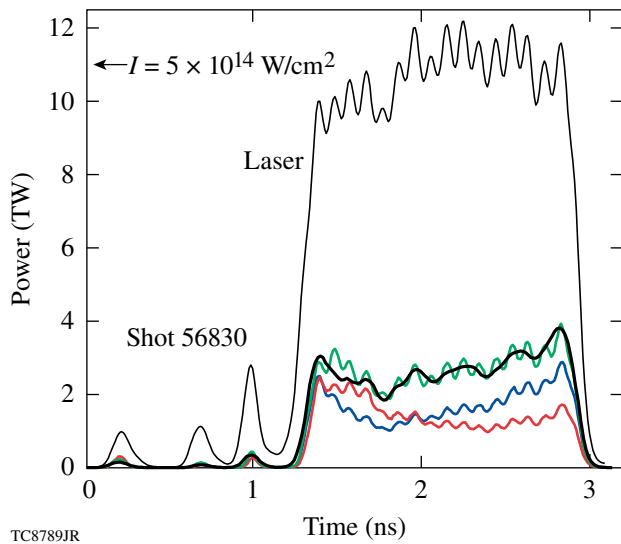


Figure 122.16 Scattered-light power for an 830- μm -diam plastic shell (9 atm of D_2 -gas fill, 26- μm CH wall) imploded with 18.3 kJ. The incident laser power and experimental scattered power (within $\pm 5\%$ accuracy) are shown by the thin and thick black lines, respectively. The *LILAC* predictions with flux-limited ($f = 0.06$) and nonlocal transports are shown in red and blue, respectively, and with nonlocal transport and CBET ($\eta = 0.75$) in green.

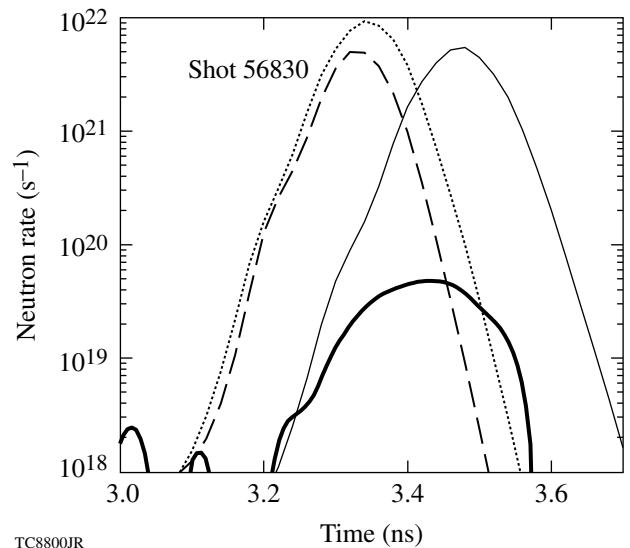


Figure 122.17 Neutron-production history for the same implosion as in Fig. 122.16. The measured history (thick solid line) is determined with ~ 50 -ps uncertainty. The *LILAC* predictions with flux-limited ($f = 0.06$) and nonlocal transports are shown by the dashed and dotted lines, respectively, and with nonlocal transport and CBET ($\eta = 0.75$) by the thin solid line.

be explained using a somewhat-reduced CBET, in which η is assumed between 0.5 and 1. This relatively wide uncertainty interval of η can be partially attributed to the uncertainties of experimental results. It is apparent, however, that the experimentally suggested mean value $\eta \sim 0.75$ is smaller than the theoretical prediction $\eta = 1$. This suggests the inaccuracy of the simplified CBET model [Eqs. (1)–(3)] is of the order of $\sim 25\%$.

Since the light refraction and frequency shift are sensitive to the corona's spatial structure, the simulated coronal structure can be validated using time-dependent scattered-light spectral measurements.⁹ Figure 122.18 shows an example of the measurement and simulations for an 843- μm -diam plastic shell (20- μm CH wall) imploded with 1-ns square pulse at $I \sim 8 \times 10^{14} \text{ W/cm}^2$ (OMEGA shot 50601). Two simulations are compared using (1) flux-limited transport [Fig. 122.18(b)] and (2) nonlocal transport and CBET [Fig. 122.18(c)]. Both simulated spectra reproduce reasonably well the basic structure of the measured spectrum [Fig. 122.18(a)]. The initial (at $t \lesssim 0.5 \text{ ns}$) blue shift is attributed to the Doppler shift of light reflected in the expanding part of the corona and the late-time (at $t \gtrsim 0.5 \text{ ns}$) red-shifted “fan tails” are produced by light reflected in the inward-moving part. However, these simulations reveal important differences. The flux-limited model predicts an insufficient initial blue shift [Ref. 26, feature A in Fig. 122.18(b)], which clearly deviates from the measured spectrum. The blue shift predicted by the model with nonlocal transport [Fig. 122.18(c)] shows much closer agreement to the experiment. The insufficient blue shift in the flux-limited model can be explained by a more-diluted corona [see Fig. 122.14(b)],

and, consequently, a deeper location of the light-ray turning points toward the critical radius, where the coronal outflow velocity is reduced.

The structure of the fan tails is less susceptible to the choice of a thermal-transport model but depends more on the presence of CBET. The most-red-shifted parts of the fan tail are produced by light rays that penetrate deeply into the corona, almost reaching the critical-density region. The larger the fraction of the incident light that reaches the critical radius, the more intense the red-shifted spectrum. Such red-shifted fan tails were found in simulations without CBET [Ref. 26, feature B in Fig. 122.18(b)]. In contrast and in agreement with measurements, simulations with CBET predict a less-red-shifted fan tail [Fig. 122.18(c)].

Splitting the incident laser light into two or more colors can reduce the CBET by shifting and suppressing the coupling resonances [Eq. (3)]. This color-splitting technique can be employed to increase the laser absorption in direct-drive implosions. Figure 122.19 shows the predicted variation of the absorption fraction (solid line) for two-color light with a wavelength separation $\Delta\lambda$. Here, the same implosion was assumed as in Fig. 122.16 and the laser energy is equally distributed between the colors. The dashed line in Fig. 122.19 shows the absorption fraction for the model with the expected asymptotic 50% reduction of CBET at $\Delta\lambda \gg \lambda_L (c_a/c)$, which corresponds to $\Delta\lambda = 0$ and η reduced by 0.5 (i.e., $\eta = 0.375$). The increase in the absorption is moderate ($\approx 5\%$) for $\Delta\lambda \sim 5 \text{ \AA}$ and takes the maximum ($\approx 8\%$) for $\Delta\lambda \sim 8$ to 10 \AA . There is

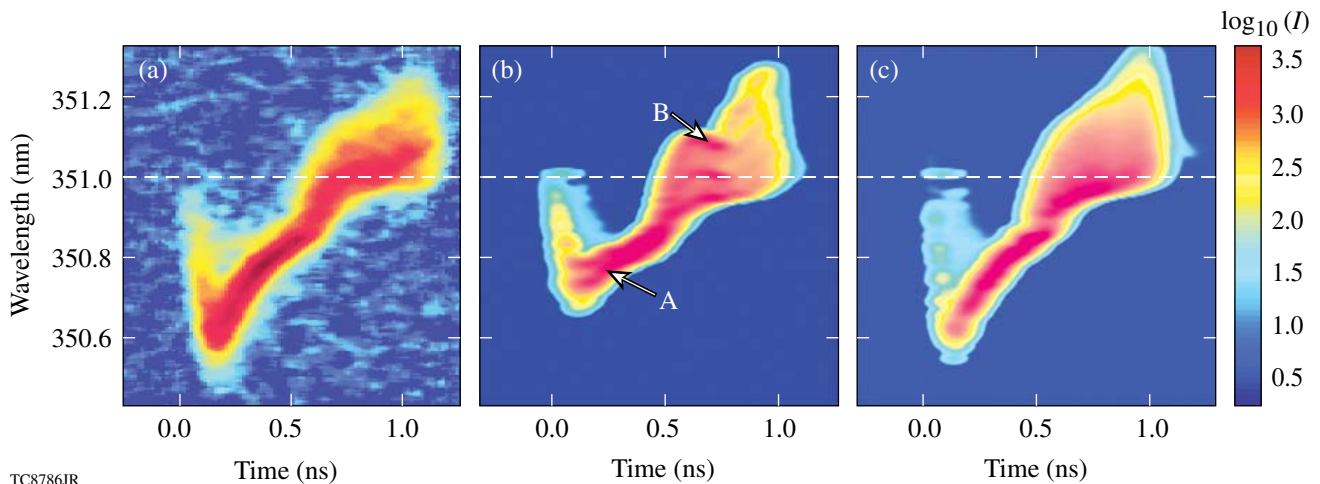
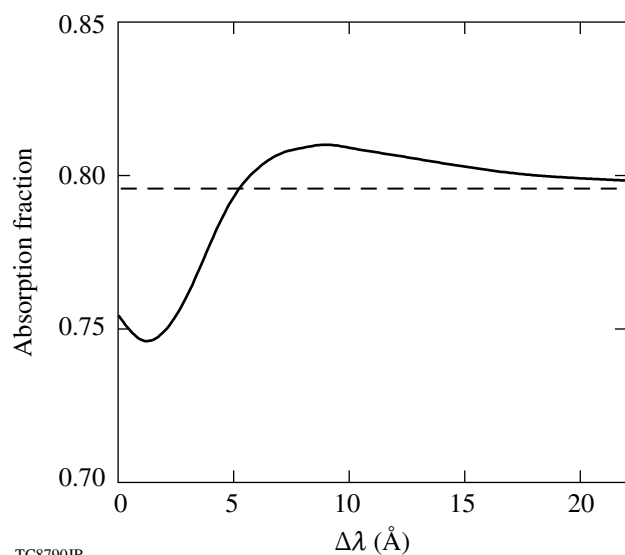


Figure 122.18

(a) Measured and [(b),(c)] simulated scattered-light spectra for a plastic-shell implosion (OMEGA shot 50601). *LILAC* predictions with flux-limited transport are shown in (b), and nonlocal transport with CBET ($\eta = 0.75$) in (c). The laser wavelength is indicated by the dashed lines.



TC8790JR

Figure 122.19

Absorption fraction (solid line) as a function of the wavelength separation $\Delta\lambda$ in two-color laser light. The dashed line corresponds to $\Delta\lambda = 0$ and 50%-reduced CBET.

little change in the absorption for $\Delta\lambda < 4 \text{ \AA}$, which confirms the experimental finding that the absorption is insensitive to the use of 1-THz smoothing by special dispersion (SSD),²⁷ which widens the laser bandwidth by ~ 3 to 4 \AA . It should be noted that this color-splitting technique may be more efficient in direct-drive implosions at the National Ignition Facility²⁸ because of larger CBET in larger-scale targets.

In summary, it has been shown that the effect of CBET in direct-drive ICF implosions on OMEGA is significant and results in the reduced laser absorption (by $\sim 20\%$ to 30%). *LILAC* simulations using CBET and nonlocal thermal transport show good agreement with bang-time and scattered-light measurements for warm and cryogenic implosions using different pulse shapes and plastic (CH or CD) as an ablator. The simulations, using flux-limited transport ($f=0.06$) and without CBET, overpredict the absorption for long pulses ($>1 \text{ ns}$), resulting in earlier bang-time predictions. The absorption can be increased by employing two-color laser light with a wavelength separation of $\Delta\lambda \sim 5$ to 8 \AA .

ACKNOWLEDGMENT

This work was supported by the U.S. Department of Energy Office of Inertial Confinement Fusion under Cooperative Agreement No. DE-FC52-08NA28302, the University of Rochester, and the New York State Energy Research and Development Authority. The support of DOE does not constitute an endorsement by DOE of the views expressed in this article.

REFERENCES

1. J. D. Lindl, *Inertial Confinement Fusion: The Quest for Ignition and Energy Gain Using Indirect Drive* (Springer-Verlag, New York, 1998), Chap. 6, pp. 39, 61.
2. R. L. McCrory, J. M. Soures, C. P. Verdon, F. J. Marshall, S. A. Letzring, S. Skupsky, T. J. Kessler, R. L. Kremens, J. P. Knauer, H. Kim, J. Delettrez, R. L. Keck, and D. K. Bradley, *Nature* **335**, 225 (1988).
3. W. L. Kruer, *The Physics of Laser-Plasma Interactions, Frontiers in Physics*, Vol. 73, edited by D. Pines (Addison-Wesley, Redwood City, CA, 1988), Chap. 4, pp. 45, 87.
4. C. J. Randall, J. R. Albritton, and J. J. Thomson, *Phys. Fluids* **24**, 1474 (1981).
5. J. Myatt, A. V. Maximov, W. Seka, R. S. Craxton, and R. W. Short, *Phys. Plasmas* **11**, 3394 (2004).
6. W. Seka, H. A. Baldis, J. Fuchs, S. P. Regan, D. D. Meyerhofer, C. Stoeckl, B. Yaakobi, R. S. Craxton, and R. W. Short, *Phys. Rev. Lett.* **89**, 175002 (2002).
7. T. R. Boehly, D. L. Brown, R. S. Craxton, R. L. Keck, J. P. Knauer, J. H. Kelly, T. J. Kessler, S. A. Kumpan, S. J. Loucks, S. A. Letzring, F. J. Marshall, R. L. McCrory, S. F. B. Morse, W. Seka, J. M. Soures, and C. P. Verdon, *Opt. Commun.* **133**, 495 (1997).
8. J. Delettrez, R. Epstein, M. C. Richardson, P. A. Jaanimagi, and B. L. Henke, *Phys. Rev. A* **36**, 3926 (1987).
9. W. Seka, D. H. Edgell, J. P. Knauer, J. F. Myatt, A. V. Maximov, R. W. Short, T. C. Sangster, C. Stoeckl, R. E. Bahr, R. S. Craxton, J. A. Delettrez, V. N. Goncharov, I. V. Igumenshchev, and D. Shvarts, *Phys. Plasmas* **15**, 056312 (2008).
10. R. A. Lerche, D. W. Phillion, and G. L. Tietbohl, *Rev. Sci. Instrum.* **66**, 933 (1995).
11. V. N. Goncharov, O. V. Gotchev, E. Vianello, T. R. Boehly, J. P. Knauer, P. W. McKenty, P. B. Radha, S. P. Regan, T. C. Sangster, S. Skupsky, V. A. Smalyuk, R. Betti, R. L. McCrory, D. D. Meyerhofer, and C. Cherfils-Cl  rouin, *Phys. Plasmas* **13**, 012702 (2006).
12. V. N. Goncharov, T. C. Sangster, P. B. Radha, R. Betti, T. R. Boehly, T. J. B. Collins, R. S. Craxton, J. A. Delettrez, R. Epstein, V. Yu. Glebov, S. X. Hu, I. V. Igumenshchev, J. P. Knauer, S. J. Loucks, J. A. Marozas, F. J. Marshall, R. L. McCrory, P. W. McKenty, D. D. Meyerhofer, S. P. Regan, W. Seka, S. Skupsky, V. A. Smalyuk, J. M. Soures, C. Stoeckl, D. Shvarts, J. A. Frenje, R. D. Petrasso, C. K. Li, F. S  guin, W. Manheimer, and D. G. Colombant, *Phys. Plasmas* **15**, 056310 (2008).
13. J. A. F. Hittinger *et al.*, *J. Comput. Phys.* **209**, 695 (2005).
14. P. Michel *et al.*, *Phys. Rev. Lett.* **102**, 025004 (2009).
15. T. Dewandre, J. R. Albritton, and E. A. Williams, *Phys. Fluids* **24**, 528 (1981).

16. E. A. Williams, R. L. Berger, R. P. Drake, A. M. Rubenchik, B. S. Bauer, D. D. Meyerhofer, A. C. Gaeris, and T. W. Johnston, *Phys. Plasmas* **2**, 129 (1995).
17. A. Shvydky, P. W. McKenty, J. A. Delettrez, I. V. Igumenshchev, D. H. Edgell, S. Skupsky, and R. L. McCrory, *Bull. Am. Phys. Soc.* **54**, 307 (2009).
18. L. Spitzer, Jr. and R. Härm, *Phys. Rev.* **89**, 977 (1953).
19. R. C. Malone, R. L. McCrory, and R. L. Morse, *Phys. Rev. Lett.* **34**, 721 (1975).
20. T. R. Boehly, E. Vianello, J. E. Miller, R. S. Craxton, T. J. B. Collins, V. N. Goncharov, I. V. Igumenshchev, D. D. Meyerhofer, D. G. Hicks, P. M. Celliers, and G. W. Collins, *Phys. Plasmas* **13**, 056303 (2006).
21. V. N. Goncharov, J. P. Knauer, P. W. McKenty, P. B. Radha, T. C. Sangster, S. Skupsky, R. Betti, R. L. McCrory, and D. D. Meyerhofer, *Phys. Plasmas* **10**, 1906 (2003).
22. K. Anderson and R. Betti, *Phys. Plasmas* **11**, 5 (2004).
23. A. Sunahara, J. A. Delettrez, C. Stoeckl, R. W. Short, and S. Skupsky, *Phys. Rev. Lett.* **91**, 095003 (2003).
24. N. A. Krall and A. W. Trivelpiece, *Principles of Plasma Physics* (San Francisco Press, Inc., San Francisco, 1986), p. 316.
25. I. V. Igumenshchev, V. N. Goncharov, W. Seka, D. Edgell, and T. R. Boehly, *Phys. Plasmas* **14**, 092701 (2007).
26. D. Edgell, W. Seka, J. A. Delettrez, R. S. Craxton, V. N. Goncharov, I. V. Igumenshchev, J. Myatt, A. V. Maximov, R. W. Short, T. C. Sangster, and R. E. Bahr, *Bull. Am. Phys. Soc.* **52**, 195 (2007); *ibid.*, *Bull. Am. Phys. Soc.* **53**, 168 (2008); *ibid.*, *Bull. Am. Phys. Soc.* **54**, 145 (2006).
27. S. Skupsky and R. S. Craxton, *Phys. Plasmas* **6**, 2157 (1999).
28. S. W. Haan, S. M. Pollaine, J. D. Lindl, L. J. Suter, R. L. Berger, L. V. Powers, W. E. Alley, P. A. Amendt, J. A. Futterman, W. K. Levedahl, M. D. Rosen, D. P. Rowley, R. A. Sacks, A. I. Shestakov, G. L. Strobel, M. Tabak, S. V. Weber, G. B. Zimmerman, W. J. Krauser, D. C. Wilson, S. V. Coggeshall, D. B. Harris, N. M. Hoffman, and B. H. Wilde, *Phys. Plasmas* **2**, 2480 (1995).

Characterization of Highly Stable, Mid-IR, GaSb-Based Laser Diodes

Introduction

Mid-IR, 3000- to 3500-nm laser sources are important for various applications including gas sensing, spectral analysis, infrared illumination, countermeasures, medical diagnostics, and others. One particular application is layering cryogenic targets for inertial confinement fusion (ICF) implosions at the Omega Laser Facility.¹ Careful layering of cryogenic targets is important to maximize the fuel density in ICF implosions. These targets consist of $\sim 900\text{-}\mu\text{m}$ -diam microcapsules that contain frozen D_2 (deuterium–deuterium) gas. The frozen deuterium is “layered” so that it is uniformly distributed around the inner surface of the capsule.^{2,3} The layering process relies on the target being in a spherical isotherm that is uniformly illuminated by mid-IR light. The wavelength is tuned to the absorption peak in the fuel material (3160 nm with $\sim 20\text{-nm}$ FWHM for D_2 targets⁴). Since thicker regions of ice will have a longer path length, they absorb more radiation, so they will be relatively hot spots. Fuel material sublimates from the hotter regions and condenses and refreezes on the thinner, colder regions, leading to a uniform distribution of fuel material. For this process to produce layers with the required uniformity, the

temperature must be held very close to the material’s melting point. As a result, the mid-IR source’s output power and spectrum must be temporally stable to avoid over- or underheating.

Currently a mid-IR optical parametric oscillator (OPO) is used to layer the targets.⁵ It was shown in Ref. 6 that mid-IR, GaSb-based quantum-well laser diodes can be used for target layering. Here we report on selection and characterization of a mid-IR laser diode that performs optimally for the cryogenic target layering.

Laser-Diode Selection

Three laser diodes emitting at ~ 3160 nm have been grown and assembled as described in Ref. 6. During the selection process, the output power versus driver current and spectral shape at 3160 nm were measured (see Fig. 122.20).

Diode #1 delivered the highest output power of >50 mW at 2400 mA of driver current. Its spectrum was centered at 3160 nm and had a compact envelope with $<20\text{-nm}$ FWHM. Diode #2 had the same slope efficiency as diode #1 with lower

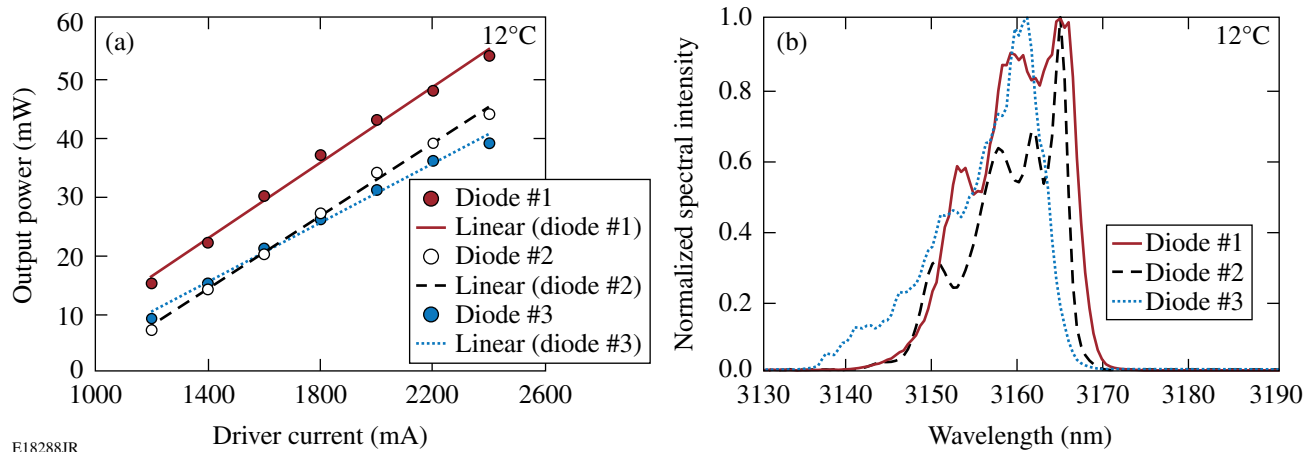


Figure 122.20

(a) Output power versus driver current and (b) spectra at 3160 nm for three tested laser diodes.

output power. Its spectrum had more-pronounced intensity variations than diode #1. Diode #3 had lower slope efficiency and output power than both diodes #1 and #2. Its spectrum was asymmetric and had a wide short-wavelength wing. Diode #1 has been selected for further characterization.

Laser-Diode Characterization

The output power of diode #1 was measured at various driver currents and heatsink temperatures (see Fig. 122.21). The highest power—54 mW—was produced at 12°C and 2400 mA of the driver current. A further temperature decrease might cause condensation and higher current might damage the diode. The output-power variations over 24 h of operation were ~1.3% rms and might be reduced by improving temperature stabilization of the diode.

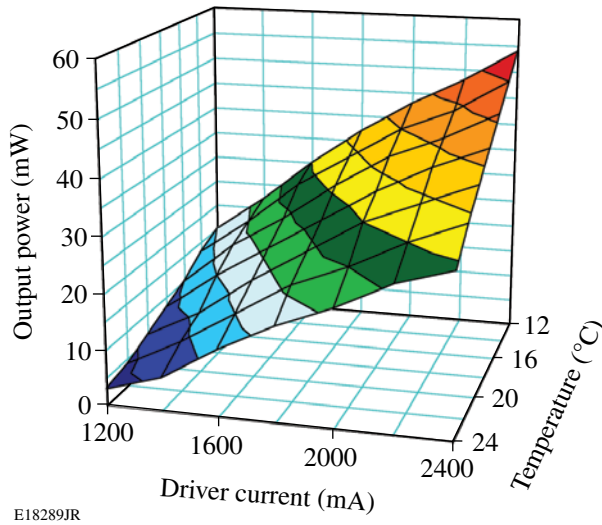


Figure 122.21
Output power versus driver current at various temperatures for diode #1.

The spectral position and shape were measured at various temperatures and currents (Fig. 122.22). The output spectrum moved toward a longer wavelength at a rate of ~2 nm per °C of temperature increase and at a rate of ~2.5 nm per 100 mA of current increase.

Providing constant absorbed power and preventing target melting require irradiation with a highly stable spectrum that matches the D₂ absorption band. The 3160-nm-centered, 20-nm FWHM D₂ absorption band⁴ is well represented by a fourth-order super-Gaussian shown in Fig. 122.23 (red). The diode #1 spectra at various diode temperatures and driver currents were multiplied by the D₂ absorption curve to find

a relative power absorbed by D₂. After integration over the wavelength, the absorbed power, plotted in Fig. 122.24, showed optimal temperature and current settings for the maximum absorbed power –12°C and 1800 mA, which correspond to ~37 mW of absorbed power. Figure 122.23 shows spectral

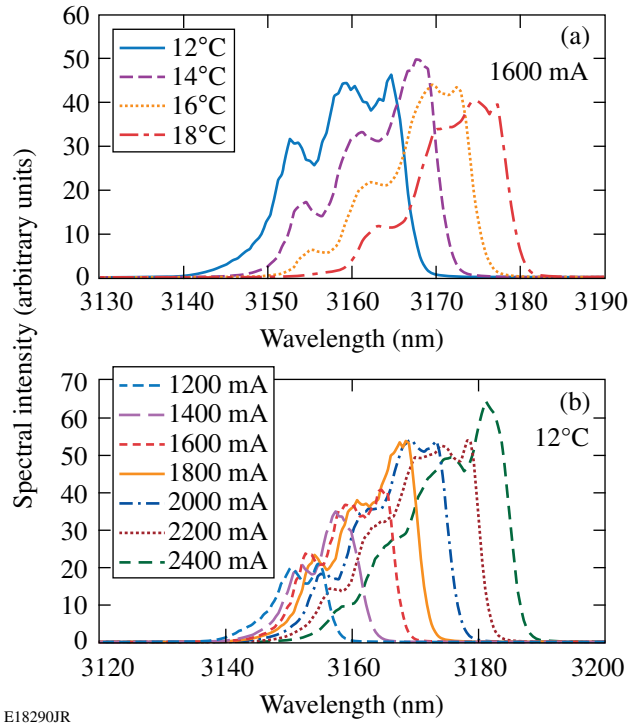


Figure 122.22
Output spectral shape and positions for various (a) temperatures and (b) currents for diode #1.

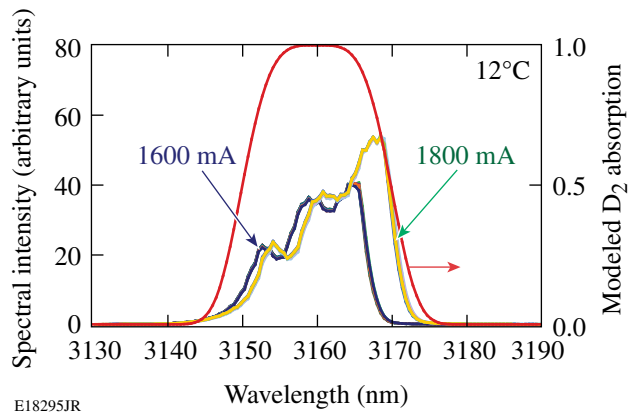
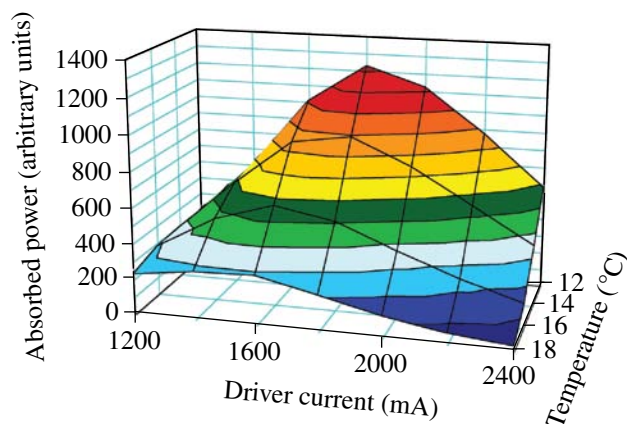


Figure 122.23
Diode #1 spectral stability at 1600- and 1800-mA driver currents. The D₂ absorption band is shown in red.



E18291JR

Figure 122.24

Diode #1 output power absorbed by the D₂ target at various diode temperatures and driver currents.

diode #1 stability at 12°C and 1600- and 1800-mA current settings. Plotted for each current setting are nine spectra that were taken at 15-min intervals over 2 h. Diode #1 represents high spectral stability and a compact spectral envelope over optimal temperature and current settings.

Conclusion

We demonstrated and characterized a highly spectrally stable, mid-IR, GaSb-based laser diode with a 3160-nm-centered, <20-nm FWHM spectrum and >35-mW output power at room temperature for cryogenic target layering at the Omega Laser Facility. A highly stable operation with output-power variations of ~1.3% rms has been demonstrated over 24 h. Future research will consist of optimizing the growing process to achieve consistent laser-diode performance with >100 mW of output power to meet the mid-IR layering-source requirement.

ACKNOWLEDGMENT

This work was supported by the U.S. Department of Energy Office of Inertial Confinement Fusion under Cooperative Agreement No. DE-FC52-08NA28302, the University of Rochester, and the New York State Energy Research and Development Authority. The support of DOE does not constitute an endorsement by DOE of the views expressed in this article. SUNY work was supported by US Air Force Office of Scientific Research under grant FA9550-08-1-0458.

REFERENCES

1. T. R. Boehly, D. L. Brown, R. S. Craxton, R. L. Keck, J. P. Knauer, J. H. Kelly, T. J. Kessler, S. A. Kumpan, S. J. Loucks, S. A. Letzring, F. J. Marshall, R. L. McCrory, S. F. B. Morse, W. Seka, J. M. Soures, and C. P. Verdon, *Opt. Commun.* **133**, 495 (1997).
2. T. C. Sangster, R. Betti, R. S. Craxton, J. A. Delettrez, D. H. Edgell, L. M. Elasky, V. Yu. Glebov, V. N. Goncharov, D. R. Harding, D. Jacobs-Perkins, R. Janezic, R. L. Keck, J. P. Knauer, S. J. Loucks, L. D. Lund, F. J. Marshall, R. L. McCrory, P. W. McKenty, D. D. Meyerhofer, P. B. Radha, S. P. Regan, W. Seka, W. T. Shmayda, S. Skupsky, V. A. Smalyuk, J. M. Soures, C. Stoeckl, B. Yaakobi, J. A. Frenje, C. K. Li, R. D. Petrasso, F. H. Séguin, J. D. Moody, J. A. Atherton, B. D. MacGowan, J. D. Kilkenny, T. P. Bernat, and D. S. Montgomery, *Phys. Plasmas* **14**, 058101 (2007).
3. D. R. Harding, D. D. Meyerhofer, T. C. Sangster, S. J. Loucks, R. L. McCrory, R. Betti, J. A. Delettrez, D. H. Edgell, L. M. Elasky, R. Epstein, V. Yu. Glebov, V. N. Goncharov, S. X. Hu, I. V. Igumenshchev, D. Jacobs-Perkins, R. J. Janezic, J. P. Knauer, L. D. Lund, J. R. Marciante, F. J. Marshall, D. N. Maywar, P. W. McKenty, P. B. Radha, S. P. Regan, R. G. Roides, W. Seka, W. T. Shmayda, S. Skupsky, V. A. Smalyuk, C. Stoeckl, B. Yaakobi, J. D. Zuegel, D. Shvarts, J. A. Frenje, C. K. Li, R. D. Petrasso, and F. H. Séguin, *J. Phys., Conf. Ser.* **112**, 022001 (2008).
4. A. Crane and H. P. Gush, *Can. J. Phys.* **44**, 373 (1966).
5. L. M. Elasky, D. J. Lonobile, W. A. Bittle, D. R. Harding, A. V. Okishev, and J. D. Zuegel, presented at the 15th Target Fabrication Specialists' Meeting, Glendon Beach, OR, 1–5 June 2003.
6. A. V. Okishev, D. Westerfeld, L. Shterengas, and G. Belenky, *Opt. Express* **17**, 15760 (2009).

A Reduced Particle-in-Cell Model for Two-Plasmon-Decay Instability

Introduction

Two-plasmon-decay (TPD) instability [the parametric decay of a laser (photon) into two Langmuir waves (plasmons)] has recently experienced renewed experimental and theoretical interest, largely based on recent experimental results obtained at the Omega Laser Facility.^{1–4} The TPD instability has been the subject of previous theoretical^{5,6} and experimental⁷ studies. Recent experiments using the OMEGA laser¹ have produced unambiguous evidence that TPD is driven in both spherical and planar targets. The diagnostic evidence includes the simultaneous emission of odd half-harmonic radiation and hard x rays.^{1,8} There is also some evidence^{2–4} that these hot electrons may be inhibiting the efficient implosion of spherical targets by preheating the core to a higher adiabat.

Although effort has been devoted to the linearized theory of the TPD instability in various regimes,^{5,6} it is clear, *a priori*, that a nonlinear theory is necessary to describe its evolution beyond the subpicosecond time to be relevant to experiments. This article is devoted to the development of a new theoretical tool for the study of the nonlinear development of TPD. It describes initial results from the implementation of the reduced particle-in-cell (RPIC) technique to treat the nonlinear evolution of TPD in homogeneous plasmas. The RPIC model is not limited to homogeneous plasma, and future work will include inhomogeneous plasma densities and flow velocities, which are present in experiments. The RPIC modeling and the closely related extended Zakharov (ZAK) modeling⁹ are useful tools for studying the nonlinear regimes of parametric instabilities. The RPIC and ZAK models have been previously applied to the nonlinear development of stimulated Raman scattering (SRS)¹⁰ and to the nonlinear development of the parametric decay instability (PDI).¹¹ In these studies, nonlinear processes such as the Langmuir decay instability (LDI) [the parametric decay of a Langmuir wave (LW) into another LW and an ion-acoustic wave (IAW)], Langmuir cavitation, and electron trapping have been observed to compete. Several predictions of this modeling have been experimentally verified.¹²

The RPIC model, while fully kinetic in regards to both electron and ion dynamics, shares certain features with the

reduced, fluid-like ZAK modeling.¹³ Both models represent the transverse fields, longitudinal fields, and density fields in terms of slowly varying envelopes of rapidly oscillating phase factors. This approach assumes a well-defined separation of time scales between the laser, LW, and IAW oscillations. This representation of field quantities stands in contrast with the standard particle-in-cell (PIC) technique in which the full-time variations are followed explicitly.¹⁴ In **Appendix B** (p. 103), a derivation of the extended Zakharov model directly from the RPIC equations of motion is presented. This derivation provides a direct theoretical connection between the kinetic RPIC and the fluid-like ZAK models. Furthermore, such a theoretical connection provides guidance on how one should proceed with *quantitative* comparison of the two models.

In the RPIC simulations, unique signatures of LDI are found that are suggestive of LDI as one of the primary saturation processes. Spectral signatures of LDI processes are strikingly similar, at least semi-quantitatively, to those found from ZAK modeling. In addition, the RPIC model also predicts heated-electron velocity distributions in the quasi-stationary nonlinear regime. Previous RPIC modeling has been extremely successful in modeling the nonlinear behavior of parametric instabilities involving the Langmuir decay instability, largely because RPIC eliminates the often unphysically high electron–ion collision rate present in explicit PIC codes, while at the same time allowing for the use of a modest number of simulation particles per simulation cell. For instance, for a plasma in quasi-thermodynamic equilibrium with $T_e/T_i \gg 1$, RPIC will preserve the temperature ratio perfectly over an extended time, whereas in standard PIC codes, this ratio will become unity prematurely because of the unphysically rapid electron–ion energy equilibration rate.¹⁵ This is problematic when ion modes are involved, such as in LDI, since the IAW damping rate is sensitive to this ratio (cf. Ref. 16). Additional effects expected from the strong electron–ion collisions (even when $T_{e0} = T_{i0}$) include unphysically large collisional damping of LW’s and IAW’s. Elimination of unphysical electron–ion collisions makes it possible for RPIC simulations to operate with fewer particles per simulation cell than standard PIC codes. It is important to

observe that the earliest application of PIC codes to TPD by Langdon *et al.*⁵ and more recently by Yan *et al.*¹⁴ observed a high level of ion-density fluctuations. It is not clear in retrospect that these can be interpreted as resulting from IAW fluctuations excited by LDI as found in this work.

In previous work using ZAK modeling⁹ it was found, among other things, that LDI produces a distinct, rich Fourier spectrum of electron- and ion-density fluctuations. Furthermore, this modeling provided an explanation for the well-known problem that the primary, i.e., most linearly unstable, TPD Langmuir waves cannot couple locally to the (observed) radiation at $3\omega_0/2$, where ω_0 is the laser frequency. In Russell *et al.*,¹⁷ it was shown that there is an efficient local coupling of the secondary LDI-produced LW's to the $3\omega_0/2$ emission and this coupling in turn produced, in an inhomogeneous plasma, a distinctive double-peaked $3\omega_0/2$ frequency spectrum. RPIC has the advantage that the envelope fields can be used directly to compute the currents for the $3\omega_0/2$ radiation, as was done in Russell *et al.*¹⁷ and also more recently for the $\omega_0/2$ radiation current as shown in DuBois *et al.*¹⁸ The latter application of RPIC to $\omega_0/2$ radiation is proposed for future work.

The article is organized as follows: (1) The equations for the physical model underlying RPIC are discussed. This involves expressing the electromagnetic vector potential, the longitudinal scalar potential, and the plasma density in temporal envelope representations (the primary objective of the RPIC formulation is to eliminate the laser time scale from the electron equation of motion and the laser and LW time scales from the ion equation of motion). (2) A sketch of the derivation of the RPIC model for TPD is given, with the details provided in **Appendix A**, p. 101. An important element in this derivation (as in previous implementations of RPIC¹⁵) is the closure of the model set of equations with an auxiliary electron equation of state. (3) Results of both RPIC and ZAK simulations of TPD in a homogeneous plasma are presented (including the standard problem of a single coherent laser beam) along with simulations of oblique overlapped beams propagating at angles of $\pm 23^\circ$ relative to the x axis common in OMEGA geometry.¹ Finally, a summary and conclusions are presented.

Physical Model

The vector potential, scalar potential, and electron density are written as¹⁹

$$\mathbf{A}(\mathbf{x}, t) = \frac{1}{2}[\mathbf{a}_0 \exp(-i\omega_0 t) + \text{c.c.}], \quad (1)$$

$$\phi(\mathbf{x}, t) = \phi_S + \frac{1}{2}[\phi_F \exp(-i\omega_{LW} t) + \text{c.c.}], \quad (2)$$

$$n(\mathbf{x}, t) = n_S + \frac{1}{2}[n_F \exp(-i\omega_{LW} t) + \text{c.c.}], \quad (3)$$

where ω_0 is the laser frequency and ω_{LW} is the carrier frequency of the LW density and electric-field perturbations. In the RPIC model, ω_{LW} is an input parameter and is typically chosen to be $\omega_{LW} = \omega_{pe0}$ (where $\omega_{pe0}^2 = 4\pi e^2 n_{e0}/m_e$), e is the unsigned electronic charge, n_{e0} is the electron number density, and m_e is the mass of an electron. The subscripts S and F refer to the slow (ion-acoustic wave and profile modification) and fast (Langmuir wave) time scales, respectively. It is assumed that the density is at, or near, quarter-critical density so that $\omega_0 \approx 2\omega_{LW}$. The model is also restricted to two spatial dimensions (x, y), with z the ignorable coordinate.

The goal of the RPIC formulation is to eliminate the laser time scale from the electron equations of motion and the laser and Langmuir wave time scales from the ion equations of motion. The particle velocities and positions in RPIC, by necessity, are measured in an oscillating and, therefore, non-inertial frame.

1. Single-Particle Equation in an Oscillating Frame

The nonrelativistic equation of motion for the single-particle velocity $\mathbf{u} [= u_x(x, y)\hat{\mathbf{x}} + u_y(x, y)\hat{\mathbf{y}}]$ is given by

$$m \frac{d\mathbf{u}}{dt} = q \left(-\nabla \phi - \frac{1}{c} \frac{\partial \mathbf{A}}{\partial t} + \frac{\mathbf{u} \times \nabla \times \mathbf{A}}{c} \right). \quad (4)$$

Rewriting the above equation with the change of variable $\mathbf{u} \equiv \tilde{\mathbf{u}} - q\mathbf{A}/mc$, one obtains

$$\begin{aligned} m \left(\frac{d\tilde{\mathbf{u}}}{dt} - \frac{q}{mc} \frac{\partial \mathbf{A}}{\partial t} - \frac{q}{mc} \mathbf{u} \cdot \nabla \mathbf{A} \right) \\ = q \left(-\nabla \phi - \frac{1}{c} \frac{\partial \mathbf{A}}{\partial t} + \frac{\mathbf{u} \times \nabla \times \mathbf{A}}{c} \right) \end{aligned} \quad (5a)$$

and

$$\begin{aligned} m \frac{d\tilde{\mathbf{u}}}{dt} = -\nabla \left(q\phi + \frac{q^2}{2mc^2} \mathbf{A} \cdot \mathbf{A} \right) \\ + \frac{q}{c} (\tilde{\mathbf{u}} \times \nabla \times \mathbf{A} + \tilde{\mathbf{u}} \cdot \nabla \mathbf{A}). \end{aligned} \quad (5b)$$

Note that the operators ∇ and d/dt in the above equation are measured in the laboratory frame. The above equation can be written in the oscillating frame $(\tilde{\mathbf{x}}, \tilde{t})$, which moves with velocity $-q\mathbf{A}/mc$ relative to the lab frame (\mathbf{x}, t) by using the following coordinate transformation:

$$\mathbf{u} = \tilde{\mathbf{u}} - \frac{q\mathbf{A}(\mathbf{x}, t)}{mc}, \quad (6)$$

$$\mathbf{x} = \tilde{\mathbf{x}} - \frac{q}{mc} \int_0^t \mathbf{A}[\mathbf{x}(\tau), \tau] d\tau, \quad (7)$$

$$t = \tilde{t}. \quad (8)$$

The various partial derivatives required for the transformation $(\mathbf{x}, t) \rightarrow (\tilde{\mathbf{x}}, \tilde{t})$ are

$$\frac{\partial \tilde{t}}{\partial t} = 1, \quad (9)$$

$$\frac{\partial \tilde{t}}{\partial \mathbf{x}} = 0, \quad (10)$$

$$\frac{\partial \tilde{\mathbf{x}}}{\partial t} = \frac{q\mathbf{A}}{mc}, \quad (11)$$

$$\frac{\partial \tilde{\mathbf{x}}}{\partial \mathbf{x}} = \mathbf{I}. \quad (12)$$

By using the chain rule and the partial derivatives shown above, one obtains

$$\frac{\partial}{\partial t} = \frac{\partial \tilde{t}}{\partial t} \frac{\partial}{\partial \tilde{t}} + \frac{\partial \tilde{\mathbf{x}}}{\partial t} \cdot \frac{\partial}{\partial \tilde{\mathbf{x}}} = \frac{\partial}{\partial \tilde{t}} + \frac{q\mathbf{A}}{mc} \cdot \frac{\partial}{\partial \tilde{\mathbf{x}}}, \quad (13)$$

$$\frac{\partial}{\partial \mathbf{x}} = \frac{\partial \tilde{t}}{\partial \mathbf{x}} \frac{\partial}{\partial \tilde{t}} + \frac{\partial \tilde{\mathbf{x}}}{\partial \mathbf{x}} \cdot \frac{\partial}{\partial \tilde{\mathbf{x}}} = \frac{\partial}{\partial \tilde{\mathbf{x}}}. \quad (14)$$

The transformation from (\mathbf{x}, t) to $(\tilde{\mathbf{x}}, \tilde{t})$ proceeds as

$$\begin{aligned} \frac{d}{dt} &= \frac{\partial}{\partial t} + \mathbf{u} \cdot \frac{\partial}{\partial \mathbf{x}}, \\ &= \frac{\partial}{\partial \tilde{t}} + \frac{q\mathbf{A}}{mc} \cdot \frac{\partial}{\partial \tilde{\mathbf{x}}} + \mathbf{u} \cdot \frac{\partial}{\partial \tilde{\mathbf{x}}}, \\ &= \frac{\partial}{\partial \tilde{t}} + \tilde{\mathbf{u}} \cdot \frac{\partial}{\partial \tilde{\mathbf{x}}}, \\ \frac{d}{dt} &= \frac{d}{d\tilde{t}}. \end{aligned} \quad (15)$$

Equation (5) can now be rewritten as

$$\begin{aligned} m \frac{d\tilde{\mathbf{u}}}{d\tilde{t}} &= -\tilde{\nabla} \left(q\phi + \frac{q^2}{2mc^2} \mathbf{A} \cdot \mathbf{A} \right) \\ &+ \frac{q}{c} [\tilde{\nabla} (\tilde{\mathbf{u}} \cdot \mathbf{A}) - \mathbf{A} \times \tilde{\nabla} \times \tilde{\mathbf{u}} - \mathbf{A} \cdot \tilde{\nabla} \tilde{\mathbf{u}}], \end{aligned} \quad (16)$$

$$\frac{d\tilde{\mathbf{x}}}{d\tilde{t}} = \tilde{\mathbf{u}}, \quad (17)$$

where the vector identity

$$\tilde{\nabla} (\tilde{\mathbf{u}} \cdot \mathbf{A}) = \tilde{\mathbf{u}} \times \tilde{\nabla} \times \mathbf{A} + \mathbf{A} \times \tilde{\nabla} \times \tilde{\mathbf{u}} + \mathbf{A} \cdot \tilde{\nabla} \tilde{\mathbf{u}} + \tilde{\mathbf{u}} \cdot \tilde{\nabla} \mathbf{A}$$

has been used. Note that Eqs. (16) and (17), which are valid for both electrons and ions, are exact.

2. Fluid Equations

The electron fluid momentum equation is obtained by integrating Eq. (16) (the single-particle equation of motion) over the distribution function, writing explicitly $d/d\tilde{t} \equiv \partial/\partial\tilde{t} + \tilde{\mathbf{U}} \cdot \tilde{\nabla}$,

$$\begin{aligned} mn \left(\frac{\partial \tilde{\mathbf{U}}}{\partial \tilde{t}} + \tilde{\mathbf{U}} \cdot \tilde{\nabla} \tilde{\mathbf{U}} \right) &= -n \tilde{\nabla} \left(q\phi + \frac{q^2}{2mc^2} \mathbf{A} \cdot \mathbf{A} \right) \\ &+ \frac{qn}{c} [\tilde{\nabla} (\tilde{\mathbf{U}} \cdot \mathbf{A}) - \mathbf{A} \times \tilde{\nabla} \times \tilde{\mathbf{U}} - \mathbf{A} \cdot \tilde{\nabla} \tilde{\mathbf{U}}] - \tilde{\nabla} p, \end{aligned} \quad (18)$$

where n , $\tilde{\mathbf{U}}$, and p are the electron density, fluid velocity, and fluid pressure in the oscillating frame. For an isotropic background electron-velocity distribution f ,

$$n \equiv \int f(|\tilde{\mathbf{u}}|) d^3\tilde{\mathbf{u}},$$

$$n\tilde{\mathbf{U}} \equiv \int \tilde{\mathbf{u}} f(|\tilde{\mathbf{u}}|) d^3\tilde{\mathbf{u}},$$

$$p \equiv \int m|\tilde{\mathbf{u}} - \tilde{\mathbf{U}}|^2 f(|\tilde{\mathbf{u}}|) d^3\tilde{\mathbf{u}}.$$

In the special case of an isotropic Maxwellian distribution function, $p = n_e T_e$.

The RPIC Model

The derivation of the RPIC model for TPD can be divided into three separate tasks: First, the fluid momentum equation [Eq. (18)] is averaged over the fast laser time scale to derive an electron equation of state, which itself provides closure for the RPIC model. Second, Eq. (18) is also used to derive the transverse electron current, which provides the driving sources in the nonlinear Schrödinger equation for the incident EM waves. Third, the single-particle equation [Eq. (16)] is averaged over the fast laser time scale to derive a reduced-description, single-particle equation of motion (only a summary of the RPIC model is given below; detailed derivations of these equations can be found in **Appendix A**, p. 101).

The electrons are advanced using the following reduced-description equations of motion:

$$\begin{aligned} m_e \frac{d\tilde{\mathbf{u}}_e}{d\tilde{t}} &\approx -e\mathbf{E} - \frac{e^2}{4m_e c^2} \tilde{\nabla} |\mathbf{a}_0|^2 \\ &- \frac{e^2}{4cm_e \omega_{LW}} \left\{ i \tilde{\nabla} (\mathbf{E}_F^* \cdot \mathbf{a}_0) \exp[-i(\omega_0 - \omega_{LW})\tilde{t}] + \text{c.c.} \right\} \\ &- \frac{e^2}{4cm_e \omega_{LW}} \left\{ -i(\mathbf{a}_0 \cdot \tilde{\nabla}) \mathbf{E}_F^* \exp[-i(\omega_0 - \omega_{LW})\tilde{t}] + \text{c.c.} \right\}, \end{aligned} \quad (19)$$

$$\frac{d\tilde{\mathbf{x}}_e}{d\tilde{t}} = \tilde{\mathbf{u}}_e,$$

$$\mathbf{E} \equiv -\tilde{\nabla} \phi, \quad (20)$$

$$\mathbf{E}_F \equiv -\tilde{\nabla} \phi_F,$$

and the ions by

$$m_i \frac{d\tilde{\mathbf{u}}_i}{d\tilde{t}} = Z_i e \mathbf{E}_S - \frac{Z_i^2 e^2}{4m_i c^2} \tilde{\nabla} |\mathbf{a}_0|^2,$$

$$\frac{d\tilde{\mathbf{x}}_i}{d\tilde{t}} = \tilde{\mathbf{u}}_i,$$

$$\mathbf{E}_S \equiv -\tilde{\nabla} \phi_S. \quad (21)$$

Here, Z_i and m_i are the ion charge state and ion mass, respectively. The electron and ion charge densities are interpolated from the particle data onto the computational mesh:

$$-en_e(\tilde{\mathbf{x}}, \tilde{t}) = \sum_{p \in e} q_p S[\tilde{\mathbf{x}} - \tilde{\mathbf{x}}_p(\tilde{t})], \quad (22)$$

$$eZ_i n_i(\tilde{\mathbf{x}}, \tilde{t}) = \sum_{p \in i} q_p S[\tilde{\mathbf{x}} - \tilde{\mathbf{x}}_p(\tilde{t})]. \quad (23)$$

The particle shape function $S(\mathbf{x})$ is the bi-quadratic B-spline of compact supports Δx and Δy (Δx and Δy are the discrete grid spacings of the computational mesh).¹⁵ The symbols $\sum_{p \in e}$ and $\sum_{p \in i}$ denote summations over the finite-size electron particles and finite-size ion particles, respectively. The electrostatic potentials ϕ , ϕ_S , and ϕ_F are obtained by solving the Poisson equation in conjunction with the auxiliary electron equation of state:

$$\tilde{\nabla}^2 \phi = 4\pi e \left(n_e - \sum_i Z_i n_i \right), \quad (24)$$

$$\tilde{\nabla}^2 \phi_S = 4\pi e \left(n_{eS} - \sum_i Z_i n_i \right), \quad (25)$$

$$\alpha(t) = e\phi_S - \frac{e^2}{4m_e \omega_{LW}^2} |\mathbf{E}_{\text{eff}}|^2 - \frac{e^2}{4m_e^2 c^2} |\mathbf{a}_0|^2 - f(\gamma, n_{eS}), \quad (26)$$

where

$$f(\gamma, n_{eS}) = \begin{cases} T_{e0} \ln(n_{eS}/n_{e0}) & \text{for } \gamma = 1, \\ T_{e0} \left(\frac{\gamma}{\gamma - 1} \right) (n_{eS}/n_{e0})^{\gamma - 1} & \text{otherwise.} \end{cases} \quad (27)$$

$$\mathbf{E}_{\text{eff}} \equiv \mathbf{E}_F - \frac{e}{2im_e c \omega_{\text{LW}}} \exp(-i\Delta\omega\tilde{t}) \left[\tilde{\nabla} \left(\mathbf{E}_F^* \cdot \mathbf{a}_0 \right) + \mathbf{a}_0 \cdot \tilde{\nabla} \mathbf{E}_F^* \right], \quad (28)$$

$$\phi_F \approx \exp(i\omega_{\text{LW}}\tilde{t}) \left[-\frac{1}{i\omega_{\text{LW}}} \frac{\partial\phi}{\partial\tilde{t}} + (\phi - \phi_S) \right], \quad (29)$$

$$\Delta\omega \equiv \omega_0 - 2\omega_{\text{LW}}. \quad (30)$$

Here, α is the constant of integration chosen to satisfy global charge conservation and γ is the ratio of specific heats (isothermal electrons: $\gamma = 1$; adiabatic electrons: $\gamma = 5/3$), and n_{e0} is the background electron number density. Finally, the incident EM field is advanced self-consistently in time by solving the nonlinear Schrödinger equation

$$\begin{aligned} & i \left(\frac{2\omega_0}{c^2} \right) \frac{\partial \mathbf{a}_0}{\partial \tilde{t}} + \tilde{\nabla}^2 \mathbf{a}_0 + \frac{1}{c^2} \left(\omega_0^2 - \frac{4\pi e^2 n_S}{m_e} \right) \mathbf{a}_0 \\ & = -\frac{4\pi}{c} \tilde{\nabla} \chi_0 + \frac{4\pi e^2 n_{eF}}{2im_e c \omega_{\text{LW}}} \tilde{\mathbf{E}}_{\text{eff}} \exp(i\Delta\omega\tilde{t}), \end{aligned} \quad (31)$$

where

$$\nabla^2 \chi_0 = -\nabla \cdot \mathbf{J}_0, \quad (32)$$

$$\mathbf{J}_0 = -\frac{e^2 n_{eS} \mathbf{a}_0}{m_e c} - \frac{e^2 n_{eF}}{2im_e \omega_{\text{LW}}} \mathbf{E}_{\text{eff}} \exp(i\Delta\omega\tilde{t}). \quad (33)$$

The projection operator in Eq. (32) ensures that the gauge condition $\nabla \cdot \mathbf{a}_0 = 0$ is preserved.

Equations (19)–(33) are solved self-consistently on a rectangular simulation domain with $0 \leq x \leq x_{\text{max}}$ and $0 \leq y \leq y_{\text{max}}$, consisting of $N_x \times N_y$ computational cells of equal size. The EM wave of the laser is permitted to propagate along an arbitrary direction in the x – y plane and is linearly polarized (normal to the direction of wave propagation). The field boundary conditions are periodic in the y direction but are aperiodic in the x direction with $\phi(x=0,y) = \phi(x=x_{\text{max}},y) = 0$. At all boundary

surfaces, i.e., $x=0$, $x=x_{\text{max}}$, $y=0$, and $y=y_{\text{max}}$, particles leaving the domain are absorbed (removed), and new particles are injected consistent with a Maxwellian bath (with a temperature given by the plasma's initial state) surrounding the simulation domain (see Fig. 122.25). Modification of the particle boundary conditions (for example, to account for recirculation of hot electrons²⁰) is an important problem for future research, as discussed in **Summary and Conclusions** (p. 101). Finally, the RPIC code is fully parallel, based on the Message Passing Interface (MPI),¹⁵ and has a number of built-in spectral, hot-electron, and spatial diagnostics.

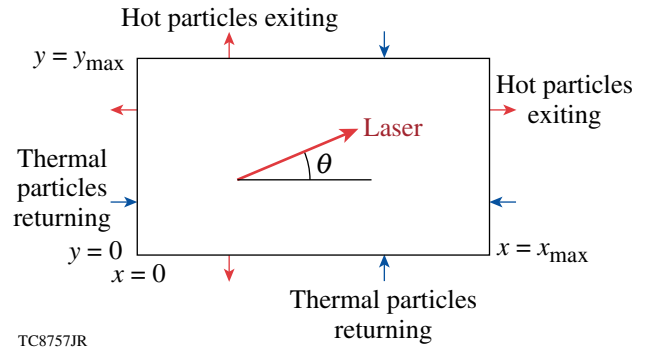


Figure 122.25

The two-dimensional simulation geometry. A Maxwellian bath of electrons at temperature T_{e0} is assumed to surround the rectangular simulation domain. The laser light can be specified as multiple plane-wave sources, propagating at arbitrary angles θ to the x direction.

Simulation Results

Three sets of simulations are presented in this section. For each set, two simulations were performed with identical parameters on the domain $x_{\text{max}} = 20 \mu\text{m}$, $y_{\text{max}} = 10 \mu\text{m}$, and consisting of $N_x \times N_y = 2048 \times 1024$ computational cells of equal size (see Fig. 122.25). In all cases the incident laser light had a vacuum wavelength of $\lambda_0 = 0.351 \mu\text{m}$ and the plasma was fully ionized hydrogen ($Z = 1$). The two simulations highlight the qualitative similarities and quantitative differences between the kinetic RPIC model [Eqs. (19)–(33)] and its (fluid) limiting form that has been derived in Appendix B [Eqs. (B40)–(B41)]. The limiting form, given by Eqs. (B40)–(B41), is solved using the existing extended-Zakharov code “ZAK,” which is described in DuBois *et al.*⁹ The equations solved by ZAK are advanced in time using split steps: spatial gradients are computed in configuration space, and Landau damping of LW’s and IAW’s, which are k dependent, are computed in Fourier space. These results, which are by no means exhaustive, are presented to illustrate the utility and capability of the RPIC code and to motivate further studies.

The first simulation set investigated the decay of a single-plane electromagnetic (EM) wave propagating in the positive x direction. Pump depletion was not considered, i.e., $\mathbf{a}_0 = a_{00}\hat{\mathbf{y}}\exp(ik_0x)$, where a_{00} is a constant [Eq. (31) is not solved]. The pump laser had an intensity of $I_0 = 2 \times 10^{15}$ W/cm², corresponding to a linear (amplitude) growth rate of $\gamma_{\text{TPD}}/\omega_{\text{pe}0} \simeq 6.4 \times 10^{-3}$, which is 50 \times above the collisional threshold (the collision frequency $\nu_{e0}/\omega_{\text{pe}0}$ was taken to be $\sim 9.1 \times 10^{-4}$). The plasma was of uniform initial density $n_{e0}/n_c = 0.23$ [where $n_c = m_e \omega_0^2/(4\pi e^2)$ is the critical density] and the electron- and ion-plasma temperatures were $T_{e0} = 4$ keV and $T_{i0} = 2$ keV, respectively. This electron temperature was about a factor of 2 higher than typically found in OMEGA experiments and was chosen because the spectral components (e.g., due to LDI) were more widely separated because of the large value of $k\lambda_{\text{De}}$, where $\lambda_{\text{De}} \equiv v_{\text{the}}/\omega_{\text{pe}0}$ is the electron Debye length and $v_{\text{the}} \equiv (T_{e0}/m_e)^{1/2}$ is the electron thermal speed. The electrons and ions were each represented by 16 particles per computational cell. The discrete time step was $\omega_{\text{pe}0}\Delta t = 0.1$ or, alternatively, $\Delta t \approx 3.88 \times 10^{-5}$ ps.

Figure 122.26 shows, from strictly linear-fluid considerations, the locations of frequency- and wave-number-matched LW's (circle),

$$\left(k_x\lambda_{\text{De}} - \frac{1}{2}k_0\lambda_{\text{De}}\right)^2 + (k_y\lambda_{\text{De}})^2 = \kappa^2, \quad (34)$$

and the locations of maximum TPD growth (hyperbola),

$$\left(k_x\lambda_{\text{De}} - \frac{1}{2}k_0\lambda_{\text{De}}\right)^2 - (k_y\lambda_{\text{De}})^2 = \left(\frac{1}{2}k_0\lambda_{\text{De}}\right)^2. \quad (35)$$

Here κ is defined as

$$\kappa \equiv \sqrt{\frac{1}{2}\Omega - \left(\frac{1}{2}k_0\lambda_{\text{De}}\right)^2}, \quad \text{with } \Omega \equiv \frac{2}{3}\left(\frac{\omega_0}{\omega_{\text{pe}0}} - 2\right), \quad (36)$$

and $k_0 = \omega_0/c\sqrt{1 - n_{e0}/n_c}$ is the laser light's wave number in the plasma. The intersections of the circle and the hyperbola are locations where TPD-produced LW's are expected to be the most intense. In Fig. 122.26, the two linear modes indicated by the label "1" and located at

$$\mathbf{k}\lambda_{\text{De}} \equiv (k_x\lambda_{\text{De}}, k_y\lambda_{\text{De}}) = (0.20, \pm 0.087)$$

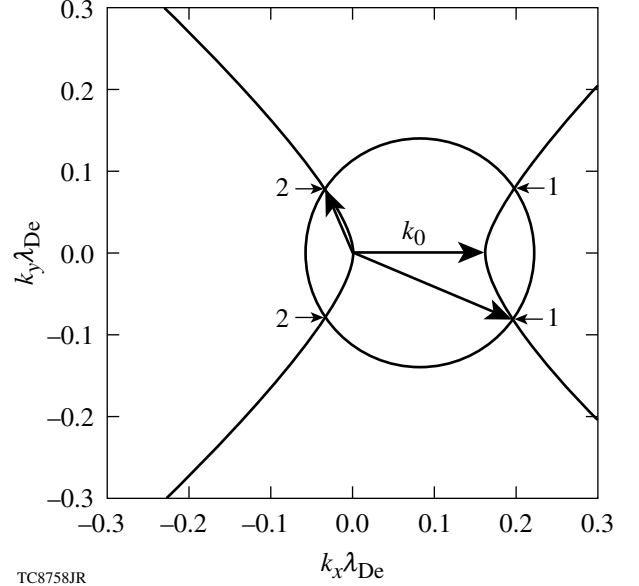


Figure 122.26

The expected wave numbers for plasmons occurring in the TPD instability of a single pump laser propagating in the x direction with parameters $T_{e0} = 4$ keV and $n_e/n_c = 0.23$. The circle represents all possible wave-number- and frequency-matched decay LW's [Eq. (34)], and the hyperbola represents the locations in k space where the TPD growth rate is maximized [Eq. (35)]. The intersections of the circle and the hyperbolae are the spectral locations where TPD LW's are expected to occur. Labels 1 and 2 denote the forward propagating (blue-shifted) and backward propagating (red-shifted) LW's, respectively.

correspond to forward-propagating, blue-shifted LW's and the two modes labeled "2" at $\mathbf{k}\lambda_{\text{De}} = (-0.038, \pm 0.087)$ correspond to backward-propagating, red-shifted plasmons.

Figure 122.27 shows the normalized LW spectra

$$W_k \equiv \frac{x_{\text{max}}}{2\pi} \frac{y_{\text{max}}}{2\pi} \frac{|E_{\text{LW}}(k_x, k_y)|^2}{4\pi n_{e0} T_{e0}},$$

time-averaged over the full 20-ps duration of the simulation, for both the (a) RPIC and (b) ZAK models. The RPIC and ZAK results are displayed on the same color scale to facilitate a direct comparison. The RPIC and ZAK results exhibit good qualitative similarity, with the dominant spectral features falling at exactly the same location in k space. The labels 1 and 2 in Fig. 122.27 refer to the same unstable modes as were identified previously in Fig. 122.26. In addition, two LDI steps of the blue-shifted plasmons are seen in the RPIC calculations [labeled 1' and 1'', respectively, in Fig. 122.27(a)], while only one LDI step is clearly seen in the ZAK calculations [labeled 1' in Fig. 122.27(b)]. As a measure of the level of laser-induced LW

excitation, the integrated value $W \equiv \int d\mathbf{k} W_k$ is defined, where the integration is carried out over the disk $|\mathbf{k}\lambda_{De}| \leq 0.25$. For the RPIC simulation $W = 1.0 \times 10^{-1}$, while the ZAK simulation

gives the almost $2\times$ stronger value of $W = 1.8 \times 10^{-1}$. However, the peak values in the RPIC simulation are narrower and more intense than for the ZAK case.

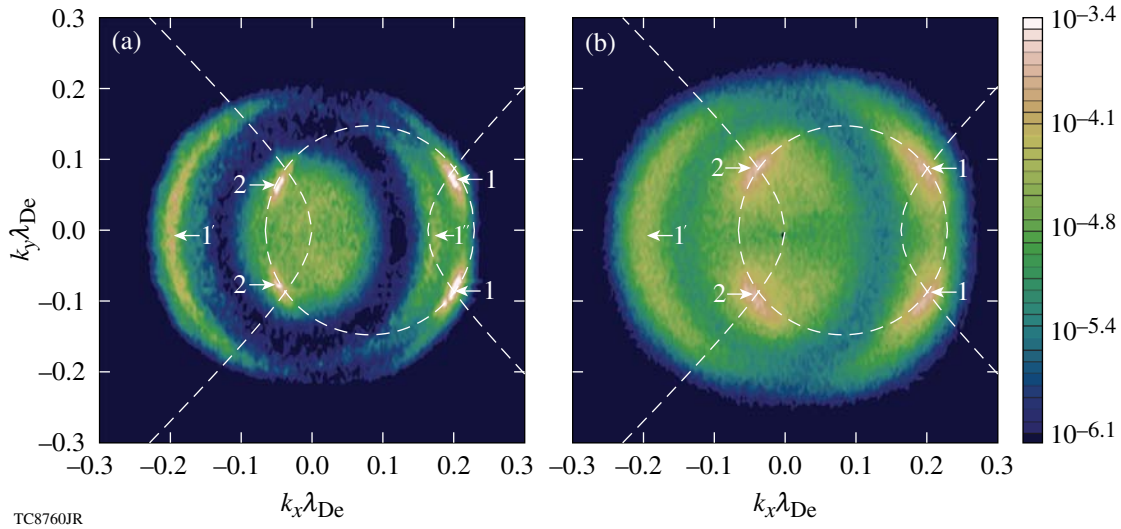


Figure 122.27

The time-averaged LW spectral intensity W_k is shown for both (a) RPIC and (b) ZAK simulations for a single plane-wave pump light wave and the parameters $T_{e0} = 4$ keV and $n_{e0}/n_c = 0.23$. Labels 1 and 2 denote the forward-propagating (blue-shifted) and backward-propagating (red-shifted) TPD LW's, respectively. Label 1' indicates that the LW's wave corresponding to the first LDI step of blue TPD plasmon (1), which is evident in both the RPIC and ZAK calculations. The second decay step (1'') can be seen in (a).

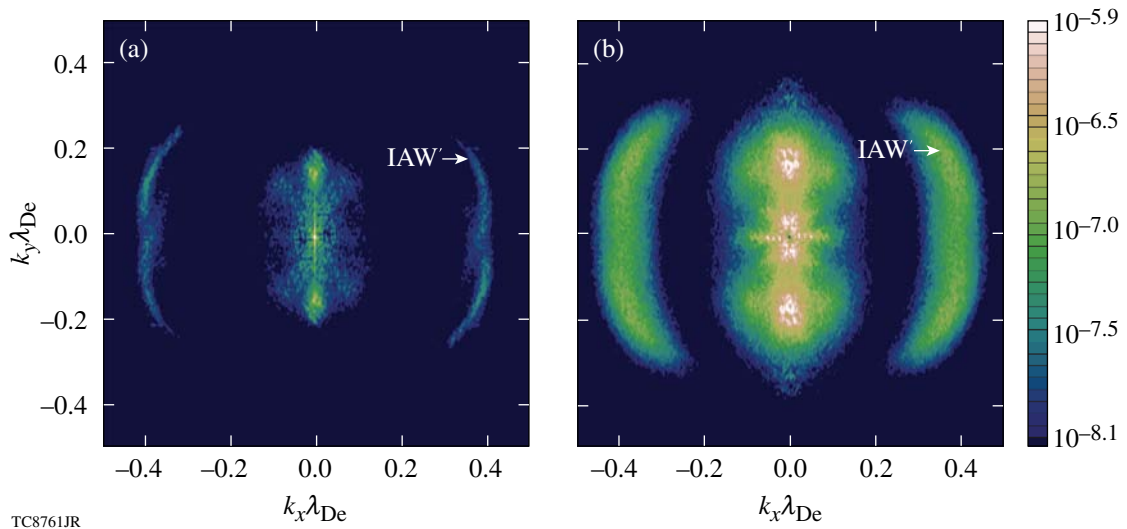


Figure 122.28

The time-averaged IAW density fluctuation spectrum $|\delta N_k|^2$ is shown for (a) RPIC and (b) ZAK simulations of TPD driven by a single plane-wave pump with the parameters $T_{e0} = 4$ keV and $n_{e0}/n_c = 0.23$. IAW's corresponding to the first LDI step of the blue TPD plasmon are evident in both sets of simulations, although narrower and weaker in (a) than in (b), and are indicated by the label IAW'.

The corresponding IAW spectra

$$|\delta N_k|^2 \equiv \frac{x_{\max}}{2\pi} \frac{y_{\max}}{2\pi} \left| \delta n_{eS}(k_x, k_y) / n_{e0} \right|^2$$

are shown in Fig. 122.28. Ion-acoustic waves caused by LDI are clearly visible in both the RPIC and ZAK simulations and are labeled IAW'. The IAW from the second LDI step is very weak and difficult to identify in the displayed spectrum. The integrated LDI density perturbations are estimated by the quantity $\mathcal{N}_{\text{LDI}} \equiv \int d\mathbf{k} |\delta N_k|^2$. In this case, the domain of integration is the annulus $0.3 \leq |\mathbf{k}\lambda_{\text{De}}| \leq 0.5$. The choice of domain is intended to avoid including the structures in $|\delta N_k|^2$ found near $k_x = 0$ that arise from the beating of pairs of LW's with equal and opposite values of k_y and equal values of k_x . Using this criterion, RPIC gives $\mathcal{N}_{\text{LDI}} = 1.4 \times 10^{-4}$, whereas ZAK gives $\mathcal{N}_{\text{LDI}} = 5.3 \times 10^{-4}$. If it is assumed that the ponderomotive drive for the IAW's is proportional to \mathcal{W} , comparing the \mathcal{N}_{LDI} values would indicate that LDI plays a relatively smaller role in the nonlinear saturation in RPIC. Kinetic saturation mechanisms, such as trapping of electrons (and ions) in the LW's (and IAW's) in the case of RPIC, cannot be ruled out. All of the simulations reported here reach saturation after about 15 ps, which is also the time at which LDI features become well established in the spectra.

In the second simulation set, two overlapping incident laser beams, again plane waves, were prescribed at angles θ relative to the x axis of $\theta_{\pm} = \pm 23^\circ$. This type of crossed-beam geometry is generic to direct-drive ICF, where large numbers of beams are overlapped to provide uniform illumination of the target (the precise angles of $\theta_{\pm} = \pm 23^\circ$ are specific to OMEGA¹). The individual beam intensity $I_0 = 1 \times 10^{15}$ W/cm² was chosen such that the crossed-beam overlapped intensity was the same as the previous single-beam case, shown in Figs. 122.26–122.28, and all other parameters were identical, with the exception of the plasma density, which was slightly increased to $n_{e0}/n_c = 0.231$ (the reason for choosing this particular density is given below).

The locations of the most linearly unstable TPD-produced LW waves, for an arbitrary irradiation angle in a homogeneous plasma, can be obtained simply by rotating Eqs. (34) and (35) in k space (see **Appendix C**, p. 109). In general, for two overlapping beams there are eight distinct LW's since each beam will produce four LW's (as previously shown in Fig. 122.26): two corresponding to the forward (blue-shifted) plasmons and two corresponding to the backward (red-shifted) plasmons. In the case of beams symmetrically oriented about the x axis, for a

given set of plasma parameters (T_{e0} and $0.2 \lesssim n_{e0}/n_c \lesssim 0.25$), a particular beam angle θ exists in which two of the forward (blue-shifted) plasmons are degenerate, or common. This overlap, or sharing of a common plasmon, allows for the cooperative nonlinear interaction between the two crossed beams. Conversely, for a prescribed beam angle θ and electron temperature T_{e0} , a particular density n_{e0}/n_c exists that will result in degenerate forward plasmons. In monotonic inhomogeneous plasmas, a location will always exist along the beam path where this degeneracy condition is satisfied, but in homogeneous simulations it must be specially selected, which is the choice made here. The relationship between the beam angle θ , electron density n_{e0}/n_c , and electron temperature T_{e0} for degeneracy to occur is derived in **Appendix C** and is given by Eq. (C8). For an electron temperature $T_{e0} = 4$ keV and angles $\theta_{\pm} = \pm 23^\circ$, Eq. (C8) yields degenerate forward plasmons for an electron density of $n_{e0}/n_c = 0.231$. This is depicted graphically in Fig. 122.29, where two sets of circles and hyperbolae are shown: (1) solid lines for the laser propagating at $\theta_+ (= +23^\circ)$ and (2) dashed lines for the laser propagating at $\theta_- (= -23^\circ)$. As before, the intersections of the circle and the hyperbola for

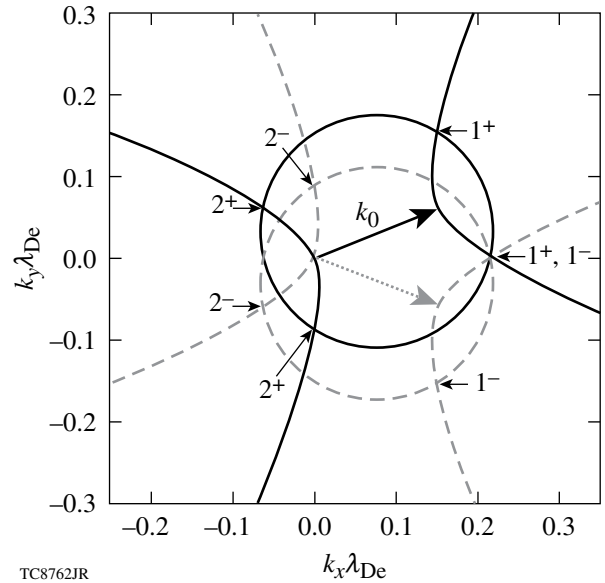


Figure 122.29

Expected wave numbers for TPD LW's resulting from the decay of two EM plane waves propagating with angles $\theta = \pm 23^\circ$ with respect to the x axis (the parameters are $T_e = 4$ keV and $n_e/n_c = 0.231$). Points 1^+ (1^-) and 2^+ (2^-) denote the expected locations of the red- and blue-shifted plasmons from the EM wave propagating with angle $\theta = +23^\circ$ (-23°), respectively. The solid (dashed) circle [Eq. (C1)] represents all frequency- and wave-number-matched LW's for the $\theta = +23^\circ$ (-23°) beam. Likewise, the solid (dashed) hyperbolae [Eq. (C4)] show the maximum growth rate for the $\theta = +23^\circ$ (-23°) beam. The blue-shifted plasmons 1^+ and 1^- are degenerate.

each respective laser beam are the spectral locations where LW's are expected to be observed. These are labeled as in Fig. 122.26, with the superscripts \pm corresponding to decays of the beam incident at angle θ_{\pm} . The on-axis, blue-shifted LW's of both beams (1^+ and 1^-) are degenerate—the common LW wave. This has a wave number $k\lambda_{De} \approx (0.23, 0.0)$ and a phase velocity $v_{\phi}/v_{the} \approx 4.7$. This notion of a “shared” plasma wave,

which can generally occur in cases of multiple-beam irradiation where a symmetry exists, has been discussed by Short *et al.*²¹

Figures 122.30 and 122.31 show the LW spectral intensity W_k and IAW density spectra $|\delta N_k|^2$, respectively, time averaged over the full 20-ps duration of the simulation. Although the RPIC and ZAK results are not in exact quantitative agreement,

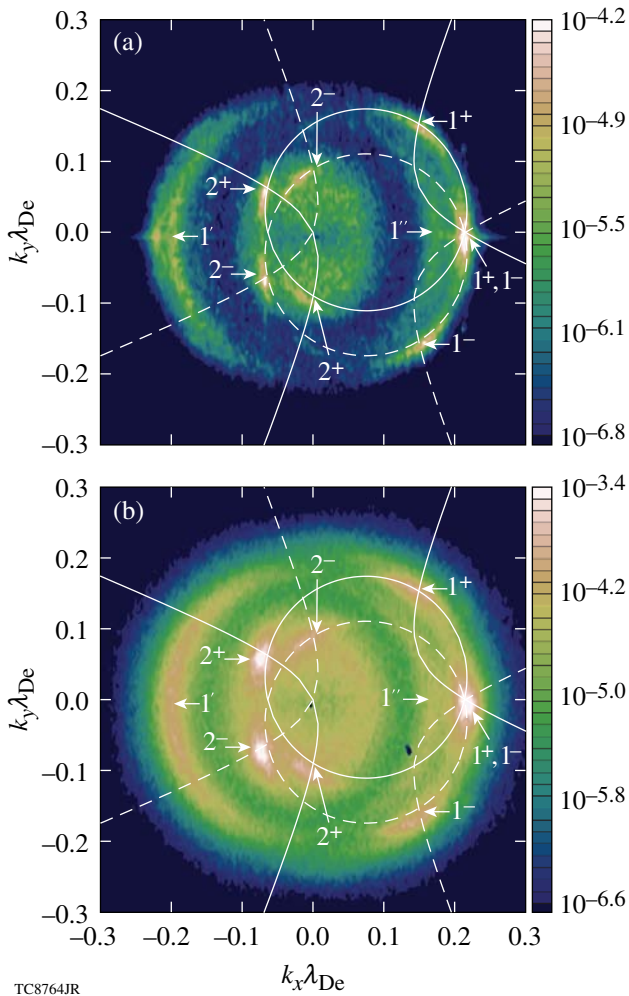


Figure 122.30

The time-averaged LW spectrum W_k is shown for both (a) RPIC and (b) ZAK simulations for the parameters $T_e = 4$ keV and $n_e/n_c = 0.231$. The pump consists of two identical EM plane waves, of intensity $I_0 = 1 \times 10^{15}$ W/cm², propagating obliquely at $\theta = \pm 23^\circ$ with respect to the x axis. Locations 1^+ (1^-) and 2^+ (2^-) denote the blue- and red-shifted LW's produced by the pump laser with angle $\theta = +23^\circ$ (-23°), respectively. The forward-going, blue-shifted LW's from each beam that are on-axis ($k_y = 0$) are degenerate. The waves marked $1'$ and $1''$ are identified as the LW's produced by the first and second LDI steps of the degenerate LW, respectively.

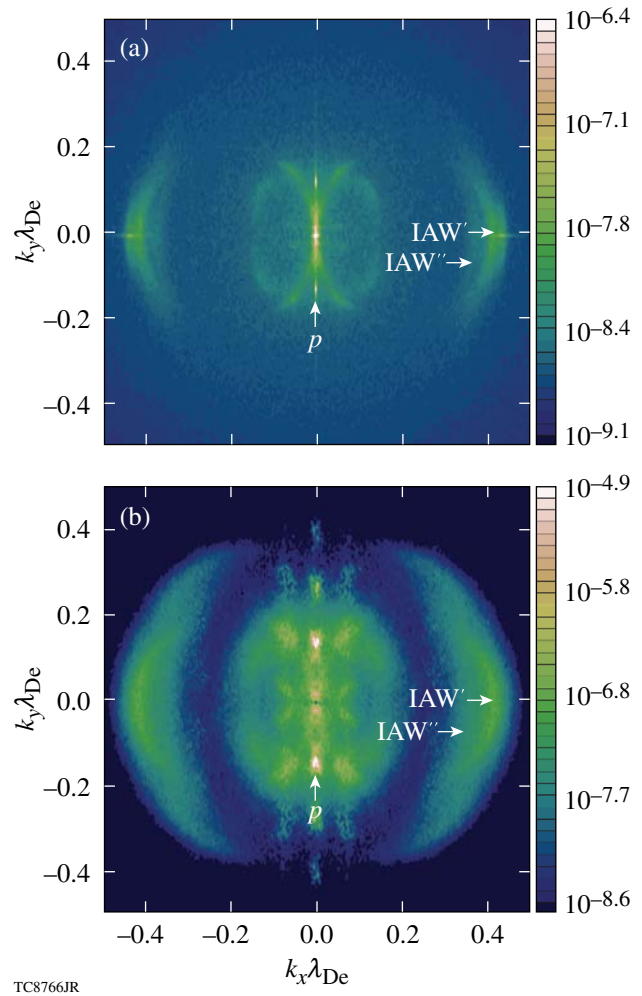


Figure 122.31

The time-averaged IAW spectrum $|\delta N_k|^2$ is shown for (a) RPIC and (b) ZAK simulations with the parameters $T_e = 4$ keV and $n_e/n_c = 0.231$. The pump consists of two EM plane waves, of intensity $I_0 = 1 \times 10^{15}$ W/cm², propagating obliquely with angle $\theta = \pm 23^\circ$ with respect to the x axis. The features labeled IAW' and IAW'' are IAW's generated by the first and second decay steps of the LDI of the common (degenerate) TPD LW. The feature indicated by the label p , with $k_x \lambda_{De} = 0$, is the density response to the ponderomotive force generated by the beating of the two incident plane waves at $k_y \lambda_{De} = \pm 2k_0 \lambda_{De} \sin(23^\circ) \sim \pm 0.123$.

their fluctuation spectra have strikingly similar features. The dominant spectral features occur at precisely the same locations in k space. In Figs. 122.30(a) and 122.30(b), all eight of the single-beam decays ($1^\pm, 2^\pm$) can be seen, with the strongest spectral feature that of the degenerate, blue-shifted LW ($1^+, 1^-$). In addition, two LDI decay steps of the forward-TPD-produced LW's can be seen in both the RPIC and the ZAK calculations [indicated by the labels $1'$ at $\mathbf{k}_{1'}\lambda_{De} \approx (-0.20, 0.0)$ and $1''$ at $\mathbf{k}_{1''}\lambda_{De} \approx (0.16, 0.0)$ (Ref. 22)]. For the RPIC simulation, the LW excitation was computed to be $W = 2.7 \times 10^{-2}$, while the ZAK simulation has a significantly stronger level of LW's, $W = 2.8 \times 10^{-1}$. Figure 122.31 shows the IAW's associated with these two LDI decay steps, $\mathbf{k}_{IAW'}\lambda_{De} \approx (0.43, 0)$ and $\mathbf{k}_{IAW''}\lambda_{De} \approx (0.39, 0)$ (Ref. 22), although the IAW from the second decay is relatively weak and not distinctly evident in the ZAK calculations [Fig. 122.31(b)]. As a measure of the strength of the LDI process, RPIC gives $\mathcal{N}_{LDI} = 6.4 \times 10^{-5}$, whereas ZAK gives $\mathcal{N}_{LDI} = 3.7 \times 10^{-4}$. Again these comparisons of the \mathcal{N}_{LDI} values would indicate that LDI plays a relatively smaller role in the nonlinear saturation in RPIC compared to its role in ZAK. Another feature (p) evident in Fig. 122.31, although unrelated to LDI, are fluctuations at $\mathbf{k}\lambda_{De} \approx (0.0, \pm 0.123)$ caused by the ponderomotive force that results from the beating of the two incident light waves in the transverse direction at $k_y\lambda_{De} = \pm 2k_0\lambda_{De} \sin(23^\circ)$. Other features near $k_x = 0$ are caused by the beating of LW's with equal values of k_x and equal and opposite values of k_y .

The electron distribution computed from discrete simulation particles provides information regarding suprathermal electron generation. The energetic electron tails are often noisy, however, because of insufficient particle numbers. To improve the statistics, the electron distribution was time averaged over 20 ps. To provide information regarding the directionality of energetic electron generation, the (time-averaged) 2-D electron distribution function $f(v_x, v_y)$ was collapsed to 1-D as follows: First, the 2-D distribution f' was computed in a rotated (primed) velocity frame, where the v'_x direction is parallel to the desired probe angle θ_{probe} :

$$f'(v'_x, v'_y) = f(v'_x \cos \theta_{\text{probe}} + v'_y \sin \theta_{\text{probe}} \\ - v'_x \sin \theta_{\text{probe}} + v'_y \cos \theta_{\text{probe}}).$$

The distribution f' was then integrated in the perpendicular v'_y direction, within the limits $\pm 2v_{\text{the}}$, to yield a 1-D velocity distribution,

$$f_{1-D}(v'_x) \equiv \int_{-2v_{\text{the}}}^{2v_{\text{the}}} f'(v'_x, v'_y) dv'_y.$$

Typically, the angle θ_{probe} is chosen so that the v'_x axis aligns with the direction of the LW propagation. With this choice of θ_{probe} , $f_{1-D}(v'_x)$ yields a 1-D velocity distribution, and therefore a hot electron temperature, in the direction of LW propagation.

The time-averaged 1-D electron-distribution function f_{1-D} along the common wave direction [$\theta_{\text{probe}} = 0$, shown in Fig. 122.32(a)] indicates a hot-electron temperature of approximately $3 \times$ the initial background electron temperature $T_{\text{hot}} \sim 3T_{e0}$, where $T_{e0} = 4$ keV. Although the electrons have departed from their initial Maxwellian state, the hot-electron temperature is modest. Since our electron distribution was averaged over 20 ps and the simulation required 15 ps to reach saturation, it is possible that if the simulation were continued longer in time, the electron distribution would continue to evolve toward higher hot-electron temperatures. An often-used simple estimate of hot-electron temperature, based on a single-plane LW, is $T/T_{e0} \sim (v_\phi/v_{\text{the}})^2 = 22$ (Ref. 23). This estimate is in excess of our observed hot-electron temperature by a factor of about 7.4, although $v_\phi^2/v_{\text{the}}^2 = 22$ is exactly the place where the distribution function begins to deviate from a Maxwellian [indicated by the arrows in Fig. 122.32]. The probe direction $\theta_{\text{probe}} = 180^\circ$ [see Fig. 122.32(b)] gives a measure of hot-electron generation by the LDI-produced LW, with $T_{\text{hot}}/T_{e0} \sim 3$. Hot-electron temperatures along the other principal directions of $\theta_{\text{probe}} = \pm 23^\circ$ (directions of the non-degenerate forward blue-shifted plasmons; results not shown) also indicate $T_{\text{hot}}/T_{e0} \sim 3$. In this particular case, the hot-electron temperature does not appear to be significantly directional.

One observation to be drawn from the single-beam and overlapping-beam simulations shown above is that while the single-beam and the overlapped intensities are identical ($\Sigma I_0 = 2 \times 10^{15}$ W/cm²), the peak value of the LW spectrum for the overlapping-beams case (Fig. 122.30) is greater than that for the single-beam case (Fig. 122.27), while for the RPIC runs, the integrated spectrum is actually weaker: $W = 1.0 \times 10^{-1}$ for the single-beam case (Figs. 122.26–122.28) while $W = 2.7 \times 10^{-2}$ for the overlapping-beam case (Figs. 122.29–122.32). This is understandable if one considers the single-beam case with $I_0 = 2 \times 10^{15}$ W/cm² (Figs. 122.26–122.28) as two perfectly coincident beams, each with an intensity of 1×10^{15} W/cm². Consequently, each one of the four TPD-produced LW's has a corresponding overlapped LW. In the case of two beams propagating at angles $\theta = \pm 23^\circ$ (Figs. 122.29–122.32), only one

TPD-produced LW has a corresponding overlapped LW (location 1^\pm shown in Fig. 122.29). The fact that the peak intensity is higher is evidence that overlapping LW's enhance the TPD instability by allowing for nonlinear interaction between the crossing laser beams.

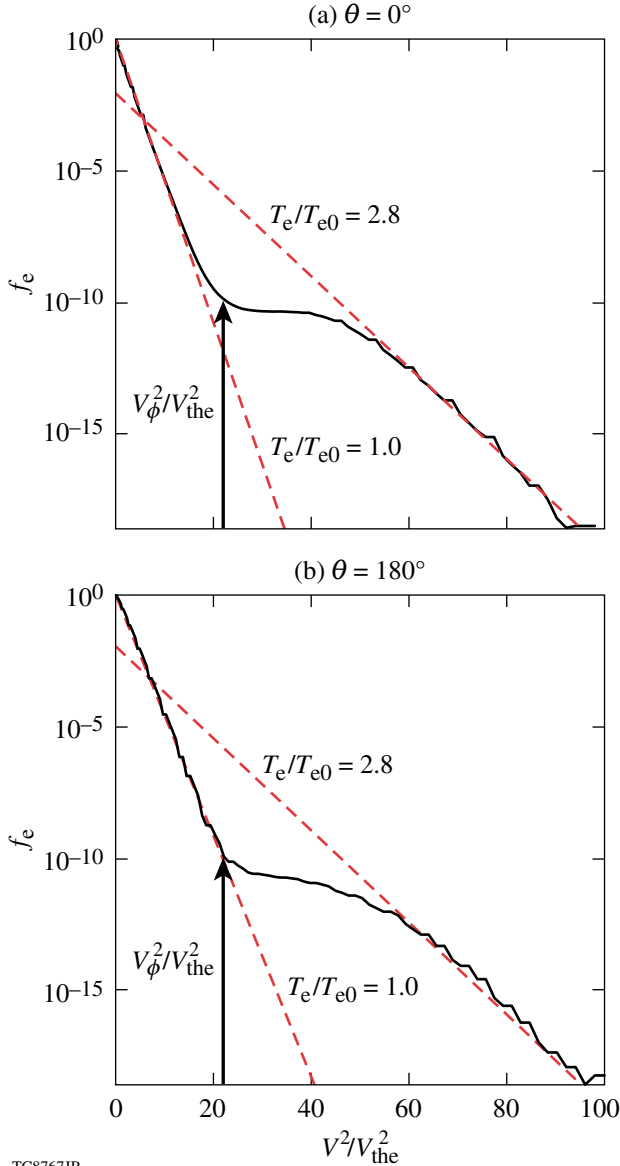


Figure 122.32 The 1-D time-averaged electron distribution shown along two directions ($\theta = 0^\circ, 180^\circ$) for two obliquely incident EM plane waves (at angles $\pm 23^\circ$ with respect to the x axis) with individual intensities of $I_0 = 1 \times 10^{15}$ W/cm² and parameters $T_{e0} = 4$ keV, $n_{e0}/n_c = 0.231$. The angle $\theta = 0^\circ$ (a) corresponds to the direction of the common LW, while the angle $\theta = 180^\circ$ (b) corresponds to the LDI LW direction of the common wave. The arrows indicate the value of v^2/v_{the}^2 corresponding to the phase velocity of the common wave.

In the final simulation set, the electron temperature was reduced to $T_{e0} = 2$ keV, which is typical of current OMEGA implosion experiments.¹ For this electron temperature and beam angle $\theta_\pm = \pm 23^\circ$, Eq. (C8) gives an electron density $n_{e0}/n_c = 0.241$, at which the simulations were performed. This was done to involve the shared plasma wave since it is believed to be important experimentally.¹ The laser geometry and intensity ($I_0 = 1 \times 10^{15}$ W/cm² for each beam) are identical to those corresponding to the previous case in Figs. 122.29–122.32. The individual beam intensity of 1×10^{15} W/cm² corresponds to a linear (amplitude) growth rate $\gamma_{TPD}/\omega_{pe0} \approx 4.3 \times 10^{-3}$, which is 83× above the single-beam collisional threshold (the collisional frequency ν_{e0}/ω_{pe0} is taken to be $\sim 4.7 \times 10^{-4}$). This final case is therefore more strongly driven than the second case, which was 50× the collisional threshold. The linear TPD wave geometry is illustrated in Fig. 122.33, the labels having the same meaning as in previous figures. The common LW now occurs at $\mathbf{k}\lambda_{De} \approx (0.16, 0.0)$ and corresponds to a phase velocity $v_\phi/v_{the} \approx 6.5$.

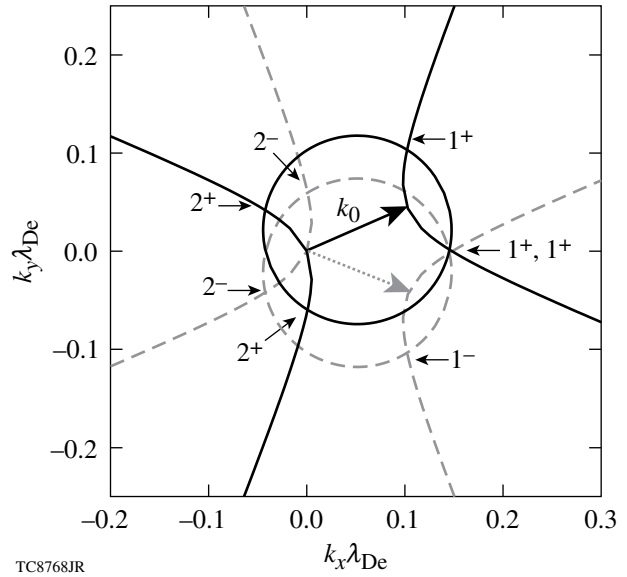


Figure 122.33 Decay diagram for the TPD instability of two EM plane-wave pump beams propagating with angles $\theta = \pm 23^\circ$ relative to the x direction in a plasma with $T_e = 2$ keV and $n_e/n_c = 0.241$. The solid (dashed) curves correspond to the individual decays of the beam with incident angle of $\theta = +23^\circ$ (-23°). The intersections of the circles (which specify frequency and wave-number matching) and the hyperbolae (which are the locations of maximum growth rate) [Eqs. (C1)–(C4)] that are labeled 1 and 2 give the expected location of the blue- and red-shifted TPD LW's, respectively. The on-axis ($k_y\lambda_{De} = 0$) blue-shifted LW's are degenerate.

Figures 122.34 and 122.35 show the normalized LW spectral intensity W_k and the IAW density spectra $|\delta N_k|^2$, respectively, time averaged over 20 ps. The RPIC and ZAK results bear

similar qualitative behavior to the $T_e = 4$ keV case when the reduction of $k\lambda_{De}$ is taken into account. Both the LW and IAW spectral features in the RPIC simulations are significantly nar-

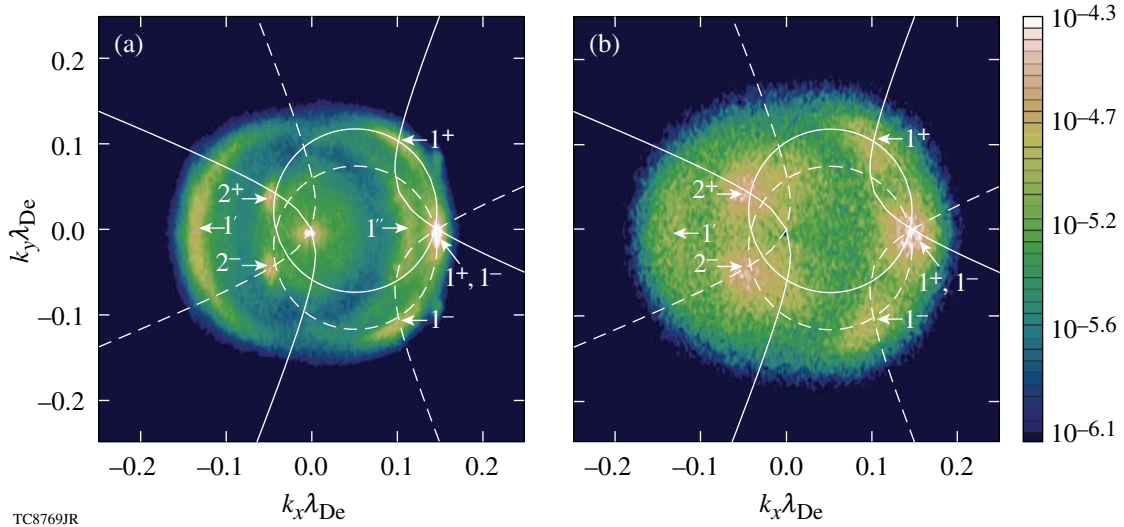


Figure 122.34 The time-averaged LW spectrum W_k is shown for (a) RPIC and (b) ZAK simulations for the parameters $T_e = 2$ keV and $n_e/n_c = 0.241$. The pump consists of two plane EM waves propagating at angles $\theta = \pm 23^\circ$ with respect to the x axis. Each pump laser beam has an intensity of $I_0 = 1 \times 10^{15}$ W/cm². The labels 1^+ (1^-) identify the forward-propagating, blue-shifted LW's resulting from the primary decay of the beam with angle $\theta = +23^\circ$ (-23°), while the labels 2^+ (2^-) mark the corresponding backward-propagating, red-shifted LW's. The degenerate LW is seen to dominate both the (a) RPIC and (b) ZAK spectra. The features marked $1'$ and $1''$ are identified as the first and second decay steps of the LDI of the shared LW. The second step is not seen in the ZAK calculations (b).

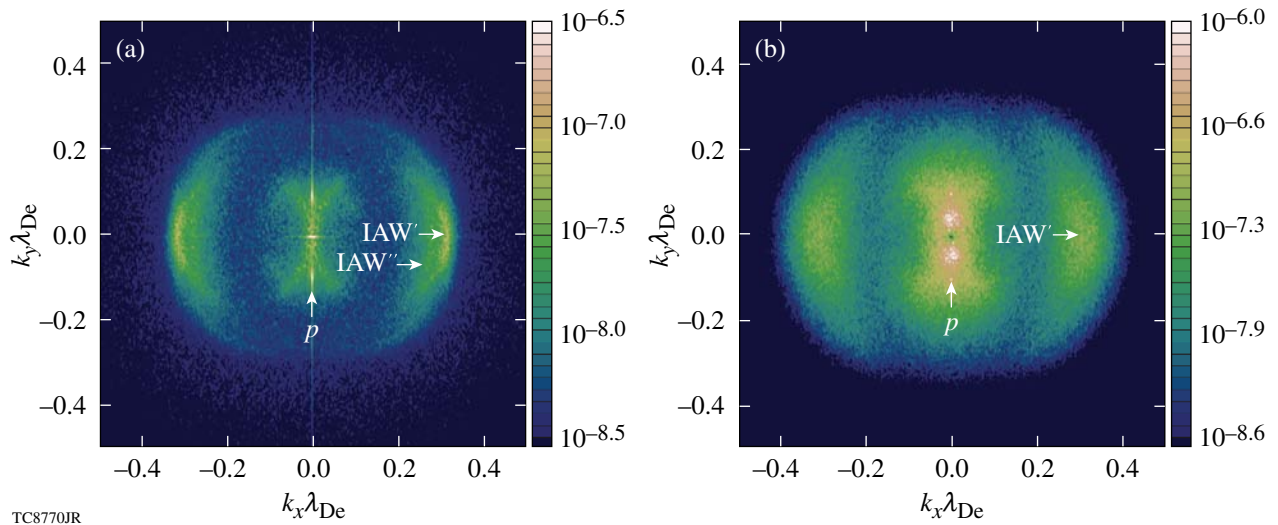


Figure 122.35 The time-averaged IAW spectrum $|\delta N_k|^2$ is shown for (a) RPIC and (b) ZAK simulations for the case with parameters $T_e = 2$ keV and $n_e/n_c = 0.241$. The pump consists of two plane EM waves propagating with angles $\theta = \pm 23^\circ$ with respect to the x axis, each with an intensity of $I_0 = 1 \times 10^{15}$ W/cm². The features labeled IAW' and IAW'' are IAW's generated by the first and second decay steps of the LDI of the common (degenerate) TPD LW. The second step is seen only in the RPIC calculation (a). The feature indicated by the label p , with $k_x\lambda_{De} = 0$, is the density response to the ponderomotive force generated by the beating of the two incident plane waves at $k_y\lambda_{De} = \pm 2k_0\lambda_{De} \sin(23^\circ) \sim \pm 0.09$.

rower and weaker than those of the ZAK simulations (RPIC: $W = 4.5 \times 10^{-2}$, ZAK: $W = 8.6 \times 10^{-2}$; for the LDI process, RPIC: $\mathcal{N} = 1.9 \times 10^{-4}$, ZAK: $\mathcal{N}_{\text{LDI}} = 4.3 \times 10^{-4}$). The RPIC LW spectrum [Fig. 122.34(a)] contains evidence of two LDI decay steps of the common LW: the primary LDI step, marked with the label 1', at $\mathbf{k}_1 \lambda_{\text{De}} \approx (-0.13, 0.0)$ and a second LDI step, marked 1'' at $\mathbf{k}_1 \lambda_{\text{De}} \approx (0.09, 0.0)$ (Ref. 22). The RPIC IAW spectrum [Fig. 122.35(a)] also shows the IAW's corresponding to these two LDI decay steps [$\mathbf{k}_{\text{IAW}} \lambda_{\text{De}} \approx (0.29, 0.0)$ and [$\mathbf{k}_{\text{IAW}} \lambda_{\text{De}} \approx (0.25, 0.0)$ (Ref. 22)], although the IAW from the second decay is relatively weak. Only one LDI step is clearly evident in the ZAK calculations [Figs. 122.34(b) and 122.35(b)]. The distinctive fluctuations in the IAW spectrum $|\delta N_k|^2$ at $\mathbf{k} \lambda_{\text{De}} \approx (0.0, \pm 0.09)$ are again due to ponderomotive force generated by the beating of the two obliquely propagating incident light waves. Although not shown, the difference between the two calculations can be reduced by comparing the ZAK spectra with those of RPIC carried out at a higher intensity. Results (not shown) indicate that the LW and IAW spectra in RPIC simulations broaden significantly. This observation is consistent with past experience.^{11,24}

The time-averaged (over 20 ps), 1-D electron-distribution function along the common-wave direction ($\theta_{\text{probe}} = 0$), shown in Fig. 122.36(a), gives $T_{\text{hot}}/T_{e0} \sim 14$. Again, the simple estimate of hot-electron temperature is $T_{\text{hot}}/T_{e0} \sim (v_\phi/v_{\text{the}})^2 = 42$ (Ref. 23). This estimate is in excess of the observed hot-electron temperature by a factor of ~ 3 . The simple estimate $T_{\text{hot}}/T_{e0} = (v_\phi/v_{\text{the}})^2$, based on a single-plane LW, is not accurate here because the LW spectrum contains a broad and complex spectrum of waves. The phase velocity of the common wave is, however, close to the position where the distribution function first begins to deviate from the initial Maxwellian (shown by the arrows in Fig. 122.36). The hot-electron temperature in the LDI direction of the common LW wave ($\theta_{\text{probe}} = 180^\circ$), shown in Fig. 122.36(b), is cooler with $T_{\text{hot}}/T_{e0} \sim 10$ most likely because the LDI-produced LW's are not as strong as the primary LW. The phase velocities of the primary and LDI LW's differ only slightly. The hot-electron temperatures along the other principal directions $\theta_{\text{probe}} = \pm 23^\circ$ (results not shown) were also determined to be $T_{\text{hot}}/T_{e0} \sim 10$. The hot-electron temperatures for the $T_{e0} = 2$ keV case are significantly higher than that for the $T_{e0} = 4$ keV case. The intensities of the degenerate LW's for the two temperature cases do not differ significantly. The TPD-produced LW's for an electron temperature of $T_{e0} = 2$ keV occur at lower values of $k\lambda_{\text{De}}$ and therefore have greater phase velocities since

$$v_\phi/v_{\text{the}} = \left[1 + (3/2)(k\lambda_{\text{De}})^2 \right] / (k\lambda_{\text{De}}).$$

Waves with greater phase velocity may lead to higher hot-electron temperatures, even though T_{hot} is not seen to scale as strongly as $(v_\phi/v_{\text{the}})^2$, as might be suggested by the simple, single-plane-LW estimate.

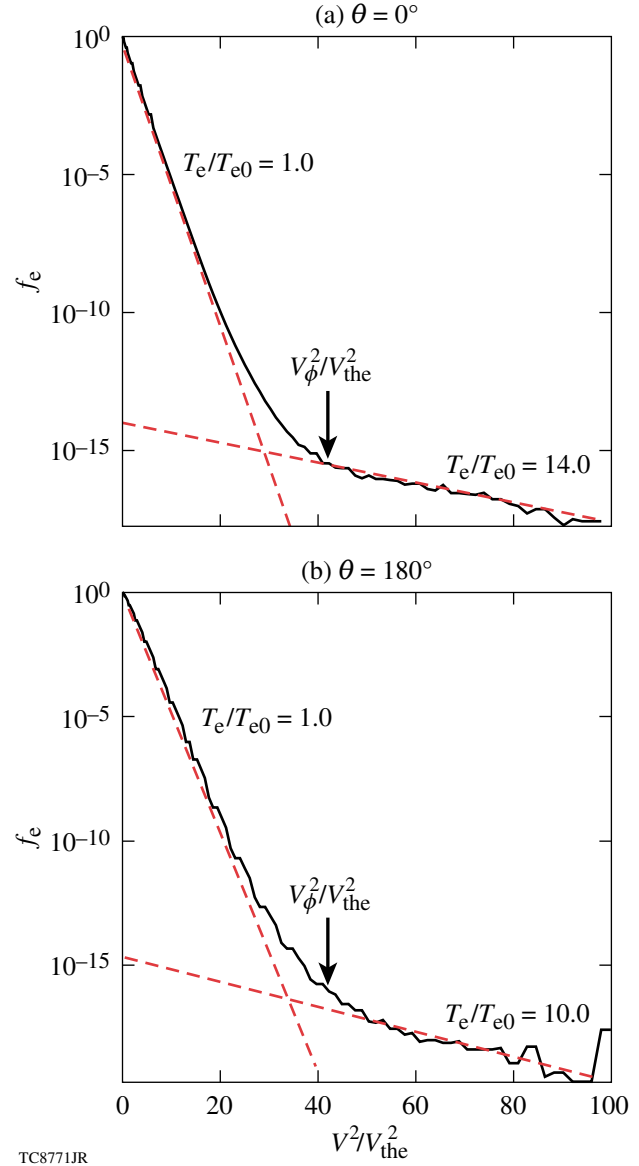


Figure 122.36

The 1-D, time-averaged electron distribution shown along two directions [$\theta = 0^\circ$ (top panel) and $\theta = 180^\circ$ (bottom panel)] for the case of two EM plane waves, each of intensity $I_0 = 1 \times 10^{15}$ W/cm², that are incident at angles of $\theta = \pm 23^\circ$ on a plasma with $T_e = 2$ keV and $n_e/n_c = 0.241$. The temperature in the direction $\theta = 0^\circ$ ($T_{\text{hot}}/T_{e0} = 14$), as determined by the fit shown by the red dashed curves, is greater than that in the direction $\theta = 180^\circ$ ($T_{\text{hot}}/T_{e0} = 10$). The arrows indicate the value of v^2/v_{the}^2 corresponding to the phase velocity of the common LW.

Summary and Conclusions

The purpose of this article has been to present the RPIC model for TPD and to establish it as a useful and reliable model for simulating the nonlinear development of TPD. The simulations were performed in homogeneous plasmas to facilitate comparisons with linear theory. Given the encouraging results in homogeneous plasma, the next step in the development of the RPIC TPD model will be to introduce experimentally relevant density gradients and flow velocities.

The RPIC model and the Zakharov limit were compared for three separate cases. In all three cases, shown in **Simulation Results** (p. 92), the level of LW turbulence excited by TPD was lower in RPIC than in ZAK, although both models displayed qualitatively similar k -space fluctuation spectra. Therefore, kinetic effects—primarily hot-electron generation—are likely a competing saturation mechanism together with LDI. This is consistent with the results of several previous works.^{11,24} Further research is required to determine the relative importance of LDI and hot-electron generation when they act simultaneously.

Two of the three cases investigated TPD excited by crossing laser beams. These simulations show that at a certain density, for a given angle between the beams, the beams can share a common primary LW, thereby enhancing the TPD instability (in an inhomogeneous plasma such a density can always be found, but here it was chosen by design). The saturation of the crossed-beam TPD instability by LDI and modification of the electron-distribution function is also apparent. The heated-electron-distribution function was observed to deviate from the initial Maxwellian at a velocity corresponding to the phase velocity of the common LW. Crossed-beam irradiation also introduced a nonzero ponderomotive force in the electron equation of motion from the transverse electric field. The effects of this term were observed in the perturbed density spectra. A strong feature in the low-frequency density fluctuation spectrum also resulted from the ponderomotive beating of two LW's sharing the same parallel wave number (with respect to the laser direction) but with equal and opposite perpendicular wave numbers.¹⁴ This feature was also evident in our previous ZAK simulations but never noted, which would imply that density channels are produced parallel to the laser direction. Whether this survives in an inhomogeneous plasma remains to be studied.

The semi-quantitative agreement of RPIC modeling and ZAK modeling, for the few survey cases presented here, highlights the similarities and differences between the kinetic RPIC model and its limiting (fluid) form. In this way, the RPIC

modeling provides a bridge to systematically improve upon ZAK modeling. This is desirable because fluid-type codes are much more efficient than PIC codes and can therefore include more of the essential experimental realities (e.g., three spatial dimensions and speckled laser beams). Of particular interest is the possibility, currently under investigation, that the discrepancy between the two models might be recoverable by including modifications of the electron-distribution function in the quasi-linear approximation.¹¹ If possible, this would have the benefit of greatly reduced computational expense, allowing for more-realistic simulations to be made, for example, in three spatial dimensions. The resulting modified electron energy distributions are expected to be strongly dependent on the boundary conditions used for electrons entering and leaving the simulation box (this is consistent with conclusions in Sanbonmatsu *et al.*¹¹). Indeed, the present calculations should not be regarded as predicting experimental hot-electron spectra since it has been argued that the recirculation of hot electrons through the TPD-active region must be accounted for by any physically realistic model of hot-electron generation in spherical implosions.²⁰

Finally, the currents generating experimentally observable EM signatures of TPD (the secondary radiation emissions at $\omega_0/2$ and $3\omega_0/2$), which typically involve a tiny fraction of the LW and IAW energy, can be calculated by postprocessing the high-frequency electric-field envelopes and the low-frequency electron-density fluctuations generated in either the RPIC or the ZAK modeling. This technique is exactly the same as used in Refs. 9 and 17 for the ZAK modeling. This is another advantage of the RPIC modeling, which uses the same envelope representations as ZAK, over standard PIC methods. With this procedure future studies of the correlation of hot-electron effects with $\omega_0/2$ radiation may be possible.

ACKNOWLEDGMENT

We are pleased to acknowledge useful discussions with Drs. A. V. Maximov, W. Seka, R. W. Short, and B. Langdon.

This research was supported by (1) the U.S. Department of Energy, Office of Inertial Confinement Fusion under Cooperative Agreement No. DE-FC52-08NA28302, the University of Rochester, and the New York State Energy Research and Development Authority and (2) the National Nuclear Security Agency through its High-Energy-Density Laboratory Plasmas Grant No. DE-FG52-09NA29545. The support of DOE does not constitute an endorsement by DOE of the views expressed in this article.

Appendix A: Derivation of the RPIC Equations

In this Appendix, a derivation of the RPIC model is presented. One notable difference between standard PIC methods and RPIC is the explicit removal of the laser time scale from

RPIC equations of motion. As a result of removing the laser time scale, it is essential that RPIC equations of motion are expressed in an oscillating, non-inertial frame. There are three major components of the RPIC derivation: the electron equation of state (closure for our RPIC model), the nonlinear Schrödinger equation (EM propagation and pump depletion model), and the reduced-description particle equations of motion.

1. Electron Equation of State

Assume that the velocity $\tilde{\mathbf{U}}$, electrostatic potential ϕ , and pressure p are of the following form:

$$\tilde{\mathbf{U}} = \tilde{\mathbf{U}}_S + \frac{1}{2} [\tilde{\mathbf{U}}_F \exp(-i\omega_{\text{LW}}t) + \text{c.c.}].$$

$$\phi = \phi_S + \frac{1}{2} [\phi_F \exp(-i\omega_{\text{LW}}t) + \text{c.c.}],$$

$$p \approx p_S.$$

Substituting the above expression for $\tilde{\mathbf{U}}$ into Eq. (18), keeping only terms of frequencies $\omega = 0, \pm\omega_{\text{LW}}, \pm(\omega_0 - \omega_{\text{LW}}), \pm(\omega_0 - 2\omega_{\text{LW}})$, the individual terms in Eq. (18) are approximated as

$$\frac{\partial \tilde{\mathbf{U}}}{\partial t} \approx -\frac{\omega_{\text{LW}}}{2} [i\tilde{\mathbf{U}}_F \exp(-i\omega_{\text{LW}}t) + \text{c.c.}], \quad (\text{A1})$$

$$\tilde{\mathbf{U}} \cdot \tilde{\nabla} \tilde{\mathbf{U}} \approx \frac{1}{4} \tilde{\nabla} (\tilde{\mathbf{U}}_F \cdot \tilde{\mathbf{U}}_F^*) - \frac{1}{4} (\tilde{\mathbf{U}}_F \times \tilde{\nabla} \times \tilde{\mathbf{U}}_F^* + \text{c.c.}), \quad (\text{A2})$$

$$\mathbf{A} \cdot \mathbf{A} \approx \frac{1}{2} \mathbf{a}_0 \cdot \mathbf{a}_0^*, \quad (\text{A3})$$

$$\tilde{\mathbf{U}} \cdot \mathbf{A} \approx \frac{1}{4} \left\{ \tilde{\mathbf{U}}_F^* \cdot \mathbf{a}_0 \exp[-i(\omega_0 - \omega_{\text{LW}})t] + \text{c.c.} \right\}, \quad (\text{A4})$$

$$\mathbf{A} \times \tilde{\nabla} \times \tilde{\mathbf{U}}$$

$$\approx \frac{1}{4} \left\{ \mathbf{a}_0 \times \tilde{\nabla} \times \tilde{\mathbf{U}}_F^* \exp[-i(\omega_0 - \omega_{\text{LW}})t] + \text{c.c.} \right\}, \quad (\text{A5})$$

$$\mathbf{A} \cdot \tilde{\nabla} \tilde{\mathbf{U}}$$

$$\approx \frac{1}{4} \left\{ \mathbf{a}_0 \cdot \tilde{\nabla} \tilde{\mathbf{U}}_F^* \exp[-i(\omega_0 - \omega_{\text{LW}})t] + \text{c.c.} \right\}, \quad (\text{A6})$$

where it has been assumed that $|\partial \tilde{\mathbf{U}}_F / \partial t| \ll \omega_{\text{LW}} |\tilde{\mathbf{U}}_F|$ and $|\mathbf{U}_S| \ll |\mathbf{U}_F|$. Substituting these approximations in Eqs. (A1)–(A6) into Eq. (18), neglecting the second-order convective term $\tilde{\mathbf{U}} \cdot \tilde{\nabla} \tilde{\mathbf{U}}$, and collecting terms of similar frequencies, one obtains

$$\begin{aligned} \tilde{\mathbf{U}}_F = & \frac{q}{im\omega_{\text{LW}}} \tilde{\nabla} \left[\phi_F - \frac{1}{2c} \tilde{\mathbf{U}}_F^* \cdot \mathbf{a}_0 \exp(-i\Delta\omega t) \right] \\ & + \frac{q \exp(-i\Delta\omega t)}{2imc\omega_{\text{LW}}} (\mathbf{a}_0 \times \tilde{\nabla} \times \tilde{\mathbf{U}}_F^* + \mathbf{a}_0 \cdot \tilde{\nabla} \tilde{\mathbf{U}}_F^*), \end{aligned} \quad (\text{A7})$$

and

$$\begin{aligned} \frac{1}{4} \tilde{\nabla} (\tilde{\mathbf{U}}_F \cdot \tilde{\mathbf{U}}_F^*) = & \frac{1}{4} [\tilde{\mathbf{U}}_F \times \tilde{\nabla} \times \tilde{\mathbf{U}}_F^* + \tilde{\mathbf{U}}_F^* \times \tilde{\nabla} \times \tilde{\mathbf{U}}_F] \\ & - \frac{q}{m} \tilde{\nabla} \phi_S - \frac{\tilde{\nabla} p_S}{n_S m} - \frac{q^2}{4m^2 c^2} \tilde{\nabla} (\mathbf{a}_0 \cdot \mathbf{a}_0^*), \end{aligned} \quad (\text{A8})$$

where $\Delta\omega \equiv \omega_0 - 2\omega_{\text{LW}}$. Setting $q = -e$ and $m = m_e$, Eq. (A7) is solved approximately to give

$$\tilde{\mathbf{U}}_F \approx \frac{e}{im_e \omega_{\text{LW}}} \mathbf{E}_{\text{eff}}, \quad (\text{A9})$$

where \mathbf{E}_{eff} was previously defined in Eq. (28). Substituting Eq. (A9) into Eq. (A8), neglecting the term in the square brackets on the right-hand side (rhs) of Eq. (A8) and integrating the resulting equation, assuming a pressure profile $p_S = n_0 T_{e0} (n_S/n_0)^\gamma$, with γ being the ratio of specific heats (isothermal electrons: $\gamma = 1$; adiabatic electrons: $\gamma = 5/3$), one obtains the electron equation of state, Eq. (26). This provides closure for the RPIC model.

2. Field Equations

The driving current \mathbf{J} resulting from self-consistent electron motion is

$$\begin{aligned}\mathbf{J} &= -en\mathbf{U}, \\ &= -en\left(\tilde{\mathbf{U}} - \frac{q\mathbf{A}}{mc}\right), \\ &= -en\left(\tilde{\mathbf{U}} + \frac{e\mathbf{A}}{m_e c}\right).\end{aligned}$$

The components of \mathbf{J} with frequencies $\pm\omega_0$ and $\pm 2\omega_{\text{LW}}$ (since $\omega_0 \approx 2\omega_{\text{LW}}$ for TPD) are of importance:

$$\begin{aligned}\mathbf{J} &\approx -\frac{1}{2}\left\{\left[\frac{e^2 n_{eS}\mathbf{a}_0}{m_e c} + \frac{en_{eF}\tilde{\mathbf{U}}_F}{2}\exp(i\Delta\omega\tilde{t})\right]\exp(-i\omega_0\tilde{t}) + \text{c.c.}\right\}, \\ \mathbf{J} &\equiv \frac{1}{2}\left[\mathbf{J}_0\exp(-i\omega_0\tilde{t}) + \text{c.c.}\right],\end{aligned}\quad (\text{A10})$$

$$\mathbf{J}_0 = -\left[\frac{e^2 n_{eS}\mathbf{a}_0}{m_e c} + \frac{en_{eF}\tilde{\mathbf{U}}_F}{2}\exp(i\Delta\omega\tilde{t})\right],$$

where $\tilde{\mathbf{U}}_F$ is given in Eq. (A9). On substituting Eq. (A9) into Eq. (A10), an equation for \mathbf{J}_0 is obtained [Eq. (33)], from which the transverse current \mathbf{J}_{0T} can be computed:

$$\mathbf{J}_{0T} \equiv \mathbf{J}_0 + \tilde{\nabla}\chi_0,$$

$$\tilde{\nabla}^2\chi_0 = -\tilde{\nabla}\cdot\mathbf{J}_0,$$

$$-\frac{1}{c^2}\frac{\partial^2\mathbf{A}}{\partial\tilde{t}^2} + \tilde{\nabla}^2\mathbf{A} = -\frac{4\pi}{c}\frac{1}{2}\left[\mathbf{J}_{0T}\exp(-i\omega_0\tilde{t}) + \text{c.c.}\right]. \quad (\text{A11})$$

A substitution of the above expression for \mathbf{J}_T into the second-order wave equation, assuming slowly varying envelopes and separating frequency components, results in a nonlinear Schrödinger equation for the evolution of the incident EM-wave envelope [Eq. (31)].

3. Time-Averaged Single-Particle Equations of Motion

The exact single-particle equation of motion is time averaged to obtain the RPIC single-particle equation of motion. Recall that Eq. (16) is exact and is applicable to both electrons and ions.

The electron particle velocity can be conveniently cast in the form

$$\tilde{\mathbf{u}}_e = \tilde{\mathbf{u}}_{e0} + \tilde{\mathbf{u}}_{eS} + \frac{1}{2}\left[\tilde{\mathbf{u}}_{eF}\exp(-i\omega_{\text{LW}}\tilde{t}) + \text{c.c.}\right], \quad (\text{A12})$$

where $\tilde{\mathbf{u}}_{e0}$ is the initial electron velocity, $\tilde{\mathbf{u}}_{eS}$ the low-frequency velocity perturbation, and $\tilde{\mathbf{u}}_{eF}$ is the high-frequency velocity perturbation. Equation (16) is solved approximately as follows: First, neglecting contributions from the laser pump and assuming $|\partial\tilde{\mathbf{u}}_{eS}/\partial\tilde{t}| \ll \omega_{\text{LW}}|\tilde{\mathbf{u}}_{eF}|$, Eq. (16) yields

$$\begin{aligned}\tilde{\mathbf{u}}_{eF} &\approx -\frac{e}{im_e\omega_{\text{LW}}}\tilde{\nabla}\phi_F, \\ &= \frac{e}{im_e\omega_{\text{LW}}}\mathbf{E}_F.\end{aligned}$$

Then, substituting the above approximate expression for $\tilde{\mathbf{u}}_{eF}$ into Eqs. (A12) and (16) and keeping only electron responses at the ion-acoustic and Langmuir time scales, i.e., $\omega \sim 0, \pm\omega_{\text{LW}}, \pm(\omega_0 - \omega_{\text{LW}})$, Eq. (19) is obtained, the electron reduced-description equation of motion in the oscillating frame.

Specifying these results to 2-D, assuming polarization in the y direction and a fixed pump wave $a_0 = a_{00}\exp(ik_0x)$, Eq. (19) further reduces to give

$$\begin{aligned}m_e\frac{d\tilde{\mathbf{u}}_e}{d\tilde{t}} &\approx -e\mathbf{E} - \frac{e^2}{4m_e c^2}\tilde{\nabla}\left|\mathbf{a}_0\right|^2 \\ &+ \hat{\mathbf{x}}\frac{e^2 k_0}{4cm_e\omega_{\text{LW}}}\left\{\mathbf{a}_0 \cdot \mathbf{E}_F^* \exp[-i(\omega_0 - \omega_{\text{LW}})\tilde{t}] + \text{c.c.}\right\}.\end{aligned}\quad (\text{A13})$$

The ion-particle equations of motion follow similarly to yield Eq. (21).

Appendix B: Derivation of the Zakharov Equations from RPIC

In this Appendix, it will be shown how the Zakharov equations may be obtained from the RPIC model under certain approximations. This connection ensures that the RPIC

equations have the correct limiting form (since the Zakharov equations may also be shown to be a consequence of the Vlasov equations on which the RPIC model is based), and that the Zakharov and RPIC models predict the same physical behavior in the linear regime.

It is noted that while the RPIC equations are more conveniently written in the oscillating frame, the Zakharov equations are customarily written in the laboratory frame of reference. To begin, Eq. (19) is transformed back into the laboratory frame of reference:

$$\begin{aligned}
m_e \frac{d\tilde{\mathbf{u}}_e}{dt} &\approx -e\mathbf{E} - \frac{e^2}{4m_e c^2} \nabla |\mathbf{a}_0|^2 \\
&- \frac{e^2}{4cm_e \omega_{LW}} \left[i\nabla (\mathbf{E}_F^* \cdot \mathbf{a}_0) \exp(-i\Delta\omega t) \exp(-i\omega_{LW}t) + \text{c.c.} \right] \\
&- \frac{e^2}{4cm_e \omega_{LW}} \left[-i(\mathbf{a}_0 \cdot \nabla) \mathbf{E}_F^* \exp(-i\Delta\omega t) \right. \\
&\times \exp(-i\omega_{LW}t) + \text{c.c.} \left. \right], \tag{B1}
\end{aligned}$$

since $\tilde{\nabla} = \tilde{\nabla}$, $\tilde{t} = t$, and $d/d\tilde{t} = d/dt$, as shown previously. Here, \mathbf{E} is the physical electric field reconstituted from the envelope representation

$$\mathbf{E} = \mathbf{E}_s + \frac{1}{2} \left[\mathbf{E}_1 \exp(-i\omega_{LW}t) + \mathbf{E}_2 \exp(-2i\omega_{LW}t) + \text{c.c.} \right]. \tag{B2}$$

Using the definition $\mathbf{u}_e = \tilde{\mathbf{u}}_e + e\mathbf{A}/m_e c$, one obtains from Eq. (B1)

$$\begin{aligned}
\frac{d\mathbf{u}_e}{dt} &= -\frac{e\mathbf{E}}{m_e} - \frac{e^2}{4m_e^2 c^2} \nabla |\mathbf{a}_0|^2 + \frac{e^2}{4m_e^2 c^2} (\mathbf{a}_0^* \cdot \nabla \mathbf{a}_0 + \text{c.c.}) \\
&- \frac{e^2}{4m_e^2 c \omega_{LW}} \left\{ \left[\nabla (\mathbf{E}_F^* \cdot \mathbf{a}_0) - \mathbf{a}_0 \cdot \nabla \mathbf{E}_F^* \right. \right. \\
&- \left. \left. \mathbf{E}_F^* \cdot \nabla \mathbf{a}_0 \right] i \exp[-i(\omega_{LW} + \Delta\omega)t] + \text{c.c.} \right\} \\
&- \frac{e}{m_e} \frac{\omega_0}{2c} \left\{ i\mathbf{a}_0 \exp[-i(2\omega_{LW} + \Delta\omega)t] + \text{c.c.} \right\}.
\end{aligned}$$

Changing to conventional Zakharov nomenclature, $\mathbf{E}_1 \equiv \mathbf{E}_F$ and $\mathbf{E}_2 \equiv i\omega_0 \mathbf{a}_0/c$, the above equation becomes

$$\frac{d\mathbf{u}_e}{dt} = \mathcal{A}, \tag{B3}$$

$$\begin{aligned}
\mathcal{A} &\equiv \mathcal{A}_0 + \frac{1}{2} \left[\mathcal{A}_1 \exp(-i\omega_{LW}t) + \text{c.c.} \right] \\
&+ \frac{1}{2} \left[\mathcal{A}_2 \exp(-2i\omega_{LW}t) + \text{c.c.} \right], \tag{B4}
\end{aligned}$$

$$\begin{aligned}
\mathcal{A}_0 &= -\frac{e\mathbf{E}_s}{m_e} - \frac{e^2}{4m_e^2 \omega_0^2} \nabla |\mathbf{E}_2|^2 \\
&+ \frac{e^2}{4m_e^2 \omega_0^2} (\mathbf{E}_2^* \cdot \nabla \mathbf{E}_2 + \text{c.c.}), \tag{B5}
\end{aligned}$$

$$\begin{aligned}
\mathcal{A}_1 &= -\frac{e\mathbf{E}_1}{2m_e} \\
&- \frac{e^2}{2m_e^2 \omega_0 \omega_{LW}} \left[\nabla (\mathbf{E}_1^* \cdot \mathbf{E}_2) - \mathbf{E}_2 \cdot \nabla \mathbf{E}_1^* \right. \\
&- \left. \mathbf{E}_1^* \cdot \nabla \mathbf{E}_2 \right] \exp(-i\Delta\omega t), \tag{B6}
\end{aligned}$$

$$\mathcal{A}_2 = -\frac{e\mathbf{E}_2}{2m_e} \exp(-i\Delta\omega t), \tag{B7}$$

where $\Delta\omega$ was defined previously [see Eq. (30)]. The Vlasov equation corresponding to the acceleration \mathcal{A} is

$$(\partial_t + \mathbf{v} \cdot \partial_{\mathbf{x}})F + \mathcal{A} \cdot \partial_{\mathbf{v}}F = 0, \tag{B8}$$

where the distribution function F can be written in terms of slowly varying envelopes

$$\begin{aligned}
F(\mathbf{x}, t; \mathbf{v}) &= f_0 + \frac{1}{2} \left[f_1 \exp(-i\omega_{LW}t) + \text{c.c.} \right] \\
&+ \frac{1}{2} \left[f_2 \exp(-2i\omega_{LW}t) + \text{c.c.} \right], \tag{B9}
\end{aligned}$$

$$f_0(\mathbf{x}, t; \mathbf{v}) = f_M(\mathbf{v}) + \delta f_0(\mathbf{x}, t; \mathbf{v}). \quad (\text{B10})$$

Here, $f_M(\mathbf{v})$ is the time-stationary, spatially uniform background Maxwellian distribution. Substituting Eqs. (B4)–(B7) and (B9)–(B10) into Eq. (B8) and separating frequency components, one obtains the coupled equations

$$\begin{aligned} (\partial_t + \mathbf{v} \cdot \partial_{\mathbf{x}}) \delta f_0 &= \frac{e}{m_e} \mathbf{E}_s \cdot \partial_{\mathbf{v}} (f_M + \delta f_0) \\ &+ \frac{e}{4m_e} (\mathbf{E}_1 \cdot \partial_{\mathbf{v}} f_1^* + \text{c.c.}) + \frac{e}{4m_e} (\tilde{\mathbf{E}}_2 \cdot \partial_{\mathbf{v}} f_2^* + \text{c.c.}), \end{aligned} \quad (\text{B11})$$

$$\begin{aligned} (-i\omega_{\text{LW}} + \partial_t + \mathbf{v} \cdot \partial_{\mathbf{x}}) f_1 &= \frac{e}{m_e} (\mathbf{E}_1 + \mathbf{h}_1) \cdot \partial_{\mathbf{v}} (f_M + \delta f_0) \\ &+ \frac{e}{m_e} \mathbf{E}_s \cdot \partial_{\mathbf{v}} f_1 + \frac{e}{2m_e} \tilde{\mathbf{E}}_2 \cdot \partial_{\mathbf{v}} f_1^* + \frac{e}{2m_e} (\mathbf{E}_1^* + \mathbf{h}_1^*) \cdot \partial_{\mathbf{v}} f_2, \end{aligned} \quad (\text{B12})$$

$$\begin{aligned} (-2i\omega_{\text{LW}} + \partial_t + \mathbf{v} \cdot \partial_{\mathbf{x}}) f_2 &= \frac{e}{m_e} \tilde{\mathbf{E}}_2 \cdot \partial_{\mathbf{v}} (f_M + \delta f_0) \\ &+ \frac{e}{2m_e} (\mathbf{E}_1 + \mathbf{h}_1) \cdot \partial_{\mathbf{v}} f_1 + \frac{e}{m_e} \mathbf{E}_s \cdot \partial_{\mathbf{v}} f_2, \end{aligned} \quad (\text{B13})$$

$$\tilde{\mathbf{E}}_2 \equiv \exp(-i\Delta\omega t) \mathbf{E}_2, \quad (\text{B14})$$

$$\begin{aligned} \mathbf{h}_1 &\equiv \frac{e}{2m_e \omega_0 \omega_{\text{LW}}} \left[\nabla (\mathbf{E}_1^* \cdot \tilde{\mathbf{E}}_2) \right. \\ &\left. - \tilde{\mathbf{E}}_2 \cdot \nabla \mathbf{E}_1^* - \mathbf{E}_1^* \cdot \nabla \tilde{\mathbf{E}}_2 \right], \end{aligned} \quad (\text{B15})$$

where terms that are not linear in \mathbf{E}_1 or linear in $\mathbf{E}_2 \cdot \mathbf{E}_1^*$ are neglected since only the linear parametric dispersion is of interest.

Fourier transforming Eqs. (B11)–(B13) in space and time, one obtains

$$\begin{aligned} -i(\omega - \mathbf{k} \cdot \mathbf{v}) \delta f_0(\mathbf{k}, \omega, \mathbf{v}) &= \frac{e}{m_e} \iint d\mathbf{k}' d\omega' \mathbf{E}'_s \cdot \partial_{\mathbf{v}} \delta f_0'' \\ &+ \frac{e}{4m_e} \iint d\mathbf{k}' d\omega' \mathbf{E}'_1 \cdot \partial_{\mathbf{v}} [f_1^*]'' + \text{c.c.} \\ &+ \frac{e}{4m_e} \iint d\mathbf{k}' d\omega' \mathbf{E}'_2 \cdot \partial_{\mathbf{v}} [f_2^*]'' + \text{c.c.}, \end{aligned} \quad (\text{B16})$$

$$\begin{aligned} &-i(\omega_{\text{LW}} + \omega - \mathbf{k} \cdot \mathbf{v}) f_1(\mathbf{k}, \omega, \mathbf{v}) \\ &= \frac{e}{m_e} [\mathbf{E}_1(\mathbf{k}, \omega) + \mathbf{h}_1(\mathbf{k}, \omega)] \cdot \partial_{\mathbf{v}} f_M(\mathbf{v}) \\ &+ \frac{e}{m_e} \iint d\mathbf{k}' d\omega' \mathbf{E}'_s \cdot \partial_{\mathbf{v}} f_1'' \\ &+ \frac{e}{m_e} \iint d\mathbf{k}' d\omega' \mathbf{E}'_1 \cdot \partial_{\mathbf{v}} \delta f_0'' \\ &+ \frac{e}{2m_e} \iint d\mathbf{k}' d\omega' \tilde{\mathbf{E}}'_2 \cdot [\partial_{\mathbf{v}} f_1^*]'' \\ &+ \frac{e}{2m_e} \iint d\mathbf{k}' d\omega' [\mathbf{E}'_1]^* \cdot \partial_{\mathbf{v}} f_2'', \end{aligned} \quad (\text{B17})$$

$$\begin{aligned} -i(2\omega_{\text{LW}} + \omega - \mathbf{k} \cdot \mathbf{v}) f_2(\mathbf{k}, \omega, \mathbf{v}) &= \frac{e}{m_e} \tilde{\mathbf{E}}_2(\mathbf{k}, \omega) \cdot \partial_{\mathbf{v}} f_M(\mathbf{v}) \\ &+ \frac{e}{m_e} \iint d\mathbf{k}' d\omega' \mathbf{E}'_2 \cdot \partial_{\mathbf{v}} \delta f_0'' \\ &+ \frac{e}{2m_e} \iint d\mathbf{k}' d\omega' (\mathbf{E}'_1 + \mathbf{h}'_1) \cdot \partial_{\mathbf{v}} f_1'' \\ &+ \frac{e}{m_e} \iint d\mathbf{k}' d\omega' \mathbf{E}'_s \cdot \partial_{\mathbf{v}} f_2'', \end{aligned} \quad (\text{B18})$$

where

$$\tilde{\mathbf{E}}'_2 \equiv \tilde{\mathbf{E}}_2(\mathbf{k}', \omega'),$$

$$[\tilde{\mathbf{E}}_1^*]^\dagger \equiv [\tilde{\mathbf{E}}_1(-\mathbf{k}', -\omega')]^*,$$

$$f_2'' \equiv f_2(\mathbf{k} - \mathbf{k}', \omega - \omega', \mathbf{v}),$$

$$[f_1^*]'' \equiv [f_1(\mathbf{k} - \mathbf{k}', \omega - \omega', \mathbf{v})]^*.$$

Equations (B16)–(B18) can be solved approximately. First, retaining only first-order terms in the electric fields \mathbf{E}_1 and \mathbf{E}_2 , Eqs. (B16)–(B18) give

$$\delta f_0(\mathbf{k}, \omega, \mathbf{v}) = \frac{e}{m_e} \frac{\mathbf{E}_s(\mathbf{k}, \omega) \cdot \partial_{\mathbf{v}} f_M(\mathbf{v})}{-i(\omega - \mathbf{k} \cdot \mathbf{v})}, \quad (\text{B19})$$

$$f_1(\mathbf{k}, \omega, \mathbf{v}) = \frac{e}{m_e} \frac{\mathbf{E}_1(\mathbf{k}, \omega) \cdot \partial_{\mathbf{v}} f_M(\mathbf{v})}{-i(\omega_{LW} + \omega - \mathbf{k} \cdot \mathbf{v})}, \quad (\text{B20})$$

$$f_2(\mathbf{k}, \omega, \mathbf{v}) = \frac{e}{m_e} \frac{\tilde{\mathbf{E}}_2(\mathbf{k}, \omega) \cdot \partial_{\mathbf{v}} f_M(\mathbf{v})}{-i(2\omega_{LW} + \omega - \mathbf{k} \cdot \mathbf{v})}. \quad (\text{B21})$$

Substituting the above approximate expressions for $\delta f_0(\mathbf{k}, \omega, \mathbf{v})$, $f_1(\mathbf{k}, \omega, \mathbf{v})$, and $f_2(\mathbf{k}, \omega, \mathbf{v})$ into the right-hand side (rhs) of Eq. (B17), one obtains

$$\begin{aligned} f_1(\mathbf{k}, \omega, \mathbf{v}) &= \frac{e}{m_e} \frac{[\mathbf{E}_1(\mathbf{k}, \omega) + \mathbf{h}_1(\mathbf{k}, \omega)] \cdot \partial_{\mathbf{v}} f_0(\mathbf{v})}{-i(\omega_{LW} + \omega - \mathbf{k} \cdot \mathbf{v})} \\ &- \frac{e^2}{m_e} \frac{1}{(\omega_{LW} + \omega - \mathbf{k} \cdot \mathbf{v})} \\ &\times \iint d\mathbf{k}' d\omega' \mathbf{E}_s(\mathbf{k}', \omega') \cdot \partial_{\mathbf{v}} \left[\frac{\mathbf{E}_1(\mathbf{k}' - \mathbf{k}, \omega' - \omega) \cdot \partial_{\mathbf{v}} f_M}{[\omega_{LW} + \omega' - \omega - (\mathbf{k}' - \mathbf{k}) \cdot \mathbf{v}]} \right] \\ &- \frac{e^2}{2m_e^2} \frac{1}{(\omega_{LW} + \omega - \mathbf{k} \cdot \mathbf{v})} \\ &\times \iint d\mathbf{k}' d\omega' \mathbf{E}_1(\mathbf{k}', \omega') \cdot \partial_{\mathbf{v}} \left[\frac{\mathbf{E}_s(\mathbf{k}' - \mathbf{k}, \omega' - \omega) \cdot \partial_{\mathbf{v}} f_M}{[\omega' - \omega - (\mathbf{k}' - \mathbf{k}) \cdot \mathbf{v}]} \right] \\ &+ \frac{e^2}{2m_e^2} \frac{1}{(\omega_{LW} + \omega - \mathbf{k} \cdot \mathbf{v})} \\ &\times \iint d\mathbf{k}' d\omega' \tilde{\mathbf{E}}_2(\mathbf{k}', \omega') \cdot \partial_{\mathbf{v}} \left[\frac{\mathbf{E}_1^*(\mathbf{k}' - \mathbf{k}, \omega' - \omega) \cdot \partial_{\mathbf{v}} f_M}{[\omega_{LW} + \omega' - \omega - (\mathbf{k}' - \mathbf{k}) \cdot \mathbf{v}]} \right] \\ &- \frac{e^2}{2m_e^2} \frac{1}{(\omega_{LW} + \omega - \mathbf{k} \cdot \mathbf{v})} \\ &\times \iint d\mathbf{k}' d\omega' \mathbf{E}_1^*(-\mathbf{k}', -\omega') \\ &\cdot \partial_{\mathbf{v}} \left[\frac{\tilde{\mathbf{E}}_2(\mathbf{k} - \mathbf{k}', \omega - \omega') \cdot \partial_{\mathbf{v}} f_M}{[2\omega_{LW} + \omega - \omega' - (\mathbf{k} - \mathbf{k}') \cdot \mathbf{v}]} \right]. \end{aligned} \quad (\text{B22})$$

In order to solve Eq. (B22), $\mathbf{E}_1(\mathbf{k}, \omega)$ must first be computed. The Poisson equation, in conjunction with the continuity equation and the gauge condition $\nabla \cdot \mathbf{A} = 0$, gives

$$\mathbf{k} \cdot \mathbf{E}_1(\mathbf{k}, \omega) = \frac{4\pi \mathbf{k} \cdot \mathbf{J}_1(\mathbf{k}, \omega)}{i\omega_{LW}}, \quad (\text{B23})$$

$$\mathbf{J}_1(\mathbf{k}, \omega) = -e \int d^3 \mathbf{v} \mathbf{v} f_1(\mathbf{k}, \omega, \mathbf{v}), \quad (\text{B24})$$

where, consistent with the envelope approximation, $|\omega| \ll \omega_{LW}$.

Substituting Eq. (B22) into Eq. (B24) leads to

$$\mathbf{J}_1 = \mathbf{J}_1^0 + \delta \mathbf{J}_1^0 + \delta \mathbf{J}_1^1 + \delta \mathbf{J}_1^2, \quad (\text{B25})$$

$$\mathbf{J}_1^0 = \frac{e^2}{m_e} \int d^3 \mathbf{v} \left[\frac{\mathbf{v} \mathbf{E}_1(\mathbf{k}, \omega) \cdot \partial_{\mathbf{v}} f_0}{i(\omega_{LW} + \omega - \mathbf{k} \cdot \mathbf{v})} \right], \quad (\text{B26})$$

$$\begin{aligned} \delta \mathbf{J}_1^0 &= \frac{e^2}{m_e} \int d^3 \mathbf{v} \left[\frac{\mathbf{v} \mathbf{h}_1(\mathbf{k}, \omega) \cdot \partial_{\mathbf{v}} f_0}{i(\omega_{LW} + \omega - \mathbf{k} \cdot \mathbf{v})} \right] \\ &+ \frac{e^3}{m_e^2} \int d\mathbf{k}' \int d\omega' \int d^3 \mathbf{v} \frac{\mathbf{v} \mathbf{E}_s(\mathbf{k}', \omega')}{(\omega_{LW} + \omega - \mathbf{k} \cdot \mathbf{v})} \\ &\cdot \partial_{\mathbf{v}} \left[\frac{\mathbf{E}_1(\mathbf{k}' - \mathbf{k}, \omega' - \omega) \cdot \partial_{\mathbf{v}} f_M}{[\omega_{LW} + \omega' - \omega - (\mathbf{k}' - \mathbf{k}) \cdot \mathbf{v}]} \right] \\ &+ \frac{e^3}{m_e^2} \int d\mathbf{k}' \int d\omega' \int d^3 \mathbf{v} \frac{\mathbf{v} \mathbf{E}_1(\mathbf{k}', \omega')}{(\omega_{LW} + \omega - \mathbf{k} \cdot \mathbf{v})} \\ &\cdot \partial_{\mathbf{v}} \left[\frac{\mathbf{E}_s(\mathbf{k}' - \mathbf{k}, \omega' - \omega) \cdot \partial_{\mathbf{v}} f_M}{[\omega' - \omega - (\mathbf{k}' - \mathbf{k}) \cdot \mathbf{v}]} \right], \end{aligned} \quad (\text{B27})$$

$$\begin{aligned} \delta \mathbf{J}_1^1 &= -\frac{e^3}{2m_e^2} \int d\mathbf{k}' \int d\omega' \int d^3 \mathbf{v} \frac{\mathbf{v} \tilde{\mathbf{E}}_2(\mathbf{k}', \omega')}{(\omega_{LW} + \omega - \mathbf{k} \cdot \mathbf{v})} \\ &\cdot \partial_{\mathbf{v}} \left[\frac{\mathbf{E}_1^*(\mathbf{k}' - \mathbf{k}, \omega' - \omega) \cdot \partial_{\mathbf{v}} f_0}{[\omega_{LW} + \omega' - \omega - (\mathbf{k}' - \mathbf{k}) \cdot \mathbf{v}]} \right], \end{aligned} \quad (\text{B28})$$

$$\delta \mathbf{J}_1^2 = \frac{e^3}{2m_e^2} \int d\mathbf{k}' \int d\omega' \int d^3\mathbf{v} \frac{\mathbf{v} \mathbf{E}_1^*(-\mathbf{k}', -\omega')}{(\omega_{\text{LW}} + \omega - \mathbf{k} \cdot \mathbf{v})} \cdot \partial_{\mathbf{v}} \left[\frac{\tilde{\mathbf{E}}_2(\mathbf{k} - \mathbf{k}', \omega - \omega') \cdot \partial_{\mathbf{v}} f_0}{2\omega_{\text{LW}} + \omega - \omega' - (\mathbf{k} - \mathbf{k}') \cdot \mathbf{v}} \right]. \quad (\text{B29})$$

Note that since \mathbf{E}_1 is a longitudinal field,

$$\mathbf{E}_1(\mathbf{k}, \omega) = \frac{\mathbf{k} [\mathbf{k} \cdot \mathbf{E}_1(\mathbf{k}, \omega)]}{k^2}. \quad (\text{B30})$$

Equation (B26) is evaluated, using the approximation $|\omega| \ll \omega_{\text{LW}}$ to give

$$\frac{4\pi \mathbf{k} \cdot \mathbf{J}_1^0}{i\omega_{\text{LW}}} = -\chi_e(\mathbf{k}, \omega + \omega_{\text{LW}}) \mathbf{k} \cdot \mathbf{E}_1(\mathbf{k}, \omega), \quad (\text{B31})$$

where

$$\chi_e(\mathbf{k}, \omega) \equiv \frac{4\pi e^2}{m_e k^2} \int d^3\mathbf{v} \left[\frac{\mathbf{k} \cdot \partial_{\mathbf{v}} f_0}{\omega - \mathbf{k} \cdot \mathbf{v}} \right].$$

Equation (B27) is evaluated similarly to yield

$$\frac{4\pi \mathbf{k} \cdot \delta \mathbf{J}_1^0(\mathbf{k}, \omega)}{i\omega_{\text{LW}}} = -\chi_e(\mathbf{k}, \omega + \omega_{\text{LW}}) \mathbf{k} \cdot \mathbf{h}_1(\mathbf{k}, \omega) + i \int d\mathbf{k}' \int d\omega' \left[\mathbf{k} \cdot \mathbf{E}_1(\mathbf{k}', \omega') \frac{\delta n_{eS}(\mathbf{k}' - \mathbf{k}, \omega' - \omega)}{n_{e0}} \right]. \quad (\text{B32})$$

To obtain the right-hand side of Eq. (B32), it was assumed that $|\omega|, |\omega'| \ll \omega_{\text{LW}}$,

$$|\omega' - \omega| \leq |\mathbf{k}' - \mathbf{k}| c_s \ll |(\mathbf{k}' - \mathbf{k}) \cdot \mathbf{v}| \sim |\mathbf{k}' - \mathbf{k}| v_{\text{the}},$$

and the relation

$$\delta n_{eS}(\mathbf{k}, \omega) = -e\phi_{eS}(\mathbf{k}, \omega)/T_{e0},$$

where $\mathbf{E}_s(\mathbf{k}, \omega) = -i\mathbf{k}\phi_{eS}(\mathbf{k}, \omega)$ was used.

Using the approximations $|\omega - \mathbf{k} \cdot \mathbf{v}| \ll \omega_{\text{LW}}$ and

$$|\omega' - \omega - (\mathbf{k}' - \mathbf{k}) \cdot \mathbf{v}| \ll \omega_{\text{LW}},$$

neglecting smaller terms of the order $\mathbf{k} \cdot \mathbf{v}/\omega_{\text{LW}} \sim k\lambda_{\text{De}} \ll 1$, and applying two successive integration by parts in velocity space, Eq. (B28) is evaluated:

$$\begin{aligned} \delta \mathbf{J}_1^1(\mathbf{k}, \omega) &= -\frac{e^3 n_{e0}}{2m_e^2 \omega_{\text{LW}}^3} \int d\mathbf{k}' \int d\omega' \left[\mathbf{E}_1^*(\mathbf{k}' - \mathbf{k}, \omega' - \omega) \cdot \mathbf{k} \right] \tilde{\mathbf{E}}_2(\mathbf{k}', \omega') \\ &\quad - \frac{e^3 n_{e0}}{2m_e^2 \omega_{\text{LW}}^3} \int d\mathbf{k}' \int d\omega' \mathbf{E}_1^*(\mathbf{k}' - \mathbf{k}, \omega' - \omega) \left[\tilde{\mathbf{E}}_2(\mathbf{k}', \omega') \cdot \mathbf{k} \right] \\ &\quad - \frac{e^3 n_{e0}}{2m_e^2 \omega_{\text{LW}}^3} \int d\mathbf{k}' \int d\omega' \tilde{\mathbf{E}}_2(\mathbf{k}', \omega') \\ &\quad \times \left[\mathbf{E}_1^*(\mathbf{k}' - \mathbf{k}, \omega' - \omega) \cdot (\mathbf{k}' - \mathbf{k}) \right]. \end{aligned} \quad (\text{B33})$$

Similarly, using the same approximations and integration by parts, Eq. (B30) is evaluated:

$$\begin{aligned} \delta \mathbf{J}_1^2(\mathbf{k}, \omega) &= \frac{e^3 n_{e0}}{4m_e^2 \omega_{\text{LW}}^3} \int d\mathbf{k}' \int d\omega' \mathbf{E}_1^*(-\mathbf{k}', -\omega') \left[\tilde{\mathbf{E}}_2(\mathbf{k} - \mathbf{k}', \omega - \omega') \cdot \mathbf{k} \right] \\ &\quad + \frac{e^3 n_{e0}}{4m_e^2 \omega_{\text{LW}}^3} \int d\mathbf{k}' \int d\omega' \left[\mathbf{E}_1^*(-\mathbf{k}', -\omega') \cdot \mathbf{k} \right] \\ &\quad \times \tilde{\mathbf{E}}_2(\mathbf{k} - \mathbf{k}', \omega - \omega'). \end{aligned} \quad (\text{B34})$$

Equation (B34) is recast using the change of variables $\mathbf{k}'' = \mathbf{k} - \mathbf{k}'$ and $\omega'' = \omega - \omega'$:

$$\begin{aligned} & \delta \mathbf{J}_1^2(\mathbf{k}, \omega) \\ &= \frac{e^3 n_{e0}}{4m_e^2 \omega_{\text{LW}}^3} \int d\mathbf{k}'' \int d\omega'' \mathbf{E}_1^*(\mathbf{k}'' - \mathbf{k}, \omega'' - \omega) [\tilde{\mathbf{E}}_2(\mathbf{k}'', \omega'') \cdot \mathbf{k}] \\ &+ \frac{e^3 n_{e0}}{4m_e^2 \omega_{\text{LW}}^3} \int d\mathbf{k}'' \int d\omega'' [\mathbf{E}_1^*(\mathbf{k}'' - \mathbf{k}, \omega'' - \omega) \cdot \mathbf{k}] \\ &\times \tilde{\mathbf{E}}_2(\mathbf{k}'', \omega''). \end{aligned} \quad (\text{B35})$$

Summing Eqs. (B33) and (B35), rearranging the resulting equation, and using the fact that $\tilde{\mathbf{E}}_2$ is a transverse field, i.e., $\tilde{\mathbf{E}}_2(\mathbf{k}', \omega') \cdot \mathbf{k}' = 0$, one obtains

$$\begin{aligned} & \delta \mathbf{J}_1^1 + \delta \mathbf{J}_1^2 \\ &= \frac{ie^3 n_{e0}}{4m_e^2 \omega_{\text{LW}}^3} \int d\mathbf{k}' \int d\omega' [\mathbf{E}_1^*(\mathbf{k}' - \mathbf{k}, \omega' - \omega) \cdot i\mathbf{k}'] \tilde{\mathbf{E}}_2(\mathbf{k}', \omega') \\ &- \frac{ie^3 n_{e0}}{4m_e^2 \omega_{\text{LW}}^3} \int d\mathbf{k}' \int d\omega' [\mathbf{E}_1^*(\mathbf{k}' - \mathbf{k}, \omega' - \omega) \cdot i(\mathbf{k} - \mathbf{k}')] \tilde{\mathbf{E}}_2(\mathbf{k}', \omega') \\ &+ \frac{ie^3 n_{e0}}{4m_e^2 \omega_{\text{LW}}^3} \int d\mathbf{k}' \int d\omega' [\tilde{\mathbf{E}}_2(\mathbf{k}', \omega') \cdot i(\mathbf{k} - \mathbf{k}')] \\ &\times \mathbf{E}_1^*(\mathbf{k}' - \mathbf{k}, \omega' - \omega). \end{aligned} \quad (\text{B36})$$

Using the approximations $\chi_e(\mathbf{k}, \omega + \omega_{\text{LW}}) \approx -\omega_{\text{pe0}}^2 / \omega_{\text{LW}}^2$ and $\omega_0 \sim 2\omega_{\text{LW}}$, and transforming Eq. (B32) back to configuration space with $i\mathbf{k} \rightarrow \nabla$, results in

$$\begin{aligned} \nabla \cdot \delta \mathbf{J}_0^1 &= \frac{ie^3 n_{e0}}{4m_e^2 \omega_{\text{LW}}^3} \nabla \cdot \left[\nabla (\mathbf{E}_1^* \cdot \tilde{\mathbf{E}}_2) \right. \\ &\left. - (\tilde{\mathbf{E}}_2 \cdot \nabla) \mathbf{E}_1^* - (\mathbf{E}_1^* \cdot \nabla) \tilde{\mathbf{E}}_2 \right]. \end{aligned} \quad (\text{B37})$$

Transforming Eq. (B36) back to configuration space, one obtains

$$\begin{aligned} \nabla \cdot (\delta \mathbf{J}_1^1 + \delta \mathbf{J}_1^2) &= \frac{ie^3 n_{e0}}{4m_e^2 \omega_{\text{LW}}^3} \nabla \cdot \left[(\mathbf{E}_1^* \cdot \nabla) \tilde{\mathbf{E}}_2 \right. \\ &\left. - \tilde{\mathbf{E}}_2 (\nabla \cdot \mathbf{E}_1^*) - (\tilde{\mathbf{E}}_2 \cdot \nabla) \mathbf{E}_1^* \right]. \end{aligned} \quad (\text{B38})$$

Substituting Eqs. (B25), (B31), (B32), and (B36) into Eq. (B23) and transforming back to configuration space with $i\mathbf{k} \rightarrow \nabla$, one finds

$$\begin{aligned} & \mathcal{F}^{-1} \left[i\mathbf{k} \cdot \mathbf{E}_1(\mathbf{k}, \omega) \epsilon(k, \omega + \omega_{\text{LW}}) \right] \\ &+ \mathcal{F}^{-1} \left\{ i \int d\mathbf{k}' \int d\omega' \left[\mathbf{k} \cdot \mathbf{E}_1(\mathbf{k}', \omega') \frac{\delta n_{eS}(\mathbf{k}' - \mathbf{k}, \omega' - \omega)}{n_{e0}} \right] \right\} \\ &= \frac{e\omega_{\text{pe0}}^2}{4m_e \omega_{\text{LW}}^4} \nabla \cdot \left[\nabla (\mathbf{E}_1^* \cdot \tilde{\mathbf{E}}_2) - \tilde{\mathbf{E}}_2 (\nabla \cdot \mathbf{E}_1^*) \right], \end{aligned} \quad (\text{B39})$$

where the operator \mathcal{F}^{-1} denotes the inverse Fourier transform in space and time, and

$$\begin{aligned} \epsilon(\mathbf{k}, \omega + \omega_{\text{LW}}) &= 1 + \chi_e(\mathbf{k}, \omega + \omega_{\text{LW}}), \\ &\approx \frac{2\omega_{\text{pe0}} [\omega(k) + i\gamma_L(k)] - 3k^2 v_{\text{the}}^2}{-\omega_{\text{pe0}}^2}. \end{aligned}$$

In this approximation, Eq. (B39) can then be evaluated explicitly to yield the well-known Zakharov equation

$$\begin{aligned} \nabla \cdot \left\{ \left[2i\omega_{\text{pe0}} (\partial_t + \gamma_L \circ) + 3v_{\text{the}}^2 \nabla^2 + \omega_{\text{pe0}}^2 \frac{\delta n_{eS}}{n_{e0}} \right] \mathbf{E}_1 \right\} \\ = \frac{e}{4m_e} \nabla \cdot \left[\nabla (\mathbf{E}_1^* \cdot \tilde{\mathbf{E}}_2) - \tilde{\mathbf{E}}_2 (\nabla \cdot \mathbf{E}_1^*) \right], \end{aligned} \quad (\text{B40})$$

where the operator “ \circ ” is used to denote a convolution in configuration space (see DuBois *et al.*⁹). The iterative procedure

leading to Eq. (B22) is based on the assumption that the perturbations of the distribution function are small compared to the background distribution function f_M . This leads to the validity estimates for the Zakharov model: $|\mathbf{E}_1|^2/4\pi n_{e0}T_{e0} \ll 1$, $|\mathbf{E}_2|^2/4\pi n_{e0}T_{e0} \ll 1$, $|e\phi_{eS}/T_{e0}| \ll 1$, $|\delta n_{eS}/n_{e0}| \ll 1$, and $k_{LW}\lambda_{De} \ll 1$. These involve qualitative arguments, and the quantitative strengths of the inequalities are not known *a priori*. Furthermore, this derivation does not account for the evolution of the background electron-velocity distribution function, which is here taken to be a fixed Maxwellian, $f_M(v)$. This is why detailed quantitative comparison of the ZAK model with RPIC is desirable.

The equation for the low-frequency density fluctuation can be derived in a similar way. The result is

$$\begin{aligned} & \left[\partial_t^2 + 2iv_i \circ \partial_t - c_s^2 \nabla^2 \right] \delta n \\ &= \frac{1}{16\pi m_i} \nabla^2 \left[|\mathbf{E}_1|^2 + \frac{1}{4} |\mathbf{E}_2|^2 \right]. \end{aligned} \quad (\text{B41})$$

In the simulations reported in the text where the laser is a uniform plane wave, the ponderomotive pressure of the pump [the second term on the right-hand side of Eq. (41)] does not contribute.

Appendix C: Degenerate LW's with Overlapping Beams

In the presence of two identical beams propagating at angles $\theta = \pm\theta_b$ with respect to the x axis, the locations of the most linearly unstable LW are given by algebraic solutions of the following two sets of equations:

$$\begin{aligned} & \left(k_{x1} \cos \theta_b + k_{y1} \sin \theta_b - \frac{1}{2} k_0 \lambda_{De} \right)^2 \\ & + \left(-k_{x1} \sin \theta_b + k_{y1} \cos \theta_b \right)^2 = \kappa^2, \end{aligned} \quad (\text{C1})$$

$$\begin{aligned} & \left(k_{x1} \cos \theta_b + k_{y1} \sin \theta_b - \frac{1}{2} k_0 \lambda_{De} \right)^2 - \left(-k_{x1} \sin \theta_b + k_{y1} \cos \theta_b \right)^2 \\ & = \left(\frac{1}{2} k_0 \lambda_{De} \right)^2, \end{aligned} \quad (\text{C2})$$

$$\begin{aligned} & \left(k_{x2} \cos \theta_b - k_{y2} \sin \theta_b - \frac{1}{2} k_0 \lambda_{De} \right)^2 \\ & + \left(k_{x2} \sin \theta_b + k_{y2} \cos \theta_b \right)^2 = \kappa^2, \end{aligned} \quad (\text{C3})$$

$$\begin{aligned} & \left(k_{x2} \cos \theta_b - k_{y2} \sin \theta_b - \frac{1}{2} k_0 \lambda_{De} \right)^2 \\ & - \left(k_{x2} \sin \theta_b + k_{y2} \cos \theta_b \right)^2 = \left(\frac{1}{2} k_0 \lambda_{De} \right)^2, \end{aligned} \quad (\text{C4})$$

where κ is defined by

$$\begin{aligned} \kappa^2 &\equiv \frac{1}{2} \Omega - \left(\frac{1}{2} k_0 \lambda_{De} \right)^2, \\ \Omega &\equiv \frac{2}{3} \left(\frac{\omega_0}{\omega_{pe0}} - 2 \right). \end{aligned}$$

Equations (C1)–(C4) are obtained by rotating Eqs. (34) and (35) through angles $\pm\theta_b$. For arbitrary temperature T_{e0} and density n_{e0} , the solutions of Eqs. (C1)–(C2) and (C3)–(C4) result in eight distinct modes since each set of circles and hyperbolae will have four distinct intersections. There exists, however, a combination of temperature and density such that two of the eight solutions become degenerate, i.e., there will be only seven distinct solutions for (k_{x1}, k_{y1}) and (k_{x2}, k_{y2}) . By symmetry, this special condition occurs when $k_{y1} = k_{y2} = 0$, in which case the location $k_x = k_{x1} = k_{x2}$ of the degenerate mode is given by

$$\begin{aligned} & \left(k_x \cos \theta_b - \frac{1}{2} k_0 \lambda_{De} \right)^2 + k_x^2 \sin^2 \theta_b \\ & = \frac{1}{3} \left(\frac{\omega_0}{\omega_{pe0}} - 2 \right) - \left(\frac{1}{2} k_0 \lambda_{De} \right)^2, \end{aligned} \quad (\text{C5})$$

$$\left(k_x \cos \theta_b - \frac{1}{2} k_0 \lambda_{De} \right)^2 - k_x^2 \sin^2 \theta_b = \left(\frac{1}{2} k_0 \lambda_{De} \right)^2. \quad (\text{C6})$$

Equations (C5) and (C6) are augmented by the electromagnetic dispersion relation

$$\omega_0^2 = \omega_{pe0}^2 + k_0^2 c^2. \quad (C7)$$

Equations (C5)–(C7) are solved for the background electron density given by

$$\frac{n_{e0}}{n_c} = 4 \left[-\sigma + (\sigma^2 - 8\sigma + 4)^{1/2} \right]^{-2},$$

$$\sigma \equiv \frac{2}{3} \left[\frac{511}{T_e(\text{keV})} \right] \cos^2(2\theta_b). \quad (C8)$$

REFERENCES

1. W. Seka, D. H. Edgell, J. F. Myatt, A. V. Maximov, R. W. Short, V. N. Goncharov, and H. A. Baldis, *Phys. Plasmas* **16**, 052701 (2009).
2. J. A. Delettrez, V. N. Goncharov, P. B. Radha, C. Stoeckl, A. V. Maximov, T. C. Sangster, J. A. Frenje, and D. Shvarts, *Bull. Am. Phys. Soc.* **53**, 248 (2008).
3. V. A. Smalyuk, D. Shvarts, R. Betti, J. A. Delettrez, D. H. Edgell, V. Yu. Glebov, V. N. Goncharov, R. L. McCrory, D. D. Meyerhofer, P. B. Radha, S. P. Regan, T. C. Sangster, W. Seka, S. Skupsky, C. Stoeckl, B. Yaakobi, J. A. Frenje, C. K. Li, R. D. Petrasso, and F. H. Séguin, *Phys. Rev. Lett.* **100**, 185005 (2008).
4. B. Yaakobi, T. R. Boehly, T. C. Sangster, D. D. Meyerhofer, B. A. Remington, P. G. Allen, S. M. Pollaine, H. E. Lorenzana, K. T. Lorenz, and J. A. Hawreliak, *Phys. Plasmas* **15**, 062703 (2008).
5. M. V. Goldman, *Ann. Phys.* **38**, 117 (1966); C. S. Liu and M. N. Rosenbluth, *Phys. Fluids* **19**, 967 (1976); A. B. Langdon, B. F. Lasinski, and W. L. Kruer, *Phys. Rev. Lett.* **43**, 133 (1979); S. J. Karttunen, *Plasma Phys.* **22**, 151 (1980); A. M. Rubenchik, *Sov. Phys.-JETP* **41**, 498 (1975); B. Bezzerides and D. F. DuBois, *Phys. Rev. Lett.* **36**, 729 (1976); R. Z. Sagdeev *et al.*, *Sov. Phys.-JETP* **55**, 74 (1982); H. H. Chen and C. S. Liu, *Phys. Rev. Lett.* **39**, 881 (1977); J. Meyer, *Phys. Fluids B* **4**, 2934 (1992).
6. A. Simon, R. W. Short, E. A. Williams, and T. Dewandre, *Phys. Fluids* **26**, 3107 (1983); B. B. Afeyan and E. A. Williams, *Phys. Rev. Lett.* **75**, 4218 (1995).
7. H. A. Baldis and C. J. Walsh, *Phys. Rev. Lett.* **47**, 1658 (1981); D. M. Villeneuve, H. A. Baldis, and C. J. Walsh, *Phys. Fluids* **28**, 1454 (1985); K. A. Tanaka, B. Boswell, R. S. Craxton, L. M. Goldman, F. Guglielmi, W. Seka, R. W. Short, and J. M. Soures, *Phys. Fluids* **28**, 2910 (1985); W. Seka, B. B. Afeyan, R. Boni, L. M. Goldman, R. W. Short, K. Tanaka, and T. W. Johnston, *Phys. Fluids* **28**, 2570 (1985); P. E. Young *et al.*, *Phys. Rev. Lett.* **61**, 2766 (1988); W. Seka, R. E. Bahr, R. W. Short, A. Simon, R. S. Craxton, D. S. Montgomery, and A. E. Rubenchik, *Phys. Fluids B* **4**, 2232 (1992).
8. Hard x rays are signatures for hot-electron generation and preheat.
9. D. F. DuBois, D. A. Russell, and H. A. Rose, *Phys. Rev. Lett.* **74**, 3983 (1995).
10. H. X. Vu, D. F. DuBois, and B. Bezzerides, *Phys. Rev. Lett.* **86**, 4306 (2001); *ibid.*, *Phys. Plasmas* **14**, 012702 (2007).
11. K. Y. Sanbonmatsu *et al.*, *Phys. Rev. Lett.* **82**, 932 (1999); *ibid.*, *Phys. Plasmas* **7**, 1723 (2000).
12. J. L. Kline *et al.*, *Phys. Rev. Lett.* **94**, 175003 (2005); J. L. Kline *et al.*, *Phys. Plasmas* **13**, 055906 (2006).
13. In point of fact, we show in Appendix B that the ZAK model can be derived from the basic equations of the RPIC model under certain conditions.
14. R. Yan *et al.*, *Phys. Rev. Lett.* **103**, 175002 (2009).
15. H. X. Vu, B. Bezzerides, and D. F. DuBois, *J. Comput. Phys.* **156**, 12 (1999).
16. H. X. Vu, J. M. Wallace, and B. Bezzerides, *Phys. Plasmas* **1**, 3542 (1994).
17. D. A. Russell and D. F. DuBois, *Phys. Rev. Lett.* **86**, 428 (2001).
18. D. F. DuBois, D. A. Russell, H. X. Vu, J. F. Myatt, and W. Seka, “The Nonlinear Source for Radiation, from the Two-Plasmon-Decay Instability, at One-Half of the Laser Frequency,” in preparation (2010).
19. In the absence of SRS, the vector potential envelopes \mathbf{a}_{-1} and \mathbf{a}_1 (with carrier frequencies $\omega_0 - \omega_{pe0}$ and $\omega_0 + \omega_{pe0}$, respectively) are set to 0.
20. J. F. Myatt, J. A. Delettrez, W. Seka, D. H. Edgell, A. V. Maximov, R. W. Short, D. F. DuBois, D. A. Russell, and H. X. Vu, *Bull. Am. Phys. Soc.* **54**, 145 (2009).
21. R. W. Short, *Bull. Am. Phys. Soc.* **54**, 144 (2009).
22. If above the LDI threshold, a Langmuir wave with wave number $k_{LW}\lambda_{De}$ will decay into a pair of LW and IAW with $k_{LW1}\lambda_{De} = -k_{LW}\lambda_{De} + \Delta k\lambda_{De}$ and $k_{IAW1}\lambda_{De} = 2k_{LW}\lambda_{De} - \Delta k\lambda_{De}$, where $\Delta k\lambda_{De} = 1.5(m_e/m_i)^{1/2}$ (cf. Ref. 11). This process can continue where the LW resulting from the primary LDI step can result in a secondary LDI decay step. Repeated LDI decays may occur until the resulting LW’s are of sufficiently long wavelengths that LW cavitation can be nucleated.⁹
23. W. L. Kruer, *The Physics of Laser-Plasma Interactions*, *Frontiers in Physics*, Vol. 73, edited by D. Pines (Addison-Wesley, Redwood City, CA, 1988), p. 133.TM
24. The Workshop on SRS/SBS Non-Linear Saturation at Wente Vineyards, Livermore, CA, University of California Report UCRL-JC-148983-SUM (2002).

Two-Dimensional Simulations of the Neutron Yield in Cryogenic-DT Implosions on OMEGA

Introduction

Inertial confinement fusion (ICF) has been actively pursued for decades¹ since it was proposed in the early 1970s (Ref. 2). In the so-called “hot-spot” ignition designs, a capsule containing a cryogenic deuterium–tritium (DT) ice layer and low-density DT gases is imploded directly by intense laser pulses³ or indirectly by x rays in a hohlraum.⁴ The ultimate goal of ICF is to ignite the imploding target, producing net energy gain. To reach this goal, the cryogenic-DT shell must be sufficiently low in temperature that it can be compressed to an extremely high density ($>1000\times$ solid-DT density), resulting in an areal density ($\rho R \geq 1$ g/cm²) to provide sufficient inertial confinements for burn-wave propagation. The temperature in the hot spot must be sufficiently high so that the resulting fusion α particles can “trigger” the burn-wave propagation for ignition. Both conditions are necessary for the success of hot-spot ICF ignition. Nonuniformities seeded by target and laser perturbations grow exponentially via Rayleigh–Taylor (RT) instability⁵ during the acceleration and deceleration of the fuel shell. This perturbation growth can disrupt the neutron yield (α -particle production) from the core through cooling the hot spot by either injecting “cold” material into the core or increasing heat flow out of the hot spot because of the increased surface area. This reduces the effective hot-spot volume, density, and temperature.⁶ The yield-over-clean (YOC), defined as the ratio of experimental neutron yield to its value from one-dimensional (1-D) simulations, is conventionally used to describe the neutron-yield reduction caused by perturbations. It has been shown⁷ that a minimum YOC requirement ($YOC_{\min} \geq 40\%$ to 50%) must be met at the National Ignition Facility (NIF)⁸ for both direct- and indirect-drive–ignition designs to be successful. By scaling the hydro-equivalent NIF-ignition designs to OMEGA, it has been suggested that the YOC of cryogenic-DT implosions on OMEGA should be $\sim 15\%$ to 20% (Ref. 7) to have confidence that a scaled NIF target will ignite.

Over the past years RT growth of various perturbations has been extensively studied for both planar and spherical targets through theoretical analyses/simulations⁹ and experiments.^{10–14} These perturbations include the target offset from

target chamber center, the ice roughness of the cryogenic-DT layer, and the laser nonuniformities. Understanding the effects of each of the perturbation sources and their combination on the neutron-yield reduction through multidimensional simulations compared with experiments is critical to identifying the major nonuniformity sources that should be improved. For ICF ignition designs, the perturbation growth generally depends on the target design and laser pulse shapes. A comprehensive study of cryogenic deuterium (D₂) implosions on OMEGA¹⁵ has been presented in Ref. 16. As opposed to the cryogenic-D₂, continuous-pulse implosions, the high-compression [$\langle \rho R \rangle > 200$ mg/cm²] cryogenic-DT implosions are driven by triple-picket designs with a higher convergence ratio and small hot spot. This article is devoted to a thorough understanding of the neutron-yield performance in cryogenic-DT implosions on OMEGA.^{17,18} Two-dimensional (2-D) *DRACO*¹⁹ simulations have been performed to systematically investigate each of the perturbation sources and their combined effects on the neutron yield. The *DRACO* simulations reproduced the trends observed in experiments. The simulated YOC’s agree with the experimental YOC within a factor of 2 or better, and the simulated neutron-averaged ion temperatures agree with measurements within the experimental uncertainty. Major nonuniformity sources are identified for the triple-picket plus step-pulse designs:^{17,18} the target offset with respect to the target chamber center and laser imprinting. This is in contrast to the cryogenic-D₂ implosions¹⁶ where the ice-layer roughness is much more dominant. The simulations of DT implosions suggest that to increase YOC from the current level of $\sim 5\%$ to the hydro-equivalent ignition level of $\sim 15\%$ to 20% (maintaining $\langle \rho R \rangle = 200$ to 300 mg/cm²), the target offset must be less than ~ 10 μ m and smoothing by spectral dispersion (SSD) must be applied.

The following sections (1) briefly describe the experiments and the basics of 2-D radiation–hydrodynamic simulations for cryogenic-DT implosions, respectively; (2) describe the detailed simulation results that examine each of the nonuniformity sources and their combined perturbation effects on the neutron-yield reduction; (3) discuss the integrated *DRACO* simulations

for individual cryogenic-DT shots by including the actual target and laser nonuniformities in experiments; (4) compare the simulated YOC and the neutron-averaged ion temperature with experiments; and (5) formulate the relationship between YOC and the temperature-over-clean (TOC), indicating how much distortion occurs in the hot-spot formation. Conclusions are presented in the last section.

Experiments of Cryogenic-DT Implosions on OMEGA

Low-adiabat ($\alpha \sim 2.0$ to 2.5, which is conventionally defined as the ratio of DT-fuel pressure to the Fermi-degenerate pressure), cryogenic-DT implosion experiments have been conducted on OMEGA with the multiple-picket drive pulses^{17,18} shown in Figs. 123.1(a) and 123.1(b). The targets, shown in Fig. 123.1(c), were energy scaled from the ignition design on the National Ignition Facility (NIF).¹⁷ The OMEGA target had an 860- μm diameter, with an $\sim 10\text{-}\mu\text{m}$ plastic (CD) ablator filled with approximately 650 atm of DT (nominally 50:50) gas at standard temperature and pressure. When cooled to the triple point (approximately 18.7 K), a DT-ice layer ($\sim 65\ \mu\text{m}$ thick) formed inside the shell. The targets were mounted on 17- μm -diam SiC stalks. The triple-picket design^{17,18} is motivated by the desire to precisely tune the multiple shock waves to maintain a low-implosion adiabat and to minimize shock preheating of the fuel. The pickets launch a series of decaying shocks that are designed to coalesce nearly simultaneously with the main shock near the inner surface of the cold fuel. Shock-timing measurements in liquid deuterium with a velocity interferometer system for any reflector (VISAR)²⁰ are used to obtain a laser pulse shape that places the DT fuel on the desired adiabat. By adjusting the picket energies, low-adiabat ($\alpha \sim 2$), high-compression [$\langle \rho R \rangle_n \sim 300 \pm 47\ \text{mg}/\text{cm}^2$ inferred by a magnetic recoil spectrometer (MRS)²¹] implosions have been demonstrated on OMEGA.^{17,18}

For the OMEGA cryogenic-DT experiments, both the triple-picket (TP) plus square main pulse [Fig. 123.1(a)] and triple-picket plus step main pulse [Fig. 123.1(b)] have been used to drive target implosions. The former design resulted in an in-flight adiabat of $\alpha \sim 2.5$ and a convergence ratio of $C_R \sim 19$, while the step main pulse drove a lower-adiabat ($\alpha \sim 2.0$) implosion with a higher convergence ratio of $C_R \sim 24$ (resulting in higher $\langle \rho R \rangle$). The total laser energy was 23 kJ for the square main pulse and 25 kJ for the step main pulse. With a peak intensity of $\sim 8 \times 10^{14}\ \text{W}/\text{cm}^2$, the predicted implosion velocity in these designs is $v_{\text{imp}} = 3 \times 10^7\ \text{cm}/\text{s}$. Details of the compression dynamics, the areal-density (ρR) measurement, and the triple-picket ignition design for the NIF can be found in Refs. 17 and 18.

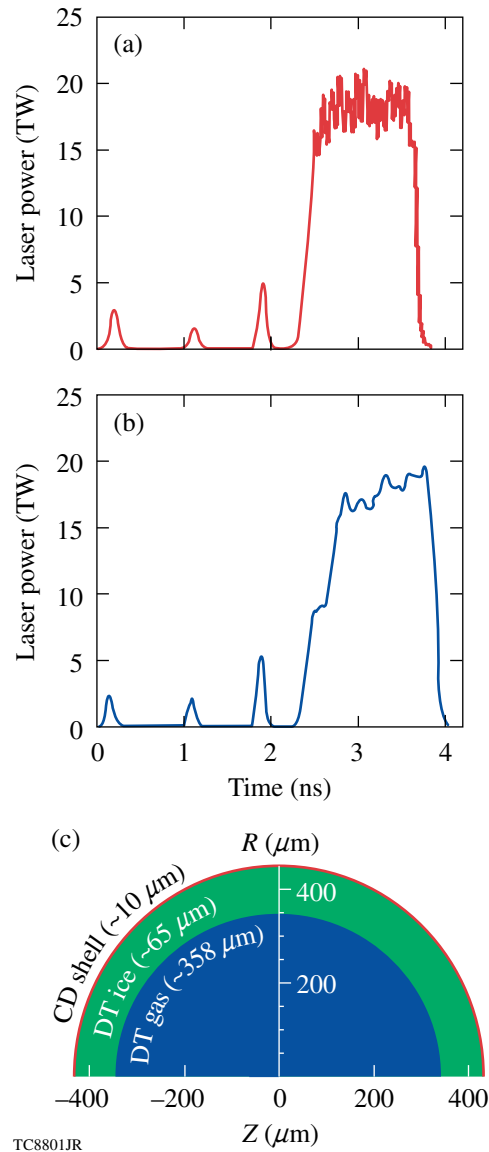


Figure 123.1

(a) The triple-picket plus square main pulse and (b) the triple-picket plus step main pulse used for cryogenic-DT implosions on the OMEGA laser. (c) A schematic diagram of a cryogenic-DT target.

The neutron yields from DT fusion were measured with a combination of activation, scintillation, and track recorder detectors. The yield of these implosions, 1×10^{12} to 6×10^{12} neutrons, varied from $\sim 3\%$ to $\sim 10\%$ of the 1-D hydrodynamic simulation prediction, depending on the pulse shape, target offset, ice roughness, and beam smoothing. The neutron-averaged ion temperature ($\langle T_i \rangle_n$) was inferred using neutron time-of-flight spectroscopy.²² The accuracy of these measurements was approximately $\pm 0.5\ \text{keV}$, depending on the measurement

configuration and the neutron-hit statistics in the detectors. Improvements to reduce the error bar in $\langle T_i \rangle_n$ measurements are underway. The measured $\langle T_i \rangle_n$ and the absolute neutron yields are lower than the 1-D–predicted values, as a consequence of laser and target perturbations including ice roughness, laser-drive nonuniformity (primarily pointing- and single-beam nonuniformity), capsule-surface imperfections associated with the stalk mount, and target offsets from the locus of laser-beam pointing. The subsequent sections provide a systematic investigation of how these nonuniformities reduce the neutron yield and the ion temperature in the hot spot. The simulations are used to identify the major perturbation sources and to suggest possible improvements for the implosion-yield performance.

Two-Dimensional DRACO Simulations

To understand the various laser and target perturbation effects on the cryogenic-DT implosion experiments, multi-dimensional hydrodynamic simulations were performed. The two-dimensional, radiation hydrodynamics code *DRACO* has been developed at LLE for both implosion and planar-target simulations.¹⁹ For spherical implosion simulations, the *DRACO* coordinates are defined by the cylindrical axis \mathbf{Z} and the radius \mathbf{R} , with the assumption of azimuthal symmetry. This study used *DRACO*'s Lagrangian version. Laser absorption in the plasma corona by inverse bremsstrahlung was modeled by three-dimensional (3-D) ray tracing with OMEGA's port geometry.²³ The equation-of-state (EOS) of materials was determined from the *SESAME* EOS table.²⁴ The radiation transport in *DRACO* used the multigroup diffusion model, in which the Astrophysics Opacity Table (AOT)²⁵ is applied.

In direct-drive ICF implosions, the laser energy absorbed near the critical-density region is thermally transported to the ablation surface mainly by electrons. The thermal-transport model in direct-drive ICF is crucial for properly simulating the target drive. Flux-limited Spitzer thermal conductivity is often used in laser-plasma fluid modeling.²⁶ The standard flux limiter $f = 0.06$ was used in the 2-D simulations. Previous experiments with planar and spherical targets^{27–29} have shown that this flux limiter works well for the laser intensities used here. The 1-D simulations of the cryogenic-DT implosions were modeled using both classical (flux-limited) heat transport and a nonlocal heat-transport model³⁰ and were found to be insensitive to the transport model.

A series of planar and spherical experiments were conducted to benchmark the *DRACO* simulations.^{11–14,16,19,29,31,32} The code capability of simulating the Rayleigh–Taylor instability growth has been demonstrated with intense laser-driven planar/

spherical target experiments on OMEGA.^{11–14} The RT growth of perturbations either by pre-imposed mass modulation^{11,12} or by direct laser imprinting^{13,14} has been properly predicted by *DRACO* simulations. A systematic study of the neutron yield in cryogenic-D₂ implosions on OMEGA was performed with 2-D *DRACO* simulations.¹⁶ The simulation results generally reproduced the experimental trend in YOC versus target offset and ice roughness for 5- μm -thick CD-shell targets, while for 10- μm -thick CD-shell targets, laser imprinting reduced the yield by a factor of 2. Following our previous experience in simulating cryogenic-D₂ implosions, cryogenic-DT implosions are systematically investigated for each of the perturbation sources and their combined effects on the yield performance. Comparing simulations with experiments elucidates the major perturbations and suggests how to increase the neutron yield in the experiments.

Simulation Results for Various Laser and Target Perturbations

In cryogenic-DT experiments, a variety of laser and target perturbations determine the implosion performance. Two kinds of laser perturbations will be addressed: (a) long-wavelength beam-to-beam perturbations ($\ell < 20$) such as mistiming, mispointing, and power imbalance among beams and (b) single-beam laser imprinting in the high-mode regime (up to $\ell \sim 200$). The target perturbations include the target offset from the target chamber center and the inner surface roughness of the ice layer. In this section, each of the nonuniformity sources will be investigated separately and their combined effect on yield performance will be examined.

1. Long-Wavelength Laser Nonuniformities

The 60-beam OMEGA Laser Facility¹⁵ can deliver up to 30-kJ, 351-nm UV energies on target. Each laser beam, coming from ports in a 3-D geometry, is equipped with a super-Gaussian (SG-4) phase plate³³ and polarization smoothing³⁴ is employed. The low-mode (long-wavelength) perturbation effects include the power imbalance (PIB) among beams, the beam-to-beam mistiming (MT), and the static mispointing (MP) of each beam. Their effects have been investigated separately with *DRACO* simulations of cryogenic-DT target performance using different levels of perturbation σ_{rms} . The results are summarized in Tables 123.I–123.III. A normal distribution of random perturbation amplitudes from each laser beam is assumed for a given σ_{rms} . For example, Table 123.I shows that for the square main pulse, the YOC decreases from 94.1% to 81.1% as the mistiming changes from $\sigma_{\text{rms}} = 9$ ps to $\sigma_{\text{rms}} = 40$ ps. Table 123.II shows that a static mispointing of $\sigma_{\text{rms}} = 50$ μm reduces the YOC to 65%. For power imbalance

among the beams, the pickets' power imbalance is more important than the main drive pulse because the PIB nonuniformity can be more efficiently seeded during the pickets. As shown in Table 123.III, a PIB of $\sigma_{\text{rms}} = 10\%$ during the pickets can reduce the YOC to 74%, even when the main pulse's PIB is $\sigma_{\text{rms}} = 3\%$. This level of PIB during the pickets has been seen in cryogenic-DT experiments. The PIB in cryogenic-DT pulse shapes has recently been improved to an overall $\sigma_{\text{rms}} = 3\%$ to 4%, which recovers the YOC to a level of $\sim 90\%$.

Table 123.I: YOC dependence on beam-to-beam mistiming for the square main pulse.

Beam-to-beam mistiming	YOC (%)
$\sigma_{\text{rms}} = 9$ ps	94.1
$\sigma_{\text{rms}} = 25$ ps	90.4
$\sigma_{\text{rms}} = 40$ ps	81.1

Table 123.II: YOC dependence on beam mispointing for the step main pulse.

Static beam mispointing	YOC (%)
$\sigma_{\text{rms}} = 10$ μm	91.9
$\sigma_{\text{rms}} = 30$ μm	77.0
$\sigma_{\text{rms}} = 50$ μm	65.0

Table 123.III: YOC dependence on beam-power imbalance for the step main pulse.

Beam-power imbalance	YOC (%)
$\sigma_{\text{rms}} = 3\%$ (pickets) and 3% (main pulse)	92.9
$\sigma_{\text{rms}} = 3\%$ (pickets) and 10% (main pulse)	90.3
$\sigma_{\text{rms}} = 10\%$ (pickets) and 3% (main pulse)	74.0

By using a nominal laser perturbation level for each source on OMEGA, the simulation results of their combined effects on the cryogenic-DT yield performance are listed in Table 123.IV for both pulse shapes. The combined effects of the three nominal perturbations (MT: $\sigma_{\text{rms}} = 9$ ps; MP: $\sigma_{\text{rms}} = 10$ μm ; PIB: $\sigma_{\text{rms}} = 3\%$ overall) reduce the yield by $\sim 7\%$ for the square main pulse and by $\sim 17\%$ for the step main pulse. The latter is more sensitive to perturbations since it drives a lower-adiabat, high-convergence implosion. In the following sections, these nominal low- ℓ -mode laser nonuniformities have been included since they are always present in OMEGA experiments.

2. Target Offset

The target can be offset from the target chamber center as a result of vibration when the cryogenic shroud is retracted. It is measured at shot time using time-integrated x-ray pinhole cameras. As shown in cryogenic-D₂ implosions,¹⁶ the target offset imposes a dominant $\ell = 1$ perturbation. This is due to the asymmetry of laser illumination on the target, which results in less laser absorption in the offset direction. As a result, the shock breaks out asymmetrically and the overdriven side converges more and achieves a higher density. The uneven drive compresses the target asymmetrically, reducing the final hot-spot volume, temperature, and density. The density contours for the square-main-pulse design are plotted in Figs. 123.2(a) and 123.2(b) at peak compression for the cases of 20- μm and 40- μm offsets from the target chamber center. The corresponding ion-temperature contour plots are shown in Figs. 123.2(c) and 123.2(d). As the target offset increased, the compression asymmetry increased; the ion temperature and effective volume for neutron production in the hot spot were reduced, leading to a reduction in neutron yield. The target offsets of 20 μm and 40 μm caused the YOC to decrease to 72% and 36.4%, respectively.

Carrying out *DRACO* simulations for different target offsets, the YOC was plotted as a function of target offset in Fig. 123.3 for both the square main pulse (red circles) and the step main

Table 123.IV: YOC degradation caused by the smallest low-mode beam perturbations on OMEGA.

Smallest OMEGA beam nonuniformities	YOC (%)	YOC (%)
	(square main pulse)	(step main pulse)
Mistiming ($\sigma_{\text{rms}} \sim 9$ ps)	94.1	92.2
Mispointing ($\sigma_{\text{rms}} \sim 10$ μm)	93.8	91.9
Power imbalance ($\sigma_{\text{rms}} \sim 3\%$ overall)	93.6	92.9
All above perturbations together	93.4	83.3

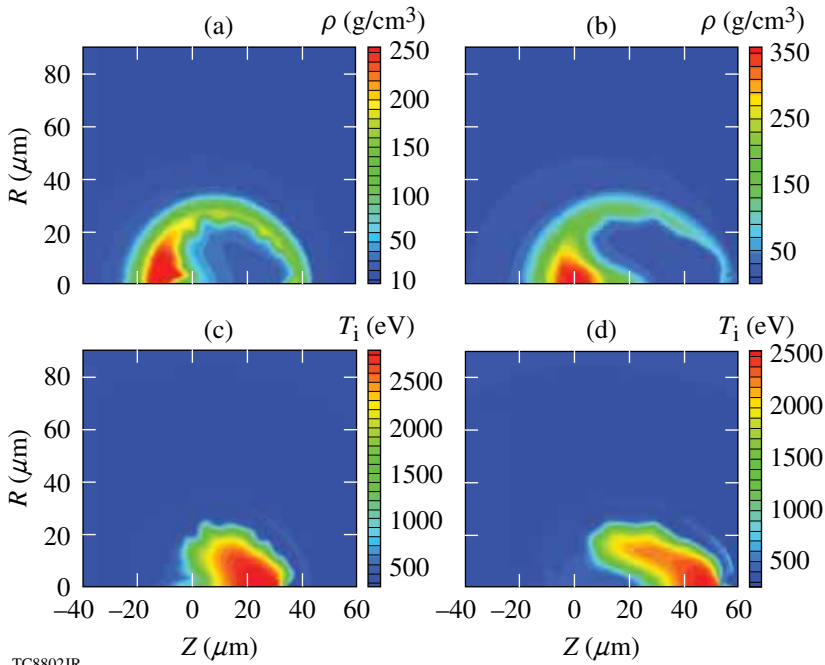


Figure 123.2
The density contour plots at peak compression for target offsets of (a) 20 μm and (b) 40 μm from the target chamber center, for the square-main-pulse case. The corresponding ion temperatures are shown in (c) and (d), respectively.

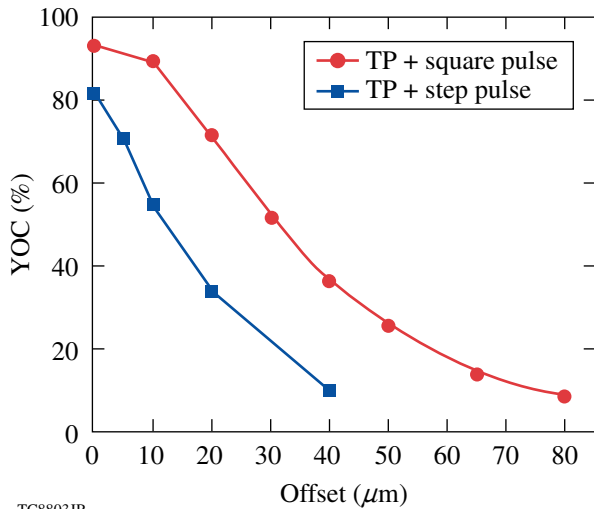


Figure 123.3
The YOC is plotted as a function of target offset for the two types of pulses shown in Figs. 123.1(a) and 123.1(b).

pulse (blue squares). The step main pulse is more sensitive to the target offset than the square main pulse. For example, at 20- μm offset the YOC is $\sim 72\%$ for the square main pulse, while it is $\sim 34\%$ for the step-main-pulse design. This factor of ~ 2 reduction is consistent with the experimental observations for these two pulse shapes (see **DRACO Simulations of Individual Cryogenic-DT Shots**, p. 122). The dominant $\ell = 1$ perturbation has been confirmed by experimental ρR

measurements. As shown in Fig. 123.2(b), if the ρR detector is sitting along the $+z$ axis (along the target offset), it measures the smallest ρR ; while, if it sits on the $-z$ axis (against the target offset), it will measure the largest ρR . Indeed, two shots with large offsets (35 μm and 39 μm) have shown such asymmetric ρR results [$\langle \rho R \rangle_{\text{CPS}_1} = 50 \text{ mg/cm}^2$ and $\langle \rho R \rangle_{\text{CPS}_2} = 180 \text{ mg/cm}^2$], experimentally inferred from the knock-on-deuteron (KOD) spectrum following elastic (n,D) scattering.³⁵ For these two shots, the two charged-particle spectrometers (CPS₁ and CPS₂) were roughly in line with the direction of target offset. The shape of the KOD spectrum evolves dramatically as the fuel areal density increases up to 180 mg/cm^2 ; above 180 mg/cm^2 , the shape of the spectrum no longer changes with increasing areal density and the measurement is saturated.³⁵

3. Ice Roughness

For the cryogenic-DT targets imploded on OMEGA, 10- μm CD shells were permeation filled with an equimolar mixture of DT to 650 atm. The shell and gas were then slowly cooled to just below the DT triple point (18.7 K). By controlling the exchange-gas pressure and the temperature of the copper-layering sphere, a spherical isotherm can be maintained at the ice surface inside the capsule, and β -layering produces high-quality layers.^{36,37} During formation of the ice layer, the inner ice surface was characterized using optical shadowgraphy.³⁸ A typical shadowgraph of a cryogenic-DT target is shown in Fig. 123.4(a); the inner-surface position is “unwrapped” azimuthally around the center of the capsule to form a line in

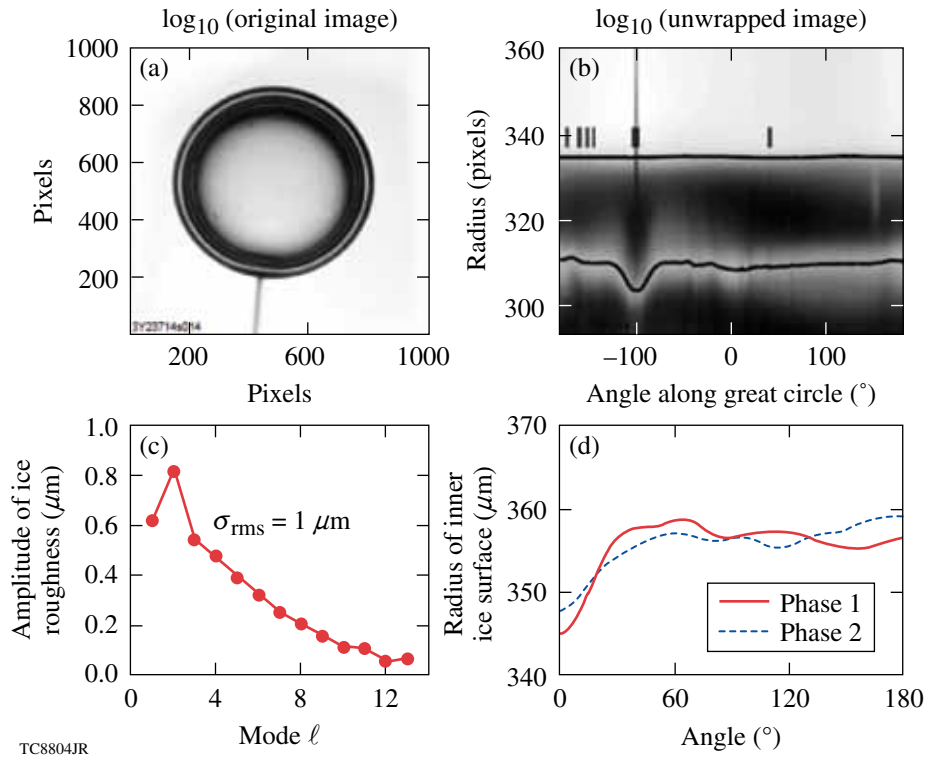


Figure 123.4

(a) A typical cryogenic-DT target view; (b) the ice-layer radius plotted versus angle; (c) a typical spectrum of ice roughness ($\sigma_{\text{rms}} = 1.0 \mu\text{m}$) at the inner surface (the thick part near the stalk has been excluded); (d) the angle-dependent radius of the inner ice surface for two different phases but same σ_{rms} , which were composed for our *DRACO* simulations.

radius–azimuth space [Fig. 123.4(b)]. Figure 123.4(c) shows the typical power spectrum of the ice roughness ($\sigma_{\text{rms}} = 1 \mu\text{m}$) as a function of the mode number, which was generated by fitting the Fourier amplitudes of the radial variation as a function of the azimuth.³⁹ Using the measured spectrum, the ice-layer thickness (ΔR) was composed for the *DRACO* simulations,

$$\Delta R(\theta) = \Delta R_0 + \sum_{\ell=1}^n \pm A_{\ell} \cos(\ell\theta), \quad (1)$$

where ΔR_0 is the average thickness of the ice layer and A_{ℓ} is the perturbation amplitude of the ℓ th mode. Because of the azimuthal symmetry imposed in 2-D *DRACO*, the phase among different modes must be either 0 or π , giving a plus (+) or minus (−) sign in the superposition of each mode. Different combinations of these signs provide various “phases” of the ice layer, which give different perturbed shell thicknesses along the polar angle θ , even though σ_{rms} is the same. The inner-surface radius as a function of angle has been plotted in Fig. 123.4(d) for two such phases, respectively, by solid (red) and dashed (blue) lines. The “dips” in radius around the stalk were modeled with the superposition of a Gaussian bump, around $\theta = 0^\circ$.

Different phases of ice roughness can vary the target-yield performance. Examples are shown in Figs. 123.5(a) and 123.5(b) for density contours at peak compression for phase 1 and phase 2 [shown in Fig. 123.4(d)], respectively, at $\sigma_{\text{rms}} = 1.0 \mu\text{m}$ with the step main pulse. The simulations show a neutron yield of $\text{YOC} = 78\%$ for phase 1 and $\text{YOC} = 56\%$ for phase 2. The “ice bump” around the stalk has not yet been included in the ice-roughness-only studies but will be included in the individual shot simulations. Considering only the ice roughness (without the localized ice bump), Fig. 123.5(c) shows the YOC as a function of ice roughness σ_{rms} from *DRACO* simulations for both $\sigma_{\text{rms}} = 1.0 \mu\text{m}$ and $\sigma_{\text{rms}} = 3.0 \mu\text{m}$ with three random phases. The error bar for each case represents the range of YOC’s caused by the different phases. As expected, the YOC decreases with increasing ice roughness.

4. Combined Target Offset and Ice Roughness

The combined effects of target offset and ice roughness on cryogenic-DT implosion yields are studied in this subsection. Both pulse shapes shown in Figs. 123.1(a) and 123.1(b) are simulated for ice roughnesses of $\sigma_{\text{rms}} = 1.0 \mu\text{m}$ and $\sigma_{\text{rms}} =$

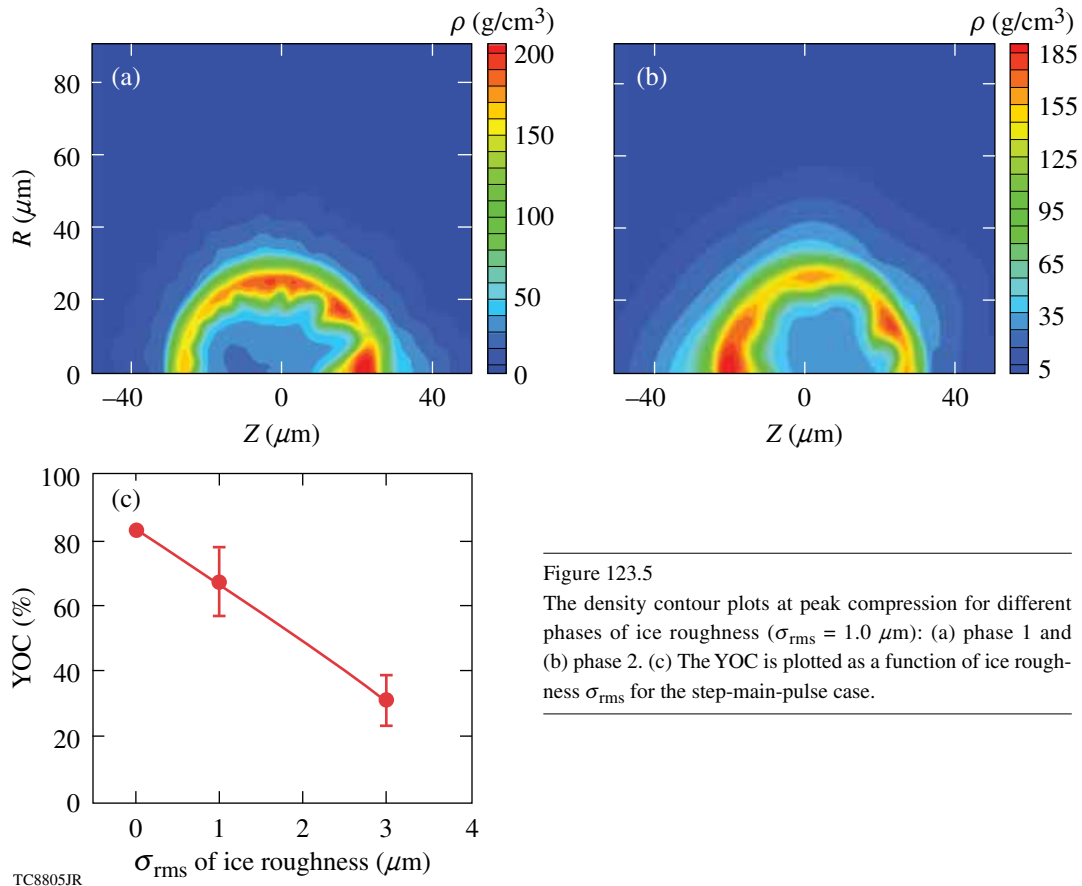


Figure 123.5
The density contour plots at peak compression for different phases of ice roughness ($\sigma_{\text{rms}} = 1.0 \mu\text{m}$): (a) phase 1 and (b) phase 2. (c) The YOC is plotted as a function of ice roughness σ_{rms} for the step-main-pulse case.

3.0 μm . The simulation results are shown in Figs. 123.6 and 123.7, respectively, by red circles (square main pulse) and blue squares (step main pulse). For the typical cryogenic-DT target ice roughness ($\sigma_{\text{rms}} = 1.0 \mu\text{m}$), Fig. 123.6 shows that the step main pulse resulted in more yield reduction than the square main pulse, again because of its lower adiabat and higher convergence. At an offset of about 20 μm , the square main pulse gives a factor-of-2-higher YOC than the step-main-pulse case, which is consistent with the experimental observation (discussed in *DRACO Simulations of Individual Cryogenic-DT Shots*, p. 122). A steeper drop in YOC is found for a target offset larger than 10 μm , especially for the step-main-pulse design, as illustrated in Fig. 123.6.

At a large ice roughness $\sigma_{\text{rms}} = 3.0 \mu\text{m}$, the YOC difference between the two pulse shapes is no longer significant since an increase in ice roughness dominates the performance and reduces the YOC to 30% to 40% (indicated by Fig. 123.7), even for target offsets $\leq 30 \mu\text{m}$. The step main pulse is more sensitive to the phase of the ice roughness, as indicated by the large YOC ranges in Fig. 123.7. To reach a high YOC level ($\geq 50\%$), the target must have a small offset ($\leq 10 \mu\text{m}$ for the step pulse

and $\leq 20 \mu\text{m}$ for the square pulse) and maintain a high-quality ice layer (ice roughness $\sigma_{\text{rms}} \leq 1 \mu\text{m}$).

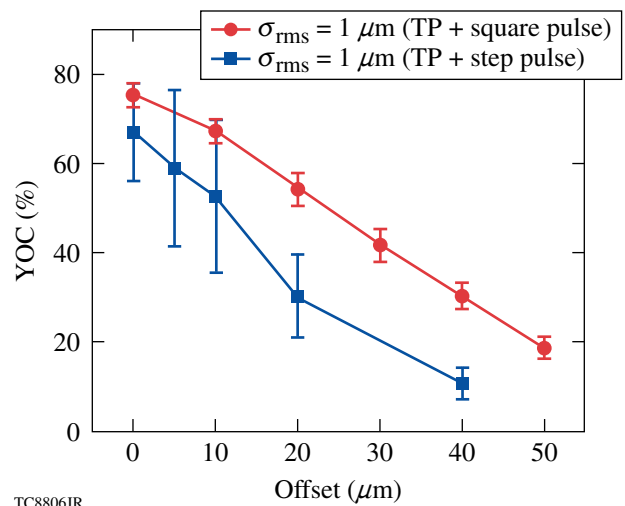


Figure 123.6
The YOC is plotted as a function of target offset with ice roughness $\sigma_{\text{rms}} = 1.0 \mu\text{m}$ for the two pulse shapes shown in Figs. 123.1(a) and 123.1(b).

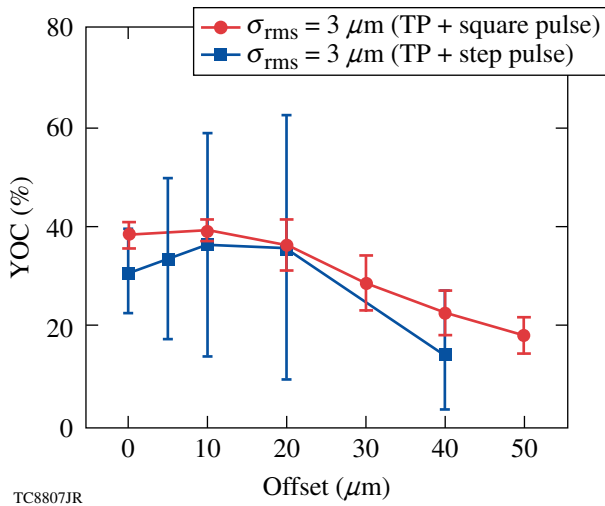


Figure 123.7

Same as Fig. 123.6 but for ice roughness $\sigma_{\text{rms}} = 3.0 \mu\text{m}$.

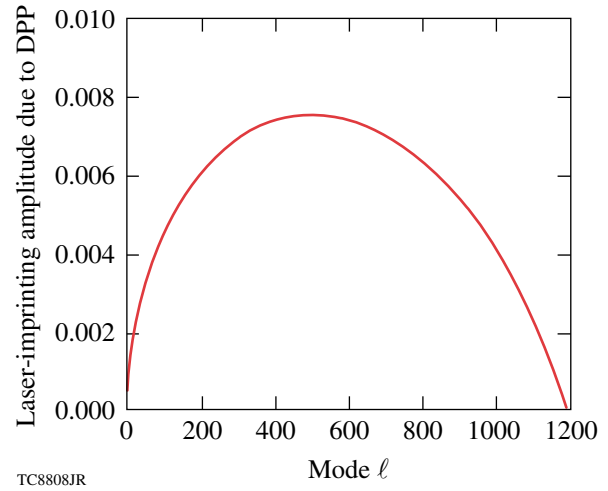


Figure 123.8

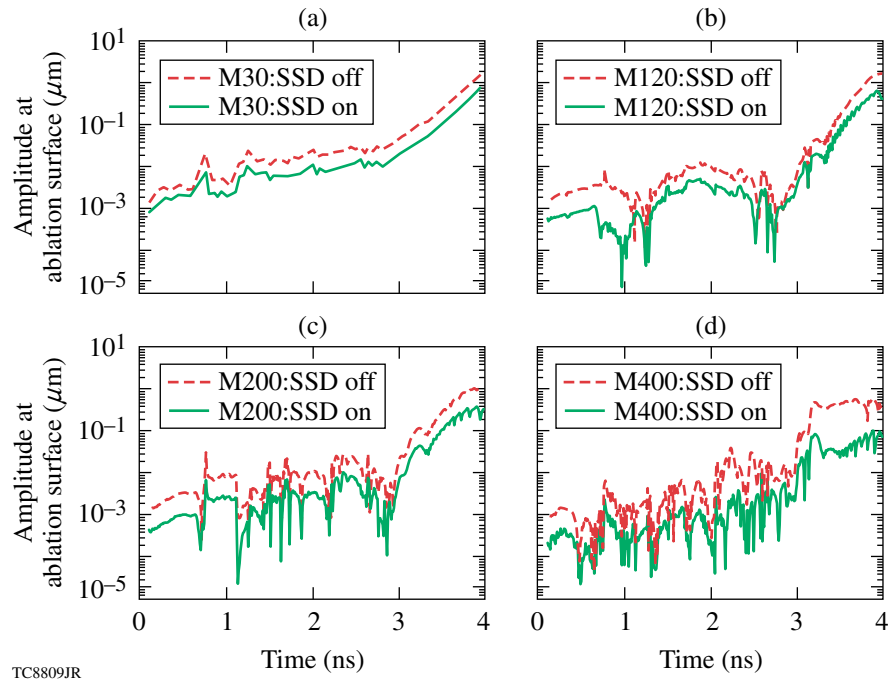
A typical SG-4 DPP spectrum on the OMEGA laser.

5. Laser Imprinting

Laser nonuniformities seed the instabilities at the ablation surface and can be categorized into long- and short-wavelength perturbations. The long-wavelength perturbations caused by beam mistiming, beam mispointing, and power imbalance have been discussed in **Long-Wavelength Laser Nonuniformities**, p. 113. The short-wavelength, single-beam nonuniformity caused by laser imprinting is addressed here.⁴⁰ An analytical model⁴¹ describing the nonuniformity of super-gaussian (SG) distributed phase plates (DPP's) is used to modulate the laser illumination on target. The experimentally confirmed SG-4 DPP spectrum⁴² is shown in Fig. 123.8. Polarization smoothing reduces the amplitudes by $\sqrt{2}$ (Ref. 34). Smoothing by spectral dispersion (1-THz, 2-D SSD) with one-color cycle⁴³ is applied for some shots. SSD is simulated using an analytical model.⁴⁴ The amplitudes of laser imprinting at the ablation surface are defined at the outer $1/e$ point of maximum density. These amplitudes seed the RT growth during the acceleration phase. Laser-imprinting effects are considered for both SSD-on and SSD-off cases.

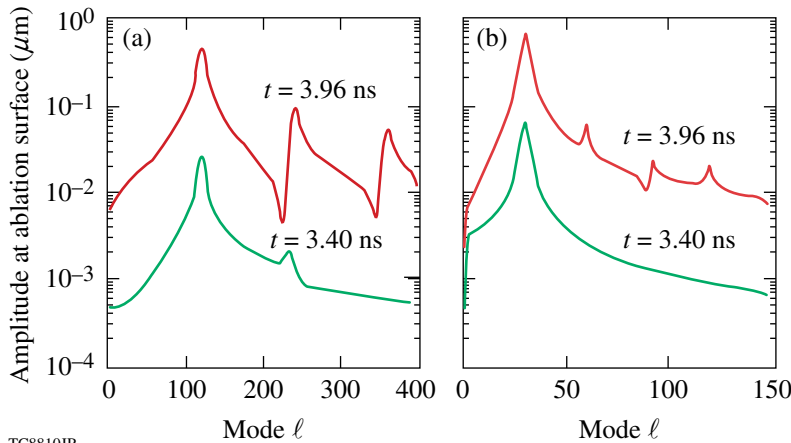
Single-mode laser-imprinting simulations for the step-main-pulse design up to mode $\ell = 500$ were performed with *DRACO* simulations either in a 45° wedge or in a half sphere. The resulting modulation amplitude at ablation surface is plotted as a function of time in Figs. 123.9(a)–123.9(d) for laser-imprinting modes $\ell = 30$ ($\lambda \approx 73.3 \mu\text{m}$), $\ell = 120$ ($\lambda \approx 18.3 \mu\text{m}$), $\ell = 200$ ($\lambda \approx 11.0 \mu\text{m}$), and $\ell = 400$ ($\lambda \approx 5.5 \mu\text{m}$), respectively.

The SSD-off cases are represented by dashed (red) curves and the SSD-on cases by solid (green) lines. For mode $\ell = 30$, Fig. 123.9(a) shows continuous imprinting before the start of acceleration at $t \approx 2.8$ ns. For modes $\ell \geq 120$, the laser imprinting decoupled during the first picket, when the distance from the laser deposition to the ablation surface became larger than the imprinting wavelength. The Richtmyer–Meshkov and preliminary RT growth caused by the unstable interference between the CD shell and the ice layer increase the amplitude. Phase reversals are seen in the high-mode laser-imprinting simulations, shown in Figs. 123.9(b)–123.9(d). After the acceleration starts at $t \approx 2.8$ ns, the $\ell = 30$ mode continuously grows until the end of acceleration ($t = 3.98$ ns), while the high modes of $\ell = 200$ and $\ell = 400$ quickly grow and nonlinearly saturate. The intermediate mode $\ell = 120$ grows linearly for about 600 ps; when its amplitude reaches $\sim 10\%$ of its wavelength, nonlinear behavior in RT growth begins. This can be seen in Fig. 123.10(a) where the Fourier transform of the single mode ($\ell = 120$) at the ablation surface (SSD on) is shown at two distinct times of $t = 3.4$ ns and $t = 3.96$ ns. At $t = 3.4$ ns, the $\ell = 120$ mode grows linearly, but at $t = 3.96$ ns, harmonics emerge as evidence of nonlinear growth.⁹ At the end of the acceleration phase, the shell radius converges to $R = 100 \mu\text{m}$ so that for the $\ell = 120$ mode, its wavelength is about $\sim 5 \mu\text{m}$, but $\lambda = 21 \mu\text{m}$ for a low mode $\ell = 30$. At $t = 3.96$ ns, the $\ell = 120$ mode grows to an amplitude of $\sim 0.8 \mu\text{m}$ [see Fig. 123.9(b)], which is $\sim 16\%$ of its wavelength. The mode $\ell = 120$ becomes nonlinear at the end of acceleration. For the low-mode $\ell = 30$



TC8809JR

Figure 123.9 The laser-imprinting mode growth as a function of time for both SSD-off and SSD-on cases from single-mode simulations: (a) $\ell = 30$, (b) $\ell = 120$, (c) $\ell = 200$, and (d) $\ell = 400$.



TC8810JR

Figure 123.10 The modal spectrum for our single-mode simulations (SSD on) at two distinct times $t = 3.40$ ns and $t = 3.96$ ns, for two cases (a) $\ell = 120$ and (b) $\ell = 30$.

case, the RT growth remained in a linear stage to the end of acceleration, which is confirmed by the absence of harmonics in Fig. 123.10(b).

By scanning the different single-mode simulations, the modulation amplitudes at the ablation surface as a function of laser-imprinting mode are shown in Figs. 123.11(a) and 123.11(b) at the start and end of acceleration, respectively. Both SSD-on (green squares) and SSD-off (red circles) cases

are shown in Fig. 123.11. The simulation results show that SSD reduces the modulation amplitude by a factor of 3 to 4, depending on the mode range. Overall, the laser-imprinting spectra (at the end of acceleration) show two distinct peaks around $\ell = 30$ and $\ell = 120$ for the triple-picket, step-main-pulse, cryogenic-DT design. The laser-imprinting spectra for the triple-picket design are compared with previous continuous-pulse, 5- μ m-CD-shell designs^{45,46} in Fig. 123.12(a) at the start of the acceleration phase and Fig. 123.12(b) at the end of the

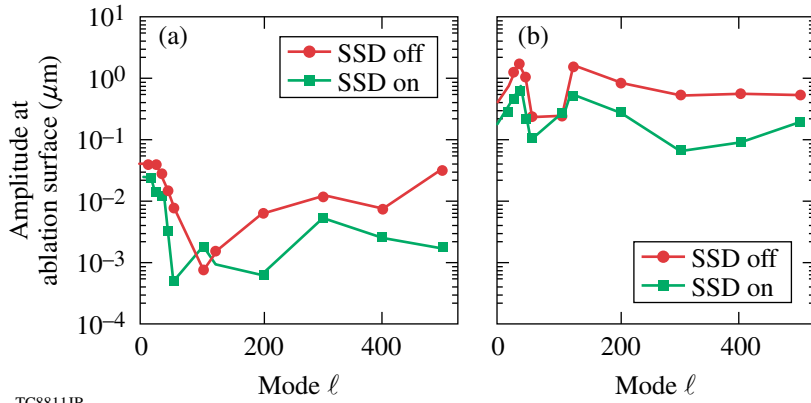


Figure 123.11

The laser-imprinting spectrum at (a) the start of acceleration and (b) the end of acceleration, for both SSD-off and SSD-on cases.

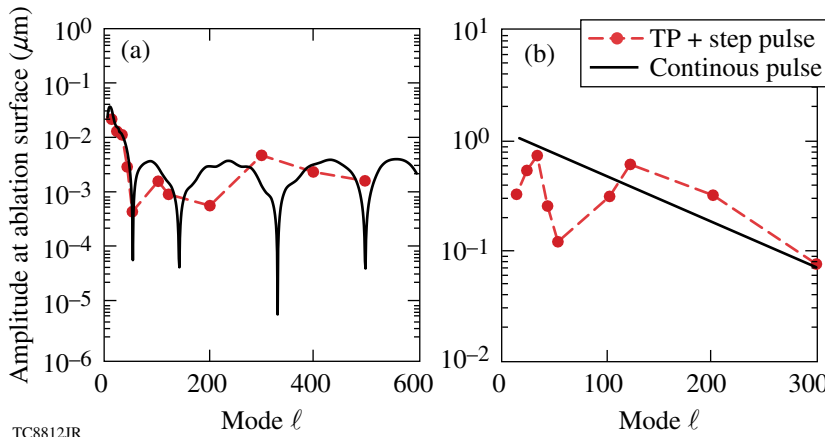


Figure 123.12

The laser-imprinting comparison between the triple-picket plus step-pulse (circles) and the continuous-pulse designs (solid lines) at (a) the start of acceleration and (b) the end of acceleration for the SSD-on case.

acceleration phase for the SSD-on case. The laser imprinting for the triple-picket design is comparable to the imprinting of the continuous-pulse and 5- μm -CD-shell designs, even though a 10- μm -thick CD shell was used in the triple-picket design (for the purpose of reducing potential fast-electron preheat⁴⁷). This is accomplished with the strong adiabat shaping^{46,48} caused by the three pickets.

The single-mode studies were performed up to a very high mode of $\ell = 500$, where there was evidence that short-wavelength (high-mode) RT growth can be stabilized in high-intensity drives at $I \sim 10^{15} \text{ W/cm}^2$ in planar experiments.^{11,12} At such high intensity, the corona temperature is about $T_e \approx 3 \text{ keV}$, resulting in a heat-carrying electron energy of around 15 to 20 keV. These electrons nonlocally affect the heat transport.^{29,49} They can penetrate to provide an extra heating at the ablation surface, which may in turn cause the ablation velocity to increase, leading to the short-wavelength RT stabilization, as the growth rate⁵⁰ scales as $\gamma - 0.94 \sqrt{\text{kg}/(1 + kL_m)} - 1.5 kV_a$, with wave number k , acceleration g , density scale length L_m , and ablation velocity V_a . Planar experiments with a wavelength

of $\lambda = 20 \mu\text{m}$ have shown no RT growth at such high-intensity drive conditions.^{11,12} For the cryogenic-DT, triple-picket designs, the laser intensity peaks at $I \sim 8 \times 10^{14} \text{ W/cm}^2$, which results in a corona temperature of $\sim 2.7 \text{ keV}$. Since the mean free path of the heat-carrying electrons scales with $\sim T_e^{-2}$, it is estimated that perturbations with $\lambda < 15$ to $16 \mu\text{m}$ should be stabilized, which corresponds to modes $\ell \geq 150$ to 200 (at the initial radius of $R = 350 \mu\text{m}$ at the start of acceleration). Therefore, for the multimode simulations the maximum mode was chosen to be $\ell_{\text{max}} = 200$. The multimode simulations were performed using a 45° wedge. To satisfy the boundary conditions, every fourth mode was included in the simulations. The amplitudes of the skipped ($\Delta \ell = 4$) modes were added in quadrature to conserve the total σ_{rms} of laser imprinting. Sixteen grid points per wavelength were used for the maximum laser-imprinting mode. The grid can support the harmonic growth of lower laser-imprinting modes ($\ell < 100$). The result of a simulation with $\ell_{\text{max}} = 200$ is shown in Fig. 123.13(a), where the density contours are plotted in the SSD-on case at the end of acceleration. It indicates two distinct features: (a) the dominant mode is around $\ell = 32$; (b) the second laser-

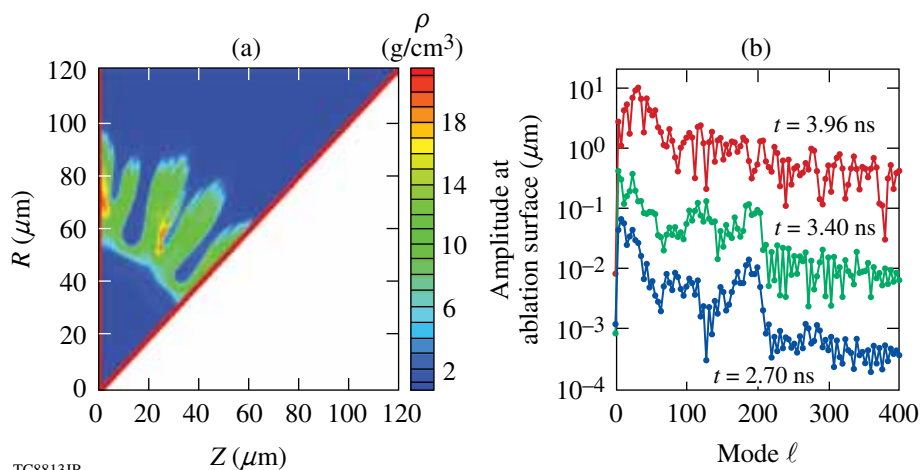


Figure 123.13

(a) The density contour plot for a multimode simulation (up to mode $\ell_{\max} = 200$ with SSD on) at the end of acceleration; (b) the modal spectrum at different times for the same simulation.

imprinting peak is located around $\ell = 120$. Both features are consistent with the single-mode simulation results shown in Fig. 123.11(b). Figure 123.13(a) shows the “bubble” and “spike” growth, indicating the nonlinear growth and mode coupling.⁹ The Fourier transform of the ablation surface [Fig. 123.13(b)] shows the history of RT-growth modal spectra at times of $t = 2.7$ ns, $t = 3.4$ ns, and $t = 3.96$ ns. At $t = 2.7$ ns, the lower (blue) curve in Fig. 123.13(b) indicates a sharp cutoff at $\ell = 200$, the same as the maximum laser-imprinting seeds included. The modal spectra grow almost linearly to $t = 3.4$ ns with distinct features peaking at $\ell = 32$ and $\ell = 120$ beginning to appear. At the end of acceleration, the two overall peaks around $\ell = 32$ and $\ell = 120$ appear in the upper curve ($t = 3.96$ ns), which is consistent with the single-mode predictions. The nonlinear growth for imprinting modes $\ell = 100$ to 200 has washed out the mode cutoff around $\ell = 200$. Mode coupling caused by high-mode nonlinear growth enhances the low-mode growth that leads to effective disruption of the neutron production from the hot spot.

By including the maximum modes up to $\ell_{\max} = 50$, $\ell_{\max} = 100$, and $\ell_{\max} = 200$ separately in six multimode simulations, we obtained the laser-imprinting effects on the YOC. The results are shown in Fig. 123.14 for the step-main-pulse design in the SSD-on (red squares) and SSD-off (blue circles) cases. Figure 123.14 shows that simulations with multimodes up to $\ell_{\max} = 50$ hardly reduce the yield, even though the first imprinting peak around $\ell = 30$ has been included. This again indicates the laser imprinting to the yield-reduction effect is through the enhanced low-mode growth that is “fed” by the high-mode nonlinear saturation. High modes $\ell > 150$ may be stabilized by nonlocal electron heating of the ablation surface. This effect was not included in the *DRACO* simulations; therefore, the $\ell_{\max} = 200$ results may overestimate the

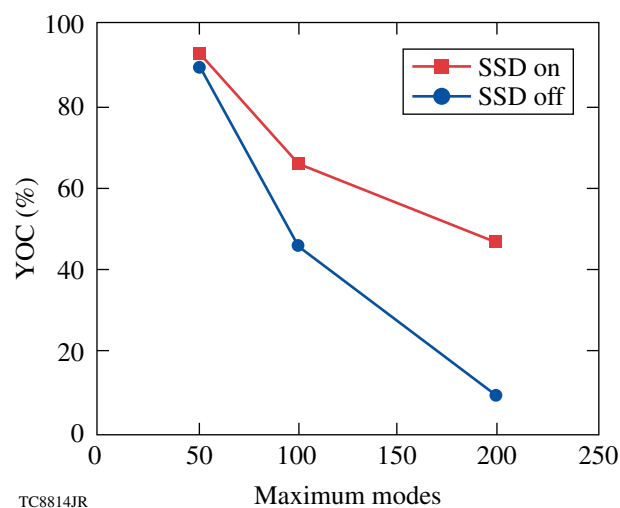


Figure 123.14

The YOC is plotted as a function of maximum modes included in multimode simulations, for the step main pulse in SSD-off and SSD-on cases.

laser-imprinting effects. The multimode simulation up to about $\ell_{\max} = 150$ shows that the resultant YOC ratio of the SSD-on case to the SSD-off is ~ 2 . This agrees well with experimental observations that will be discussed in **DRACO Simulations of Individual Cryogenic-DT Shots**, p. 122. Laser-imprinting effects reduced the YOC to $\sim 50\%$ in the SSD-on case and further to $\sim 25\%$ in the SSD-off case. Turning on the SSD improved the yield by a factor of ~ 2 , which has been seen in both *DRACO* simulations and experiments.

Separate studies for each nonuniformity source (in the case of the step main pulse) have identified three dominant nonuniformities that affect the cryogenic-DT implosion performance: (a) a power imbalance ($\ell < 10$) of $\sim 10\%$ (pickets) and $\sim 3\%$ (main

pulse) reduce the YOC to $\sim 74\%$; (b) even with a high-quality ice layer ($\sigma_{\text{rms}} = 1 \mu\text{m}$), a target offset ($\ell = 1$) $> 20 \mu\text{m}$ reduces the YOC to $\sim 30\%$; and (c) the laser imprinting ($\ell = 20$ to 150) decreases the YOC to a level of $\sim 25\%$ (SSD off) and $\sim 50\%$ (SSD on). If these three major perturbation effects were taken as a product (assuming they behave independently in a different modal range), the yield would be about $\text{YOC} \simeq 5\%$ (SSD off) and $\text{YOC} \simeq 10\%$ (SSD on). This is in agreement (within a factor of ~ 2) with the measured YOC.

DRACO Simulations of Individual Cryogenic-DT Shots

A series of low-adiabat ($\alpha = 2.0$ to 2.5), cryogenic-DT target implosions have been performed using the triple-picket pulse designs [Figs. 123.1(a) and 123.1(b)] on OMEGA. Detailed compression dynamics and areal-density measurements up to $\langle \rho R \rangle \simeq 300 \text{ mg/cm}^2$ have been described in Refs. 17 and 18. Integrated DRACO simulations for nine individual cryogenic-DT shots that resulted in a large, absolute areal density of $\langle \rho R \rangle > 180 \text{ mg/cm}^2$ ($> 80\%$ of their 1-D designs) have been performed, including the actual experimental laser and target conditions. Low-mode ($\ell \leq 50$) DRACO simulations included the long-wavelength laser nonuniformities, target offset, and ice roughness (high-mode laser imprinting was not included). The low-mode simulation results (blue squares) shown in Fig. 123.15(a) compare the simulated YOC with the experimental values (red symbols) versus the target offset. Three phases of ice roughness have been examined for each shot in the DRACO simulations. The nine experimental shots are divided into three laser conditions: (1) triple-picket plus square main pulse with SSD on (red diamonds); (2) triple-picket plus square main pulse

with SSD off (red triangles); and (3) triple-picket plus step main pulse with SSD off (red circles). Figure 123.15(a) shows that for those shots with an offset larger than $\sim 25 \mu\text{m}$, the low-mode DRACO predictions can explain the experimental YOC since the target offset together with ice roughness ($\sigma_{\text{rms}} = 1$ to $2 \mu\text{m}$) is the dominant perturbation source. The low-mode DRACO neutron-yield predictions at small offsets are generally higher, however, than the experimental observations, in which the laser imprinting dominates.

A full simulation including both the low-mode perturbations discussed above and the high-mode laser imprinting has been performed up to $\ell_{\text{max}} = 200$ for a shot with a $3\text{-}\mu\text{m}$ offset. The resultant YOC is shown by the orange square in Fig. 123.15(b). Compared to the low-mode modeling ($\ell < 50$), the high-mode simulation reduces the YOC by a factor of ~ 4 for this shot (SSD off). This is in agreement with the results presented in **Laser Imprinting**, p. 118. For other shots, the laser-imprinting effects were taken into account by “scaling” low-mode simulation results by either a factor of ~ 2 reduction in the case of SSD on or a factor of ~ 4 reduction in the case of SSD off. The resultant high-mode predictions shown in Fig. 123.15(b) are compared with experiments. The high-mode DRACO predictions with laser-imprinting effects now agree with experimental YOC within a factor of 2 or better for all shots. From Fig. 123.15(b), two distinct features can be seen: (a) the square-main-pulse shots with SSD on give an experimental YOC of $\sim 9\%$ (red diamonds), which is twice as high as that of the same pulse shape with SSD off (red triangles); (b) the three step-main-pulse shots (red circles) with SSD off

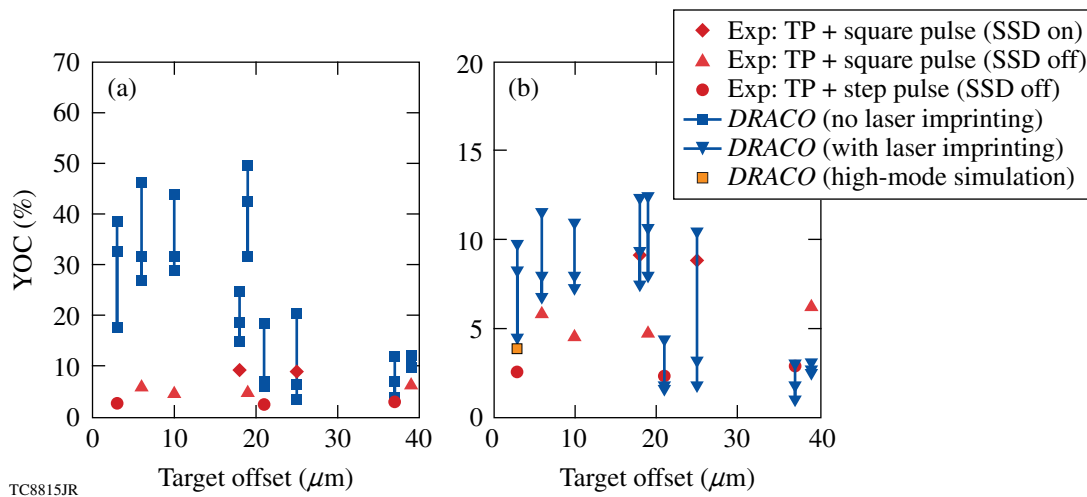


Figure 123.15

The YOC comparison between experiments and DRACO simulations for individual shots: (a) without laser imprinting and (b) with laser imprinting considered.

have a YOC level of 2% to 3%, which is a factor of 2 below the square main pulse (red triangles) with SSD off. All of these behaviors are well reproduced by the *DRACO* simulations (see also Figs. 123.6 and 123.14).

The simulated ion temperatures for these individual shots are compared with experimental measurements in Fig. 123.16. In experiments, the neutron-averaged ion temperature $\langle T_i \rangle$ is inferred by neutron time-of-flight spectroscopy.²² The measurement uncertainty is about ± 0.5 keV, shown in Fig. 123.16. The simulated $\langle T_i \rangle$ for each shot has three entries based on the phases examined. To take into account laser-imprinting effects, the high-mode scaling of $\langle T_i \rangle$ was done by either 10% or 15% reduction to the low-mode simulated $\langle T_i \rangle$, respectively, to the shots with SSD on and SSD off, as has been seen in the direct high-mode simulations. Figure 123.16 indicates that the *DRACO*-simulated $\langle T_i \rangle$ agrees with measurements within the experimental error bars. The TOC is defined as the ratio of experimental or *DRACO*-simulated $\langle T_i \rangle$ to its 1-D–designed value, e.g., $\text{TOC} = \langle T_i \rangle_{\text{exp or 2-D}} / \langle T_i \rangle_{\text{1-D}}$. The YOC versus TOC for all the shots is shown in Fig. 123.17. The experimental points are represented by red circles and the *DRACO* simulations by blue squares. The *DRACO* simulations tracked the experimental trend very well. The experimental error bar and simulation range of TOC are shown. A fitting line, $\text{YOC} \simeq 0.25 \times (\text{TOC})^4$, just passes through both experimental and simulated points for the SSD-off shots. For the cryogenic-DT implosion conditions, the neutron yield N is proportional to the hot-spot volume (V), density (ρ), ion temperature (T_i), and the burn time (t_b) as

$$N \propto V \times t_b \times \rho^2 \times T_i^4. \quad (2)$$

If Eq. (2) is divided by the 1-D clean values on each side, it gives

$$\text{YOC} = \left[\frac{\rho \sqrt{V t_b}}{(\rho \sqrt{V t_b})_{\text{1-D}}} \right]^2 \times (\text{TOC})^4. \quad (3)$$

The prefactor “0.25” of the solid green fitting line in Fig. 123.17 means that the product of hot-spot density and the square root of its volume and burn time reduced to $\sim 50\%$ of its 1-D value. This fitting characterizes the hot-spot distortion. The two shots with SSD on are above the fitting line. To have a fitting line with the same format passing through these two points, the prefactor is roughly about 0.49, meaning less hot-spot distortion (i.e., the product of hot-spot density and the square root of its volume

and burn time has been reduced to $\sim 70\%$ of its 1-D value when SSD is turned on). The dashed red fitting line for the SSD-on case plotted in Fig. 123.17 confirms the importance of SSD for these implosions.

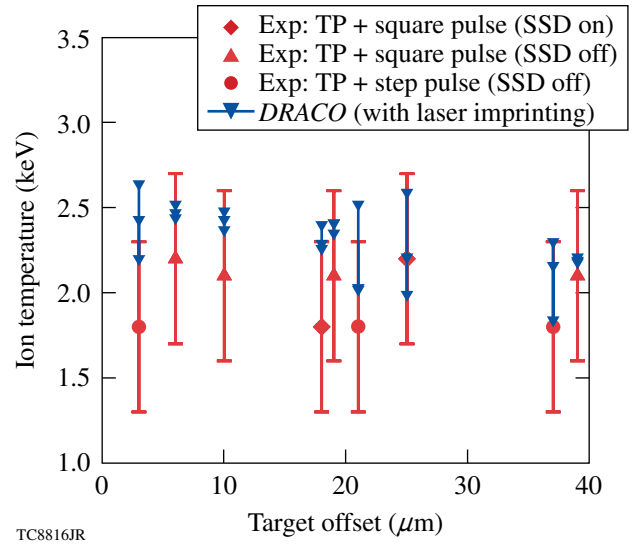


Figure 123.16 The neutron-averaged ion temperature comparison between experiments and *DRACO* simulations (with laser imprinting) for individual shots.

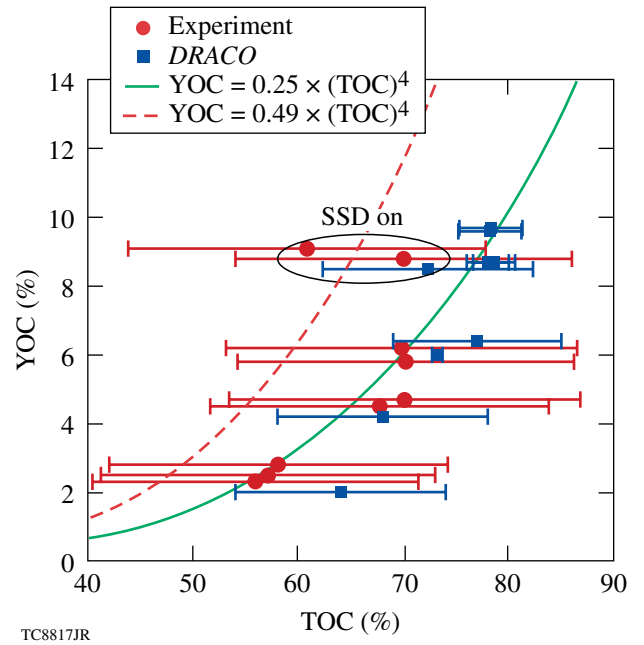


Figure 123.17 The relationship between YOC and TOC indicates the distortion of the hot-spot volume and density.

To have an insight into the hot-spot distortion caused by different perturbations, we calculated the clean volume fraction (CVF) and the volume-weighted surface area at the peak neutron-production time for different perturbed cases. The CVF is defined as the ratio of perturbed volume within the $T_i = 3$ -keV contour to the uniform case, i.e., $CVF = V(T_i > 3 \text{ keV}) / V_{1-D}(T_i > 3 \text{ keV})$. The surface area (A) along the $T_i = 3$ -keV contour can also be calculated from the simulations. Since the heat conduction loss is proportional to the surface area, we define the volume-weighted surface-area increase factor (SAIF) to be $SAIF = (A/V) / (A/V)_{1-D}$. In Fig. 123.18, we plot the YOC as a function of CVF and SAIF for (a) different target offsets of 40 μm , 20 μm , 10 μm , and 5 μm , and (b) the laser-imprinting effect. Figure 123.18(a)

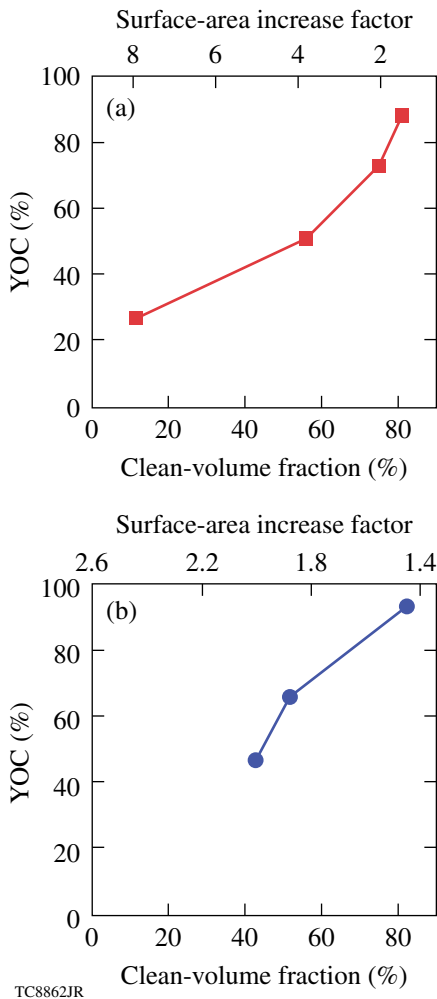


Figure 123.18 YOC as a function of the clean-volume fraction and the hot-spot surface-area-increase factor for (a) the target-offset effect and (b) the laser-imprinting effect (with step-pulse design).

shows that as the target offset increases, the CVF decreases and the volume-weighted surface area increases, leading to a smaller effective volume for neutron production and more heat loss. Therefore, when the target offset increases, the YOC becomes smaller and smaller, as does the neutron burn width. A similar analysis was also carried out for the laser-imprinting effect. The results, plotted in Fig. 123.18(b), show the different maximum modes ($\ell_{\text{max}} = 50, 100, \text{ and } 200$) included in the SSD-on-simulations (same as Fig. 123.14). When more modes were included, the clean volume fraction decreased and the surface area increased, resulting in a decrease in YOC. We noticed that the target offset did not change the peak neutron-production time, while the laser imprinting caused peak neutron production earlier than in the uniform case. This was caused by the laser imprinting inducing “spikes” that pinched into the hot spot to increase the hot-spot pressure so that the shell tended to stagnate earlier. These analyses indicate that the major perturbations of both the target offset and laser imprinting cause a reduction in hot-spot volume and an increase in hot-spot surface area (leading to quick hot-spot cooling), which ultimately lead to neutron-yield reduction.

The areal density inferred from 2-D simulations is discussed briefly here; detailed discussions were presented in Ref. 18. Using the 2-D simulations, the down-scattered neutron spectrum from which the areal density $\langle \rho R \rangle$ is inferred was calculated. An example is shown in Fig. 123.19, where the blue diamonds indicate the angle-averaged $\langle \rho R \rangle$ expected from 2-D simulations, which compare to the 1-D–designed value represented by the dashed red line. This is for the square-main-pulse case with the offset-only perturbation. The $\langle \rho R \rangle$ range

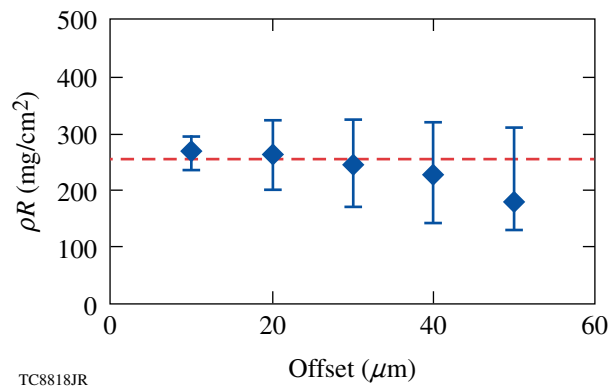


Figure 123.19 The areal density ($\langle \rho R \rangle$) inferred from the down-scattered neutron spectrum is plotted against the target offset. The dashed red line represents the corresponding 1-D value of $\langle \rho R \rangle$.

(error bar) is due to the different viewing angles around the target. Figure 123.19 indicates that the angle-averaged $\langle \rho R \rangle$ agrees with its 1-D–designed value if the offset is less than $20 \mu\text{m}$. The angle-dependent range of $\langle \rho R \rangle$ is within the MRS measurement uncertainty of $\pm 20\%$. Examinations of other perturbation sources show that the $\langle \rho R \rangle$ variation caused by perturbations is within the MRS measurement uncertainty.

Conclusions

In summary, the neutron-yield performance caused by a variety of nonuniformity sources for the cryogenic-DT implosions on OMEGA has been systematically investigated. The experimental trends are well-reproduced by 2-D *DRACO* hydrodynamic simulations: the simulated YOC agrees with experiments within a factor of 2 or better and the simulated ion temperatures $\langle T_i \rangle$ fall within the experimental uncertainty of measurements. The relationship between YOC and TOC provides an indication of how much the hot-spot volume, density, and burn time are reduced. Based on the simulations, two dominant nonuniformity sources have been identified: the target offset and laser imprinting, which mainly account for the yield reduction in the cryogenic-DT shots. Another important issue is the laser power imbalance during the pickets, which has now been improved to 3% to 4% from the previous $\sim 10\%$. The simulations suggest that to increase the YOC to an ignition-scaled level of $\sim 15\%$ to 20% for the step-main-pulse design (maintaining high-compression $\langle \rho R \rangle = 200$ to 300 mg/cm^2), the target offset must be $\leq 10 \mu\text{m}$ and SSD must be used.

ACKNOWLEDGMENT

This work was supported by the U.S. Department of Energy (DOE) Office of Inertial Confinement Fusion under Cooperative Agreement No. DE-FC52-08NA28302, the University of Rochester, and the New York State Energy Research and Development Authority.

REFERENCES

1. S. Atzeni and J. Meyer-ter-Vehn, *The Physics of Inertial Fusion: Beam Plasma Interaction, Hydrodynamics, Hot Dense Matter*, International Series of Monographs on Physics (Clarendon Press, Oxford, 2004); J. D. Lindl, *Inertial Confinement Fusion: The Quest for Ignition and Energy Gain Using Indirect Drive* (Springer-Verlag, New York, 1998).
2. J. Nuckolls *et al.*, *Nature* **239**, 139 (1972).
3. R. L. McCrory, D. D. Meyerhofer, R. Betti, R. S. Craxton, J. A. Delettrez, D. H. Edgell, V. Yu Glebov, V. N. Goncharov, D. R. Harding, D. W. Jacobs-Perkins, J. P. Knauer, F. J. Marshall, P. W. McKenty, P. B. Radha, S. P. Regan, T. C. Sangster, W. Seka, R. W. Short, S. Skupsky, V. A. Smalyuk, J. M. Soures, C. Stoeckl, B. Yaakobi, D. Shvarts, J. A. Frenje, C. K. Li, R. D. Petrasso, and F. H. Séguin, *Phys. Plasmas* **15**, 055503 (2008).
4. J. D. Lindl, *Phys. Plasmas* **2**, 3933 (1995).
5. S. E. Bodner, *Phys. Rev. Lett.* **33**, 761 (1974); H. Takabe *et al.*, *Phys. Fluids* **28**, 3676 (1985); H. J. Kull and S. I. Anisimov, *Phys. Fluids* **29**, 2067 (1986); A. B. Bud'ko and M. A. Liberman, *Phys. Fluids B* **4**, 3499 (1992); V. V. Bychkov, S. M. Goldberg, and M. A. Liberman, *Phys. Plasmas* **1**, 2976 (1994); J. Sanz, *Phys. Rev. Lett.* **73**, 2700 (1994); J. G. Wouchuk and A. R. Piriz, *Phys. Plasmas* **2**, 493 (1995).
6. R. Betti, V. N. Goncharov, R. L. McCrory, P. Sorotokin, and C. P. Verdon, *Phys. Plasmas* **3**, 2122 (1996); V. N. Goncharov, P. McKenty, S. Skupsky, R. Betti, R. L. McCrory, and C. Cherfils-Clérouin, *Phys. Plasmas* **7**, 5118 (2000).
7. P. Y. Chang, R. Betti, B. K. Spears, K. S. Anderson, J. Edwards, M. Fatenejad, J. D. Lindl, R. L. McCrory, R. Nora, and D. Shvarts, *Phys. Rev. Lett.* **104**, 135002 (2010).
8. J. Paisner *et al.*, *Laser Focus World* **30**, 75 (1994); E. M. Campbell and W. J. Hogan, *Plasma Phys. Control. Fusion* **41**, B39 (1999).
9. S. W. Haan, *Phys. Rev. A* **39**, 5812 (1989); M. M. Marinak *et al.*, *Phys. Rev. Lett.* **80**, 4426 (1998).
10. B. A. Remington *et al.*, *Phys. Rev. Lett.* **73**, 545 (1994); K. S. Budil *et al.*, *Phys. Rev. Lett.* **76**, 4536 (1996); C. J. Pawley *et al.*, *Phys. Plasmas* **6**, 565 (1999); J. P. Knauer, K. Anderson, R. Betti, T. J. B. Collins, V. N. Goncharov, P. W. McKenty, D. D. Meyerhofer, P. B. Radha, S. P. Regan, T. C. Sangster, V. A. Smalyuk, J. A. Frenje, C. K. Li, R. D. Petrasso, and F. H. Séguin, *Phys. Plasmas* **12**, 056306 (2005); V. A. Smalyuk, O. Sadot, J. A. Delettrez, D. D. Meyerhofer, S. P. Regan, and T. C. Sangster, *Phys. Rev. Lett.* **95**, 215001 (2005); H. Azechi *et al.*, *Phys. Rev. Lett.* **98**, 045002 (2007).
11. V. A. Smalyuk, S. X. Hu, V. N. Goncharov, D. D. Meyerhofer, T. C. Sangster, D. Shvarts, C. Stoeckl, B. Yaakobi, J. A. Frenje, and R. D. Petrasso, *Phys. Rev. Lett.* **101**, 025002 (2008).
12. V. A. Smalyuk, S. X. Hu, V. N. Goncharov, D. D. Meyerhofer, T. C. Sangster, C. Stoeckl, and B. Yaakobi, *Phys. Plasmas* **15**, 082703 (2008).
13. V. A. Smalyuk, S. X. Hu, J. D. Hager, J. A. Delettrez, D. D. Meyerhofer, T. C. Sangster, and D. Shvarts, *Phys. Rev. Lett.* **103**, 105001 (2009).
14. V. A. Smalyuk, S. X. Hu, J. D. Hager, J. A. Delettrez, D. D. Meyerhofer, T. C. Sangster, and D. Shvarts, *Phys. Plasmas* **16**, 112701 (2009).
15. T. R. Boehly, D. L. Brown, R. S. Craxton, R. L. Keck, J. P. Knauer, J. H. Kelly, T. J. Kessler, S. A. Kumpan, S. J. Loucks, S. A. Letzring, F. J. Marshall, R. L. McCrory, S. F. B. Morse, W. Seka, J. M. Soures, and C. P. Verdon, *Opt. Commun.* **133**, 495 (1997).
16. S. X. Hu, P. B. Radha, J. A. Marozas, R. Betti, T. J. B. Collins, R. S. Craxton, J. A. Delettrez, D. H. Edgell, R. Epstein, V. N. Goncharov, I. V. Igumenshchev, F. J. Marshall, R. L. McCrory, D. D. Meyerhofer, S. P. Regan, T. C. Sangster, S. Skupsky, V. A. Smalyuk, Y. Elbaz, and D. Shvarts, *Phys. Plasmas* **16**, 112706 (2009).
17. V. N. Goncharov, T. C. Sangster, T. R. Boehly, S. X. Hu, I. V. Igumenshchev, F. J. Marshall, R. L. McCrory, D. D. Meyerhofer, P. B. Radha, W. Seka, S. Skupsky, C. Stoeckl, D. T. Casey, J. A. Frenje, and R. D. Petrasso, *Phys. Rev. Lett.* **104**, 165001 (2010).

18. T. C. Sangster, V. N. Goncharov, R. Betti, T. R. Boehly, D. T. Casey, T. J. B. Collins, R. S. Craxton, J. A. Delettrez, D. H. Edgell, R. Epstein, K. A. Fletcher, J. A. Frenje, V. Yu. Glebov, D. R. Harding, S. X. Hu, I. V. Igumenshchev, J. P. Knauer, S. J. Loucks, C. K. Li, J. A. Marozas, F. J. Marshall, R. L. McCrory, P. W. McKenty, D. D. Meyerhofer, P. M. Nilson, S. P. Padalino, R. D. Petrasso, P. B. Radha, S. P. Regan, F. H. Séguin, W. Seka, R. W. Short, D. Shvarts, S. Skupsky, V. A. Smalyuk, J. M. Soures, C. Stoeckl, W. Theobald, and B. Yaakobi, *Phys. Plasmas* **17**, 056312 (2010).
19. P. B. Radha, T. J. B. Collins, J. A. Delettrez, Y. Elbaz, R. Epstein, V. Yu. Glebov, V. N. Goncharov, R. L. Keck, J. P. Knauer, J. A. Marozas, F. J. Marshall, R. L. McCrory, P. W. McKenty, D. D. Meyerhofer, S. P. Regan, T. C. Sangster, W. Seka, D. Shvarts, S. Skupsky, Y. Srebro, and C. Stoeckl, *Phys. Plasmas* **12**, 056307 (2005); D. Keller, T. J. B. Collins, J. A. Delettrez, P. W. McKenty, P. B. Radha, B. Whitney, and G. A. Moses, *Bull. Am. Phys. Soc.* **44**, 37 (1999).
20. T. R. Boehly, D. H. Munro, P. M. Celliers, R. E. Olson, D. G. Hicks, V. N. Goncharov, G. W. Collins, H. F. Robey, S. X. Hu, J. A. Marozas, T. C. Sangster, O. L. Landen, and D. D. Meyerhofer, *Phys. Plasmas* **16**, 056302 (2009).
21. J. A. Frenje, K. M. Green, D. G. Hicks, C. K. Li, F. H. Séguin, R. D. Petrasso, T. C. Sangster, T. W. Phillips, V. Yu. Glebov, D. D. Meyerhofer, S. Roberts, J. M. Soures, C. Stoeckl, K. Fletcher, S. Padalino, and R. J. Leeper, *Rev. Sci. Instrum.* **72**, 854 (2001).
22. T. J. Murphy, R. E. Chrien, and K. A. Klare, *Rev. Sci. Instrum.* **68**, 610 (1997).
23. J. A. Marozas, F. J. Marshall, R. S. Craxton, I. V. Igumenshchev, S. Skupsky, M. J. Bonino, T. J. B. Collins, R. Epstein, V. Yu. Glebov, D. Jacobs-Perkins, J. P. Knauer, R. L. McCrory, P. W. McKenty, D. D. Meyerhofer, S. G. Noyes, P. B. Radha, T. C. Sangster, W. Seka, and V. A. Smalyuk, *Phys. Plasmas* **13**, 056311 (2006).
24. B. I. Bennett *et al.*, Los Alamos National Laboratory, Los Alamos, NM, Report LA-7130 (1978).
25. W. F. Huebner *et al.*, Los Alamos National Laboratory, Los Alamos, NM, Report LA-6760-M (1977).
26. R. C. Malone, R. L. McCrory, and R. L. Morse, *Phys. Rev. Lett.* **34**, 721 (1975).
27. S. P. Regan, R. Epstein, V. N. Goncharov, I. V. Igumenshchev, D. Li, P. B. Radha, H. Sawada, W. Seka, T. R. Boehly, J. A. Delettrez, O. V. Gotchev, J. P. Knauer, J. A. Marozas, F. J. Marshall, R. L. McCrory, P. W. McKenty, D. D. Meyerhofer, T. C. Sangster, D. Shvarts, S. Skupsky, V. A. Smalyuk, B. Yaakobi, and R. C. Mancini, *Phys. Plasmas* **14**, 056305 (2007).
28. T. R. Boehly, E. Vianello, J. E. Miller, R. S. Craxton, T. J. B. Collins, V. N. Goncharov, I. V. Igumenshchev, D. D. Meyerhofer, D. G. Hicks, P. M. Celliers, and G. W. Collins, *Phys. Plasmas* **13**, 056303 (2006).
29. S. X. Hu, V. Smalyuk, V. N. Goncharov, S. Skupsky, T. C. Sangster, D. D. Meyerhofer, and D. Shvarts, *Phys. Rev. Lett.* **101**, 055002 (2008).
30. V. N. Goncharov, O. V. Gotchev, E. Vianello, T. R. Boehly, J. P. Knauer, P. W. McKenty, P. B. Radha, S. P. Regan, T. C. Sangster, S. Skupsky, V. A. Smalyuk, R. Betti, R. L. McCrory, D. D. Meyerhofer, and C. Cherfils-Clérouin, *Phys. Plasmas* **13**, 012702 (2006).
31. S. X. Hu, V. A. Smalyuk, V. N. Goncharov, J. P. Knauer, P. B. Radha, I. V. Igumenshchev, J. A. Marozas, C. Stoeckl, B. Yaakobi, D. Shvarts, T. C. Sangster, P. W. McKenty, D. D. Meyerhofer, S. Skupsky, and R. L. McCrory, *Phys. Rev. Lett.* **100**, 185003 (2008).
32. I. V. Igumenshchev, F. J. Marshall, J. A. Marozas, V. A. Smalyuk, R. Epstein, V. N. Goncharov, T. J. B. Collins, T. C. Sangster, and S. Skupsky, *Phys. Plasmas* **16**, 082701 (2009).
33. Y. Lin, T. J. Kessler, and G. N. Lawrence, *Opt. Lett.* **20**, 764 (1995).
34. T. R. Boehly, V. A. Smalyuk, D. D. Meyerhofer, J. P. Knauer, D. K. Bradley, R. S. Craxton, M. J. Guardalben, S. Skupsky, and T. J. Kessler, *J. Appl. Phys.* **85**, 3444 (1999).
35. J. A. Frenje, C. K. Li, F. H. Séguin, D. T. Casey, R. D. Petrasso, T. C. Sangster, R. Betti, V. Yu. Glebov, and D. D. Meyerhofer, *Phys. Plasmas* **16**, 042704 (2009).
36. D. R. Harding, D. D. Meyerhofer, S. J. Loucks, L. D. Lund, R. Janezic, L. M. Elasky, T. H. Hinterman, D. H. Edgell, W. Seka, M. D. Wittman, R. Q. Gram, D. Jacobs-Perkins, R. Early, T. Duffy, and M. J. Bonino, *Phys. Plasmas* **13**, 056316 (2006).
37. T. C. Sangster, R. Betti, R. S. Craxton, J. A. Delettrez, D. H. Edgell, L. M. Elasky, V. Yu. Glebov, V. N. Goncharov, D. R. Harding, D. Jacobs-Perkins, R. Janezic, R. L. Keck, J. P. Knauer, S. J. Loucks, L. D. Lund, F. J. Marshall, R. L. McCrory, P. W. McKenty, D. D. Meyerhofer, P. B. Radha, S. P. Regan, W. Seka, W. T. Shmayda, S. Skupsky, V. A. Smalyuk, J. M. Soures, C. Stoeckl, B. Yaakobi, J. A. Frenje, C. K. Li, R. D. Petrasso, F. H. Séguin, J. D. Moody, J. A. Atherton, B. D. MacGowan, J. D. Kilkenny, T. P. Bernat, and D. S. Montgomery, *Phys. Plasmas* **14**, 058101 (2007).
38. J. A. Koch *et al.*, *Fusion Technol.* **38**, 123 (2000).
39. D. H. Edgell, W. Seka, R. S. Craxton, L. M. Elasky, D. R. Harding, R. L. Keck, and M. D. Wittman, *Fusion Sci. Technol.* **49**, 616 (2006).
40. V. N. Goncharov, S. Skupsky, T. R. Boehly, J. P. Knauer, P. McKenty, V. A. Smalyuk, R. P. J. Town, O. V. Gotchev, R. Betti, and D. D. Meyerhofer, *Phys. Plasmas* **7**, 2062 (2000).
41. R. Epstein, *J. Appl. Phys.* **82**, 2123 (1997).
42. S. P. Regan, J. A. Marozas, J. H. Kelly, T. R. Boehly, W. R. Donaldson, P. A. Jaanimagi, R. L. Keck, T. J. Kessler, D. D. Meyerhofer, W. Seka, S. Skupsky, and V. A. Smalyuk, *J. Opt. Soc. Am. B* **17**, 1483 (2000).
43. S. Skupsky, R. W. Short, T. Kessler, R. S. Craxton, S. Letzring, and J. M. Soures, *J. Appl. Phys.* **66**, 3456 (1989); J. E. Rothenberg, *J. Opt. Soc. Am. B* **14**, 1664 (1997).
44. J. A. Marozas, J. D. Zuegel, and T. J. B. Collins, *Bull. Am. Phys. Soc.* **54**, 306 (2009).
45. *LLE Review Quarterly Report* **82**, 49, Laboratory for Laser Energetics, University of Rochester, Rochester, NY, LLE Document No. DOE/SF/19460-344 (2000).
46. V. N. Goncharov, J. P. Knauer, P. W. McKenty, P. B. Radha, T. C. Sangster, S. Skupsky, R. Betti, R. L. McCrory, and D. D. Meyerhofer, *Phys. Plasmas* **10**, 1906 (2003).

47. V. A. Smalyuk, D. Shvarts, R. Betti, J. A. Delettrez, D. H. Edgell, V. Yu. Glebov, V. N. Goncharov, R. L. McCrory, D. D. Meyerhofer, P. B. Radha, S. P. Regan, T. C. Sangster, W. Seka, S. Skupsky, C. Stoeckl, B. Yaakobi, J. A. Frenje, C. K. Li, R. D. Petrasso, and F. H. Séguin, *Phys. Rev. Lett.* **100**, 185005 (2008).
48. K. Anderson and R. Betti, *Phys. Plasmas* **10**, 4448 (2003).
49. G. Schurtz *et al.*, *Phys. Rev. Lett.* **98**, 095002 (2007).
50. R. Betti, V. N. Goncharov, R. L. McCrory, and C. P. Verdon, *Phys. Plasmas* **5**, 1446 (1998).

X-Ray Radiography of Cryogenic Implosions on OMEGA

Introduction

Radiographs of cryogenic implosions on OMEGA¹ have been obtained using short-pulse, aluminum K-shell emission-line backlighters driven by the OMEGA EP short-pulse laser.² These experiments³ have been designed to implode cryogenic D₂/DT shells and to achieve conditions that scale up to the thermonuclear ignition conditions⁴ that can be attained with the much greater energy available on the NIF (National Ignition Facility).⁵ X-ray radiography is being developed to verify the integrity of the imploding cryogenic shells and to corroborate the compression performance measured from charged-particle spectra.³ The backlighter is chosen so that the emission-line energies occur where the energy-dependent optical thicknesses of the imploded cores will provide a measurable range of radiographic transmission near the time of peak compression. Backlighter simulations show that it can overcome the imploded core self-emission. The OMEGA EP short-pulse capability provides a backlight exposure time that is short enough to discern the overall shell integrity and convergence, as well as shell structure resulting from the low-order hydrodynamic effects of drive nonuniformity, target positioning offset, and ice-layer nonuniformity. Numerical simulations of the first measured cryogenic implosion radiographs⁶ are used to assess the implosion performance in advance of peak compression. The radiographic simulation takes into account the spatial and temporal resolution, the camera spectral response, and the backlighter spectrum. Radial mass distributions are obtained from the radiographs using Abel inversion and the known temperature and density dependence of the free-free (FF) opacity of the hydrogen shell. This extends similar analyses of warm-shell radiographs, based on the simpler temperature and density dependence of the CH bound-free (BF) opacity, which has been applied to warm polar-drive implosions.⁷ Radiography based on Compton scattering of hard backlight x rays approaching 100-keV energy^{8,9} is being investigated as an alternative approach.

The measurements presented here are preliminary but are consistent with simulated implosion performance and radiography in advance of peak compression. They are valuable in

planning future measurements that will be extended to the final phases of the implosion.

This article describes the experimental configurations. The atomic physics of both FF and Compton radiography, which is the basis for analyzing radiographs and for anticipating the relative advantages of each method, is described. The simulations demonstrate the feasibility of soft x-ray FF radiography and hard x-ray Compton radiography. Simulations of backlighters and radiographs are based on quantitative atomic physics and radiative transport. Finally, the available FF radiographs are analyzed, and conclusions are presented.

Experimental Configurations

The initial experimental configuration with FF radiography of cryogenic implosions includes a 10- μm -thick, 1-mm-sq Al-foil area backlighter target attached to the wire support for a silk-mounted target (Fig. 123.20). The backlighter foil is irradiated with a single 1-kJ, 10-ps OMEGA EP beam. Time-resolved backlit images are recorded through a pinhole array with an x-ray framing camera that provides 30-ps time gating.¹⁰ The energy band, including the Al K-shell lines, is isolated using transmission filters and Ir-coated mirrors that reject hard backlighter x rays above 2 keV. One measured image is shown. The shadow of the imploding shell is visible against the emission from the irradiated spot on the backlighter foil. Further development of this diagnostic will include narrowing the camera bandwidth, possibly employing a monochromatic imaging device to further reduce the background caused by self-emission from the imploded target.

The experimental configuration for Compton radiography, shown in Fig. 123.21, is very similar to the configuration for FF backlighting.¹¹ The backlighter target is a 10- μm Au microwire embedded in a 300- μm -sq CH foil substrate. The 1-kJ, 10-ps OMEGA EP beam is focused onto a small 100- μm -diam spot to create a pulse of suprathermal electrons that drive a burst of K α and bremsstrahlung emission from the microwire in a broad spectral range centered near 90 keV. By aligning the wire along the line of sight to the target, the end-on view

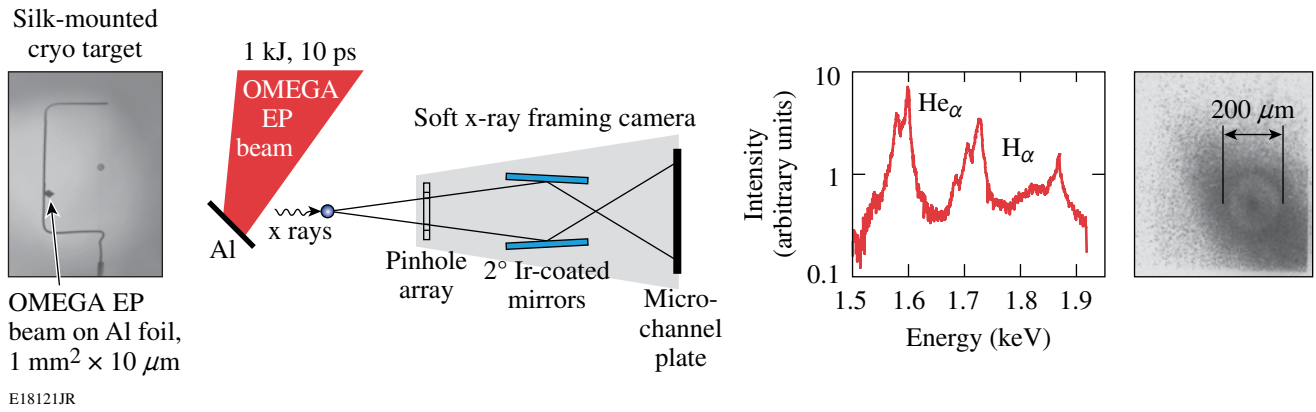


Figure 123.20

The configuration of our initial experiments with free-free (FF) radiography of cryogenic implosions includes an Al-foil area backlighter target attached to the wire support of a silk-mounted target. The backlight from the foil is driven with a single 1-kJ, 10-ps OMEGA EP beam. Time-resolved backlit images are recorded through a pinhole array with an x-ray framing camera. One measured image is shown. The shadow of the imploding shell is visible against the emission from the irradiated spot on the backlighter foil. The imaged photon energy band, including the Al K-shell lines, is isolated using transmission filters and Ir-coated mirrors.

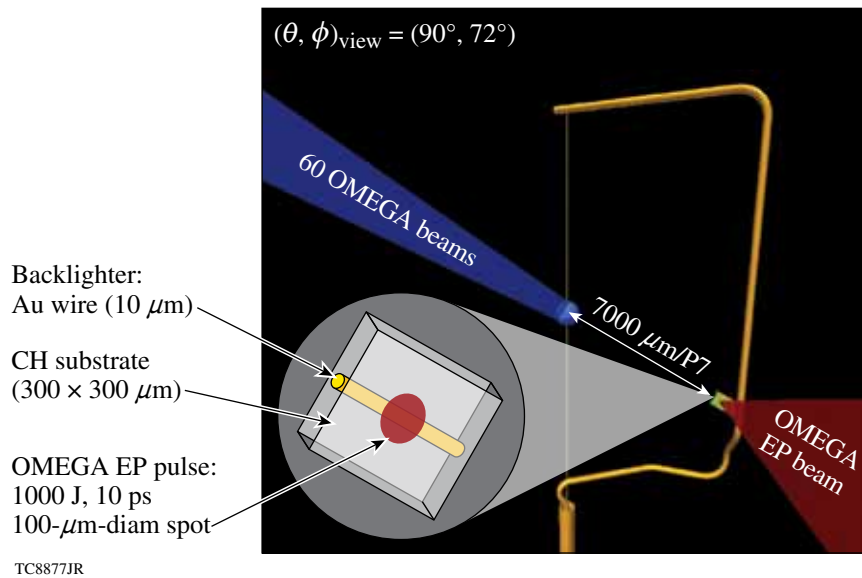


Figure 123.21

The configuration under development for Compton radiography is very similar to the configuration for FF backlighting. The backlighter target is a 10- μ m Au microwire embedded in a CH-foil substrate. The 1-kJ, 10-ps OMEGA EP beam is focused to a small 100- μ m-diam spot to create a burst of K α and bremsstrahlung emission from the microwire in a broad spectral range centered near 90 keV. The end-on view of this wire appears to the image plate as a point backlighter.

of this wire appears from the direction of the image plate as a point backlighter. Preliminary radiographs of warm CH target implsions have been obtained with this configuration on OMEGA by Tommasini.⁹ This method is currently being applied to cryogenic implsions.

Atomic Physics Basis for Radiography

A radiograph is formed by the attenuation of backlighter emission by an object, creating a shadow of the object in an imaging device. This process is illustrated in Fig. 123.22 for a spherical object creating a circularly symmetric shadow. The image intensity $I(x)$ is a central lineout of the measured intensity distribution along the x axis of the image plane coordinates x,y with y fixed accordingly. All the backlighter rays, propagating in parallel, create an orthographic projection of the object on the image plane, as if the backlighter were infinitely far away. The intensity $I(x)$ is the attenuated backlighter intensity I_{BL} . The attenuation is given by $I(x) = I_{BL} \exp[-\tau(x)]$, where $\tau(x)$, the optical thickness of the object along a particular line of sight from the backlighter to the point x on the image plane, is the path integral $\tau(x) = \int \kappa(s) ds$ of the opacity of the object $\kappa(s)$, expressed as a function of position along the path, indicated by the path-length parameter s (Ref. 12). If the opacity of the object is a known function of its conditions, an optical thickness measurement will provide a diagnostic of conditions along the line of sight. Writing $\kappa[r(s)]$ in Fig. 123.22 shows that the points on the path s correspond to points r in a spherical opacity distribution and that the two are related in a well-defined way.

This relationship forms the basis for inferring $\kappa(r)$ from $\tau(x)$ by Abel inversion,¹³ as described below.

The FF, bound-free (BF), and Compton radiography techniques are distinguished by the properties of the respective dominant absorption or scattering processes involved. The FF and BF processes have strong material dependence and share the same ν^{-3} spectral dependence, while the effective radiographic mass absorption coefficient of Compton scattering is only weakly dependent on material composition and the backlighter spectrum. Figure 123.23 shows these three individual contributions [FF (red), BF (blue), Compton (black)] plotted for deuterium (solid lines) at a typical coasting-phase shell condition, $\rho = 3 \text{ g/cm}^3$ and $kT = 25 \text{ eV}$, and for carbon (dashed lines) at $\rho = 0.5 \text{ g/cm}^3$ and at a higher temperature, $kT = 100 \text{ eV}$, where it might exist in trace concentrations at the outer edge of the imploding shell, near a cooling remnant of the hot ablation region. Blue ovals indicate the key process and typical spectral range for FF radiography of cryogenic D_2 shells, BF radiography of warm CH shells, and Compton radiography of most materials. For the purpose of radiography, it is acceptable to think of opacity or attenuation being caused by Compton scattering, even though Compton scattering is not an absorption process in which photons are destroyed. At the photon energies being considered, the scattering is only about 30% stronger in the forward direction than the backward direction.¹⁴ This is sufficiently isotropic that nearly every scattered photon is effectively removed from the field of view, as if it has

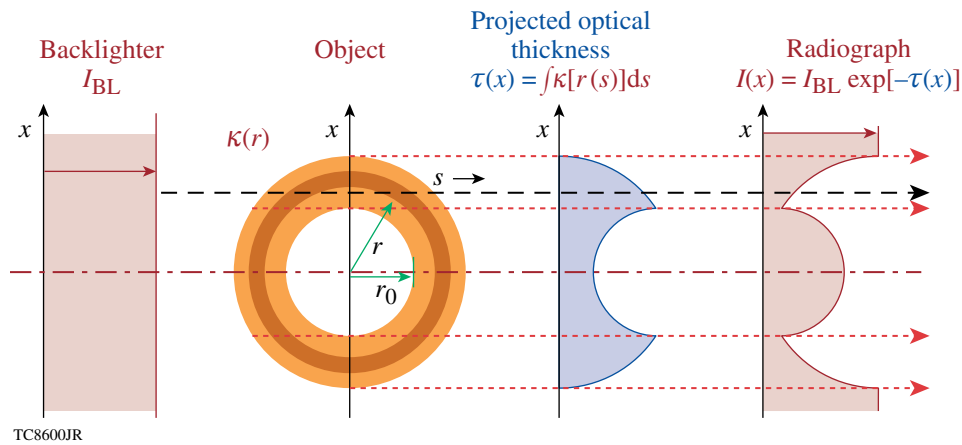
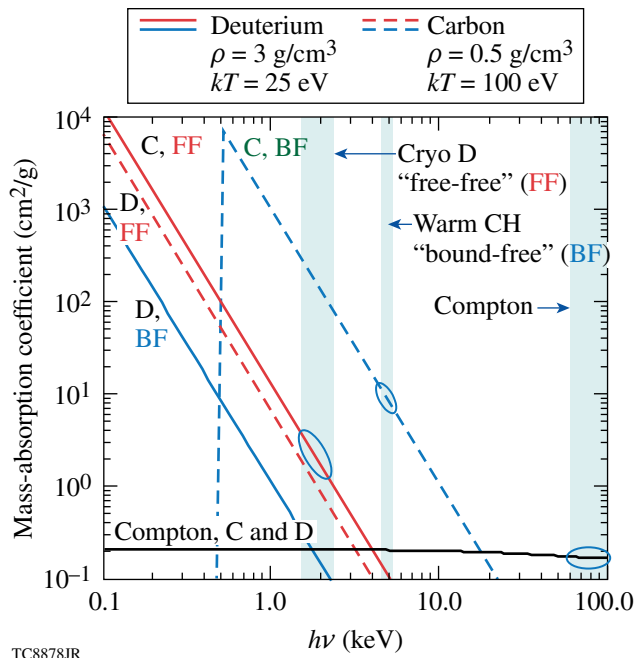


Figure 123.22 Hollow shells with radial opacity profiles $\kappa(r)$ form characteristically limb-darkened circularly symmetric shadows in the image plane, here represented as $I(x)$. A typical backlighter emission ray is shown sampling the absorbing shell on its way to the image plane, where the recorded intensity is determined by the integral of the opacity along its path, the projected optical thickness. Abel inversion recovers the radial opacity distribution from the optical depth profile projected onto the image plane.



TC8878JR

Figure 123.23

The FF, BF, and Compton radiographies are distinguished by the properties of the respective attenuation processes involved. FF and BF mass-absorption coefficients have strong material and spectral dependence, while the effective mass-absorption coefficient of Compton scattering is only weakly dependent on material composition and the backlighter spectrum. The individual process [FF (red), BF (blue), Compton (black)] contributions are plotted for carbon (dashed lines) and deuterium (solid lines) at a typical set of coasting-phase conditions for an imploding deuterium shell. Blue ovals indicate the key process and spectral region for FF radiography of cryogenic deuterium shells, BF radiography of warm CH shells, and Compton radiography of most materials.

been absorbed, so the total Compton-scattering cross section for radiography may be treated as an absorption cross section.

Target optical thicknesses of order unity are desirable for radiography. As a typical OMEGA target implosion approaches peak compression, the mass areal density of a shell grows by more than an order of magnitude within roughly 100 ps, peaking at roughly 0.3 g/cm^2 (Ref. 3). Based on this, the mass-absorption coefficients in the neighborhood of $10 \text{ cm}^2/\text{g}$ are appropriate. For BF and FF radiography, which share the same strong ν^{-3} spectral dependence, this determines the appropriate range of backlighter energy. The Compton cross section, on the other hand, given by the Klein–Nishina formula, varies very slowly with photon energy out to 100 keV (Ref. 15), the upper limit of hard x-ray backlighters proposed thus far.⁸ This makes Compton scattering the dominant radiography process for light elements at high-photon energies. The advantage

of radiography with hard x rays is that the self-emission of the imploded target, which decreases rapidly with photon energy as $\exp(-h\nu/kT)$, does not create significant background intensity at these high backlighter photon energies. The main disadvantage of Compton radiography is that the attenuation by OMEGA-imploded shells is small, of the order of several percent at peak compression. An advantage of Compton scattering is that its very weak spectral dependence simplifies the analysis of Compton radiographs. With broadband BF and FF radiography, the spectral content of the backlighter and the spectral response of the imaging system must be known accurately because of the strong spectral dependence of BF and FF opacity. The weak spectral dependence of Compton scattering is also a disadvantage because one cannot adjust the backlighter energy to obtain anything more favorable than weak attenuation. Compton radiography will be better suited to the NIF,⁵ where implosions approaching the 3.0-g/cm^2 mass areal density required for ignition¹⁶ will provide optical thicknesses an order of magnitude larger than on OMEGA.

The mass-absorption-coefficient curves for Compton scattering by carbon and deuterium are indistinguishable, so they are represented by the same black curve in Fig. 123.23. For hard x rays, all electrons, free and bound, contribute identically to the mass-absorption coefficient.¹⁵ Since most of the naturally occurring elements from helium through chlorine have equal proton and neutron numbers, they have very nearly the same number of electrons per mass and, therefore, very nearly equal Compton mass-absorption coefficients. The mass-absorption coefficient of heavier elements decreases slowly with atomic number, as the proton/neutron number ratio decreases. Under compressed-shell conditions beyond the late coasting phase, carbon is more opaque than hydrogen by a few orders of magnitude, due, in large part, to the strong atomic-number Z^4 scaling of the K-shell photoionization cross section and the dominant abundance of helium-like carbon, with two bound K-shell electrons per ion. Hydrogen, on the other hand, has a negligible population of bound states under these conditions and, as a result, absorbs primarily through FF absorption. This means that a trace of carbon impurity in an imploding hydrogen shell will dominate its radiograph. If the purpose of the radiograph is to observe the mass distribution, then a hydrodynamically irrelevant trace of carbon contaminant can substantially alter the apparent mass distribution in a FF radiograph of an imploding cryogenic shell, while Compton radiographs will remain largely unaffected. If the purpose of the radiograph is to detect carbon contamination by fuel–shell mix, it will be visible through its high BF opacity at the soft

energies of FF radiography and invisible at the hard energies of Compton radiography.

In the case of radiography of CD shells,⁷ the opacity is dominated by the BF opacity of the helium-like species of carbon over the wide range of temperature and density expected in imploding shells. The remaining dependencies are $\rho\nu^{-3}$. Assuming that the backlighter spectrum and the detector response define a single effective photon energy, the opacity becomes simply a product of the mass density ρ and a known constant factor. Consequently, each optical thickness measurement is equivalent to a measurement of $\int \rho ds$, the areal density along a particular line of sight. The analysis of D₂ shell FF radiographs is simplified by the fact that ionization under imploded shell conditions is likely to be sufficiently complete that BF transitions will not compete with the FF opacity. The remaining parameter dependencies are $\rho^2 T^{-1/2} \nu^{-3}$, so each optical thickness measurement in a FF radiograph at a known ν is equivalent to a $\int \rho^2 T^{-1/2} ds$ measurement. Given an independent determination of the temperature T , such as from another diagnostic or from a simulation, the integral $\int \rho^2 ds$ remains. The radial density-squared profile can be obtained from this data by Abel inversion, just as has been done with CD shells.⁷ The uncertainty of the density inferred from FF opacity is correlated with the uncertainty in the temperature, but only weakly, since the temperature scaling of FF opacity is $T^{-1/4}$, relative to the density dependence.

The opacities of both CD and D₂ follow these simple temperature and density-scaling laws over much of the range of conditions of compressed imploded shells. This is shown in Fig. 123.24 in two plots of their respective temperature-and-density-scaled opacities as functions of temperature. The photon energy is fixed at $h\nu = 2$ keV, and the scaled opacity is plotted for four different densities roughly a factor of 10 apart. In Fig. 123.24(a), the plotted quantity is equal to the opacity divided by ρ , corresponding to the scaling of BF absorption, which dominates the opacity of CD; Fig. 123.24(b) shows the opacity of D₂ divided by $\rho^2/T^{1/2}$, corresponding to the scaling of FF absorption, which dominates the opacity of D₂ under these conditions. The nearly constant value over a wide range of temperature indicates the validity of the respective temperature and density scalings. The CD opacity drops from this scaling at temperatures above 100 eV because the bound electrons are removed by collisional ionization and rises above this scaling at the highest density because of the contribution of FF absorption that grows with density as ρ^2 . The simple scaling of the FF opacity of D₂ is seen to hold for all the conditions plotted, except for the lowest density, where bound electron

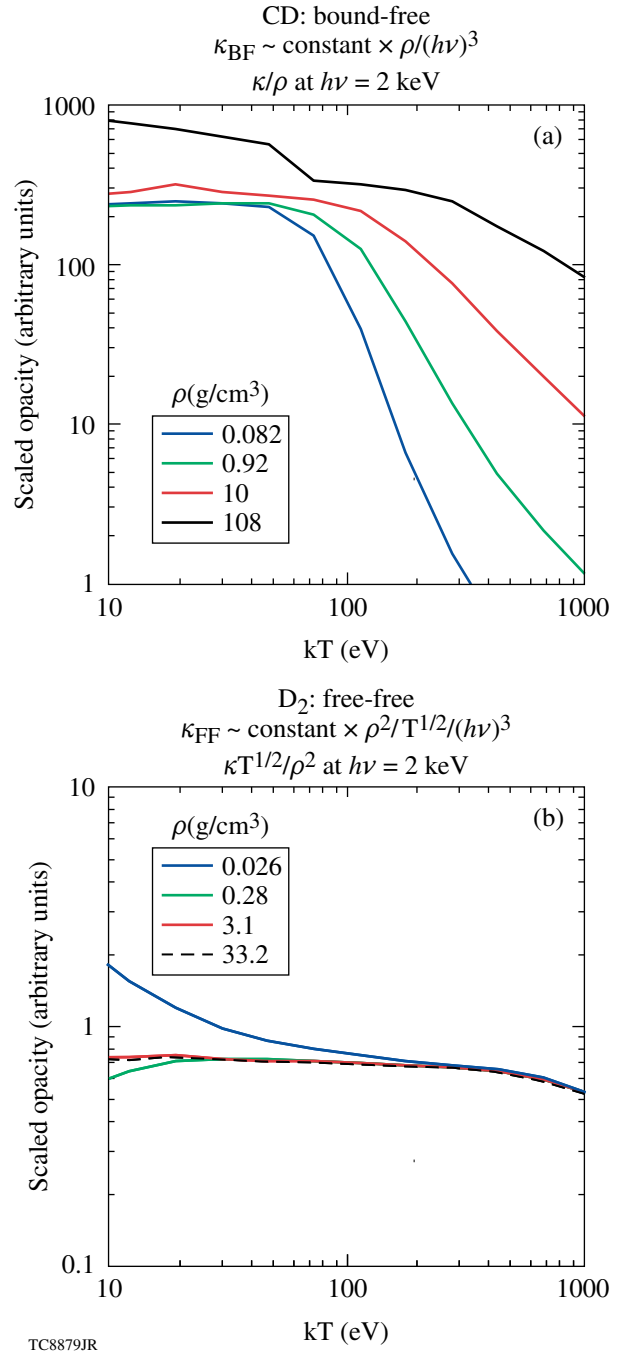


Figure 123.24 The opacities of CD and D₂ both follow simple temperature- and density-scaling laws that cover much of the range of conditions of compressed imploded shells. This is shown in two plots of their respective scaled opacities as functions of temperature. Plot (a) shows the opacity divided by ρ , corresponding to the scaling of BF absorption, which dominates the opacity of CD. Plot (b) shows the opacity of D₂ divided by $\rho^2/T^{1/2}$, corresponding to the scaling of FF absorption, which dominates the opacity of D₂ under these conditions. The scaled opacities are plotted for four different densities at roughly a factor of 10 apart. The photon energy is fixed at $h\nu = 2$ keV.

states become marginally abundant at the lowest temperatures. The scaling of the FF opacity is not as simple as that of BF opacity, but it appears to be slightly more reliable, at least over the conditions and spectral range shown.

Ideally, the backlighter should be monochromatic so that ν is a known constant. If the opacity of the object varies significantly over the joint bandwidth defined by the backlighter spectrum and the detector response, it can significantly alter the transmitted backlighter spectrum. Therefore, however one might define a spectrum-averaged backlighter energy, its value may vary over the plane of the radiograph. This almost certainly will not be an issue with Compton radiography since the effective opacity, as shown in Fig. 123.23, varies very slowly with photon energy. In any case, the main benefit of a narrow-bandwidth detector is that it limits the background caused by self-emission from the target.

Feasibility of Soft X-Ray Free-Free Radiography

The simulation of cryogenic implosion radiography employs several tools. The target implosions are simulated in 1-D by *LILAC*¹⁷ and in 2-D by *DRACO*,¹⁸ which includes the effects of target offset and irradiation nonuniformity (see “Two-Dimensional Simulations of the Neutron Yield in Cryogenic-DT Implosions on OMEGA,” p. 111). The short-pulse foil hydrodynamics are simulated in 1-D by *LILAC*. Both the backlight emission and the implosion radiography are simulated separately by the post-processor Spect3D.¹⁹ Spect3D calculates radiation transport using tabulated opacity and emissivity data based on detailed atomic models for the radiograph simulations. For the backlighter simulations, these quantities are calculated in real time, using time-dependent, non-LTE atomic-level kinetics, including self-consistent nonlocal photoexcitation.

The radiographs are simulated from the opacity distributions within the object that are obtained from hydrodynamic simulations. The calculation takes into account the spectral, spatial, and temporal responses of the imaging device as well as the backlighter spectrum. This fully accounts for the finite-bandwidth effect discussed above.

Figure 123.25 shows a *DRACO*/Spect3D-simulated radiograph of a successful OMEGA cryogenic implosion. This implosion, shot 47206, reached a measured areal density of 202 ± 7 mg/cm² (Ref. 20). The radiograph, which is shown in (b), shows the shadow of the simulated mass-density profile at the time of peak compression, which is shown in (a). This contour plot is a cross section of the density distribution in a plane intersecting the imploded shell along its vertical symme-

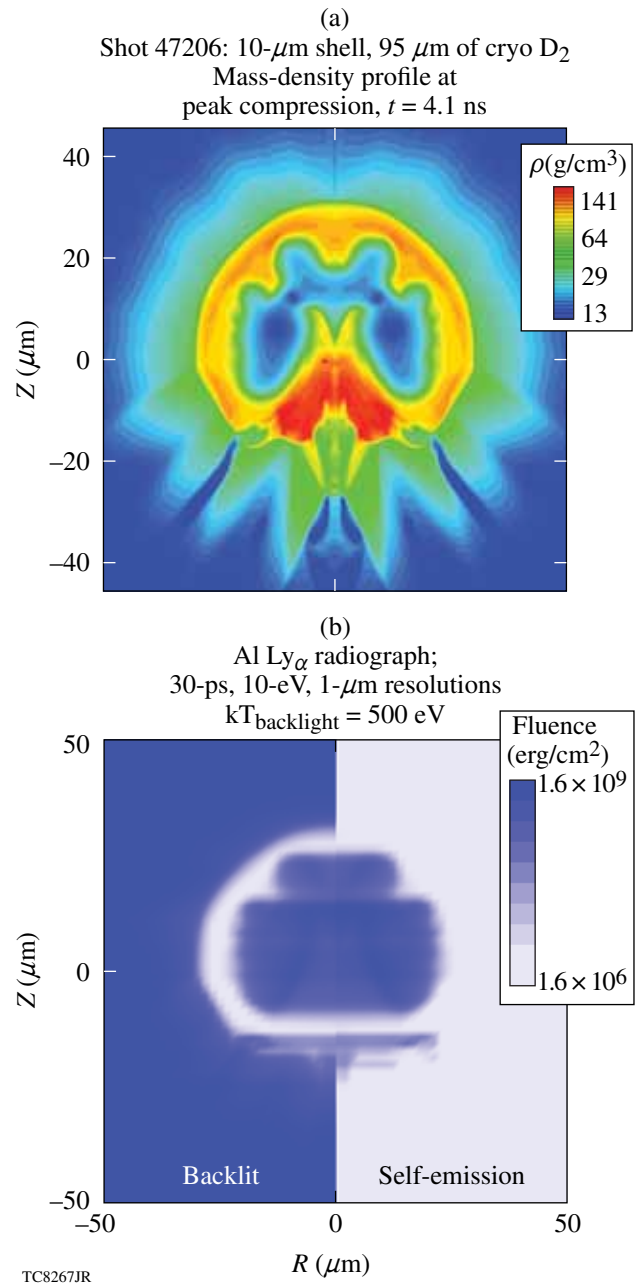


Figure 123.25

A *DRACO*/Spect3D-simulated radiograph of a successful OMEGA cryogenic implosion at peak compression is shown in the left “backlit” half of the split frame in (b). This implosion, shot 47206, reached a measured areal density of 202 mg/cm² (Ref. 20). The simulated mass density profile at this time is shown in cross section in the contour plot in (a). The coordinates (R, Z) refer to a cylindrical geometry with the symmetry (Z) axis in the vertical direction. The simulated radiograph in the left side of the split image in (b) was backlit at the H-like aluminum Ly_α emission line energy at a brightness temperature of 500 eV. The right half of the split image in (b) shows only the self-emission with no backlighter contribution. The imaging device is restricted to a 10-eV bandwidth, a 30-ps integration time, and a 1- μm spatial resolution.

try axis. The asymmetries of the imploded shell are the result of irradiation nonuniformity caused by target offset, beam imbalance, and the shape of the individual beam profile at the target surface. The cylindrical coordinates (R, Z) are defined with the symmetry (Z) axis in the vertical direction. The left-hand side of the split image in (b) shows the simulated radiograph of this density distribution, including the backlighter. The right-hand half of the image is the exact mirror image of the radiograph in (a), except that the backlighter contribution is not included, leaving only the self-emission. The imaging device is restricted to a bandwidth of 10 eV. The backlighter is assumed to be the Ly_α emission line of H-like aluminum at a brightness temperature of 500 eV, which corresponds to an intensity of about twice that of the shell's self-emission at this line energy, which peaks at about this time. This intensity has been exceeded in backlighter development experiments,²¹ but it has been chosen here to illustrate the useful information available with a backlighter that does not overwhelm the self-emission. The 30-ps integration time, which is comparable to currently available gating times, takes into account the blurring effects of source motion. The 1- μm spatial resolution of the simulation is much better than will be available with current instrumentation, but it shows the amount of information that could be available with improved resolution.

Most of the structure seen in the shell mass distribution is visible in the radiograph [Fig. 123.25(b)]. At the bottom of the shell, the flow appears to have formed a dense concentration of mass that has preceded the rest of the shell toward the center. The shadow of such a dense concentration of shell material should be seen distinctly in the backlit portion of the image on the left-hand side of the frame, but it is very faint. Seeing how similar this cone-shaped concentration appears in the backlit side of the frame and in the self-emission side, one concludes that it is filling in its own shadow with its own emission. The inner-surface emission from the shell behind it is being blocked along with the backlighter. The falling radial temperature gradient and the rising radial density gradient create a surface of maximum emissivity at the interior of the shell. As has been shown with BF radiographs of warm polar-drive implosions,⁷ the portion of the shell outside this emitting surface forms a shadow on the radiograph that may be analyzed. As long as this shell absorption is physically separated in the radiograph from the inner-surface self-emission, it can be measured. As this example demonstrates, however, self-emission is capable of hiding substantial amounts of shell mass.

Over the 30-ps integration time, the self-emission is dimmer than the hypothetical backlight but strong enough to reduce

confidence in the absorption of the shadow of the shell limb. The shape of the shell is still apparent with this marginally intense hypothetical backlighter. Higher backlight intensity will be available that will compensate for the excess self-emission admitted by gating times that are longer than the backlight pulse and by spectral pass bands that extend past the spectral width of the backlighter.

The image contrast in a FF radiograph of an imploding cryogenic shell can change from nothing to saturation in a very short time because of the rapid approach to peak shell density, coupled with the strong ρ^2 density scaling of the FF opacity. The spectrum of the backlighter must be chosen so that the shell transmission produces optimum radiographic contrast at a chosen time. The contour plot in Fig. 123.26 shows the transmission of a ray passing through the center of the *DRACO* simulation shown in Fig. 123.25 as a function of time and backlighter photon energy. This plot is repeated, once with the Al K-shell line energies indicated and once with the energies of the H-like Ly_α lines of several possible backlighter materials indicated. At any one of these line energies, the lineout across the plot gives the transmission as a function of time. This transmission varies dramatically, reaching a minimum at maximum compression near 4.15 ns. For a particular backlighter energy, Fig. 123.26 shows the times at which a desired transmission value is likely to occur. Similarly, the contour corresponding to a desired transmission value gives, as a function of time, the backlighter photon energy that would provide this transmission value. If, for example, the contour at the transition from yellow to orange indicates a suitable transmission value, it crosses the aluminum K-shell line energies roughly 100 ps before peak compression, indicating that these lines are suitable backlight sources at this time. Materials with higher line energies will provide the same degree of contrast later in time.

Figure 123.27 shows the expected performance of an Al backlighter. The time-resolved spectrum in (a) represents the simulated spectral flux from a 10- μm aluminum foil irradiated with an 8-ps Gaussian pulse at 10^{18} W/cm². The strongest feature is the Ly_α emission line of the hydrogen-like species, but a great deal of energy is emitted in other spectral features, including continuum above 2.2 keV. This continuum would create a uniform background, were it not removed by iridium reflectors, as was explained earlier and shown in Fig. 123.20. The specific intensity at the Ly_α line center is shown in (b) as a function of time. This emission appears as a pulse lasting 5 ps, centered close to the laser pulse. The specific intensity of this emission line can be compared with that of the time-dependent self-emission expected from a cryogenic implosion

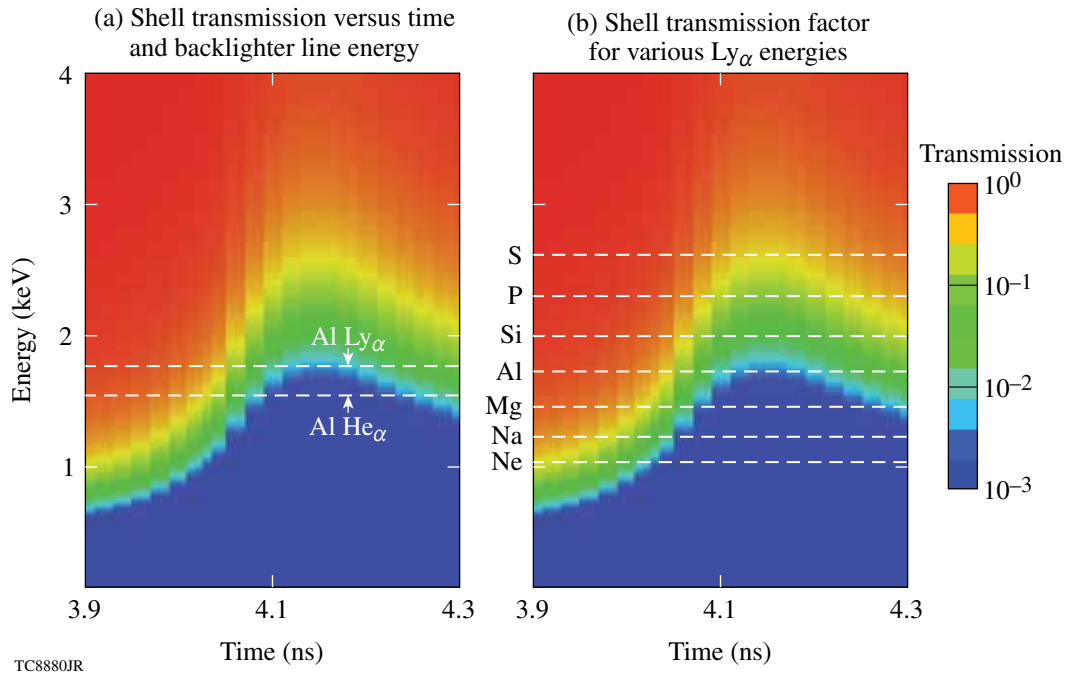


Figure 123.26

The image contrast in a FF radiograph is determined by the transmission of the imploded shell at the effective photon energy of the backlighter. The transmission of a ray at the center of a *DRACO*-simulated radiograph of shot 47206 is shown plotted as contours as a function of time and backlighter photon energy. This plot is repeated, once with the Al K-shell line energies indicated and once with the energies of the H-like Ly_α lines of several possible backlighter materials indicated. The backlighter energy giving a particular transmission value at a particular time can be read as a function of time by following the corresponding contour.

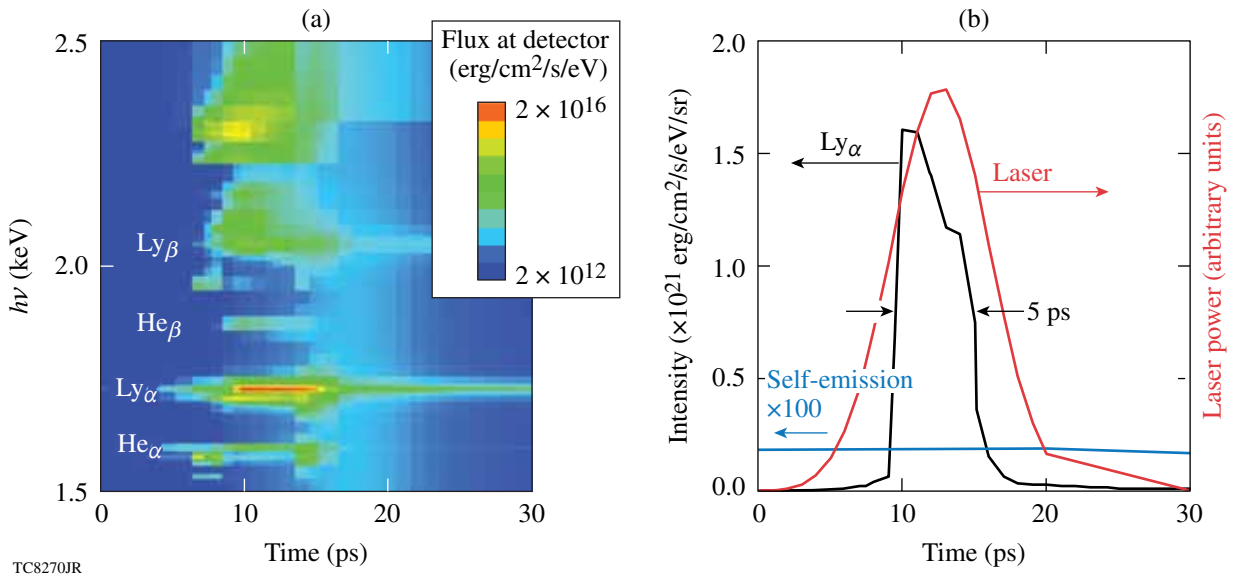


Figure 123.27

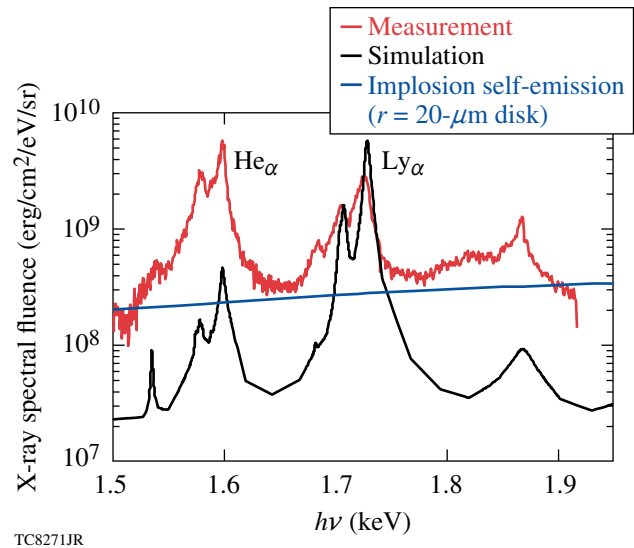
The simulated time-resolved spectrum in (a) represents the spectral flux from the surface of a 10- μm aluminum foil irradiated with an 8-ps Gaussian pulse at 10^{18} W/cm^2 . The specific intensity centered at the Ly_α line is shown in (b) plotted as a function of time. This emission appears as a pulse lasting 5 ps, centered near that of the laser pulse, plotted in red. This emission line is much more intense than the self-emission expected from a cryogenic implosion on OMEGA. The blue curve represents 100 \times the specific intensity obtained from an implosion simulation, assuming that all the self-emission of a simulated imploded cryogenic core emerges from within a 20- μm -radius circle.

on OMEGA. The time scale of the simulated implosion has been shifted so that the peaks of the self-emission and the backlight line intensity coincide. The blue curve represents $100\times$ the specific intensity obtained assuming that the entire self-emission of a simulated imploded cryogenic core emerges from within a $20\text{-}\mu\text{m}$ -radius circle. Clearly, the Ly_α line can provide a backlight source that is potentially two orders of magnitude more intense than the self-emission background. The self-emitted continuum lasts much longer, however, than the short duration of the backlighter and covers a much wider bandwidth than the backlighter spectral line, so short framing times and narrow bandwidths are essential for restricting the self-emission background to acceptable levels.

The simulated spectral fluence is compared in Fig. 123.28 with the measured time-integrated spectral emission from a similar experiment on the OMEGA EP laser. The consistency of the simulated and measured aluminum Ly_α fluence is encouraging. The irradiance of $1.25 \times 10^{18} \text{ W/cm}^2$ in the simulation is slightly higher than the $5 \times 10^{17} \text{ W/cm}^2$ average in the experiment, which anticipates the likelihood that more-intense portions of the nonuniform beam are dominating the spectral emission. To convert the measured fluence to a time-integrated specific intensity that can be compared directly with the simulated time-integrated emission, it is assumed that the measured fluence was emitted within a length of time equal to the backlighter laser pulse width and from within its nominal $23\text{-}\mu\text{m}$ laser-spot radius. With these assumptions, the simulated and measured Ly_α fluences are close. The measured He_α fluence, on the other hand, is much higher than the simulated level. The measured background continuum is also much higher than the simulated level. These discrepancies are probably due to emission from the foil outside the directly illuminated spot that has been heated by both thermal and nonthermal electron transport. The formation of a large, relatively cool radiating area surrounding the laser spot, following the absorption within the laser spot, has not been taken into account in the 1-D *LILAC* simulation. Even though the colder radiating area would be dimmer than the original hot area under the laser, it could be larger and longer lasting, resulting in a substantial contribution to the total fluence. The agreement in the Ly_α emission indicates that the prompt emission from the laser spot is modeled reasonably well. The He_α emission certainly comes from a lower temperature and a larger area than the Ly_α source because material producing more He_α emission than Ly_α emission can have a temperature of no more than about 500 eV. At this temperature, the blackbody limit on the line emission rules out the possibility that such a source could produce the observed He_α fluence in a time as short as the laser

pulse width and from an area as small as the laser-spot area. If the Ly_α emission is prompt and the He_α emission is over an extended period of time, then it is the Ly_α emission that will be favored by the time gating of the x-ray framing camera. Given the ν^{-3} dependence of the FF opacity of the imploded shell, uncertainty as to which of these two spectral lines is dominating the backlighter over the gating time corresponds to less than a 24% uncertainty in the shell opacity to be used in the radiographic analysis. With reasonable progress in backlighter spectroscopy or by implementing narrow-band imaging, this uncertainty will diminish substantially.

For comparison, the time-integrated self-emission intensity from the previous simulated cryogenic implosion example is plotted as the blue curve in Fig. 123.28, assuming for the purposes of this estimate that the source is a disk with a $20\text{-}\mu\text{m}$ radius, which is very close to the image size at peak core emission. This self-emission is much lower than the Ly_α spectral fluence, indicating that the implosion radiographs can be substantially free of self-emission, with some tolerance of longer



TC8271JR
Figure 123.28

The measured and simulated spectral fluence from an aluminum foil target are compared, assuming identical pulse widths and similar irradiances and assuming that all emission comes from within a $23\text{-}\mu\text{m}$ laser spot. The simulated aluminum Ly_α time-integrated spectral fluence is consistent with the measured spectral emission. Agreement over the entire spectrum cannot be expected from a 1-D simulation like this because nonthermal electron transport to non-irradiated portions of the foil is not modeled. Agreement in the Ly_α fluence indicates that emission from the directly irradiated spot is modeled reasonably well and that useful backlighter intensities can be attained. The time-integrated intensity from a simulated cryogenic implosion is plotted for comparison, assuming that the effective source is a $20\text{-}\mu\text{m}$ -radius disk, which is very close to the core image size at peak core emission.

integration times and camera bandwidths that are slightly wider than the backlighter spectral line.

DRACO/Spect3D-simulated radiographs of the cryo implosion shown in Fig. 123.25, shot 47206, have been obtained using the simulated backlighter spectrum shown in Fig. 123.27. Three images, representing the 100 ps leading up to the time of peak compression, are shown in Fig. 123.29. The spectral interval used is 10 eV in width, centered at the aluminum $\text{Ly}\alpha$ energy. These radiographs show a very rapid increase in image contrast, roughly an order of magnitude in each 50-ps time step. At this backlighter energy, the 100 ps shown is the extent of the useful time interval for radiography with Al lines, because of the loss of contrast at the early end of this interval. As explained above, the degree of radiographic contrast obtained at a given time in the implosion can be adjusted by changing the backlighter material. The simulated backlighter intensity is high enough in these radiographs to overcome the self-emission. The image at 4.1 ns shows the shadow of the mass concentration at the bottom of the imploded shell, which was not visible in the simulated radiograph in Fig. 123.25, obtained with marginally adequate backlighter intensity. The simulated spatial resolution of $5\ \mu\text{m}$ allows one to see much of the detail of the mass distribution in Fig. 123.25. The assumed temporal resolution is 30 ps and the shell motion is taken into account. The effects of the assumed spatial resolution of $5\ \mu\text{m}$ and the smearing resulting from shell motion during the 30-ps time gate are comparable.

Feasibility of Hard X-Ray Compton Radiography

Simulated Compton radiographs are obtained from *DRACO* and *LILAC* simulations using the same Spect3D postprocessor as the simulated FF radiographs. The effective opacity is much simpler. Along any line of sight, the density path integral $\int \rho ds$, and the effective optical depth τ are very simply related by

$$\tau = \frac{\sigma_{\text{KN}}(h\nu)}{m_{Z,A}/Z} \int \rho ds, \quad (1)$$

where $\sigma_{\text{KN}}(h\nu)$ is the Klein–Nishina total cross section for the Compton scattering of a photon.^{14,15} This cross section varies very slowly over the 50- to 100-keV spectral range used for Compton radiography, and, at these energies, all electrons in the material, both bound and free, contribute equally to the effective opacity. Consequently, the areal electron density is obtained from the areal mass density by dividing by $m_{Z,A}/Z$, the mass per electron of the shell material, specified here by its atomic number Z and mass A . Since the mass per electron is about two atomic mass units, decreasing slowly with increasing atomic number, the effective opacity has a very weak material dependence.

The three *DRACO*/Spect3D-simulated radiographs of shot 47206 in Fig. 123.29 are calculated again and shown in Fig. 123.30 at the same times and spatial resolutions, but with

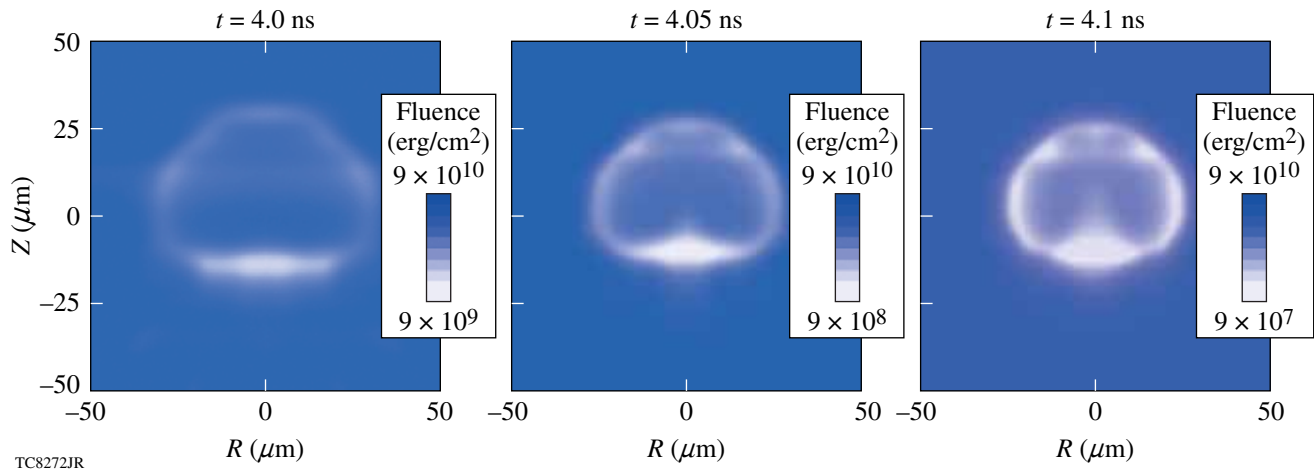


Figure 123.29

Three simulated FF radiographs leading up to the time of peak compression are shown, based on the same simulation shown in part in Fig. 123.25 and the backlighter spectrum shown in Fig. 123.28. The spectral interval used is 10 eV in width, centered at the aluminum $\text{Ly}\alpha$ energy. The assumed spatial resolution is $5\ \mu\text{m}$ and the temporal resolution is 30 ps. These images illustrate that useful detail is visible and also that radiographic contrast increases very rapidly as peak compression is approached.

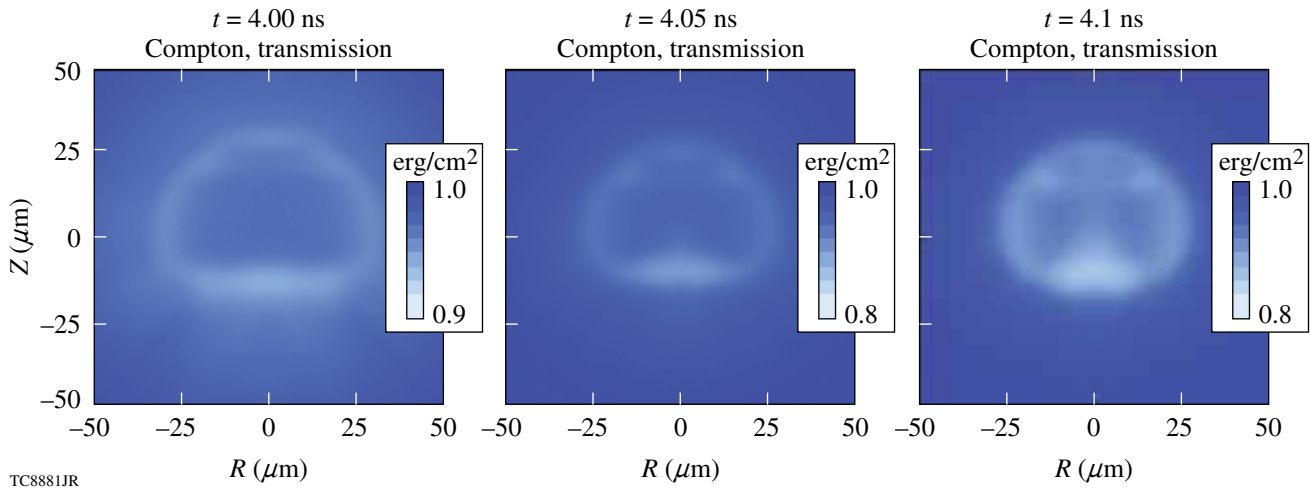


Figure 123.30

The three *DRACO/Spect3D*-simulated radiographs of shot 47206 in Fig. 123.29 have been obtained at the same times and spatial resolutions but with a backlighter energy of 57 keV, where Compton scattering forms the image. The time resolution is 10 ps, the pulse width claimed for recent Compton radiograph experiments with warm CH shells. The Compton radiographs appear almost identical to the FF radiographs, except for their very weak transmission signal.

a backlighter energy of 57 keV, where Compton scattering forms the image. The time resolution is 10 ps, the pulse width claimed for recent Compton radiograph experiments with warm CH shells.⁹ The Compton radiographs appear almost identical to the FF radiographs, except for their very weak transmission signal. The contour scales are linear and cover only the range of transmission needed to bring out the image, while the FF radiographic images in Fig. 123.29 require logarithmic scales covering up to three decades to span their full dynamic range. The backlighter photon energy of 57 keV corresponds to the inner-shell K_{α} decay transition of tantalum. Since this simulation was done, higher energy sources have been considered, including bremsstrahlung up to 100 keV (Ref. 8), but the result of this simulation would change negligibly if this were taken into account, owing to the weak energy dependence of the Klein–Nishina cross section.

A *LILAC/Spect3D* simulation of a sequence of Compton radiographs has been obtained for the 120 ps leading up to the time of peak compression of a more-recent cryogenic implosion, shot 55723. The simulated peak areal density was 370 mg/cm², and the measured value was 300 mg/cm² (Ref. 3). The simulated shell areal density and neutron emission rate are plotted as functions of time in Fig. 123.31(a). The simulated radiographs are circularly symmetric because the *LILAC* simulation is spherically symmetric, so the simulated radiographs are represented as radial transmission profiles in Fig. 123.31(b). The transmission profile curves are color keyed to a legend giving the image times and also to time markers in (a). This

shows that the imaging device must be sensitive to a 15% attenuation signal. A much greater sensitivity will be required for quantitative radiography at earlier times. Sensitivity to less than 4% attenuation will be needed to make measurements 120 ps before peak compression. This series of radiographs shows that both the radial convergence and the transmission are measurable indicators of compression. The core shadow shrinks and sharpens with the approach to peak compression, but the opaque limb of the image converges by only 10 μm over the 120 ps shown, making this motion difficult to measure, given the 10-μm image resolution imposed by the size of the point backlighter. These radiographs were simulated without allowance for temporal or spatial resolution.

Analysis of Free-Free Radiographs

The FF radiographs obtained thus far have been analyzed as if they were shadows of spherically symmetric objects. The formation and analysis of the radiograph of a spherically symmetric object are illustrated schematically in Fig. 123.22 for the case of a hollow spherical shell. Generally, the radial opacity profile $\kappa(r)$ of a hollow spherical shell forms a circularly symmetric intensity distribution $I(x)$, which appears as a characteristically limb-darkened shadow, relative to a uniform backlighter intensity I_{BL} . The optical thickness $\tau(x)$ of a spherically symmetric object is the Abel transform of the opacity profile

$$\tau(x) = \int \kappa[r(s)] ds, \quad (2)$$

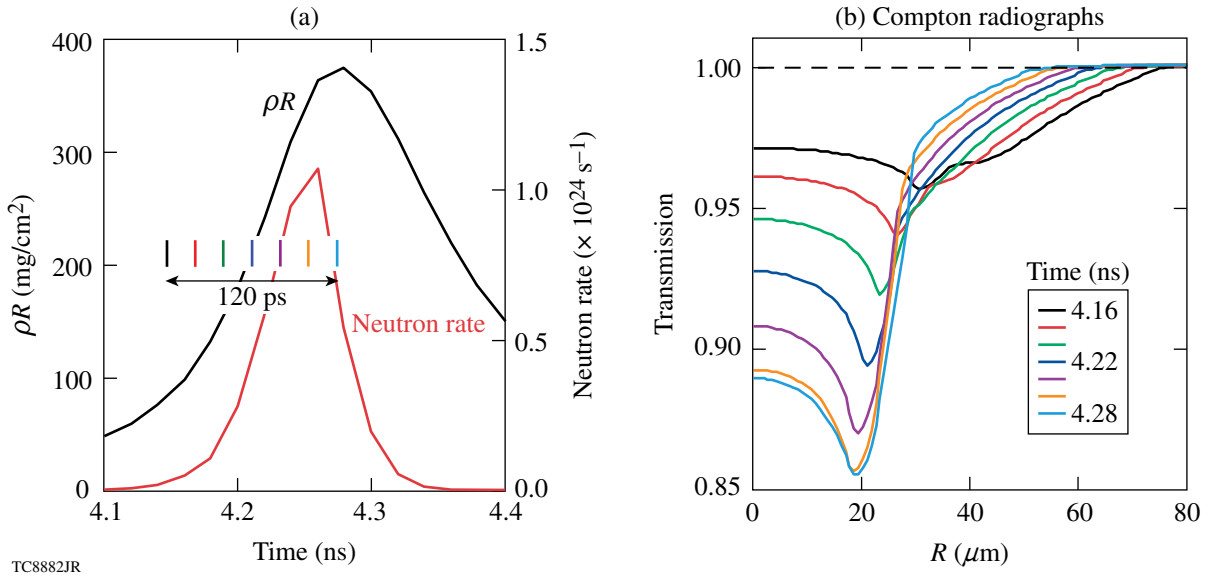


Figure 123.31
 A 1-D *LILAC/Spect3D* simulation of a sequence of Compton radiographs has been obtained over the 120 ps leading up to the time of peak compression of shot 55723, which recently attained an areal density of 300 mg/cm². The shell areal density and neutron emission rate are plotted in (a) as functions of time. The radiographs are represented in (b) as radial transmission profiles, color-keyed to the time labels in the legend and to time markers in (a). The backlighter photon energy was chosen to be 57 keV. Spatial and temporal resolutions were not taken into account.

where each point on the backlighter ray path s is identified with its distance r from the center of the object. The inverse Abel transform of $\tau(x)$

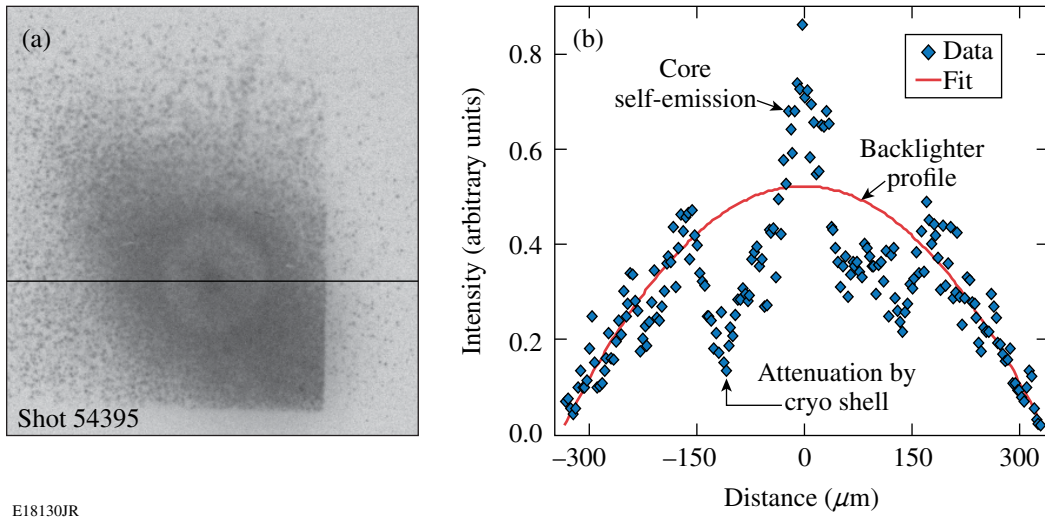
$$\kappa(r) = -\frac{1}{\pi} \int_r^\infty \frac{d\tau(x)}{dx} \frac{dx}{\sqrt{x^2 - r^2}} \quad (3)$$

recovers the spherical opacity profile from the shadow. Limb darkening is the tendency for the radiographic shadow of a uniformly absorbing shell to have a sharp minimum of intensity at a radius equal to the inner radius of the absorbing shell because of the strong peak in $\tau(x)$ at that radius. Obtaining the opacity at a given radius r by Abel inversion requires information from the radiograph only for $x > r$. If, for example, there is an emitting core within a radius r_0 , Abel inversion of the radiograph still gives the opacity distribution for $r > r_0$, as long as the shadow is visible for all $x > r_0$. The radial optical thickness can be obtained by evaluating $\int_{r_0}^\infty \kappa(r) dr$ using Eq. (3) and performing the radial integration analytically to derive a new expression,

$$\int_{r_0}^\infty \kappa(r) dr = \frac{r_0}{\pi} \int_{r_0}^\infty \frac{\tau(x)}{x\sqrt{x^2 - r_0^2}} dx, \quad (4)$$

which is easier to apply than Eq. (3) if the radial integral is all that is wanted.

A preliminary estimate of the areal density of the imploding target in shot 54395 obtained from a lineout of its radiograph is shown in Fig. 123.32, which illustrates the basic steps of the radiographic analysis. The imploding shell is seen as a crisp shadow near the center of the elliptical backlighter emission spot in (a). The transmission/emission profile is first isolated from this nonuniform backlighter intensity distribution in a highly approximate fashion shown in (b) by fitting an inverted parabola to reconstruct the symmetric rounded top of the backlighter intensity distribution from the portion of the backlighter that is exposed. Emission from the core and from a thin unablated remnant of the original CD shell can be seen peaking above the backlighter intensity in (b). The FF opacity of deuterium at the Al K-shell line energies and a uniform shell temperature estimate of 25 eV from a *LILAC* simulation gives a $\rho^2 R \approx 0.097 \text{ g}^2/\text{cm}^5$ for the absorbing shell based on the measured transmission profile and Eq. (4). Assuming that the shell density is uniform, we obtain an areal density of $\rho R \approx 33 \text{ mg}/\text{cm}^2$ within a shell thickness of 110 μm centered at a mean radius of about 140 μm . This areal-density value is consistent with the imploded mass from the *LILAC* simulation of this implosion confined within the shadow radius. Assuming a temperature based on a simulation introduces a weak model dependence into this estimate. The unablated shell mass can be used instead of the shell temperature as a simulation-based parameter.⁷ This may be a better choice since, unlike the shell



E18130JR

Figure 123.32

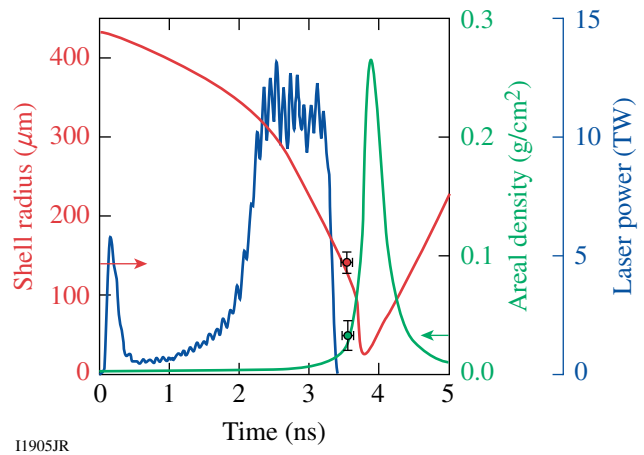
A preliminary estimate of the target areal density obtained from a radiograph lineout of shot 54395 illustrates the basic steps of radiograph analysis. The attenuation contribution to the radiograph in (a) is obtained by fitting an inverted parabola model to the backlighter intensity profile shown in (b), where it is not obscured by the imploding shell, and then using this fitted backlighter model profile to infer the backlighter intensity behind the imploding shell. Emission from the core and from a thin unablated remnant of the original CD shell can be seen peaking above the backlighter intensity in (b). The FF opacity of deuterium and a shell-temperature estimate of 25 eV from a *LILAC* simulation give a $\rho^2 R \approx 0.097 \text{ g}^2/\text{cm}^5$ value within the absorbing shell. Assuming that the shell density is uniform, $\rho R \approx 33 \text{ mg}/\text{cm}^2$ can be inferred, which is consistent with the imploded mass from the *LILAC* simulation of this implosion.

temperature, it is nearly constant throughout the approach to peak compression, and it allows one to treat the opacity simply as ρ^2 times a constant determined by the imploded mass value. The flat transmission level within the shell's shadow and the crisp outer boundary defined by the self-emission help to define the shell boundaries, but the extra self-emission at this late time, after the laser pulse has turned off, implies an unablated residue of the original CD shell. Simulation of this implosion verifies that shells must be slightly thinner than in this example to avoid an unablated shell remnant. As has been discussed above, even a trace of residual CD can add significantly to the opacity of the shell. Clearly, this compromises our ability to analyze this imploding shell reliably in terms of the FF opacity of pure D_2 .

These areal-density and shell-radius estimates are consistent with a *LILAC* simulation of this implosion roughly 300 ps in advance of peak compression, as can be seen in Fig. 123.33. The time uncertainty indicated by the error bars corresponds to the 80-ps gating time of the x-ray framing camera. These estimates are uncertain due to the small amount of radiographic data sampled by the single lineout and the resulting difficulty in identifying the limits of the shell. These results are sensitive to the fitting model of the backlighter intensity profile.

The radiograph of shot 54395 shown in Fig. 123.32(a) is shown again in Fig. 123.34(b). Another view of the same

implosion from another pinhole on the framing camera, approximately 40 ps earlier, is shown in Fig. 123.34(a). The separation of the pinholes on the framing camera creates a parallax effect that changes the position of the imploding target relative to the backlighter spot. The radiograph in (a)



I1905JR

Figure 123.33

The areal density and shell diameter inferred from the preliminary analysis of the first radiograph of shot 54395 are consistent with the *LILAC* simulation of this implosion at a time well before peak compression. Further simulation and analysis of the radiograph indicate that complicating effects of a trace remnant of the original CD shell lends a large uncertainty to the inferred ρR value.

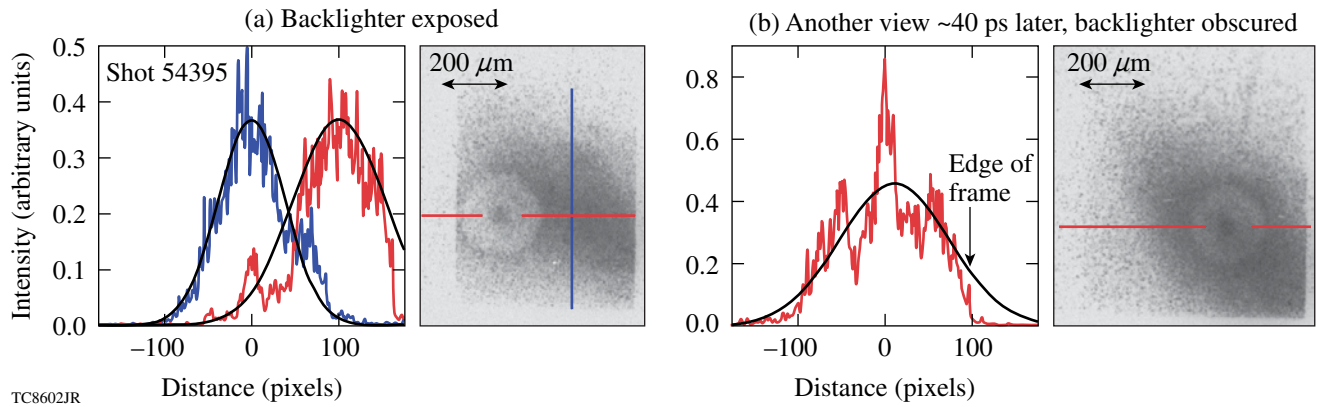


Figure 123.34

Two framing camera views of the same imploding shell, shot 54395, taken at nearly the same time are shown in (a) and (b). Parallax caused by the separation of the pinholes on the framing camera creates images with different target-backlighter orientations. These radiographs are flat fielded with an elliptical Gaussian backlighter distribution model. The superposition of lineouts of the fitted backlighter profile and the radiograph in (a) shows that the elliptical Gaussian profile fits the backlighter profile well. The color of each lineout matches that of the line on the radiograph, indicating the row or column of data represented by the lineout. The good fit of the model distribution to the two orthogonal lineouts in (a) indicates that the attenuation of the center of the backlighter by the imploding target seen in the radiograph in (b) is probably being isolated properly with this model.

shows the center of the backlighter spot exposed, while the radiograph in (b) shows the target well-centered over the backlighter spot, providing a strong absorption signal over the entire target. These radiographs are flat fielded, assuming that the backlighter has an elliptical Gaussian distribution. The plots show lineouts of the radiographs superimposed on the same lineout of the fitted backlighter model. Each lineout is taken along the row or column of data indicated on the radiographs by the line with the matching color. Plot (a) shows that a good fit is obtained over nearly the entire spot, which indicates that the backlighter is being represented properly when this fitting model is applied to the radiograph in (b), where the center of the backlighter distribution is obscured. After the radiograph is flat fielded with the fitted backlighter distribution, the transmission image of the target remains, which is then circularly averaged and Abel inverted to obtain the radial opacity profile of the imploded shell.

The radiograph of shot 54395 in Fig. 123.32(a) has been analyzed using an elliptical Gaussian intensity model fit to the exposed portion of the backlighter spot. The resulting transmission distribution is circularly averaged about the center of the shell shadow and plotted as the blue curve in both frames of Fig. 123.35. The inverse Abel transform given by Eq. (3) is applied to this transmission profile, obtaining a radial opacity profile. This opacity profile is the ρ^2 profile, the density scaling of FF opacity, to within a constant factor that is determined by the total unablated shell mass $34.8 \mu\text{g}$ obtained from a *LILAC* simulation. The resulting density profile is plotted in

red in both frames of Fig. 123.35. Radial transmission profiles were obtained from a *LILAC/Spect3D* simulation at three times covering a 200-ps range centered at the time of the measurement indicated in Fig. 123.33. These are plotted in Fig. 123.35(a), where the measured radial transmission profile is emphasized as a heavy blue curve for easier comparison. The simulated mass density profiles at these three times are plotted in Fig. 123.35(b) along with the measured mass-density profile, plotted in this frame as a heavy red curve. The mass-density distribution is strongly peaked toward the outside of the shell, resulting in an areal density $\rho R = 19 \text{ mg/cm}^2$, not quite consistent with the preliminary estimate shown in Fig. 123.33. Assuming a 25-eV shell temperature, which is applicable to this time interval, an analysis based on the FF opacity of pure D_2 gives a much higher value of $\rho R = 47 \text{ mg/cm}^2$, suggesting that the shell is more opaque than a simple understanding of D_2 opacity would lead one to expect.

The simulated and measured transmission profiles in Fig. 123.35 both show transmission factors greater than unity at some radii, which indicates self-emission contributions from the core and from near the outer radius of the shell. The absolute backlighter intensity was not available for the radiographic simulation, so the simulation uniform backlighter intensity value was chosen to have roughly the observed strength of the backlighter relative to the self-emission at the time when the rapidly rising core self-emission and the outer-shell self-emission are comparably intense. The result in Fig. 123.35 is that the exterior self-emissions compare well, while the

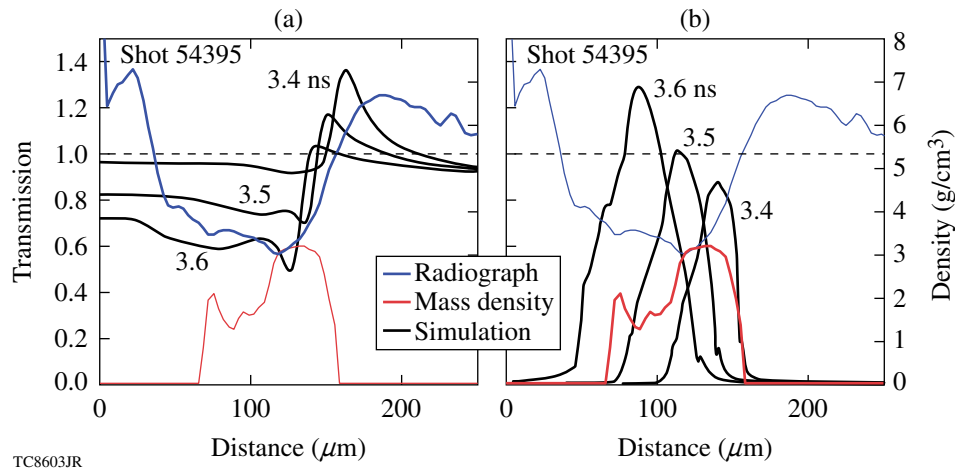


Figure 123.35

The simulation of shot 54395 by *LILAC* shows that a trace of the original CD shell remains unablated. The Spect3D simulated radiographs take this into account and show some resemblance to the measured radiograph between 3.5 and 3.6 ns. The central self-emission is underpredicted at this time, relative to the exterior self-emission, but the amount of unablated CD is known well enough for the simulated and measured exterior self-emissions to match reasonably well. Plots (a) and (b) both show the circularly averaged radial transmission profile and the mass-density profile that is recovered from it by Abel inversion. In (a), the transmission profile (blue) is emphasized and compared with simulated transmission profiles; in (b), the inferred mass-density profile is emphasized (red) and compared with the corresponding simulated mass-density profiles. The inferred density profiles are normalized to the simulated imploded mass. The mass-density profile inferred from analyzing the radiograph in terms of the opacity of D_2 is compromised by the unablated CD, even though it is a small remnant of minimal hydrodynamic importance. The dashed line indicates unit transmission.

simulated core self-emission has not grown to the measured level. It is probably more reliable to match the exterior self-emission since the source is the residual and unablated shell CD, which is predicted to be present in the 1-D simulation, while the strength of the measured shell absorption suggests that shell CD may have mixed into the center of the implosion, which would increase the core self-emission relative to the 1-D prediction by an uncertain factor. The unablated CD remnant is indicated in the simulated mass-density profiles, and its presence accounts for the sharp limb-darkened feature on the simulated transmission profile, which is particularly distinct at the later two times. The generally flat appearance of the shadow in the radiographs in Figs. 123.32(a), 123.34(a), and 123.34(b) suggests that the radial opacity profile is distinctly weighted toward the exterior, which is borne out in the more thorough analysis summarized in Fig. 123.35. The presence of unablated CD compromises the analysis of the radiograph in terms of the opacity of pure D_2 , even if the amount of CD involved is of minor hydrodynamic significance. In another shot, a slight reduction in the initial CD thickness produces an imploded shell where the CD is predicted to be completely ablated away, providing a case that is potentially much better suited for this kind of analysis.

This analysis of the radiograph of shot 54395 has been repeated for shot 55133 and is shown in Fig. 123.36. The

polymer shell of this target was $9.6 \mu\text{m}$ thick, initially, which was sufficiently reduced from the $10.1\text{-}\mu\text{m}$ shell thickness of shot 54395 that no polymer remains in the unablated shell in the *LILAC* simulation. As expected, the radiograph, included in Fig. 123.36 as an inset, shows no apparent self-emission at its outer edge, indicating that there is no residual polymer. Plots (a) and (b) both show the same circularly averaged radial transmission profile and the mass-density profile that was recovered from it by Abel inversion. The inferred density profile, normalized to the simulated imploded mass of $33.5 \mu\text{g}$, has an areal density of 20 mg/cm^2 , much lower than the value based on the opacity, 56 g/cm^2 . In this figure, the simulated density profiles were time averaged over the 80-ps time gate of the framing camera.

The inferred mass-density profile is flatter and broader than any of the time-averaged simulated profiles. Consistent with this, the measured radiographic transmission profile is broader than the simulated radiographs at any time. Since the measured radiograph shows no sign of self-emission other than from the core, the simulated radiographs were calculated without self-emission to obtain a pure transmission signal. Consequently, the simulated and measured radiographs cannot be compared within the emitting core radius. This does not affect the inferred density profile outside the emitting core. The simulated and measured radiographs and density profiles bear

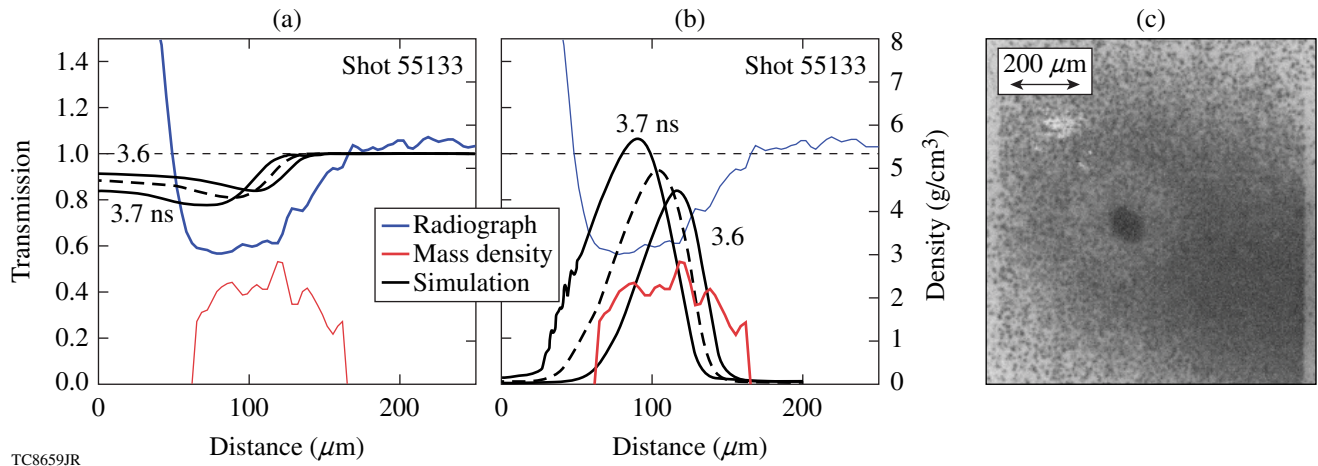


Figure 123.36

The analysis of the radiograph of shot 54395 illustrated in Fig. 123.35 is repeated here for a radiograph of shot 55133, shown in (c). This polymer shell is $9.6 \mu\text{m}$ thick, less than $10.1 \mu\text{m}$ for shot 54395. As a result, all of the polymer is expected to be ablated away, and no self-emission or absorption from unablated polymer is either expected or seen. The mass-density profile (red curve) in (b) that has been inferred from the transmission profile in (a) matches the position of the simulated shell most closely at 3.6 ns. The plotted simulated density profiles have been averaged over the 80-ps time gate of the framing camera. The areal density from the inferred mass distribution, normalized to the simulated imploded mass of $33.5 \mu\text{g}$, is $20 \text{ mg}/\text{cm}^2$, much lower than the value based on the opacity, $56 \text{ mg}/\text{cm}^2$. The observed attenuation at this time is significantly greater than expected, as if an excess opacity were distributed uniformly over the shell.

a closer qualitative resemblance in this case than in the case of shot 45395, primarily because there is no localized external self-emission, but the measured radiographic attenuation is still greater than expected.

This unaccounted absorption remains under investigation. Small-scale mix of the shell polymer into the D_2 shell is a possibility, although an amount of carbon sufficient to diminish the transmission should be visible as self-emission at the outer surface of the shell, still warm from the ablation phase of the implosion. The D_2 opacity model must be examined. Additional BF opacity could add significantly to the opacity if the D ions are not as completely stripped by continuum lowering as the model indicates.¹⁹

Conclusions

Radiography of cryogenic implosions with OMEGA EP-driven backlighting is being developed on OMEGA. Analysis of the first OMEGA/OMEGA EP FF radiographs has provided useful measurements at times well in advance of peak compression. Simulated radiographs based on a multidimensional cryogenic implosion demonstrate that FF radiography at peak compression is feasible with the demonstrated backlighter intensity. Compton radiography with hard x-ray point backlighters, an alternative to radiography with soft area backlighters, has been demonstrated on OMEGA with CH implosions and is also under development for cryogenic implosion imaging on OMEGA. There is a balance of advantages between FF

and Compton radiography. Compton radiographs, with simpler backlighter attenuation physics and lower background from self-emission, are easier to analyze. Simulated Compton radiographs show measurable contrast that is interpreted with simple attenuation physics with little dependence on the backlight spectrum or the target material. The strong material dependence of FF opacity can compromise the soft radiograph of a cryo shell, even if only a trace of polymer shell material mixes into the imploded ice. While the very weak material dependence of Compton scattering makes radiography of the ice shell possible in the presence of hydrodynamically irrelevant contaminants, the stronger material sensitivity of FF radiography could be useful for detecting significant contamination or mix. Not only is the radiograph contrast much stronger in FF radiography, as compared with the marginally detectable contrast in Compton radiography, but the contrast can be optimized for a particular stage in the compression history by changing the backlighter material, while in Compton radiography almost nothing can be done to improve or adjust the contrast.

With either method, backlighter sources driven by OMEGA EP will provide useful images of cryogenic shells imploded on OMEGA. The images obtained from the radiography of cryogenic implosions will be crucial for demonstrating the continuing success of cryogenic implosion campaigns by supplementing the data currently obtained. The preliminary results presented here show similarities between the simulated

implosion performance and radiography well in advance of peak compression. These results are valuable and encouraging in planning for future measurements that will be extended to the final phases of the implosion.

ACKNOWLEDGMENT

This work was supported by the U.S. Department of Energy Office (DOE) of Inertial Confinement Fusion under Cooperative Agreement No. DE-FC52-08NA28302, the University of Rochester, and the New York State Energy Research and Development Authority. The support of DOE does not constitute an endorsement by DOE of the views expressed in this article.

REFERENCES

1. T. R. Boehly, D. L. Brown, R. S. Craxton, R. L. Keck, J. P. Knauer, J. H. Kelly, T. J. Kessler, S. A. Kumpan, S. J. Loucks, S. A. Letzring, F. J. Marshall, R. L. McCrory, S. F. B. Morse, W. Seka, J. M. Soures, and C. P. Verdon, *Opt. Commun.* **133**, 495 (1997).
2. L. J. Waxer, D. N. Maywar, J. H. Kelly, T. J. Kessler, B. E. Kruschwitz, S. J. Loucks, R. L. McCrory, D. D. Meyerhofer, S. F. B. Morse, C. Stoeckl, and J. D. Zuegel, *Opt. Photonics News* **16**, 30 (2005).
3. V. N. Goncharov, T. C. Sangster, T. R. Boehly, S. X. Hu, I. V. Igumenshchev, F. J. Marshall, R. L. McCrory, D. D. Meyerhofer, P. B. Radha, W. Seka, S. Skupsky, C. Stoeckl, D. T. Casey, J. A. Frenje, and R. D. Petrasso, *Phys. Rev. Lett.* **104**, 165001 (2010); T. C. Sangster, V. N. Goncharov, R. Betti, T. R. Boehly, D. T. Casey, T. J. B. Collins, R. S. Craxton, J. A. Delettrez, D. H. Edgell, R. Epstein, K. A. Fletcher, J. A. Frenje, V. Yu. Glebov, D. R. Harding, S. X. Hu, I. V. Igumenshchev, J. P. Knauer, S. J. Loucks, C. K. Li, J. A. Marozas, F. J. Marshall, R. L. McCrory, P. W. McKenty, D. D. Meyerhofer, P. M. Nilson, S. P. Padalino, R. D. Petrasso, P. B. Radha, S. P. Regan, F. H. Séguin, W. Seka, R. W. Short, D. Shvarts, S. Skupsky, V. A. Smalyuk, J. M. Soures, C. Stoeckl, W. Theobald, and B. Yaakobi, *Phys. Plasmas* **17**, 056312 (2010).
4. C. D. Zhou and R. Betti, *Phys. Plasmas* **14**, 072703 (2007).
5. E. I. Moses, *J. Phys., Conf. Ser.* **112**, 012003 (2008).
6. R. Epstein, V. A. Smalyuk, F. J. Marshall, J. Delettrez, V. N. Goncharov, P. W. McKenty, D. D. Meyerhofer, P. B. Radha, S. P. Regan, T. C. Sangster, and W. Theobald, *Bull. Am. Phys. Soc.* **54**, 306 (2009).
7. F. J. Marshall, P. W. McKenty, J. A. Delettrez, R. Epstein, J. P. Knauer, V. A. Smalyuk, J. A. Frenje, C. K. Li, R. D. Petrasso, F. H. Séguin, and R. C. Mancini, *Phys. Rev. Lett.* **102**, 185004 (2009).
8. R. Tommasini *et al.*, *Rev. Sci. Instrum.* **79**, 10E901 (2008).
9. *LLE Review Quarterly Report* **120**, 239, Laboratory for Laser Energetics, University of Rochester, Rochester, NY, LLE Document No. DOE/NA/28302-910 (2009).
10. D. K. Bradley *et al.*, *Rev. Sci. Instrum.* **66**, 716 (1995).
11. S. Regan (Laboratory for Laser Energetics) and R. Tommasini (Lawrence Livermore National Laboratory), private communication (2009).
12. S. Chandrasekhar, *Plasma Physics* (University of Chicago Press, Chicago, 1960).
13. R. N. Bracewell, *The Fourier Transform and Its Applications*, 3rd ed. (McGraw-Hill, Boston, 2000).
14. E. Sergrè, *Nuclei and Particles: An Introduction to Nuclear and Subnuclear Physics* (W. A. Benjamin, New York, 1965).
15. J. Castor, *Radiation Hydrodynamics* (Cambridge University Press, Cambridge, England, 2004), pp. 291–293.
16. J. D. Lindl, *Phys. Plasmas* **2**, 3933 (1995).
17. J. Delettrez, R. Epstein, M. C. Richardson, P. A. Jaanimagi, and B. L. Henke, *Phys. Rev. A* **36**, 3926 (1987).
18. P. B. Radha, V. N. Goncharov, T. J. B. Collins, J. A. Delettrez, Y. Elbaz, V. Yu. Glebov, R. L. Keck, D. E. Keller, J. P. Knauer, J. A. Marozas, F. J. Marshall, P. W. McKenty, D. D. Meyerhofer, S. P. Regan, T. C. Sangster, D. Shvarts, S. Skupsky, Y. Srebro, R. P. J. Town, and C. Stoeckl, *Phys. Plasmas* **12**, 032702 (2005).
19. J. J. MacFarlane *et al.*, *High Energy Density Phys.* **3**, 181 (2006).
20. T. C. Sangster, V. N. Goncharov, P. B. Radha, V. A. Smalyuk, R. Betti, R. S. Craxton, J. A. Delettrez, D. H. Edgell, V. Yu. Glebov, D. R. Harding, D. Jacobs-Perkins, J. P. Knauer, F. J. Marshall, R. L. McCrory, P. W. McKenty, D. D. Meyerhofer, S. P. Regan, W. Seka, R. W. Short, S. Skupsky, J. M. Soures, C. Stoeckl, B. Yaakobi, D. Shvarts, J. A. Frenje, C. K. Li, R. D. Petrasso, and F. H. Séguin, *Phys. Rev. Lett.* **100**, 185006 (2008).
21. W. Theobald, C. Stoeckl, P. A. Jaanimagi, P. M. Nilson, M. Storm, D. D. Meyerhofer, T. C. Sangster, D. Hey, A. J. MacKinnon, H.-S. Park, P. K. Patel, R. Shephard, R. A. Snavely, M. H. Key, J. A. King, B. Zhang, R. B. Stephens, K. U. Akli, K. Highbarger, R. L. Daskalova, L. Van Woerkom, R. R. Freeman, J. S. Green, G. Gregori, K. Lancaster, and P. A. Norreys, *Rev. Sci. Instrum.* **80**, 083501 (2009).

A Gated Liquid-Scintillator–Based Neutron Detector for Fast-Ignitor Experiments and Down-Scattered Neutron Measurements

Introduction

Neutron detectors in inertial confinement fusion experiments are predominantly used to measure the neutron yield¹ and ion temperature² of the primary fusion reaction. These experiments produce nearly monoenergetic neutron spectra with energies of ~ 2.45 MeV for deuterium–deuterium (D–D) reactions and 14.1 MeV for deuterium–tritium (DT)–filled targets. The neutron spectra are broadened only slightly by the temperature of the core plasma,² which is of the order of a few keV. Neutron detectors are also utilized to detect secondary DT neutrons from targets filled with pure deuterium to infer the areal density of the fuel.³ The secondary DT neutrons show a broad spectrum that depends on the fuel areal density, typically from 10 to 18 MeV, with a yield of the order of 10^{-3} of the primary neutrons. Since these secondary DT neutrons are faster than the primary DD neutrons, they can be easily detected with a time-resolved detector at a sufficient distance from the target to allow for neutron time-of-flight dispersion, which is of the order of ~ 25 ns/m. Even though the large background from the primary neutrons generally saturates the detector and recording system, this does not significantly affect the secondary neutron measurements because the secondary neutrons are recorded well before the background arrives. Recently, two new applications for neutron detectors have been proposed: (1) fast-ignition (FI) experiments with cone-in-shell targets⁴ and (2) down-scattered neutron measurements in inertial fusion experiments,⁵ which are much more challenging since they require the measurement of a small signal after a large background. In FI experiments the neutron spectrum of interest is quasi-monoenergetic, generally at ~ 2.45 MeV from D–D reactions. The background consists of hard x rays from the interaction of the high-energy short-pulse laser with the gold cones with an apparent spectral temperature of the order of ~ 1 MeV. The temporal dispersion between signal and background is high (~ 40 ns/m), but the background can easily be 10^5 times higher than the signal. For the down-scattered neutron measurements, the background is the primary DT neutrons and the signal is the neutrons with energies below 12 MeV, typically 6 to 10 MeV. The signal-to-background ratio depends on the areal density of the target and is of the order of

10^{-2} for full-scale ignition targets. The temporal time-of-flight dispersion is small, approximately 4 ns/m for 10-MeV neutrons, compared to the primary 14.1-MeV DT neutrons. This article describes a current-mode neutron detector developed at LLE using a fast oxygen-enriched liquid scintillator coupled to a gated microchannel plate photomultiplier for FI and down-scattered neutron measurements.

X-Ray Shielding

While shielding cannot be used for down-scattered neutron measurements to separate signal from background since there is no significant attenuation difference between 14.1-MeV and 6- to 12-MeV neutrons in any material, x-ray shielding has been used successfully to measure neutrons in high-energy short-pulse laser experiments at ~ 500 -J laser energy and 1-ps pulse duration.⁶ The detector described in Ref. 6 [an 18-cm-diam, 10-cm-thick Pilot B⁷ scintillator, coupled to a conventional XP2020⁸ photomultiplier tube (PMT)] was set up 2 m from the target for integrated FI experiments on the OMEGA Laser System.⁹ Lead shielding with 15-cm thickness toward the target and 5 cm in all other directions was used to attenuate the hard x-ray background [see Fig. 123.37(a)]. The expected neutron yield from the FI experiments are of the order of 10^7 , which would produce a signal of ~ 1 V in the PMT. Figure 123.37(b) shows an example from a neutron-producing shot with a yield of 1.1×10^7 without the short-pulse laser firing. In an integrated FI experiment with a short-pulse laser energy of 1 kJ at 10 ps, the PMT is heavily saturated and no neutron signal is visible at all [Fig. 123.37(c)]. An additional factor of 1000 of x-ray attenuation is a rough estimate of what would be required to avoid saturation. The attenuation coefficients for Pb at photon energies of 2 to 10 MeV can be obtained from the NIST, XCOM¹⁰ database to be ~ 4 to 5×10^{-2} cm²/g, which translates into a $1/e$ attenuation length of ~ 2 cm. Therefore an additional ~ 15 cm of Pb shielding would be required to avoid saturation. The total neutron-scattering cross section at 2.45 MeV is approximately 7 barn for Pb, according to the LBL, ENDF¹¹ database, which translates into a $1/e$ attenuation length of ~ 4 cm. Consequently, the neutron signal would also be attenuated by approximately

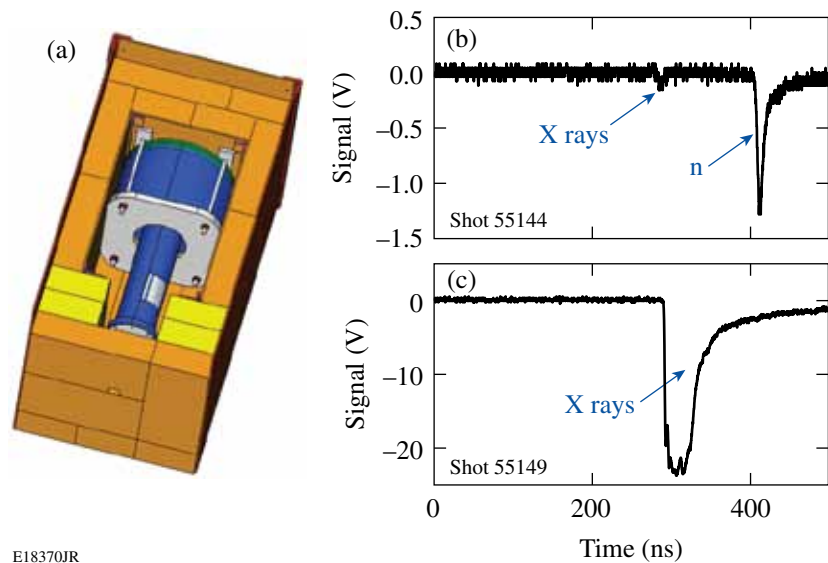


Figure 123.37
 (a) CAD model of the detector shielding. (b) Neutron signal from a shot with a yield of 1.1×10^7 . (c) X-ray background from a 1-kJ, 10-ps short pulse interacting with a fast-ignition target.

E18370JR

a factor of 50 and significantly broadened in time because of multiple scattering in the Pb shielding, making it almost impossible to detect.

Photomultiplier Gating

Another method to suppress the background signal, which works for both the FI experiments and the down-scattered neutron measurements, is to gate the PMT, rendering it inactive when the background signal is present. A PMT can be gated by applying a short positive pulse of the order of 200 V to the photocathode, which extracts the photoelectrons from the photocathode and prevents them from reaching the microchannel plate (see Fig. 123.38). A gated PMT240 from PHOTEK¹² was used in the NIF neutron time-of-flight (nTOF) detector, as described in Ref. 13, for FI experiments. The PMT was operated at a gain of 10^6 coupled to a 40-mm-diam, 20-mm-thick BC422¹⁴ plastic scintillator shielded with 25 mm of Pb. The detector was placed 5.2 m from the target. The gating pulse was set up to eliminate the hard x-ray pulse from the short-pulse interaction, which is recorded at ~ 350 ns (see Fig. 123.39). Up to an energy of ~ 500 J, the PMT gating reduces the pulse significantly, but at ~ 800 J of short-pulse energy the gating ceases to be effective and the PMT is saturated.

By removing the scintillator, it was verified that the background signal is produced predominantly by interactions with the microchannel plate (MCP). Since the MCP voltage is almost unchanged by the gate pulse, electrons generated inside the MCP will be amplified and a signal will be recorded, even if the gate voltage is applied. To avoid saturation from direct interaction with the MCP, a neutron detector was set up below the 60-cm-thick concrete floor below the target chamber at

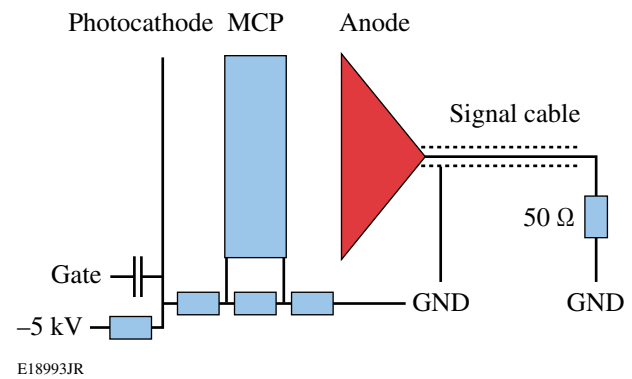
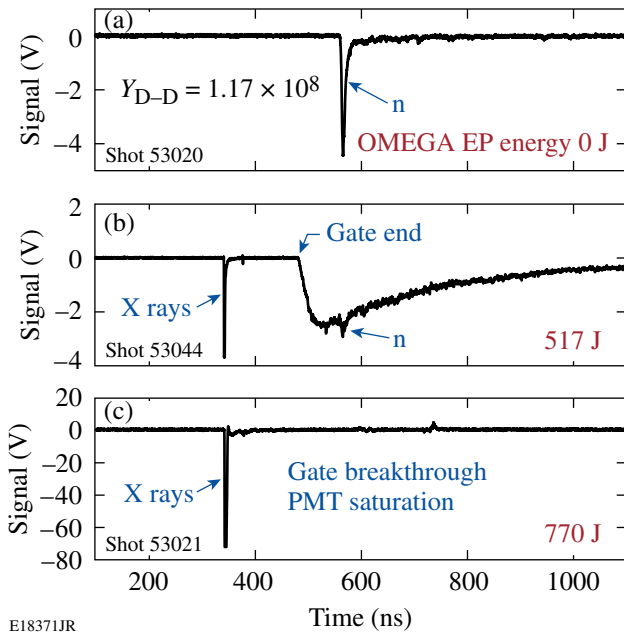


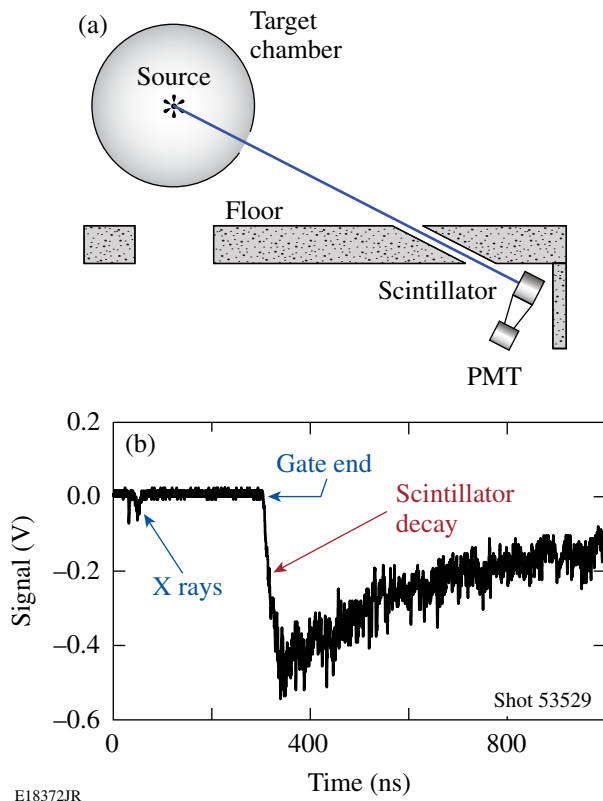
Figure 123.38
 Simplified electrical schematic of the photomultiplier gating circuit. A resistive divider sets up the voltages between the photocathode, microchannel plate (MCP), and anode. A positive pulse at the gate input extracts the photoelectrons, disabling the photomultiplier tube (PMT).

12.4 m from the target [see Fig. 123.40(a)]. A 20-cm-diam hole in the floor provided an unshielded line of sight from the target to the detector. The gated PMT240 was mounted ~ 20 cm from the scintillator outside the direct line of sight through the hole. To compensate for the larger distance to target and the reduced light-collection efficiency, the scintillator size was increased to 18-cm diameter \times 10-cm thickness.

A 2.5-cm-thick lead x-ray shield covering the hole in the floor eliminates the x-ray background with energies < 1 MeV. In this configuration the PMT gating works well and the background is reduced to a very low level, as seen in Fig. 123.40(b). Unfortunately the light output from the plastic scintillator has a significant component with a long decay constant, which produces a strong background once the PMT gate ends. This



E18371JR
 Figure 123.39
 Signal from gated PMT in NIF nTOF detector: (a) no short pulse, (b) short-pulse energy of 517 J, and (c) short-pulse energy of 770 J.

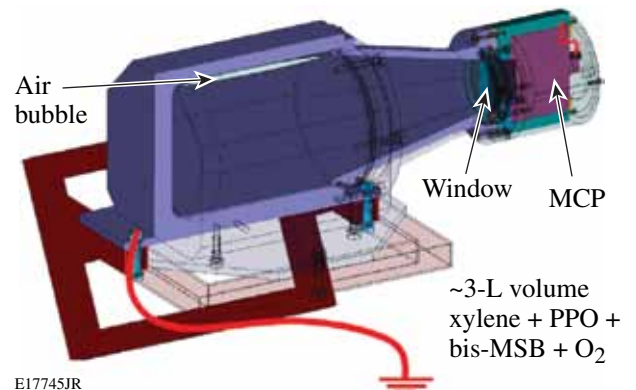


E18372JR
 Figure 123.40
 (a) Setup used to shield the PMT from direct hard x-ray irradiation; (b) signal from 1-kJ fast-ignition shot.

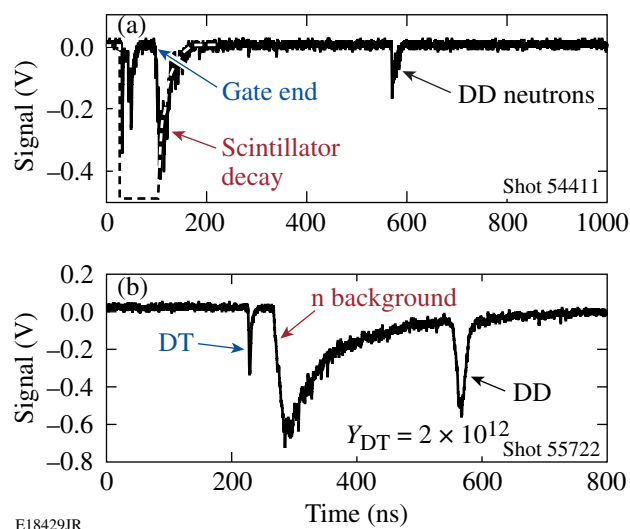
scintillator afterglow completely masks any neutron signal from D–D fusion reactions, which is expected to appear at ~550 ns, given the time-of-flight distance.

Oxygen-Enriched Liquid Scintillator

To avoid background from the scintillator decay, a scintillator material with a significantly reduced long-decay component is required. Recently a low-afterglow liquid scintillator described in the literature showed a >100× decreased light output for times >100 ns after the primary event.¹⁵ This liquid scintillator is based on a mixture of two dyes, PPO and bis-MSB, dissolved in xylene and enriched with molecular O₂. A neutron detector using this scintillator material was set up using the line of sight below the concrete floor shown in Fig. 123.40. It consists of a 3-L volume of oxygen-enriched liquid scintillator coupled to a gated PMT240 (see Fig. 123.41). A small air bubble allows for thermal expansion of the liquid without a significant pressure increase. The PMT is placed outside the direct line of sight to the target to avoid direct x-ray interactions with the MCP [see (Fig. 123.40)]. Data from integrated FI experiments with 1 kJ of short-pulse energy show a dramatically reduced scintillator decay tail and a very clear D–D neutron signal at the expected time [see Fig. 123.42(a)]. A very similar detector with a slightly smaller scintillator volume of ~1 L was fielded on high-areal-density cryogenic D–T implosions,¹⁶ for down-scattered neutron measurements. The gating of the D–T primary peak works quite well, and the 2.45-MeV D–D fusion neutron peak is very well resolved [see Fig. 123.42(b)]. Unfortunately, a large background can still be seen in the signal after the gate turns off and the PMT becomes active. This background is predominantly caused by scattered primary DT neutrons that enter the room under the target area through



E17745JR
 Figure 123.41
 Drawing of the liquid scintillator detector.



E18429JR

Figure 123.42

Signals recorded from the oxygen-enriched scintillator detector: (a) from FI experiments with 1 kJ of short-pulse energy and (b) high-areal-density cryogenic implosions.

a large hole under the target chamber and reach the detector through a large number of different pathways at different times. This was verified by blocking the direct line of sight to the target, resulting in a very similar background signal, without either the primary D–T or D–D peak.

Summary and Conclusions

The detection of a small neutron signal after a very large background of hard x rays from short-pulse-laser–target interactions in a FI experiment or neutrons of higher energy in down-scattered neutron measurements is a very challenging task. Only the proper combination of sophisticated shielding, gating of a fast MCP-PMT, and a low-afterglow scintillator made it possible to record the D–D thermal neutron peak in integrated FI experiments at 1 kJ of short-pulse energy. In experiments with high-areal-density cryogenic DT targets, it was possible to clearly observe the D–D neutron peak, but the smaller down-scattered neutron signal is still masked by scattered primary neutrons that reach the detector because of insufficient neutron shielding. An improved neutron shielding for down-scattered neutron measurements on OMEGA is currently being designed and will be fielded in the near future.

ACKNOWLEDGMENT

This work was supported by the U.S. Department of Energy Office of Inertial Confinement Fusion under Cooperative Agreement No. DE-FC52-08NA28302, the University of Rochester, and the New York State Energy Research and Development Authority. The support of DOE does not constitute an endorsement by DOE of the views expressed in this article.

REFERENCES

1. M. D. Cable and M. B. Nelson, *Rev. Sci. Instrum.* **59**, 1738 (1988).
2. T. J. Murphy, R. E. Chrien, and K. A. Klare, *Rev. Sci. Instrum.* **68**, 610 (1997).
3. V. Yu. Glebov, D. D. Meyerhofer, C. Stoeckl, and J. D. Zuegel, *Rev. Sci. Instrum.* **72**, 824 (2001).
4. R. Kodama *et al.*, *Nature* **418**, 933 (2002).
5. V. Yu. Glebov, D. D. Meyerhofer, T. C. Sangster, C. Stoeckl, S. Roberts, C. A. Barrera, J. R. Celeste, C. J. Cerjan, L. S. Dauffy, D. C. Eder, R. L. Griffith, S. W. Haan, B. A. Hammel, S. P. Hatchett, N. Izumi, J. R. Kimbrough, J. A. Koch, O. L. Landen, R. A. Lerche, B. J. MacGowan, M. J. Moran, E. W. Ng, T. W. Phillips, P. M. Song, R. Tommasini, B. K. Young, S. E. Caldwell, G. P. Grim, S. C. Evans, J. M. Mack, T. Sedillo, M. D. Wilke, D. C. Wilson, C. S. Young, D. Casey, J. A. Frenje, C. K. Li, R. D. Petrasso, F. H. Séguin, J. L. Bourgade, L. Disdier, M. Houry, I. Lantuejoul, O. Landoas, G. A. Chandler, G. W. Cooper, R. J. Leeper, R. E. Olson, C. L. Ruiz, M. A. Sweeney, S. P. Padalino, C. Horsfield, and B. A. Davis, *Rev. Sci. Instrum.* **77**, 10E715 (2006).
6. C. Stoeckl, V. Yu. Glebov, P. A. Jaanimagi, D. D. Meyerhofer, T. C. Sangster, M. Storm, S. Sublett, W. Theobald, M. H. Key, A. J. MacKinnon, P. Patel, P. A. Norreys, and D. Neely, *Rev. Sci. Instrum.* **77**, 10F506 (2006).
7. Nuclear Enterprises Ltd., Edinburgh, Midlothian EH11 4BY, United Kingdom.
8. Koninklijke Philips Electronics N.V., 1070 Amsterdam, The Netherlands.
9. C. Stoeckl, J. A. Delettrez, J. H. Kelly, T. J. Kessler, B. E. Kruschwitz, S. J. Loucks, R. L. McCrory, D. D. Meyerhofer, D. N. Maywar, S. F. B. Morse, J. Myatt, A. L. Rigatti, L. J. Waxer, J. D. Zuegel, and R. B. Stephens, *Fusion Sci. Technol.* **49**, 367 (2006).
10. Physics Laboratory, National Institute of Standards and Technology (NIST), <http://www.nist.gov/physlab/index.cfm>.
11. Experimental Nuclear Reaction Data (EXFOR/CSISRS), <http://www.nndc.bnl.gov/exfor/>.
12. Photek Ltd., St. Leonards-on-Sea, East Sussex, TN38 9NS, United Kingdom.
13. Z. A. Ali, V. Yu. Glebov, M. Cruz, T. Duffy, C. Stoeckl, S. Roberts, T. C. Sangster, R. Tommasini, A. Throop, M. Moran, L. Dauffy, and C. Horsfield, *Rev. Sci. Instrum.* **79**, 10E527 (2008).
14. Saint-Gobain Cristaux & Detecteurs, 38910 Gieres, France.
15. R. Lauck *et al.*, *IEEE Trans. Nucl. Sci.* **56**, 989 (2009).
16. V. N. Goncharov, T. C. Sangster, T. R. Boehly, S. X. Hu, I. V. Igumenshchev, F. J. Marshall, R. L. McCrory, D. D. Meyerhofer, P. B. Radha, W. Seka, S. Skupsky, C. Stoeckl, D. T. Casey, J. A. Frenje, and R. D. Petrasso, *Phys. Rev. Lett.* **104**, 165001 (2010).

On-Chip Double Emulsion Droplet Assembly for Laser-Target Fabrication

Introduction

Inertial confinement fusion (ICF) experiments use spherical organic polymer shells as mandrels for cryogenic foam targets. The targets are typically fabricated by polymerizing double-emulsion (DE) shells and then voiding the inner fluids.^{1,2} In this process, special care must be taken to ensure DE droplet uniformity because fusion experiments impose rigid requirements on the sphericity and wall thickness uniformity of foam targets.

Up to the present, the formation of uniform DE droplets has relied mainly on the controlled merging of two immiscible fluids.^{1–5} DE droplets for target fabrication are currently prepared using a triple-orifice droplet generator.¹ This method generates remarkably monodisperse emulsions with good uniformity. The DE droplet size, however, is constrained by the device dimensions, and the microfluidic devices need to be recalibrated and tuned to the correct dimensions each time they are used. In this article, we propose a DE assembly line based on a “lab-on-a-chip” droplet generator, where individual water and oil droplets generated from an on-chip dispensing system are combined directly to form DE’s. As a droplet-based microfluidic system, this scheme has the advantages of reconfigurability, flexibility, and scalability.

Background

Because the formation of DE droplets in air requires combining at least one aqueous (water) and one non-aqueous (oil) liquid droplet, we use electrowetting-on-dielectric (EWOD) and dielectrophoresis (DEP) simultaneously to dispense and transport water and oil droplets, respectively. Because all actuation is electrical, we can program each step and, in this way, obtain maximum operational flexibility.

1. Electrowetting-on-Dielectric (EWOD)

The electrowetting effect describes the observable influence of an electric field on both bulk liquid motions and the contact angle. The motive force is due to the response of the free electric surface charge to the electric field.^{6,7} In an EWOD-based micro-

fluidic device as shown in Fig. 123.43, droplets are sandwiched between parallel plates and manipulated by applying voltages to a series of adjacent electrodes on the bottom. A wide variety of fundamental fluid operations have been realized using EWOD. These operations include droplet transport,⁸ dispensing,^{9–11} separation,^{9,11} coalescence,⁹ dilution,¹² and others.

2. Dielectrophoresis (DEP)

The dielectrophoretic (or DEP) force is the force exerted on dielectrics when subjected to a nonuniform electric field.^{13,14} As another extensively studied mechanism for droplet manipulation, DEP is useful for manipulating insulating, polarizable media. For example, decane cannot be moved by EWOD¹⁵ but can be moved by DEP.¹⁶

EWOD and DEP are two observable effects of liquid under electrostatic fields, both of which are electromechanical in nature. Jones⁷ first clarified the frequency-dependent relationship between these two mechanisms. For a liquid with finite electrical conductivity and dielectric constant, there exists a critical frequency that separates conductive (EWOD) and dielectric (DEP) behavior.^{7,17,18} In the high-frequency limit, the liquid behaves as an insulator so that the electric field penetrates it. As a result, the observable electromechanical response of the liquid is virtually identical to liquid DEP.

3. General Microfluidic Platform Based on EWOD and DEP

The combination of droplet-based EWOD and DEP microfluidics makes it possible to manipulate both conductive and insulating droplets on the same chip. Conceptually, such a combination of EWOD and DEP may be visualized with the parallel-plate scheme shown in Fig. 123.43. The device consists of two parallel glass plates: a bottom plate that consists of a patterned array of individually addressable electrodes, and a top plate that is a continuous ground electrode. Usually the bottom plate is coated with a dielectric layer, and both the top and bottom surfaces are covered with a thin hydrophobic film to decrease the surface wettability.

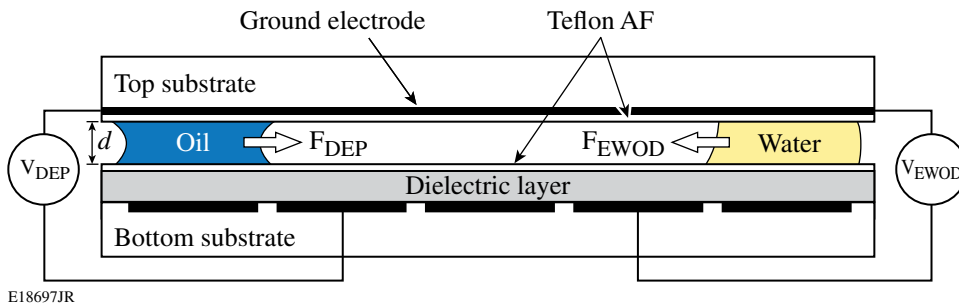


Figure 123.43

Cross section of a parallel-plate device containing a dielectric layer on the bottom plate to manipulate oil and water droplets by DEP and EWOD, respectively.

Microfabrication and Experiments

The basic features of the droplet-based microfluidic system are illustrated in a cross-sectional view in Fig. 123.43. The bottom glass substrate is evaporatively coated with 100 nm of aluminum and then photolithographically patterned into a two-dimensional electrode array. The structure is then spin coated with 0.5 μm of spin-on-glass (SOG) (Futurrex IC1-200) as the dielectric layer and 1 μm of amorphous fluoropolymer (DuPont Teflon-AF) as a hydrophobic coating. The top plate is a glass plate with a transparent indium tin oxide layer as a ground electrode covered by 1 μm of Teflon-AF as a hydrophobic coating.

The top substrate is positioned above the bottom substrate by appropriate spacers. Voltages applied to individual electrodes are controlled by a LabView-based controller. It is important to recognize that different voltages are applied for EWOD actuation and DEP actuation. For EWOD actuation, dc or low-frequency ac voltage, typically <100 V, is employed. For oil DEP actuation, dc or ac voltage (50 to 100K Hz) is used, but usually >250 V.

Droplet-Dispensing Reproducibility

In a typical dispensing operation, a liquid finger is drawn from a large reservoir droplet. Liquid pinch-off occurs by activating the electrode at the front end of the liquid finger and the reservoir electrode and deactivating the electrodes in between (the cutting electrode) until the liquid front is separated from the liquid bulk. Successful pinch-off requires an application of electrode voltages above some threshold value.⁶ The sequence of steps of droplet dispensing is shown in Fig. 123.44. EWOD-based water droplet dispensing has been widely studied,^{9–11} but dielectric-droplet (oil) dispensing has not received much attention. Here we demonstrate repeatable dielectric droplet dispensing on a microfluidic chip as shown in Fig. 123.44. Because of the difference in the electric-actuation mechanism, oil-droplet manipulation by DEP requires much higher voltages than EWOD dispensing of aqueous droplets.

Dispensing reproducibility is of paramount importance in laser-target fabrication because the uniformity of subsequently formed DE droplets is largely determined by the initial liquid volume control. The requirements for double emulsion droplet uniformity are described in **Appendix A** (p. 156). It has been observed that the final extracted drop volume is usually somewhat larger than the volume subtended by a square electrode (volume = a^2d , where a is the length of a square electrode in the electrode array and d is the spacing between bottom and top substrates).¹¹ The reason is that a liquid tail formed after separation adds some additional liquid to the already-formed

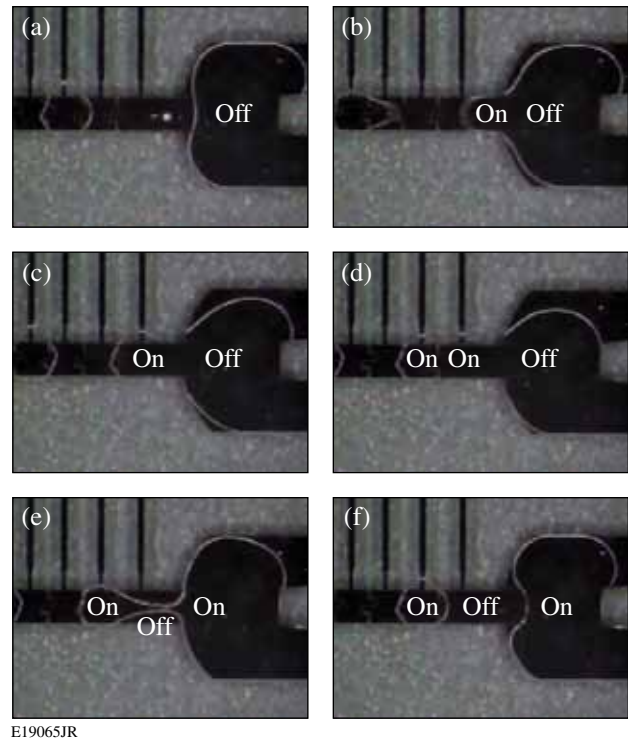


Figure 123.44

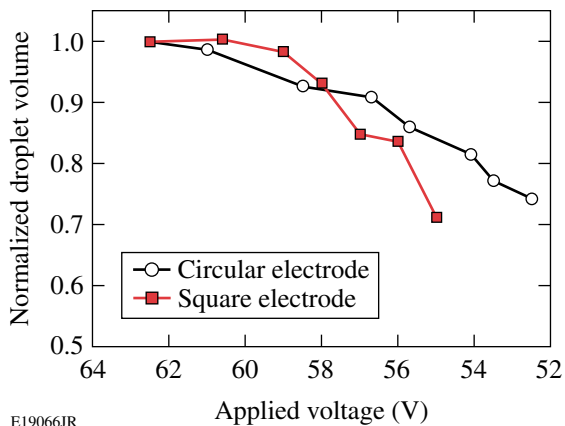
Top view of an on-chip dispenser showing the sequence of a silicone oil droplet being formed. (a) The reservoir and an already-formed droplet; (b)–(d) the liquid finger is formed, and, meanwhile, the first droplet is delivered away; (e) the pinch-off occurs; (f) a new droplet is formed.

droplet. It is this volume that produces variability in the dispensing operation. In this research we investigated the effects of applied voltage and electrode shape on droplet volume control for an on-chip dispensing system because they both impact the tail volume directly.

1. Effect of Applied Voltage on Droplet Volume Variations

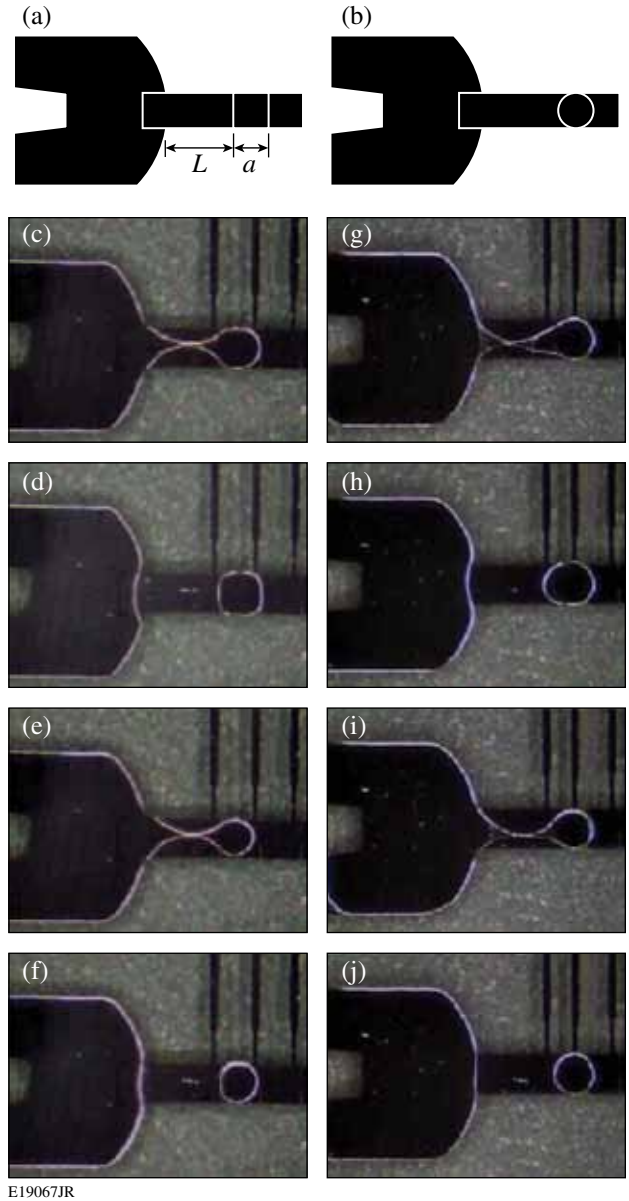
We investigated the dependence of dispensed water drop volume on the actuation voltage in a structure with 1-mm-sq electrodes. The droplet volume becomes sensitive when the applied voltage is close to the minimum required value for pinch-off. For example, when applied voltage decreased from 62.5 V to the minimum pinch-off voltage of 55.0 V, the droplet volume dropped by almost 30% as shown in Fig. 123.45. The same result is observed with both square and circular dispensing electrodes. The voltage effect is a result of the effect on the tail shapes during pinch-off. As shown in Fig. 123.46, a smaller tail is observed at lower voltage, and the pinch-off position also moves closer to the individual droplet. The shape of the tail changes because the liquid finger necking depends on the electrowetting force, which is directly related to applied voltage.⁶

Figures 123.46(c) and 123.46(e) show that with square electrodes, a smaller area of the dispensing electrode is filled by liquid during pinch-off at lower voltage. This smaller finger front may also contribute to reduced dispensed-droplet volume. No obvious change in the finger front is observed for circular electrode structures, as shown in Figs. 123.46(g) and 123.46(i), but the droplet volume remains very sensitive to voltage change. In general, the tail volume plays the most important role in determining variation in droplet volume.



E19066JR

Figure 123.45
The normalized volume variation of a series of droplets generated by different applied voltages. All tests were done with DI water. The gap between the top and bottom substrates was 85 μm , and the voltage applied was 100 Hz ac.



E19067JR

Figure 123.46

The effect of applied voltage on droplet volume variation. [(a),(b)] Square and circular dispensing electrodes used for the dispensing experiments. The square electrode is 1 mm \times 1 mm and the diameter of the circular electrode is 1 mm. The length of the cutting electrode is 2 mm. [(c),(d)] Pinch-off and the formed droplet on the square electrode by applying 62.5- V_{rms} , 100-Hz ac voltage; [(e),(f)] pinch-off and the formed droplet on the square electrode by applying 55- V_{rms} , 100-Hz ac voltage; [(g),(h)] pinch-off and the formed droplet on the circular electrode by applying 62.5- V_{rms} , 100-Hz ac voltage; [(i),(j)] pinch-off and the formed droplet on the circular electrode by applying 52.5- V_{rms} , 100-Hz ac voltage. In all cases, the gap between top and bottom substrates is 85 μm .

2. Effect of Cutting Electrode on Droplet Volume and Reproducibility

We tested electrode structures with different cutting electrode length (L) to investigate its effect on droplet volume and reproducibility. As shown in Fig. 123.47, the dispensed droplet volume increases directly with L . Droplets with an average volume of 103 nL and 183 nL were dispensed on a 1-mm \times 1-mm-sq electrode using cutting electrodes of lengths $L = 2$ mm and 3 mm, respectively. These droplet volumes are greater than the volume subtended by one electrode (85 nL). The increase in droplet volume is due to the larger tail formed on longer cutting electrodes during pinch-off. Similar behavior is also observed on 2-mm \times 2-mm-sq electrodes.

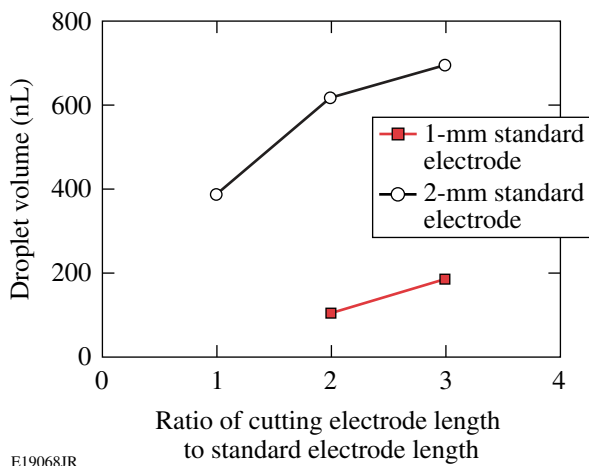


Figure 123.47 Average droplet volume versus cutting electrode length. All tests were performed with DI water. The gap between top and bottom substrates was 85 μm , and 90- V_{rms} , 100-Hz ac voltage was applied.

Droplet volume reproducibility suffers as L is increased. As indicated in Fig. 123.48 and Table 123.V, the coefficient of variation ($\text{CV} = \text{standard deviation}/\text{mean}$) increases significantly when the ratio of the cutting electrode length to standard electrode length (L/a) approaches $L/a = 3$. The reason for this behavior is the reduced influence of the cutting electrode on the radius of curvature in the pinch-off region. In fact, the pinch-off position becomes indeterminate for sufficiently large L/a . Large droplet volume variation ($\text{CV} = 40\%$) is observed when $L/a = 3$ on a 2-mm \times 2-mm electrode because of the instability of the pinch-off position (see Fig. 123.49).

The best reproducibility ($\text{CV} = 3.0\%$) is achieved for a cutting electrode of the same length as that of the standard electrodes. This reproducibility is adequate for laser target fabrication (see **Appendix A**, p. 156, for detailed discussion).

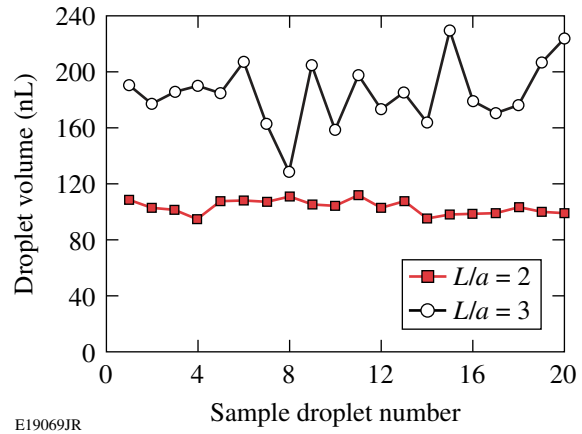


Figure 123.48

Droplet volume variation for two lengths of the cutting electrode. All tests were performed with DI water on 1-mm \times 1-mm dispensing electrodes. The gap between the top and bottom substrates was 85 μm , and 90- V_{rms} , 100-Hz ac voltage was applied.

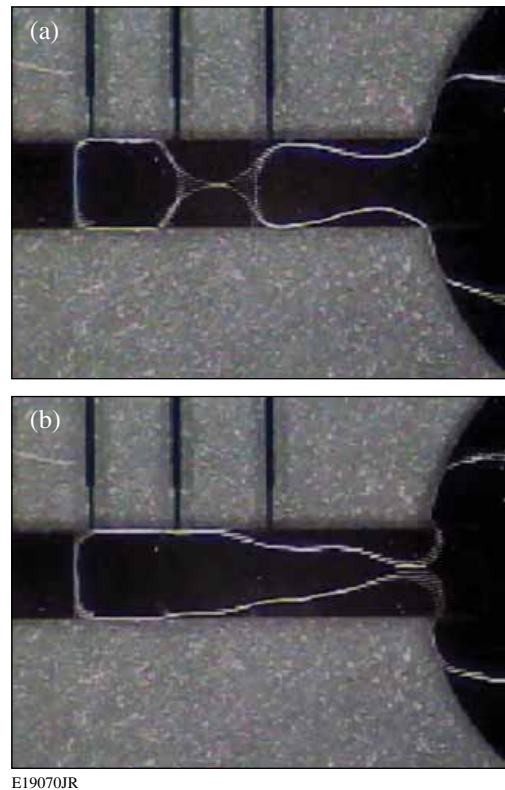


Figure 123.49

Instability of the pinch-off position for a droplet dispensing on a 2-mm standard electrode and a 6-mm cutting electrode. The gap between the top and bottom substrates was 85 μm , and 90- V_{rms} , 100-Hz ac voltage was applied.

Table 123.V: Effect of cutting electrode length on volume reproducibility (CV) for droplets dispensed on 1-mm and 2-mm dispensing electrodes and an 85- μm channel gap. In all cases, the voltage applied was 90 V_{rms} , 100 Hz ac.

Electrode size	$L/a = 1$	$L/a = 2$	$L/a = 3$
1 mm \times 1 mm	—	4.7%	12.7%
2 mm \times 2 mm	3.0%	5.3%	40%

On-Chip Double Emulsion Formation

1. Gibbs Free Energy Model

When two immiscible droplets are brought together, a DE droplet forms spontaneously if the Gibbs free energy is reduced by the emulsification process. The Gibbs surface energy change between initial and final states of a DE formation process is

$$\Delta G = G_{\text{DE}} - (G_{\text{water}} + G_{\text{oil}}), \quad (1)$$

where G_{DE} is the total Gibbs interfacial energy of a DE droplet and G_{water} and G_{oil} are Gibbs surface energies of the individual water and oil droplets forming that DE droplet. The Gibbs energy change ΔG is a convenient criterion for testing the likelihood of DE formation. A negative ΔG means the DE formation is favored. In the following, we develop a simple model to calculate the Gibbs surface energy changes associated with double emulsion formation.

The Gibbs surface energy is a sum of the product of interfacial tensions and corresponding surface areas. The surface shape of a droplet sandwiched between parallel plates is strongly affected by the contact angle against the substrate and the spacing between top and bottom substrates. For the geometry model shown in Fig. 123.50, the droplet volume is

$$\begin{aligned} V &= 2 \int_0^h \pi x^2 dz \\ &= 2\pi \left[(x_0^2 + R^2)h - \frac{1}{3}h^3 + 2x_0R^2 \left(\frac{1}{2}\theta_0 + \frac{1}{4}\sin 2\theta_0 \right) \right], \quad (2) \end{aligned}$$

where the spacing between substrates is $2h$, $\theta_0 = \theta - \pi/2$, θ is the contact angle on a hydrophobic surface ($\theta > 90^\circ$), and $R = -h/\cos\theta$.

The lateral surface area and base areas are then

$$\begin{aligned} S_L &= 2 \int_0^{\theta_0} 2\pi(x_0 + R \cos \theta') R d\theta' \\ &= 4\pi R(x_0\theta_0 + R \sin \theta_0), \quad (3) \end{aligned}$$

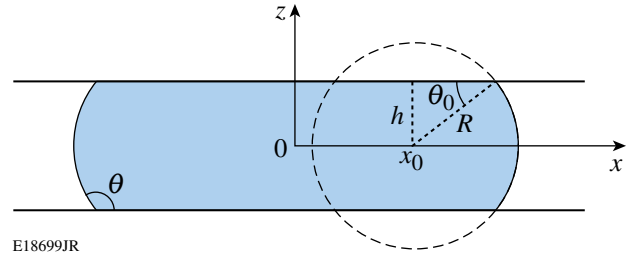


Figure 123.50

Droplet geometry when sandwiched between parallel plates.

$$S_B = 2\pi(x_0 + R \cos \theta_0)^2. \quad (4)$$

When $\theta < 90^\circ$, droplet volume and droplet surfaces can be derived as

$$V = 2\pi \left[(x_0^2 + R^2)h - \frac{1}{3}h^3 - 2x_0R^2 \left(\frac{1}{2}\theta_0 + \frac{1}{4}\sin 2\theta_0 \right) \right], \quad (5)$$

$$\begin{aligned} S_L &= 2 \int_0^{\theta_0} 2\pi(x_0 - R \cos \theta') R d\theta' \\ &= 4\pi R(x_0\theta_0 - R \sin \theta_0), \quad (6) \end{aligned}$$

$$S_B = 2\pi(x_0 - R \cos \theta_0)^2, \quad (7)$$

where $\theta_0 = \pi/2 - \theta$ and $R = h/\cos \theta$.

Several studies^{19,20} have reported that, for a water-in-oil DE droplet in the parallel-plate structure, the oil becomes entrapped underneath the inner water droplet as illustrated in Fig. 123.51(b). We analyzed the Gibbs surface energy change for both cases of the water droplet resting on the Teflon surface and the water droplet on a thin layer of oil. Using Eqs. (2)–(7) and the interfacial tension data shown in Table 123.VI, we calculate ΔG for water-in-silicone oil (20 cst) DE for the configurations of Figs. 123.51(a) and 123.51(b). ΔG per unit total liquid volume is expressed as the ratio of the volume of water to the total volume of water and oil in the DE. Both configurations give $\Delta G < 0$, but the configuration with the oil entrapped underneath the water system is energetically favored.

As noted above, a water droplet and an oil droplet usually combine to form a water-in-oil DE because water has a higher surface tension than most oils, but we can reverse this tendency if we add surfactant Silwet L-77 to the water. The interfacial tension for Silwet-treated water (at the surfactant concentration of 0.0625 wt%, listed in Table 123.VI) is greater than silicone

oil, but lower than mineral oil. Therefore it is not effective to choose silicone oil for oil-in-water DE's. Instead, we chose mineral oil and then calculated ΔG for water treated with mineral oil-in-Silwet as a function of the volume ratio of mineral oil.

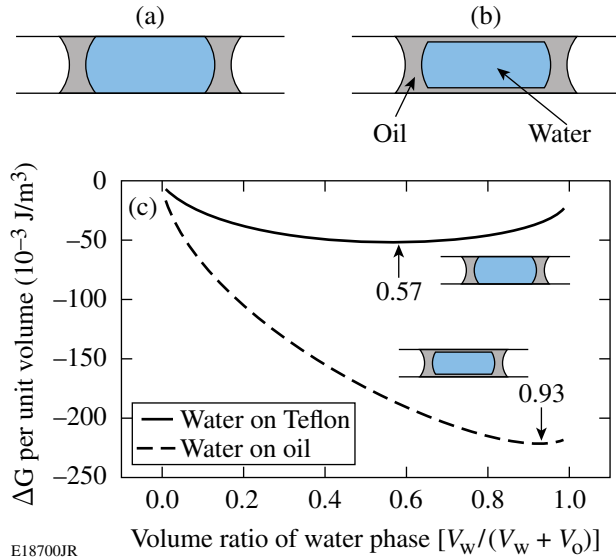


Figure 123.51 Water-in-silicone oil (20 cst) DE droplet in the parallel-plate structure: (a) the inner water droplet rests on the Teflon surface; (b) the inner water droplet rests on a thin layer of oil; (c) ΔG of DE formation for both cases (a) and (b).

Table 123.VI: Interfacial tension data at room temperature (mN/m).

Interface	Interfacial tension
Water/air	74
Silicone oil (20 cst)/air	20.6
Mineral oil/air	28.1
Silicone oil (20 cst)/water	35
Mineral oil/water	49
Water/Teflon TM	49
Silicone oil (20 cst)/Teflon TM	5.6
Mineral oil/Teflon TM	10.25
Teflon TM /air	18
W_{S-t} /air	24.7
Mineral oil/ W_{S-t}	4.5
W_{S-t} /Teflon TM	2.46

W_{S-t} : Silwet-treated water (0.0625 wt%)

As shown in Fig. 123.52, the requirement for DE formation, $\Delta G < 0$, is met. Similar to water-in-oil DE's, one might also wonder whether a thin layer of water could be entrapped underneath the oil droplet. To test for this possibility, we calculated ΔG for both this case and the case of oil resting directly on Teflon surface. Figure 123.52 shows that the energy is minimized when the inner oil droplet is separated from the Teflon surface by a layer of water. We have some evidence for this configuration but further experimental verification is needed.

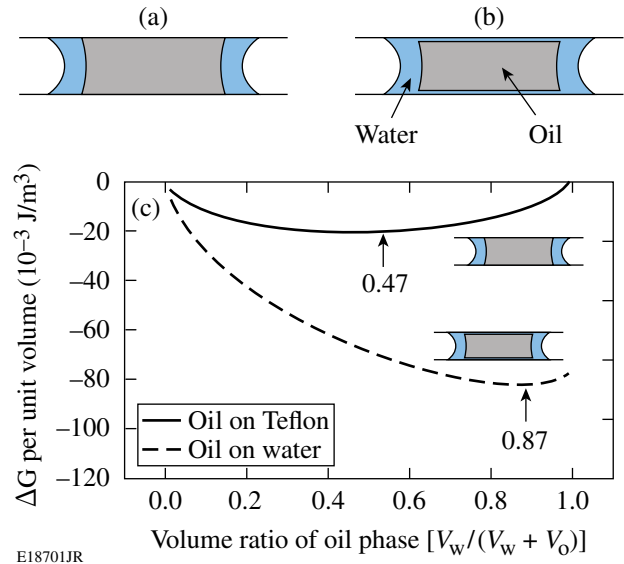
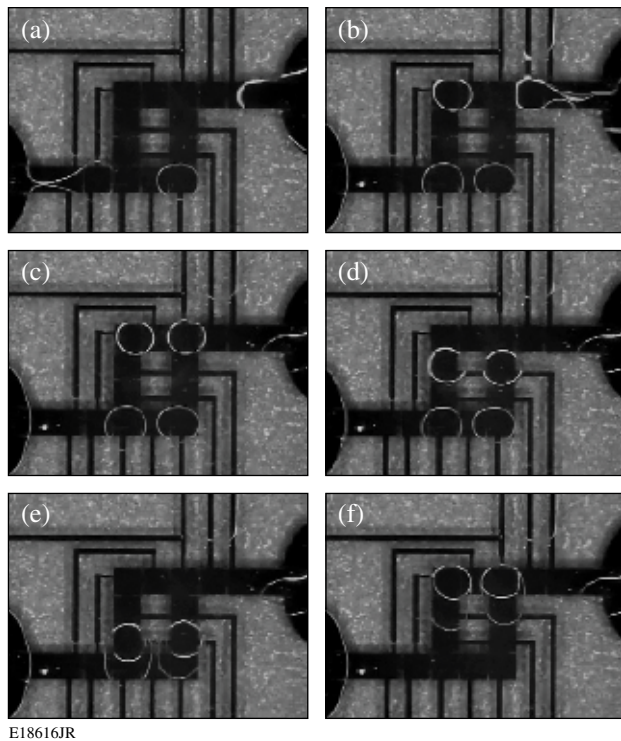


Figure 123.52 Mineral oil-in-Silwet-treated-water DE formation in parallel plates; (a) the inner oil droplet rests on the Teflon surface; (b) the inner oil droplet rests on a thin layer of water; (c) ΔG of DE formation for both cases (a) and (b).

2. Experiments for Water-in-Oil DE Formation

We tested the electric-field-actuated formation of water-in-silicone oil DE as shown in Fig. 123.53. Two silicone oil droplets were first dispensed from the left reservoir through DEP by applying $330\text{-}V_{\text{rms}}$, 100-Hz ac voltage on the lower array of electrodes. Then, two DI water droplets were dispensed from the right reservoir through EWOD actuation by application of $85\text{-}V_{\text{rms}}$, 100-Hz ac voltage on the upper array of electrodes. With the same EWOD actuation voltages, the water droplets were then transported toward the oil droplets as shown in Figs. 123.53(c) and 123.53(d). After the water droplets touched the oil droplets, they were engulfed by the oil droplets to form DE droplets [see Fig. 123.53(e)]. Furthermore, the water droplets were able to pull the whole merged water-in-oil DE droplets by low-voltage EWOD transport [Fig. 123.53(f)].



E18616JR

Figure 123.53

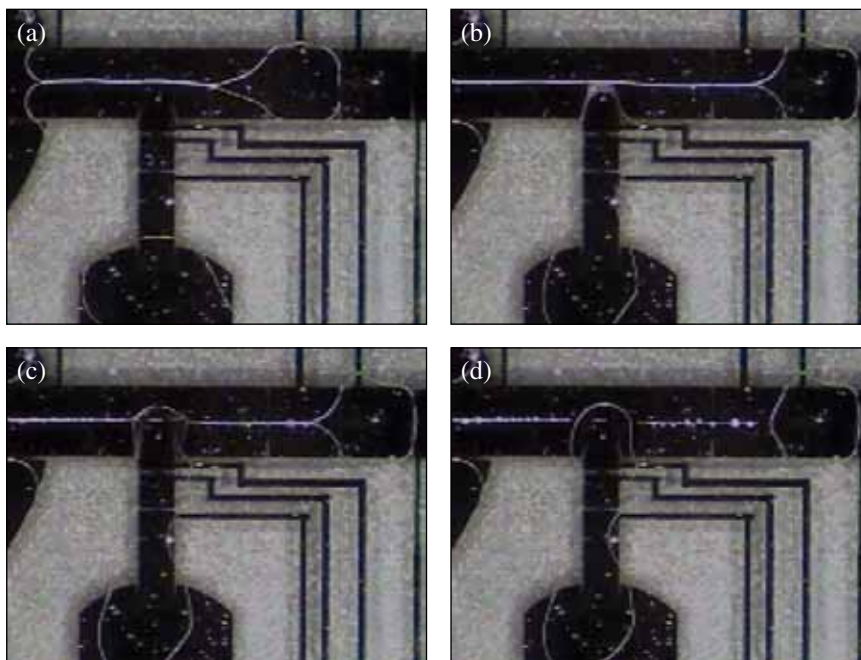
The formation of water-in-silicone oil DE droplets. (a) Two silicone oil droplets are dispensed through DEP actuation by applying $330\text{-}V_{\text{rms}}$, 100-Hz ac voltage; (b) two DI water droplets are dispensed by EWOD actuation by applying $85\text{-}V_{\text{rms}}$, 100-Hz ac voltage; [(c)–(e)] the water droplets are delivered and combined with oil droplets to form DE droplets; (f) the water droplets drag merged water-in-oil DE droplets by EWOD actuation.

3. Experiments for Oil-in-Water DE Formation.

We performed dispensing experiments with Silwet-treated water solutions of five wide ranging concentrations: 0.00625, 0.0125, 0.025, 0.0625, and 0.125 wt%. Only the 0.00625-wt% Silwet solution could be dispensed smoothly. All the others formed a remarkably persistent “tether” during the pinch-off process. As shown in Fig. 123.54(a), the thin liquid tether is formed between the reservoir and the droplet, preventing its separation. A full understanding of the tether formation is still lacking, but similar experiments in oil media show that surfactant-treated water can be successfully dispensed without tether formation.^{10,11}

One way to break the tether is to use a second liquid finger to disturb it; this mechanism is shown in Fig. 123.54. The secondary liquid used was pure DI water. When the pure-water finger touches the tether, the Silwet solution in the contact area is diluted locally and the tether breaks because of the increased surface tension. The entire tether disintegrates into many satellite droplets because of hydrodynamic instability [see Fig. 123.54(d)].

This method does not work when the Silwet concentration exceeds 0.125 wt%, in which case the second water finger seems to mix with the tether instead of breaking it. Apparently the local dilution is not sufficient to increase the surface tension when the Silwet concentration is far above critical micelle concentration. Another problem with the tether formed during dispensing is that



E18703JR

Figure 123.54

Breaking the tether with a second water liquid finger. (a) The second liquid (DI water) in a reservoir; (b) the second liquid finger approaches the “tether”; (c) the tether breaks inside the second liquid finger; (d) the entire tether disintegrates into many satellite droplets.

the electrode shape loses some of its influence in defining the pinch-off curvature, resulting in a poor volume reproducibility.

4. Other Possible Solutions to the Tether Problem

A second method to avoid the tether is by taking advantage of the pH effect on spreading of Silwet solutions. Radulovic²¹ found that the wetting ability of Silwet solutions is drastically reduced with the addition of acetic acid, possibly because of the polarization of the trisiloxane head. We also found in experiments that the Silwet surfactant could be strongly affected by the addition of other acids (such as HCl) or bases (such as KOH), and the change in wetting ability by the pH effect is reversible by neutralization. In our work, we have demonstrated that the addition of acid to Silwet-treated water can prevent the tether formation. Then, the dispensed droplet is neutralized by mixing with another base droplet. In this way, the required low surface tension is recovered. The droplet now containing some salts can be used for oil-in-water DE's. The problem with this method is that the reversal process using a base solution takes a long time, typically more than an hour. This waiting time would be a major disadvantage for mass production of DE droplets. Also, evaporation of water during such a long period must be prevented.

A third approach would be to add the surfactant to the oil to avoid tether formation. We have found that Silwet has little influence on the wetting property of oils and Silwet-doped oil can be dispensed smoothly. When a pure water droplet and a Silwet-doped oil droplet are placed together, an oil-in-water DE droplet is formed because Silwet tends to stay in water phase. Unfortunately, the DE droplet formation takes some time because the Silwet diffuses gradually across the interface from the oil phase into the water phase. Using 0.125% (v/v) Silwet-added mineral oil and DI water droplets, the process takes several minutes. When a 0.5% (v/v) Silwet-modified mineral oil drop is used, the diffusion time is reduced to about 10 s.

Conclusion

In this article, we have demonstrated that aqueous and non-aqueous liquid droplets can be dispensed from reservoirs on a microfluidic chip and the dispensed droplets can then be combined to form oil-in-water-in-air (O/W/A) or water-in-oil-in-air (W/O/A) DE droplets. In the dispensing process, droplet volume reproducibility has been tested over a range of operational parameters, including applied voltage and the length of the cutting electrode. We find that drop volume variability is caused mainly by variability in the tail volume during pinch-off. When the length of the cutting electrode is increased,

volume reproducibility is degraded because longer cutting electrodes reduce the influence of the electrode structure on the radius of curvature in the pinch-off region.

The Gibbs free energy change can be used to test the ability to form stable DE droplets. The result indicates that (1) water-in-oil DE droplets form through spontaneous emulsification and (2) oil-in-water DE droplets can also be formed by the addition of surfactant and the proper selection of oil. Experimental results show the formation of water-in-oil DE droplets. Using simultaneous DEP and EWOD actuation on a microfluidic chip, dielectric (oil) and conductive (water) droplets have been dispensed, and merged, and the transport of the merged water-in-oil DE droplet has been demonstrated.

The formation of water DE droplets treated with mineral oil-in-Silwet has been demonstrated. We find that a tether is formed during the dispensing of Silwet-treated water. Although the tether can be broken by the disturbance of a second liquid finger, it interferes with the dispensing operation and degrades dispensing reproducibility. Other methods to avoid the tether include taking advantage of the pH effect on Silwet solutions and adding the surfactant to the oil phase. Further effort to develop a more reliable formation method for oil-in-water DE is needed; for example, a surfactant more sensitive to pH might react more quickly so that its recovery of wetting ability (the contact angle reversal) would take much less time. Alternatively, low-surface-tension water could be dispensed in an oil medium without forming a tether. These schemes will be tested for oil-in-water DE formation.

ACKNOWLEDGMENT

This work was supported by the U.S. Department of Energy Office of Inertial Confinement Fusion under Cooperative Agreement No. DE-FC52-08NA28302, the University of Rochester, and the New York State Energy Research and Development Authority. The support of DOE does not constitute an endorsement by DOE of the views expressed in this article.

Appendix A: Requirements on DE Droplet Uniformity for Laser-Target Fabrication

The foam shell structure of a concentric laser target is shown in Fig. 123.55. V_1 and V_2 are the volumes of the inner oil phase and the outer water phase, respectively:

$$V_1 = \frac{4\pi}{3} R_1^3 \text{ and } V_1 + V_2 = \frac{4\pi}{3} R_2^3.$$

The shell thickness is $d = R_2 - R_1$; therefore, d can be written

$$d = \frac{\left(\frac{3}{\pi}\right)^{1/3} \cdot (V_1 + V_2)^{1/3}}{2^{2/3}} - \frac{\left(\frac{3}{\pi}\right)^{1/3} \cdot V_1^{1/3}}{2^{2/3}}. \quad (A1)$$

By taking partial derivatives of Eq. (A1), we obtain an expression for the uncertainty of d in terms of the uncertainties of V_1 and V_2

$$\Delta d = \left| \Delta V_1 \cdot \left[\frac{1}{6^{2/3} \pi^{1/3} (V_1 + V_2)^{2/3}} - \frac{1}{6^{2/3} \pi^{1/3} V_1^{2/3}} \right] \right| + \left| \Delta V_2 \cdot \frac{1}{6^{2/3} \pi^{1/3} (V_1 + V_2)^{2/3}} \right|. \quad (A2)$$

The specified dimensions of an inertial fusion energy (IFE) target are $2R_2 = 4 \pm 0.2$ mm, $d = 289 \pm 20$ μ m. By substituting these values into Eq. (A2), we can determine wall-thickness variation ($\Delta d/d$) in terms of water and oil volume variations ($\Delta V/V$) (refer to Fig. 123.56). Different wall thickness variations ($\Delta d/d$) are represented by a set of straight lines in the ($\Delta V_1/V_1$) versus ($\Delta V_2/V_2$) chart. These lines have the same slope, and small ($\Delta d/d$) lines are closer to the original point. The shaded area indicates where the requirement on wall thickness variation is satisfied, i.e., $\Delta d/d < 20/289 = 6.92\%$. For example, if the oil volume variation ($\Delta V_1/V_1$) is 5% and the water volume

variation ($\Delta V_2/V_2$) is 4%, the corresponding point indicated by a star in Fig. 123.56 is located within the shaded area, which means the wall thickness condition meets the requirement.

The red line in Fig. 123.56 represents where the changes of water- and oil-phase absolute volumes are the same, and the blue line represents where the relative volume variations of water and oil phases are the same. Under the condition of identical relative volume variations, $|\Delta V_1/V_1| = |\Delta V_2/V_2|$ must be smaller than 4.97% to meet the laser target requirement.

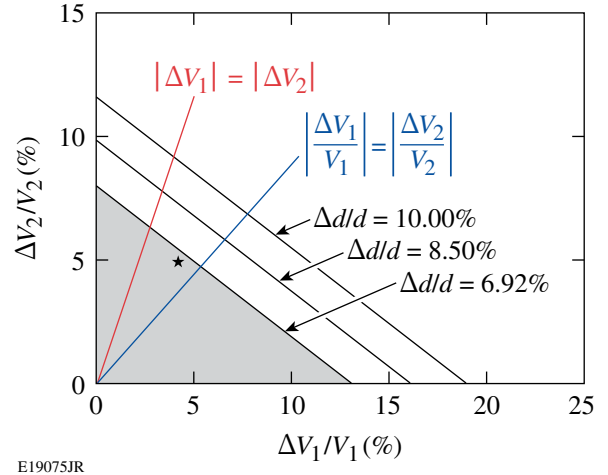


Figure 123.56 Sensitivity analysis of shell wall thickness for an IFE target.

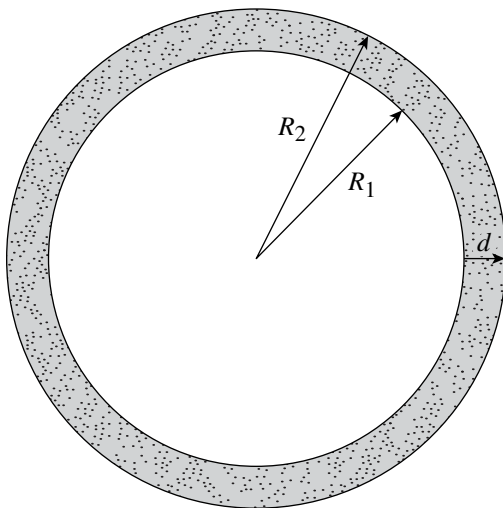


Figure 123.55 The foam shell structure of a concentric laser target.

REFERENCES

1. S. M. Lambert *et al.*, *J. Appl. Polym. Sci.* **65**, 2111 (1997).
2. R. Paguio *et al.*, in *Assembly at the Nanoscale—Toward Functional Nanostructured Materials*, edited by C. S. Ozkan *et al.*, *Mat. Res. Soc. Symp. Proc.* Vol. 901E (Materials Research Society, Warrendale, PA, 2006), Paper 0901-Ra05-23-Rb05-23.
3. N. Pannacci *et al.*, *Phys. Rev. Lett.* **101**, 164502 (2008).
4. A. S. Utada *et al.*, *Science* **308**, 537 (2005).
5. S. Okushima *et al.*, *Langmuir* **20**, 9905 (2004).
6. R. B. Fair, *Microfluid Nanofluid* **3**, 245 (2007).
7. T. B. Jones, *Langmuir* **18**, 4437 (2002).
8. M. G. Pollack, R. B. Fair, and A. D. Shenderov, *Appl. Phys. Lett.* **77**, 1725 (2000).
9. S. K. Cho, H. Moon, and C.-J. Kim, *J. Microelectromech. Syst.* **12**, 70 (2003).

10. H. Ren, R. B. Fair, and M. G. Pollack, *Sens. Actuators B, Chem.* **98**, 319 (2004).
11. J. Berthier *et al.*, *Sens. Actuators A, Phys.* **127**, 283 (2006).
12. R. B. Fair *et al.*, in *IEEE International Electron Devices Meeting (IEDM 2003)* (IEEE, New York, 2003), pp. 32.5.1–32.5.4.
13. T. B. Jones and M. Washizu, *J. Electrostatics* **37**, 121 (1996).
14. P. R. C. Gascoyne and J. V. Vykoukal, *Proc. IEEE* **92**, 22 (2004).
15. D. Chatterjee *et al.*, *Lab Chip* **6**, 199 (2006).
16. S.-K. Fan, T.-H. Hsieh, and D.-Y. Lin, *Lab Chip* **9**, 1236 (2009).
17. T. B. Jones, K.-L. Wang, and D.-J. Yao, *Langmuir* **20**, 2813 (2004).
18. K.-L. Wang and T. B. Jones, *J. Micromech. Microeng.* **14**, 761 (2004).
19. M. Bienia *et al.*, *Physica A* **339**, 72 (2004).
20. A. Staicu and F. Mugele, *Phys. Rev. Lett.* **97**, 167801 (2006).
21. J. Radulovic, K. Sefiane, and M. E. R. Shanahan, *J. Colloid Interface Sci.* **332**, 497 (2009).

Charge-Injection-Device Performance in the High-Energy-Neutron Environment of Laser-Fusion Experiments

Introduction

Electronic devices such as charge-coupled devices (CCDs)¹ or charge-injection devices (CIDs)² (the subject of this work) are used to image x rays emitted by laser-generated plasmas. The laser beam or beams interact with the target in various ways depending on the total energy- and intensity-generating, short-lived plasmas whose temperatures are such that either thermal or nonthermal x-ray emission takes place. X-ray imaging and x-ray spectroscopy are used in such research to diagnose conditions in the plasma. The laser–target interactions for laser intensities exceeding $\sim 10^{14}$ W/cm² result in plasma temperatures in the keV regime. During ablation and implosion of targets in laser-driven fusion experiments, stagnation core temperatures as high as ~ 10 keV can be obtained³ and are expected for conditions approaching ignition at the National Ignition Facility (NIF).⁴ Simultaneously with the x-ray emission, a burst of fusion-generated neutrons is emitted by the imploding target at the time of implosion stagnation. Maximum neutron yields of $\sim 10^{14}$ (DT, neutron energy 14.1 MeV) are currently generated at LLE’s Omega Laser Facility⁵ and are expected to be far exceeded on the NIF. At a yield of 10^{14} the neutron fluence at 1 m from the target, if unattenuated, is $\sim 8 \times 10^8$ neutrons/cm². In a typical $25\text{-}\mu\text{m} \times 25\text{-}\mu\text{m}$ pixel region of an imaging array, this neutron fluence corresponds to $\sim 5 \times 10^3$ neutrons per pixel. Clearly, if the solid-state device is sensitive to either the neutrons or neutron-induced γ rays or neutron-generated charged particles, this flux level could cause the device to be incapable of being used for imaging x rays.

The effects of ionizing radiation, both γ rays and charged particles, on silicon⁶ and on silicon-based photodetectors such as CCDs⁷ have been studied. γ rays and, therefore, neutron-induced γ rays, can cause bulk damage through Compton scattering of the γ rays by atomic electrons. The displaced Si atoms can permanently affect the noise level of the device or, if enough defects are created, render it unusable. While not immune to such effects, the unique architecture of the CID² makes it radiation tolerant.⁸ CID cameras able to withstand radiation levels of 10^6 -rad/h and 10^7 -rad accumulated dose are available.⁹

In this work the effects of high-energy (DT) neutrons on the CID cameras are examined. The experiments were performed on the 60-beam, UV OMEGA Laser.⁵ Implosions of DT-filled capsules on OMEGA can generate neutron yields of up to $\sim 10^{14}$ (Ref. 10). CID cameras are used on this system in a number of x-ray imaging diagnostics¹¹ at a range of distances (0.8 to 2.6 m) experiencing neutron fluences ranging from 10^7 to 10^9 neutrons/cm². It is demonstrated in this work that the resulting background and noise levels in the CID cameras are a function of the neutron fluence and that usable images are obtained throughout this fluence range. Furthermore, numerical processing of the images reduces neutron-induced noise in the x-ray images obtained during high-yield target experiments, extending the useful range to higher neutron yields/fluences.

Neutron-Induced Signal in CID Cameras

The CID cameras used in this work (model CID4150-DX3)¹² are the primary means of image acquisition at the Omega Laser Facility in a set of x-ray pinhole cameras (XPHCs)¹³ and an x-ray microscope that uses a Kirkpatrick–Baez reflection optic to obtain x-ray images. The x-ray microscope system, known as the gated monochromatic x-ray imager (GMXI),¹⁴ was used with CID cameras at the image plane in a time-integrating broadband mode. The sensitive x-ray range of the GMXI is ~ 2 to 7 keV, limited at the low end by transmission through a Be blast shield and at the high end by Ir-mirror reflectivity.¹⁴ The XPHCs are similarly limited at low x-ray energies but contain no high-energy mirror cutoff. Target-emission spectral shape makes the energy ranges comparable.

The model CID4150-DX3 is an 812×607 -pixel array of square photodiodes with $38.5\text{-}\mu\text{m}$ center-to-center spacing. The active area is $31.3 \times 23.2\text{ mm}^2$ and is housed inside an aluminum case with $48\text{-} \times 30\text{-mm}$ outside dimensions. The well depth for each pixel is $\sim 1.4 \times 10^6$ e–h pairs and the depletion region depth is $\sim 7\text{-}\mu\text{m}$ (Ref. 15). The sensors are front-side illuminated and have an equivalent dead layer of $\sim 1\text{-}\mu\text{m}$ Si (Ref. 15). The sensors do not have a phosphor coating, and all cameras in this study were operated in vacuum with a $25\text{-}\mu\text{m}$ -thick Be window in front of the sensor (toward target). In general the images in

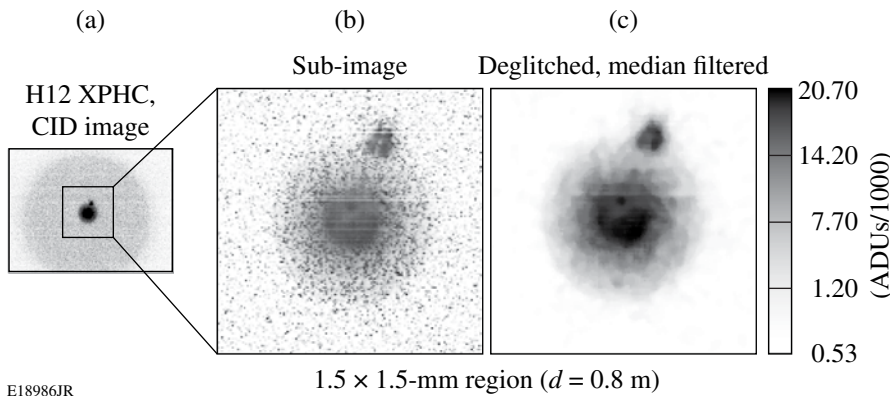
this study consist of an accumulated signal caused by x rays in the range of 2 to 7 keV.

Figures 123.57 and 123.58 show example x-ray images taken on typical D-T neutron-generating target experiments with an XPHC and the GMXI. The images are displayed in units of ADUs (analog-to-digital units). The XPHC image [Fig. 123.57(a)] is at a high neutron fluence ($\sim 4 \times 10^8$ neutrons/cm²) because of its proximity to the target (0.8 m), while the GMXI image [Fig. 123.58(a)] was taken at a much lower neutron fluence ($\sim 3 \times 10^7$ neutrons/cm²). Both target shots had the same approximate yield (3×10^{13} neutrons). The images are improved [Figs. 123.57(c) and 123.58(c)] by processing the images using deglitching and filtering (described later in the text).

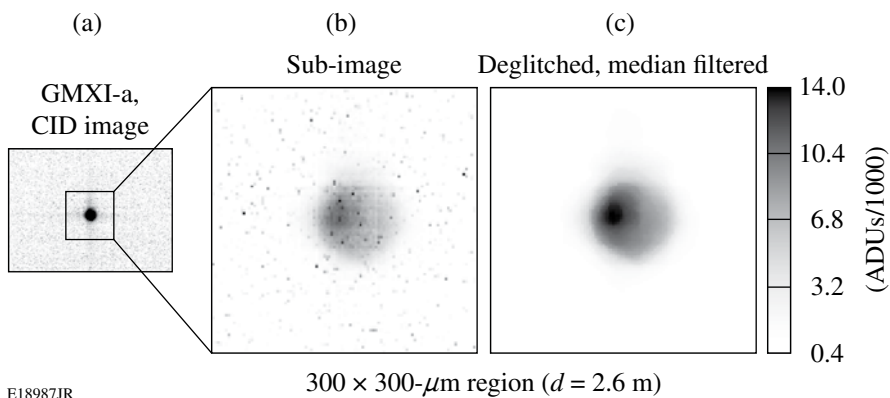
The neutron-induced effects in a set of images (~ 100) with neutron yields ranging from 3×10^{12} to 6×10^{13} , with CID cameras in both XPHCs and the GMXI, were determined as follows: The average signal level in the camera was determined in a 400×400 -pixel region not containing the x-ray image and

not shielded by any of the pinhole-camera support structure. The root-mean-square fluctuations (σ_{rms}) were computed from the variations of the mean signal in the same region. In all cases, the images are corrected for non-target-induced background (primarily dark current) by subtracting a frame taken before the laser shot (1.2 s before shot). The subtraction of the background frame is always a good idea and in the mode of operation of the CID cameras used in this work (uncooled) is essential. All values of background and σ_{rms} are plotted as a function of neutron fluence (yield over $4\pi d^2$, where d is the distance). Two CID cameras were in XPHC's at a distance of 0.8 m to the target, and one was in an XPHC at a distance of 1.9 m. Additionally, two CID cameras were in the GMXI at a distance of 2.6 m. The DT-neutron yields were obtained from a fully cross-calibrated set of neutron detectors.¹⁶ The absolute neutron yields measured by these detectors are accurate to better than 10%.

Figure 123.59 shows the average neutron-induced signal level for all cameras as a function of neutron fluence. The signal level is seen to follow a straight line of slope ~ 1 , meaning



E18986JR



E18987JR

Figure 123.57

An x-ray image obtained with a CID camera in an OMEGA XPHC on a high-(DT) neutron-yield target shot (yield $\sim 3 \times 10^{13}$). (a) The full image with neutron-induced background and noise, (b) An unprocessed sub-image representing a 2×2 -mm region at the target. Single-pixel events are evident as are some line upsets. (c) A deglitched and median-filtered version of the same sub-image.

Figure 123.58

An x-ray image obtained with a CID camera in the GMXI on a target shot with similar yield to the XPHC image in Fig. 123.57 (yield $\sim 3 \times 10^{13}$). (a) Full image, (b) unprocessed sub-image representing a 500×500 - μm region at the target, and (c) a deglitched and median-filtered version of the same.

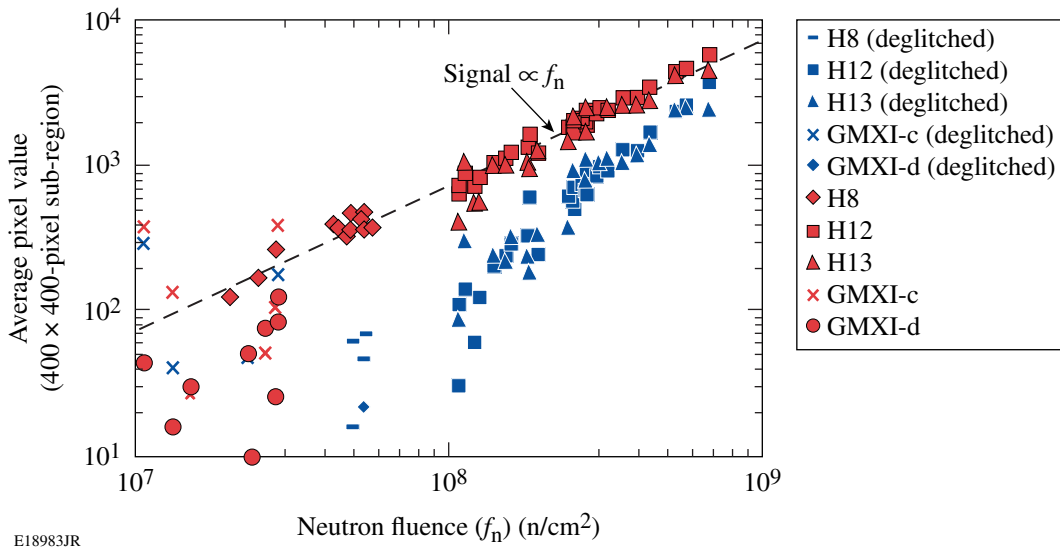


Figure 123.59

The average pixel value in ADUs for 400×400 -pixel regions in all of the CID cameras for regions not containing x-ray images as a function of the neutron fluence. The red (upper) values are from non-deglitched images and the blue (lower) values are from deglitched images.

it is proportional to the neutron fluence (f_n). As is noticed in Figs. 123.57 and 123.58, the neutron-induced signal consists of a near-single-pixel component as well as a more-uniform background. The single-pixel events are likely to be induced by n-p protons generated by neutron interaction with the $25\text{-}\mu\text{m}$ -thick Be window just in front of the CID sensor, while the uniform background is a consequence of n-gammas interacting with the CID sensor. (A study of the charged-particle sensitivity of this model of CID camera can be found in Fletcher *et al.*¹⁷). Jaanimagi *et al.*¹⁸ found a similar phenomenological effect on CCDs used for streak-camera recording at the Omega Facility.

The single-pixel events are effectively removed by deglitching the images. That is accomplished here by running a program that tests the values found in a 5×5 -pixel region. If the value of the pixel is greater than 1.25 times the median of that region, then the value is replaced by the median. This first step removes most of the high-signal-level single-pixel events. A second pass over the image, where the pixel value is replaced by the median of the pixel values resulting from the first pass, further reduces noise in the image. (More sophisticated noise-removal algorithms such as those compared in Chen and Yang¹⁹ are capable of even more thorough noise removal but are outside the scope of this article.) Examples of the improvements in the images are shown in Figs. 123.57(c) and 123.58(c). The lowering of the average signal level caused by deglitching is seen in the lower curve of values in Fig. 123.59 (deglitched values are those of step 1; no additional median filtering is applied).

The variation of the neutron-induced signal σ_{rms} is shown in Fig. 123.60. The variation is seen to follow a curve of slope $\sim 1/2$ making it proportional to $(f_n)^{1/2}$. Again, deglitching suppresses the noise by eliminating the high-signal-level single-pixel events (lower curve of values seen in Fig. 123.60). The maximum signal level detected in any given pixel (taken here to be $\sim 1.4 \times 10^6$ electron-hole pairs, corresponding to $\sim 20,000$ ADUs) limits the maximum detected x-ray signal. For instance, at 1 keV for an assumed e-h pair energy of 3.3 eV, the maximum number of absorbed photons is 4600. The maximum signal-to-noise ratio (SNR_{max}) achievable is therefore $\sim (n)^{1/2}$, where n is the number of photons absorbed. At 1 keV this is ~ 68 per pixel for the CID camera or, using the same argument, ~ 21 at 10 keV.

Figure 123.61 shows the computed SNR_{max} after background subtraction, with and without deglitching, for the same set of target experiments. Usable images are obtained for the highest neutron fluences encountered, with deglitching increasing the SNR by a factor of 3 or more. For comparison, the SNR_{max} achievable from photon-counting statistics for the 1-keV and 10-keV photon-energy cases are shown as horizontal dashed lines in Fig. 123.61. For the non-deglitched images the SNR is affected above neutron fluences of $\sim 3 \times 10^7$ neutrons/cm². For the deglitched images the SNR is restored to more than can be achieved with counting statistics alone for neutron fluences of up to $\sim 10^8$ neutrons/cm² for 1-keV photons or $\sim 3 \times 10^8$ neutrons/cm² for 10-keV photons.

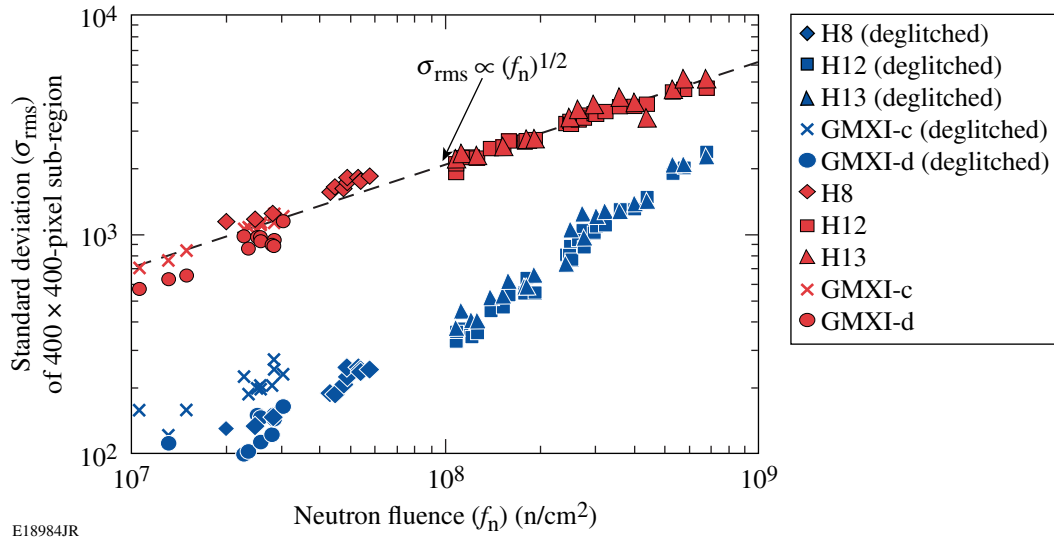


Figure 123.60
The standard deviation of the pixel values σ_{rms} as a function of neutron fluence for CID images from non-deglitched (red, upper) and deglitched (blue, lower) images.

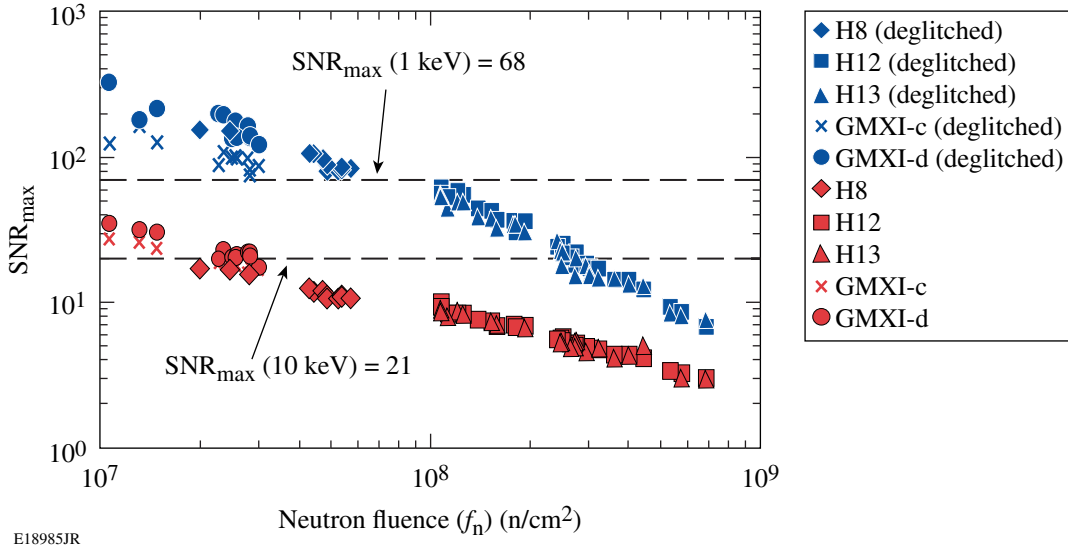
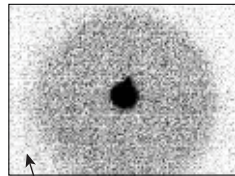


Figure 123.61
The computed maximum signal-to-noise ratio (SNR_{max}) as a function of neutron fluence from non-deglitched and deglitched images from all CID cameras. The dashed lines are the maximum SNR's obtainable from photon-counting statistics for 1- and 10-keV photons.

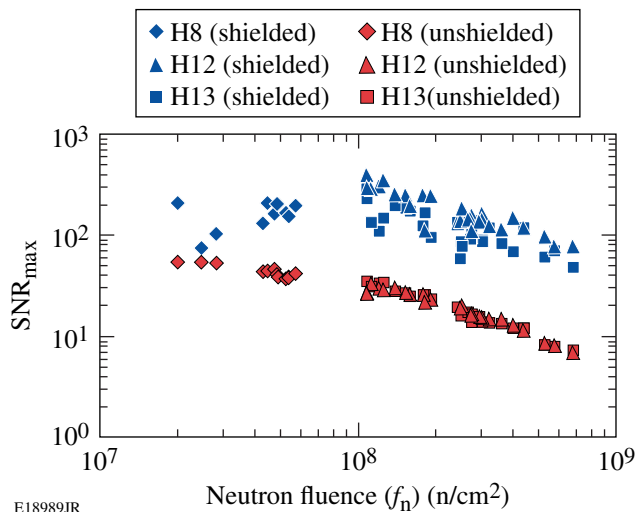
A further improvement of the SNR is achieved if the CID camera is shielded from the direct line of sight to the target with sufficient material to attenuate the neutron-induced signal. In the case described here (Fig. 123.62) the regions of the CID cameras in the XPHCs that are shielded by the body of the pinhole camera (~13 mm of stainless steel in the path) have a reduced background signal induced by the high-energy neutrons. For the cases shown, the shielding decreases the background and noise and increases the SNR, making it possible to use the CID cameras at inferred neutron fluences up to $\sim 10^{10}$ neutrons/cm² (extrapolation of the shielded SNR trend). At 1 m this corresponds to a neutron yield of $\sim 10^{15}$. To make practical use of shielding, however, the direct path to the target must be blocked. The diagnostic must therefore incorporate reflectors such as grazing-incidence mirrors, as in a KB microscope, or crystal-diffraction elements, as in a spectrometer.

undertaken at the Omega Laser Facility, where yields up to $\sim 10^{14}$ can be generated. The neutron-induced effects on the cameras are seen to scale with neutron fluence and therefore are inversely proportional to the square of the distance from the target to the camera. Deglitching the x-ray images obtained during high-energy neutron-target experiments reduces the noise and increases the fluence range that useful x-ray images can be obtained up to $\sim 3 \times 10^8$ neutrons/cm². Shielding the cameras from the direct line of sight to the target can further reduce the neutron-induced background, and an inferred yield of $\sim 10^{15}$ at 1 m could be tolerated if shielding comparable to or better than that used in this study is incorporated into the diagnostic. This, however, requires the use of reflectors or diffractors. This study indicates that the CID camera will be a useful means of obtaining time-integrated x-ray images on the NIF up to yields of $\sim 10^{15}$ or more depending on distance to the target and shielding.

H9 XPHC, CID image



Shielded region



E18989JR

Figure 123.62 The computed SNR_{max} for shielded and unshielded regions of CID cameras in OMEGA XPHCs as a function of neutron fluence. Both cases are for deglitched images.

Conclusions

The CID camera used in this work (model CID4150-DX3)¹¹ is seen to maintain usability in the high-energy neutron environment of DT-bearing target experiments currently being

ACKNOWLEDGMENT

This work was supported by the U.S. Department of Energy Office of Inertial Confinement Fusion under Cooperative Agreement No. DE-FC52-08NA28302, the University of Rochester, and the New York State Energy Research and Development Authority. The support of DOE does not constitute an endorsement by DOE of the views expressed in this article.

REFERENCES

1. J. R. Janesick *et al.*, *Opt. Eng.* **26**, 156 (1987).
2. J. Carbone *et al.*, in *Solid State Sensor Arrays: Development and Applications II*, edited by M. M. Blouke (SPIE, Bellingham, WA, 1998), Vol. 3301, pp. 90–99.
3. J. D. Lindl, *Inertial Confinement Fusion: The Quest for Ignition and Energy Gain Using Indirect Drive* (Springer-Verlag, New York, 1998).
4. W. J. Hogan, E. I. Moses, B. E. Warner, M. S. Sorem, and J. M. Soures, *Nucl. Fusion* **41**, 567 (2001).
5. T. R. Boehly, D. L. Brown, R. S. Craxton, R. L. Keck, J. P. Knauer, J. H. Kelly, T. J. Kessler, S. A. Kumpan, S. J. Loucks, S. A. Letzring, F. J. Marshall, R. L. McCrory, S. F. B. Morse, W. Seka, J. M. Soures, and C. P. Verdon, *Opt. Commun.* **133**, 495 (1997).
6. R. Korde *et al.*, *IEEE Trans. Nucl. Sci.* **36**, 2169 (1989).
7. J. Janesick, T. Elliott, and F. Pool, *IEEE Trans. Nucl. Sci.* **36**, 572 (1989).
8. J. Carbone, S. Czebiniaik, and R. Carta, in *Robotics and Remote Systems*, edited by L. M. Kostelnik, Proceedings of the Conference on Robotics and Remote Systems (American Nuclear Society, La Grange Park, IL, 1996), Vol. 43, pp. 43–50.
9. J. J. Zarnowski *et al.*, in *Charge-Coupled Devices and Solid State Optical Sensors IV*, edited by M. M. Blouke (SPIE, Bellingham, WA, 1994), Vol. 2172, pp. 187–198.

10. J. M. Soures, R. L. McCrory, C. P. Verdon, A. Babushkin, R. E. Bahr, T. R. Boehly, R. Boni, D. K. Bradley, D. L. Brown, R. S. Craxton, J. A. Delettrez, W. R. Donaldson, R. Epstein, P. A. Jaanimagi, S. D. Jacobs, K. Kearney, R. L. Keck, J. H. Kelly, T. J. Kessler, R. L. Kremens, J. P. Knauer, S. A. Kumpan, S. A. Letzring, D. J. Lonobile, S. J. Loucks, L. D. Lund, F. J. Marshall, P. W. McKenty, D. D. Meyerhofer, S. F. B. Morse, A. Okishev, S. Papernov, G. Pien, W. Seka, R. Short, M. J. Shoup III, M. Skeldon, S. Skupsky, A. W. Schmid, D. J. Smith, S. Swales, M. Wittman, and B. Yaakobi, *Phys. Plasmas* **3**, 2108 (1996).
11. F. J. Marshall, T. Ohki, D. McInnis, Z. Ninkov, and J. Carbone, *Rev. Sci. Instrum.* **72**, 713 (2001).
12. Thermo Fisher Scientific Instruments Division, CIDTEC Cameras and Imagers, Liverpool, NY 13088.
13. R. A. Forties and F. J. Marshall, *Rev. Sci. Instrum.* **76**, 073505 (2005).
14. F. J. Marshall and J. A. Oertel, *Rev. Sci. Instrum.* **68**, 735 (1997).
15. R. Forties, *2000 Summer Research Program for High School Juniors at the University of Rochester's Laboratory for Laser Energetics*, Rochester, NY, LLE Report No. 319, LLE Document No. DOE/SF/19460-383 (2000).
16. V. Yu. Glebov, C. Stoeckl, T. C. Sangster, S. Roberts, G. J. Schmid, R. A. Lerche, and M. J. Moran, *Rev. Sci. Instrum.* **75**, 3559 (2004).
17. K. A. Fletcher, B. Apker, S. Hammond, J. Punaro, F. J. Marshall, J. Laine, and R. Forties, *Rev. Sci. Instrum.* **78**, 063301 (2007).
18. P. A. Jaanimagi, R. Boni, and R. L. Keck, *Rev. Sci. Instrum.* **72**, 801 (2001).
19. S. Chen and X. Yang, *Opt. Eng.* **46**, 097003 (2007).

Grating Inspection System for Large-Scale Multilayer-Dielectric Gratings for High-Energy Laser Systems

Introduction

The OMEGA EP Laser System at LLE is a petawatt-class laser system capable of producing high-energy laser pulses with lengths shorter than a picosecond. Short-pulse production is achieved in a pulse compressor composed of large-aperture (meter-scale) multilayer-dielectric diffraction gratings.¹ The pulse compressor consists of four tiled-grating assemblies (TGA's) within a vacuum grating compressor chamber (GCC).² The fourth TGA handles the highest compressed power and is, therefore, most prone to laser-induced damage, requiring frequent inspection. A grating inspection system (GIS) has been developed to provide *in-situ* detection of potential damage features on the fourth TGA without disturbing the vacuum environment or the alignment of the TGA's.

In this article we describe the GIS, which provides high-resolution damage-sensitive imaging of the diffraction grating's optical surface. Selective sensitivity to damage is achieved by using a dark-field imaging system that collects scattered (as opposed to reflected or diffracted) light from the optical surface. This technique is not, in principle, dependent on the diffractive nature of the surface under test and should be applicable to any flat optical surface that causes minimal scattering when in an undamaged state.³

This article will (1) discuss the GIS system with design requirements and constraints; (2) present an alignment method that optimizes performance; (3) discuss the background and thermal issues that arise from using the GIS system in a vacuum environment; (4) present a data-reduction scheme that addresses various unique issues posed by the system; (5) demonstrate measurement results obtained from the GIS during a recent energy ramp campaign; and (6) present conclusions.

System Description

A number of key requirements were imposed on the GIS system design to ensure compatibility with the OMEGA EP pulse compression system:

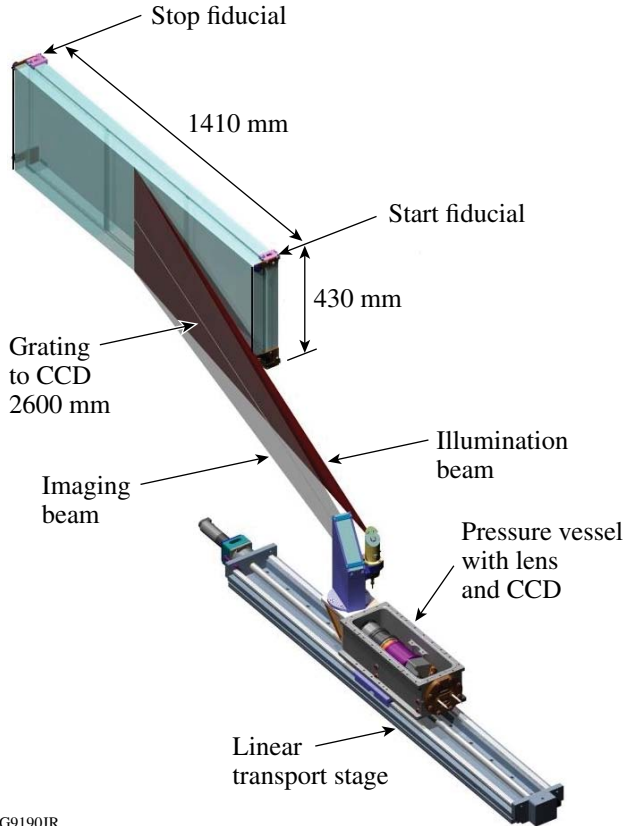
1. The GIS may not enter a volume assigned to any other GCC devices.
2. The GIS must not obstruct shot and alignment beams.
3. GIS heat output must be less than 1 W/h per measurement.
4. All material must be rated as vacuum compatible and satisfy class-100-level cleanliness requirements.
5. GIS must be capable of detecting damage features as small as 250 μm .

To best satisfy these requirements, a linearly scanned, dark-field imaging concept was selected. A scanning system allows one to sample a number of object points greater than the number of pixels on the sensor, which is a significant advantage over other design concepts given the size of the object to be imaged ($\sim 6 \times 10^5 \text{ mm}^2$) and the feature size requirement [see requirement (5) above]^a. In the context of imaging a highly angle dependent surface such as a diffraction grating, a scanning system has the additional advantage that the viewing angle is constant with respect to position along the scan-parallel direction.

The GIS consists of three subsystems: (1) a line-illumination system, (2) a line-imaging system aligned to view the illuminated portion of the grating surface, and (3) a transport mechanism that scans these across the width of the TGA to form a two-dimensional image. Figure 124.1 shows an overview of the system, and Table 124.I outlines the specifications of the as-built system, which satisfies the design requirements.

The illumination system consists of a line generator that projects an elongated Gaussian pattern onto the grating surface.

^aNote that requirement (5) concerns *detection*, not *resolution*. It is invoked here only as an estimator of the required resolution and, in turn, the required number of object plane samples.



G9190JR

A line generator is used rather than a simpler area illumination concept to provide sufficient irradiance in the region imaged by the camera, while requiring only a modest total power. Light is provided by a 1053-nm fiber laser external to the GCC and transported to the line generator via a single-mode, polarization-maintaining fiber. Since both high illumination intensity and a long optical fiber to deliver illumination to the GIS are required, special care was necessary to prevent stimulated Brillouin scattering from destroying the fiber. This was achieved by using a custom fiber-laser source with a relatively short coherence length as compared to commercial products at this wavelength.

As closely as possible, the illumination light matches the polarization (vertical), incidence angle ($\sim 72^\circ$), and wavelength (1053 nm) for which the gratings are designed to exhibit their highest diffraction efficiency. Mechanical restrictions on the location of the GIS within the GCC [see requirement (1) above] preclude, however, an exact match to the desired angle of incidence. As a compromise, an angle of incidence of 78.5°

Figure 124.1

Grating inspection system is shown scanning across a 1.41-m \times 0.43-m tiled-grating assembly. Note that the pressure vessel housing cover is absent in this image for illustrative purposes.

Table 124.I: System parameters.

Imaging System	
Working (object) distance	2.6 m
Viewing angle w.r.t grating surface	76°
Focal length	250 mm
Full field of view	14°
Feature detection	$250 \mu\text{m}$ or larger
Sensor	Dalsa Piranha 2 8192-pixel array, 10 bits/pixel, $7\text{-}\mu\text{m}$ pixel size
Lens	Mamiya KL 4.5/250L-A (Ref. 4)
Illumination	
Wavelength	1053 nm
Angle of incidence	78.5° from surface normal
Power at line generator	180 mW
Line shape on grating surface	Gaussian $1 \times 500 \text{ mm}$ at $1/e^2$
Mechanical	
Alignment fiducial	$250\text{-}\mu\text{m}$ -diam acid-etched wires, coplanar with grating surface
Vacuum-compatible reticulating stage	Straightness = $100 \mu\text{m}$ over 1.5 m, effective drive/encoder resolution = $2 \mu\text{m}$

from the grating surface normal is used. This is close enough to the ideal angle that diffraction efficiency is not significantly affected. Most of the incident light is therefore diffracted, minimizing stray light from reflections in the grating substrate or nearby mechanical components. Light striking a damaged portion of the grating will be diffracted less efficiently, leading to scatter that may be detected by the imaging system.

The imaging system consists of a commercial medium-format photographic lens that images the optic surface to a linear charge-coupled-device (CCD) array camera. The camera captures light from one vertical strip of the optic during each acquisition, building an image as the scanner moves horizontally across the TGA surface. The camera and imaging lens are housed in an airtight case, along with temperature and pressure sensors. This casing preserves atmospheric pressure to facilitate heat dissipation from the camera (see **Mitigation of Thermal and Background Effects**, p. 168) and to prevent contamination of the GCC by outgassing from the camera, lens, or associated electronics. A periscope assembly, external to the airtight case, keeps the camera and imaging lens out of the on-shot and alignment beam envelopes. Figure 124.2 gives an overhead view of the GIS camera and pressure vessel including the periscope and illumination and imaging systems.

The imaging lens provides a reduction from object to image by a factor of 8.9, mapping the $7\text{-}\mu\text{m}$ pixels of the camera to about $62.5\ \mu\text{m}$ in the object plane.⁴ The camera views the grating surface at a shallow angle, however, which spreads the object space footprint of each pixel by a factor of 3.8 in the horizontal direction, covering an area of $62.5 \times 237.5\ \mu\text{m}$ in the plane of the grating surface. The GIS typically acquires

a line of data per $16\ \mu\text{m}$ of travel across the grating surface, which, in combination with the horizontal extent of the pixel footprint in object space, means that every point on the grating surface contributes to the signal in adjacent lines of data in the output image. Acquiring data in this way provides a low-pass effect and strong oversampling, which is an advantage in data reduction for reducing noise and eliminating a particular type of image defect (see **Data Reduction**, p. 169).

The linear transport is parallel to the surface of the grating and offset from it along the scan direction. The placement of the GIS transport was chosen to accommodate existing GCC equipment and satisfied the top-level requirements. Custom drive electronics for the linear transport provide a trigger signal for the camera, which is synchronized to the rotary encoder output from the drive motor. This prevents fluctuations in transport velocity from producing distortions in the image data and ensures that the scale of the image will be highly repeatable.

Installation and Alignment

To maximize the sensitivity of the GIS, the illumination line and the line imaged by the CCD must overlap precisely. Using a high-precision coordinate measuring machine,⁵ the transport stage was aligned to be parallel to the grating surface at the correct distance to yield a nominal viewing angle of 14° relative to the scan direction (76° relative to the grating surface normal). This angle was mandated by the mechanical constraints discussed in the previous section. To facilitate the alignment between illumination and imaging beams, alignment fiducials are installed on the TGA for use with the GIS. The fiducials are $250\text{-}\mu\text{m}$ -diam stainless-steel wire, strung 3 mm from the edge of the grating, parallel to the edge, and copla-

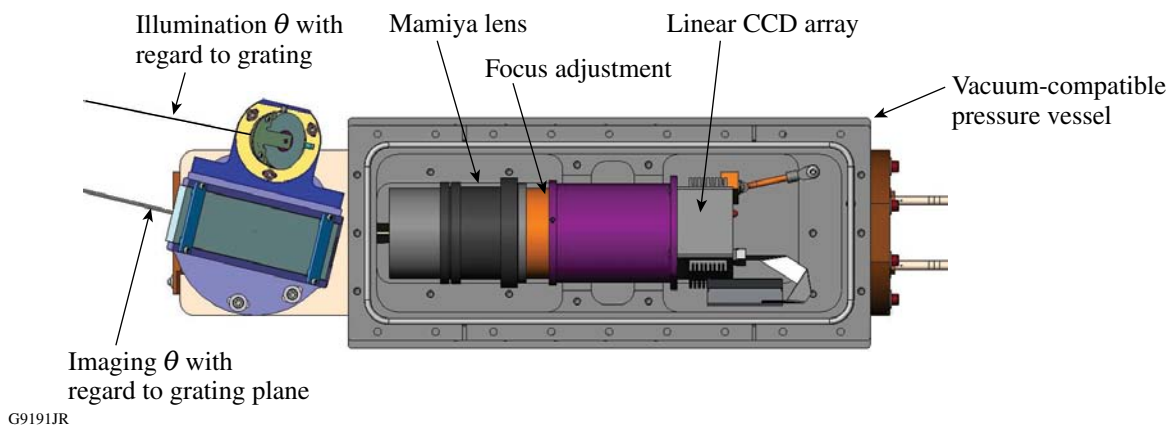


Figure 124.2

An engineering top-view drawing shows the vacuum-compatible pressure vessel housing the major components of the imaging system. This reduces contamination and out-gassing while keeping the camera functioning in air. The separation between illumination and imaging is also indicated.

nar with the grating surface. They are imaged in every GIS scan, providing information on the GIS alignment and focus state and verification that the illumination source is functioning properly. The fiducials also play an important role in the installation and alignment of the GIS, where they serve as a reference for the rotation and pointing of both the camera and the illumination line.

Alignment was achieved using the following procedure: First, the top and bottom of the fiducial wire were illuminated with small “marker” beams from a HeNe laser. With the camera moved to the limit of travel corresponding to the illuminated fiducial, the periscope was tipped and tilted until the HeNe illumination was detected and centered on the CCD. The camera was then rotated to bring both HeNe illuminated portions of the fiducial into view. Next, the 1.053- μm line generator was added and pointed at the fiducial wire. The line had to be rotated to be within the field of view of the linear CCD array, corresponding to a 120- μrad tolerance. Finally, the focus and polarization of the line generator were checked to maximize the return signal and minimize transmitted light through the grating, respectively. These alignment steps had to be iteratively repeated until the desired signal level was achieved.

Mitigation of Thermal and Background Effects

The GIS camera generates a significant quantity of heat whenever it is receiving power and suffers from severely limited thermal dissipation because it operates in a vacuum environment. This creates a number of consequences when operating the instrument: Unnecessary thermal pollution of the GCC by the GIS can impact the optical alignment of the grating compressor, which must be avoided. The CCD temperature can vary strongly over the scan duration of roughly 8 min, which directly influences the dark current background. Finally, the long-term equilibrium temperature of the camera, while energized, is potentially damaging to the CCD.

The pressure vessel housing the camera mitigates these effects to some degree by providing a significant thermal mass in close contact with the camera, while the vessel itself remains in poor contact with the GCC as a whole. Thermal effects, however, must also be minimized procedurally.

A study of the thermal behavior of the GIS was conducted during installation within the vacuum GCC, which was used as a guide in developing a set of usage protocols that mitigate thermal effects. Data were continuously acquired from the GIS camera for roughly 45 min, and the temperature was recorded from an in-camera thermistor. Temperature data were collected

once per 500 lines of image data at a 0.5 °C resolution. A model function was fitted to the data, consisting of a single exponential function rounded to the nearest half-degree. Figure 124.3 shows the raw data and the rounded-fit function, as well as the exponential component of the model, before rounding.

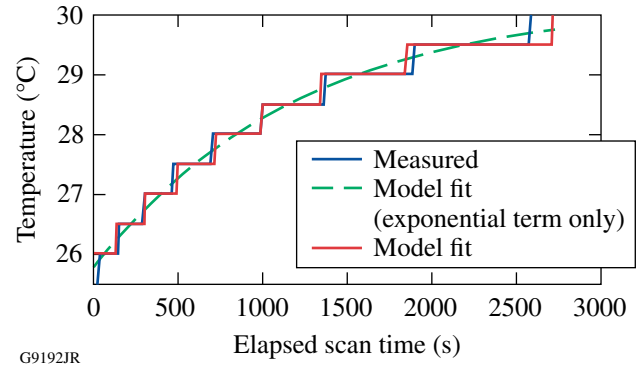


Figure 124.3

Measured temperature, fitted-model data, and the exponential component of the fitted model.

The exponential component of the fitted model is used to estimate the temperature, from which a value is interpolated to correspond with each line of image data. Figure 124.4 shows the background level versus temperature for each line of data from the CCD. This establishes a thermal variation of the background of 2.0 counts/degree.

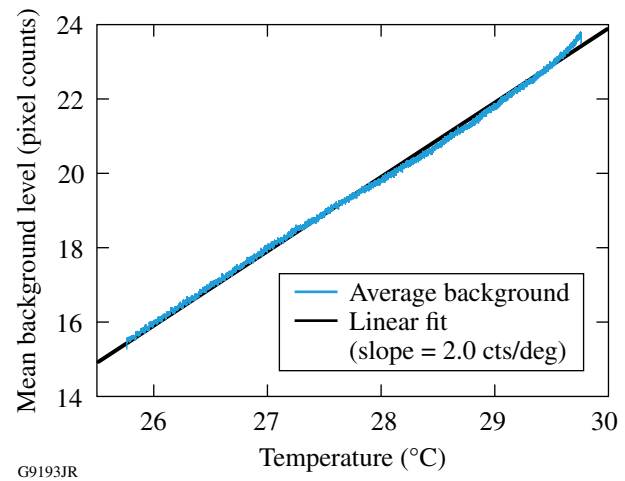


Figure 124.4

Mean background level versus temperature during the thermal study.

Over an 8-min scan, the rise in temperature could be many degrees, which would produce unacceptable variations in background. This is mitigated in GIS operation by a series of operations carried out by the GIS acquisition software. When

a scan is initiated by the user, this software ensures that the camera is at or above 23 °C to reduce the second derivative of the temperature with respect to time. If the camera is below this temperature, it is energized and warmed up before the scan is initiated. Once scanning begins, 500 lines of image data are acquired to provide pre-scan background data. Post-scan background is similarly measured immediately after the scan is concluded. The pre- and post-scan background data are used quite effectively by the GIS data-reduction algorithms to compensate for variation in the background, as described in the next section. The variance in the background will, of course, also increase with temperature; this variation has been undetected in testing, however, and is assumed to be negligible.

Data Reduction

Raw data from the GIS, as from practically all imaging systems, have a number of undesirable characteristics that must be corrected during data reduction to provide the most-accurate possible representation of the surface being inspected. Some characteristics of the GIS data are relatively unique, and their treatment will be described in detail. Double exposures (DE's) are the most notable of these because of their strong impact on image quality if uncorrected. DE errors, as they occur in a scanning system like the GIS, are quite unique and cannot be corrected using basic image-processing techniques, such as smoothing or filtering. The GIS data reduction also performs background subtraction, which is, in principle, a common operation. However, because of the thermally induced background variation over the duration of a GIS scan, this process is carried out in a somewhat unique manner. Finally, the GIS data reduction must correct for the nonuniform illumination level, which varies strongly across the vertical extent of the image as a result of the Gaussian shape of the illumination line.

DE's are caused by a known issue in the trigger logic of the Dalsa Piranha2 camera when running at line rates below 1 kHz. During a DE, the camera fails to respond to a trigger signal,

resulting in a line of data being exposed for two integration periods. DE's are relatively infrequent; it is typical to gather a full scan (roughly 88,000 lines) without a single occurrence. An uncorrected DE would be problematic, however, for later analysis and must be removed. DE's are corrected by inspecting the column sums of a region at the top of the GIS image. The region spans the full image, is 400 pixels tall, and was chosen for its absence of any significant image features (i.e., it is dominated by background). Figure 124.5 identifies this region.

The column sums are divided by a median-filtered copy of themselves, and DE's are identified by points where this ratio exceeds six standard deviations above its mean value. Figure 124.6 displays the column sums and the same data after a median filter. DE reduction in this manner is highly effective because the median filter is ideal for identifying isolated extreme values in the raw data.

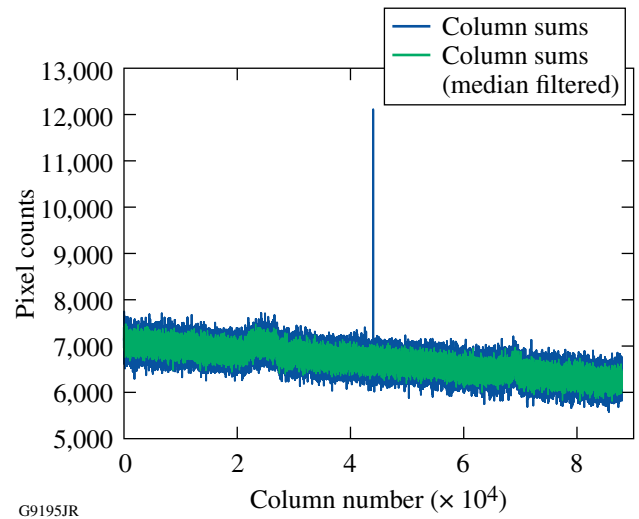


Figure 124.6
Column sums of the image data in the region of interest are shown. A DE is simulated at line 40,000 because real DE's are very infrequent.

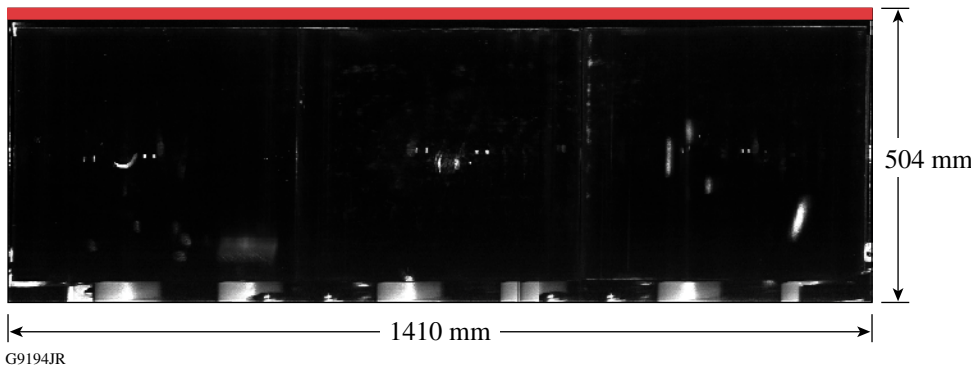


Figure 124.5
A typical GIS image (the region used to detect DE is identified in red).

Once identified, columns affected by a DE are eliminated and replaced with interpolated values from their neighboring columns. This interpolation is justified in this case by the large oversampling in the horizontal (scan) direction. As described in **System Description** (p. 165), the pixel footprint in the plane of the grating has a horizontal extent of roughly $237.5 \mu\text{m}$, while acquisition occurs every $16 \mu\text{m}$. This implies that 93% of the area imaged by each pixel is also imaged in each of the adjacent data lines, making interpolation between adjacent pixels highly reliable.

After correcting DE's in the image data and in the pre- and post-scan background data by the same process, the data reduction corrects for the variable background level. The background values are interpolated linearly across the GIS image from the pre-scan to the post-scan levels, and these interpolated values are subtracted from the image. In effect, this assumes that the background level increases linearly with time as the scan progresses, which of course, it does not. However, because the second derivative of the temperature change versus time has been constrained by the data acquisition process (see **Mitigation of Thermal and Background Effects**, p. 168), the deviation of the background from the linear interpolation is also bounded. Figure 124.7 shows the exponential model for the temperature data, extrapolated to the 7-min period immediately after the camera reaches $23 \text{ }^\circ\text{C}$. The start-to-end linear approximation deviates from the exponential by a maximum of $\sim 0.09 \text{ }^\circ\text{C}$, which translates into a maximum error in the background estimation of roughly 0.18 CCD counts. This subcount departure should be insignificant to further image processing and will be even smaller if the scan begins at a temperature higher than

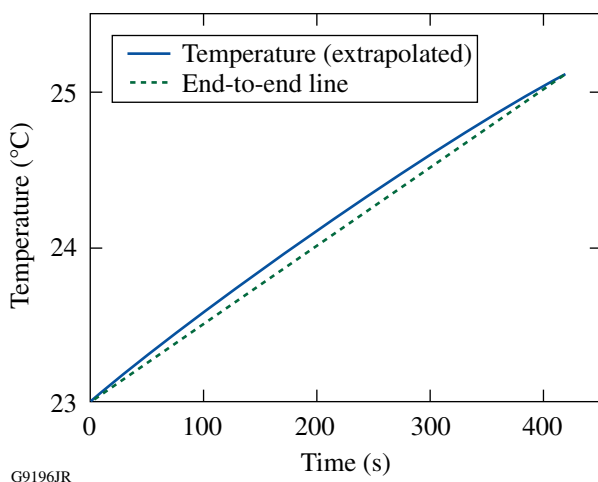


Figure 124.7
Temperature data are shown extrapolated over the travel scan time.

$23 \text{ }^\circ\text{C}$, where the exponential behavior of the temperature is more closely approximated by a line.

Finally, the data reduction corrects for strong variations in signal strength across the vertical extent of the image, such as from illumination nonuniformity. This variation would confound any image analysis based on a fixed binarization threshold. To correct the signal level, an equalization coefficient is applied to the data from each pixel of the CCD array. Equalization coefficients are calculated from a GIS scan of a reference surface, which is collected during installation and maintenance of the GIS. The reference surface is a uniform scattering surface composed of white Delrin.⁶ Note that this measurement includes more than just the Gaussian shape of the illumination. By using measured data from the GIS, rather than a pre-characterization of the illumination profile, this equalization also accounts for variations in photoresponse for each pixel, vignetting in the imaging lens, and other properties of the as-built system.

Figure 124.8 shows the measured equalization coefficient for each pixel in the CCD array, demonstrating that the Gaussian illumination profile clearly dominates other effects. It must be noted that the scattering properties of the reference target and of scattering sites on the optic being imaged are certainly non-Lambertian and likely not identical. It is unclear to what extent this distorts the equalization coefficients, but it is assumed to be negligible. It is also important to understand that equalizing the signal level cannot alter the signal-to-noise ratio, which inevitably varies across the vertical dimension of the image.

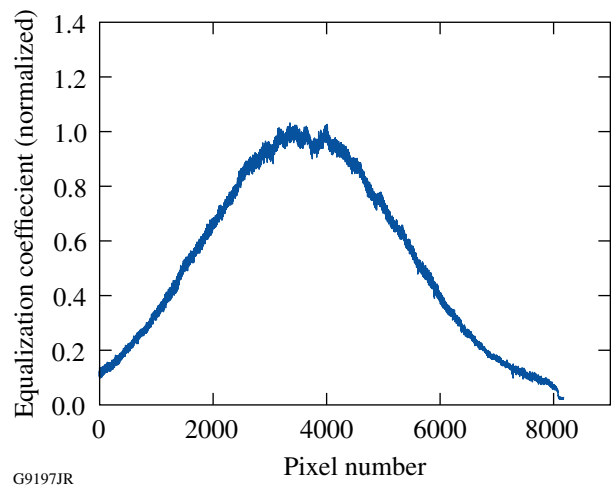


Figure 124.8
Signal equalization coefficients for each pixel in the CCD array.

A 3×3 median filter is applied to the image to suppress noise. Median filtering typically provides good noise suppression without compromising image detail as heavily as, for example, a smoothing filter. A median filter is particularly effective on GIS images at this point because, as discussed above, they are heavily oversampled in the horizontal direction. So, the noise suppression from the median filter comes at the cost of virtually no loss of image structure in the horizontal direction and acceptable loss in the vertical direction.

At this point the anomalies in the GIS data are sufficiently corrected to give an image that represents, as accurately as possible, the scattering sites on the optic under test. The final step in data reduction is to re-scale the GIS image to a standard pixel scale of 16 pixels/mm. This simplifies future processing and measurements and offers an opportunity for further noise suppression. The scale factors for this transformation are determined to sufficient precision by measuring the size of a known feature in a raw GIS image, such as the outline of a grating tile. Raw GIS data have a scale of roughly 61.26 and 16.25 pixels/mm in the horizontal and vertical directions, respectively. The image is re-scaled via bi-cubic interpolation with an anti-aliasing filter.⁷

Results

The GIS allows one to make frequent *in-situ* measurements of the TGA surface. The optics are also inspected visually during semi-annual maintenance periods when the GCC is vented to atmospheric pressure. This visual inspection is the conventionally accepted method for observing morphological change (MC) on optical surfaces and serves as a performance benchmark for the GIS in terms of sensitivity to damage features. Visual inspection also provides a point of comparison for determining whether all MC's that appear under visual inspection are detected by the GIS. Figure 124.9 compares (a) a photograph of a damaged region of a grating taken during visual inspection and (b) the same region as imaged by the GIS.

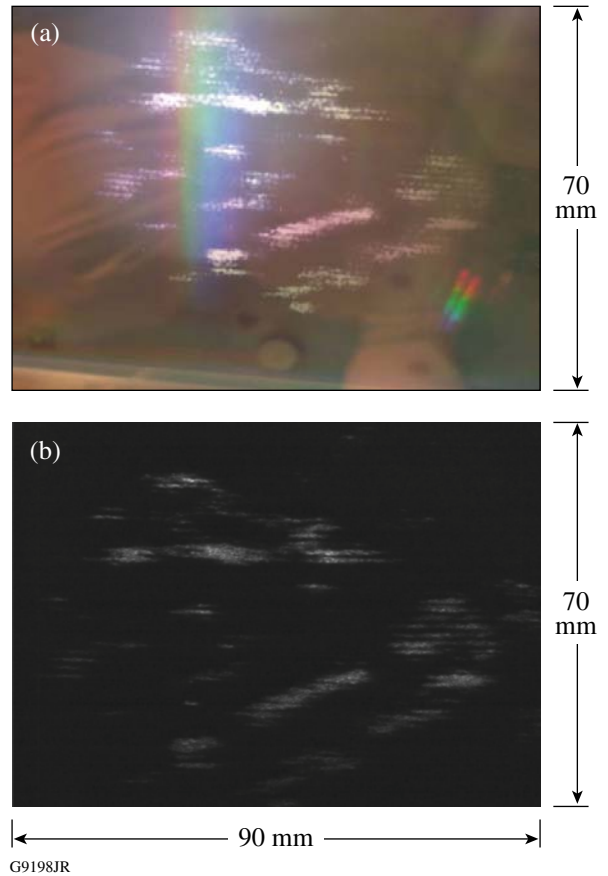


Figure 124.9
 (a) A photograph taken during visual inspection on 19 June 2009 and (b) the same region of the TGA surface imaged by the GIS on 7 September 2009. Clear correlation can be seen between the surface features detected by both methods.

Such correspondence between GIS observations and visual inspections has now been repeatedly supported and represents an important measure of the success of the GIS.

Final output from the GIS is a high-quality, high-resolution image ready to use to identify and analyze damage on the TGA surface. Figure 124.10 shows a typical image. Note that in this

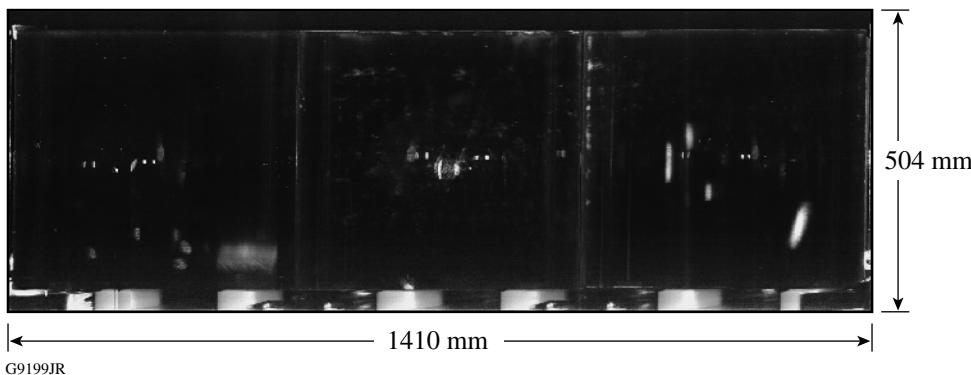


Figure 124.10
 A typical image of a TGA as produced by the GIS. A variety of common non-damage features are visible.

image, and most others presented in this article, the contrast has been significantly adjusted to make details visible to the reader. In their original state, for use in analysis, the dynamic range of the GIS is very large, and much of the interesting structure is present at the lower end of the intensity scale. The TGA was in good condition at the time of the scan in Fig. 124.10, and very little scattering was present from damage or other MC on the optical surface. Therefore, this image is a good illustration of the “background” features in a “pre-damaged” GIS image. In the central region of each grating tile can be observed two pairs of bright circular features, in some cases with another one or two larger oval-shaped features between them. These are inherent to the grating tiles and are not fully understood. They are not visible under human inspection of the gratings. The inter-tile gaps are clearly visible, as well as the fiducial wires at the extreme edges of the image. A number of other optical ghosts are visible, generally appearing as oblong “blemishes.” Some of these ghosts are assumed to be stray-light artifacts, possibly resulting from some part of the TGA mechanical assembly. Finally, along the bottom of the image, one can observe a portion of the TGA mechanical structure. Particularly prominent

here are the six white rectangular features that result from a set of Delrin cylinders on the TGA support structure. Recognizing and measuring these background features are vital to any analysis seeking to identify MC on the grating surface. Clearly, it is necessary to employ techniques that compare a potentially damaged grating to an earlier reference. These analysis methods, however, are beyond the scope of this article.

The GIS has been highly successful in detecting MC attributable to high-energy operation of the OMEGA EP system. Figure 124.11 shows a GIS image gathered after a recent energy-ramp campaign. Even without rigorous analysis, MC is clearly visible in the lower portion of the center tile and the upper-right quadrant of the left tile. The region highlighted by the red box contains the two most-severe MC’s on the grating surface, with severity being judged by the surface area of the MC.

The progression of this damage can be investigated in greater detail. Figure 124.12 shows a sequence of images of this region at full resolution, demonstrating the progression of MC during the energy ramp.

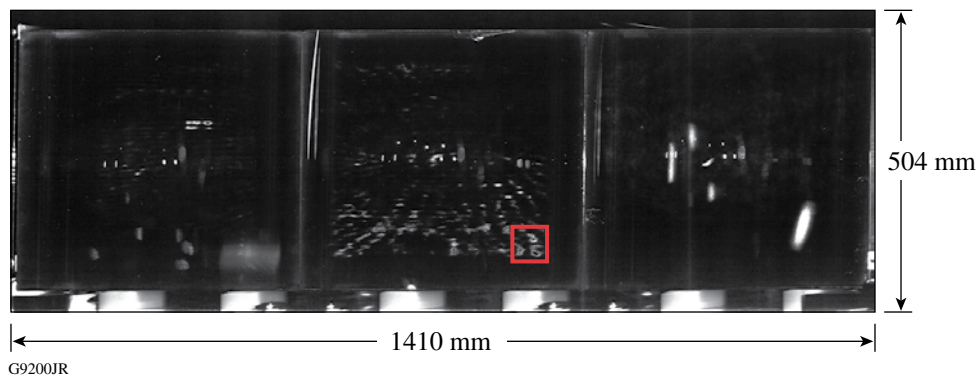


Figure 124.11

GIS image taken after the final shot in the OMEGA EP energy-ramp campaign. Damage-induced scattering is visible in multiple areas. The area outlined in red highlights the two most severely damaged sites in terms of affected area.

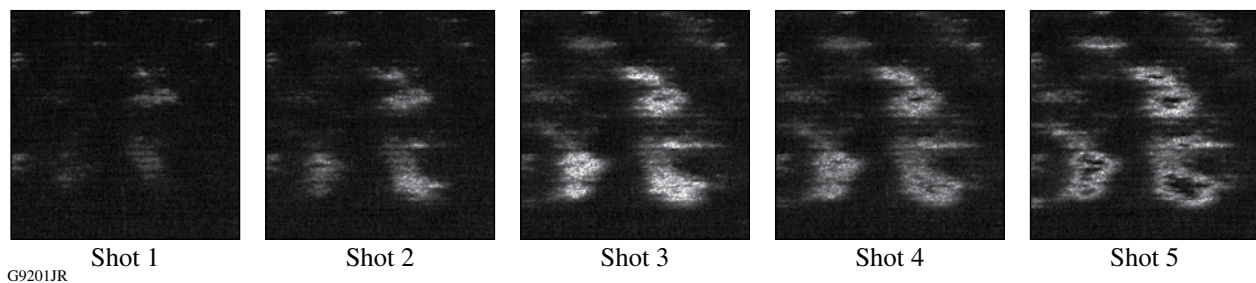


Figure 124.12

A progression of images of a region of the final TGA in the OMEGA EP upper compressor during the energy-ramp campaign. This is the region identified in Fig. 124.11.

It is interesting to note that, as MC's progress, the scattering signal becomes stronger until a point is reached (shot 3) at which the scattering signal is abruptly reduced. This effect becomes visible on shot 4 and is dramatically apparent on shot 5. Subsequent analysis of this and other regions of the grating tile using an atomic force microscope reveal that, in the region where scattering has ceased, the pillars comprising the diffractive surface structure have been completely ejected from the surface.

Conclusion

The grating inspection system has been integrated into the OMEGA EP vacuum grating compression chamber. It operates reliably within the allowed operational window between shots and has successfully demonstrated the ability to detect features in the specified 250- μm scale. Statistical techniques have been applied to GIS observations to establish system fluence limits that minimize the threat of damage to the gratings, while making it possible for OMEGA EP to satisfy its short-pulse mission.⁸ There is great potential for further investigation of the *in-situ* behavior of large-aperture diffraction gratings, and the GIS will continue to play a vital role in this work.

ACKNOWLEDGEMENT

This work was supported by the U.S. Department of Energy Office of Inertial Confinement Fusion under Cooperative Agreement No. DE-FC52-08NA28302, the University of Rochester, and the New York State Energy Research and Development Authority. The support of DOE does not constitute an endorsement by DOE of the views expressed in this article.

Special thanks to LLE software engineers Steve Smith and Mark Wilson and LLE electrical engineer Scott Ingraham for their excellent work and support in developing the GIS image acquisition software and drive electronics. We also extend thanks to system scientist Jie Qiao, optical engineer Damon Diehl (ASE Instrument, Inc.), and LLE engineering director/chief safety officer Dr. D. W. Jacobs-Perkins for their great guidance and support.

REFERENCES

1. T. J. Kessler, J. Bunkenburg, H. Huang, A. Kozlov, and D. D. Meyerhofer, *Opt. Lett.* **29**, 635 (2004).
2. J. Qiao, A. Kalb, M. J. Guardalben, G. King, D. Canning, and J. H. Kelly, *Opt. Express* **15**, 9562 (2007).
3. M. Commandré, in *Laser-Induced Damage in Optical Materials: 2008*, edited by G. J. Exarhos *et al.* (SPIE, Bellingham, WA, 2008), Vol. 7132, p. 713200.
4. This lens is listed as $f/4.5$, EFL = 250 mm. The mechanical requirements of the pressure vessel housing impose, however, a number of noncircular apertures. In practice, this system has different effective apertures in the vertical and horizontal directions and is likely slower, overall, than $f/4.5$.
5. FARO Technologies, Inc., Lake Mary, FL 32746 (<http://www.faro.com>).
6. McMaster Carr Supply, Aurora, OH 44202 (<http://www.mcmaster.com>).
7. See MATLAB 7.8.0.347 documentation for the image resize function in the Image Processing Toolkit.
8. J. Qiao, A. W. Schmid, L. J. Waxer, T. Nguyen, J. Bunkenburg, C. Kingsley, A. Kozlov, and D. Weiner, *Opt. Express* **18**, 10,423 (2010).

Scaling Hot-Electron Generation to High-Power, Kilojoule-Class Laser–Solid Interactions

High-intensity laser–solid interactions ($>10^{18}$ W/cm²) accelerate large numbers of thermal electrons to relativistic energies. These high-energy, MeV-scale electrons are a source of significant energy deposition within plasmas and are used extensively in plasma-based particle acceleration,^{1–3} creation of warm dense matter,⁴ laboratory high-energy astrophysics,⁵ ultrafast γ -ray generation,⁶ and fast-ignition research.^{6,7} Efficient hot-electron generation is of great importance for the energetic feasibility of these applications and has been studied intensively.^{6,8–17}

Previous solid-target experiments showed energy-conversion efficiencies into hot electrons ($\eta_{L\rightarrow e}$) of up to several tens of percent for picosecond or shorter pulses of 1- μ m light and laser intensities from 10^{18} W/cm² $\leq I \leq 10^{20}$ W/cm² (Refs. 6,8–17). With recent developments in laser technology, it is now possible to generate kilojoule-class, $\tau_p = 10$ -ps pulses that can be focused to intensities of $I > 10^{18}$ W/cm² (Ref. 18). Such long-duration, high-intensity laser pulses hold great promise for high-energy applications that require rapid electron-energy deposition over time scales that are short compared to the typical hydrodynamic decompression times of solid and laser-compressed targets.

In fast ignition, laser-compressed deuterium and tritium are rapidly heated and ignited by a high-intensity laser pulse.^{6,7} An intense, multikilojoule, 10- to 20-ps-long laser pulse is required to generate the ignition spark with optimal electron-beam energies and currents for energy deposition within the fuel assembly. Knowledge of the coupling of a high-intensity laser into energetic electrons that heat the fuel, in addition to how this scales to ignition-class lasers, is critical to understanding spark generation and fast ignition.

Hot-electron generation in this regime is only partially understood, however, particularly at high laser energies ($E_L > 1000$ J) and long laser-pulse durations ($\tau_p \sim 10$ ps), where no previous data exist because of the unavailability of suitably high-energy lasers. With increasing laser-pulse duration, a number of processes affect energy coupling to solid targets,

including pre-plasma formation,^{19,20} electron transport,²¹ hole boring,²² and laser-driven shock formation.²³ Understanding these effects on energy coupling is crucial for scaling hot-electron generation to long-pulse, high-intensity lasers. Definitive measurements of the effect of laser-pulse duration on $\eta_{L\rightarrow e}$ are reported in this article.

X-ray spectroscopic measurements of hot-electron generation in high-intensity laser–solid interactions show that the conversion efficiency is independent of laser-pulse duration. Thin-foil targets have been heated with hot electrons generated by $\tau_p = 10$ -ps pulses focused to intensities of $I > 10^{18}$ W/cm², and $\eta_{L\rightarrow e}$ has been inferred with K-photon spectroscopy. Comparing the energy emitted in K photons to target-heating calculations shows an energy-coupling efficiency to hot electrons of $\eta_{L\rightarrow e} \sim 20\%$ with laser powers from $1 \text{ TW} \leq P_L \leq 210 \text{ TW}$. These are the first experiments to study hot-electron generation with intense, $\tau_p = 10$ -ps pulses at such high laser powers. Time-resolved x-ray emission measurements suggest that hot electrons are generated over the entire duration of the incident laser drive. The K-photon emission data are compared to other published data at similar laser intensities, showing for the first time that $\eta_{L\rightarrow e}$ is independent of laser-pulse duration from $1 \text{ ps} \leq \tau_p \leq 10 \text{ ps}$.

The experiments were carried out using LLE’s Multi-Tera-watt (MTW)^{24,25} and Omega EP¹⁸ Laser Facilities. For these experiments, the MTW laser delivered an energy of $E_L = 10$ J in a $\tau_p = 10$ -ps pulse at a wavelength of $\lambda_L = 1.054 \mu\text{m}$. The laser pulse was focused by an $f/3$, off-axis parabolic mirror at normal incidence to the target with an $R_{80} = 5 \mu\text{m}$, where R_{80} is the spot radius containing 80% of the laser energy, providing a laser intensity of $I = 1 \times 10^{18}$ W/cm². OMEGA EP delivered higher laser energies from $300 \text{ J} \leq E_L \leq 2100 \text{ J}$ in a $\tau_p = 10$ -ps pulse at a wavelength of $\lambda_L = 1.054 \mu\text{m}$. An $f/2$, off-axis parabolic mirror focused the laser pulse at either 45° or normal incidence to the target with an $R_{80} = 25 \mu\text{m}$, providing laser intensities of up to $I \sim 10^{19}$ W/cm². The targets were Cu foils with dimensions that were varied between $600 \times 600 \times 50 \mu\text{m}^3$ and $75 \times 75 \times 3 \mu\text{m}^3$, mounted on a 17- μ m-thick silicon-carbide stalk.

Pre-plasma expansion prior to intense laser irradiation affects the energy coupling to solid targets,^{19,20} particularly at high laser energies, and is caused by low laser contrast. For these OMEGA EP shots, fast-diode measurements indicate that the laser pedestal typically reaches 6×10^{-7} of the peak laser power and contains 10^{-4} of the total laser-pulse energy. For the experiments reported here, the energy contained in the pedestal varied from $40 \text{ mJ} \leq E_{\text{ped}} \leq 210 \text{ mJ}$. Over this energy range, calculations made using the 1-D radiation hydrodynamic code *LILAC*²⁶ indicate that the pre-plasma extends up to 5 to $10 \mu\text{m}$ between the critical- and the solid-density plasma.

The main diagnostic for measuring K-photon emission from the target was an absolutely calibrated, single-photon-counting x-ray spectrometer based on an SI-800 x-ray charge-coupled device.²⁷ A combination of heavy shielding and collimation, and a large target-to-spectrometer distance, reduces the number of Cu K-photon hits that are detected, satisfying the single-photon-counting regime, while reducing the hard x-ray flux. Cu filters that transmit Cu K_{α} and K_{β} photons below the filter K edge further optimize the signal to background of the measured spectrum. A graphite (HOPG) crystal spectrometer provided a complementary measurement of the K-photon yield.²⁸ The radiation emission time was measured using an ultrafast x-ray streak camera with a temporal resolution of about 2 ps (Ref. 29).

Typical K-photon spectra obtained in the experiment are shown in Fig. 124.13. Figure 124.13(a) shows a time-integrated x-ray emission spectrum from a $500 \times 500 \times 20\text{-}\mu\text{m}^3$ Cu target irradiated with an $E_L = 1000\text{-J}$, $\tau_p = 10\text{-ps}$ pulse. Figure 124.13(b) shows an x-ray emission spectrum from a $75 \times 75 \times 5\text{-}\mu\text{m}^3$ Cu target irradiated with the same laser conditions.

The emission spectra show peaks at 8.05 keV and 8.91 keV, where the Cu plasma emits K_{α} and K_{β} inner-shell radiation. As hot electrons move through the target, the atomic electrons in the 1s shell of copper ions are ejected by electrons with energies 2 to $3 \times$ the copper K-shell ionization potential (~ 20 to 25 keV). During de-excitation, the system relaxes to a lower-energy state, with $2p \rightarrow 1s$ and $3p \rightarrow 1s$ transitions generating K_{α} and K_{β} photons. The emission lines are fit to Gaussian line shapes with a full width at half maximum (FWHM) of 220 eV. The emission spectra contain the thermal He_{α} and Ly_{α} ionic-line emission that is generated from hot surface plasma on the laser-irradiated side of the target.

The main observation from these measurements is the suppressed K-photon yield from the reduced-mass target.

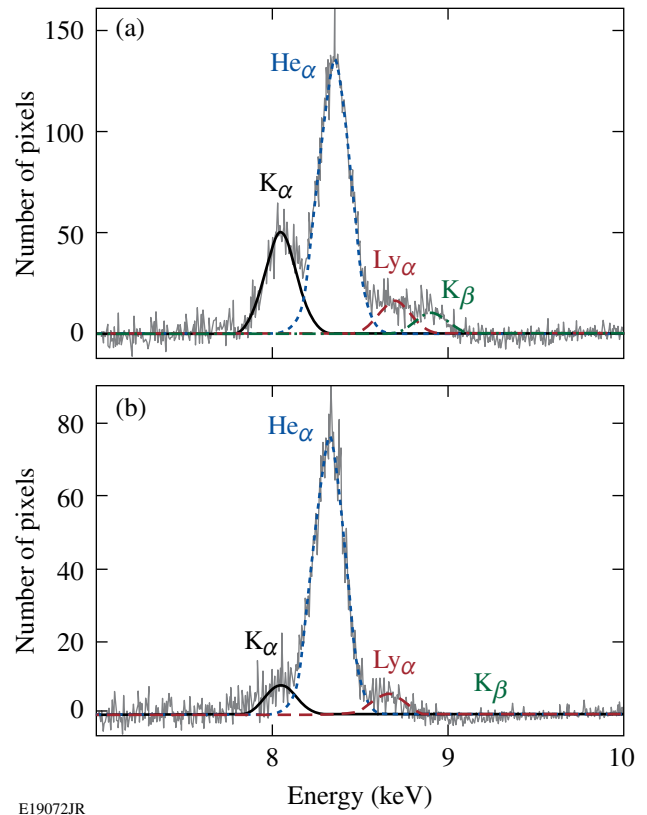


Figure 124.13 Comparison of K-photon emission spectra from (a) $500 \times 500 \times 20\text{-}\mu\text{m}^3$ and (b) $75 \times 75 \times 5\text{-}\mu\text{m}^3$ Cu targets irradiated with $E_L = 1000\text{-J}$, $\tau_p = 10\text{-ps}$ laser pulses.

The $75 \times 75 \times 5\text{-}\mu\text{m}^3$ Cu target generates no K_{β} radiation and has a dramatically suppressed K_{α} yield compared to the larger-volume target. The suppressed K-photon yield suggests higher-energy-density conditions and high thermal-electron temperatures in the reduced-mass target. This is expected for these high-energy interaction conditions.^{15–17,30}

The method for calculating $\eta_{L \rightarrow e}$ involves comparing K-photon emission from reduced-mass targets to target-heating calculations and was described previously in Ref. 16. It relies on a significant fraction of the laser-generated hot electrons being trapped by the target potential that develops because of the charge separation that occurs between the hot escaping electrons and the relatively immobile ions.¹² This effect has been studied theoretically¹⁶ and confirmed experimentally.^{15,17,30} The collisional range of MeV electrons in cold, solid-density copper is several hundred microns and is much greater than the target thickness used in the experiment (up to tens of microns). Hot electrons recirculate (reflux) throughout the target, efficiently transferring energy to the target material

until they range out. Capacitance model calculations indicate that hot-electron refluxing efficiencies in these targets reach >90%, making K-photon spectroscopy measurements of the contained hot electrons highly representative of $\eta_{L \rightarrow e}$.

Time-resolved x-ray emission measurements support the electron-refluxing interpretation for $\tau_p = 10$ -ps pulses. Figure 124.14 shows the radiation time history for a $100 \times 100 \times 10$ - μm^3 Cu target irradiated with an $E_L = 1000$ -J, $\tau_p = 10$ -ps pulse. The ultrafast x-ray streak camera was filtered as shown in Fig. 124.14 (inset), providing sensitivity to bremsstrahlung, inner-shell radiation, and thermal ionic-line emission.

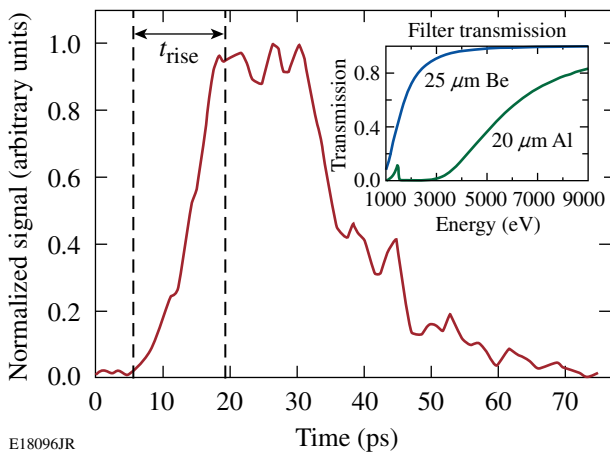


Figure 124.14
Time-resolved x-ray emission from a $100 \times 100 \times 10$ - μm^3 Cu target ($E_L = 1000$ J, $\tau_p = 10$ ps). The transmission functions for the x-ray streak-camera filters are shown (inset).

An increase in radiation emission correlated with the laser-pulse duration, implying an increasing hot-electron number density within the target over this period. This occurs because hot electrons reflux, suggesting constant laser-energy coupling to hot electrons over the entire duration of the incident laser drive. After the laser pulse ends, a radiation afterglow persists for around 20 ps (FWHM) and is likely a combination of inner-shell radiation and thermal radiation, emitted in response to the electron-energy deposition within the target. Thermal radiation persists until the hot electrons thermalize and target decompression dominates.

The absolute K-photon yield generated during the recirculation phase is sensitive to the time-varying number density of hot electrons within the target and target heating. The target-charging process governs the number of hot electrons contained

within the target, while target heating is caused mainly by electron–electron collisional energy deposition from the hot electrons. The ionization state of the target depends on collisions between bound and free conduction electrons. Once the thermal electron temperature inside the target exceeds a few hundred electron volts, the Cu M shell is depleted by thermal ionization, suppressing the plasma’s ability to generate K_β photons. Several hundreds of electron volts are required to deplete the Cu L shell. Time-integrated K-photon emission measurements quantify the target heating, making it possible for $\eta_{L \rightarrow e}$ to be inferred by comparison to target-heating calculations, which are used to predict the ratio of K_β to K_α (K_β/K_α) for a given hot-electron conversion efficiency.

The data show that suppression of the K-photon yield is governed by target energy density. Figure 124.15 shows the experimentally measured values for (K_β/K_α) from reduced-mass targets plotted as a function of the ratio of the laser energy to the target volume (in units of J/mm^3). The data obtained with 10-ps pulses (blue data points) are compared to previously published data with 1-ps pulses (black data points).¹⁷ The measured values for K_β/K_α are normalized to those measured from Cu foils when target heating is negligible ($K_\beta/K_\alpha \sim 0.14$).

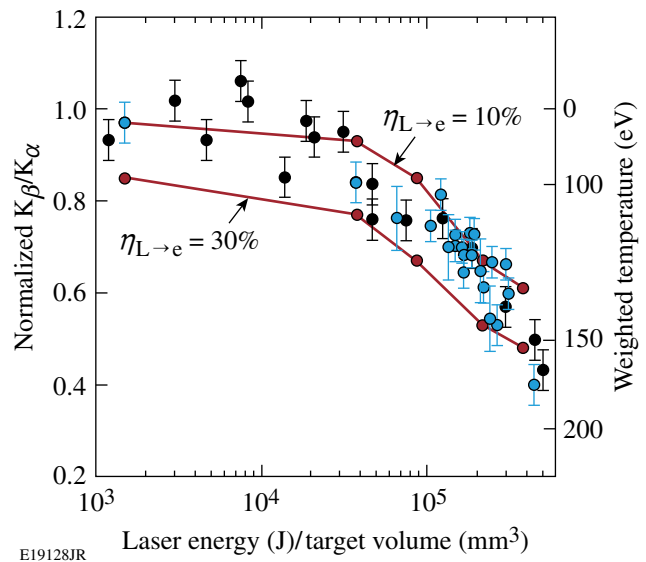


Figure 124.15
Experimental K_β/K_α data [normalized to the cold-material value (left axis)] and inferred bulk-electron temperature (right axis) as a function of laser energy (J)/target volume (mm^3). Data for 10-ps pulses (blue) and 1-ps pulses (black reproduced from Ref. 17); target-heating calculations for $\eta_{L \rightarrow e} = 10\%$ and 30%.

A reduction in the K_β/K_α ratio is observed with increasing laser energy and decreasing target volume. At the lowest target-energy densities studied ($\sim 1.5 \times 10^3 \text{ J/mm}^3$), laser-generated hot electrons interact with cold target material. When the target energy density is increased to greater than $1 \times 10^5 \text{ J/mm}^3$, target heating and thermal ionization suppress K_β/K_α . For target energy densities of $\sim 5 \times 10^5 \text{ J/mm}^3$, K_β/K_α is suppressed to $40 \pm 4\%$ of the cold-material value.

The experimental trend in K_β/K_α with $\tau_p = 10$ -ps pulses is in excellent agreement with previous studies that were performed at significantly lower, joule-class laser energies and picosecond-pulse durations.¹⁷ The same rate of change in K_β/K_α is observed with increasing energy density, independent of laser-pulse duration from $1 \text{ ps} \leq \tau_p \leq 10 \text{ ps}$. For the parameter space studied, variations in laser spot size, laser intensity, laser prepulse, and angle of incidence do not alter this observation. Scaled for laser energy and target mass, the results from these experiments suggest that the same fraction of laser energy is transferred into K-photon-generating hot electrons, independent of laser-pulse duration.

This interpretation is supported by two-dimensional, cylindrically symmetric target-heating calculations using the implicit-hybrid particle-in-cell code *LSP*.³¹ Self-generated fields are included in the model and are calculated self-consistently. Target charging and heating in the calculations were produced by a hot-electron population that had an exponential energy distribution, with a temperature of up to several hundred keV, as defined by the ponderomotive scaling²² and the range of experimental laser irradiation conditions. Spatial and temporal heating variations are accounted for when determining K-photon emission, with the emission probability calculated using the local temperature at the time of emission. The Thomas-Fermi equation-of-state model used was appropriate for the range of temperatures achieved in this experiment.

The calculated values for K_β/K_α as a function of increasing energy density are shown in Fig. 124.15. Calculations were performed assuming $\eta_{L \rightarrow e} = 10\%$ and 30% . The target-heating model predicts suppression in K_β/K_α very similar to that observed in the experiment. The thermal electron temperature inferred from the model for different target interactions is shown in Fig. 124.15 (right axis). This temperature represents a measure of the degree of target heating by hot-electron energy deposition and is weighted by the K-photon emission rate. Weighted thermal electron temperatures approaching several hundred electron volts are achieved in the smallest-mass tar-

gets. Regions of the target that do not emit K photons could reach higher thermal temperatures.

Strong reduction of K_β/K_α in the calculations support the interpretation that in hot Cu-foil targets, thermal ionization causes K-photon suppression with hot-electron refluxing being the dominant energy transfer mechanism. An energy-coupling efficiency to hot electrons of $\eta_{L \rightarrow e} = 20 \pm 10\%$ reproduces the majority of the experimental $\tau_p = 10$ -ps data. This range of $\eta_{L \rightarrow e}$ is in good agreement with previous $\tau_p = 1$ -ps studies at similar laser intensities.^{16,17}

Calculations indicate that around 5% of the hot-electron energy is ohmically dissipated in the high-temperature, low-resistivity plasma. The calculations do not account for fast-proton acceleration by sheath fields at the target surface, with previous measurements indicating 1% to 2% energy-transfer efficiencies to protons.^{32,33} The inferred value for $\eta_{L \rightarrow e}$ therefore represents a lower bound on the energy-conversion efficiency into hot electrons that is required to generate the experimentally observed K-photon emission.

In summary, thin-foil targets have been heated with hot electrons generated by a $\tau_p = 10$ -ps pulse at focused intensities of $I > 10^{18} \text{ W/cm}^2$. K-photon spectroscopy and target-heating calculations show an energy-coupling efficiency into hot electrons of $\eta_{L \rightarrow e} \sim 20\%$ with laser powers from $1 \text{ TW} \leq P_L \leq 210 \text{ TW}$. These measurements are in excellent agreement with previous $\tau_p = 1$ -ps data at similar laser intensities, demonstrating that the energy-conversion efficiency into hot electrons is independent of laser-pulse duration from $1 \text{ ps} \leq \tau_p \leq 10 \text{ ps}$. Ultrafast x-ray streak camera measurements suggest that laser energy is coupled into hot electrons over the entire duration of the incident laser drive. These results are important for the understanding of hot-electron generation in long-pulse, high-intensity laser-solid interactions, such as those found in fast-ignition and high-brightness x-ray-generation experiments.

ACKNOWLEDGMENT

This work was supported by the U.S. Department of Energy Office of Inertial Confinement Fusion under Cooperative Agreement Nos. DE-FC52-08NA28302 and DE-FC02-04ER54789, the University of Rochester, and the New York State Energy Research and Development Authority. The support of DOE does not constitute an endorsement by DOE of the views expressed in this article.

REFERENCES

1. M. I. K. Santala *et al.*, Phys. Rev. Lett. **84**, 1459 (2000).
2. E. L. Clark *et al.*, Phys. Rev. Lett. **84**, 670 (2000).

3. R. A. Snavely, M. H. Key, S. P. Hatchett, T. E. Cowan, M. Roth, T. W. Phillips, M. A. Stoyer, E. A. Henry, T. C. Sangster, M. S. Singh, S. C. Wilks, A. MacKinnon, A. Offenberger, D. M. Pennington, K. Yasuike, A. B. Langdon, B. F. Lasinski, J. Johnson, M. D. Perry, and E. M. Campbell, *Phys. Rev. Lett.* **85**, 2945 (2000).
4. P. K. Patel *et al.*, *Phys. Rev. Lett.* **91**, 125004 (2003).
5. B. A. Remington *et al.*, *Science* **284**, 1488 (1999).
6. M. H. Key, M. D. Cable, T. E. Cowan, K. G. Estabrook, B. A. Hammel, S. P. Hatchett, E. A. Henry, D. E. Hinkel, J. D. Kilkenny, J. A. Koch, W. L. Kruer, A. B. Langdon, B. F. Lasinski, R. W. Lee, B. J. MacGowan, A. MacKinnon, J. D. Moody, M. J. Moran, A. A. Offenberger, D. M. Pennington, M. D. Perry, T. J. Phillips, T. C. Sangster, M. S. Singh, M. A. Stoyer, M. Tabak, G. L. Tietbohl, M. Tsukamoto, K. Wharton, and S. C. Wilks, *Phys. Plasmas* **5**, 1966 (1998).
7. M. Tabak *et al.*, *Phys. Plasmas* **1**, 1626 (1994).
8. D. F. Price *et al.*, *Phys. Rev. Lett.* **75**, 252 (1995).
9. H. Chen, B. Soom, B. Yaakobi, S. Uchida, and D. D. Meyerhofer, *Phys. Rev. Lett.* **70**, 3431 (1993).
10. K. B. Wharton *et al.*, *Phys. Rev. Lett.* **81**, 822 (1998).
11. K. Yasuike *et al.*, *Rev. Sci. Instrum.* **72**, 1236 (2001).
12. S. P. Hatchett, C. G. Brown, T. E. Cowan, E. A. Henry, J. S. Johnson, M. H. Key, J. A. Koch, A. B. Langdon, B. F. Lasinski, R. W. Lee, A. J. MacKinnon, D. M. Pennington, M. D. Perry, T. W. Phillips, M. Roth, T. C. Sangster, M. S. Singh, R. A. Snavely, M. A. Stoyer, S. C. Wilks, and K. Yasuike, *Phys. Plasmas* **7**, 2076 (2000).
13. F. N. Beg *et al.*, *Phys. Plasmas* **4**, 447 (1997).
14. Y. Ping *et al.*, *Phys. Rev. Lett.* **100**, 085004 (2008).
15. W. Theobald, K. Akli, R. Clarke, J. Delettrez, R. R. Freeman, S. Glenzer, J. Green, G. Gregori, R. Heathcote, N. Izumi, J. A. King, J. A. Koch, J. Kuba, K. Lancaster, A. J. MacKinnon, M. Key, C. Mileham, J. Myatt, D. Neely, P. A. Norreys, H.-S. Park, J. Pasley, P. Patel, S. P. Regan, H. Sawada, R. Shepherd, R. Snavely, R. B. Stephens, C. Stoeckl, M. Storm, B. Zhang, and T. C. Sangster, *Phys. Plasmas* **13**, 043102 (2006).
16. J. Myatt, W. Theobald, J. A. Delettrez, C. Stoeckl, M. Storm, T. C. Sangster, A. V. Maximov, and R. W. Short, *Phys. Plasmas* **14**, 056301 (2007).
17. P. M. Nilson, W. Theobald, J. F. Myatt, C. Stoeckl, M. Storm, J. D. Zuegel, R. Betti, D. D. Meyerhofer, and T. C. Sangster, *Phys. Rev. E* **79**, 016406 (2009).
18. L. J. Waxer, D. N. Maywar, J. H. Kelly, T. J. Kessler, B. E. Kruschwitz, S. J. Loucks, R. L. McCrory, D. D. Meyerhofer, S. F. B. Morse, C. Stoeckl, and J. D. Zuegel, *Opt. Photonics News* **16**, 30 (2005).
19. A. G. MacPhee *et al.*, *Phys. Rev. Lett.* **104**, 055002 (2010).
20. F. Perez *et al.*, *Phys. Rev. Lett.* **104**, 085001 (2010).
21. A. J. Kemp, Y. Sentoku, and M. Tabak, *Phys. Rev. Lett.* **101**, 075004 (2008).
22. S. C. Wilks *et al.*, *Phys. Rev. Lett.* **69**, 1383 (1992).
23. K. U. Akli, S. B. Hansen, A. J. Kemp, R. R. Freeman, F. N. Beg, D. C. Clark, S. D. Chen, D. Hey, S. P. Hatchett, K. Highbarger, E. Giraldez, J. S. Green, G. Gregori, K. L. Lancaster, T. Ma, A. J. MacKinnon, P. Norreys, N. Patel, J. Pasley, C. Shearer, R. B. Stephens, C. Stoeckl, M. Storm, W. Theobald, L. D. Van Woerkom, R. Weber, and M. H. Key, *Phys. Rev. Lett.* **100**, 165002 (2008).
24. V. Bagnoud, I. A. Begishev, M. J. Guardalben, J. Puth, and J. D. Zuegel, *Opt. Lett.* **30**, 1843 (2005).
25. V. Bagnoud, J. D. Zuegel, N. Forget, and C. Le Blanc, *Opt. Express* **15**, 5504 (2007).
26. J. Delettrez, R. Epstein, M. C. Richardson, P. A. Jaanimagi, and B. L. Henke, *Phys. Rev. A* **36**, 3926 (1987).
27. C. Stoeckl, W. Theobald, T. C. Sangster, M. H. Key, P. Patel, B. B. Zhang, R. Clarke, S. Karsch, and P. Norreys, *Rev. Sci. Instrum.* **75**, 3705 (2004).
28. A. Pak *et al.*, *Rev. Sci. Instrum.* **75**, 3747 (2004).
29. C. Stoeckl, W. Theobald, P. A. Jaanimagi, P. Nilson, M. Storm, J. A. Delettrez, R. Epstein, T. C. Sangster, D. Hey, A. J. MacKinnon, H.-S. Park, P. K. Patel, R. Shepherd, J. Green, K. L. Lancaster, and P. A. Norreys, *Bull. Am. Phys. Soc.* **52**, 67 (2007).
30. S. D. Baton *et al.*, *High Energy Density Phys.* **3**, 358 (2007).
31. D. R. Welch *et al.*, *Phys. Plasmas* **13**, 063105 (2006).
32. L. Robson *et al.*, *Nat. Phys.* **3**, 58 (2007).
33. J. Fuchs *et al.*, *Nat. Phys.* **2**, 48 (2006).

Measurement of the Self-Phase Modulation on OMEGA

Introduction

The safe operation of a multikilojoule-class laser system requires that the accumulated nonlinear phase remain low enough to avoid beam filamentation and resulting damage to the laser-amplifier glass. A rule of thumb for infrared lasers is to keep the so-called ΔB -integral below 2 radians,¹ where the B -integral is given by

$$B(t) = \frac{2\pi}{\lambda} \int_0^L \gamma(z) \times I(z,t) \times dz \quad (1)$$

for a wavelength λ , optical path length L , nonlinear coefficient γ , and intensity $I(z,t)$, which equals the power divided by the area $P(z,t)/A(z)$. While ΔB , which is calculated per stage, where a stage is defined as all of the components between sequential spatial filters, is of most interest, a potentially more easily measured quantity is the ΣB of the system or the sum of B -integral through all stages of the system.² The protocols for safe operation become particularly important on a system like LLE's OMEGA laser. The OMEGA Laser System consists of 60 beamlines with nine amplification stages employing Nd:phosphate glass (LHG8). Each beamline typically produces about 800 J of infrared energy ($\lambda_{IR} = 1053$ nm) in a 1-ns super-Gaussian pulse. This energy is converted to the UV ($\lambda_{UV} = 351$ nm) by frequency tripling in KDP crystals with approximately 60% conversion efficiency. The temporal pulse shape is adjusted from shot to shot as specified by the principal investigator. Some of these pulse shapes have rapid changes in intensity that can increase the self-phase modulation (SPM) beyond acceptable limits.

Before any of these pulse shapes is propagated down the system, a computer code that incorporates the Frantz–Nodvik model of light propagation in a laser amplifier chain³ simulates the pulse through the system. These simulations have been extensively tested with respect to the temporal pulse shape. The code also predicts the SPM experienced by the pulse due to the B -integral. By introducing an imaging spectrometer at the output of the laser system, it is possible for the first time

to directly compare the model's prediction of the ΣB -integral with a shift in the laser frequency.

The change in instantaneous frequency, $\Delta\nu$, of the pulse caused by SPM is given by⁴

$$\Delta\nu(t) = -\frac{1}{2\pi} \frac{dB(t)}{dt} = -\frac{1}{\lambda} \int_0^L \frac{\gamma(z)}{A(z)} \times \frac{dP(z,t)}{dt} \times dz. \quad (2)$$

Therefore, the instantaneous change in the optical frequency is proportional to the time derivative of the B -integral. If the temporal pulse shape is assumed to be independent of z , the derivative of intensity can be removed from the integrand in Eq. (2) and the instantaneous frequency is simply proportional to dP/dt . This assumption is not valid in most laser amplifier systems. Typically a low-energy pulse injected at the front end of the system is continuously amplified as it propagates. On OMEGA, a single laser pulse feeds all 60 beamlines. The intensity increases as the beam passes through an amplifier stage and then decreases as the beam is split to feed subsequent amplifier stages. The pulse shape, injected at the input of the system, is typically a monotonically increasing temporal ramp. The leading edge of this ramp is preferentially amplified relative to the trailing edge because of the gain–saturation dynamics of the glass amplifiers. Depending on the exact shape of the input pulse, the output pulse shape can be a rising ramp, a super-Gaussian flattop, or a falling ramp. For the purposes of this article, only Gaussian and flattop pulses will be considered. The correct way to handle all these pulse shapes is to calculate $\Delta\nu(z)$ at every point in the laser-amplifier chain and produce an integrated frequency shift for the entire system. This ability is incorporated in the laser system model mentioned above.

Based on temporal and spatial measurements that can be made on the system, we have verified the predictions of the model both in terms of pulse shape and ΣB -integral. Additionally, we have demonstrated that $\Delta\nu$ is approximately proportional to dP/dt as measured in the UV at the output of the laser chain. This relationship is the basis of an empirical analysis

that assumes that the intensity is independent of z . Although this empirical analysis is less accurate than the full-system model, it has the advantage of being available immediately after a shot has been taken, as opposed to more than 1 h for a full simulation. Therefore, this relationship provides a real-time diagnostic that can immediately determine if the laser system is being operated safely. The agreement between the empirical model and the measurements is sufficient for a “go/no-go” decision in terms of shot operations.

The primary modeling tool used here—the *RAINBOW* code—calculates energy transport in solid-state laser systems and uses ray tracing to propagate a pulse through all components of a laser chain. Laser amplifiers are modeled by numerically solving the Frantz–Nodvik³ equations as modified by Avizonis and Grotbeck⁵ on a time-resolved basis for one or more locations in the aperture of the laser. Arbitrary spatial and temporal pulse shapes may be input, allowing for detailed predictions of the spatial and temporal shapes of the laser output. Gain saturation is modeled using a variant of the two-ion model⁶ derived from fits to gain-saturation data.⁷ Disk- and rod-geometry gain elements are modeled. Passive losses are input for each component. Frequency conversion to the third harmonic uses intensity look-up tables from *MIXER* code⁸ calculations.

RAINBOW accurately tracks the accumulated phase retardation of each temporal element of each ray (the “ B ” integral) and includes a phenomenological model of spatial-filter transmission.⁹ Using the determined SPM, it calculates the output pulse spectrum by a Fourier transformation.

Measurement

The temporal pulse shape is measured at both the input and output of the system. After an initial temporal pulse-shaping system, the infrared pulse shape is measured with either an 18-GHz InGaAs photodiode¹⁰ or a streak camera with an S-1 photocathode. The IR measurements are used as the input to the model. At the output of the system, the intensity as a function of time is measured for each of the 60 beamlines on OMEGA with a set of six streak cameras that have a 50-ps temporal resolution.¹¹ Figure 124.16 shows a measured IR pulse shape at the input of the system (scaled to match the peak UV power), a predicted UV pulse shape at the end of the system, and a measured UV output pulse. The excellent agreement between the model and the measurement provides an experimental verification of the model. In addition, an imaging spectrometer measures the UV spectra of all 60 beams with a 2.5-pm (7.6-GHz) resolution.¹² These two sets of measurements can be

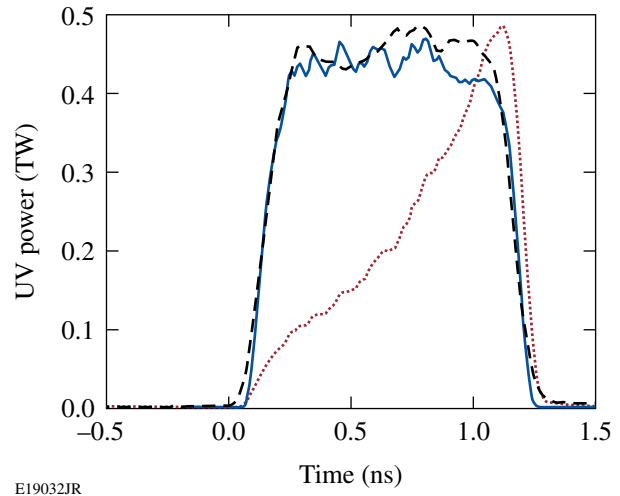


Figure 124.16

The temporal UV pulse shape at the output of the system as measured by the streak cameras (dashed black curve) matches the predicted pulse shape (solid blue curve) derived from the rescaled input IR pulse (dotted red curve).

combined to demonstrate a linear relationship between dP/dt and the frequency shift caused by SPM.

When relatively benign pulse shapes are propagated on the OMEGA Laser System, such as a 200-J, 2-ns square pulse, only negligible amounts of additional bandwidth are generated. Any observed broadening represents the instrument response function of the spectrometer with a full width, $\Delta\nu$, at 1/20th of the peak of 20 GHz. In contrast, the most-pronounced frequency shifts occur when the amplifier chains generate 40 J of UV energy in a 100-ps FWHM asymmetric Gaussian pulse given approximately by

$$P(t) = P_0 \times e^{-[(t-t_0)/\tau]^2}, \quad (3)$$

where $\tau = 49$ ps if $t < t_0$ and $\tau = 80$ ps if $t \geq t_0$. In this case dP/dt is non-negligible (>1 GW/ps) for most of the duration of the pulse, so most of the energy is shifted out of the narrow bandwidth defined by the instrument response function. Figure 124.17 shows the spectra from three different laser shots. The dashed green curve from a 63-J, 3-ns square pulse essentially represents the instrument-response function. The solid blue curve, from the 100-ps pulse described above, shows significant spectral broadening.

Similar shifts occur with 1-ns square pulses that rise to the same intensity as the 100-ps pulses with approximately the same rise time. For the 1-ns square pulses, however, most of the pulse energy remains within a narrow spectral bandwidth defined by a monochromatic seed laser because dP/dt

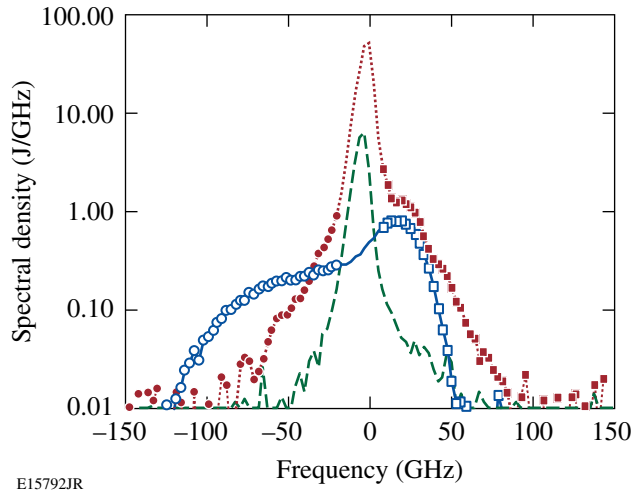


Figure 124.17

The UV spectrum at the output of the system for a 1-ns, 556-J square pulse (dotted red curve), a 100-ps, 48-J pulse (solid blue curve), and a 3-ns, 63-J square pulse (dashed green curve). The squares represent spectral components that have been frequency upshifted; the circles and dots have been downshifted. The 3-ns pulse does not undergo SPM.

is approximately zero (<1 GW/ps) over much of the pulse. The 100-ps pulses produce frequencies that are shifted by as much as 50 GHz from the laser carrier frequency. The integrated effective red and blue spectral shifts for each beamline can be determined from the spectral measurements. From Eq. (2), it can be shown that the rising edge of a pulse ($dP/dt > 0$) gives rise to a red shift ($\Delta\nu < 0$) and the falling edge ($dP/dt < 0$) generates a blue shift ($\Delta\nu > 0$). An effective $\langle dP/dt \rangle$ for the rising edge of the UV pulse is determined by computing a normalized, weighted integral of the time derivative of the power from the 10% to the 80% points on the rising edge:

$$\left\langle \frac{dP_{UV}}{dt} \right\rangle_{\text{rise}} = \frac{\int_{0.1 P_{\text{max}}}^{0.8 P_{\text{max}}} \frac{dP_{UV}(t)}{dt} \times P_{UV} \times dt}{\int_{0.1 P_{\text{max}}}^{0.8 P_{\text{max}}} P_{UV} \times dt}. \quad (4)$$

A similar equation can be generated for the falling edge.

Just as the temporal pulse shape can be divided into rising and falling edges, the UV spectra can be divided into red and blue components by determining where energy has been shifted to lower or higher frequencies. To calculate the frequency-shifted spectra, the instrument response function was scaled to represent the same energy as was measured for

each beamline. The scaled waveform $S_{\text{resp}}(\nu)$ was subtracted from the measured waveform $S_{\text{meas}}(\nu)$:

$$S_{\Delta}(\nu) = [S_{\text{meas}}(\nu) - S_{\text{resp}}(\nu)]. \quad (5)$$

Anywhere the result is positive represents frequency-shifted energy. Negative numbers represent energy that remained at the center-line frequency of the laser, ν_0 . An average, downshifted frequency $\langle \nu_- \rangle$ is defined in a manner similar to $\langle dP/dt \rangle_{\text{rise}}$:

$$\langle \nu_- \rangle = \frac{\int_{-\infty}^{\nu_0} \nu \times S'_{\Delta}(\nu) \times d\nu}{\int_{-\infty}^{\nu_0} S'_{\Delta}(\nu) \times d\nu}, \quad (6)$$

where $S'_{\Delta} = S_{\Delta}$, if $S_{\Delta} > 0$, and $S'_{\Delta} = 0$, if $S_{\Delta} < 0$. In analogy with the temporal pulse shape, an average upshifted frequency $\langle \nu_+ \rangle$ can be similarly defined. The spectral and temporal measurements were combined by pairing $\langle dP/dt \rangle_{\text{rise}}$ with $\langle \nu_- \rangle$ and $\langle dP/dt \rangle_{\text{fall}}$ with $\langle \nu_+ \rangle$. This pairing follows the premise that the rising edge generates red shifts and the falling edge generates blue shifts. When the spectral shifts, recorded for both 1-ns and 100-ps pulses, are plotted versus $\langle dP/dt \rangle$, we find a linear relationship with a slope of -7.8 GHz-ns/TW as shown in Fig. 124.18. As expected, the intercept is approximately zero, which indicates that there is no frequency shift when the intensity is constant. If the amplifier system was characterized by constant power, area, and uniform optical material properties, the slope of the fit in Fig. 124.18 would be directly proportional

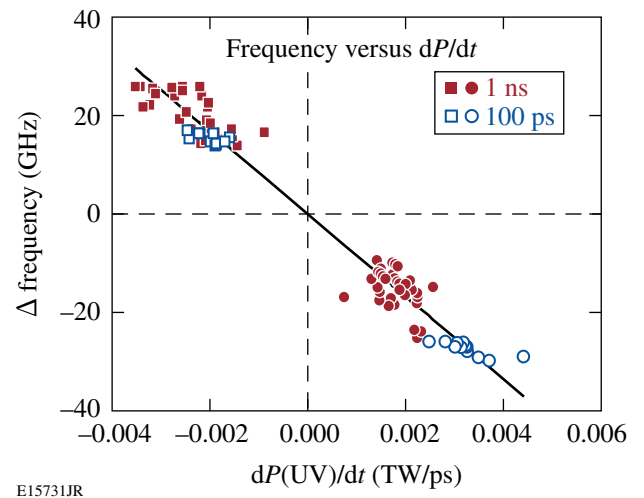


Figure 124.18

Combined plot of $\langle \nu_- \rangle$ versus $\langle dP_{\text{rise}}/dt \rangle$ and $\langle \nu_+ \rangle$ versus $\langle dP_{\text{fall}}/dt \rangle$. Data were acquired for both 100-ps double-Gaussian pulses and 1-ns super-Gaussian pulses.

to the nonlinear coefficient of the material, γ . The evolving temporal pulse shape in the amplifier chain implies, however, that the slope represents an effective aggregate value. The fact that there is a linear relationship that extends over different pulse shapes, beamlines, and beam energies is indicative of the reproducibility of the laser system configuration. The utility of the slope lies in the reconstruction of the spectrum from the temporal pulse shape and the extraction of the ΣB -integral from the measured spectrum.

The slope relates the average frequency shift to the average dP/dt . If the relation holds in detail, the same slope relates the instantaneous frequency to the instantaneous dP/dt . The quantity dP/dt was therefore calculated for every time interval dt in the temporal waveform and mapped, via the fitted slope, to a frequency shift. For the simulated curve, dP/dt was derived from the UV power calculated at the end of the amplifier chain by the system model based on the measured IR input pulse. The energy associated with that frequency shift is given by $P(t)dt$. For comparison with the measured spectrum, this energy is distributed over all frequencies using the instrument response function centered at the instantaneous frequency. Finally, the full spectrum is computed by summing the contributions of all time intervals. The result (Fig. 124.19) shows a comparison of the calculated spectra using this technique as derived from the temporal pulse shape (red curve with diamonds) with the directly measured spectra (black curve with \times 's) and the spec-

trum predicted for the full-system model (solid blue curve). In all three curves, the frequency components with spectral shifts less than ± 6 GHz, corresponding to the spectrometer resolution, have been removed to highlight the SPM-induced frequencies. The agreement is remarkably good despite violating the assumption about the constancy of the intensity throughout the system.

There is even better agreement between the model-generated spectrum and the measured spectrum. To achieve this agreement, the measured IR pulse shape at the input of the system had to be deconvolved with the 20-ps impulse response of the streak camera used to measure the pulse shape. This deconvolved pulse shape was applied to the laser system model to generate the predicted spectrum. The fact that deconvolution was necessary to match the measured spectrum indicates the high sensitivity of the spectroscopic measurement.

The IR and UV streak cameras and the UV spectrometer have been permanently installed on the system and are monitored on every shot. To further verify the model, a UV streak camera coupled to a spectrometer was temporarily installed to measure the time-resolved spectrum of the UV beam.¹³ The centroid of the UV spectrum increases by approximately 0.2 \AA from the nominal 3510.1 \AA on the rising edge and decreases by 0.1 \AA on the falling edge. The UV power history had a double Gaussian shape with a faster rising edge and slower falling edge as indicated by the dotted red curve in Fig. 124.20. The experimentally measured spectral shifts (black \times 's) closely

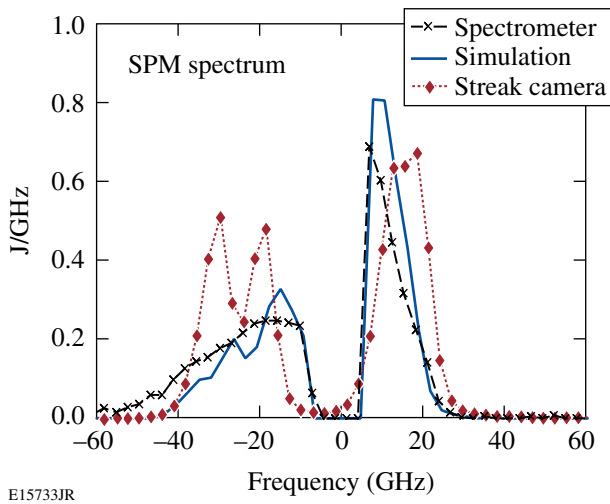


Figure 124.19
A comparison of the frequency-shifted spectra derived from the spectrometer (black curve with \times) with that derived from dP/dt as measured by the streak camera (red curve with diamonds) and predicted by the system model (solid blue curve). Frequencies within the resolution bandwidth of the spectrometer have been removed to highlight the shifted frequencies.

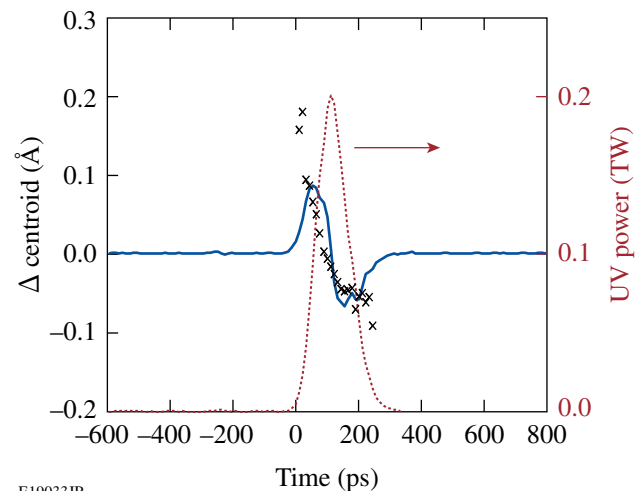


Figure 124.20
The time-resolved centroid of the UV spectrum (black \times 's) matches the derivative of the UV scaled by the constant 32 \AA ps/TW (solid blue curve). The UV temporal shape is overlaid in red (dotted)

match the scaled temporal derivative of the UV power (solid blue curve). This verifies the temporal associations assumed in compiling Fig. 124.18.

These measurements help ensure the safety of the laser system. A scenario for safe operation of the laser system would be as follows: The IR pulse shape is measured at the input of the system, and the instrument temporal response is deconvolved to produce a high-bandwidth estimate of the input shape. This input pulse shape is processed by the model to determine if the pulse shape can be safely propagated through the system. The laser system is then fired and the spectrum is acquired. The measured SPM spectrum can then be converted into a ΣB -integral number to verify the pre-shot prediction.

Conclusion

We have, for the first time, demonstrated the ability to directly monitor the contribution of SPM to the spectrum at the output on a multikilojoule laser system. We have also demonstrated for the first time, to our knowledge, a direct measurement of the important laser parameter ΣB . This provides a real-time diagnostic that can be used to ensure safe operation of the system. This is particularly important as more-complex pulse shapes employing multiple pickets (i.e., 100-ps pulses preceding longer shaped pulses)¹⁴ are deployed on the system.

ACKNOWLEDGMENT

This work was supported by the U.S. Department of Energy Office of Inertial Confinement Fusion under Cooperative Agreement No. DE-FC52-08NA28302, the University of Rochester, and the New York State Energy Research and Development Authority. The support of DOE does not constitute an endorsement by DOE of the views expressed in this article.

REFERENCES

1. D. C. Brown, in *High-Peak-Power Nd:Glass Laser Systems*, edited by D. L. MacAdam, Springer Series in Optical Sciences (Springer-Verlag, New York, 1981), Vol. 25, Chap. 7, Sec. 7.4, p. 214.
2. Common usage of the term “ B ”-integral: ΔB is always the B -integral accumulated between laser stages, usually defined as pinhole-to-pinhole. ΔB determines the damage threat from small-spatial-scale self-focusing and should never exceed 2 rad. ΣB refers to the total B -integral through the entire laser system from oscillator to target. It usually is a determining factor for the focal-spot size. It regulates the growth of the highest-frequency ripple that can make it through all of the pinholes. When used alone, B can refer to either ΔB or ΣB and is used when no distinction is necessary.
3. L. M. Frantz and J. S. Nodvik, *J. Appl. Phys.* **34**, 2346 (1963).
4. Y. R. Shen, *The Principles of Nonlinear Optics* (Wiley, New York, 1984), p. 242.
5. P. V. Avizonis and R. L. Grotbeck, *J. Appl. Phys.* **37**, 687 (1966).
6. C. Bibeau, “Evaluation of the $^4I_{11/2}$ Terminal Level Lifetime for Several Neodymium-Doped Laser Crystals and Glasses,” Ph.D. thesis, Lawrence Livermore National Laboratory, 1995.
7. S. M. Yarema and D. Milam, *IEEE J. Quantum Electron.* **QE-18**, 1941 (1982).
8. R. S. Craxton, *IEEE J. Quantum Electron.* **QE-17**, 1771 (1981).
9. J. Trenholme *et al.*, Shiva Nova CP&D Interim Report, Laser Fusion Program, Lawrence Livermore National Laboratory, Misc. 107, 2-3-2-324 (1977).
10. J. R. Marciante, W. R. Donaldson, and R. G. Roides, *IEEE Photonics Technol. Lett.* **19**, 1344 (2007).
11. W. R. Donaldson, R. Boni, R. L. Keck, and P. A. Jaanimagi, *Rev. Sci. Instrum.* **73**, 2606 (2002).
12. W. R. Donaldson, M. Millecchia, and R. Keck, *Rev. Sci. Instrum.* **76**, 073106 (2005).
13. S. P. Regan, D. K. Bradley, A. V. Chirokikh, R. S. Craxton, D. D. Meyerhofer, W. Seka, R. W. Short, A. Simon, R. P. J. Town, B. Yaakobi, J. J. Carroll III, and R. P. Drake, *Phys. Plasmas* **6**, 2072 (1999).
14. V. A. Smalyuk, V. N. Goncharov, K. S. Anderson, R. Betti, R. S. Craxton, J. A. Delettrez, D. D. Meyerhofer, S. P. Regan, and T. C. Sangster, *Phys. Plasmas* **14**, 032702 (2007).

Large-Aperture, Plasma-Assisted Deposition of Inertial Confinement Fusion Laser Coatings

Introduction

As inertial confinement fusion (ICF) laser systems continue to evolve, the need for large-aperture optical coatings suitable for use in vacuum continues to increase.^{1,2} Laser pulses that are temporally compressed to the picosecond scale or shorter must propagate in vacuum because of *B*-integral and self-focusing effects.³ While reducing the oxygen backfill during silica evaporation may make multilayer coatings less tensile, traditional electron-beam-deposited coatings tend to experience tensile stress failures in vacuum environments.⁴ More-energetic techniques such as magnetron sputtering, ion-beam sputtering, and ion-assisted deposition result in films with compressive stresses, but these techniques tend to have difficulties with low laser-damage resistance, high film stresses, and/or scale-up to large apertures.^{2,5,6} It is essential for ICF laser-system components to establish a coating process that is stable, with a low-compressive stress in vacuum, and a high laser-damage resistance, particularly for picosecond-scale pulses.

This effort focuses on the development and implementation of a hafnia/silica coating process for meter-scale optical coatings with a controlled compressive stress and high laser-damage resistance. Establishing a low-magnitude compressive stress in the coating is critical for large optics to avoid tensile stress failures while maintaining the optical surface figure without unacceptably thick, heavy, and expensive substrates. A plasma source utilizing a lanthanum hexaboride cathode (LaB₆) was selected for modification of the film because of its low defect density, smooth resulting film structure, and high plasma current necessary for densification of hafnia.^{7,8} In this article, results using a single plasma source to modify electron-beam-deposited coatings are presented. Deposition conditions were modified to provide controlled film stresses and high laser-damage thresholds under various wavelengths and pulse durations. This work was then adapted to develop and implement a dual-plasma-source system in a 72-in. coating chamber, suitable for processing meter-scale optics. This process has been used to coat a 0.8-m mirror for use in vacuum at 1053 nm with a 10-ps pulse duration on the OMEGA EP Laser System.

Background

Ion-assisted deposition (IAD) and plasma-assisted deposition, or plasma-ion-assisted deposition (PIAD), have been used to create environmentally stable optical coatings, coating processes suitable for use on temperature-sensitive substrates, and more mechanically durable coatings.^{9–12} These processes utilize an ionized gas that is accelerated with a magnetic field toward the substrate surface during the coating process. Some ion sources can operate on O₂ gas alone, while others require the addition of a neutral gas, such as argon.^{7,8,10,13,14}

Using ion and plasma sources to modify a standard electron-beam evaporation process provides a significant benefit by introducing many additional control variables that may be used to influence film properties such as humidity stability, film stress, mechanical durability, and material refractive indices. Evaporation is a low-energy deposition process, leading to porous coatings that adsorb moisture, making the optical thickness of the film, as well as the coating stress, a function of the relative humidity in the use environment.¹² Variables such as beam voltage, current, gas selection, and gas flow, in addition to source location and pointing, can be utilized to alter these film properties by transferring momentum from incident ions to the condensing film, altering the structure, and collapsing the pores present in the coating.¹⁵ The introduction of these variables requires care in determining the appropriate operating conditions for each to achieve the desired film performance without negatively influencing other film characteristics.

The choice of gas used in a plasma or ion process can have a significant impact on the resulting film densification. Ions with greater mass provide a correspondingly greater momentum, resulting in additional influence on the condensing film structure.^{10,16} The deposition of oxide films by evaporation typically requires the addition of oxygen to the vacuum environment, introducing it directly into the chamber, where it is dispersed. By passing the oxygen through an ion or plasma source, the gas is ionized and accelerated, imparting momentum to the oxygen molecules, leading to densification of the growing film

as the oxygen impacts the surface. As greater densification is required, more argon may be used in the plasma to benefit from its greater atomic mass. If a further increase in momentum is required, higher-atomic-mass gases such as krypton or xenon may be used to provide additional ion momentum. As the relative content of oxygen is decreased, however, the film must be carefully evaluated to prevent an increase in optical absorption, leading to a reduced laser-damage threshold.

Plasma or ion-beam current is simply related to the flow of ions, each of which carries a charge equivalent to the charge of an electron. Increased current in a plasma- or ion-assisted process tends to provide greater densification of the coating being deposited without the risk associated with increased absorption, as is the case with increased ion voltage. Since current will influence the film density, it will also play a role in the ultimate stress achieved in the film. In particular, the impact of ions modifies the film porosity and reduces or eliminates the exchange of water vapor, leading to changes in film stress.^{4,15}

The operating voltage of a plasma source determines the energy of an arriving ion at the substrate surface. By increasing the source voltage, higher ion energies and a correspondingly greater densification of the film structure are achieved; however, ions with too high an energy may break atomic bonds in the film, leading to damage of the coating material and the formation of localized absorption sites. Ion voltage may also influence crystalline content in the film since the film structure exhibits characteristics of deposition at a higher temperature with an increased crystallite size; surface roughness and film stress are also modified.¹⁷ Ion beams and plasmas impart energy to the condensing film, causing the displacement of surface atoms and the compaction of the film structure. Using ions to assist the deposition process may lead to energies at the surface equivalent to deposition temperatures in excess of 10^6 K (Ref. 18). This enables one to continuously modify the film structure from a porous, columnar structure realized with electron-beam evaporation to a highly crystalline film in an extremely compressive state resulting from significant ion impingement. This change in film structure is described by structure-zone models with equivalent deposition temperatures.^{19–21} By adjusting the characteristics of the plasma flux and the evaporant conditions, the desired film stress and density may be achieved.

Coating stress is comprised of intrinsic and thermal stresses. The influence of energetic deposition is such that the intrinsic stress becomes significantly more important, able to balance or dominate the thermal stresses present in the film resulting from the differing coefficients of thermal expansion for coating and

substrate materials when depositing at elevated temperatures. The relationship between the film stress and the substrate surface deflection is described by Stoney's equation²²

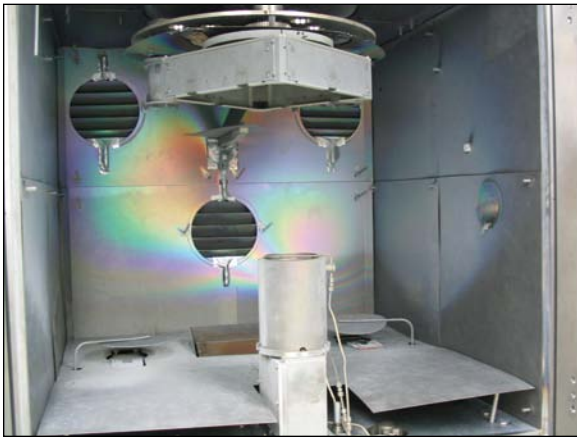
$$\sigma = \frac{E_s t_s^2}{6(1 - \nu_s) t_f R}, \quad (1)$$

where σ is the stress in the film, R is the radius of curvature of the surface, E_s is Young's modulus of the substrate, ν_s is Poisson's ratio for the substrate, and t_f and t_s are the thickness of the film and substrate, respectively. It should be noted that Stoney's equation is an approximation, suitable when $t_f \ll t_s$. Plasma-assisted deposition controls film properties in a way that the deposition process may be tuned for each substrate material with its corresponding thermal stresses by altering the intrinsic stress of the film. The degree of control achievable with a plasma-assisted process will determine the magnitude of the film stress that can be realized and, consequently, the substrate thickness necessary to meet the required surface flatness for an optical component.

The distribution of the ion flux from an ion or plasma source may be modeled much like a deposition source, using a cosine distribution.^{23,24} A primary advantage of plasma sources is that the extraction coil enables one to alter the source flux by changing the strength of the magnetic field in the extractor coil.²⁵ Also, unlike deposition, the influence of the impinging ions is not simply a linear process. To a large extent is a thresholding process, where a minimum ion flux is required to achieve film densification.⁶ The primary goal in this work, however, is the establishment of a low-magnitude compressive-film stress, without the need for complete densification. The source placement and flux-distribution tuning must be performed in such a manner that the film densification and corresponding structure are controlled over the aperture of the substrates.

Experimental Procedure

An initial series of coatings was prepared in a cryo-pumped, 56-in. coating chamber equipped with quartz heater lamps, dual electron-beam guns, multipoint quartz crystal monitoring, and planetary substrate rotation as shown in Fig. 124.21. Granular silicon dioxide was evaporated from a continuously rotating pan, while hafnium metal was deposited in the presence of oxygen from a stationary six-pocket electron-beam gun to form hafnium dioxide. A single Satis PDS plasma source was installed in the chamber at a radius of 15 in. from chamber center to provide a uniform ion flux over the aperture of the substrate.



G9089JR

Figure 124.21

The 56-in. coating chamber with planetary rotation, dual electron-beam guns, and a single Satis PDS plasma source. The plasma source is positioned off-center in the chamber to provide a more-uniform plasma flux over the substrate aperture.

The primary concern with energetically assisting the deposition process for high-peak-power laser applications is that the laser-damage threshold will be compromised, leading to reduced fluence capabilities for the laser.² Hafnia monolayers were deposited on cleaved float glass with an optical thickness of four quarter-waves at 351 nm to form an absentee layer that minimizes the influence of the standing-wave electric field in the film. The cleaved-glass substrate eliminates the effects of substrate fabrication and cleaning processes on laser-damage thresholds.²⁶ The plasma settings for the initial samples were 140 to 180 V/35 A (acceleration voltage/beam current), a nominal 10 sccm of argon gas surrounding the LaB₆ cathode in the plasma source controlled to maintain constant beam current/voltage, and 50 sccm of O₂ gas injected into the plasma using a gas-distribution ring on the top of the source. Chamber pressure was controlled through oxygen backfill to maintain a constant pressure of 4.0×10^{-4} Torr. Laser-damage testing was performed in a standard 1:1 testing configuration at 351 nm at a 0.5-ns pulse duration.²⁷ Finally, x-ray diffraction (XRD) measurements of the hafnia films were collected using a Philips Materials Research diffractometer (MRD) with a CuK α source to evaluate the crystallinity of the hafnia structure. The coated samples were oriented in a near-grazing incidence configuration, with an incident angle $\theta = 2.2^\circ$ and a diffracted angle 2θ incremented in steps of 0.02° , with a 13-s integration time at each position.

The film stress in hafnia monolayers was also evaluated as a function of plasma-assist voltage since this is the primary benefit for large-aperture laser coatings. Hafnia layers with a

140-nm thickness were deposited on 25-mm-diam \times 1-mm-thick BK7 substrates. Surface flatness was measured using a Zygo New View interferometer at controlled relative humidities of 0% and 40%, measuring the uncoated surface of the substrate to avoid the influence of phase effects from the coating. The optics were supported horizontally on a three-point mounting fixture, using equally spaced ball bearings placed at 65% of the radius of the substrate to minimize deflection caused by mounting. The resulting stress in the hafnia films was evaluated as a function of plasma voltage to determine appropriate operating conditions for low-stress coatings.

Development of the plasma-assist process continued with the deposition of multilayer high-reflector coatings using a broad range of deposition conditions, including variations of plasma voltage, current, gas flows, deposition rates, substrate temperature, and chamber pressure. The influence of the deposition conditions on film stress and laser-damage resistance was evaluated to determine optimal deposition conditions. Selected deposition processes were used to deposit high-reflector coatings centered at $\lambda_0 = 1053$ nm on 310-mm-diam \times 14-mm-thick fused-silica substrates for evaluation on an 18-in. Zygo interferometer and a large-aperture laser conditioning station according to National Ignition Facility (NIF) protocol.²⁸

Finally, the plasma-assist process was installed in a 72-in. coating chamber (as shown in Fig. 124.22) utilizing two Thin



G9090JR

Figure 124.22

A Thin Film Solutions Ltd. dual-plasma-source system installed in LLE's 72-in. electron-beam evaporation system. The plasma sources provide a high ion flux over the entire surface of the meter-scale substrates.

Films Solutions Ltd. plasma sources, based on the original Satis PDS source design.^{8,25} Two sources were implemented to ensure adequate plasma flux over the surface of a large optic, given a significantly greater source-to-substrate distance than that in the 56-in. coating chamber, as well as to provide redundancy in the event of a source failure. Custom control software was developed to ramp the source in a series of steps to prevent the poisoning of one source cathode by the operation of the second source. The plasma sources were installed at a radial position of 8.3 in. from chamber center, compromising between maximum ion flux and uniformity. Additional mounting locations were machined in the chamber base plate to provide the ability to tune the flux distribution over the substrate aperture as needed. Uniformity masks were reconfigured to avoid significant impingement of the plasma on the film-correction masks.²³ The sources were operated at 145 V with a beam current of 20 A each, introducing 50 sccm of O₂ during hafnia deposition and 15 sccm of O₂ during silica deposition. Cathode temperatures were kept as low as possible by minimizing the rf power to reduce film defects caused by cathode ejections. Interaction between the sources was determined to be negligible during operation.

Results

Throughout this effort to develop plasma-assisted-deposition processes, the plasma conditions (current, voltage, and gas flows) were modified, as well as chamber conditions (oxygen backfill, deposition rates, and substrate temperature). A qualitative understanding of the influence of each parameter is of primary importance since the process space becomes much larger as the number of process variables is increased. Different chamber configurations will require different operational parameters since the influence of a given plasma voltage, current, and gas flow will be strongly dependent on the source location, distance to the substrate, substrate size, and the substrate motion.

As the use of different gas flows and corresponding chamber pressures was evaluated, one consideration was where to introduce the gas. Oxygen is typically introduced during reactive electron-beam deposition, but the inclusion of a plasma-assist source allows one to introduce some or all of the oxygen through the plasma source. Deposition tests were undertaken with oxygen introduced in the chamber or through the plasma source at different controlled operating pressures. As shown in Fig. 124.23, as the chamber pressure is increased, there is a greater change in optical thickness of the hafnia coating between 0%- and 40%-relative-humidity environments caused by water movement into the pores of the film. By introducing

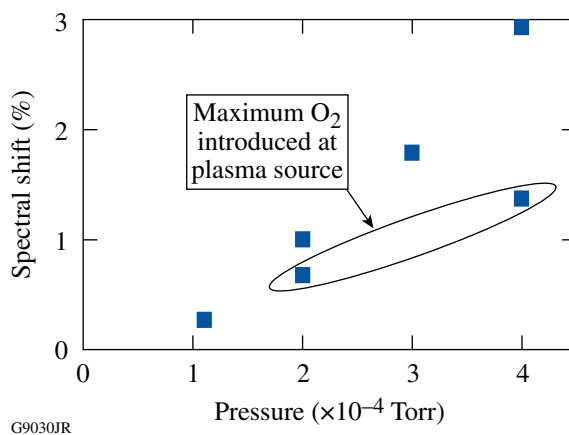


Figure 124.23

Influence of O₂ backfill pressure on the resulting sensitivity of hafnia films to relative humidity. A larger spectral shift between 0% and 40% relative humidity indicates greater film porosity.

the oxygen through the plasma source with all other plasma operating conditions constant, film porosity is reduced 30% to 50%.

It has been found previously that laser-damage thresholds of electron-beam-deposited hafnia improve as the porosity of the film increases.^{29,30} The influence of plasma-assisted deposition on the laser-damage threshold of hafnia coatings was explored for 351-nm light. To minimize the influence of substrate preparation on laser-damage thresholds, coatings were deposited on cleaved float-glass surfaces.²⁶ Laser-damage testing was performed in a standard 1:1 testing configuration at 351 nm at a 0.5-ns pulse duration.³⁰ Laser-damage characterization at 351 nm provides greater sensitivity to changes in film absorption than evaluation at 1053 nm, which tends to be dominated by film defects. These tests demonstrate minimal rate or plasma-voltage influence over the range of parameters tested, as shown in Fig. 124.24. The relatively insignificant change in laser-damage threshold for a plasma voltage in the range of 140 to 180 V indicates the corresponding change in optical absorption of the film must also be negligible. Since the film is deposited with plasma assist, it has a reduced porosity and a correspondingly greater density than a film deposited at the equivalent pressure by electron-beam evaporation. Additionally, the use of plasma assist makes low-porosity deposition no longer necessary to maintain high-laser-damage resistance.^{29,30}

The crystallinity of the hafnia monolayers deposited at 180 V with a 35-A plasma current measured using XRD is shown in Fig. 124.25. The electron-beam-evaporated hafnia exhibits a relatively weak monoclinic crystalline signature, while the crystalline peaks become much more defined as the

ion/evaporant ratio is increased. As the deposition rate of the hafnia is decreased, the relative ion flux is effectively increased and the crystallites grow to approximately 12 nm as calculated using Scherrer's equation.^{30,31} This increase in film crystallinity is equivalent to an increased substrate temperature as described in a structure-zone model.¹⁹⁻²¹ It was determined in a previous study that a reduction in film crystallinity could be correlated with improved laser-damage thresholds for 351-nm light.³⁰ This does not appear to hold true for PIAD films based on the results shown in Figs. 124.24 and 124.25.

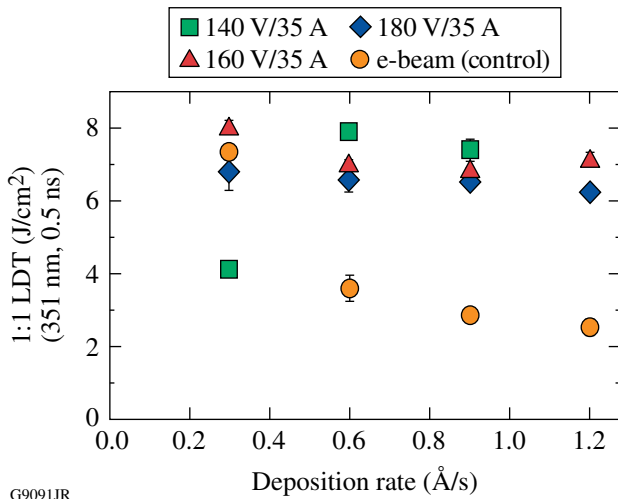


Figure 124.24 Laser-damage thresholds of hafnia deposited with PIAD exhibit minimal deposition-rate dependence, unlike typical electron-beam deposition of hafnia. The control electron-beam coating was deposited with an oxygen backfill pressure of 2×10^{-4} Torr.

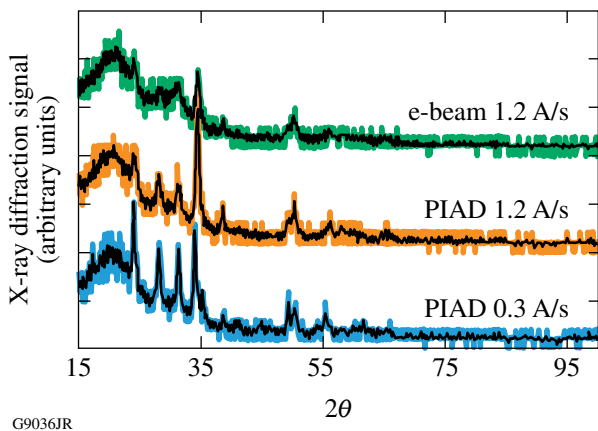


Figure 124.25 X-ray diffraction measurements of hafnia monolayers indicate increasing crystallinity as the plasma/evaporant flux is increased. This may be achieved by increasing the plasma current or decreasing the deposition rate.

The film stress in hafnia monolayers was also evaluated as a function of plasma-assist voltage. Hafnia layers of 140-nm thickness were deposited on 25-mm-diam \times 0.25-mm-thick BK7 substrates. Surface-flatness measurements were performed on a Zygo New View interferometer at relative humidities of 0% and 40%. Using Eq. (1), these measurements were used to calculate the film stress. The resulting stress in the hafnia films is plotted in Fig. 124.26(a) as a function of plasma voltage when operated at 35 A to determine appropriate operating conditions for low-stress coatings. The stress transitioned from a tensile state below 145 V to an increasingly compressive state above this plasma potential. All film stresses for plasma-assisted silica films plotted in Fig. 124.26(b) were found to be compressive, with an increasing compressive stress as the plasma voltage was increased.

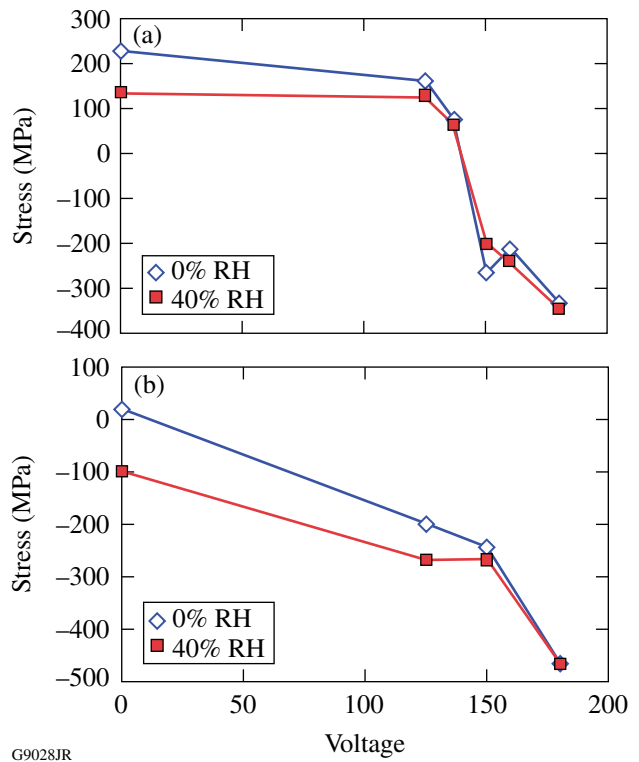
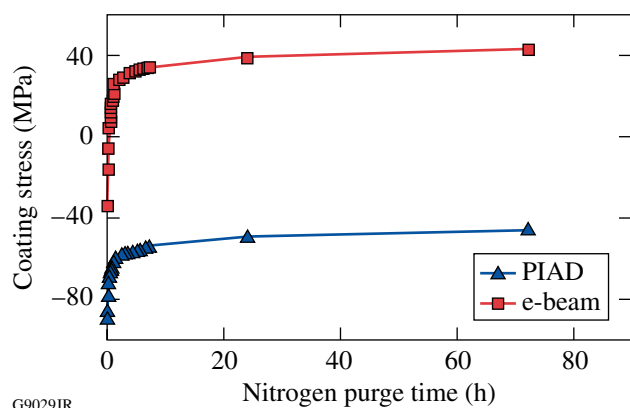


Figure 124.26 (a) Influence of plasma-assist voltage on the stresses in hafnia monolayers. An assist of approximately 145 V at 35 A is sufficient to transition from tensile to compressive stress. (b) Influence of plasma-assist voltage on the stresses in silica monolayers. Note that all silica stresses are compressive, except the evaporated silica (no PIAD) in a dry environment.

Development of the plasma-assist process continued with the deposition of multilayer high-reflector coatings using a broad range of deposition conditions, including variations of plasma voltage, current, gas flows, deposition rates, substrate temperature, and chamber pressure. The influence of the depo-

sition conditions on film stress and laser-damage resistance was evaluated to determine optimal deposition conditions. In general, the addition of energetic ions through PIAD resulted in a more-compressive coating with a reduced sensitivity to relative humidity than a comparable coating produced with only electron-beam evaporation, as shown in Fig. 124.27. The PIAD results shown are from a coating deposited with a 170-V/40-A plasma, leading to greater densification of the film and a reduced sensitivity to humidity. The chamber temperature was adjusted to 140 °C, which is as low as possible while maintaining a controlled, constant temperature during PIAD operation.



G9029JR

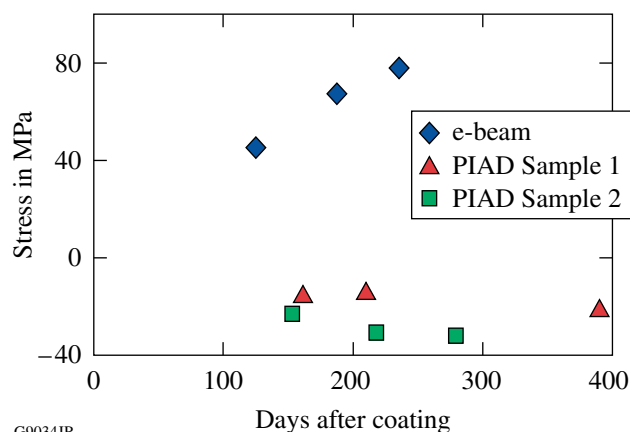
Figure 124.27

Change in film stress for PIAD and electron-beam-deposited coatings as the ambient relative humidity changes from 40% RH to 0% RH. While the % RH of the measurement environment changes almost immediately, the removal of water from the film pores is a much slower process, dependent on the diffusion of water through the film structure. Note that PIAD coatings are more compressive, with a smaller change in film stress as the coating is dried.

The densification of only single materials within multilayer coatings was explored by operation of the plasma source during hafnia or silica layers. Hafnia was considered since it is the primary source of tensile stress, as shown in Fig. 124.26(a). Silica was pursued since it undergoes the most significant change in stress as a function of time.⁴ However, the presence of porous layers between dense diffusion barriers led to irregular water penetration around film defects, leading to subsequent spotting of the coating. Furthermore, the argon backfill required to idle the plasma sources resulted in a poorer vacuum during nondensified layers. The densification of alternating layers was determined to be problematic and not pursued further.

Selected deposition processes were used to deposit high-reflector coatings centered at $\lambda_0 = 1053$ nm on 310-mm-diam \times 14-mm-thick fused-silica substrates for evaluation on an 18-in. Zygo interferometer and large-aperture laser conditioning sta-

tion according to NIF protocol.²⁸ As shown in Fig. 124.28, the stress in the electron-beam-deposited coating continued to become more tensile as the coating aged, with changes in film stress apparent more than six months after deposition. PIAD samples 1 and 2 show a film stress that remained constant, within ± 10 MPa, over an extended duration. A controlled compressive stress with a magnitude of 20 to 30 MPa is ideal to avoid difficulties arising from tensile-stress failures (crazing), while imparting minimal reflected wavefront deformation caused by stress.



G9034JR

Figure 124.28

Change in film stress for PIAD and electron-beam-deposited coatings at 0% RH as a function of aging. While e-beam-deposited coatings continue to change significantly over periods of months, partially dense PIAD coatings with near-neutral stress maintain a consistent film stress.

The dual-source system was operated at 145 V with a beam current of 20 A from each source, introducing 50 sccm of O₂ during hafnia deposition and 15 sccm of O₂ during silica deposition. Meter-scale high-reflector coatings were produced with a compressive stress of the order of 50 to 80 MPa in a use environment of 0% relative humidity and a laser-damage threshold of 6.7 J/cm² at 1053 nm with a pulse length of 10 ps. Laser-damage testing was performed in an ambient humidity environment at 29° incidence. This process was used to fabricate an 0.8-m mirror, designated as SPHR10, on a BK7 substrate for use in vacuum on the OMEGA EP Laser System, as shown in Fig. 124.29. Measurement of the coated surface indicated 0.38 waves peak-to-valley of surface power on a 1064-nm-wavelength interferometer. Measurement of the film stress for BK7 substrates in a dry environment indicated a stable film stress of approximately 50 MPa. The stress aging of the PIAD coating, as shown in Fig. 124.30, indicated that the aging effects typical of evaporated hafnia silica coatings have been effectively eliminated, even for a PIAD coating with significant porosity and humidity susceptibility.^{4,28} The

spectral shift in the optical thickness of the coating from a 0%- to 40%-relative-humidity environment was measured as $1.54 \pm 0.14\%$ over a 0.9-m aperture, indicating significant but quite uniform film porosity, although the film was more dense than the reference electron-beam–deposited film with a typical 2.7% spectral shift. The consistency of the film porosity, as determined by the spectral shift in different humidity environ-

ments, demonstrated that film densification was quite uniform over the substrate aperture, particularly since the film was only partially densified. Laser-damage thresholds for 1053-nm, 1-ns pulses were measured at 22.09 J/cm^2 in a 1:1 defect-targeting mode. The laser-damage threshold for defect-free sites was determined to be 26.67 J/cm^2 , indicating a decrease in laser-damage threshold relative to standard evaporated coatings, which tend to be $>85 \text{ J/cm}^2$ for defect-free sites.^{1,28}

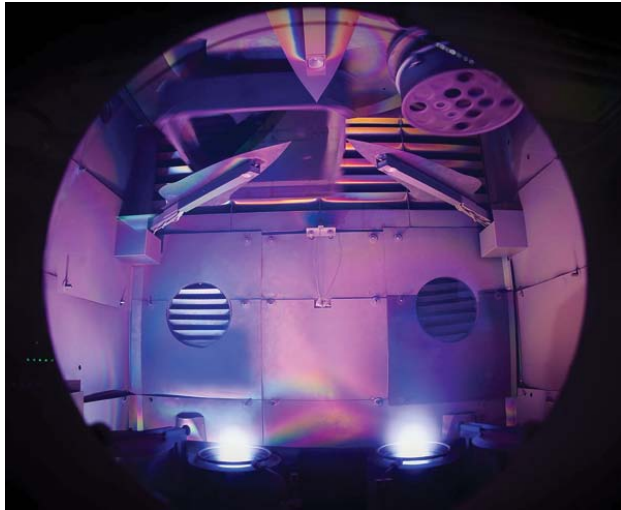
Conclusions

Plasma-assisted deposition provides a means of tuning the film stress of optical coatings while maintaining high-peak-power laser-damage thresholds. Installation of a plasma-assist process is unique for a given deposition system since each chamber configuration will have a different set of optimal operating parameters for neutral film stress based on the substrate size, rotation geometry, radial position of the source, and other considerations. This development effort provides guidance for tuning the process in different systems. Increased plasma voltage leads to greater densification of the film and a more-compressive film stress. The use of more-energetic oxygen, by ionizing it with a plasma source, leads to a denser coating and improved laser-damage thresholds, particularly for lasers in the ultraviolet region of the spectrum, which are more susceptible to film absorption. Likewise, reduced chamber pressures lead to decreased evaporant scattering and a less-porous film structure.

Controlled compressive film stresses of $<50 \text{ MPa}$ can be established and maintained in a dry-use environment on fused-silica substrates through plasma-assisted deposition, providing a means of avoiding tensile-stress failures in vacuum while maintaining high-quality surface flatness of the laser components. A plasma-assist process for multilayer coatings has been demonstrated with a low-magnitude compressive stress utilizing a nominal voltage of 145 V during hafnia and silica deposition, with plasma current being adjusted to achieve the desired film stress and densification. This process was integrated in a 72-in. coating chamber to deposit high-precision coatings over 0.9-m aperture optics. The measured laser-damage threshold for a 29° high-reflector coating is 6.7 J/cm^2 (1053 nm, 10-ps pulse) with a compressive film stress of 50 MPa.

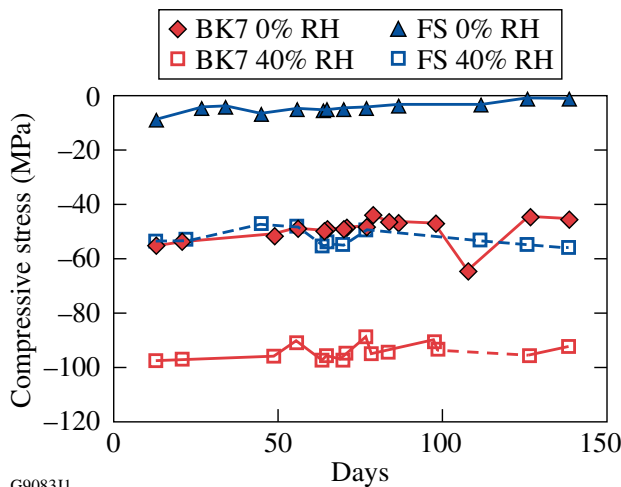
ACKNOWLEDGMENT

The authors wish to express their appreciation to Alex Maltsev for his efforts on the fabrication of extremely high quality, high-aspect-ratio substrates for this study. This work was supported by the U.S. Department of Energy Office of Inertial Confinement Fusion under Cooperative Agreement No. DE-FC52-08NA28302, the University of Rochester, and the New York State Energy Research and Development Authority. The support of DOE does not constitute an endorsement by DOE of the views expressed in this article.



G9092JR

Figure 124.29 The dual-source PIAD system in the 72-in. coating chamber was used to deposit the SPHR10 coating. The plasma effectively fills the entire deposition region, providing a uniform densification of the film over the full aperture of the substrate.



G9083J1

Figure 124.30 Stress-aging measurements of PIAD coatings indicate negligible changes in stress as a function of time after deposition. In comparison, the stress of the e-beam–deposited coating in Fig. 124.28 continues to change significantly six months after deposition.

REFERENCES

1. J. B. Oliver, A. L. Rigatti, J. D. Howe, J. Keck, J. Szczepanski, A. W. Schmid, S. Papernov, A. Kozlov, and T. Z. Kosc, in *Laser-Induced Damage in Optical Materials: 2005*, edited by G. J. Exarhos *et al.* (SPIE, Bellingham, WA, 2005), Vol. 5991, pp. 394–401.
2. E. Lavastre *et al.*, in *Optical Interference Coatings*, OSA Technical Digest (Optical Society of America, Washington, DC, 2004), p. TuF3.
3. Y.-H. Chuang, L. Zheng, and D. D. Meyerhofer, *IEEE J. Quantum Electron.* **29**, 270 (1993).
4. H. Leplan *et al.*, *J. Appl. Phys.* **78**, 962 (1995).
5. D. J. Smith *et al.*, in *Laser-Induced Damage in Optical Materials: 2008*, edited by G. J. Exarhos *et al.* (SPIE, Bellingham, WA, 2008), Vol. 7132, p. 71320E.
6. M. Alvisi *et al.*, *Thin Solid Films* **358**, 250 (2000).
7. R. Thielsch *et al.*, *Thin Solid Films* **410**, 86 (2002).
8. F. Placido *et al.*, in *Advances in Thin-Film Coatings for Optical Applications III*, edited by M. J. Ellison (SPIE, Bellingham, WA, 2006), Vol. 6286, p. 628602.
9. H. R. Kaufman and J. M. Harper, in *Advances in Thin Film Coatings for Optical Applications*, edited by J. D. T. Kruschwitz and J. B. Oliver (SPIE, Bellingham, WA, 2004), Vol. 5527, pp. 50–68.
10. M. Kennedy, D. Ristau, and H. S. Niederwald, *Thin Solid Films* **333**, 191 (1998).
11. E. H. Hirsch and I. K. Varga, *Thin Solid Films* **69**, 99 (1980).
12. B. G. Bovard, in *Thin Films for Optical Systems*, edited by F. R. Flory (Marcel Dekker, New York, 1995), pp. 117–132.
13. J. R. Kahn, H. R. Kaufman, and V. V. Zhurin, in *46th Annual Technical Conference Proceedings* (Society of Vacuum Coaters, Albuquerque, NM, 2003), pp. 621–625 (Paper 110).
14. D. E. Morton and V. Fridman, in *Proceedings of the 41st Annual Technical Conference of the Society of Vacuum Coaters* (Society of Vacuum Coaters, Albuquerque, NM, 2003), pp. 297–302 (Paper 53).
15. K.-H. Müller, *J. Vac. Sci. Technol. A* **4**, 184 (1986).
16. J. D. Targove and H. A. Macleod, *Appl. Opt.* **27**, 3779 (1988).
17. G. Atanassov *et al.*, *Thin Solid Films* **342**, 83 (1999).
18. H. Kersten *et al.*, *Vacuum* **46**, 305 (1995).
19. J. V. Sanders, in *Chemisorption and Reactions on Metallic Films*, edited by J. R. Anderson, *Physical Chemistry, A Series of Monographs* (Academic Press, London, 1971), pp. 1–38.
20. J. A. Thornton, in *Modeling of Optical Thin Films*, edited by M. R. Jacobson (SPIE, Bellingham, WA, 1988), Vol. 821, pp. 95–103.
21. B. A. Movchan and A. V. Demchishin, *Fiz. Met. Metalloved* **28**, 653 (1969).
22. G. G. Stoney, *Proc. R. Soc. Lond. A* **82**, 172 (1909).
23. J. B. Oliver and D. Talbot, *Appl. Opt.* **45**, 3097 (2006).
24. H. R. Kaufman, R. S. Robinson, and R. I. Seddon, *J. Vac. Sci. Technol. A* **5**, 2081 (1987).
25. D. Gibson, European Patent No. EP 1 154 459 A2 (14 November 2001).
26. S. Papernov, D. Zaksas, J. F. Anzellotti, D. J. Smith, A. W. Schmid, D. R. Collier, and F. A. Carbone, in *Laser-Induced Damage in Optical Materials: 1997*, edited by G. J. Exarhos *et al.* (SPIE, Bellingham, WA, 1998), Vol. 3244, pp. 434–445.
27. S. Papernov and A. W. Schmid, *J. Appl. Phys.* **82**, 5422 (1997).
28. J. B. Oliver, J. Howe, A. Rigatti, D. J. Smith, and C. Stolz, in *Optical Interference Coatings*, OSA Technical Digest (Optical Society of America, Washington, DC, 2001), p. ThD2.
29. B. Andre, J. Dijon, and B. Rafin, U.S. Patent No. 7,037,595 (2 May 2006).
30. J. B. Oliver, S. Papernov, A. W. Schmid, and J. C. Lambropoulos, in *Laser-Induced Damage in Optical Materials: 2008*, edited by G. J. Exarhos *et al.* (SPIE, Bellingham, WA, 2008), Vol. 7132, p. 71320J.
31. B. D. Cullity, *Elements of X-Ray Diffraction*, 2nd ed. (Addison-Wesley, Reading, MA, 1978).

Improved On-Shot Focal-Spot Measurement on OMEGA EP Using Phase-Retrieval-Enhanced Wavefront Measurements

Introduction

Intensity at the target plane is a critical parameter in many inertial confinement fusion (ICF) experiments conducted on the short-pulse OMEGA EP laser.¹ Measuring the focal-spot intensity at the target plane on a high-energy shot, however, is a challenging task. Remote camera measurements can be made with a sampled diagnostic beam, but it is not easy to account for the effect of the final optics that focus the beam to target and the optics for the diagnostic. For OMEGA EP, a remote wavefront-measurement system has been developed to make on-shot target-plane focal-spot predictions for the short-pulse beams.² Limitations in the wavefront sensor and errors in the calibration and on-shot measurement, however, can lead to erroneous wavefront measurements that in turn yield poor focal-spot predictions.

In many applications where wavefront information is desired, phase-retrieval techniques have been effective in estimating wavefront based on a series of intensity measurements.^{3–7} Often, these measurements are made simultaneously in two different planes, e.g., a pupil plane and a far-field plane, or two or more far-field planes at different defocus distances. A variety of algorithms have been used to estimate the phases of the optical fields in these planes based on the rules of propagation between them. These can generally be classified into two categories: iterative-transform methods and gradient-search methods.⁵ In the former category, an initial guess is made about the phase profile in one plane, and the field is propagated back and forth between the planes with the magnitude of the field being replaced with the measured value and the phase being based on the calculated phase at each iteration.³ In the latter category, a merit function is produced and minimized by utilizing its gradient over a discrete set of variables.^{5,6} Gradient-search algorithms can be point-by-point (independently varying the wavefront at discrete points over the planes of interest) or modal (modifying the coefficients of a modal expansion of the wavefront).

In this article, we demonstrate the use of phase retrieval to improve the focal-spot measurement on OMEGA EP. As

a result of this work, the on-shot focal-spot measurement has been improved to the point that it reliably matches direct measurements of the focal-spot intensity at low energy. This article is organized as follows: OMEGA EP and the on-shot target-plane focal-spot measurement technique are reviewed and initial performance of the focal-spot measurement is assessed; four problems with the focal-spot measurements are described and phase-retrieval techniques for mitigating them are described; the results of applying these improvements to the focal-spot measurement are described with the accuracy and reliability assessed over a population of shot data; and finally, conclusions are presented.

Overview of Focal-Spot Measurement

The focal-spot diagnostic (FSD) was deployed on OMEGA EP to characterize on-shot, target-plane fluence distributions for the short-pulse beamlines. The OMEGA EP short-pulse system uses optical parametric chirped-pulse amplification (OPCPA) to generate a high-energy, high-peak-power laser pulse.¹ A seed pulse is stretched and amplified using both parametric amplification and conventional amplification in the front-end laser system and large-aperture beamline. At its fully amplified level, the beam is stretched to approximately 1-ns duration and amplified to multiple kilojoules. It then propagates into a grating compression chamber (GCC), a large vacuum chamber containing a four-grating pulse compression system, where it is compressed to between 700 fs (best compression) and 100 ps.

Figure 124.31 shows a diagram of one of the compressors in the OMEGA EP short-pulse system, indicating the location of key diagnostics relative to the beam for the on-shot focal-spot measurement. After undergoing amplification, pulse recompression, and wavefront correction, the beam propagates to a leaky diagnostic mirror within the GCC. A small percentage of the beam (~0.5%) transmits through the diagnostic mirror and is provided to a suite of laser diagnostics—the short-pulse diagnostics package (SPDP). The main beam, i.e., the portion reflected from the diagnostic mirror, is transported to the target chamber via a series of mirrors and focused by an $f/2$ off-axis parabola (OAP).

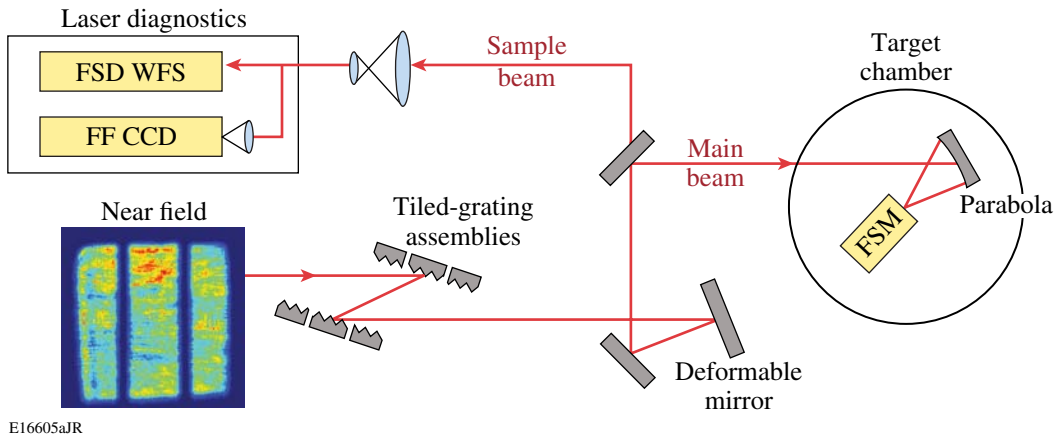


Figure 124.31

A diagram of the OMEGA EP short-pulse system indicates the location of key diagnostics relative to the beam for on-shot focal-spot measurement. After undergoing amplification, pulse recompression, and wavefront correction, the main OMEGA EP beam propagates to a leaky diagnostic mirror within the vacuum grating compression chamber. A small percentage of the beam (~0.5%) leaks through the diagnostic mirror and is provided to a suite of laser diagnostics, including the focal-spot diagnostic wavefront sensor (FSD WFS) and a far-field camera (FF CCD). The main beam is transported to the target chamber and focused at target chamber center by an $f/2$ off-axis parabola. For low-energy qualification shots, a focal-spot microscope (FSM) was inserted to directly image the focal spot at the target plane.

The FSD is a high-resolution wavefront sensor installed in the SPDP,⁸ denoted FSD WFS in Fig. 124.31. The FSD wavefront sensor provides a full measurement of the (temporally and spectrally averaged) near-field amplitude and phase of the sample beam that can be numerically propagated to calculate the focal-spot fluence distribution.⁹

In close proximity to the FSD is a 16-bit, cooled, far-field charge-coupled-device (CCD) camera (FF CCD in Fig. 124.31) that records the focal-spot fluence distribution of the sample beam. Both the FSD and this FF CCD acquire data on every OMEGA EP shot. In addition, for some low-energy shots, a focal-spot microscope (FSM) has been inserted into the target chamber to directly image the focal spot at the target plane

onto another 16-bit cooled CCD camera.² These two cameras provide the direct focal-spot intensity measurements that are used as inputs to the phase-retrieval algorithms discussed in this article. The image data from both of these CCD's also provide a check of the quality of the phase-retrieval results.

One of the challenges of this approach to measuring the target-plane focal spot is the indirect nature of the wavefront measurement. The measurement requires a careful calibration of the FSD wavefront sensor to “transfer” (or reference) the wavefront of the sample beam measured in the SPDP to the wavefront of the main beam inside the target chamber. The FSD is calibrated using the two-step process described in detail in Ref. 2 and illustrated in Fig. 124.32. A brief description is

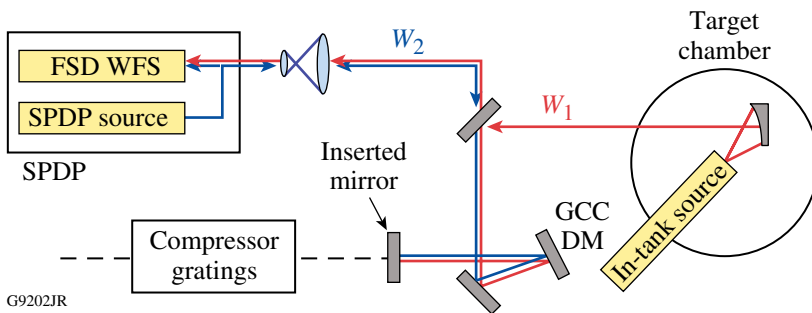


Figure 124.32

The FSD is calibrated using the two-step process illustrated. In the first step, a laser source is inserted into the target chamber with a focus at target chamber center (TCC) and propagated backward to the FSD wavefront sensor via an inserted alignment mirror. The wavefront W_1 is measured in this configuration. Next, a laser source on the SPDP diagnostic table is propagated to the alignment diagnostic mirror (DM) and back to the wavefront sensor, where the wavefront contribution W_2 is measured. The transfer wavefront, essentially $W_1 - W_2$ with pre-measured source wavefront contributions also compensated, is added to on-shot wavefront measurements to obtain the wavefront error of the main beam inside the target chamber.

given here. In the first step, an in-tank laser source is focused to target chamber center (TCC) and propagated backward to the FSD wavefront sensor via an inserted alignment mirror. The wavefront W_1 is measured in this configuration. Next, a laser source in the SPDP is propagated to the alignment mirror and back to the FSD wavefront sensor, where the wavefront contribution W_2 is measured.

A “transfer wavefront” is defined essentially as $W_1 - W_2$. When added to the directly measured sample-beam wavefront, the transfer wavefront removes the wavefront contributions from the diagnostic beam path (between the diagnostic mirror and the FSD sensor) and adds the wavefront contributions from the beam transport to the target (between the diagnostic mirror and the target). Additionally, another correction factor is applied, based on the pre-characterized wavefront contributions of the two sources used for the calibration. The measurement of the wavefront contributions from these two sources is thought to be one of the primary sources of error in the calibration process.

To evaluate the focal-spot measurement, the far-field distribution calculated from the FSD near-field measurement is compared to the directly measured far field from the appropriate CCD camera (either the far-field CCD or the FSM). The agreement is quantified by the cross-correlation

$$C = \frac{\max \left[\iint F_{\text{FSD}}(x - \Delta_x, y - \Delta_y) F_{\text{CCD}}(x, y) dx dy \right]}{\left[\left(\iint F_{\text{FSD}}^2 dx dy \right) \left(\iint F_{\text{CCD}}^2 dx dy \right) \right]^{1/2}}, \quad (1)$$

where F_{FSD} and F_{CCD} are the far-field fluence distributions from the FSD and the camera, respectively. The cross-correlation is normalized in such a way that a perfect agreement results in a value of unity. In practice, a value $C > 0.9$ has been found to normally indicate an acceptable measurement.

Initially, when focal-spot intensity distributions were measured using the FSD wavefront sensor, the results were often quite poor. An example of this is shown in Fig. 124.33, where the focal spot of the sample beam as predicted by the FSD wavefront sensor [Fig. 124.33(a)] and measured by the SPDP far-field CCD camera [Fig. 124.33(b)] are displayed side by side. Both focal spots are plotted as normalized fluence (fluence divided by total energy, in cm^{-2}) over a square 100- μrad field of view. The poor agreement ($C = 0.71$) between these two diagnostics, which measured the same beam in close proximity, illustrates the challenge of the on-shot focal-spot measurement.

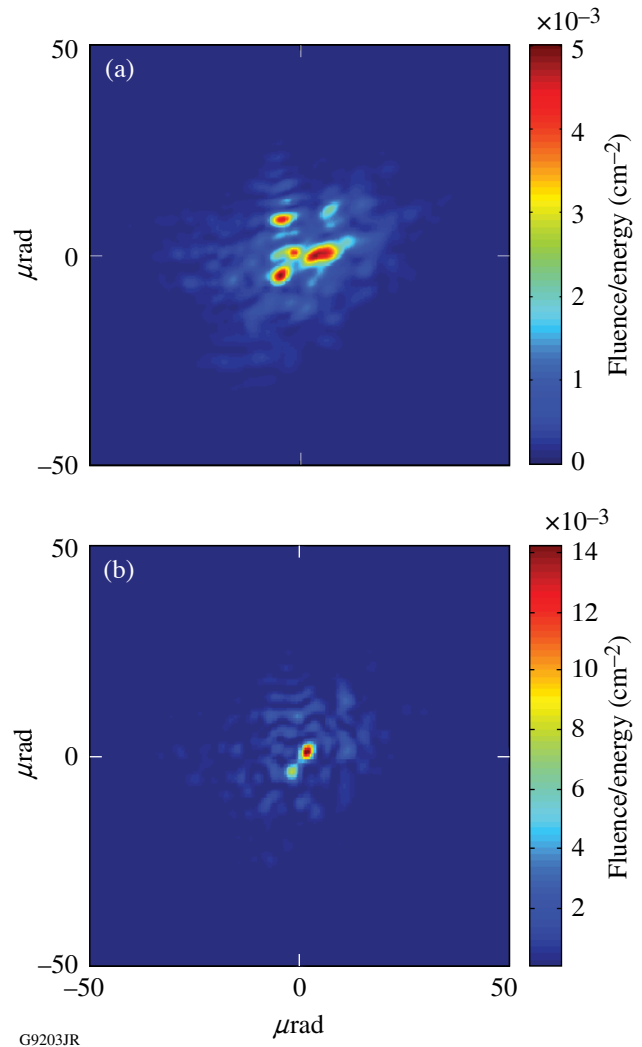


Figure 124.33

An example of an early focal-spot measurement of the sample beam. The color map (a) is a direct measurement using the FF CCD camera, while (b) shows the initial result using the FSD near-field measurement. Both focal spots are expressed in normalized fluence (fluence divided by total energy, in cm^{-2}) and are plotted over a square 100- μrad field of view. The poor agreement by two diagnostics measuring the same beam in close proximity illustrates the challenge of the on-shot focal-spot measurement.

Four problems, discussed in further detail in the next section, have led to poor FSD focal-spot measurements of the type shown in Fig. 124.33. The first problem is a fixed wavefront error between the FSD wavefront measurement and the wavefront incident on the FF CCD. The second is the inability of a Shack–Hartmann wavefront sensor to measure the mean relative wavefront (piston phase) between discrete beam segments that are generated by the tiled-grating compressor. The third problem is chromatic wavefront errors that are undetectable by the Shack–Hartmann wavefront sensor and have a significant

effect on the fidelity of the focal spot. Finally, fixed errors in the FSD calibration process further degrade the quality of the remote focal-spot measurement at the target plane. Each of these problems has been mitigated by retrieving phase information embedded within the focal-spot measurements from the FF CCD and the focal-spot microscope.

Phase-Retrieval Applications and Results

1. Phase Retrieval of SPDP Transfer Wavefront from Multiple Measurements

Whereas the FSD wavefront sensor is in very close proximity to the FF CCD camera, differences between the measured wavefront and the actual wavefront of the focusing beam at the FF CCD must be considered. First, the Shack–Hartmann wavefront measurement is a relative measurement against a reference beam. Wavefront errors in the reference beam translate directly into errors in the measured wavefront. For the FSD, a reference wavefront was acquired using an alignment laser located in the diagnostic package (the SPDP source in Fig. 124.32), reflected from a reference mirror back into the FSD. In principle, this removes the wavefront contributions from the four-element relay lens used to image the pupil onto the FSD wavefront sensor. Wavefront error in the reference laser itself, however, will introduce errors in the reference measurement. These errors were characterized separately and compensated for; however the accumulation of errors can be significant.

In addition, the optics between the FSD and the FF CCD must be considered. Aside from two planar reflective optics, a four-element focusing lens produces a far-field image on the sensor plane of the FF CCD. There is also a window on the camera (wedged and tilted to remove artifacts) as well as various neutral density filters, but these are all in close proximity to the far-field plane and therefore have little effect on the focal spot.

To account for these errors, an SPDP transfer wavefront analogous to the transfer wavefront used to produce target-plane wavefront measurements was defined. The SPDP transfer wavefront is a static quantity (assuming no system configuration changes) that is added to every FSD wavefront sensor measurement to obtain the wavefront at the exit pupil of the FF CCD lens. It was inferred from simultaneous FSD and FF CCD measurements over multiple laser shots using phase retrieval.

The classical iterative transform methods of phase retrieval were attempted on this problem but were generally unsuccessful. These included the so-called Gerchberg–Saxton algorithm³ and various refinements such as the input–output algorithm of Fienup.⁵ These algorithms produced nonphysical results

in which zeros would appear in the near field around which the phase would process continuously over a 2π range. When the phase was unwrapped, branch cuts would be required, leading to unphysical discontinuities in the wavefront. The problem appears to have been caused by a combination of polychromatic effects and a small incoherent background in the far-field measurements.

To improve focal-spot predictions, a modal phase-retrieval method that has proven to be successful and robust was employed. It is based closely on a gradient-search algorithm reported by Fienup.⁶ A block diagram of the algorithm is shown in Fig. 124.34. The inputs to the algorithm are the measured near-field intensity and wavefront from the FSD wavefront sensor and the measured focal-spot intensity from the FF CCD camera. The algorithm produces a single low-order SPDP transfer wavefront expressed as a two-dimensional Legendre polynomial, as well as the piston phases in the left and right beam segments (as discussed in the following subsection). Multiple shots are evaluated simultaneously to improve accuracy.

The algorithm proceeds from the near-field intensities and wavefronts measured by the FSD wavefront sensor. The current SPDP transfer wavefront is added to all the wavefronts, and the wavefront offsets are added to the outer tiles of the appropriate wavefronts. The far-field fluence distributions are then calculated from the near-field intensity and the corrected wavefront. These are compared to the measured values to generate a merit function, which is based on the root-sum-square (rss) error,

$$\text{rss error} = \left\{ \iint [F_{\text{FSD}}(x,y) - F_{\text{CCD}}(x,y)]^2 dx dy \right\}^{1/2}. \quad (2)$$

The rss errors from all shots are summed to produce an overall merit function that takes into account errors over the entire data set.

A nonlinear optimization algorithm is employed to modify the optimization parameters for the subsequent iterations. In most cases, a quasi-Newton, Broyden–Fletcher–Goldfarb–Shanno (BFGS) algorithm¹⁰ is used, which is a true gradient-search algorithm. Alternatively, to attempt to find a global solution, a simulated annealing algorithm has initially been employed¹¹ to identify the approximate solution, followed by a gradient search algorithm to obtain a more-accurate estimate. The algorithm continues until the merit function is minimized.

This modal phase-retrieval algorithm was used to measure the SPDP transfer wavefront for the FSD sensors in both the upper and lower compressors on OMEGA EP. A fourth-order

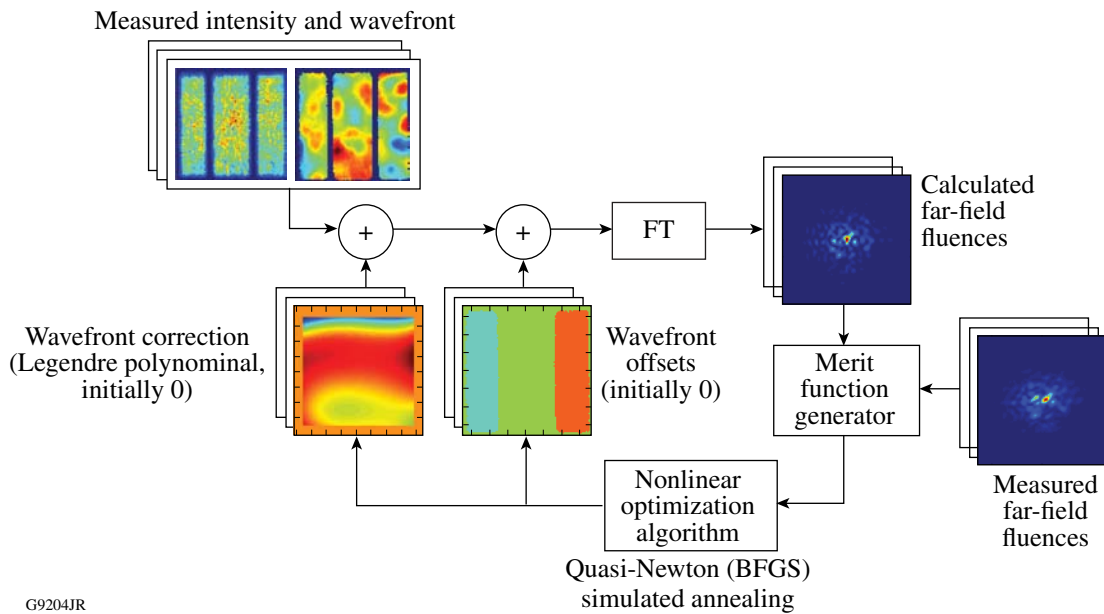


Figure 124.34

A block diagram illustrating the modal phase-retrieval algorithm used to measure the SPDP transfer wavefront. The inputs to the algorithm are the measured near-field intensity and wavefront from the FSD wavefront sensor and the measured focal-spot intensity from the FF CCD camera. Multiple shots are evaluated simultaneously to improve accuracy. The far-field fluence distributions are calculated from the measured near fields using Fourier transforms (FT) and compared to the measured values to generate a merit function. This merit function is minimized by using a nonlinear optimization algorithm to vary the SPDP transfer wavefront (estimated as a Legendre polynomial) and the average phase in the outer beam segments for each shot. The SPDP transfer wavefront and average phases are added to the original measurements in the subsequent iteration. The algorithm continues until the merit function is minimized.

Legendre polynomial was used to estimate the SPDP transfer wavefront in the phase-retrieval algorithm. The result for the upper compressor, retrieved from approximately 20 low-energy shots, is displayed in Fig. 124.35. The SPDP transfer wavefront is added to all FSD wavefront measurements.

To evaluate the improvement gained by use of the SPDP transfer wavefront measurement, focal-spot measurements at the SPDP were performed with a narrowband laser¹² propagated through the beamline and through the compressor to the diagnostic table. The outer segments of the beam were obscured in order to illuminate only the central grating tile in the grating compressor (see the next section). Therefore, the pupil had a single rectangular area and the spectral width was essentially monochromatic compared to the 8-nm OPCPA spectrum.

Figure 124.36 shows how the application of the SPDP transfer wavefront improves the focal-spot prediction in this single-segment, quasi-monochromatic scenario. The cross-correlation between the FSD-generated far-field distribution and the measured intensity from the FF CCD is shown for six different shots. For each shot, the correlation before (blue diamonds) and after (red squares) applying the SPDP transfer

wavefront correction is shown. The correction was seen to improve the focal-spot cross-correlation from an average of 0.944 to 0.990, and the standard deviation was reduced from 0.021 to 0.003.

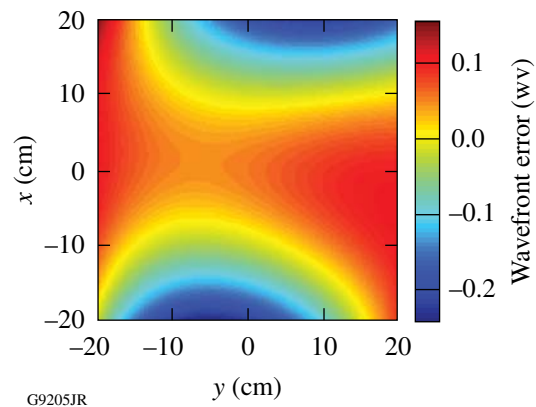
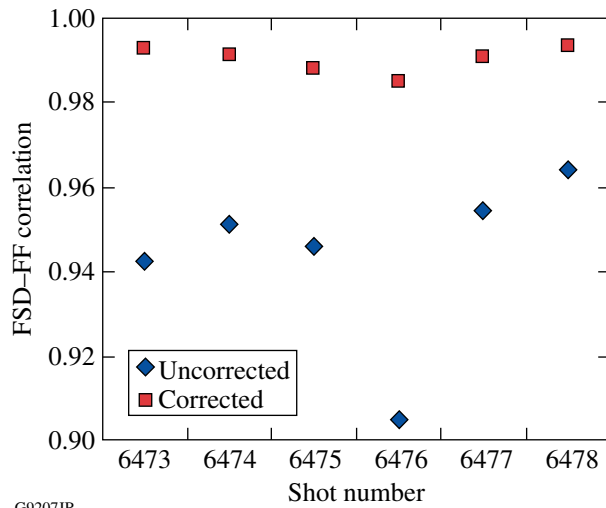


Figure 124.35

The SPDP transfer wavefront for the upper compressor. This wavefront was retrieved from a large number of shot measurements using the modal phase-retrieval algorithm with FSD wavefront sensor and FF CCD image data. The SPDP transfer wavefront was added to all FSD wavefront measurements to improve agreement with the FF CCD images.



G9207JR

Figure 124.36

The effect of the SPDP transfer wavefront on the quality of the FSD measurement is shown for the single-tile monochromatic beam. The cross-correlation between the FSD-generated far-field distribution and the measured intensity from the FF CCD is shown for six different shots. For each shot, the correlation before (blue diamonds) and after (red squares) applying the SPDP transfer wavefront correction is shown. The correction was seen to improve the correlation from an average of 0.944 to 0.990, and the standard deviation was reduced from 0.021 to 0.003.

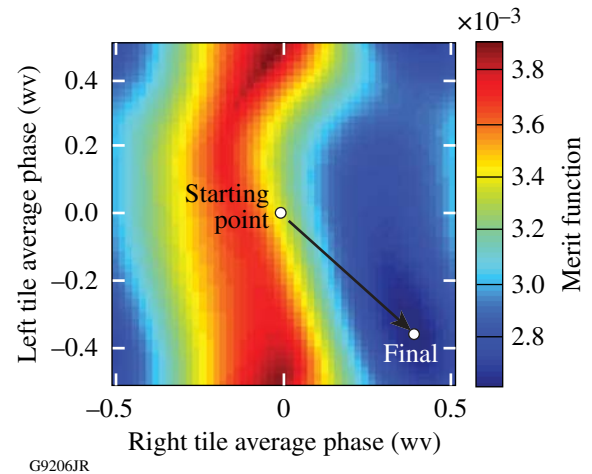
2. Single-Shot Retrieval of Average Relative Wavefront in Outer-Beam Segments

The pulse-compression system in OMEGA EP uses four tiled-grating assemblies, each comprised of three closely spaced, interferometrically aligned grating segments, to produce an effective meter-scale grating.¹³ To prevent damage associated with high-energy illumination of the edges of the grating tiles, the short-pulse beams in OMEGA EP are apodized in the region of the gaps between tiles. This produces the three-segment beam profile shown in the inset of Fig. 124.31 and further complicates the focal-spot measurement.

The FSD wavefront sensor, being a Shack–Hartmann type, fundamentally measures the local wavefront slopes across the pupil. Spatial-integration algorithms are used to reconstruct the wavefront,¹⁴ but there is an inherent uncertainty in the average wavefront in each discrete segment of the beam. This is normally not an important issue when measuring a beam with a single continuous pupil area because the overall piston phase is unimportant. In the case of OMEGA EP's three-segment beams, however, this limitation results in an inherent uncertainty in the relative average wavefront between the adjacent segments. Consequently, there is a differential piston artifact in the measurement that can significantly impact the focal-spot

prediction. Fortunately, this uncertainty can again be resolved by retrieving the relative average phase in the outer-beam segments from the FF CCD image.

Figure 124.37 shows a typical plot of the rss error merit function in Eq. (2) versus the relative piston phase (in waves) in the two outer beam segments. To retrieve the average relative wavefront in the outer segments, one searches for the minimum of the merit function in this plot. Note that the merit function has periodic boundary conditions, with one full period shown. A grid search followed by a quasi-Newton gradient-minimization search has proven to be a reliable means of finding the optimum solution for all shots encountered.



G9206JR

Figure 124.37

A typical plot of the merit function versus the piston wavefront in the outer beam segments. To retrieve the average relative wavefront in the outer segments, one searches for the minimum of the merit function in this plot. Note that the merit function has periodic boundary conditions, with one full period shown.

To test the retrieval of the relative phase in the outer beam segments, the experiment with the narrowband laser described in the previous subsection was repeated, illuminating multiple beam segments. The obscuration in the beam was removed to propagate first two, then all three beam segments through the compressor. The results of this experiment are summarized in Fig. 124.38. The plot shows the average and range of cross-correlations over six shots, illuminating one, two, and three beam segments. For each configuration, the red squares and error bars were generated with the outer-segment piston phase retrieved, while the blue diamonds were generated without performing that step (by optimizing wavefront continuity across beam segments). The error bars represent the minimum and maximum values over the six measurements. The SPDP transfer wavefront

was applied for all shots. Note that the corrected measurements remained at a high value (>0.97 for all measurements) for all the shots in this monochromatic case. Conversely, when the average relative phase in the outer segments was not retrieved, the cross-correlation and variability became progressively worse as more beam segments were introduced.

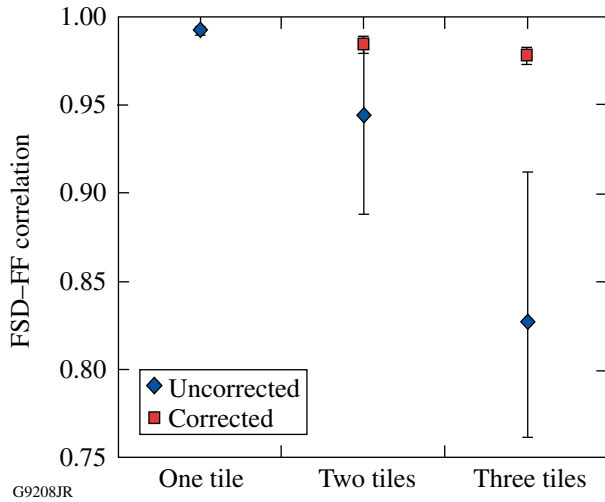


Figure 124.38

Monochromatically illuminating multiple tiles, the effect of the average relative wavefront between the beam segments is illustrated. The plot shows the average and range of correlations over six shots illuminating one, two, and three tiles. For each configuration, the correlations with (red squares) and without (blue diamonds) solving for the relative wavefront in the outer segments are shown, and the error bars represent the minimum and maximum values over six measurements. The SPDP transfer wavefront was applied for all shots. The corrected measurements remained at a high value (>0.97 for all measurements) for all three beam segments for this monochromatic case.

3. Estimating Effects of Polychromatism on Focal-Spot Structure

Despite the relatively narrow spectral widths involved (~ 8 nm unamplified and ~ 3.3 nm amplified), the short-pulse system on OMEGA EP can exhibit strong chromatic aberrations. The dominant chromatic aberration observed thus far has been attributed to residual angular dispersion, which can arise either in the stretcher or in the pulse compressor, and produces a wavelength-dependent tilt term. The polychromatism has been observed to significantly affect the far field, as demonstrated in Fig. 124.39. The focal-spot distribution in Fig. 124.39(a) shows the predicted focal-spot fluence based on monochromatic propagation of the measured near field of the FSD. The actual focal spot from the full 8-nm OPCPA bandwidth as measured by the FF CCD is shown in Fig. 124.39(b). The polychromatism is evident in the reduced sharpness of the focal spot and the peak fluence, which is lower by a factor of ~ 2 . The blurring

of the focal spot is typically along a preferential axis, which is indicative of a wavelength-dependent tilt term as expected from residual angular dispersion. Note that the blurring of the sort shown was not observed in the narrowband experiment described in the previous subsections and, consequently, cannot be explained by the modulation transfer function of the FF CCD lens.

The polychromatic blurring cannot be explained simply by the spectral content of the beam without a chromatically vary-

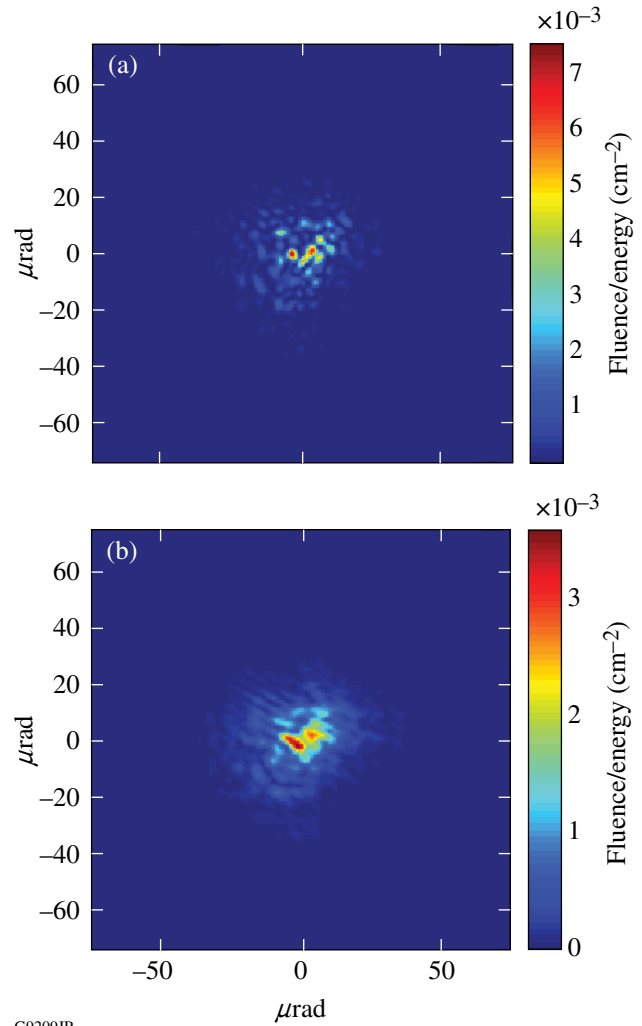


Figure 124.39

Polychromatism has been observed to blur the fine features of the far-field intensity pattern when the OPCPA beam is measured. The focal-spot distribution in (a) shows the predicted focal-spot fluence based on monochromatic propagation of the measured near field of the FSD. The actual focal spot from the full 8-nm OPCPA bandwidth as measured by the FF CCD is shown in (b). The polychromatism degrades the sharpness of the focal spot and reduces the peak fluence by approximately a factor of 2 in this case.

ing component of the wavefront. In other words, if the far field is polychromatically generated from the measured wavefront, by incoherently summing the far fields propagated from the near field using a range of wavelengths, the effect on the predicted focal spot is insignificant. The type of blurring we have observed would be seen over this narrow spectral width only if there was a significant variation in the wavefront (particularly tilt) over the spectral range.

Because the FSD wavefront sensor is not spectrally sensitive, it cannot provide information on the chromatic aberrations and, instead, produces a spectrally averaged wavefront measurement. To estimate the effects on polychromatism,

however, a Fourier analysis has been developed (Fig. 124.40). In the first step of the process, the focal-spot intensities measured by the FF CCD and monochromatically calculated from the FSD wavefront sensor are both Fourier transformed. A polychromatic transfer function is then estimated by taking the ratio of the Fourier transforms, smoothing, and fitting an elliptical Gaussian function. In the third step, the polychromatic transfer function is inverse Fourier transformed to generate a polychromatic impulse response. Finally, the original monochromatically calculated FSD focal-spot measurement is convolved with the polychromatic impulse response to obtain a focal-spot fluence distribution that includes an estimate for polychromatic effects.

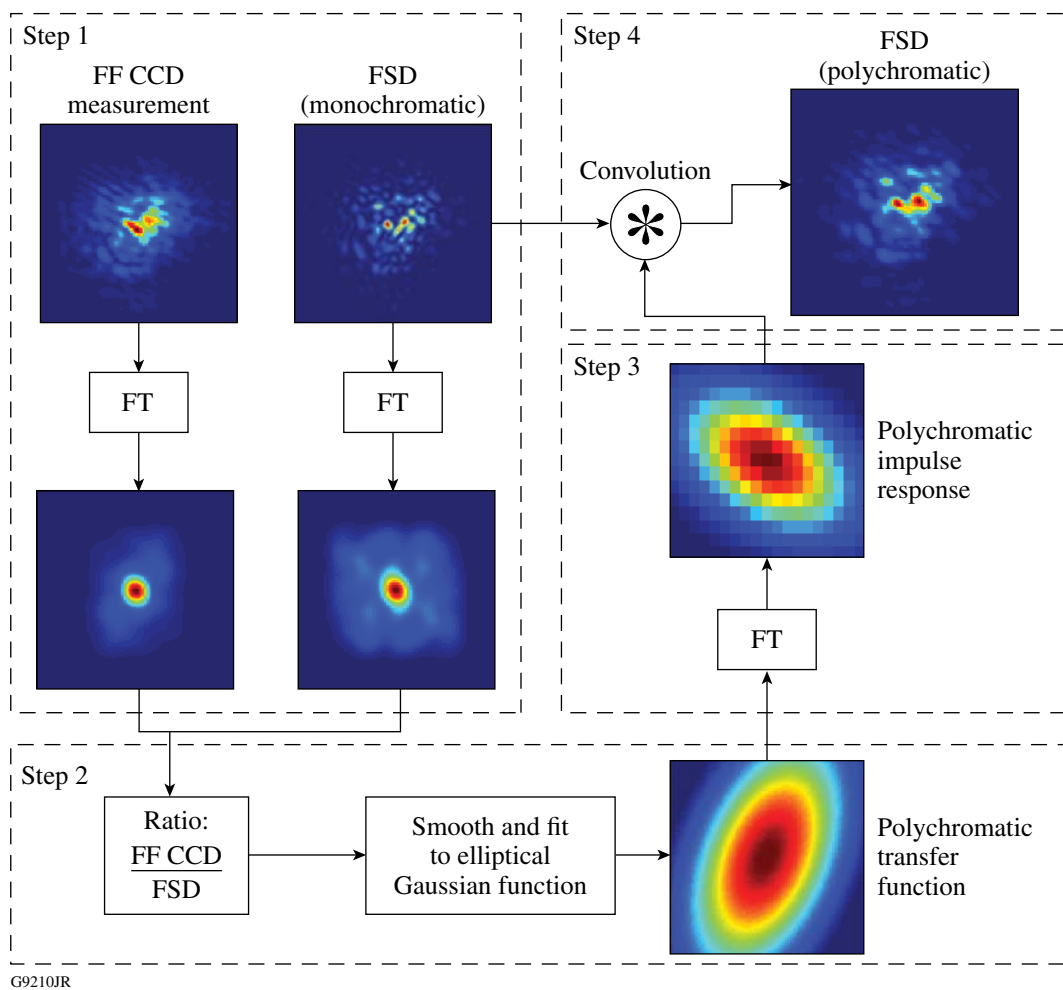


Figure 124.40

The four-step algorithm for estimating the effects of polychromatic blurring. In Step 1 of the process, the focal-spot intensities measured by the FF CCD and monochromatically calculated from the FSD wavefront sensor are Fourier transformed. In Step 2, the polychromatic transfer function is estimated by taking the ratio of the Fourier transforms from Step 1, smoothing, and fitting to an elliptical Gaussian function. The polychromatic transfer function is then inverse Fourier transformed to generate the polychromatic impulse response in Step 3. Finally, in Step 4 the original monochromatically calculated FSD focal-spot measurement is convolved with the polychromatic impulse response to obtain a focal-spot fluence distribution that includes an estimate for polychromatic effects.

We emphasize that this system provides only an *estimate* for polychromatism and is, in fact, only appropriate if residual angular dispersion is the dominant mechanism. Other sources of polychromatic error will affect the focal spot in a more-complex way than can be modeled with an intensity impulse response. For example, there is longitudinal chromatic aberration in the spatial-filter lenses in the beamline. This, in principle, is corrected using a diffractive optical element in the injection lens,¹⁵ although its performance in the system has not yet been experimentally verified. There is also a chromatic contribution associated with the spatial chirp on the beam at the second and third gratings in the compressor. The surface errors in those tiled-grating assemblies produce a wavefront error that has a wavelength-dependent horizontal displacement on the beam. These effects, which are not addressed with this method, will be a subject for further development.

4. Phase Retrieval to Improve FSD Calibration

The final issue that was addressed was the appearance of fixed errors in the calibration of the FSD wavefront sensor. It is believed that the primary source of error in the FSD calibration process is contributed by the two reference sources used in the calibration measurements. These were characterized offline and compensated as part of the calibration process, but changes in the wavefront performance of the laser sources and measurement errors both contribute to calibration errors. There also exist optical elements that are inserted into the beam path for the calibration process but removed under normal operating conditions, which could contribute fixed wavefront errors. Finally, because the FSD wavefront is effectively “transferred” to the FF CCD to use the earlier phase-retrieval techniques, any wavefront error in the far-field lens is effectively added to the

wavefront measurement. This wavefront error in the far-field lens must be removed via the transfer wavefront, introducing another error in the FSD calibration.

These fixed calibration errors were inferred using the modal phase-retrieval process described above, but this time using image data from the FSM from a number of low-energy shot campaigns. In each campaign, a series of shots was acquired with the OPCPA beam propagating through both the passive beamline and the compressor. The deformable mirror (see Fig. 124.31) was used to introduce phase diversity in the shot sequence to improve the phase-retrieval results. The FSM was inserted into the target chamber and aligned to image the focal spot at the center of the target chamber. For each shot, the techniques described earlier were used to correct the FSD wavefront measurement and to retrieve the polychromatic impulse response to obtain agreement between the FSD and the SPDP far-field CCD. The transfer wavefront measured during FSD calibration prior to each shot campaign was then applied to obtain an initial estimate for the wavefront converging to the target plane. A transfer-wavefront correction was then retrieved by using a variant of the modal phase-retrieval process described above using FSD and FSM data as inputs from a large number of shots. One key difference from the earlier modal phase-retrieval application is that the average phase in the outer beam segments was not varied when retrieving the transfer wavefront correction. These parameters were determined via phase retrieval using the FF CCD image and are therefore fixed at this stage. Furthermore, the transfer-wavefront correction is expected to be continuous over the beam aperture.

The resulting transfer-wavefront corrections (Fig. 124.41) have been evaluated for three different target configurations:

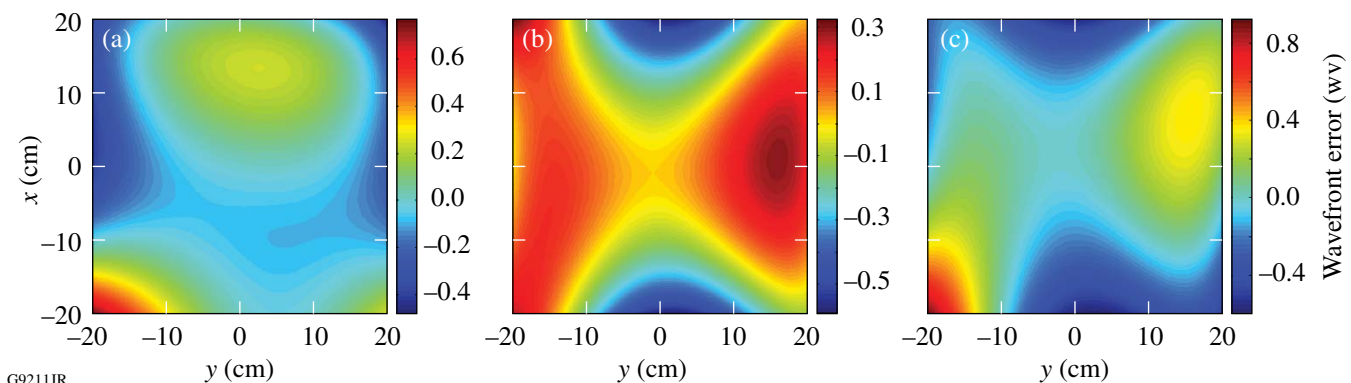


Figure 124.41

Transfer-wavefront corrections are shown for (a) upper compressor to the OMEGA EP backlighter, (b) lower compressor to the OMEGA EP sidelighter, and (c) upper compressor to the OMEGA backlighter. These were retrieved from low-energy shot campaigns using FSM measurements in conjunction with FSD wavefront measurements using a phase-retrieval process similar to that shown in Fig. 124.34. These correction wavefronts were applied to all FSD calibration measurements obtained using the technique in Fig. 124.32.

(a) the upper compressor propagating to the backlighter OAP in the OMEGA EP target chamber, (b) the lower compressor to the OMEGA EP sidelighter OAP, and (c) the upper compressor to the OMEGA target chamber OAP. As before, the correction wavefront is estimated by a fourth-order Legendre polynomial. It is important to also note that the transfer-wavefront correction has been confirmed to be reasonably stable over multiple shot campaigns conducted over approximately one year. The transfer-wavefront correction measurements will be performed periodically in the future to confirm its stability or adapt to changes in the system performance. Variability observed in the transfer-wavefront correction is used to estimate the uncertainty of the target-plane measurement.

Note that special consideration must be made for defocus when measuring the transfer-wavefront correction. In shot campaigns in general, defocus within the target chamber is an unknown parameter, affected by both the positioning of the OAP and the target itself. Furthermore, during the FSD calibration, longitudinal errors in the placement of the in-tank source will lead to a defocus error. Finally, during the FSM shot campaigns, errors in alignment of the FSM to the OAP focal plane led to defocus in the measured focal spot that introduced a defocus term into the transfer-wavefront correction via the phase-retrieval process. To deal with the defocus uncertainty, a through-focus scan was conducted as part of each FSM shot campaign to measure the FSM defocus relative to the OAP. As a result, defocus was effectively removed from the transfer-wavefront correction.

Results

To evaluate the performance of the phase-retrieval techniques described in the previous section, they have been applied to a number of on-shot focal-spot measurements and compared to available direct focal-spot measurements. First, the accuracy of the sample-beam focal-spot measurement is considered by comparing the FSD result with the FF CCD.

As an example of the impact of these phase-retrieval improvements, the sample-beam focal-spot measurement shown in Fig. 124.33 is again considered in Fig. 124.42. The direct focal-spot measurement from the FF CCD camera is repeated in Fig. 124.42(a). The far-field fluence calculated using near-field measurements by the FSD wavefront sensor, including correction for the SPDP transfer wavefront, the average phase in the outer beam segments, and estimation of polychromatic effects, is shown in Fig. 124.42(b). The corrected FSD prediction shows a much-better qualitative correspondence with the direct FF CCD measurement than the uncorrected

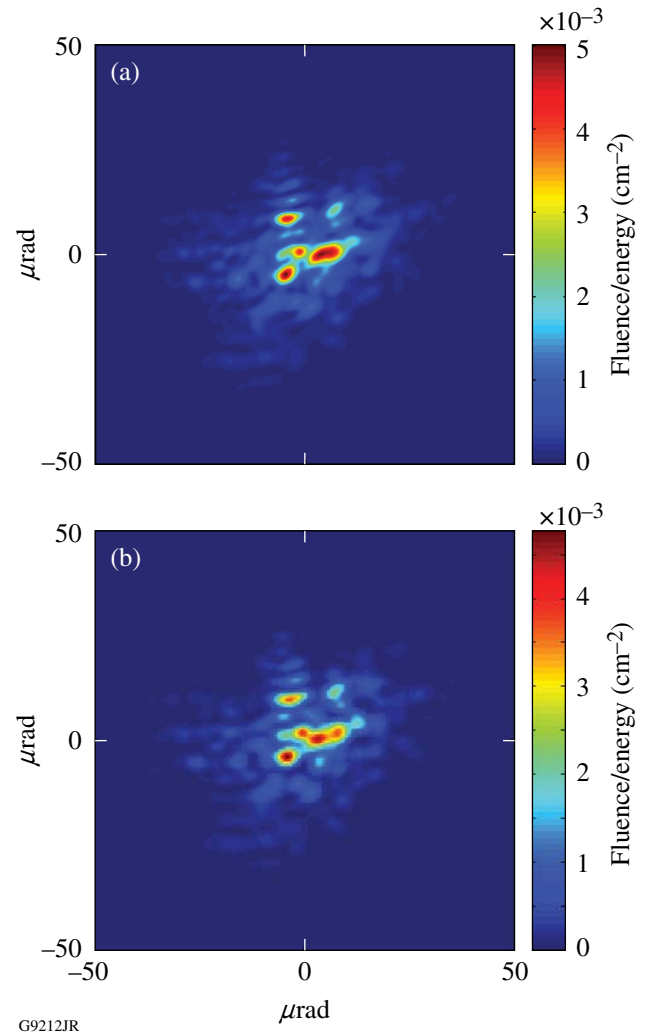


Figure 124.42

The sample-beam focal-spot measurement shown in Fig. 124.33 is repeated here using the phase-retrieval techniques described. (a) The direct focal-spot measurement from the FF CCD camera. (b) The far-field fluence calculated using near-field measurements by the FSD wavefront sensor, including correction for the SPDP transfer wavefront, the average phase in the outer beam segments, and estimation of polychromatic effects. The two focal-spot agreements match much better qualitatively than the uncorrected case shown in Fig. 124.33. The quantitative agreement is also much better, with the cross-correlation improving from 0.71 to 0.95.

case shown in Fig. 124.33. The quantitative agreement is also much better, with the cross-correlation improving from 0.71 to 0.95. The prediction of the peak intensity has also improved to within 10% accuracy, compared to the initial estimate that overpredicted the peak intensity by $>2\times$.

The improved focal-spot measurement of the sample beam has also proven to be very reliable and stable over a large number of shots. To illustrate this, the cross-correlation has been

evaluated over a population of 175 low-energy shots, which spanned approximately 18 months. Figure 124.43 is a histogram showing the frequency of cross-correlations within intervals of 0.01. The filled bars correspond to the corrected measurements, i.e., when the SPDP transfer wavefront (assumed static over the entire time period), the average phase in the outer segments, and the effects of polychromatism have all been applied. The white bars give the cross-correlation values without these corrections. There is a clear improvement in performance after applying the phase-retrieved corrections, with the mean cross-correlation increasing from 0.826 to 0.965. The consistency of the measurement was also much improved, with the standard deviation of the cross-correlation reduced from 0.044 to 0.010.

Amplifying the beam did not adversely affect the quality of focal-spot measurement, as demonstrated in the histogram in Fig. 124.44. The cross-correlation between the FSD and the FF CCD was calculated after applying all the phase-retrieved corrections. The white bars represent the rate of occurrence for each cross-correlation value for all high-energy shots over a recent 6-month period, representing a population of 220 samples. The filled bars represent the same data for all the low-energy FSM campaign shots evaluated in Fig. 124.43. The statistics are quite similar: the low-energy and high-energy mean cross-correlations are 0.965 and 0.967, respectively, which are effectively identical considering the standard deviations (0.010 and 0.009, respectively).

To achieve consistent performance over the wide range of shot conditions included in this study, it was necessary to account for changes in the system configuration in the diagnostic package. Specifically, wavefront contributions from neutral-density filters inserted in front of the FSD wavefront sensor can be significant. The wavefront introduced by each of these filters is characterized *in situ* in an offline measurement and removed from each on-shot wavefront measurement as appropriate.

The true test of the FSD measurement accuracy is its ability to accurately measure the focal spot remotely in the target chamber. The cross-correlation between the FSD focal-spot prediction and the direct measurement using the FSM was evaluated for all the low-energy shot campaigns described earlier. A histogram of the cross-correlation data is presented in Fig. 124.45. The histogram in Fig. 124.45(a) shows the effect of the phase-retrieval corrections on the focal-spot measurement. The white bars give the distribution of cross-correlation values between the FSD and direct FSM measurements when no phase-retrieval corrections have been applied. The filled bars, which show the corresponding cross-correlations with the addition of the phase-retrieval corrections, demonstrate the improvement in overall quality and reliability. The histogram in Fig. 124.45(b) compares the quality of the measurement of the sample beam at the SPDP table (filled bars) and the main beam in the target chamber (white bars). All phase-retrieval corrections were applied for this data. The measurement accuracy

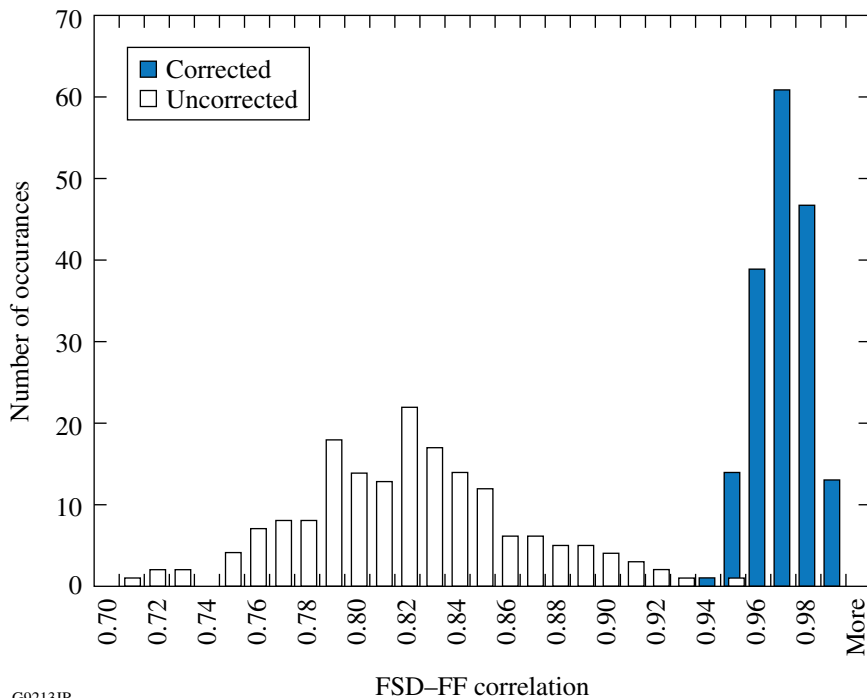


Figure 124.43

A histogram of the cross-correlations between the FSD and FF CCD measurements. The filled bars give the values when the SPDP transfer wavefront, the average phase in the outer segments, and the effects of polychromatism have all been retrieved. The white bars give the values without these corrections. The histograms consist of low-energy shots with the full OPCPA bandwidth, acquired during the shot campaigns to the FSM, which spanned approximately 18 months.

G9213JR

is slightly worse in the target chamber, likely because of the variability in the transfer-wavefront correction from campaign to campaign; however, the measured cross-correlation reliably exceeds 0.9 with >95% probability.

Unfortunately, confirming an accurate measurement of the focal-spot measurement at high energy is currently not possible since a high-energy shot cannot be sufficiently attenuated to the level required for the focal-spot microscope. Other target

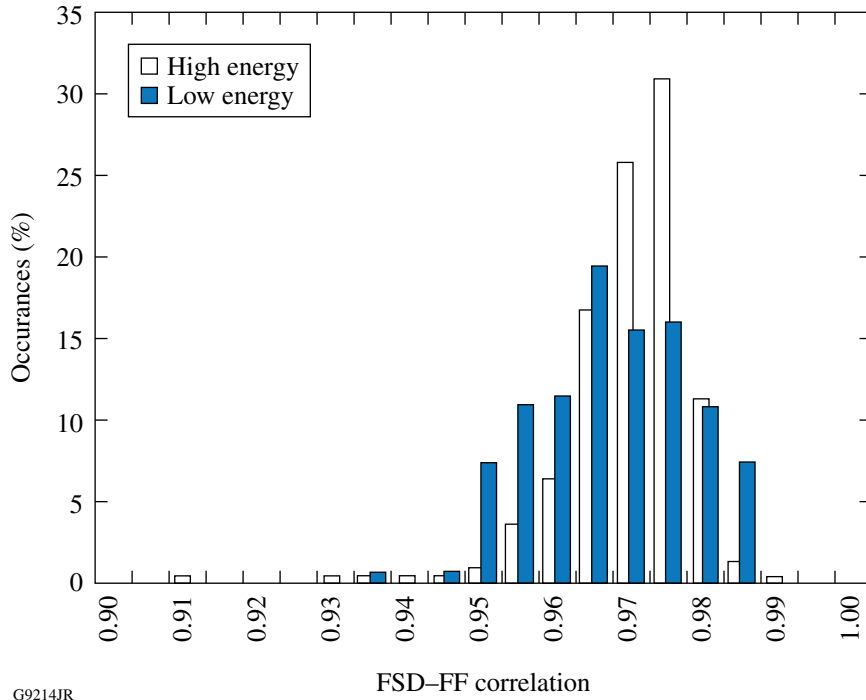
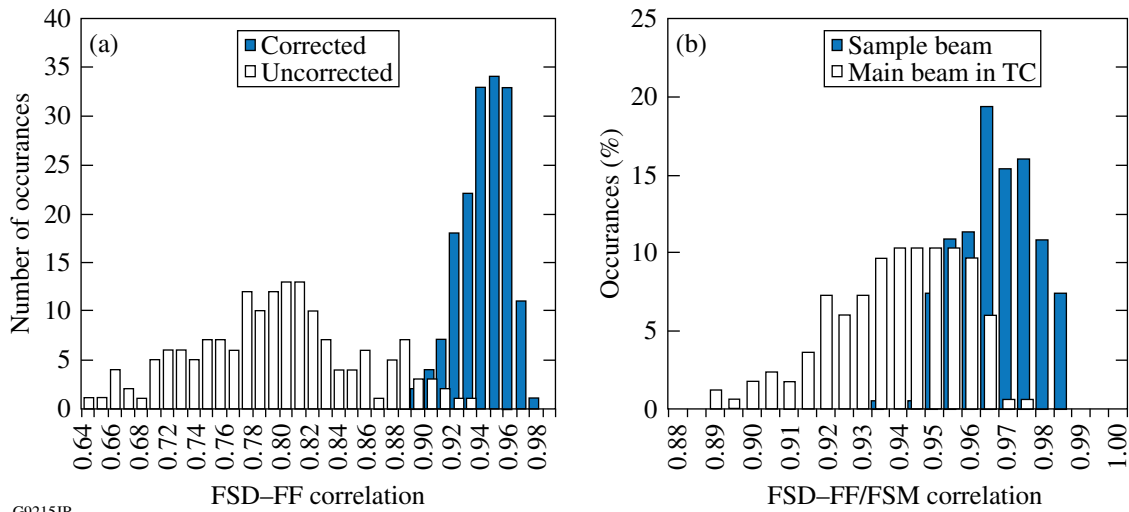


Figure 124.44

A histogram demonstrating that the consistently high sample-beam focal-spot measurement accuracy is maintained for high-energy OMEGA EP shots. The white bars represent the rate of occurrence for each cross-correlation between the FSD and the far-field CCD for all high-energy shots over a recent 6-month period. The filled bars represent the same data for all the low-energy FSM campaign shots, as also plotted in Fig. 124.43. The values are calculated with all phase-retrieved corrections.

G9214JR



G9215JR

Figure 124.45

The accuracy of the focal-spot measurement of the main beam in the target chamber is evaluated in the histograms. (a) The effect of the phase-retrieval corrections on the focal-spot measurement. The white bars give the distribution of cross-correlation values between the FSD and direct FSM measurements when no phase-retrieval corrections have been applied. The filled bars, which show the corresponding cross-correlations with the addition of the phase-retrieval corrections, demonstrate the improvement in overall quality and reliability. (b) A comparison of the quality of the measurement of the sample beam at the SPDP table (filled bars) and the main beam in the target chamber (TC) (white bars). All phase-retrieval corrections were applied for this data. The measurement accuracy is slightly worse in the target chamber, likely because of the variability in the transfer-wavefront correction from campaign to campaign.

diagnostics, such as x-ray pinhole cameras, have poor resolution and do not provide a true measure of focal-spot fluence because of the complexities of the target interaction. For this reason we must rely on the low-energy results to assess the performance of the focal-spot measurement at the target plane. To maximize the confidence in the measurement at high energy, we have accounted for all changes to the system configuration for these shots, e.g., attenuators inserted before the SPDP. The wavefront errors contributed by all configuration changes were measured individually offline. On high-energy shots, the wavefront contributed by each inserted aberrator was removed from the measurement to correct for potential measurement error.

Conclusions

Phase retrieval has been a useful technique for obtaining consistently high quality remote predictions of the on-shot target-plane fluence distribution. A modal phase-retrieval technique based on a gradient-search algorithm was used to retrieve correction wavefronts for the FSD that produce focal spots in consistent agreement with direct measurements of the sample beam and main beam at the target plane for low energy. Phase retrieval was also used to provide phase information beyond the capabilities of the Shack–Hartmann wavefront sensor. The relative piston phase between the discrete segments of the OMEGA EP beam was retrieved on each shot using an image of the sample-beam focal spot. Further, an estimate of the effects of chromatic aberration on the focal-spot fluence distribution was obtained from the sample-beam focal-spot image using a Fourier technique.

Analysis of a large population of on-shot measurements has proven the focal-spot measurement to be reliable. Cross-correlation with direct focal-spot fluence measurements using the far-field CCD and the FSM consistently exceeded 90%, although no direct measurement at the target plane at high energy is currently possible.

As a result of the improved accuracy of the on-shot focal-spot measurement, scientists conducting experiments on the OMEGA EP short-pulse beamlines now have critical information about on-target intensity distributions. This information is proving to be very useful and is enhancing the value of OMEGA EP experiments for furthering our understanding of ICF physics.

ACKNOWLEDGMENT

The authors thank Prof. James Fienup for insightful discussions on phase-retrieval algorithms. This work was supported by the U.S. Department of Energy Office of Inertial Confinement Fusion under Cooperative Agreement No. DE-FC52-08NA28302, the University of Rochester, and the New York State Energy Research and Development Authority. The support of DOE does not constitute an endorsement by DOE of the views expressed in this article.

REFERENCES

1. J. H. Kelly, L. J. Waxer, V. Bagnoud, I. A. Begishev, J. Bromage, B. E. Kruschwitz, T. J. Kessler, S. J. Loucks, D. N. Maywar, R. L. McCrory, D. D. Meyerhofer, S. F. B. Morse, J. B. Oliver, A. L. Rigatti, A. W. Schmid, C. Stoeckl, S. Dalton, L. Folnsbee, M. J. Guardalben, R. Jungquist, J. Puth, M. J. Shoup III, D. Weiner, and J. D. Zuegel, *J. Phys. IV France* **133**, 75 (2006).
2. J. Bromage, S.-W. Bahk, D. Irwin, J. Kwiatkowski, A. Pruyne, M. Millecchia, M. Moore, and J. D. Zuegel, *Opt. Express* **16**, 16,561 (2008).
3. R. W. Gerchberg and W. O. Saxton, *Optik* **35**, 237 (1972).
4. R. A. Gonsalves, *J. Opt. Soc. Am.* **66**, 961 (1976).
5. J. R. Fienup, *Appl. Opt.* **21**, 2758 (1982).
6. J. R. Fienup, *Appl. Opt.* **32**, 1737 (1993).
7. S.-W. Bahk, J. Bromage, I. A. Begishev, C. Mileham, C. Stoeckl, M. Storm, and J. D. Zuegel, *Appl. Opt.* **47**, 4589 (2008).
8. Imagine Optic, 91400 Orsay, France (<http://www.imagine-optic.com/>).
9. J. W. Goodman, *Introduction to Fourier Optics* (McGraw-Hill, New York, 1968).
10. C. G. Broyden, *IMA J. Appl. Math.* **6**, 76 (1970); R. Fletcher, *Comput. J.* **13**, 317 (1970); D. Goldfarb, *Math. Comput.* **24**, 23 (1970); D. F. Shanno, *Math. Comput.* **24**, 647 (1970).
11. S. Kirkpatrick, C. D. Gelatt, Jr., and M. P. Vecchi, *Science* **220**, 671 (1983).
12. A Q-switched diode-pumped Nd:YLF laser from Photonics Industries was used, model DS10-1053; Photonics Industries International, Inc., Bohemia, NY 11716 (<http://www.photonix.com>).
13. J. Qiao, A. Kalb, T. Nguyen, J. Bunkenburg, D. Canning, and J. H. Kelly, *Opt. Lett.* **33**, 1684 (2008).
14. cf. D. L. Fried, *J. Opt. Soc. Am.* **67**, 370 (1977); this work used the method described in S.-W. Bahk, *Opt. Lett.* **33**, 1321 (2008).
15. T. J. Kessler, H. Huang, and D. Weiner, in *International Conference on Ultrahigh Intensity Laser Development, Science and Emerging Applications 2006* (ICUIL, Cassis, France, 2006), pp. 126–128.

The Second Omega Laser Facility Users Group Workshop 28 April–1 May 2010

Overview

More than 115 researchers from 44 universities and laboratories and 9 countries gathered at the Laboratory for Laser Energetics (LLE) for the second Omega Laser Facility Users Group (OLUG) Workshop (see Fig. 124.46). The purpose of the three-day workshop was to facilitate communications and exchanges among individual OMEGA users and between users and LLE; to present ongoing and proposed research; to encourage research opportunities and collaborations that could be undertaken at the Omega Laser Facility and in a complementary fashion at other

facilities [such as the National Ignition Facility (NIF) or the Laboratoire pour l'Utilisation des Lasers Intenses (LULI)]; to provide an opportunity for students and postdoctoral fellows to present their research at LLE in an interactive and informal atmosphere; and to provide feedback to LLE about ways to improve the facility and future experimental campaigns. The interactions were stimulating and lively, as can be seen in photographs shown in this document. There are 180 members in the OMEGA Users Group; their names and affiliations can be found at www.lle.rochester.edu/about/omega_laser_users_group.php.



U1092JR

Figure 124.46

More than 115 researchers from around the world and from 44 universities and laboratories participated in this year's OMEGA Laser Users Workshop. Plans for the next workshop, on 27–29 April 2011, are well underway, with significant NNSA support already allocated for student/postdoctoral travel expenses.

During the first two mornings of the workshop, 17 science and facility talks were presented. The facility talks proved especially useful for those not familiar with the art and complexities of performing experiments on OMEGA. The overview science talks, given by leading world authorities, described the breadth and excitement of high-energy-density (HED) science undertaken at the Omega Laser Facility. The next section of this document contains a summary of the presentations.

A total of 45 students and postdoctoral fellows, 37 of whom were supported by travel grants from the National Nuclear Security Administration (NNSA), attended the workshop and presented 31 of the 59 contributed poster and oral presentations. The presentations ranged from target fabrication to simulating important aspects of supernovae, all of which generated spirited discussions, probing questions, and many suggestions. In total there were 76 presentations, including both invited and contributed.

An important function of the workshop was to develop a set of recommendations and findings to help set future priorities for the Omega Laser Facility. These findings were grouped into three areas—60-beam OMEGA, OMEGA EP, and broader facility-improvement issues—and comprise a report given to the management of the Omega Facility. The report, along with management's response, can be found at the end of this document. LLE management is using these recommendations as a guide for making decisions about the Omega Laser Facility operations, priorities, and future changes.

One highlight of the workshop was a panel of students and postdoctoral fellows who discussed their experiences at the facility and their thoughts and recommendations on facility improvements. Wide-ranging and engaging discussions were sparked by this forum, which resulted in the student/postdoctoral report reproduced at the end of this document.

Another important event was a job fair designed to bring students together with potential future employers. This fair will be expanded at the next workshop.

Finally, one of the important decisions made at the workshop was to schedule the next one, which will be held at LLE on 27–29 April 2011. During their meetings, the Users Group and interested members of the HED community are formulating plans for this third workshop and reviewing progress on the **Findings and Recommendations** (p. 208) of the second workshop. In the future, a semiannual meeting will always take place at a satellite meeting during the fall American Physical Society's Division of Plasma Physics Conference.

The Presentations

A wide-ranging series of 76 talks and posters were presented over a two-day period. In the morning sessions, invited talks covered the facility and science. The invited science talks focused on several important topics, including high-energy-density plasmas, laboratory astrophysics, ignition in inertial confinement fusion (ICF), the physics of fast ignition, and future experiments on OMEGA and the NIF.

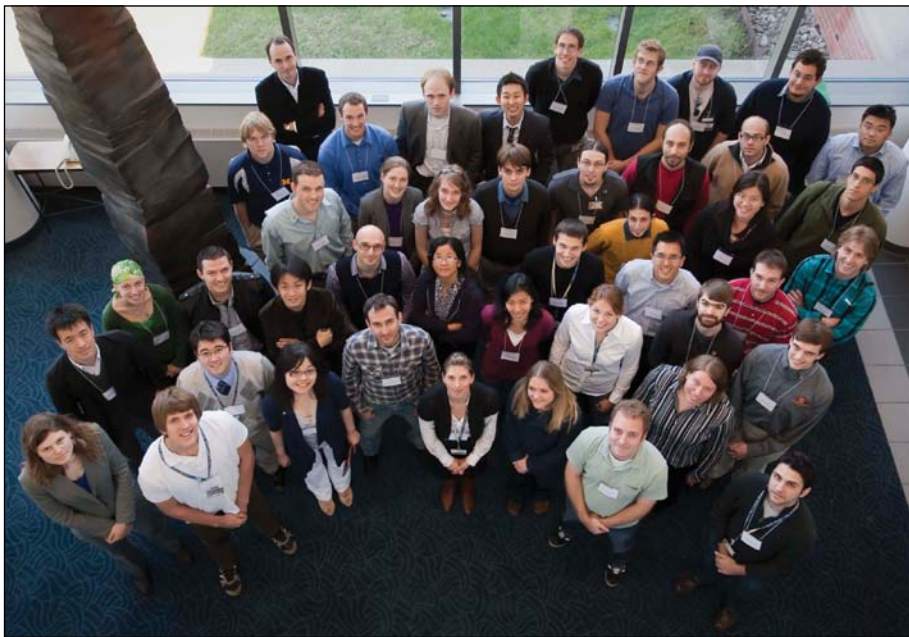


Figure 124.47

A total of 45 students and postdoctoral fellows attended and made 31 engaging presentations.

U1093JR



U1094JR

Figure 124.48

In the plenary sessions, 17 authorities spoke about the science and opportunities of high-energy-density physics and described the evolving capabilities of the Omega Laser Facility needed to reach new science frontiers.

The facility talks presented important details and developments on the status and performance of OMEGA/OMEGA EP from pulse shaping and duration to beam smoothing; the qualification process for interfacing new experiments; the present, and soon-to-be operating, set of diagnostics; and the critical role of targets, from design to procurement, full characterization, fielding, and, finally, shooting.

In addition to the 17 invited presentations, 59 contributed posters and talks covered a wide spectrum of work on OMEGA from target fabrication to fast-ignition experiments to basic and novel nuclear physics experiments. Additional presentations covered opportunities for taking physics platforms developed at OMEGA to larger (the NIF) and smaller (e.g., Jupiter, Trident, and LULI) facilities. The invited, contributed, and poster presentations formed much of the basis for wide-ranging lively discussions resulting in the **Findings and Recommendations** (p. 208) for the Omega Facilities and future capabilities, found at the end of this document.

The photographs on the following pages provide a representative sampling of the workshop's talks, interactions, and ambience.



U1095JR

Figure 124.49

Professor Robert Rosner of the University of Chicago kicked off the workshop with an astrophysicist's perspective on high-energy-density physics.

Findings and Recommendations of the Executive Committee

Executive Committee:

Richard Petraso, Committee Chair,
Massachusetts Institute of Technology
Hector Baldis, University of California–Davis
James Cobble, Los Alamos National Laboratory
Paul Drake, University of Michigan
James Knauer, LLE, University of Rochester (designated)
Roberto Mancini, University of Nevada–Reno
Peter Norreys, Rutherford Appleton Laboratory

1. Introduction

The OMEGA Laser Users Group warmly thanks LLE’s management for taking actions on the recommendations from our last report and for expeditiously addressing the issues identified therein. It is a strong testament to the professionalism of the facility staff that the tasks were executed with good speed and due diligence. The activities undertaken are a great credit to the Laboratory and to the University of Rochester. They are certainly highly appreciated by the academic and research user community.



U1096JR

Figure 124.50

The challenges and science of fast ignition were the focus of Professor Peter Norreys of Rutherford Appleton Laboratory (RAL). Professor Norreys is a member of the Users Executive Committee.



U1097JR

Figure 124.51

Dr. Guy Dimonte of Los Alamos National Laboratory (LANL) discussed the role of particle interactions in the equilibration of high-energy-density plasmas.

The OMEGA and OMEGA EP lasers are world-class facilities that provide academic access to cutting-edge energies and intensities on target. As with any high-performance device, however, critical enhancements are needed to continue to see progress in forefront science. This document describes the academic and research user community’s observations, distilled from its April 2010 workshop, of those elements and components that can maintain LLE’s leading position at the forefront of high-energy-density physics (HEDP). The OLUG looks forward to hearing progress on these recommendations at the semiannual satellite meeting in November (at the APS Conference) and at its next annual workshop (27–29 April 2011).



U1098JR

Figure 124.52

Dr. Brent Blue from General Atomics discussed the science and technology of developing and fielding complex targets for OMEGA experiments.

2. OMEGA (60 beams)

a. Three independent legs will add substantial improvement and flexibility to future experiments. Greatly expanded experimental design options would develop if it were possible to use all three of the existing drivers, with each driving one of the OMEGA legs. Ideally, each driver would be able to drive any leg to accommodate the constraints imposed by diagnostic configurations. Improved experiments and new classes of experiments would then become possible. The OLUG considers this a high priority.

Request: Present a plan to the Executive Committee on the implementation of three independent legs. In addition, include this and additional options for discussion at next year's workshop.

LLE Response: Preliminary concepts for this project have been developed and will be advanced further in FY11. Pending the availability of LLE resources, the implementation will commence in FY11. At a minimum, LLE will complete a plan for the implementation.

b. Request: Compile a list of qualified diagnostics that can be fielded for joint operations.



U1099JR

Figure 124.53
Moving physics platforms and experiments from OMEGA to the NIF was the focus of remarks by General Atomics' Joe Kilkenny. Dr. Kilkenny gave many concrete examples of this migration including x-ray, neutron, and charged-particle diagnostics.



U1100JR

Figure 124.54
(a) Professor Roberto Mancini from the University of Nevada and (b) Dr. Carolyn Kuranz from the University of Michigan posed questions in a plenary session. Prof. Mancini is a member of the Users Executive Committee.

LLE Response: The requested information will be made more readily accessible, and the OLUG Executive Committee will be notified as soon as the data are published on the Website.

c. It is common to drive experiments with ten OMEGA beams and very common to conduct two separate experiments in one day. The workhorse distributed phase plates (DPP's) are the SG8's. Many users have found that the limited number of these specific DPP's has compromised the quality or productivity of their experiments, especially when they had shots on the second half-day of a shared day. In the area of chamber optics, OLUG would prioritize this item second behind the provision of four 750- μm phase plates for OMEGA EP.

Request: Acquire enough SG8's to make 20 available to the user community (if this will not jeopardize the higher-priority 750- μm phase plate purchase needed for OMEGA EP).

LLE Response: The acquisition of additional SG8 DPP's is included in LLE's FY11 budget. The implementation date is contingent on vendor availability. There are currently 12 SG8

DPP's available, and these can continue to be shifted to accommodate campaign transitions as required in the interim period.

d. Request: Acquire a high-resolution neutron spectrometer to measure neutrons with energies in the 2- to 3-MeV range.

LLE Response: LLE is working with users to develop the requirements for this diagnostic and will then determine if it is feasible. If so, LLE will initiate a project to implement it.

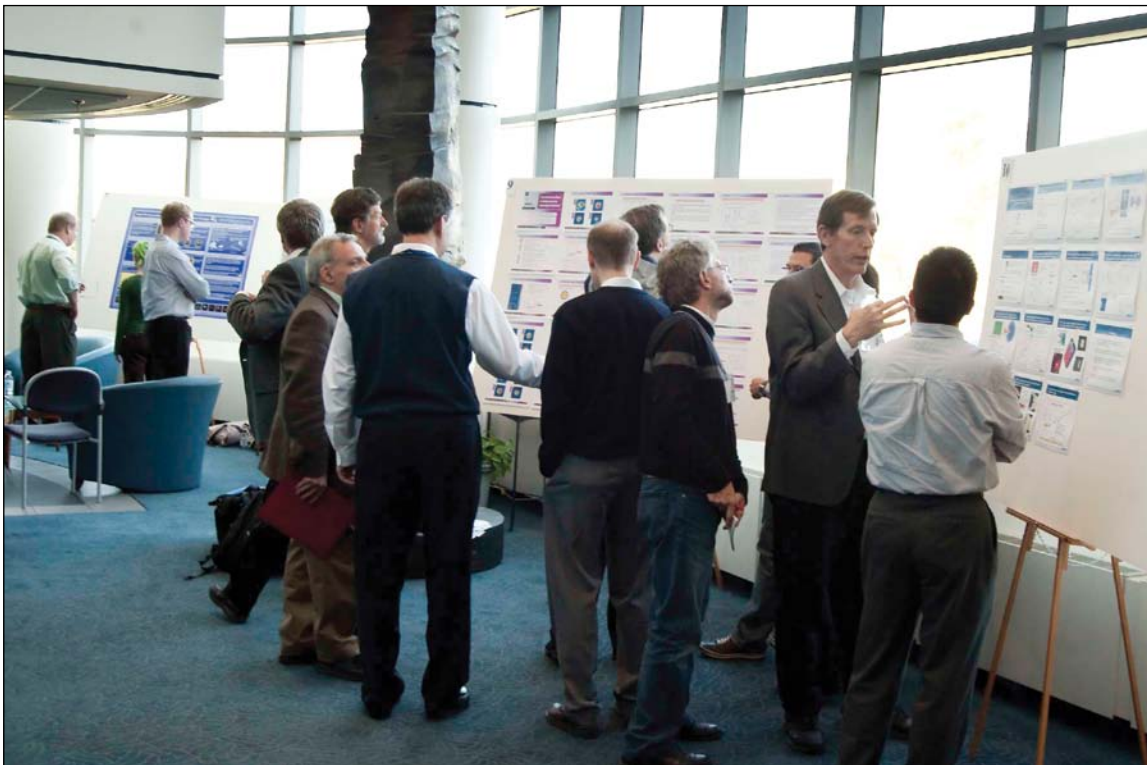
e. Upgrade the backlighter driver to operate at the nominal specified performance. The existing backlighter driver is unable to support the full energy that OMEGA's 60 beams are capable of producing. Because most backlighting and x-ray-probing experiments are photon limited, this is a significant shortfall for some experiments.

Recommendation: Improve the backlighter driver in order to support full-energy operation of the beams that it drives.

LLE Response: The backlighter source will be reworked in FY11 to increase the available operating envelope to match the other laser drivers.

f. OMEGA EP petawatt (PW) beam delivering two foci onto target. There is a need for simultaneous pump/probe experiments on OMEGA using the OMEGA EP PW beam. The availability of this feature would greatly increase the capability of the facility and would lead to the undertaking of many new experiments. Examples include hard x-ray radiography of integrated fast-ignition experiments. The OLUG recognizes, however, that space limitations impose a restriction on the provision of a single off-axis focusing parabolic mirror. The OLUG considered the possibility of splitting the PW beam into two beamlets at the final turning mirror to generate two focal spots.

Request: The OLUG requests that LLE investigate the possibility of splitting the petawatt beam and report back to the Executive Committee.



U1101JR

Figure 124.55

Two poster sessions, during which 43 posters were presented, offered ample opportunities for informal discussion about OMEGA experiments and their connections to important work at other HED facilities.

LLE Response: In FY11 the beam-combiner optic in the grating compressor chamber will be reinstalled. With this optic, the two short-pulse beams can be independently directed to two foci with a small separation. This capability will be developed and demonstrated on the OMEGA EP target chamber initially in FY11 and may be available on OMEGA in late FY11. The requirements for focal-spot separation, quality, and timing need to be refined to determine if this flexibility will meet user requirements. LLE will provide status updates on this effort to the OLUG Executive Committee. Should a “split mirror” be required, the design, fabrication, and integration effort will likely take of the order of 18 to 24 months. LLE recommends that users who need this feature refine their requirements so that this assessment can be made as soon as practical.

g. Integrated experiments require smaller focal spots for the petawatt beam. This is the same problem as Issue (g) (p. 216) in the section devoted to **OMEGA EP**.

Endorsement: OLUG strongly endorses the development and implementation of the new phase-front corrector as a matter of high priority.

LLE Response: The FY11 phase-front-correction effort will initially concentrate on a proof-of-principle experiment. If this demonstration is successful, a second-generation device will be fabricated at large aperture to refine the technique. Concurrent with this work is LLE’s effort to operate the existing adaptive-optic, closed-loop system as close as practical to shot



U1102JR

Figure 124.56
University of Michigan student Elisio Gamboa discussed his work on x-ray Thomson-scattering imaging with National Nuclear Security Agency’s (NNSA) Allan Hauer. Dr. Hauer presented a talk on the importance to NNSA of high-energy-density laboratory physics.



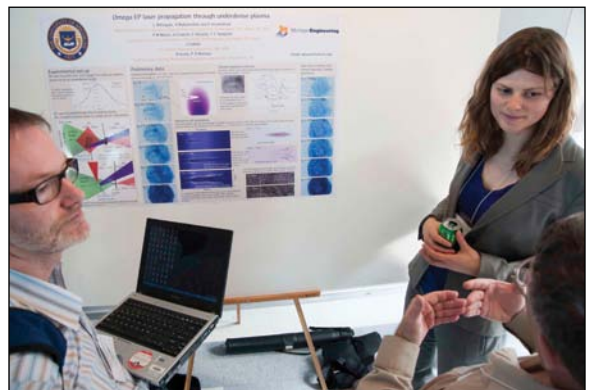
U1104JR

Figure 124.58
Frank Phillipe (left), from France (Commissariat à l’énergie atomique), chatted with Chikang Li of MIT. Drs. Phillipe and Li recently collaborated on OMEGA experiments involving rugby-shaped hohlraums.



U1103JR

Figure 124.57
Dr. Tony Caillaud, from France (Commissariat à l’énergie atomique), showed Professor Linn Van Woerkom (Ohio State University) neutron images of OMEGA DD and DT implosions.



U1105JR

Figure 124.59
Postdoctoral fellow Louise Willingale, from Prof. Karl Krushelnick’s group at the University of Michigan, and Peter Norreys of RAL listen to comments about her OMEGA EP research on proton backlighting of laser channeling.

time to improve repeatability. Finally, high-spatial-resolution phase-front control will be investigated using the active device presented to the OLUG community on 29 April 2010. Note that the implementation of dynamic control may not be complete until FY12.

h. OMEGA 60-beam timing measurement accuracy. At present, for delays or advances (offsets) of beams beyond about 10 ns from time zero, the accuracy with which one knows the beam timing drops to ± 0.5 ns. This often becomes the largest uncertainty in experiments with offsets in the 10-ns to 30-ns range.



U1106JR

Figure 124.60
Dr. Kazuo Tanaka (Osaka University) and Dr. Wolf Seka (LLE) conversed during the poster session. Dr. Tanaka presented work on the self-focusing of relativistic electrons.



U1107JR

Figure 124.61
Dr. Jim Cobble (left, from LANL), a Users Executive Committee member, spoke with Professor David Meyerhofer (LLE) about the Recommendation and Findings report for the LLE management. This report is used to help prioritize LLE facility upgrades and directions.

Request: Develop the means to determine the beam’s temporal offsets actually achieved on each shot, with an accuracy on the order of ± 0.1 ns. Such a capability would significantly improve the quality of experimental results from certain experiments.

LLE Response: The P510 streak camera system has an option currently available for a 40-ns sweep speed that is calibrated to give timing to < 0.1 ns over the requested 10- to 30-ns window. LLE recommends consulting with the Laser Facility Manager during the proposal phase (~2 months prior to shot day) to optimize configuration of the laser streak system to yield satisfactory pulse-shape measurement and precision timing simultaneously.

i. Photographic documentation of some diagnostic and related systems. To understand complex mechanical systems, it is often helpful to have photographic (and/or CAD) images to complement sets of mechanical drawings. This is definitely true of the ten-inch manipulators (TIM’s). We suggest that such images be made available online for the TIM’s. Users and the facility should both consider whether there are other systems that would also merit photographic and/or CAD documentation.

LLE Response: LLE concurs with the request to make a photograph-enhanced diagnostic glossary and will develop a standardized “cut sheet” for each diagnostic. The OLUG Executive Committee will be notified as soon as the data are published on the Website.



U1108JR

Figure 124.62
Dr. Frederick Séguin (MIT) gave a contributed talk about observations of the electromagnetic fields associated with coronal filamentation in direct-drive ICF implosions.

3. OMEGA EP

a. Bring OMEGA EP performance up to its full specification. We fully appreciate that the OMEGA EP IR and UV beam energy must be limited to ensure minimum damage to expensive and difficult-to-obtain optical components during operations with the existing gratings and UV optics. On the other hand, it is OLUG's duty to note that the user community needs access to the full performance of the laser facility to ultimately allow one to explore the exciting new regimes in high-energy-density physics. The constraints, while essential, limit the experiments that have been conducted as well as the results that have been obtained so far. Although it should be pointed out that outstanding results have been obtained with the present operating parameters of OMEGA EP, it is still the desire of the user community to have the facility operating at its specified performance at the earliest practical opportunity.

Endorsement: OLUG endorses LLE's plan to develop and acquire high-laser-damage-threshold IR and UV optics that

will make it possible for OMEGA EP to routinely operate at its design performance. OLUG requests that facility management keep the OLUG Executive Committee apprised of the research and development plans that will make it possible for OMEGA EP to reach design performance.

LLE Response: LLE is aggressively working to expand the operational envelope limits of OMEGA EP. The IR and UV energies on target are currently limited by laser-induced damage. The constraints are due to the laser-damage-threshold limits of gratings (short-pulse IR) and transmission optics (long-pulse UV). LLE will continue to share progress and plans on this item with the OLUG Executive Committee.

b. Bring design options forward to next OLUG workshop for 2 ω and 3 ω conversion of the PW beam. There are some preliminary and tentative indications, from experiments performed in France, that the fast electron energy transfer and heating of background plasma is enhanced with frequency-converted



U1109JR

Figure 124.63
Productive discussions among researchers from around the world occurred in several informal settings.



U1110JR

Figure 124.64
Benchmarks for achieving ignition were the subject of Professor Riccardo Betti's presentation.

light. This past summer at the TITAN facility, more evidence was gathered that added to the knowledge base. Certainly, much greater control over the energy content of the amplified spontaneous emission pedestal associated with petawatt laser pulses is ensured with conversion to 2ω and 3ω . This has been established as an important factor in cone-guided experiments. It is prudent to have available engineering plans for frequency conversion of the PW beam if required for future experiments by the user community.

Recommendation: The OLUG requests that facility management provide options for discussion at the next OLUG Workshop for frequency conversion of the PW beam.

LLE Response: LLE will commence a scope study to identify viable concepts for implementation of short-pulse frequency conversion. There is a high likelihood that conversion crystals, mounts, diagnostics, beam transport, and focusing systems will constitute a significant investment of LLE resources and require an NNSA-approved construction project. A case study representing the need for this item would be beneficial in garnering NNSA support for a capital project.

c. Two Cu K_{α} imaging crystal spectrometers are needed for both OMEGA 60 and OMEGA EP. Understanding the physics of fast electron energy transport from petawatt-power laser-plasma interactions with solid targets requires the deployment of sophisticated x-ray diagnostics. Cu K_{α} imaging spectrom-

eters have been developed in the United States over the past decade and have proven to be powerful tools in diagnosing the heating of dense matter using intense laser pulses. These instruments are required on both chambers so that independent experiments can be carried out simultaneously. In each target chamber, they need to be deployed in orthogonal directions so that spatial nonuniformities can be identified and characterized.

Recommendation: The OLUG requests that LLE management validate and deploy these imaging spectrometers as a matter of high priority in the coming year. The OLUG recognizes that the deployment of orthogonal instruments may pose difficulties, but the requirement for these instruments for each chamber is vital to the user program. We request that OMEGA provide a deployment plan to the Executive Committee for their consideration and report to the workshop next year on arising issues.

LLE Response: A prototype crystal imager is being developed for the Multi-Terawatt laser with plans to install a complete system on OMEGA EP in FY11. In the interim a “fast-track” crystal imager was installed on OMEGA EP in FY10. In FY11, LLE will initiate projects to add a second crystal imager on OMEGA EP and two on OMEGA. Depending on resources available and other priorities, these projects may be carried out in FY11.

d. Two electron spectrometers are needed for both target chambers. Electron spectrometers are important tools for char-



U1111JR

Figure 124.65
Dr. Al Trivelpiece (left) and Jim Decker brought some unique experience and valuable insights to the workshop.

acterizing the behavior of intense laser–plasma interactions. They have applications in many areas, including wakefield acceleration, betatron x-ray source characterization, channel formation, and positron generation, among many others. The development of a university-based program requires the deployment of spectrometers with electromagnets that provide a wide window up to GeV of particle energies. OLUG understands that Lawrence Livermore National Laboratory (LLNL) colleagues have validated and deployed low-energy electron spectrometers in their experiments; these instruments should be made available to the wider community.

Recommendation: The OLUG requests that LLE management initiate a design and validation program for an electromagnet-based electron spectrometer for wakefield acceleration studies up to GeV particle energies. They request that electron spectrometers based on the LLNL design be made available to the wider academic community.

LLE Response: In FY11, LLE will initiate projects to ensure that there are two electron spectrometers on OMEGA EP and two on OMEGA. Depending on resources available and other priorities, these projects may be carried out in FY11.

e. LLE’s contrast-ratio improvement program. The OLUG was impressed with the presentation of Christophe Dorrer relating to the intensity contrast issues of the petawatt beam. The audience appreciated the identification of all the different components in the laser chain that contribute to the pedestal over its full range—some nanoseconds ahead of the pulse, some on its leading edge. The enhancement program was warmly received by the audience.

Endorsement: The OLUG strongly endorses LLE’s contrast-ratio improvement program. They fully endorse the time frame outlined and want to be updated on progress at the next OLUG Workshop.



U1112JR

Figure 124.66

Professor Paul Drake (University of Michigan), a Users Executive Committee member, presented a talk about the opportunities for doing laboratory astrophysics on OMEGA and OMEGA EP.

LLE Response: The OLUG Executive Committee will be kept abreast of all developments in the short-pulse laser's contrast enhancement.

f. Status of the 4 ω probe. The OLUG was impressed with the presentation of Wolfgang Theobald on the fourth-harmonic probe status. The probe commissioning is proceeding with good speed and the audience was delighted with progress so far. Nevertheless, concern was raised that the seeds are not from the same source and much closer attention to minimizing and measuring timing jitter is needed. In addition, the pulse energy is marginal and needs to be increased by an order of magnitude.

Recommendation: The OLUG requests that the timing-jitter issue be addressed and an additional amplifier stage be added so that the probe energy can be increased when required. These changes should be reported to the Executive Committee.

LLE Response: The concerns of the OLUG have been communicated to the development team and will be closely monitored through the initial implementation of the 4 ω probe

laser at its baseline performance level. Any requirements analysis for specific experiments that users can provide to the team would be helpful in motivating changes to the baseline requirements for this system. LLE will work to include design features for operation of the probe with maximum precision timing and as much energy as practical.

g. OMEGA EP focal-spot size of the PW beam. The community welcomed Brian Kruschwitz's characterization of the OMEGA EP focal-spot quality. They were satisfied that the encircled energy measurements he reported were consistent with other plasma diagnostics. Concern was raised, however, that the focus of the OMEGA EP was insufficient for many future experiments and that effort is needed to reduce the 80% encircled energy radius by a least a factor of 2 (from 40 μm to 20 μm). They were delighted to hear about the new phase-front-corrector technology that will make this development possible.

Endorsement: OLUG strongly endorses the development and implementation of the new phase-front corrector as a matter of high priority.



U1113JR

Figure 124.67

From far left, Alberto Marochinno (University of Rome), Tazio Levato (INFN Frascati), Patrizio Antici (INFN Frascati), Rich Petrasso (MIT), Riccardo Betti (LLE), Lois Buitano (NNSA), Orlando Ciricosta (University of Pisa), and Angelo Schiavi (University of Rome) are captured together during the poster session.

LLE Response: See response to **OMEGA** Item (g) (p. 211).

h. Polarization smoothing on all four UV beams. The community was very impressed by the quality of the presentation from Samuel Morse. They received with great pleasure the news of the concerted effort to address issues raised at the last workshop. They were particularly struck by the quality of his argument that the polarization-smoothing technology had reached sufficient maturity to implement on OMEGA EP and that the advantages over smoothing by spectral dispersion were apparent.

Endorsement: OLUG unanimously accepted LLE's recommendation for polarization smoothing on all beams. They look forward to rapid implementation of the proposal and to receiving an updated progress report at next year's meeting.

LLE Response: User need for this feature remains unclear. If there is any specific analysis of an experiment that would benefit from this capability, please communicate to LLE since it will aid in justification of the cost. LLE is pursuing this item with no guarantee that the acquisition will be selected for funding in FY11. The time frame for implementation of polarization smoothing is 18 to 24 months after optics are ordered. Every effort will be made to expedite this acquisition as well as the

mounts that will support the optics, once the funding commitment is secured.

i. The planar cryogenic target handler should be implemented on OMEGA EP for users. A number of academics in the community raised the issue of fielding planar cryogenic-deuterium targets for the OMEGA EP chamber. They expressed concern that this technology was not available for cutting-edge transport and hydrodynamic experiments.

Recommendation: OLUG strongly endorsed the implementation of planar cryogenic target-handling technology as a high priority. The community wants to see this target-handling technology made available at the earliest opportunity.

LLE Response: LLE will consider the OLUG endorsement of this project in prioritizing laboratory resources in FY11. It is likely to take 12 to 18 months from project inception to initial capability deployment. LLE will keep the OLUG Executive Committee informed of the project status.

j. A full set (4) of 750- μ m phase plates is needed. The community expressed great pleasure that a number of phase plates had been acquired in response to their requests at last year's workshop. After considerable debate over different phase-plate



U1114JR

Figure 124.68

The student/postdoctoral panel presented important insights from young researchers working at the Omega Facility. Left to right: Dr. Maria Barrios (University of Rochester, LLE), Dr. Tammy Ma (University of California, San Diego), Dr. Hiroshi Sawada (University of California, San Diego), Dr. Ryan Rygg (LLNL), Dan Casey (MIT), Dr. Andrea Kritcher (LLNL), and Dr. Louise Willingale (University of Michigan).

sizes, it was felt that a full set (4) of 750- μm phase plates is needed. These would be useful in the context of the long-duration hydrodynamics and laboratory astrophysics experiments that OMEGA EP uniquely makes possible by stacking beams in time. By running the specified maximum of 6 kJ in a 10-ns pulse, a 750- μm phase plate produces an average intensity of $1.4 \times 10^{14} \text{ W/cm}^2$. Using an 1100- μm phase plate reduces the intensity to below $7 \times 10^{13} \text{ W/cm}^2$. This is an important difference. One definitely wants to be above 10^{14} W/cm^2 for most experiments. In solid plastics, shocks will be driven not much more than 1 mm in 40 ns; therefore, 2-D expansion is a smaller concern than having adequate intensity.

Endorsement: A full set (4) of 750- μm phase plates should be purchased and made available to the community.

LLE Response: LLE appreciates the aggregation of OLUG requirements and distillation to a well-defined recommendation. The acquisition of additional 750- μm distributed phase plates to obtain a full set of four operational optics is in the FY11 acquisition plan.

k. Requirement for a limited-reservoir gas-jet target. Some academics expressed the view that gas-jet targets should be implemented on OMEGA EP. They accepted the facility

management’s argument that an unlimited reservoir gas line might put the OMEGA EP compressor grating actuators at risk. They recognized, however, that many experiments would benefit from a gas-jet arrangement. It was felt that the burden of commissioning this technology should not fall on a single institution but should be shared as a common resource. They agreed that a limited reservoir would add capability to a wide range of experiments.

Recommendation: The facility should design, validate, and implement a limited-reservoir gas-jet target and make it available to the user community.

LLE Response: Development of equipment to provide a gas jet in the Omega Facility will require significant resources. Users interested in this capability should contact John Soures, who will facilitate formation of a subcommittee to investigate the development of this capability. LLE resource allocation to this project is subject to balancing laboratory priorities. Project selection depends on developing a set of requirements that can be met within the system’s safety constraints.

l. Requirement for added flexibility for long-pulse operation. The community was delighted by the performance of the long-pulse beams in their current configuration. The arrangement



U1115JR

Figure 124.69 A “town hall” meeting on the importance and role of high-energy-density physics, from the DOE perspective, was led by Mark Koepke (left; Office of Fusion Energy Science), Kim Budil (Office of the Under Secretary for Science), and Lois Buitano (National Nuclear Security Agency).



U1116JR

Figure 124.70 Kim Budil (Office of the Under Secretary for Science) discussed her office’s perspective on high-energy-density physics.



U1117JR

Figure 124.71

Facility presentations, like this one by Samuel Morse (LLE), related new and ongoing developments on OMEGA and briefed younger researchers on the effective use of the facility. Mr. Morse's extensive knowledge of the facility is invaluable to those planning OMEGA experiments.

had produced some outstanding results that were received by the audience with acclaim. After much debate, the community felt that if different ports, originally earmarked for long-pulse operation, were made available, it would add substantial flexibility to experiment design and effectiveness. They endorsed the option of irradiation from opposite sides as one example.

Recommendation: The OLUG recommends that all ports originally earmarked for long-pulse operation be brought into facility capability. The OLUG welcomes a report at next year's meeting on progress with options.

LLE Response: The 48°-cone-angle ports were proposed as an option in the OMEGA EP project, but it was not supported by the users or NNSA at that time. It would be very expensive to fit out with UV-beam-transport paths, which would take significant facility time and would require capital project support from NNSA. A potential smaller-scale, higher-payoff alternative, suggested at the OLUG meeting in April 2010, was to bring one or more beams to the back side of the target chamber. A feasibility study will be conducted to assess potential UV-beam routing to the opposite side of the target chamber from the existing 23° UV-beam ports.

m. Equivalent-plane monitors for all UV beams. The community felt that while the focal-spot monitor was adequate for

some experiments, all experiments were complicated by a lack of knowledge of the quality of all beams away from their foci.

Recommendation: Equivalent-plane monitors should be implemented for all beams. The OLUG welcomes a report on this issue at next year's meeting and trusts that this can be implemented with little disruption to operations.

LLE Response: The request for UV far-field measurements on all beams will be carefully considered. It would be helpful if the experimentalists requesting this feature would provide a range of spot sizes of interest for measurement. The UV diagnostic package has provision for locating a far-field monitor, and the LLE plan is to implement a phase-plate holder in the diagnostic path for at least one beam. LLE will keep OLUG apprised of the progress in meeting this recommendation.

n. A new gamma-ray spectrometer diagnostic is required. The community felt that a new gamma-ray spectrometer needs to be designed, validated, and commissioned for the facility. Users requested that the spectrometer have a spectral range up to 20 MeV.

Recommendation: The OLUG requests that management consult the Executive Committee on the design, validation, and implementation of this new instrument for the community.



U1118JR

Figure 124.72

Brian Kruschwitz (LLE) discussed the latest techniques for characterizing the OMEGA EP laser's focal spot. Such information is essential for planning experiments.

LLE Response: OLUG scientists interested in this spectrometer should contact John Soures, who will facilitate formation of a subcommittee on high-energy photon spectroscopy. Once a consensus of requirements for sensitivity, spectral range, resolution, and other features is generated, the subcommittee and OLUG Executive Committee can provide LLE with more definition of what is desired. LLE resource allocation to this project is subject to balancing laboratory priorities.

o. See also Items (f) and (g) (pp. 210,211) of OMEGA (60 beams).

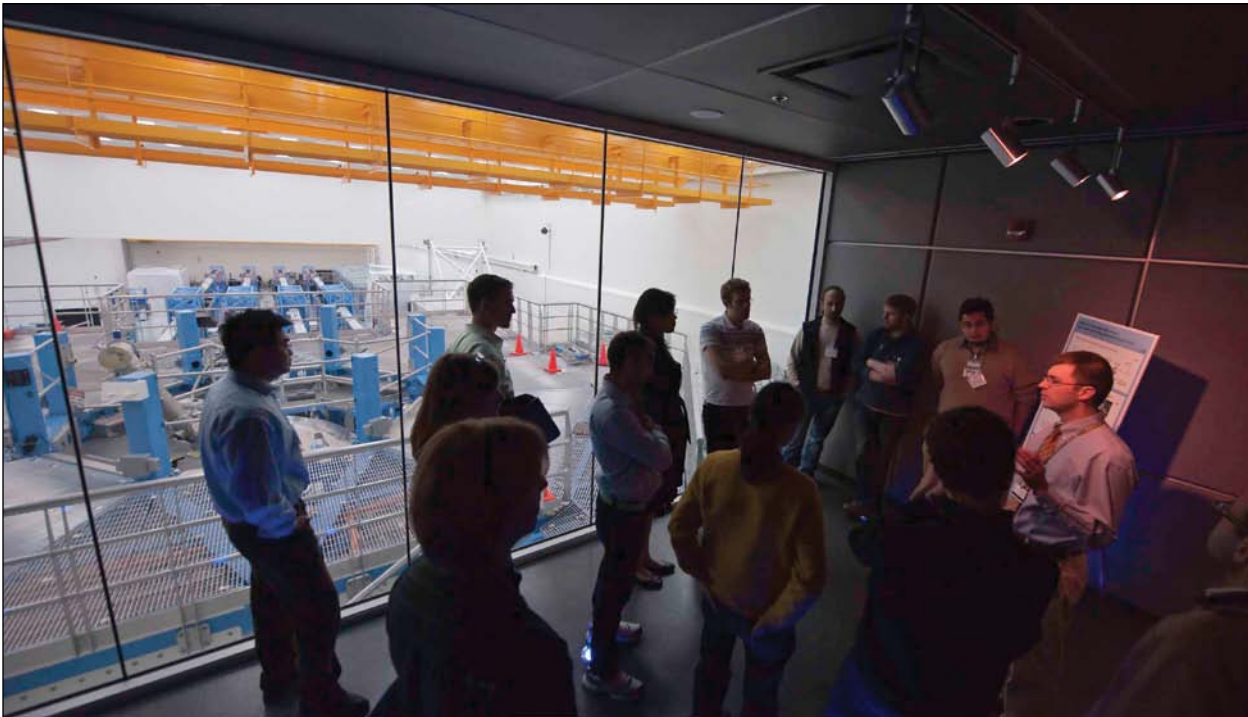
4. Other Facility Improvements

a. Dedicated user support for experiment design and theoretical modeling. To maximize the productivity of both OMEGA (60 beams) and OMEGA EP, it is important to have access to theoretical and computational support for both experiment design and data interpretation for university-based academics. Individual academics, who are motivated by curiosity-driven research in high-energy-density science, often find that they do not have access to the necessary sophisticated computational models at all stages in the training cycle. The

very nature of university life, where there is a high turnover of doctoral and postdoctoral research fellows, means that modeling skills nurtured by the teams and applied to specific problems can suddenly evaporate, leaving them without vital tools at critical stages in the research effort.

Ideally, the theoretical support team must be located within the larger-scale facilities. It must be of critical size to provide the facility users with a wide range of modeling capability (e.g., one- and two-dimensional magnetohydrodynamic simulations, implicit and explicit particle-in-cell and hybrid models for high-intensity laser-matter interactions, quantum molecular dynamics for warm dense matter studies, etc.) and have dedicated access to large-scale, high-performance computing resources. Here are some desirable characteristics of the support team:

- Team members should be involved at all stages in the experiment cycle, obviously requiring a collaborative approach by all parties.
- The team must be university focused and highly responsive to user demands. The team should assist with interpretation



U1119JR

Figure 124.73

David Canning (LLE) led a tour of the OMEGA EP laser and discussed its capabilities. For many new researchers, this was an ideal opportunity to learn about the facility.

of smaller-scale experiments undertaken on university-scale facilities. This is particularly important to the reduction in cost and size of intense laser systems and the proliferation within academic institutions.

- The team must be of sufficient size so that members have enough time to develop their own research interests, in addition to their support duties. This should allow team members time to devote to the development of new codes, algorithms, and possibly visualization routines.
- The team must be involved in training students and post-doctoral fellows in high-energy-density science, e.g., by co-supervision of Ph.D. students, etc.

Clearly, a balance must be struck between supporting experiments themselves and maintaining a critical size in the modeling support team.

Recommendation: The OLUG requests that LLE management establish a university-focused support team, ideally comprising four staff members, with academics from other programs at LLE and/or other institutions. The team will make a huge difference in the quality and depth of publications arising from the facility.

LLE Response: After the 2010 OLUG report is completed, LLE will request additional funding from NNSA and the Office

of Science to support this request. LLE may request a letter from the Executive Committee endorsing this request.

b. Increased support from DOE to the National Laser Users' Facility (NLUF) Program. The OLUG recognizes and applauds the increased funding to the NLUF Program in FY11/12 from the DOE (\$1.3M to \$1.6M). This has allowed facility management to increase access under the NLUF Program for the university community. The OLUG is also highly appreciative of the efforts of DOE officials to achieve this increase. The OLUG firmly believes that the establishment of new academic positions for young researchers in high-energy-density physics, working in partnership with the established academics and consortia (e.g., the Fusion Science Center), is a high priority for the growth of the field.

Recommendation: The OLUG strongly urges DOE to maintain the percentage increase in funding to the NLUF.

Recommendation: The OLUG urges DOE to develop and fund a program to accelerate the career progression for the brightest young dynamic researchers working in experimental high-energy-density physics by sharing the cost of their appointment with universities while they are at the assistant-professor level.

LLE Response: LLE recognizes the value of these requests, but clearly it is an issue for OLUG to communicate directly with DOE.



U1120JR

Figure 124.74

Members of the OMEGA Users Executive Committee. Back row (left to right): Paul Drake (University of Michigan), Jim Knauer (LLE), Jim Cobble (LANL), and Peter Norreys (RAL). Front row (left to right): Ryan Rygg (LLNL), Rich Petrasso (MIT), Roberto Mancini (University of Nevada).

Findings and Recommendations of the Student/Postdoctoral Panel

Student/Postdoctoral Panel

Ryan Rygg (LLNL), Chair

Maria Barrios (LLE)

Dan Casey (MIT)

Andrea Kritcher (LLNL)

Tammy Ma (University of San Diego)

Hiroshi Sawada (University of San Diego)

Louise Willingale (University of Michigan)

1. Interest continued in having extensive diagnostic information available online, such as reference papers and sample/calibration data linked from the Shot Request Form. The OMEGA staff has created a diagnostics forum, with threads for individual diagnostics. It is up to the users, however, to take the discussion there and populate it with useful information, such as optimal setup or analysis techniques.

2. Published papers typically include descriptions of the basic experimental setup, results, and conclusions, but rarely include the full nitty-gritty details necessary to run experiments at OMEGA, or to analyze the raw data produced. Completed theses of prior students were identified as often including many of the useful details left out of published articles. University of Rochester theses containing work done at the Omega Facility are available on the LLE Website. It would be useful if theses from other institutions performed using OMEGA diagnostics were also collected and made available. It was also pointed out that the LLE Review has many articles that include such useful details not contained in published articles. Although back issues of the LLE Review are available on the LLE Website, the content is not easily searchable.

3. Since HEDP is still a growing field, most academic institutions do not have enough interested students to hold dedicated classes on topics relevant to HEDP. It was suggested



U1121JR

Figure 124.75

The OMEGA Users banquet offered another opportunity for attendees to interact informally, reinforce old friendships, and create new working relationships.

that experts in the field may be able to offer lecture series or entire courses online. Roberto Mancini's recent spectroscopy class was held up as an excellent example, and additional topics would also be of interest. The MIT open courseware site was recommended as a model to enable instructors and students to share lecture notes and assignments.

4. The forum concluded with a discussion of the availability and acquisition of jobs in the field, including those in academia, government laboratories, publishing, and government administration.

Conclusions and Future Workshops

This OLUG workshop, with over 115 attendees, was part of a process that will keep members of the inertial confinement fusion and high-energy-density physics communities involved in conversations and collaborations with each other and with the Omega Facility. In addition, OLUG Executive Committee members and the LLE management have been meeting on a bi-monthly basis to assess progress, compatibility with facility resources, and impact toward the implementation of the Findings and Recommendations. Progress will be presented at a

satellite meeting at the Chicago APS Meeting (9 November 2010) and in depth at the next Users Workshop.

The next OMEGA Laser Users Workshop will be held at LLE on 27–29 April 2011; plans for it are already well underway. To this end, significant financial support from NNSA has already been procured to help defray the cost of student and postdoctoral travel. We anticipate that this next workshop will be as exciting and memorable as the first two. Come join us!

ACKNOWLEDGMENT

For capturing the ambience and spirit of the workshop through his camera lens, we thank Eugene Kowaluk. To NNSA, we gratefully acknowledge the financial assistance for student/postdoctoral travel expenses. We thank the University of Rochester Fusion Science Center, and the Office of Fusion Energy Science, for co-sponsoring the OMEGA Users Group Workshops. We thank LLE for supporting this workshop in numerous ways and for their responsiveness in addressing the Findings and Recommendations of the Users.

This synopsis was compiled and edited by R. D. Petrasso (petrasso@psfc.mit.edu) of the MIT Plasma Science and Fusion Center, with critical input and contributions from workshop attendees, the Executive and Student/Postdoctoral Workshop Committees, and the LLE management. Please send corrections to R. Petrasso. The final synopsis will be posted at www.lle.rochester.edu/about/omega_laser_users_group.php.

LLE's Summer High School Research Program

During the summer of 2010, 16 students from Rochester-area high schools participated in the Laboratory for Laser Energetics' Summer High School Research Program. The goal of this program is to excite a group of high school students about careers in the areas of science and technology by exposing them to research in a state-of-the-art environment. Too often, students are exposed to "research" only through classroom laboratories, which have prescribed procedures and predictable results. In LLE's summer program, the students experience many of the trials, tribulations, and rewards of scientific research. By participating in research in a real environment, the students often become more excited about careers in science and technology. In addition, LLE gains from the contributions of the many highly talented students who are attracted to the program.

The students spent most of their time working on their individual research projects with members of LLE's technical staff. The projects were related to current research activities at LLE and covered a broad range of areas of interest including experimental diagnostic development, computational modeling of implosion physics, opacity data for hydrodynamic simulations, laser physics, experimental and theoretical chemistry, materials science, cryogenic target characterization, target positioning and viewing systems, and database development (see Table 124.II).

The students attended weekly seminars on technical topics associated with LLE's research. Topics this year included laser physics, fusion, holography, nonlinear optics, atomic force microscopy, electrostatics, and electronic paper. The students also received safety training, learned how to give scientific presentations, and were introduced to LLE's resources, especially the computational facilities.

The program culminated on 25 August with the "High School Student Summer Research Symposium," at which the

students presented the results of their research to an audience including parents, teachers, and LLE staff. The students' written reports will be made available on the LLE Website and bound into a permanent record of their work that can be cited in scientific publications.

Two hundred and sixty-five high school students have now participated in the program since it began in 1989. This year's students were selected from over 60 applicants.

At the symposium LLE presented its 14th annual William D. Ryan Inspirational Teacher Award to Mr. Brad Allen, a physics teacher at Brighton High School. This award is presented to a teacher who motivated one of the participants in LLE's Summer High School Research Program to study science, mathematics, or technology and includes a \$1000 cash prize. Teachers are nominated by alumni of the summer program. Mr. Allen was nominated by Leela Chockalingam, Aaron Van Dyne, and Harvest Zhang, participants in the 2009 program. Leela described Mr. Allen as "one of the most fantastic science teachers I have had the opportunity to learn under. . .He took the fear and mystery out of physics and made it fun. Mr. Allen guided me toward my love of science." Aaron wrote, "Mr. Allen is a large part of why so many people learn a subject as difficult as physics so painlessly. . .He is just plain good at his job, which is preparing the next generation of scientists. . .He has an ability to make physics seem logical to everyone, and yet to challenge even the most talented students." Harvest was also very appreciative, writing, "Mr. Allen shares his brilliance with his students and stays after school almost every day to help students at all levels of physics. . . We will go on to college and learn more advanced physics. . .but it was Mr. Allen who laid the rock-solid foundation on which all future lessons in physics will rest." Brighton High School Principal Mrs. Nancy Hackett added that Mr. Allen has done "a fabulous job" and that his "good energy" has dramatically improved the level of science education at Brighton High School.

Table 124.II: High School Students and Projects—Summer 2010.

Name	High School	Supervisor	Project Title
James Baase	Victor	D. J. Lonobile, G. Brent	Optimizing the Movement of a Precision Piezoelectric Target Positioner
Andrew Chun	Brighton	F. J. Marshall	X-Ray Imaging with Compact Kirkpatrick–Baez Microscopes
Robert Cooper	Allendale-Columbia	R. W. Kidder	Designing an Ontology for Experimental Diagnostics at LLE
Luke Coy	Greece Arcadia	R. Rombaut, R. S. Craxton	A Graphical User Interface for User-Generated Opacity Data
Kyra Horne	Fairport	M. J. Guardalben	Reducing UV Near-Field Beam Modulation on OMEGA EP by Angularly Detuning the Frequency Conversion Crystals
Karin Hsieh	Webster Schroeder	W. T. Shmayda	Modeling Water Desorption from Stainless Steel
Connie Jiang	Brighton	D. W. Jacobs-Perkins, R. Huff	Testing and Installation of the Reticle Projector on OMEGA's Target Viewing System
George Liu	Pittsford Sutherland	R. Epstein	Imploded Shell Parameter Estimation Based on Radiograph Analysis
Thomas Mo	Webster Schroeder	R. S. Craxton	X-Ray Backlighting of a Shock-Ignition Experiment on the NIF
Eric Pan	Webster Thomas	T. B. Jones	Using <i>Surface Evolver</i> Software to Model the Behavior of Liquid Deuterium
Ryan Shea	Fairport	W. T. Shmayda	Water Desorption from Stainless Steel at Variable Temperatures
Laura Tucker	Brighton	R. S. Craxton	A Design for a Shock-Ignition Experiment on the NIF Including 3-D Effects
Katherine Wegman	Pittsford Mendon	K. L. Marshall	Liquid Crystal Beam-Shaping Devices Incorporating Coumarin-Based Photoalignment Layers
Francis White	McQuaid	D. H. Edgell, M. D. Wittman	Determination and Correction of Optical Distortion in Cryogenic Target Characterization
Barry Xu	Brighton	S. X. Hu	Electron-Ion Relaxation Rates in Inertial Confinement Fusion
Andrew Yu	Pittsford Sutherland	K. L. Marshall	Modeling Absorption Spectra of Optically Switchable Azobenzenes

FY10 Laser Facility Report

During FY10 the Omega Facility conducted 1343 target shots on OMEGA and 480 target shots on OMEGA EP for a record total of 1823 combined target shots (see Tables 124.III and 124.IV).

Many changes were made to the laser system to improve low-adiabat, direct-drive cryogenic implosion performance. OMEGA conducted 38 DT spherical implosions and 40 planar cryogenic target experiments in support of shock timing. Triple-picket operational improvements highlighted the ongoing

development of direct-drive cryogenic implosion capability. The OMEGA Availability and Experimental Effectiveness averages for FY10 were 93% and 94%, respectively.

OMEGA EP was operated extensively in FY10 for a variety of internal and external users. A total of 308 short-pulse IR target shots were conducted. Of these, 232 target shots were taken into the OMEGA EP target chamber and 76 joint target shots were taken into the OMEGA target chamber. A total of 117 OMEGA EP target shots included UV beams. OMEGA EP averaged 4.9 target shots per operating day with Availability and Experimental Effectiveness averages for FY10 of 86% and 94%, respectively.

Table 124.III: Omega Facility target shot summary for FY10.

OMEGA Target Shot Summary					
Laboratory	Planned Number of Target Shots	Actual Number of Target Shots	NIC	Shots in Support of NIC	Non-NIC
LLE	352	361	0	339	22
LLNL	320	376	212	0	164
NLUF	135	150	0	0	150
LANL	130	135	55	0	80
LBS	155	190	0	0	190
CEA	45	55	0	0	55
AWE	30	37	0	0	37
U. Mich.	15	19	0	0	19
FSC	20	20	0	0	20
Total	1202	1343	267	339	737

Table 124.IV: Omega EP Facility target shot summary for FY10.

OMEGA EP Target Shot Summary					
Laboratory	Planned Number of Target Shots	Actual Number of Target Shots	NIC	Shots in Support of NIC	Non-NIC
LLE	200	206	0	193	13
LLNL	95	107	31	5	71
LBS	75	89	0	0	89
NLUF	40	47	0	0	47
LANL	20	24	0	0	24
CEA	5	7	0	0	7
Total	435	480	31	198	251

Highlights of achievements in FY10 include the following:

OMEGA Three-Color-Cycle (3CC) Beam Smoothing

Three-color-cycle (3CC) smoothing by spectral dispersion (SSD) is shown to improve picket-pointing performance in simulations. In April, the OMEGA laser was returned to a 3CC-SSD configuration. For the last decade, OMEGA had operated in the 0.8-color-cycle (or terahertz) SSD configuration. The principal motivation for this action is that the three-color-cycle, 1/3-THz SSD system provides a readily available reduction in the dynamic SSD mispointing error (SSD mpe). SSD mpe became an important parameter when the drive pulse shapes for high-performance cryogenic implosions were converted from continuous foot pulses to discrete picket pulses for adiabat control. Since the ~100-ps pickets sample only a fraction of the full bandwidth, they are susceptible to a pointing deviation from the time-integrated far field. The 3CC-SSD system reduced the SSD mpe from ~40 nm to ~5 nm in the direction of the 10.4-GHz modulator. The system provides smoothing equivalent to the 1-THz, 2-D SSD system for ℓ modes < 200. The 3CC-SSD system uses less bandwidth and has the benefit of frequency converting more efficiently, providing improved power balance and greater available on-target energy.

OMEGA Pulse Shaping

OMEGA pulse-shaping capability continues to evolve to meet the demands of producing triple-picket-shaped pulses

for cryogenic experiments. Additional improvements to the Driver Electronics Room's temperature and humidity stability were implemented, significantly improving temporal pulse-shape stability. As a result, triple-picket pulse shapes now routinely achieve precision picket-pulse-shape requirements. Pulse-shape measurement diagnostics and analysis software continue to become more sophisticated to accurately predict picket energies and UV pulse shapes.

Efforts to facilitate on-target picket power balance resulted in significantly improved target-irradiation uniformity for cryogenic implosions. The P510 streak cameras were upgraded with new electronics to further improve pulse-shape measurement capability. Stage-F amplifier gain adjustments were routinely implemented for experiments to balance picket energies as measured by the enhanced P510 streak cameras. Prior to this effort, beam-to-beam picket-pulse energy performance was greater than 10%. Beam-to-beam picket-pulse energy performance of 5% or less is now routinely achieved.

To improve picket energy and pointing performance, the phase of the SSD modulators was synchronized to the system's radio frequency. Simulations indicate that this work will improve cryogenic pulse-shape performance and repeatability on target.

OMEGA Pulse-Shape Measurement Diagnostic

A new short-pulse timing diagnostic was deployed and calibrated on OMEGA EP. The pulse-shape measurement (PSM) diagnostic uses high-bandwidth oscilloscopes and photodiodes to measure short-pulse timing at the output of the grating compressor chamber (GCC). The PSM diagnostic is calibrated using target implosions on both OMEGA and OMEGA EP and is the primary diagnostic for routinely achieving short-pulse beam timings to within 50 ps on the first shot of the day. This diagnostic is also being employed to measure the drift sources of the OMEGA EP Laser System to understand and account for sources of error.

OMEGA Multilayer Dielectric Gratings

A full complement of 12 multilayer dielectric gratings was acquired from a commercial vendor to improve short-pulse energy performance on one of the OMEGA EP beamlines. These gratings followed a development effort and qualification testing of appropriate sub-aperture samples. Notable improvements were made to the production grating cleaning and vacuum-damage test protocols. The 12 compressor gratings were inserted into the GCC upper compressor in two batches: six in June in the first and second tiled-grating assemblies, and

the remaining six in the chamber vent at the end of the fiscal year. It is expected that the operational energy envelope of this compressor will be increased by ~50% to >1.5 kJ at 10 ps in the coming year.

Knowledge of the damage limits of currently available large-area diffraction gratings is being improved. A dedicated vacuum short-pulse damage facility has been developed and is being used to study multilayer dielectric gratings under use conditions to guide safe operational limits as well as improve grating-fabrication processes. Furthermore, an *in situ* grating-damage observation system (see **Grating Inspection System for Large-Scale Multilayer Dielectric Gratings for High-Energy Laser Systems**, p. 165) makes it possible to detect damage on the final gratings during operations.

OMEGA EP Focal-Spot Diagnostic

The accuracy of target-plane, on-shot focal-spot predictions using the OMEGA EP focal-spot diagnostic (FSD) has been improved. The FSD uses a wavefront measurement in the short-pulse diagnostics package to predict the target-plane fluence distribution. Phase-retrieval techniques have been implemented that produce a more reliably accurate wavefront measurement that in turn yields significantly more accurate focal-spot predictions (see **Improved On-Shot Focal-Spot Measurement on OMEGA EP Using Phase-Retrieval-Enhanced Wavefront Measurements**, p. 192). As a result, on-shot target-plane focal-spot fluence data are now provided post-shot for short-pulse shots on OMEGA EP (see Fig. 124.76). The improved FSD will

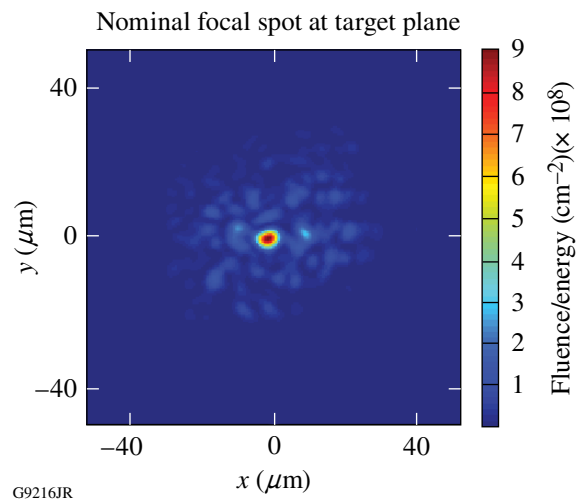


Figure 124.76
An example of an on-shot target-plane fluence measurement provided by the OMEGA EP focal-spot diagnostic on a short-pulse target shot.

play a central role in efforts to improve focal-spot repeatability and focusability.

OMEGA EP Contrast Diagnostic

Temporal contrast is now being measured in the short-pulse OMEGA EP beamlines using the high-contrast diagnostic suite (see Fig. 124.77). The on-shot contrast of short-pulse beams has been characterized using a set of calibrated fast photodiodes. This diagnostic is now operating on all high-energy shots, and nanosecond-contrast data are provided to the users. The nanosecond contrast is dominated by the parametric fluorescence from the front end that extends over a few nanoseconds, and the power of the associated pedestal is typically $10^6\times$ lower than the peak power. The contrast of the optical parametric chirped-pulse amplifier (OPCPA) front end propagating through the entire laser system has been measured using a high-resolution scanning nonlinear cross-correlator in a temporal window starting 700 ps before the main pulse. No significant discrete prepulse has been observed. These diagnostics have been used to study the contrast of OMEGA EP and support contrast-improvement campaigns. Contrast improvements have been realized by optimizing the wavelength of the seed source for the OPCPA pump, the timing between the pump and signal

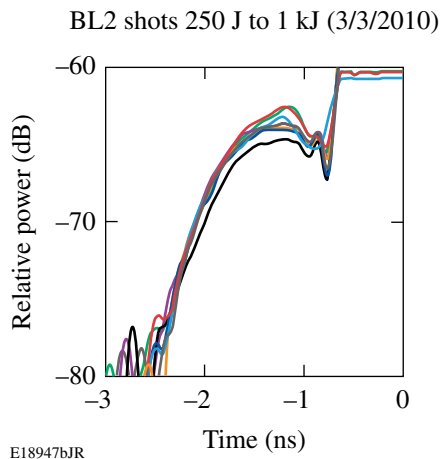


Figure 124.77
Nanosecond contrast data of shots taken on 3 March 2010. On-target contrast improvements have been measured with the high-contrast diagnostic suite.

in the OPCPA, and the nonlinear crystal configuration in the OPCPA front end. The contrast data are combined with data from the FSD to predict the on-shot intensity contrast of the pulse and the intensity of the nanosecond pedestal.

OMEGA EP Distributed Phase Plates

The first two distributed phase plates were deployed on OMEGA EP in November 2009. These UV phase plates produce 750- μm -diam focal spots and have been used extensively for experiments.

OMEGA EP Parabola Vacuum Antechambers

Vacuum antechambers for the backlighter and sidelighter off-axis parabolas (OAP's) were deployed on the OMEGA EP target chamber. These antechambers facilitate storage of the parabolas behind a protective gate valve when not in use. Access to the parabola for work such as optics replacements, installation/removal of the disposable debris shield in front of an OAP, and other maintenance no longer requires the OMEGA EP target chamber to be vented.

Experimental Diagnostics

Two new ten-inch manipulators were installed on the OMEGA EP target chamber, increasing our non-fixed diagnostic fielding capacity by 40%. A number of facility tools to better support the scientific user were implemented; for example, online availability of diagnostic documentation packages and diagnostic calibration data is now accessible by the user community.

Experimental capability evolved with the addition of 22 new diagnostics for use on OMEGA and 17 for OMEGA EP. Much of this activity involved other laboratories (e.g., LLNL, LANL, NRL, CEA, AWE), and included diagnostics such as the spherical crystal x-ray imager, electron-positron-proton spectrometers, neutron-detector test platforms for NIF diagnostics, and numerous x-ray spectrometers. Upgrades to existing diagnostic subsystems, such as the proton film pack, OMEGA high-resolution velocimeter, 4ω Thomson-scattering spectrometer, gamma reaction history diagnostic, and the DANTE x-ray diode array were also completed.

National Laser Users' Facility and External Users' Programs

Under the facility governance plan implemented in FY08 to formalize the scheduling of the Omega Laser Facility as an NNSA User Facility, Omega Facility shots are allocated by campaign. The majority (65%) of the FY10 target shots were allocated to the National Ignition Campaign (NIC) conducted by integrated teams from the national laboratories and LLE and to the high-energy-density campaigns conducted by teams led by scientists from the national laboratories.

In FY10, 30% of the facility shots were allocated to basic science experiments. Half of these were dedicated to university basic science under the National Laser Users' Facility (NLUF) Program, and the remaining shots were allotted to the Laboratory Basic Science (LBS) Program, comprising peer-reviewed basic science experiments conducted by the national laboratories and LLE/FSC.

The Omega Facility is also being used for several campaigns by teams from the Commissariat à l'énergie atomique (CEA) of France and the Atomic Weapons Establishment (AWE) of the United Kingdom. These programs are conducted on the facility on the basis of special agreements put in place by the DOE/NNSA and the participating institutions.

The facility users during this year included 11 collaborative teams participating in the NLUF Program; 12 teams led by LLNL and LLE scientists participating in the LBS Program; many collaborative teams from the national laboratories conducting experiments for the NIC; investigators from LLNL and LANL conducting experiments for high-energy-density physics programs; and scientists and engineers from CEA and AWE.

In this section, we briefly review all the external user activity on OMEGA during FY10.

FY10 NLUF Program

In FY10, DOE issued a solicitation for NLUF grants for the period of FY11–FY12. A total of 15 proposals were submitted to DOE for the NLUF FY11–12 program. An independent DOE Technical Evaluation Panel comprised of

Dr. Damien Hicks (LLNL), Prof. John K. McIver (University of Idaho), Dr. Gregory Rochau (SNL), Prof. Sharon Stephenson (Gettysburg College), Dr. Alan Wooton (University of Texas), Dr. Jonathan Workman (LANL), and Dr. John Soures (Committee Chair, non-voting) reviewed the proposals on 18 August 2010 and recommended that 11 proposals receive DOE funding and 31 days of shot time on OMEGA in each of FY11 and FY12. Table 124.V lists the successful NLUF proposals.

FY10 was the second of a two-year period of performance for the NLUF projects approved for the FY09–FY10 funding and OMEGA shots. Eleven NLUF projects were allotted Omega Facility shot time and conducted a total of 197 target shots on the facility. This work is summarized in this section.

Systematic Study of Fast-Electron Generation and Transport

Principal Investigator: F. N. Beg (University of California, San Diego)

Co-investigators: T. Yabuuchi, H. Sawada, and M. S. Wei (University of California, San Diego); R. B. Stephens (General Atomics); S. P. Regan, K. Anderson, C. Stoeckl, W. Theobald, and R. Betti (LLE); and P. K. Patel, A. J. Mackinnon, H. S. McLean, S. C. Wilks, and M. H. Key (LLNL)

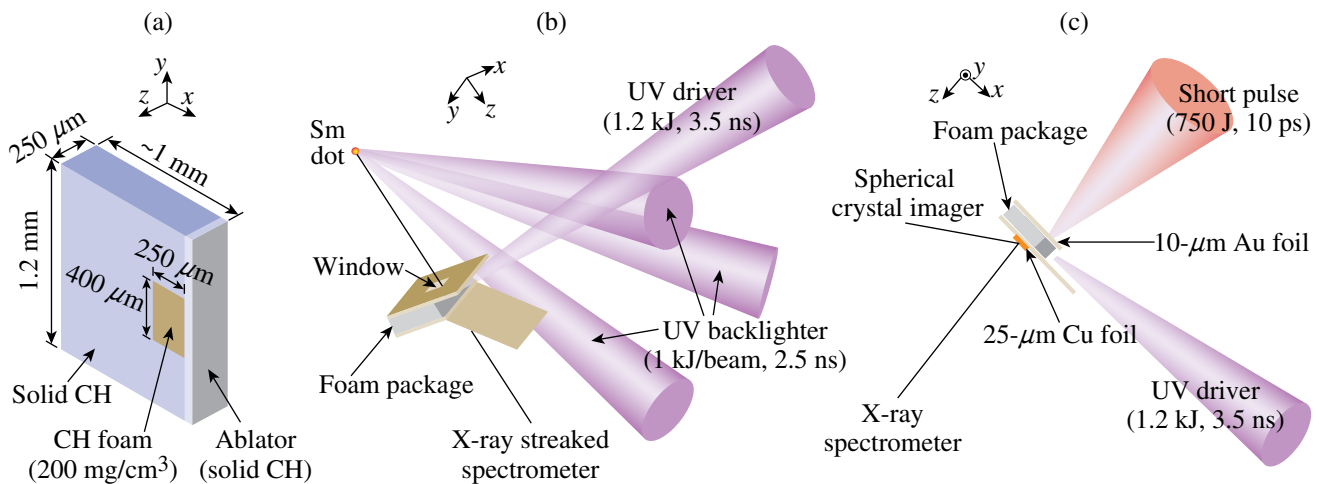
Understanding fast-electron generation and transport in the cone tip and warm dense plasma is very important for the success of the cone-guided fast ignition. We have performed two experiments in FY10 on OMEGA EP regarding this important topic. The goal of the first experiment was to characterize a plasma to be used as the transport medium in the second experiment, using the x-ray line absorption spectroscopy. The goal of the second experiment was to study the fast-electron transport in the characterized plasma. In both experiments, the warm dense plasma was created by using a shock to heat a foam target. The foam target package consisted of 200-mg/cm³ CH foam doped with aluminum inside a solid plastic container. The shock was created by irradiating a plastic foil in front of the foam with a long-pulse laser (1.2 kJ/3.5 ns in UV) as shown

in Fig. 124.78. A two-dimensional *DRACO* simulation shows that the foam plasma had a peak temperature (density) of 30 to 50 eV (110 to 180 mg/cc) at about 7 to 8 ns.

A laser-irradiated samarium dot target was used as the x-ray point source for the absorption spectroscopy. The x rays (1.4 to 1.6 keV) with a smooth, broad spectrum penetrated the foam

Table 124.V: Approved FY11 and FY12 NLUF proposals.

Principal Investigator	Affiliation	Project Title
F. Beg	University of California, San Diego	Systematic Study of Fast-Electron Transport in Imploded Plasmas
R. P. Drake	University of Michigan	Experimental Astrophysics on the OMEGA Laser
T. Duffy	Princeton University	Ramp Compression for Studying Equations of State, Phase Transitions, and Kinetics on OMEGA
R. Falcone	University of California, Berkeley	Detailed <i>In-Situ</i> Diagnostics of High-Z Shocks
P. Hartigan	Rice University	Clumpy Environments and Interacting Shock Waves: Realistic Laboratory Analogs of Astrophysical Flows
R. Jeanloz	University of California, Berkeley	Recreating Planetary Core Conditions on OMEGA
K. Krushelnick	University of Michigan	Intense Laser Interactions with Low-Density Plasma Using OMEGA EP
R. Mancini	University of Nevada, Reno	Investigation of Hydrodynamic Stability and Shock Dynamics in OMEGA Direct-Drive Implosions Using Spectrally Resolved Imaging
R. D. Petrasso	Massachusetts Institute of Technology	Charged-Particle Probing of Inertial Confinement Fusion Implosions and High-Energy-Density Plasmas
A. Spitkovsky	Princeton University	Collisionless Shocks Laboratory High-Energy-Density Plasmas
R. Stephens	General Atomics	Investigation of Laser-to-Electron Energy Coupling Dependence on Laser-Pulse Duration and Material Composition



U1124JR

Figure 124.78

(a) Schematic of the foam package target. Au foils coated with plastic on both sides were used for both experiments as seen in the experimental setup for (b) plasma characterization and (c) fast-electron transport. The foils on the target-side faces had a hole to transmit backlighter x rays for the characterization experiments. The holes were covered with Au and Cu foils in the transport experiment.

plasma through small windows on the target walls and were absorbed by aluminum atoms doped in the foam target. The line-absorption features in the spectra depend on the density and the temperature of the plasma. Figure 124.79 shows a temporal evolution of the absorbed spectra recorded with an x-ray streaked spectrometer. Preliminary analysis of the temperature of the foam using an atomic physics code *FLYCHK* indicates that the plasma temperature was about 30 eV at 7 ns after the start of the long-pulse–laser irradiation. The presence of the lower-charge-state (i.e., O-like and F-like) features later in time indicates a clear trend of the plasma cooling in time.

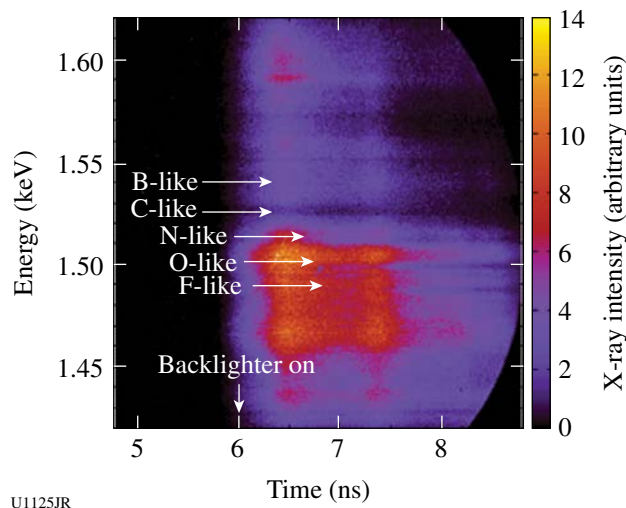


Figure 124.79

Streaked x-ray spectrum observed with Al-doped CH foam target driven by a 1.2-kJ, 3.5-ns UV long-pulse laser. Several Al absorption lines can be seen as indicated by arrows.

An OMEGA EP short-pulse laser irradiated the driven foam target at 7 ns in the transport study. The windows on the sides of the package targets were covered with Au (10- μm) and Cu (25- μm) foils. The Au foil served as the laser–plasma interaction layer, and the Cu foil served as a fluorescence layer of K_{α} x rays emitted by the binary collisions of fast electrons and the Cu atoms. The K_{α} x rays were monitored with an x-ray spectrometer and a newly developed spherical crystal imager. The transport medium was varied from the laser-driven foam plasma to undriven foam and a solid plastic, which had the same areal density as the undriven foam. As shown in Fig 124.80, a small spot of K_{α} x rays was observed with cold targets; however, no clear structure was found in the case where the foam plasma was the transport medium, which indicates a large divergence of the electron beam. In addition, a reduction of the K_{α} x-ray yield by a factor of 20 was measured when the target was driven. The physical mechanisms contributing to a large divergence angle

and low transport efficiency with the driven-foam target will be studied with hybrid particle-in-cell (PIC) codes.

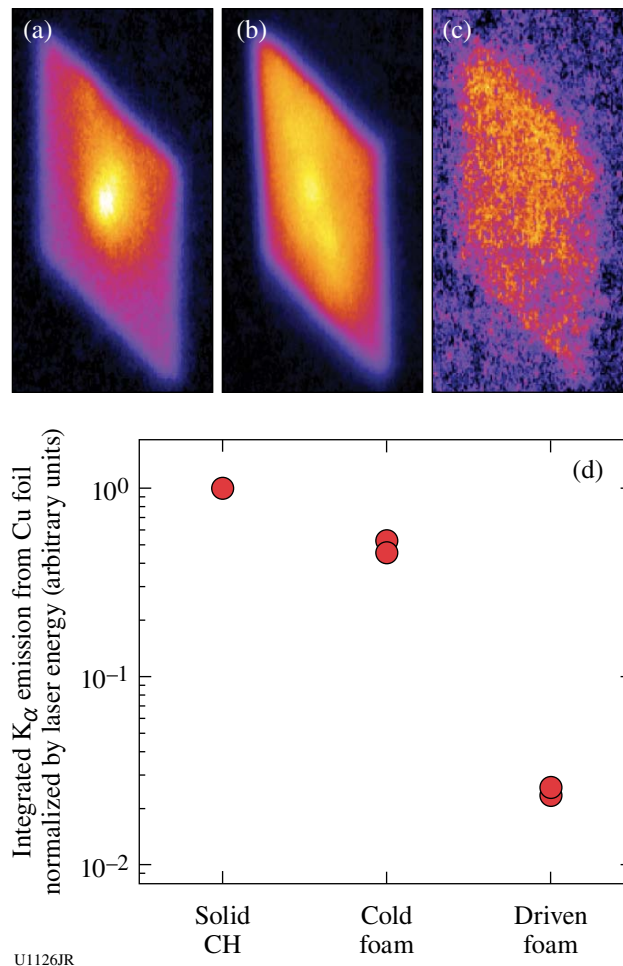


Figure 124.80

Cu K_{α} images observed with a spherical crystal imager when the transport medium was (a) 50 μm of solid CH, (b) 250 μm of cold foam, and (c) 360 μm of driven foam. (d) Integrated K_{α} x-ray yield measured with the x-ray spectrometer for three cases.

Experimental Astrophysics on the OMEGA Laser

Principal Investigator: R. P. Drake (University of Michigan)
 Co-investigators: D. Arnett (University of Arizona); T. Plewa (Florida State University); J. Glimm, D. Swesty, X. Li, and A. Calder (State University of New York–Stony Brook); I. Sokolov, J. Holloway, K. Powell, and C. Kuranz (University of Michigan); J. P. Knauer and T. R. Boehly (LLE); and B. Remington, H. Robey, F. Hansen, A. Miles, S. Glenzer, and H.-S. Park (LLNL)

The OMEGA laser can create systems with very high energy densities that are relevant to astrophysical phenomena.

This is possible because OMEGA can deposit large amounts of energy into areas measuring square millimeters, generating pressures of greater than 10 Mbars (~10-million atmospheres). In some astrophysical systems, radiation can play a dominant role in the hydrodynamic behavior of the system. This occurs, for example, in radiative shocks in which the shocked matter is so hot that it radiates away most of its energy. This project has explored two types of radiative shocks—a driven radiative shock and a radiative reverse shock. These types of shocks can be found in supernova remnants, where a fast-moving shock encounters a low-density gas, and cataclysmic variables, where a supersonic plasma flow is impeded by a dense accretion disk.

In March 2010, a campaign was continued using the OMEGA laser to create a driven radiative shock in a xenon-filled shock tube. Ten OMEGA laser beams irradiated a Be disk for 1 ns. The beams deposited a total energy of ~3.8 kJ, giving an average irradiance of $\sim 7 \times 10^{14}$ W/cm² and generating an ablation pressure of ~46 Mbars in the disk. The Be acts as a piston to drive a shock in 1.1 atm of Xe with speeds in excess of 100 km/s. This velocity exceeds the threshold where radiative effects play an important role in the dynamics of the experiment. The cooling by escaping radiation creates a collapsed dense layer of xenon, which is preceded in the tube by a radiation-heated precursor region and followed by a downstream layer of expanding Be.

The most-recent efforts to diagnose a driven radiative shock employed the streaked x-ray radiography and x-ray Thomson scattering (XRTS) diagnostic techniques simultaneously to differentiate measurements from the different regions of the shock system. For each region, x-ray Thomson scattering may provide information on electron temperature and ionization state, while streaked radiography yields shock velocity and acceleration. Example streak camera and XRTS data are shown in Figs. 124.81 and 124.82. Figure 124.81 shows a streaked x-ray radiograph indicating the distance of the shocked layer from the drive disk versus time. The fiducial wire is seen in the lower part of the image, and the sloped line moving from the left to the upper right indicates the motion of the shocked Xe layer. Figure 124.82 is a plot of intensity versus energy obtained using the XRTS technique. For this experiment, a Zn source with He_α emission near 9 keV was used to probe the dense, shocked Xe layer. The incident signal is represented by the black curve, and scattered light from free and loosely bound electrons is represented by the blue curve.

A second type of radiative shock that this project has explored is a radiative reverse shock. The first experimental

attempt at creating this type of shock took place in August 2010. In this experiment, ten OMEGA laser beams irradiated a plastic-coated tin disk for 1 ns. The beams deposited a total

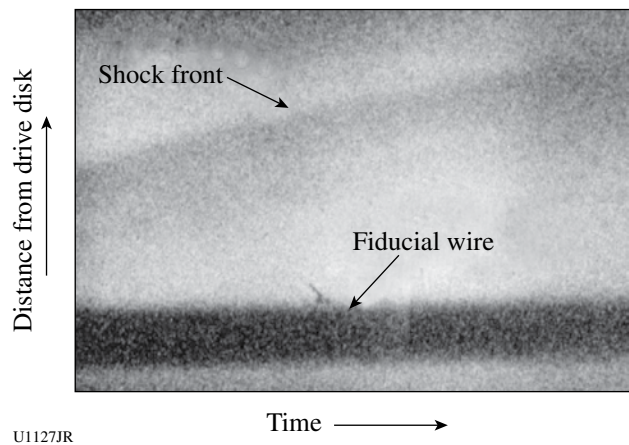


Figure 124.81

A streaked x-ray radiograph of a dense Xe layer, which provides a measure of shock velocity and acceleration. The shock is moving to the upper right in this image. An opaque wire was used to calibrate the spatial scale and determine the position of the shock at the time of imaging, while streak camera timing fiducials (not shown) calibrate the temporal scale.

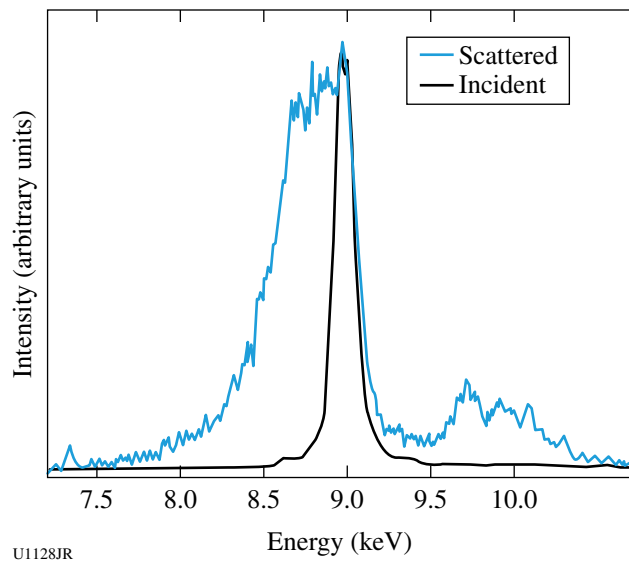
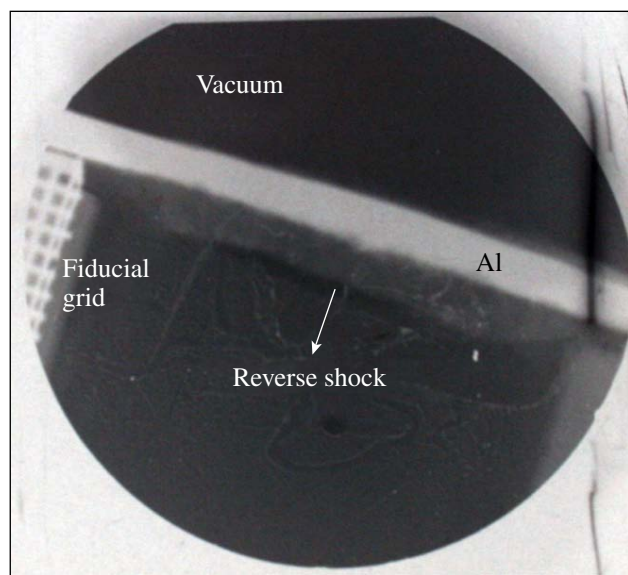


Figure 124.82

Incident and scattered spectra from March 2010 OMEGA experiments. A zinc source with He_α emission near 9 keV is used to interrogate the dense, shock-compressed Xe layer (black curve). Inelastic collisions with free and loosely bound electrons red-shift the input signal, generating the Compton feature seen below 9 keV (blue curve, normalized to match input curve's peak intensity).

energy of ~ 4.5 kJ, giving an average irradiance of $\sim 10^{15}$ W/cm². This creates a fast (greater than ~ 100 km/s) tin plasma flow through a millimeter-scale shock tube that is at vacuum. This supersonic plasma flow was impeded by a $100\text{-}\mu\text{m}$ Al “wall,” which would create a reverse shock. This shock was imaged using x-ray radiography, and self-emission from the radiative shock was recorded using a streaked optical pyrometer (SOP).

Figure 124.83 is an x-ray radiograph of a radiative reverse shock. The Al wall is labeled in the image, and the Sn plasma flow originates about 4 mm from the wall from the lower-left direction. Figure 124.84 shows data from the SOP, which captured about 100 ns of data. The directions of space and time are labeled on the image and the approximate location of the Al wall is also labeled. When the supersonic plasma flow collides with the Al, a reverse shock forms, but a strong transmitted shock is created in the Al; both are indicated in Fig. 124.84.

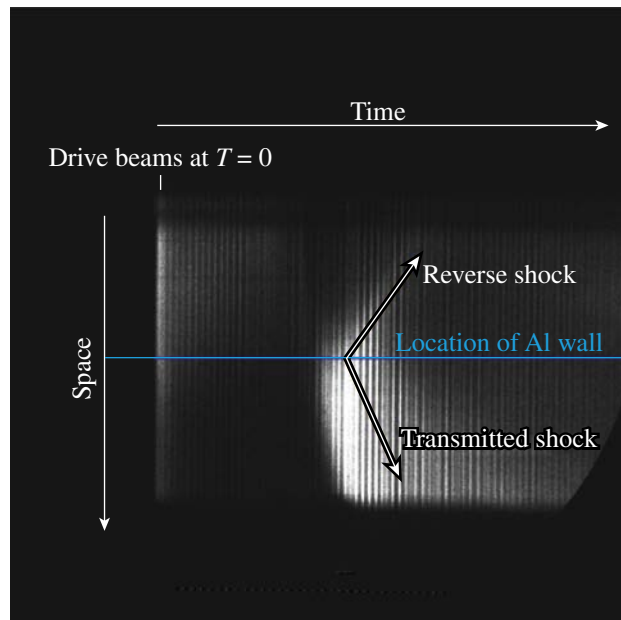


U1129JR

Figure 124.83
An x-ray radiograph of a radiative reverse shock. The Al wall is labeled in the image, and the Sn plasma flow originates about 4 mm from the wall from the lower left direction. The radiative reverse shock is moving away from the wall to the lower left.

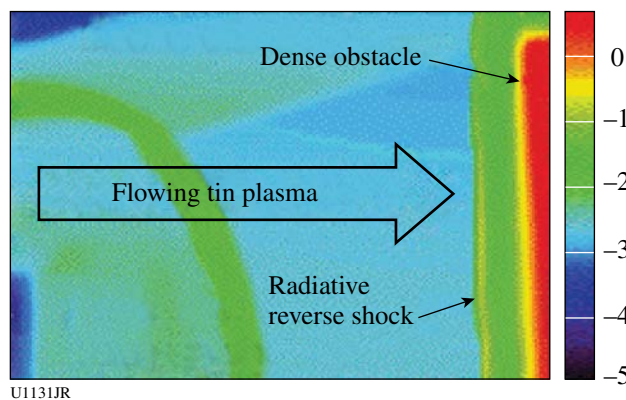
This experiment was modeled using the *CRASH* code. The *CRASH* code is a multidimensional physics code that has been developed at the University of Michigan’s Center for Radiative Shock Hydrodynamics. The density plots shown in Fig. 124.85 are simulation results from the *CRASH* code, and the laser-energy deposition was modeled using the

2-D *HYADES* code and then used to initialize the *CRASH* simulation. Figure 124.85 shows the direction of the incoming plasma flow (to the right); the Al wall is the dense obstacle in this case. The radiative reverse shock is a thin, dense layer that is moving to the left of the Al.



U1130JR

Figure 124.84
Thermal emission data over 100 ns from a streaked optical pyrometer of a radiative reverse shock. The approximate temporal location of the initial laser pulse is labeled as well as the approximate spatial location of the Al wall. Emission from reverse shock shows the shock moving away from the Al wall.



U1131JR

Figure 124.85
Results from a *CRASH* simulation of a radiative reverse shock system. The Sn plasma flow is moving to the right and collides with the dense Al. This creates a thin, dense radiative reverse shock moving to the left.

Detailed In-Situ Diagnostics of Multiple Shocks

Principal Investigator: R. W. Falcone (University of California, Berkeley)

Co-investigators: T. Ma, T. Doepfner, O. L. Landen, and S. H. Glenzer (LLNL); and H. J. Lee (SLAC Stanford Linear Accelerator Laboratory)

X-ray Thomson scattering was used to directly provide the temperature and density of shock-compressed matter.¹ Accurate characterization of dense states of matter is vital for understanding high-energy-density experiments, as well as the validation of equation of state (EOS) and plasma model assumptions. In this experiment, 250- μm Al and Be foils were shock compressed in a counter-propagating geometry using 12 drive beams with a total energy of 6 kJ at 351 nm in a 3-ns pulse. SG4 distributed phase plates were used to achieve a

smooth 800- μm focal spot, yielding a total drive intensity of $\sim 2 \times 10^{14}$ W/cm² on each side of the foil sample.

The shocked samples were probed at 140° scattering angles and varying delay times by Zn K_{α} x rays, at 8.6 keV (in the case of the Be foil), or Mo He_{α} x rays at 18.9 keV (in the case of the shocked Al foil). For both samples, the noncollective scattering regime was accessed, where $\alpha = 0.3$, $k = 8.2 \text{ \AA}^{-1}$, and $\alpha = 0.1$, $k = 17.1 \text{ \AA}^{-1}$ for the Be and the Al, respectively. The prominent Compton feature with elastic peak responding to Mo He_{α} in Fig. 124.86(b) demonstrates the feasibility as a backlighter for probing Al, the highest-Z material probed to date. The increase in the strength of the Compton feature with time as seen in Fig. 124.86(c) shows that the electron density changes with shock propagation.² The Compton feature at each time of 2.37 ns, 2.85 ns, and 3.83 ns presents the response of compressed state before, during, and

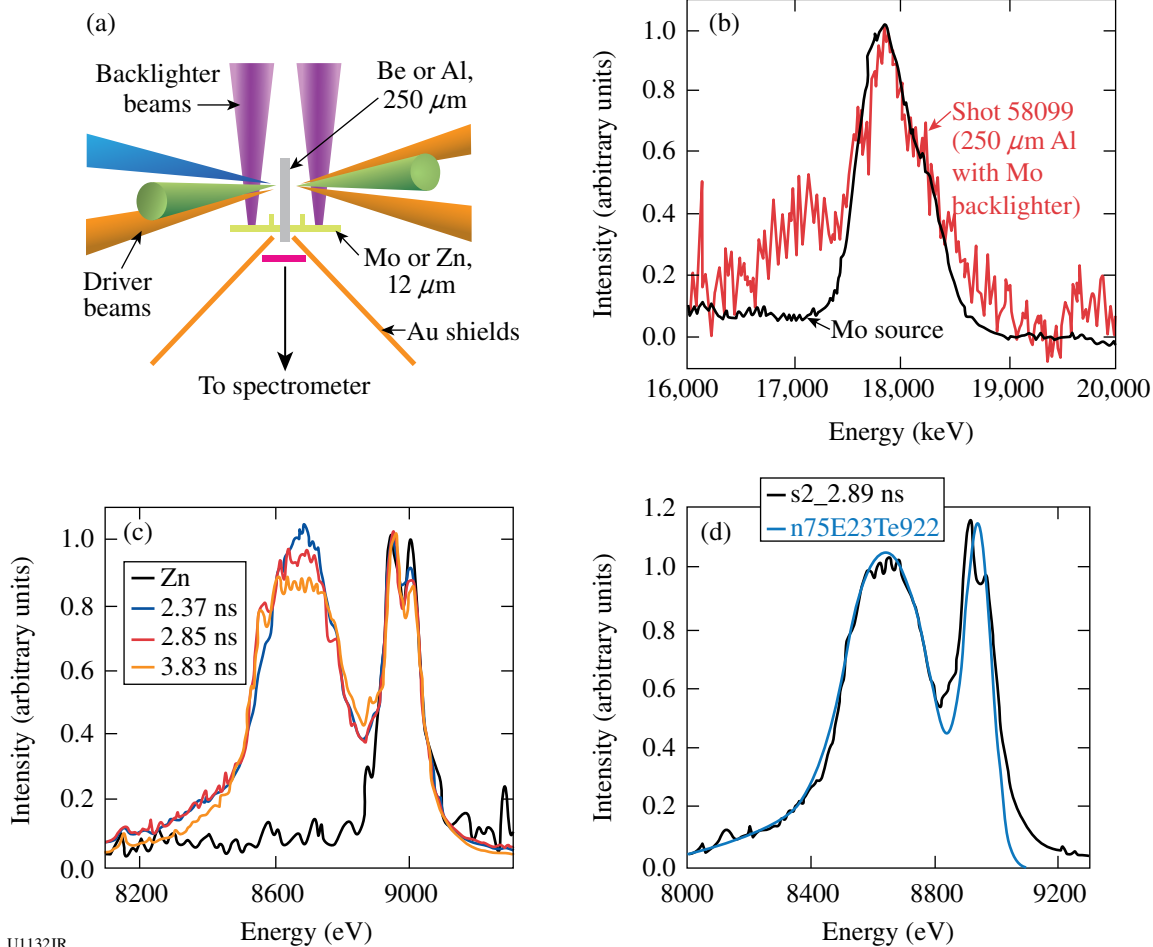


Figure 124.86

(a) Experimental configuration; (b) Mo He_{α} backlighter and scattering spectrum in compressed Al; (c) Zn K_{α} backlighter and scattering spectrum on shock-compressed Be at 2.37, 2.85, and 3.83 ns; and (d) scattering data for compressed Be and fit at 2.89 ns.

after the collision of counter-propagating shocks. A theoretical fit to the spectra at 2.89 ns in Fig. 124.86(d) allows one to infer the temperature, electron density, and ionization state. Analysis is ongoing to develop a more complete picture of the density and temperature of shock-compressed matter by counter-propagating shocks, which will address the radiation–hydrodynamic models.

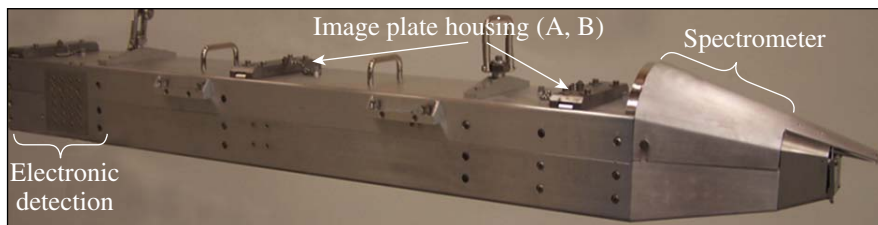
OMEGA EP–Generated X-Ray Source for High-Resolution 100- to 200-keV Point-Projection Radiography

Principle Investigator: U. Feldman (Artep Inc.)

The first-year goal of this project was to design and construct a ten-inch manipulator (TIM)–compatible OMEGA EP transmission crystal spectrometer (TCS) capable of measuring the size of the target region from which energetic (20- to 100-keV) photons produced by fast electrons are being emitted. The recording media, which could be located at distances of 20, 40, and 60 in. from target center, were designed to be image plates. During the first part of 2009, the TCS was designed and constructed (Fig. 124.87), and on 26–27 August it recorded spectra from a number of OMEGA EP shots. The recorded spectral lines indicated that, although the OMEGA EP beams were tightly focused (30 to 40 μm), the diameter of the area from which the hard x rays were emitted (a measure of the spread of the hot electrons) was 350 to 400 μm .

Our goal for the second year was to replace the image plate at the 60-in. location, which has pixel sizes of 100 μm or larger, with an electronic detector with pixel sizes of the order of ~ 25 μm . In early July 2010, the TCS was delivered to LLE, where it was mechanically and electronically checked by the LLE technical staff and Artep team members. On 15 September, the TCS was installed in the OMEGA EP chamber and recorded spectra from several specially designed targets.

The September experiments provided high-quality x-ray spectra on the TCS image-plate (IP) channels. Sample spectra from IP positions A [on the Rowland circle (RC)—focusing] and B (500 mm off the RC—source size broadened) are shown on Fig. 124.88. With careful analysis, the x-ray source size can be determined from the source-size–broadened spectrum (IP B).



U1133JR

Validating Inelastic X-Ray Scattering from H and H/He Warm Dense Matter with Shock-Velocity Measurements: Toward the Equation of State of Jupiter's Core

Principal Investigator: S. P. Regan (LLE)

Co-investigators: T. R. Boehly and P. B. Radha (LLE); and G. Gregori (Oxford)

The objective of this experiment is to measure the equation of state (P , ρ , n_e , T_e , Z) of direct-drive, shock-heated and compressed, planar cryogenic H and H/He mixtures using spectrally resolved x-ray scattering (i.e., inelastic x-ray scattering) and shock-velocity measurements on the OMEGA Laser System. The dynamics at the shock front and the plasma conditions in the bulk of the shocked material will be probed simultaneously with complementary diagnostics: the electron density (n_e) will be inferred from collective inelastic x-ray scattering (i.e., scattering from electron-plasma waves or plasmons);³ the electron temperature (T_e) and average ionization (Z) will be inferred from the noncollective x-ray scattering (i.e., scattering from individual electrons);^{1,4} and the pressure (P) and mass density (ρ) will be inferred from the velocity interferometer system for any reflector (VISAR) diagnostic.⁵ Equation-of-state (EOS) measurements typically diagnose the shock velocity (U_s) using the VISAR diagnostic and infer the particle velocity (U_p) by an impedance-matching analysis.⁶ The quantities U_s and U_p are related to P and ρ through the Rankine–Hugoniot relations.^{7–9} The ablation pressure inferred from the VISAR observation is critical for the EOS measurement. On the first LBS project shot day in FY10, the U_s in liquid D_2 irradiated for 6 ns with an intensity around 10^{13} W/cm^2 was measured with VISAR. The result is shown in Fig. 124.89 with the laser irradiation starting at $t = 0$ ns. Ionization of the CH ablator blocks the VISAR laser signal from the reflective, advancing shock front for the first 1.5 ns. The shock velocity in the time interval between 4 and 6 ns, when x-ray scattering measurements are typically performed, is 18 $\mu\text{m}/\text{ns}$. Using the U_s – U_p relation for shocked D_2 reported by Hicks *et al.*,⁶ a pressure of 0.4 Mbar and four-fold compression were inferred. Figure 124.90 presents measurements of the noncollective inelastic x-ray scattering from a liquid-deuterium target irradiated with a similar laser drive on the second

Figure 124.87

The transmission crystal spectrometer (TCS) with an electronic detector.

shot day of the experiment. Analysis is in progress to infer the shocked conditions from the VISAR and inelastic x-ray scattering measurements. The warm dense matter created in these experiments with laser-ablation-driven shock waves had plasma conditions comparable to those predicted in planetary interiors (i.e., dense, Fermi-degenerate matter). While Jupiter is mostly made of hydrogen, with only a fraction of He (<25%) and a few metals,^{10–16} the concentrations of other giant planets in the solar system are significantly enriched with C, O, and N. These form the so-called “ices” that are typical of the giant planets, such as Uranus and Neptune, and possibly extrasolar planets, such as GJ436b.^{17–19}

Development of a Platform for Laser-Ramp Compression of Planetary Materials on OMEGA

Principal Investigators: Y. M. Gupta (Washington State University) and T. S. Duffy (Princeton University)

Co-investigators: J. Montoya, J. Wang, and G. Finkelstein (Princeton University); R. F. Smith, J. H. Eggert, P. M. Celliers, D. Braun, and M. Bastea (LLNL); and T. R. Boehly (LLE)

This experiment was allocated 1.5 shot days on OMEGA in FY10 to develop a high-pressure, low-temperature ramp-compression drive, which permits one to explore new regions of thermodynamic space of particular relevance to material

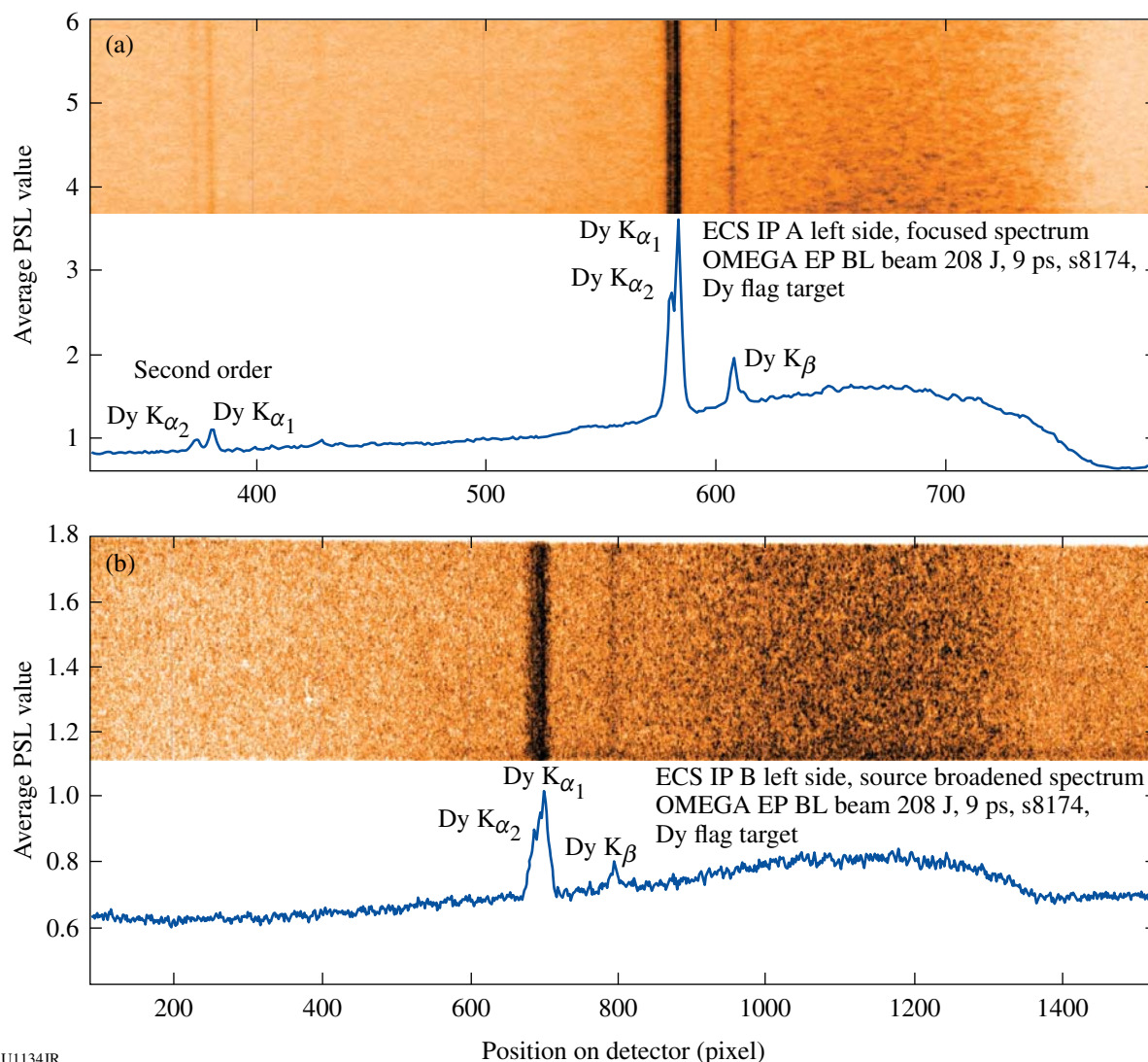
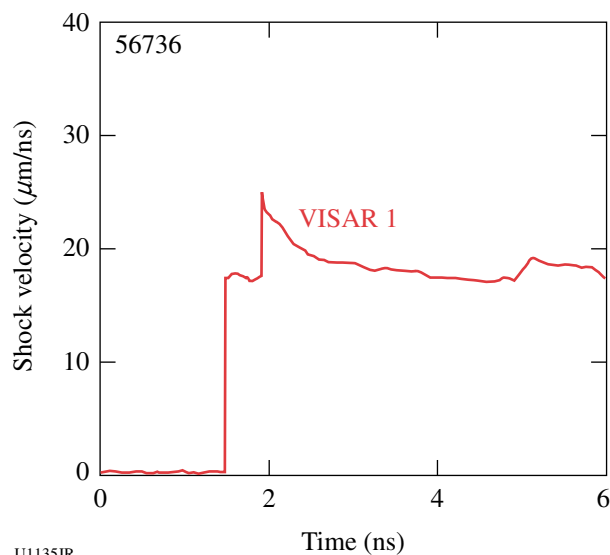


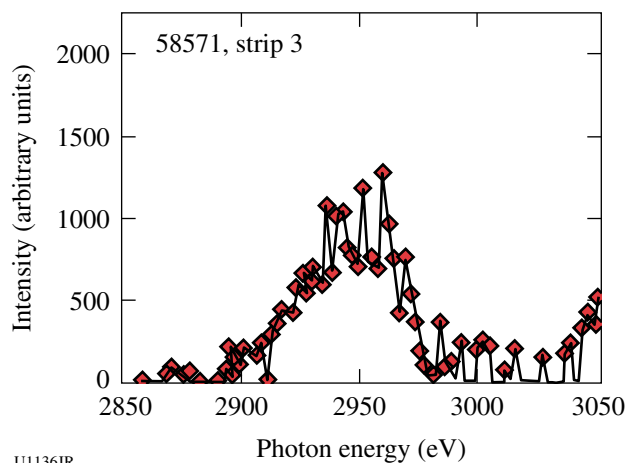
Figure 124.88 Sample spectra of the TCS taken on OMEGA EP from campaign PPRad-EP-10. Spectral images and column averages showing characteristic Dy K lines (K_{α_1} : 45.99 keV). (a) Lines in first and second order on IP A on the focusing Rowland circle and (b) IP B providing source size broadening of the spectral lines at a 500-mm distance from the focusing Rowland circle position.



U1135JR

Figure 124.89

Shock-velocity measurement taken on OMEGA shot 56736 with VISAR of a liquid-D₂ target irradiated for 6 ns with an intensity around 10^{13} W/cm² starting at $t = 0$ ns. Ionization of the CH ablator interrupts the VISAR laser signal for the first 1.5 ns. The average shock velocity in the time interval when x-ray scattering measurements are performed ($4 \text{ ns} < t < 6 \text{ ns}$) is $18 \mu\text{m/ns}$.



U1136JR

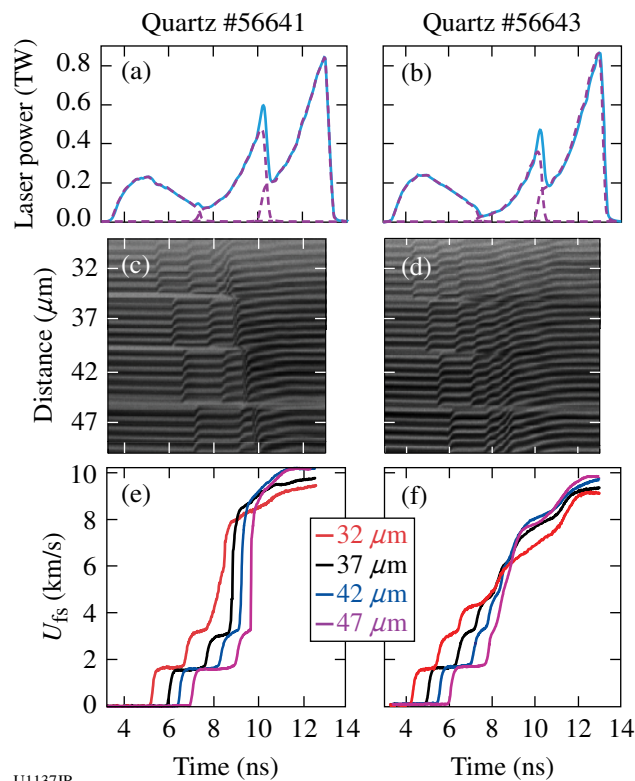
Figure 124.90

Inelastic x-ray scattering measurement taken on OMEGA shot 58571 of a liquid-D₂ target irradiated for 6 ns with an intensity around 10^{13} W/cm² starting at $t = 0$ ns. Observation was recorded at $t = 6$ ns. Analysis to infer shocked conditions in liquid D₂ is in progress.

conditions found in planetary interiors. Ramp compression achieves high compression at relatively modest temperatures and can be used to extract quasi-isentropic equation-of-state data, study solid–solid phase transitions, and compress materials in the solid state to higher pressures than can be achieved with diamond-anvil-cell (DAC) or shock-wave methods. An experimental platform for ramp loading of quartz (SiO₂) and

iron (Fe) has been established and tested in experiments at the Omega Laser Facility. Target packages consist of stepped samples and a diamond ablator attached to a Au halfraum. Composite laser pulses are used to drive a ramp-compression wave into the sample. The target and laser-ramp designs have been tested and optimized by combining experiments with computer simulations using a hydrodynamics code. A spatially planar ($\Delta t/t = 0.9\%$) ramp wave drive has been achieved in both SiO₂ and Fe stepped samples to peak stress around 250 GPa and 400 GPa, respectively, over nanosecond time scales.

Figure 124.91 shows the input laser profile, VISAR streak camera records, and corresponding free-surface velocity histories for two typical quartz experiments. The extracted free-surface velocity histories in Figs. 124.91(e,f) show a very structured breakout with a series of ramped “plateaus” consistent with drops in the bulk sound speed caused by the onset of



U1137JR

Figure 124.91

(a) and (b) Laser pulse for two representative quartz shots (56641 and 56643). The dashed lines show the individual pulses and the solid line is the composition pulse shape. (c) and (d) Line VISAR streak camera images (1.971 km/s per fringe) from ramp-compressed multi-stepped quartz targets (56641 and 56643) corresponding to (a) and (b), respectively. In (c) and (d), different step thicknesses are indicated. (e) and (f) Extracted free-surface velocity profiles from (c) and (d), respectively.

elastic-plastic deformation or a polymorphic phase transformation. The input laser profile was designed to generate an initial steady shock in quartz followed by subsequent ramp compression. An unusual feature of these profiles is the convergence of wave-arrival times for multiple steps in the 7- to 9-ns range (Fig. 124.91). It is believed that this feature is an artifact of the complicated wave interactions between free-surface reflections that combined with the onset of a phase transformation. In future experiments, the use of a lithium fluoride (LiF) window may suppress the effects of interactions. Figure 124.92 shows a sequence of measured pulses and the corresponding wave profiles for the first target step in Fe samples for several differ-

ent shots. By changing the time delay between the two pulses, it was possible to decrease the amplitude of the second shock and achieve a more ramp-like compression. However, it was not possible to completely eliminate the second shock (shots 58591 to 58593). Keeping the same delay, but increasing the power in the second pulse strongly increased the amplitude of the second shock (shot 58594). Figure 124.93 shows preliminary pressure-density curves for Fe and SiO₂ calculated with standard Lagrangian sound speed analysis. The complexity of the wave interactions caused some discrepancies among different shots. Further work will focus on the development of new analytical tools to analyze ramp-compression data for

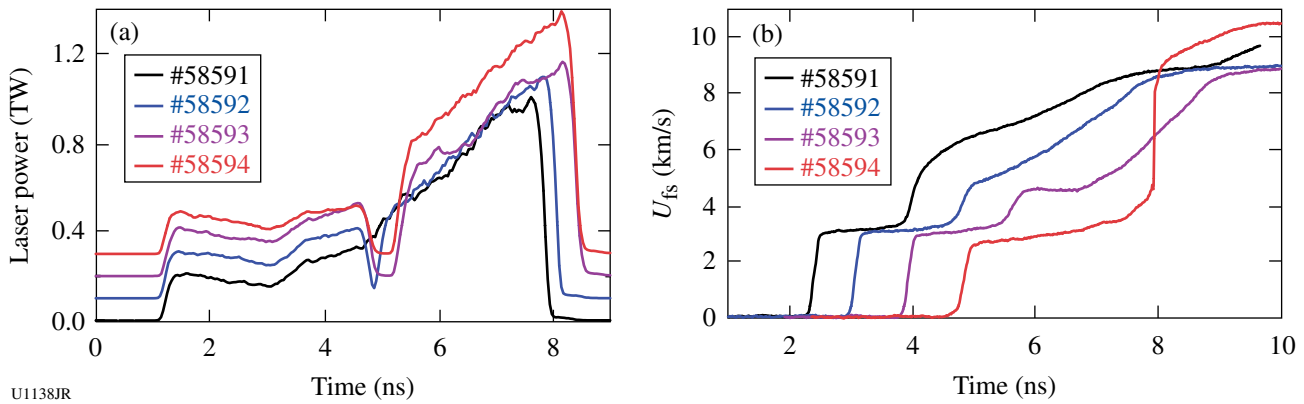


Figure 124.92

(a) Composite laser pulse shapes from a series of shots on Fe targets along with free-surface velocity profiles for the first step corresponding to each laser drive. (b) Shots 58591 to 58593 correspond to delays between the pulses of 3.5 ns, 3.65 ns, and 3.88 ns. For shot 58594, the delay was maintained the same (3.88 ns), but the power was increased. In (a), the traces are offset in amplitude (by 0.1 TW) for clarity, and the traces are offset temporally in (b).

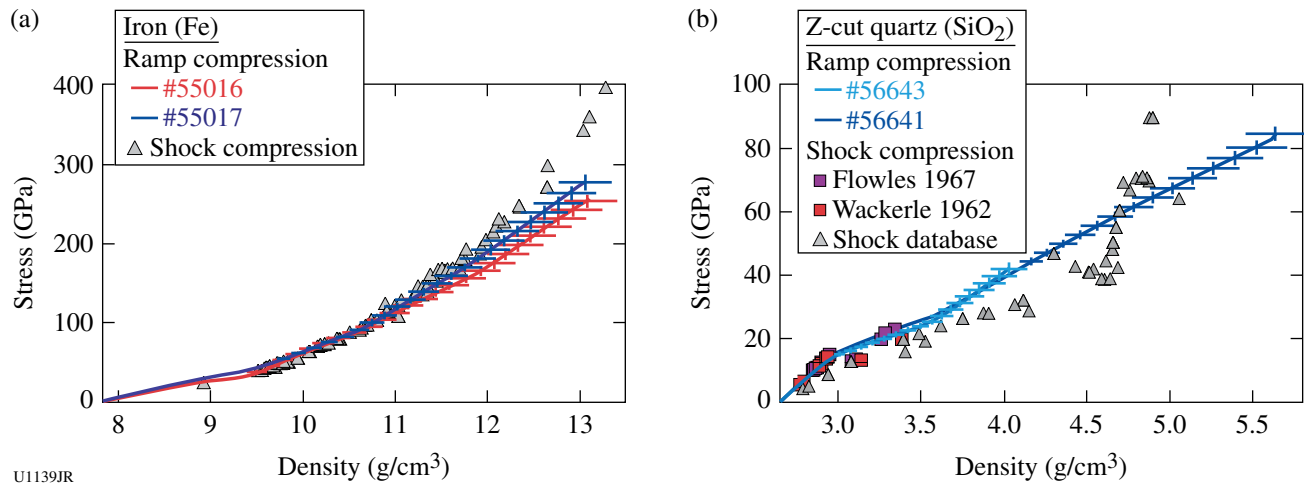


Figure 124.93

Preliminary pressure-density curves for Fe and SiO₂ calculated with standard iterative-characteristic Lagrangian sound speed analysis developed by Rothman. (a) Data are shown for two separate shots taken during an NLUF shot day on 23 July 2009. Also shown are previous data taken from shock experiments. (b) Data are shown for two different shots taken during an NLUF shot day on 20 January 2010, and shock data are shown from previous studies.

materials undergoing time-dependent compression, including treating the initial shock and phase transformation.

Laboratory Experiments of Supersonic Astrophysical Flows Interacting with Clumpy Environments

Principal Investigator: P. Hartigan (Rice University)

Co-investigators: J. Palmer (Rice University); J. Foster and P. Rosen (AWE); B. Wilde and M. Douglas (LANL); A. Frank (University of Rochester); and B. E. Blue and F. Hansen (General Atomics)

A primary goal of the NLUF program is to study how strong shock waves propagate through clumpy media such as those encountered by astrophysical jets as they interact with their nascent molecular clouds. In the current program, an experimental design was developed that allows one to observe a strong shock as it sweeps past a collection of obstacles in its path. The laboratory work complements new astrophysical images from the Hubble Space Telescope (HST) that were taken as part of a previous NLUF program.

Samples of some of the shots and numerical simulations of the experiments from the last year appear in Fig. 124.94. The target consists of cylindrical foam into which are embedded anywhere from a few to several dozen sapphire spheres. A database is being accumulated that will answer the question of how the packing fraction and clump size within the obstacle affect the propagation speed and coherence of the strong shock wave that is driven through the foam. Numerical support is provided by the *RAGE* code (see Fig. 124.94). The experiments provide important tests of the code in a complex regime that is inherently 3-D and includes multiple shocks and mixing of post-shock material. The experiments reveal dynamical changes that occur when one sphere lies in the wake of another, and they expand on previous work with two spheres, where it was learned how a planar shock creates vorticity as it interacts with the spheres.

This ongoing NLUF work is producing a series of publications in the primary refereed journals of the field, and numerous contributed and invited talks have been given at recent conferences. In 2009, this OMEGA collaboration published a large paper in the *Astrophysical Journal*,²⁰ and another paper was just accepted into *Physics of Plasmas* related to Mach stem work.²¹ This latter paper is now motivating a new line of research that the group plans to pursue in the next two years. Another large *Astrophysical Journal* paper nearing completion concerns motions within shocked jets; a paper on the vorticity between two shocked spheres is in preparation; and our current set of shot data will produce a thorough study of shocked

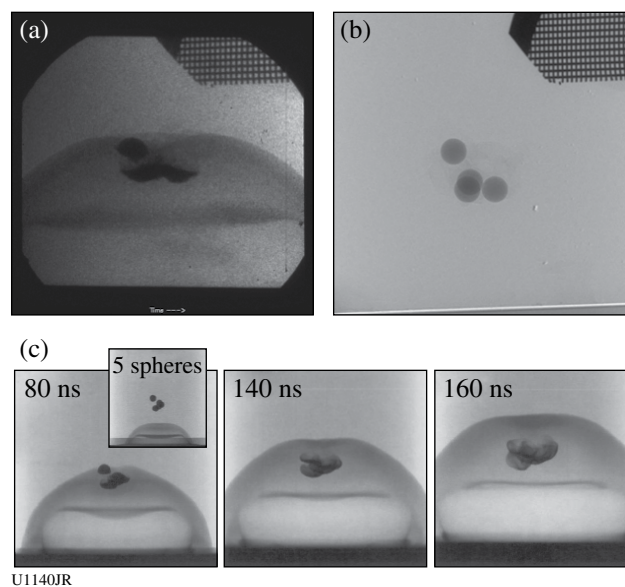


Figure 124.94

(a) Shot data (taken at 100 ns) and (b) pre-shot radiograph of a target containing four spheres. The shock wave moves upward and has just overtaken the spheres, flattening and distorting them. (c) Time-sequence numerical simulation (from *RAGE*) of a target with five spheres. A filamentary structure develops as bow shocks around each sphere interact and shadow one another. This filamentary structure resembles features we observe in the working surfaces of astrophysical jets.

clump phenomena. Student participation includes two recent Ph.D.'s (one of whom will be taking up a position at a national lab) and an M.S. thesis in its final stage.

Measurements of the Equation of State of H_2/He Mixtures Under Deep Planetary Conditions

Principal Investigator: R. Jeanloz (University of California, Berkeley)

Co-investigators: P. Loubeyre (CEA); J. H. Eggert, D. G. Hicks, P. Celliers, and G. W. Collins (LLNL); and T. R. Boehly (LLE)

Using the Omega Laser Facility, this project is demonstrating that laboratory experiments can provide crucial data to model the interior structure of the planets. Specifically, measuring the equation of state of planetary constituents is complementary to space missions for understanding the interiors and evolution of giant fluid planets. The immediate goal of these experiments is to measure the equation of state of hydrogen and helium warm dense fluids, and to quantify the miscibility gap in hydrogen/helium mixtures. The experiment is based on the generation of a laser shock in a precompressed sample. The precompressed target offers two new opportunities over the usual cryogenic targets: mixtures of H_2/He can be studied, whereas they phase-separate in a cryogenic target; the initial density of the mixture

can be significantly increased. Measurements on He, H₂, and H₂/He samples have been performed up to precompressions of 1.5 GPa. The Hugoniot data on helium have been published.^{7,22} The Hugoniot data on H₂ and D₂ have been recently measured, and their analysis is being finalized for publication (Fig. 124.95).

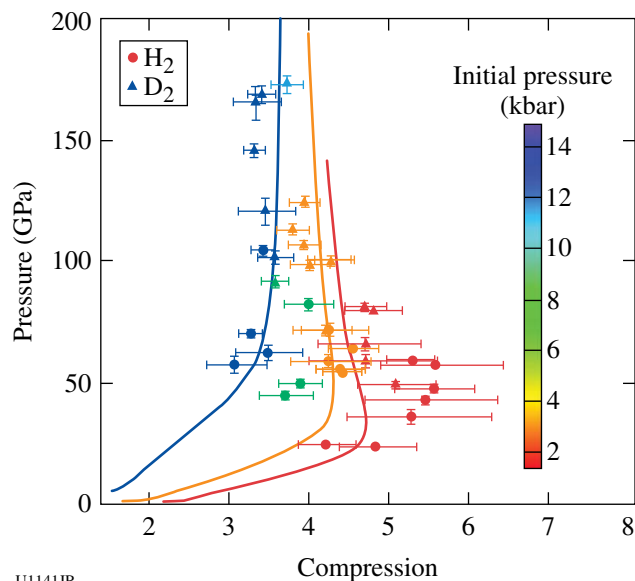


Figure 124.95

Summary of Hugoniot measurements collected at Omega on H₂ (dots) and D₂ (triangles), with the color scale indicating the initial pressure of the sample. The agreement between D₂ and H₂ measurements validates the impedance-matching construction that we used based on quartz with a Grüneisen equation of state of molten SiO₂. The full lines represent *ab-initio* calculations for comparable Hugoniots.

Last year, a special effort was made to extend the precompression on H₂/He mixtures to cover the thermodynamic domain where phase separation of the mixture is predicted to occur in the interiors of Jupiter and Saturn. To reach this domain, a precompression of more than 4 GPa is needed, and this has been achieved by a new design of diamond window with lateral support (Fig. 124.96). A typical diameter of the H₂/He sample is 300 μm, and, as a result of this new design, 6 kJ have been effectively coupled to the target.

The shock state is monitored through the back diamond using in-line imaging VISAR, along with streaked optical pyrometry (SOP) for temperature. Quartz is the reference material used as a standard for impedance-matching determination of pressure and density and relative measurements of reflectivity and temperature.

Data for H₂/He mixtures have been obtained along three Hugoniots corresponding, respectively, to a precompression of 0.4 GPa, 2 GPa, and 4 GPa (Fig. 124.97). The data have been

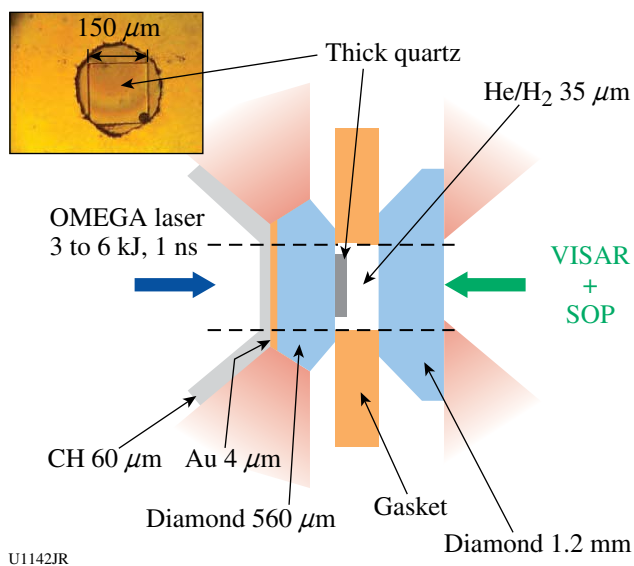


Figure 124.96

Experimental layout: schematic cross section of a precompressed target at 4 GPa. The inset (upper left) shows a picture of the sample before the shot.

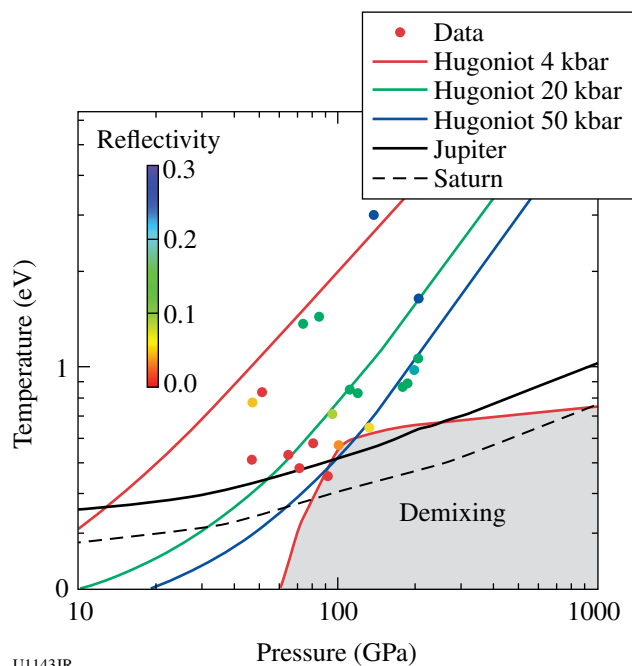


Figure 124.97

Hugoniot measurements on precompressed H₂/He mixtures collected along three paths, corresponding to precompressions of 0.4, 2, and 4 GPa at ambient temperature. The color scale gives the observed reflectivity. The phase-separation domain, calculated by *ab-initio* calculations, is given by the light red-colored domain. Isentropes for the interiors of Jupiter and Saturn are indicated by solid and dashed black lines, respectively.

collected under conditions for which H_2 is electrically conducting (metallic fluid) but He is not. The order-of-magnitude range of precompressions significantly shifts the Hugoniot points to a higher density and cooler temperature. Therefore, the measured Hugoniot of fluid H_2/He precompressed to 4 GPa crosses the Jupiter adiabat. The signature of phase separation—a jump in reflectivity along the Hugoniot—is not observed here. These data are just at the limit of the domain at which phase separation has been predicted by theoretical calculations.²³ It appears that the calculations may be overestimating phase separation; therefore, there is no phase separation within Jupiter.

Three-Dimensional Studies of Low-Adiabatic Direct-Drive Implosions on OMEGA

Principal Investigators: R. C. Mancini (University of Nevada, Reno) and R. Tommasini (LLNL)

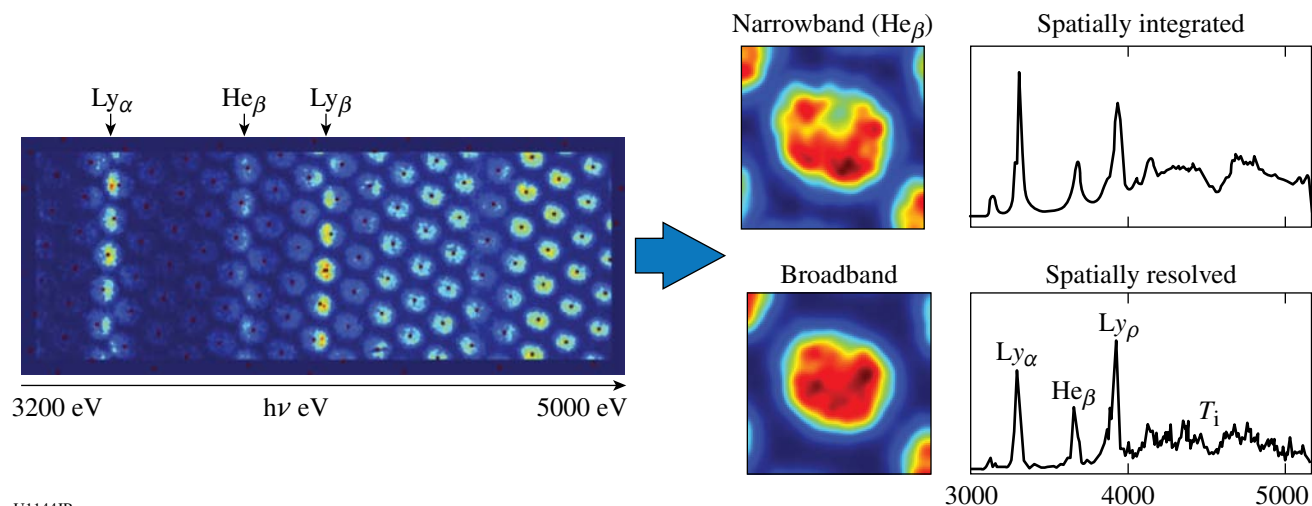
Co-investigators: J. A. Delettrez and S. P. Regan (LLE); V. A. Smalyuk (LLNL); and L. A. Welsch-Sherrill (LANL)

Determining the spatial structure of implosion core temperature conditions is important for inertial confinement fusion experiments. The emphasis of this NLUF research is to establish the direct-drive multi-monochromatic imager's (DDMMI) instrument capabilities and to develop a quantitative method for spectrally resolved image data analysis with the goal of studying the 3-D spatial structure of implosion cores in low-adiabat OMEGA direct-drive implosions. In this connec-

tion, the team has demonstrated that processing the spectrally resolved image data recorded with DDMMI produces several types of images or spectra, namely (1) broadband images, (2) narrowband images, (3) spatially integrated spectra, and (4) spatially resolved spectra. Figure 124.98 shows gated, spectrally resolved images from an argon-doped implosion core recorded by DDMMI in OMEGA shot 49956. The red dots indicate the location of the image centers.

Being able to obtain spatially resolved spectra from the spectrally resolved image data recorded with DDMMI is important because the problem of extracting the 3-D spatial structure of the implosion core can be cast in terms of analyzing a series of spatially resolved spectra recorded simultaneously along three quasi-orthogonal lines of sight (LOS's). Electron-temperature and density spatial information is encoded in the intensity and broadening changes observed in the spectra. This type of 3-D analysis for the reconstruction of spatial structure is called a *polychromatic tomography* since, unlike the tomography techniques commonly used in medicine, we work with a limited number of LOS's but we benefit from having multiple chords and multiple wavelengths associated with each LOS.

To implement the idea of polychromatic tomography, we perform searches in parameter space driven by a Pareto genetic algorithm (PGA), for the temperature and density spatial distributions that yield the best simultaneous and



U1144JR

Figure 124.98

Gated, spectrally resolved images of the implosion core recorded by the DDMMI instrument in OMEGA shot 49956, and broad- and narrowband core images and spatially integrated and a sample of spatially resolved spectra extracted from these data. The line emission spectral features are due to the Ar tracer added to the D_2 -gas fill of the core. At high photon energies, line absorption caused by a Ti tracer located in the shell is also observed. Color coding is adjusted for the visualization of each image.

self-consistent fits to all spatially resolved spectra recorded along the three quasi-orthogonal LOS's. The PGA combines a genetic algorithm with the Pareto domination technique of multi-objective optimization. This implementation of polychromatic tomography is an example of multi-objective data analysis, where the key question is what can be extracted by analyzing simultaneously and self-consistently multiple pieces of data that cannot be extracted by analyzing each piece of data on an individual basis? In previous and current NLUF research, several applications of multi-objective data analysis to x-ray spectroscopy of implosion cores have been developed. It should be noted that this method is unbiased since each PGA run with the same data starts from a randomly initialized first generation of populations (i.e., solution candidates), and the same data set can be analyzed multiple times starting from different first generations in an effort to check the uniqueness of the solution. Moreover, the result obtained with the PGA is subsequently fed to a Levenberg–Maquardt nonlinear least-squares minimization method that quickly improves the search by performing a “fine-tuning” step to find the optimal solution. Before applying this analysis method to actual data, the technique was extensively tested with a series of synthetic data test cases. Polychromatic tomography of data from several OMEGA implosion experiments has been performed, and work is in progress to compare this data with 2-D and 3-D hydrodynamic simulations.

Response of BCC Metals to Ultrahigh Strain

Rate Compression

Principal Investigator: M. Meyers (University of California, San Diego)

Co-investigators: B. Maddox, H. S. Park, B. Remington, S. Pollaine, and S. Hau-Riege (LLNL); and J. Wark (Oxford)

The goal of this campaign was to recover isentropically compressed Ta samples of various microstructures, from single crystal to nanocrystal, and to measure the loading profile using Al/LiF targets and the TIM5 ASBO (active shock breakout) on the OMEGA laser. The experimental setup is shown in Figure 124.99 and consisted of two targets simultaneously driven using a set of six beams each, one target aligned along the H3–H18 axis and the other along the H7–H14 axis. The configuration shown in Fig. 124.99 shows a VISAR witness target on H7–H14 and the Ta recovery sample on H3–H18. The VISAR witness targets were 1-mm-thick LiF coated with 10 μm of aluminum and mounted on a 10-mm-diam washer. The LiF was surrounded by a 3-mm-long Au cylinder that shielded the LiF from unconverted light. The recovery targets

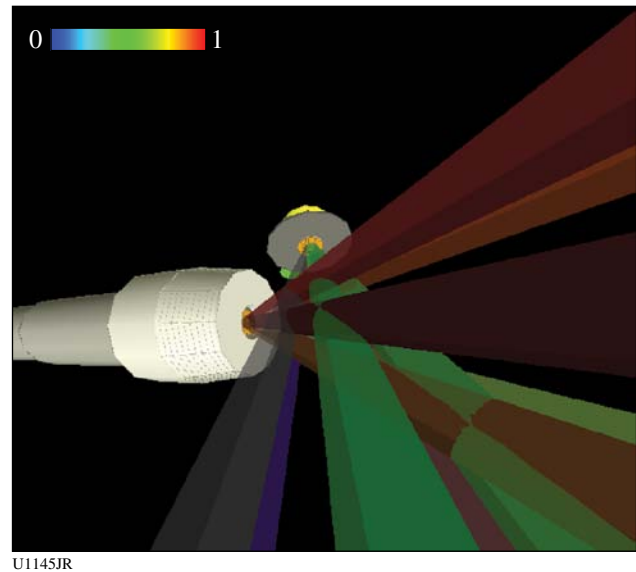


Figure 124.99

Experimental setup for BCCMet-10A showing the Ta recovery target along the H3–H18 axis and the VISAR witness target along the H7–H14 axis. The VISAR target was replaced with another recovery target after the first four shots.

consisted of a 5.5-cm-long stainless-steel recovery tube filled with 50 mg/cc of aerogel for soft recovery of laser-driven samples. The Ta target package was mounted at the end of the recovery tube and consisted of a 20- μm -thick polycarbonate ablator backed by a 180- μm BrCH (2%) reservoir. This ablator/reservoir was separated from the sample to be studied by a 300- μm -thick washer. The isentropic drive was created by the unloading of the BrCH reservoir across this gap. The VISAR target was replaced by a second Ta recovery target after the first four shots. A total of 12 successful shots were completed, resulting in 20 recovered samples, and four successful drive measurements were obtained. The recovered targets are currently being analyzed using contact profilometry, scanning electron microscopy, transmission electron microscopy, and x-ray diffraction.

Proton Radiography of Direct- and Indirect-Drive ICF Experiments and HEDP Plasmas

Principal Investigators: R. D. Petrasso and C. K. Li (Massachusetts Institute of Technology)

Co-investigators: F. H. Séguin and J. A. Frenje (MIT); J. P. Knauer (LLE); and J. R. Rygg (LLNL).

During the present and previous NLUF programs, the MIT-developed method of monoenergetic, charged-particle radiography²⁴ has been used in new types of studies of electromagnetic fields and plasmas in high-energy-density physics (HEDP) and

in inertial confinement fusion (ICF) physics. These projects, undertaken at the Omega Laser Facility,²⁵ were performed because of their importance to the future of ICF, HEDP, and the physics of fields generated by laser-plasma interactions. Topics studied include the imaging, identification, and measurement of electric and magnetic fields in laser-generated plasmas; reconnection of megagauss magnetic fields in high- β plasmas; self-generated electromagnetic fields in ICF implosions; the dynamics of ICF capsule implosions; and electromagnetic fields in laser-driven hohlraums. This work has resulted in nine publications in *Science*^{26,27} and *Physical Review Letters*,^{28–34} plus seven other papers, eleven invited talks, and many contributed talks at conferences. The experiments have successfully addressed basic physics issues and those issues directly relevant to the future success of ignition experiments at the National Ignition Facility (NIF). These NLUF experiments also provided unique research opportunities for the seven MIT graduate students in HEDP and will result in major parts of their theses.

As described in the 2010 *Science* article,²⁷ the first observations and measurements of indirect-drive ICF implosions and self-generated fields using monoenergetic proton radiography were conducted during this project.²⁴ The experimental setup and data are shown in Fig. 124.100. The hohlraums were of OMEGA scale-1.5 size with a 30- μm -thick Au wall, 100% laser entrance hole (LEH), 2.4-mm diameter, and 3.8-mm length. Each hohlraum was driven by 30 laser beams forming four irradiation rings with a total laser energy ~ 11 kJ in a 1-ns square pulse. The individual laser beams had full spatial and temporal smoothing. The radiographs, made with 15-MeV D^3He protons, covered a typical indirect-drive ICF implosion sequence. The images are displayed to show proton fluence versus position, providing time-dependent information about field distributions, capsule compression, and hohlraum plasma conditions. A striking feature in these images is a five-pronged, asterisk-like pattern surrounding the imploding capsule—a consequence of the laser-beam positions on the hohlraum wall. It was shown that the asterisk spokes were formed between two expanding plasma bubbles that were generated by “nearest neighbor” laser-beam pairs, while the periodic patterns (narrow fingers) between these spokes were associated with the remaining laser-beam distributions. Plasma flow, supersonic jets, and self-generated B fields were observed; the areal density (ρR) and implosion symmetry were determined; and different implosion phases were sampled. The views of the spatial structure and temporal evolution of both the drive and implosion properties provide essential insight into, and modeling validation of, x-ray-driven implosions.

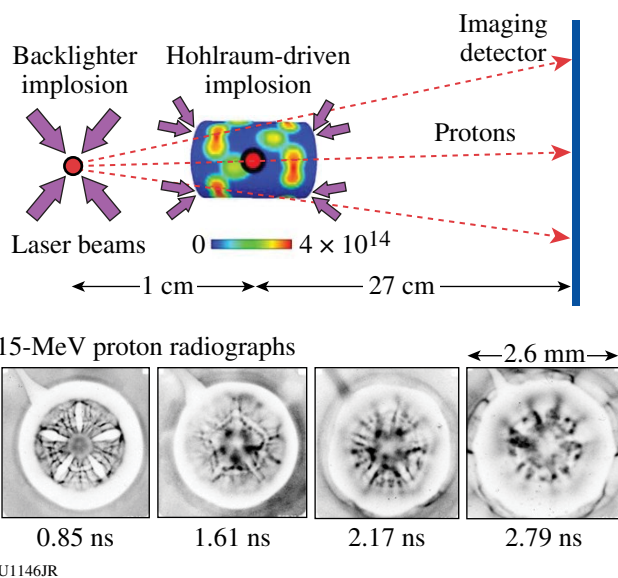


Figure 124.100

A recent experiment at the Omega Laser Facility used fusion to study fusion. A laser-driven ICF capsule produced monoenergetic 3- and 15-MeV protons through fusion reactions, and the protons were used to make radiographs of another ICF capsule imploded by x rays generated by the interaction of 30 laser beams with the inner wall of a Au hohlraum. The colors inside the hohlraum wall indicate laser intensity in units of watts per cm^2 . In the 15-MeV radiographs shown here (recorded at different times during the laser drive), the capsule is in the center, the Au hohlraum is the light-colored outer ring, and the patterns between capsule and hohlraum are due to electromagnetic fields and plasma jets. Within each image, darker means higher proton fluence. This work is discussed in Ref. 27.

Intense Laser Interactions with Low-Density Plasmas Using OMEGA EP

Principal Investigators: L. Willingale, A. Maksimchuk, and K. Krushelnick (University of Michigan)

Co-investigators: P. M. Nilson, R. S. Craxton, C. Stoeckl, and T. C. Sangster (LLE); J. Cobble (LANL); and P. Norreys and R. Scott (RAL)

Propagation of high-power, short-duration laser pulses through underdense plasma is of interest to research areas such as understanding laser beam self-focusing, channel and blast wave formation, filamentation, soliton production, electron and ion acceleration, and x-ray generation. The formation of a channel through an underdense plasma by a 740-J, 8-ps (90-TW) laser pulse focused to a peak vacuum intensity of around $2.8 \times 10^{19} \text{ W/cm}^2$ was investigated using proton probing. These parameters are relevant to conditions required for the hole-boring fast-ignition scheme.³⁵ The CH plasma-plume underdense target was created by a UV beam (2.5 ns, 1160 J in an 800- μm -diam focal spot). Two-dimensional *SAGE* modeling indicated that this produced a 650- μm -wide Gaussian density profile with

a peak density of $5.3 \times 10^{19} \text{ cm}^{-3}$ along the laser propagation axis. The proton beam was generated using the second short-pulse beam interacting with a 50- μm -thick copper target.

Figure 124.101 shows the interaction at an early time when the laser was still propagating through the plasma; the proton probe images illustrate the expansion of the channel, filamentation, and channel-wall modulations. The time at which the leading edge of the pulse arrived at focus and reached half-maximum intensity is defined as t_0 . Self-correction of the filaments into a single channel is seen from the single-shot sequence on the right side of Fig. 124.101. Bubble-like structures, which develop at later times, are illustrated in Fig. 124.102 by the proton probe images from shots with different relative beam timings. Two-dimensional particle-in-cell simulations are being performed to identify the origin of the channel-wall modulations and bubble structures.

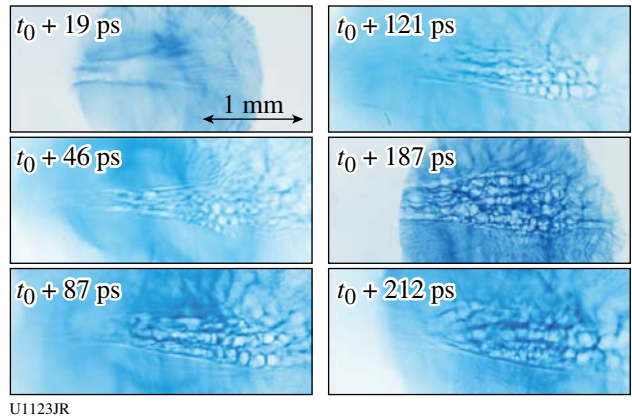


Figure 124.102
Proton probe image sequence from shots with different relative beam timings, which show the temporal evolution of the channel and the formation of bubble-like structures.

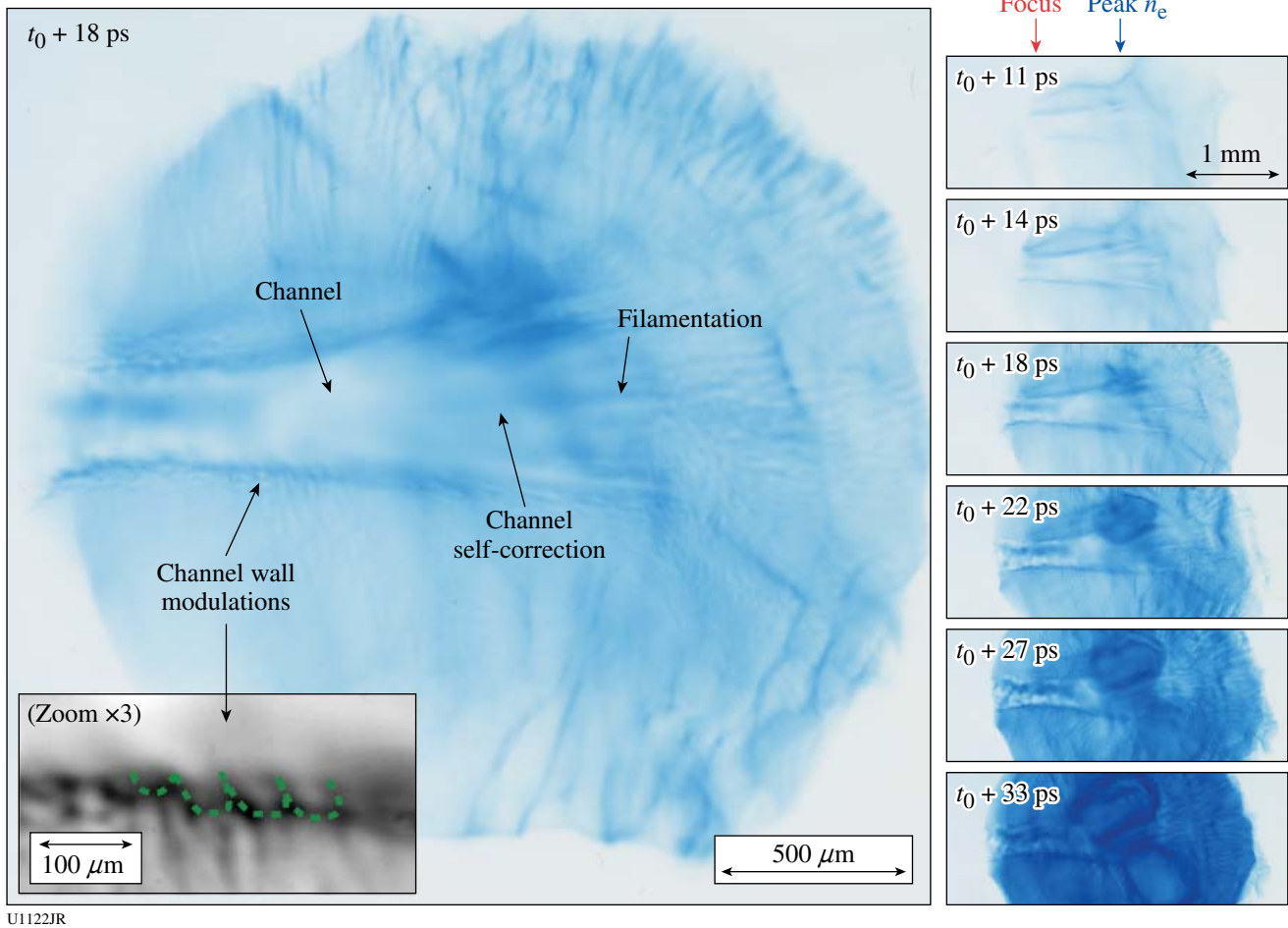


Figure 124.101
Proton probe images of the laser pulse propagating through the plasma from left to right. The time sequence is shown on the right-hand side and shows channel-wall modulations, filamentation, and channel self-correction.

FY10 Laboratory Basic Science Programs

In FY10, LLE issued a solicitation for LBS proposals to be conducted in FY11. A total of 23 proposals were submitted. An independent review committee comprised of Prof. Farhat Beg (University of California, San Diego), Dr. Robert Heeter (LLNL), Prof. Karl Krushelnick (University of Michigan), Dr. Carolyn Kuranz (University of Michigan), Dr. Nicholas Lanier (LANL), Prof. Roberto Mancini (University of Nevada, Reno), Dr. Rick Olson (SNL), Prof. Stephen Padalino (State University of New York–Geneseo), Dr. Wolf Seka (LLE), and Dr. John Soures (Committee Chair, non-voting) reviewed the proposals and recommended that 16 proposals receive 29 shot days on the Omega Laser Facility in FY11. Table 124.VI lists the successful LBS proposals.

Eleven LBS projects were allotted Omega Facility shot time and conducted a total of 303 target shots on the facility in FY10. This work is summarized in this section.

Producing Pair Plasma and Gamma-Ray Burst Using OMEGA EP

Principal Investigator: H. Chen (LLNL)

In August 2010, an LLNL/LLE/NRL team performed an LBS experiment on the OMEGA EP Laser System to study

positron production in high-intensity–laser interactions with high-Z targets. This experiment was a follow-up to that in April 2009 where a record number of positrons were produced using the 1-kJ, 10-ps OMEGA EP backlighter interacting with a 1-mm-thick Au target.³⁶ The 2010 experiment had two main objectives; to examine the positron acceleration and to measure the high-energy gamma radiation. The results are shown in Figs. 124.103 and 124.104 for the positron energy spectra and gamma spectra, respectively. Quasi-monoenergetic positrons with energies peaked at ~25 MeV, the highest positron energy from lasers, were observed. This is nearly 7 MeV higher than that observed in previous OMEGA EP experiments. It is attributed to more-efficient acceleration using laser normal incidence on the same target. The experiments were the first time that high-energy (up to 1 MeV) gamma radiation was observed in laser–solid interaction using a single-hit charge-coupled–device (CCD) detector. This information is important to understanding the physics of laser–plasma interaction that produced electron–positron pairs. The misalignment of the diagnostic and the misfocusing of the laser beam caused by the debris shield made it impossible to observe the electron–positron annihilation feature.

Positron research extends over diverse fields from particle physics and astrophysics to medical applications. These appli-

Table 124.VI: Approved FY11 LBS proposals.

Principal Investigator	Institution	Project Title
H. Chen	LLNL	Exploring Pair Plasma and its Applications Using OMEGA EP
S. X. Hu	LLE	Charged-Particle Stopping Power in Warm Dense Plasmas
R. Betti	LLE/FSC	Shock-Ignition Experiments on OMEGA
I. V. Igumenshchev	LLE	Investigation of Self-Generated Electromagnetic Fields in Directly Driven ICF Implosions Using Proton Radiography
D. Hicks	LLNL	Multi-Megabar Ramp Compression: Studies Using X-Ray Absorption Fine Structure
R. A. Kritcher	LLNL	Capsule Adiabatic Measurements with X-Ray Thomson Scattering
P. Patel	LLNL	Electron Source Characterization for Cone-Guided Fast Ignition
S. P. Regan	LLE	Diagnosing P , ρ , n_e , T_e , Z of H/He, CH ₄ , and NH ₃ Warm Dense Matter
G. Fiksel	LLE	Laser-Driven Magnetic-Flux Compression Experiments on OMEGA
V. A. Smalyuk	LLNL	Measurement of Ablative Rayleigh–Taylor Instability in Deeply Nonlinear Regime
R. Smith	LLNL	Measurement of Nucleation and Growth of the Fe α -to- ϵ Phase Transformation
B. Maddox	LLNL	Ultrahigh Pressure Lattice Dynamics in High-Z Materials
H. Park	LLNL	Astrophysical Collisionless Shock Generation in Laser-Driven Experiments
O. Hurricane	LLNL	Measurements of Linear, Nonlinear, and Turbulent-Mixing Regimes in Kelvin–Helmholtz Instability in the Subsonic Regime
C. Stoeckl	LLE	Fast-Electron Transport in Solid-Density Matter
J. M. McNaney	LLNL	Short-Pulse-Laser–Based Neutron Resonance Spectrometry

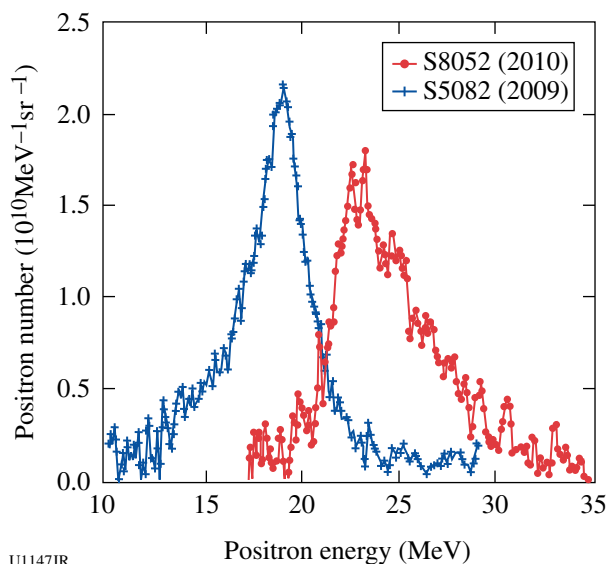


Figure 124.103
Positron spectrum measured on the OMEGA EP laser.

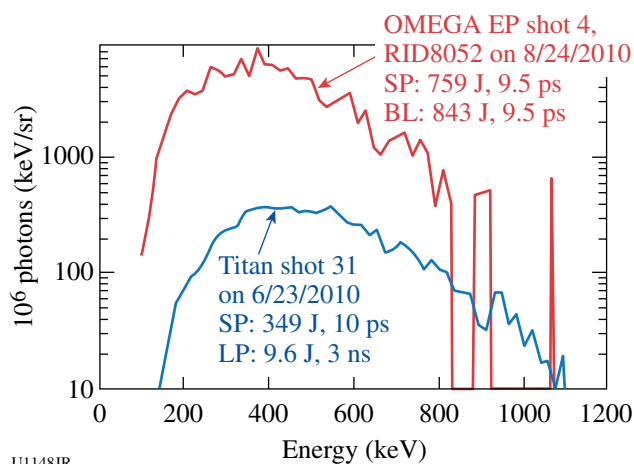


Figure 124.104
High-energy gamma spectrum measured by the NRL single-hit CCD detector.

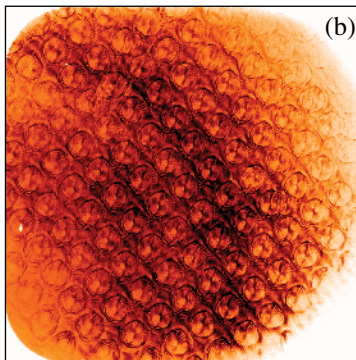
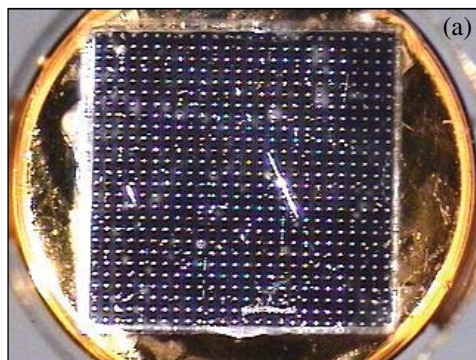


Figure 124.105
(a) Example of a fused-SiO₂ viscosity target sample with the etched array of pits clearly visible in the metrology photograph; the hohlraum is behind the sample. (b) Raw intensity record from one of the channels of the OHRV for the same target probed at 2.6 ns following the passage of a shock through the perturbed interface, showing the probe light reflected directly from the shock front and revealing the pattern of expanding ripples created by the array of etched pits.

cations often require the production of large numbers of positrons on a short time scale, which have been difficult to supply. The new OMEGA EP results could significantly affect the quest for a laser-produced positron source for research in these fields.

Measurements of the Viscosity of Shock-Compressed Fluids: Studies of Water and Silica (Viscosity-10A)

Principal Investigator: P. M. Celliers (LLNL)

The Viscosity-10A campaign was carried out as part of the LBS program. The goal was to demonstrate a method for determining the viscosity of a high-pressure fluid created by the propagation of a strong shock front through an initially transparent sample. In this campaign the sample under study was liquid silica (SiO₂), produced by propagating a shock through samples of either alpha-quartz or fused SiO₂. The viscosity of high-pressure liquid SiO₂ has obvious geophysical relevance, and measurements in the Mbar domain are not possible with conventional methods. The measurement technique is based on observing the evolution of a spectrum of perturbations imposed on a multi-Mbar shock front passing through the sample material. The viscosity of the liquid state just behind the shock front is expected to influence the decay rate of the perturbations as the shock front propagates, and detailed measurements of the perturbation state can be compared with calculations to assess the viscosity. The measurement technique employed the OMEGA high-resolution velocimeter (OHRV) to observe the velocity perturbations directly on the surface of the reflecting shock front. The shocks were driven using a hohlraum coupled to a 50- μ m polystyrene ablator followed by the sample. The perturbation spectrum was generated by an etched array of shallow pits, a few microns deep and 10 μ m in diameter, that were created on the sample surface at the interface with the ablator. As the shock passed through this interface, the perturbations created a pattern of expanding ripples riding on top of the shock front, which were detected and measured quantitatively by the OHRV (Fig. 124.105). During the campaign,

U1149JR

we carried out three drive-characterization experiments using ASBO/SOP to characterize the shock velocity. These were followed by eight perturbation experiments probing 3-Mbar and 6-Mbar shocks in the SiO₂ samples. High-quality data were recorded on all shots.

Optical Properties of LiF

Principal Investigator: D. E. Frantanduono (LLE)

Co-investigators: M. A. Barrios, T. R. Boehly, and D. D. Meyerhofer (LLE); and D. G. Hicks, J. H. Eggert, R. Smith, and P. M. Celliers (LLNL)

Direct laser ablation was used to ramp-compress lithium fluoride (LiF) to 800 GPa. LiF was observed to remain transparent over this pressure range; this is the highest-pressure insulator ever observed. The refractive index of ramp-compressed LiF was measured up to 800 GPa and observed to increase linearly with compressed density over this range. These highest-pressure measurements of refractive index to date were used to infer the pressure-induced band-gap closure of compressed LiF. An effective single-oscillator model of this behavior shows that the optical gap closes monotonically with increasing density.

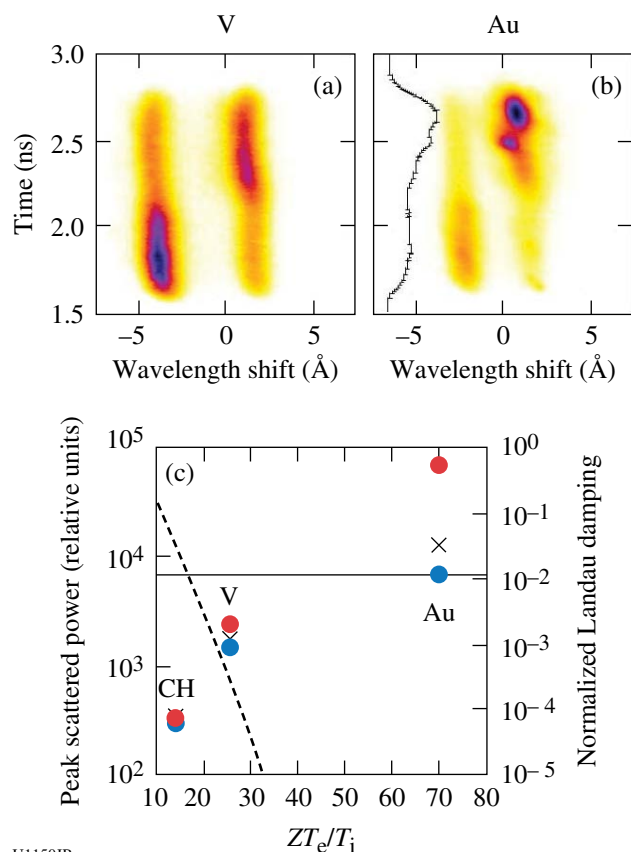
Extrapolation of these results suggests that metallization of LiF should occur at pressures of 4200 GPa. If true, LiF will prove to be a valuable window for extremely high pressure, ramp-compression experiments.

Ion-Acoustic Wave Instability from Laser-Driven Return Currents

Principal Investigators: D. H. Froula, S. X. Hu, and J. F. Myatt (LLE)

Co-investigators: J. S. Ross, L. Divol, and S. H. Glenzer (LLNL)

Thomson-scattering measurements of the amplitude and frequency of ion-acoustic waves show an instability when ion-wave damping is reduced. Experimental results from the OMEGA laser used simultaneous measurements of the electron-plasma wave and ion-acoustic wave features to characterize the plasma (T_e , T_i , Z , n_e) and to directly probe the amplitude of the ion-acoustic waves (Fig. 124.106). The ion Landau damping was varied by changing the target material: CH, V, Ag, and Au. For plasma conditions where the ion Landau damping was large ($ZT_e/T_i = 10$), the amplitude of the ion-acoustic waves was stable. Reducing the ion Landau damping ($ZT_e/T_i = 30$) increased the amplitude of the ion wave, but the electron Landau damping was sufficient to maintain stability. The ion-acoustic waves became unstable when the ion Landau damping was weak ($ZT_e/T_i = 70$). As the waves grew to wave-



U1150JR

Figure 124.106

(a) The Thomson-scattering spectrum provides a measurement of the electron temperature, density, charge state, and, from the asymmetry in the scattered power between the ion-acoustic features, the relative drift between the electrons and ions driven by the heat-flux-driven return current. (b) As the ion damping was reduced, the system became dominated by the electron Landau damping, which became Landau growth in the weakly damped systems.

breaking amplitudes, their frequency shifted and turbulence was expected. These results confirm the speculation that heat-flux-driven ion-acoustic fluctuations exist in laser-produced plasmas, which was previously invoked to increase the collision rate and account for anomalous absorption.³⁷

X-Ray Absorption Fine Structure Measurements on Multishock Compressed Iron

Principal Investigators: Y. Ping and D. G. Hicks (LLNL)

X-ray absorption fine structure (XAFS) measurements were performed on iron that was multishock compressed to a few megabar. By dynamically compressing a few-micron-thick iron sample sandwiched between thin diamond anvils, near-constant pressure conditions were produced inside the iron, the bulk of the pressure evolution taking place in the adjacent, x-ray-transparent diamond anvils. A spherical, imploding

backlighter source was used to produce a smooth, broadband source of x rays for the absorption measurement. The VISAR was used to track the rear surface of the diamond from which the pressure inside the iron sample could be inferred. An example of an XAFS spectrum obtained at 3.5 Mbar is shown in Fig. 124.107. This was analyzed using the FEFF code³⁸ and found to give a compression in Fe of 1.6 and a temperature of 6000 K. Improved fits were found for a c/a ratio of 1.73, indicating that pressure, density, temperature, and c/a ratio could be obtained from a single shot.

Capsule Adiabatic Measurements with X-Ray

Thomson Scattering

Principal Investigators: A. Kritcher, T. Doepfner, O. L. Landen, and S. H. Glenzer (LLNL)

Experiments to characterize spherically imploded inertial fusion-type targets using x-ray Thomson scattering were recorded at the Omega Laser Facility in January and May of 2010 to study the properties of compressed ICF ablaters. Measurement of the temperature and density allows one to infer the capsule adiabat—a measure of the plasma pressure normalized by the Fermi pressure—and can be used to test low-adiabat pulse-shaping methods. In these experiments the noncollective, or microscopic, particle behavior of imploding CH and Be shells was probed using a 9-keV Zn He $_{\alpha}$ x-ray source at scattering angles of 113° and 135°. Figure 124.108(a) shows a schematic of the experimental setup including time-resolved pinhole images of the imploding capsules. The capsules attached to Au

half-cones were hemispherically driven using 36 drive beams. The Zn He $_{\alpha}$ probe was created by laser irradiation of a Zn foil positioned on the inside of the Au cone. Figures 124.108(b) and 124.108(c) show radiation–hydro–dynamic calculations of the mass density as a function of time and radius for the two pulse shapes used in these experiments.

Figure 124.109 shows scattering spectra from Be (+2) capsules driven with pulse shape LA2201 shown in Fig. 124.108(b), at 4.2 ns after the start of the drive beams and a scattering angle of 135°. The measured electron density and temperature determined from theoretical fitting to the experimental data was 14 ± 3 eV and $1.1 \pm 0.15 \times 10^{24}/\text{cc}$, respectively. For these partially degenerate plasmas, the width of the inelastic Compton feature provided the electron-velocity distribution, which is a direct measure of the electron density. The electron temperature was determined from the semi-Gaussian shape of the Compton feature, independent of the choice of structure factor model. Sensitivity of theoretical fitting to the red wing of the Compton feature for varying electron temperatures is shown in Fig. 124.109. In this geometry, the larger scattering angle of 135° resulted in the Compton red wing shape depending less on the finite size of the source and scattering volume, enabling us to better determine the temperature and density. Also, with this new geometry we were able to use additional probe beams, which resulted in an increase in signal to noise. These experiments demonstrate the viability and investigate the error in using this diagnostic to study the properties of implosion targets at the National Ignition Facility.

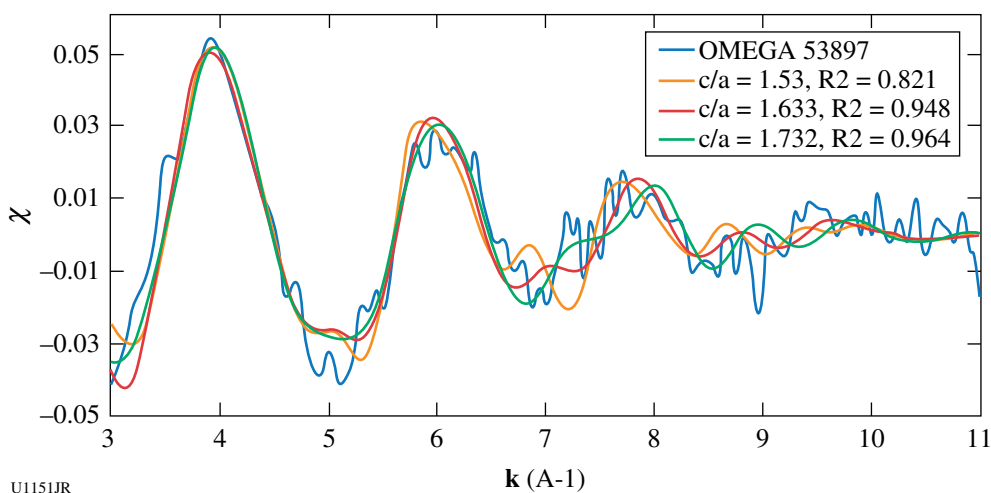
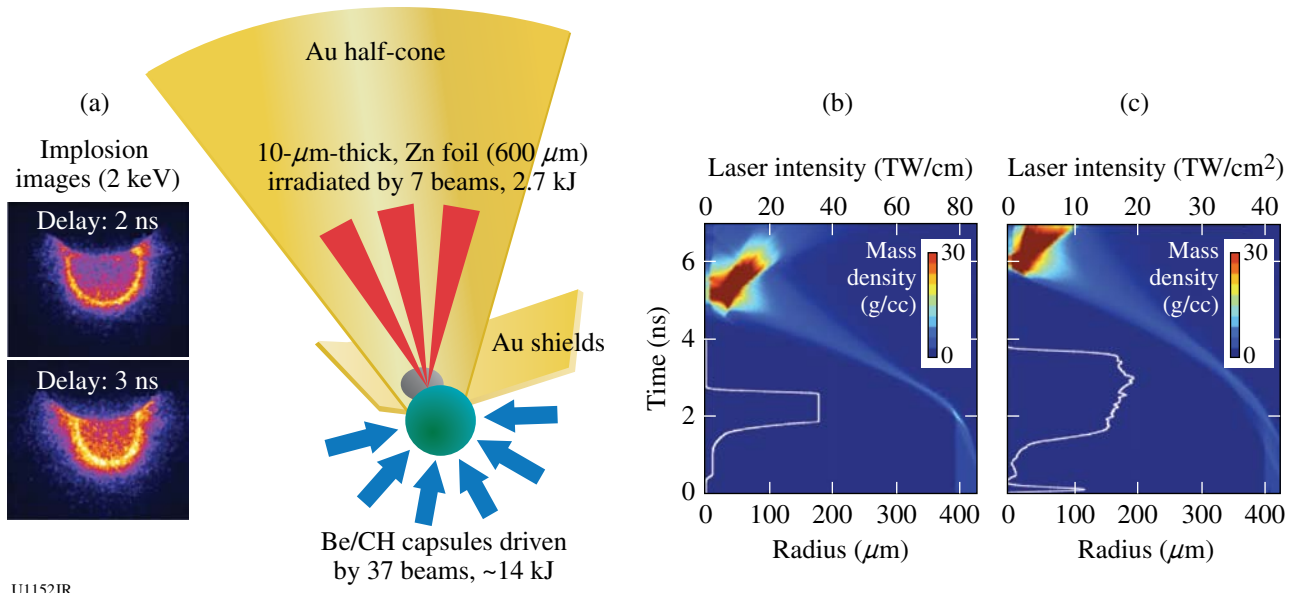


Figure 124.107

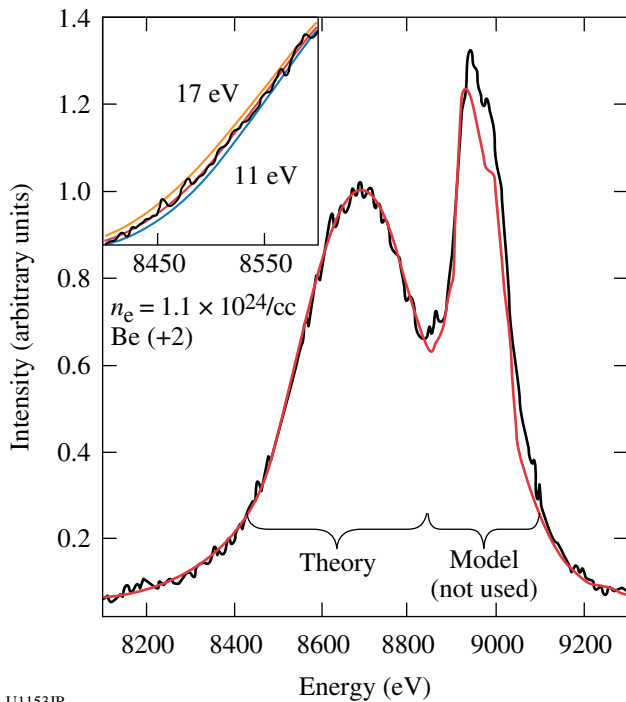
XAFS spectrum of iron compressed at 3.5 Mbar. The residual, normalized x-ray absorption coefficient χ (dimensionless) plotted versus wave vector k (inverse angstroms) is fit to an hcp crystal configuration to determine the density, temperature, and c/a ratio.



U1152JR

Figure 124.108

(a) Schematic of the experimental setup. Here, Zn He α x rays, produced via laser irradiation of a 10- μm -thick Zn foil, were scattered from imploding Be and CH capsules that were compressed using 36 additional shaped laser beams. The Zn foil was attached to gold half-cones with Au flaps that shielded the detector from the source x rays. Also shown (left) are time-resolved x-ray images of the implosion. (b) and (c) Radiation-hydrodynamic calculations of the mass density, plotted as a function of time and target thickness, where $t = 0$ denotes the start of the drive beams. Profiles of the drive-beam waveforms (white) are overlaid on the mass-density contour, listed as a function of time and laser intensity.



U1153JR

Figure 124.109

In-flight x-ray Thomson scattering data (4.2 ns) from laser-compressed Be cone-in-shell targets [see Fig. 124.108(b) for the drive-pulse shape]. Data include an elastically scattered Raleigh peak at ~ 9 keV and an inelastically scattered Compton feature at ~ 8.7 keV. Theoretical fits to the experimental data yielded an electron temperature and density of about 14 eV and $1.1 \times 10^{24}/\text{cc}$, respectively.

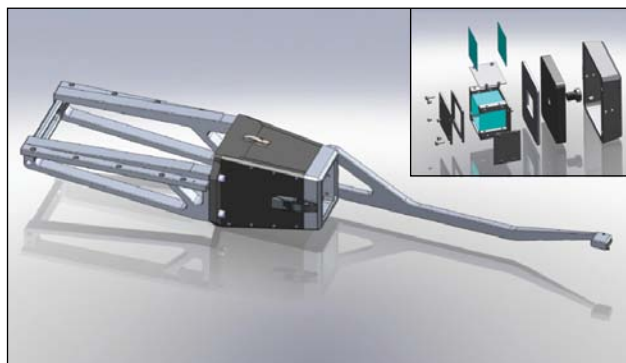
Study of High-Z Material Properties Under Compression Using High-Energy Backlighter Diffraction

Principal Investigators: B. Maddox and H. S. Park (LLNL)

This project was carried out as a series of four distinct series of shots on the OMEGA EP Laser System under the series name of DynDiff.

DynDiff-10A. This experimental campaign was designed to test two different diffraction schemes, Bragg (reflection) and Laue (transmissions), for diffraction off high-Z metals using x rays produced by laser-driven foil targets. Two new diagnostics were designed to accomplish this: For Bragg diffraction, the Bragg diffraction imager (BDI) consists of a large Hevimet housing and an Al arm that holds a Hevimet beam block close to the crystal target. The beam block prevents the x rays from the backlighter from reaching the detector while making it possible for diffracted x rays to pass. For Laue diffraction, the Laue diffraction imager (LDI) consists of the same Hevimet housing as the BDI, but with a collimator snout instead of an Al arm. This collimator snout creates a collimated x-ray beam that then diffracts off a crystal housed inside. Figure 124.110 shows a drawing of the BDI diagnostic. The inset shows the front snout that attaches to the main body to turn the BDI into the LDI. Targets for Bragg diffraction consisted of 600- μm -thick Mo (111) crystals mounted onto glass stalks. Targets for Laue dif-

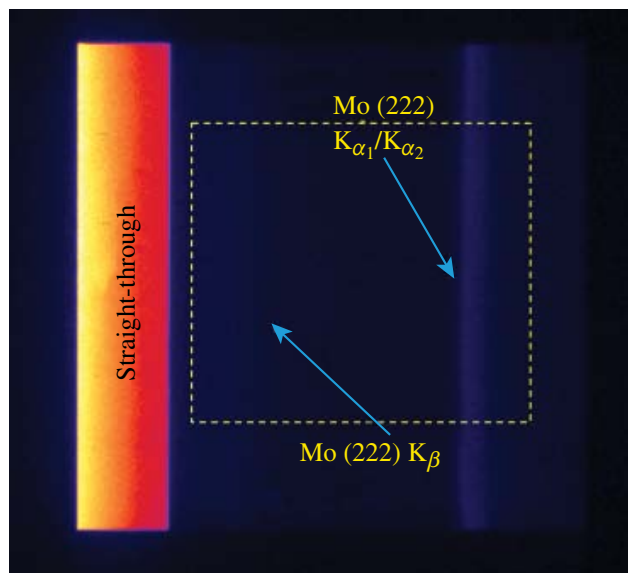
fraction consisted of 5- μm -thick Ta mounted on a rotation stage inside the LDI. X rays were produced by irradiating a metal foil using either the short-pulse backlighter beam (for Bragg diffraction) or the long-pulse UV beams (for Laue diffraction). Figure 124.111 shows an image obtained using the BDI on a Mo (111) crystal using a 17.478-keV Mo K_{α} backlighter. Similar quality results were obtained using the LDI to measure Laue diffraction from Ta single crystals. These results were used in DynDiff-10B to attempt to measure Bragg diffraction from a shock-compressed Mo crystal.



U1154JR

Figure 124.110

The Bragg diffraction imager (BDI). Inset shows the front nose assembly that turns the BDI into the Laue diffraction imager (LDI).



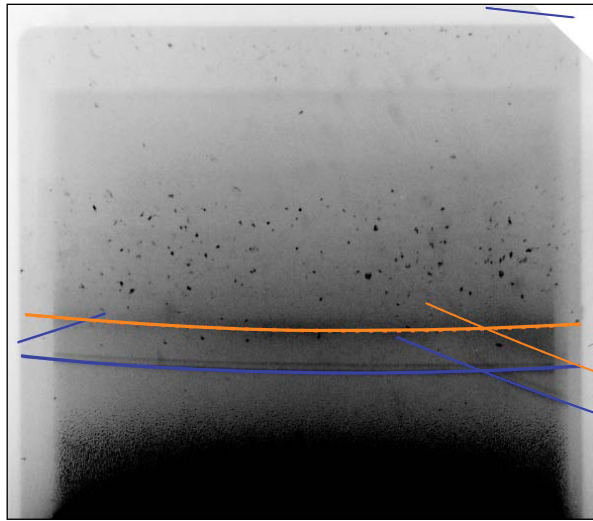
U1155JR

Figure 124.111

Diffraction image obtained using the BDI on a Mo (111) crystal using a 17.478-keV Mo backlighter.

DynDiff-10B. The goal of this campaign was to build on the success of DynDiff-10A to measure Bragg diffraction from a shock-compressed Mo (111) single crystal and to measure the drive characteristics of the OMEGA EP UV long-pulse beams using VISAR. The Mo crystal target consisted of a 600- μm -thick Mo (111) single crystal with a 20- μm parylene-n ablator and was mounted on a glass fiber stalk. The VISAR witness target was 1-mm-thick LiF coated with 10- μm -thick Al and mounted on a 7.5-mm-diam Al washer. The crystals and LiF targets were driven using a single long-pulse UV beam (Beam 4) using a 4-ns square pulse at an energy of 300 J and defocused to a 6-mm-diam spot. The x-ray backlighter target was a 250- μm -diam, 12- μm -thick Mo foil and was driven by the OMEGA EP short-pulse backlighter beam at 900 J in 100 ps with a 200- μm spot diameter. Good VISAR data were obtained; however, because of an alignment error of the BDI beam block, no driven diffraction was detected. It was concluded that the alignment tolerance was too tight and a new beam block needed to be designed that would allow for a greater alignment variance.

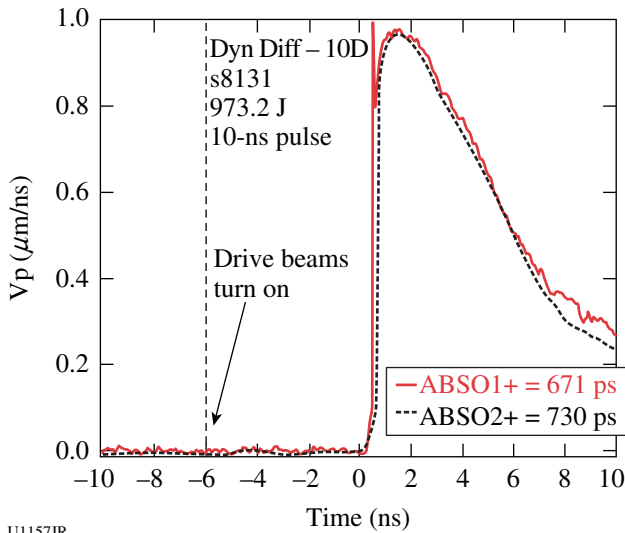
DynDiff-10C. The goal of this campaign was to measure Bragg diffraction of 17.478-keV Mo x rays off shock-compressed single-crystal Mo on OMEGA EP using a new, specially designed beam block and arm for the BDI that had a greater alignment tolerance than the original beam block. A secondary goal was to measure the shock-loading profile using Al/LiF targets and the TIM12 ASBO. A total of six target shots were conducted. The VISAR targets consisted of LiF (1 mm thick) coated with Al (10 μm thick) and a parylene-n ablator (20 μm thick), all mounted on a 7.5-mm-diam Al washer. Crystal targets consisted of a 6-mm-diam, 250- μm -thick Mo single crystal with a 20- μm -thick parylene-n ablator. Because of a target build error, no ASBO data were obtained during this campaign; however, the first driven Bragg diffraction using a petawatt-laser x-ray backlighter was observed. Figure 124.112 shows a diffraction image obtained using the BDI on a driven Mo (111) crystal along with a preliminary fit to the compressed diffraction pattern. The drive laser (UV beam 1) was set to 616 J in a 10-ns square pulse using a 5-mm-diam spot size and fired 7 ns before the backlighter beam. Although no ASBO data were obtained during this campaign, scaling from data obtained during the DynDiff-10B campaign suggests ~ 25 -GPa peak pressure. The fit to the diffraction pattern shown in Fig. 124.112 gives a strain along the compression direction of $\sim 5.8\%$. This technique was used during the DynDiff-10D campaign to measure the 3-D lattice relaxation time scale in bcc Mo by taking Bragg-diffraction snapshots, like the one shown in Fig. 124.110, at various times after the start of the laser drive.



U1156JR

Figure 124.112
Diffraction pattern obtained using the BDI of a shock-loaded Mo (111) crystal and a 17.478-keV Mo backlighter. The solid blue and orange lines show fits to the undriven and driven portions of the lattice.

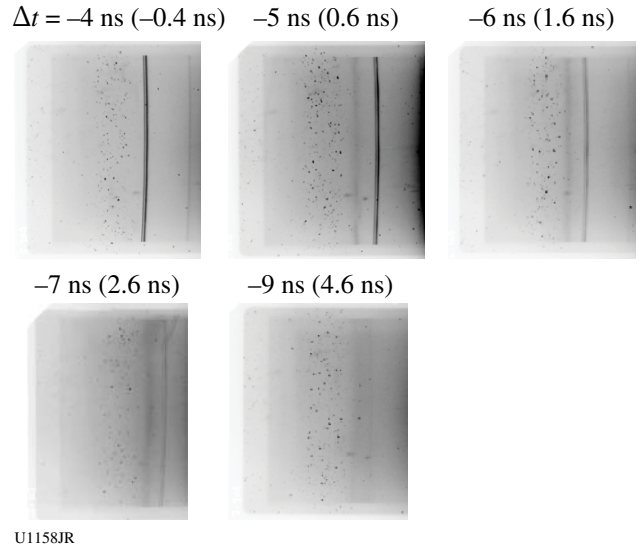
DynDiff-10D. This campaign was an extension of DynDiff-10C, and the goal was to use time-resolved Bragg diffraction to study the lattice dynamics of single-crystal bcc Mo. A total of five target shots were conducted: one VISAR shot to measure the laser drive and four successful diffraction shots at different times after initial compression. Targets were of the same design as those used in DynDiff-10C. The laser setup was also similar to that used during DynDiff-10C except for the introduction of a second UV drive beam (Beam 4) to enhance the drive uniformity across the crystal target. Figure 124.113 shows the



U1157JR

Figure 124.113
VISAR data obtained during the DynDiff-10D campaign.

VISAR data obtained. Using the shock-arrival time coupled with the Al thickness, the breakout time of the shock into the Mo crystals was calculated. Figure 124.114 shows a series of diffraction images taken at different times after the shock wave entered the crystal, starting with an undriven crystal. A compressed Mo (222) line is seen at a higher angle (left side of the images) that gradually shifts to lower compression. These data are currently being analyzed.



U1158JR

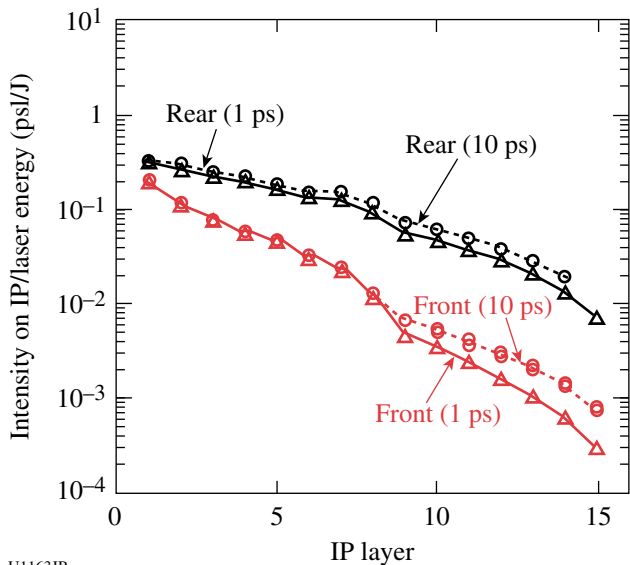
Figure 124.114
Diffraction plots as a function of time after compression for bcc Mo (111) showing a static (222) diffraction line and a compressed (222) line.

Relativistic Laser-Plasma Interaction

Principal Investigators: P. Patel (LLNL) and H. Sawada (University of California, San Diego)
Co-investigators: C. D. Chen, H. S. McLean, and M. H. Key (LLNL); T. Yabuchi and F. N. Beg (University of California, San Diego); R. B. Stephens and K. U. Akli (General Atomics); and W. Theobald, P. M. Nilson, and C. Stoeckl (LLE)

The objective of this campaign was to characterize fast electrons created by the high-energy OMEGA EP short-pulse laser interacting with planar and cone targets. The FY10 focus was on investigating two critical parameters: electron energy spectrum (T_{hot}) and conversion efficiency from laser to fast electrons (η). Experiments were performed using the OMEGA EP backlighter beam at 150 to 250 J in 1 ps and 1000 J in 10-ps-pulse duration. These laser parameters have been used in integrated fast-ignition (FI) experiments on OMEGA.³⁹ This study provided direct information about the electron source in integrated experiments.

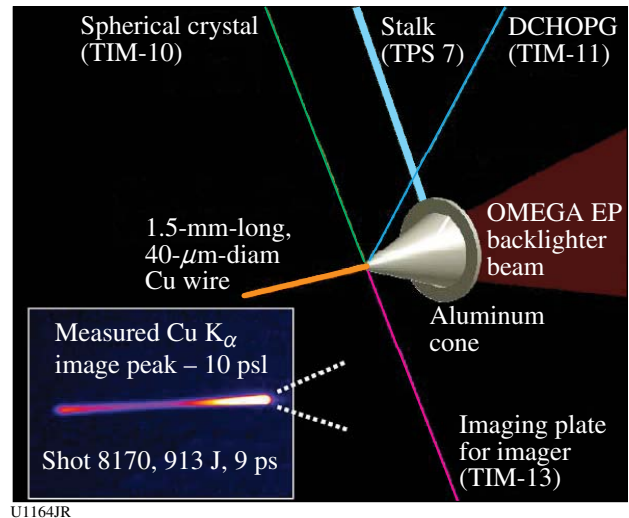
Multilayer planar targets were used to measure up-to-750-keV bremsstrahlung emission to infer T_{hot} and η . A planar target is less sensitive to the beam-pointing stability, target positioning, and pre-pulse level compared to a cone. The target consisted of an ~1-mm-thick planar Al with a 25- μm -thick Cu layer buried at 100 μm from the front surface. To prevent electron refluxing caused by the sheath fields, 1-mm-thick CH was attached to the rear side. The x rays were measured with two bremsstrahlung x-ray spectrometers (BMXS's) at the rear side on the laser axis and 49° from the incoming laser axis. Figure 124.115 compares the measured signals on the stack of 15 imaging plates in the BMXS at 150 J in the 1-ps shot and 1000 J in the 10-ps shot. These raw data normalized by the laser energy indicate similar fast-electron spectra and conversion efficiencies at a laser intensity of $\sim 5 \times 10^{18} \text{ W/cm}^2$ at both 1 and 10 ps. The preliminary analysis using a Monte Carlo code ITS⁴⁰ shows that the total conversion efficiency is estimated to be 14% to 35% for the 1-ps shot and 13% to 37% for the 10-ps shot with an assumption of the classical ejection angle. For further analyses, a PIC simulation using simulated pre-plasma profile from a radiation-hydrodynamics code *HYDRA* will be performed to calculate the divergence of the electron beam. This electron source will be fed into a hybrid transport code calculating the bremsstrahlung emission to match the measurements. The inferred T_{hot} and η will be compared to the simulated results.



U1163JR

Figure 124.115
Measured signals of front and rear bremsstrahlung spectrometers for 1-ps (shot 7694) and 10-ps (shot 7698) pulses.

The study was extended to cone-wire targets, which are more relevant to integrated experiments. Cone-wire targets were used to study the electron production in the cone and transport through the cone tip to the wire, where transport is simplified to quasi 1-D geometry in the wire direction. Figure 124.116 shows the overview of the cone-wire experiment. The backlighter beam was focused onto the Au or Al cone tip to generate electrons. The electrons transported through the cone tip were coupled to the 1.5-mm-long (40- μm -diam) Cu wire attached to the cone tip. From the wire 8.05-keV K_{α} was measured with the absolutely calibrated DCHOPG spectrometer and a spherical crystal imager (SCI) for the imaging of the wire. A version of SCI was deployed for these experiments at the end of Q4. The inset of Fig. 124.116 shows the monochromatic image of the wire at 1000 J in a 10-ps shot (shot 8170). K_{α} yields were obtained as well as wire images at both 1- and 10-ps pulse durations. The falloff of the wire emission and the Cu K_{α} yield will be modeled with a hybrid transport code to infer the T_{hot} and coupling efficiency to the wire. The SCI will enable one to study another critical parameter in future experiments: the divergence of forward-going electrons.



U1164JR

Figure 124.116
Experimental configuration of the cone-wire experiment. Inset: The measured monochromatic image of the Cu wire is shown for shot 8170.

Kinetic Behavior of Crystalline Iron Undergoing Multi-Mbar Compression and Release

Principal Investigators: R. Smith, Y. Ping, and D. G. Hicks (LLNL)

The kinetic behavior of iron during rapid compression and release was studied using x-ray absorption fine structure

(XAFS). A 4- μm iron sample, sandwiched between diamond layers, was multishock compressed up to 3.5 Mbar and then released (Fig. 124.117). The pressure history in the iron was tracked using a VISAR reflection from the rear diamond. By probing the XAFS spectrum of the iron on multiple shots before and after the peak of the compression wave, the rapid evolution of short-range atomic order in the crystal was examined. We observed that with increasing pressures, the spacing between XAFS peaks increased along with increased damping of the peaks at higher k . This indicates an increase in the density of the hcp phase from 1.65- to 1.8-fold compression and an increase in the temperature from 4000 to 10,000 K. These changes are undone on release of the wave. Detailed examinations are being made to determine whether the changes are fully reversible.

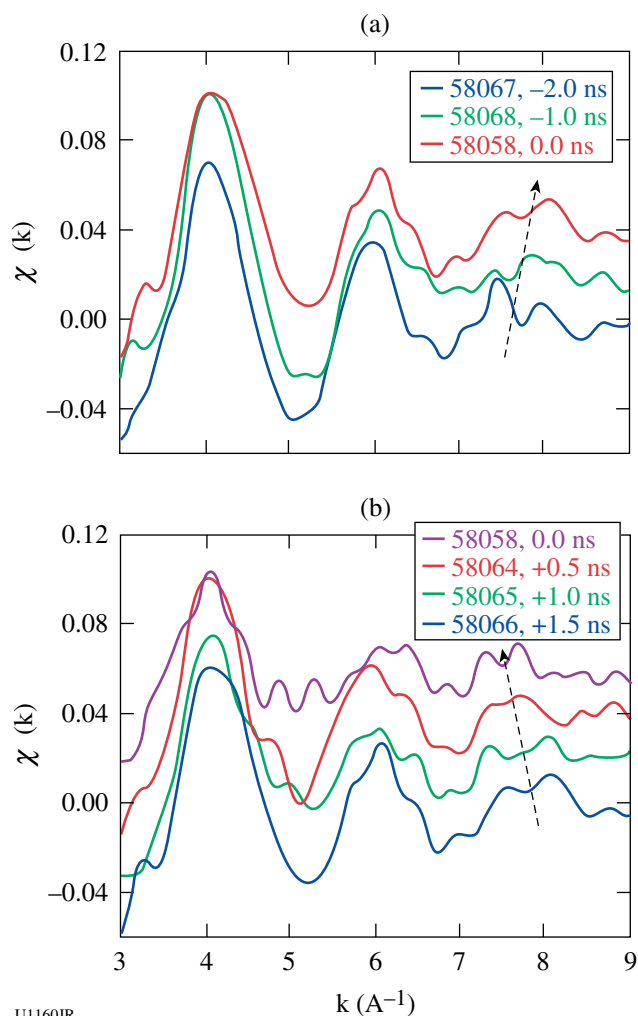


Figure 124.117
Changes in the Fe XAFS spectra observed on (a) compression and (b) release of a 3.5-Mbar pulse.

Integrated Shock-Ignition Experiments on OMEGA

Principal Investigator: R. Betti (LLE/FSC)

Co-investigators: W. Theobald, O. V. Gotchev, K. A. Anderson, and P.-Y. Chang (LLE)

Shock ignition is a two-step ICF scheme where ignition is achieved by launching a strong spherically convergent shock into the imploding capsule at the end of the compression. The laser intensities at the end of the pulse are $\sim 5 \times 10^{15} \text{ W/cm}^2$ and significantly higher than what is currently available with standard 60-beam implosions on OMEGA. A new experimental platform has been developed on OMEGA that uses 40 beams to compress D_2 -filled plastic shells on a low adiabat and the remaining 20 beams to generate a strong shock. The 20 beams are delayed and tightly focused onto the imploding shell to reach intensities of up to $\sim 8 \times 10^{15} \text{ W/cm}^2$.

Initial 40-beam implosions had a strong $l = 2$ nonuniformity as shown in the two top pinhole-camera images in Fig. 124.118(a). The implosion was improved by repointing the 40 drive beams so that a more-uniform illumination was achieved. This is clearly seen in the two bottom x-ray pinhole-camera images shown in Fig. 124.118(b). The core brightness

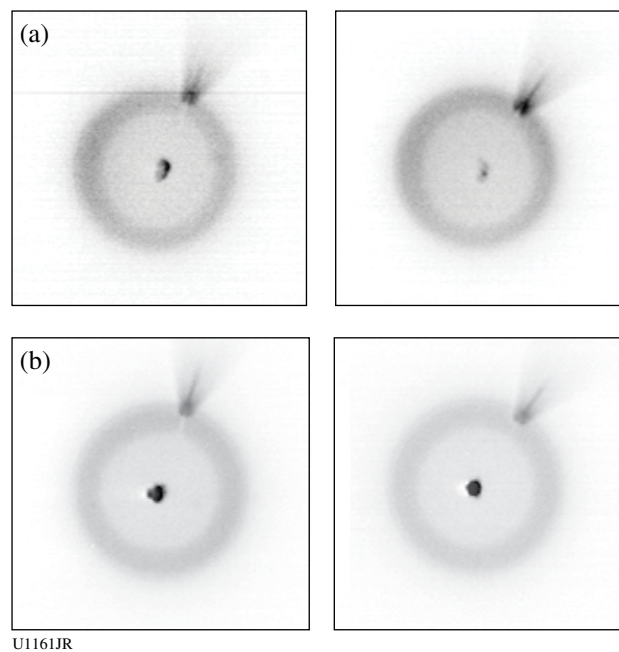


Figure 124.118
X-ray pinhole camera images from two different implosions. (a) Shot 52480, an implosion with 40 drive beams that were all pointed to the center of the capsule; (b) Shot 55737, an implosion where the 40 beams were repointed to achieve a more-uniform illumination. Two pinhole-camera images are shown for each shot.

increased and the shape of the core is more circular. By repointing the beams, the neutron yield increased by a factor of ~ 5 from $(2.6 \pm 1.1) \times 10^8$ to $(1.5 \pm 0.2) \times 10^9$. This shows that repointing significantly improved the symmetry of the implosion, reducing the calculated power imbalance from $\sim 8\%$ to $\sim 3\%$ root mean square.

Another objective of the campaign was to study the interaction of the 20 high-intensity beams. The neutron yield increased by a factor of 2 to $(3.3 \pm 0.2) \times 10^9$ when the 20 beams were added to the optimized target. The plasma reflectivity was measured for various laser intensities from ~ 2 to 8×10^{15} W/cm². This was achieved through an intensity scan by shifting the focus of the 20 shock beams relative to the center of the shell. Figure 124.119 shows the measured fraction of (a) SBS and (b) SRS laser backscatter energy of one shock beam versus laser intensity. SBS increased moderately from 7% to 12% with intensity, while SRS increased by a factor of ~ 6 from 4% to 24% and dominated the backscattering at the highest intensity. The sum of SRS and SBS (c) increased from 10% to 36%.

The backscatter is highly directional. The simultaneously measured back-reflection through a neighboring drive-beam port was $\sim 4\%$; it remained constant at all levels of intensities and was comparable to the measured backscatter for implosions without the 20 beams. About 10% of the high-intensity beam energy was converted into hot electrons with a temperature of 42 ± 5 keV, independent of laser intensity. The measurements indicate that SRS is the primary mechanism for generating the hot electrons with a relatively low temperature. No significant contribution from the two-plasmon-decay instability was observed. This would be beneficial for shock ignition since these electrons are stopped in a thin outer layer of the imploding target and might augment the strong hydrodynamic shock.

The reduction in driver energy caused by backscatter losses might be compensated by increasing the incident laser energy without the danger of preheating the target.

Integrated Core Heating for Fast Ignition

Principal Investigators: W. Theobald and C. Stoeckl (LLE)

This campaign had two primary objectives: First, the neutron-yield enhancement was measured from compressed deuterated plastic shells that were heated by fast electrons for various injection times of the short-pulse OMEGA EP laser. Second, the shock-breakout times in cone-in-shell targets were measured for the same compression condition as in the integrated fast-ignition shots for various cone-tip thicknesses.

Integrated fast-ignition experiments with hollow cone targets mounted into deuterated plastic shells were performed with 1 kJ of short-pulse energy and ~ 20 kJ of drive energy. The measured neutron yield as a function of the arrival time of the OMEGA EP pulse is shown in Fig. 124.120. The neutron yield peaks at a delay time of 3.65 ± 0.02 ns. The gray bar shows the yield without the OMEGA EP pulse. The measurement demonstrates an enhancement in neutron yield by more than a factor of 4 for a properly timed OMEGA EP beam. An additional yield of $(1.4 \pm 0.6) \times 10^7$ was produced by the ultra-intense, short-pulse laser in a narrow time window of less than 100 ps. Data points in the peak were taken on several shot days, months apart, demonstrating high reproducibility of this experimental platform.

Integrated *DRACO + LSP* simulations were performed to estimate the coupling efficiency of fast electrons to the compressed core. The fraction of OMEGA EP laser energy that is coupled into the core is $3.5 \pm 1.0\%$. The coupling is lower

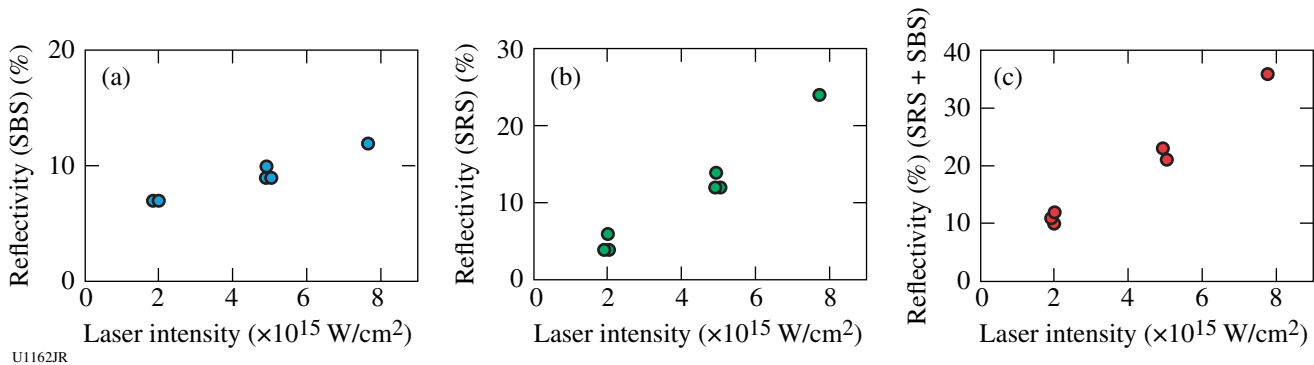
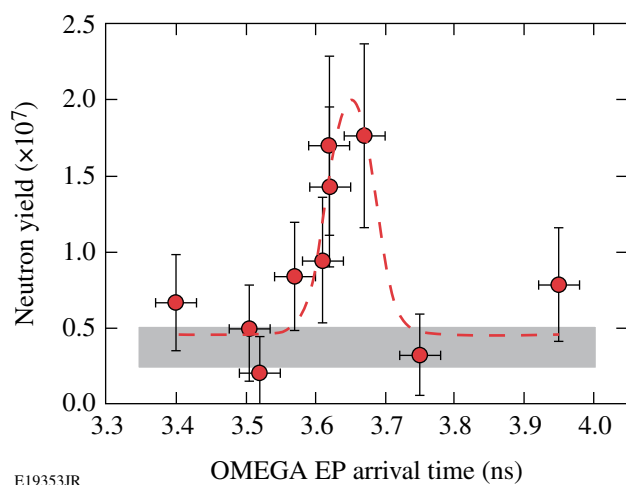


Figure 124.119
Measured backscattered light versus laser intensity for (a) SBS, (b) SRS, and (c) the sum of SBS and SRS.



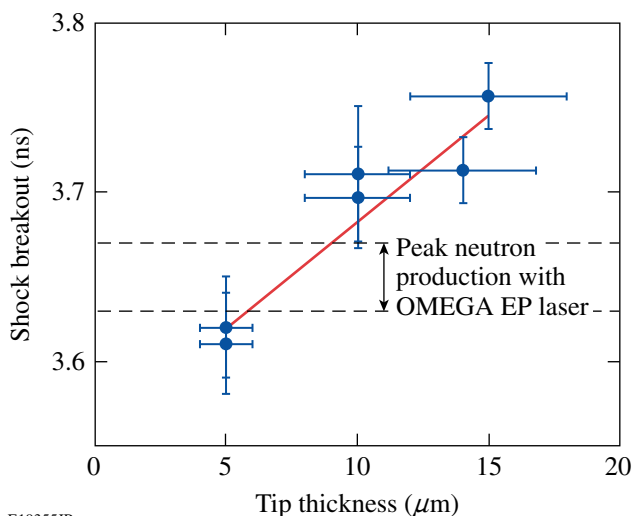
E19353JR

Figure 124.120

Measured neutron yield as a function of the arrival time of the short-pulse laser. The gray bar marks the yield without a heating beam. The dashed curve is a fit of a Gaussian profile to the integrated shot data.

compared to other experiments. A possible explanation is the formation of a pre-plasma in the cone. A pre-plasma in hollow cones has been shown in other experiments to strongly affect the ultra-intense laser-plasma interaction.

Shock-breakout measurements were performed by imploding cone-shell targets with various tip thicknesses without a short-pulse beam. VISAR and SOP diagnostics measured the time when optical emission appeared inside the cone. Figure 124.121 shows the time of shock breakout as a function



E19355JR

Figure 124.121

Measured breakout time of the shock inside the hollow Au cones. The shock breakout is later for thicker cone tips.

of tip thickness. With increasing tip thickness, the breakout is delayed. For thicknesses of 10 and 15 μm , the shock breakout time was at 3.70 ± 0.03 ns and 3.74 ± 0.03 ns, respectively. Shock breakout appeared 50 to 100 ps after the peak of neutron production, confirming that the cone tip was intact at the time when the OMEGA EP beam interacted with the target.

FY10 LLNL OMEGA Experimental Programs

In FY10, LLNL conducted several campaigns on the OMEGA and OMEGA EP Laser Systems, as well as campaigns that used the OMEGA and OMEGA EP beams jointly. Overall, LLNL led 376 target shots involving OMEGA and 107 target shots involving OMEGA EP. Approximately 50% of the total number of shots (212 OMEGA shots, 31 OMEGA EP shots) supported the National Ignition Campaign (NIC). The remainder were dedicated to experiments for high-energy-density (HED) physics (164 OMEGA shots, 64 OMEGA EP shots).

Objectives of the LLNL-led NIC campaigns at OMEGA included

- *Reactivation of the 4ω Thomson-scattering diagnostic*
- *Study of bremsstrahlung backlighters for Compton radiography of inertial confinement fusion (ICF) implosions*
- *High-resolution measurements of velocity nonuniformities created by microscopic perturbations in NIF ablator materials*
- *Equation-of-state measurements of Ge-doped CH*
- *Validation of the Compton-radiography diagnostic platform for ICF experiments*
- *Experiments to study the physical properties (thermal conductivity) of shocked-fusion fuels*
- *Characterization of hard x-ray sensitivity of MCP-based gated imagers*
- *Characterization of the plasma conditions at the laser entrance hole (LEH) of a gas-filled hohlraum using Thomson scattering*
- *Validation of the modeling of multibeam scattering occurring in NIC targets*
- *Measurement of the plasma conductivity by means of collective x-ray Thomson scattering*

The LLNL-led HED campaigns covered five main areas of research:

1. *Material dynamics and equation of state*
 - a. *Quasi-isentropic compression experiments (ICE) for material properties such as strength, equation of state, phase, and phase-transition kinetics under high pressure*
 - b. *Platform development using radiographic mea-*

measurements of instability growth in tantalum to infer material strength using the joint OMEGA-OMEGA EP configuration

- c. Properties of shocked CH and Si aerogel foams used in high-energy-density experiments
- d. The equation-of-state of a CO₂ mixture along the Hugoniot
- e. Initial experiments to develop an experimental platform to measure the melt and resolidification of tin

2. Opacity

- a. Opacity studies of high-temperature plasmas under LTE conditions
- b. Initial experiments to compare short- and long-pulse techniques to heat materials to high temperature for opacity data

3. Hydrodynamics

- a. Measurements of the Kelvin-Helmholtz instability in laser-driven shock tubes
- b. The hydrodynamic evolution of high-mach-number copper-foam jets

4. X-ray source applications

- a. Development of multi-keV x-ray sources for radiography and for the study of material response in samples

5. Diagnostic technique development

- a. Development of a target-mounted turning mirror for use with the VISAR diagnostic
- b. Demonstration of ultrafast temperature and density measurements with x-ray Thomson scattering from short-pulse-laser-heated matter
- c. Comparison of short- and long-pulse-generated x-ray backlighters
- d. Development of diffraction (white-light Laue and powder) to measure the structure of solids (Ta, Fe, Sn)

1. National Ignition Campaign Experiments

4 ω Thomson-Scattering Reactivation: The 4 ω Thomson-scattering diagnostic was reactivated using a half-day of laser time on OMEGA. The diagnostic has been redesigned to measure the high- and low-frequency Thomson-scattered features. Figure 124.122 shows the first measurement of Thomson scattering from the electron-plasma wave resonance using a 4 ω probe beam. The Thomson-scattering probe beam was aligned 400 μ m off the surface of a vanadium foil target. The target was heated with a single 3 ω beam, and the 4 ω probe beam was delayed from the heater beam by 1 ns.

The wavelength of the Thomson-scattered electron feature shown in Fig. 124.122 can be used to measure both the electron temperature and density. The density is decreasing in time

because of the expansion of the blowoff plasma, which can be seen in the increasing wavelength of the blue-shifted electron feature.

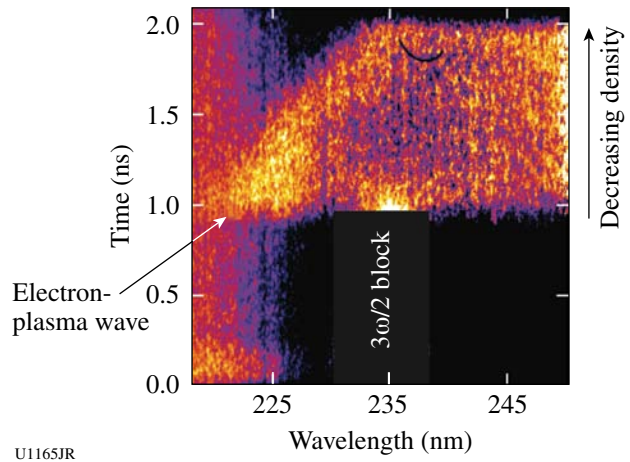


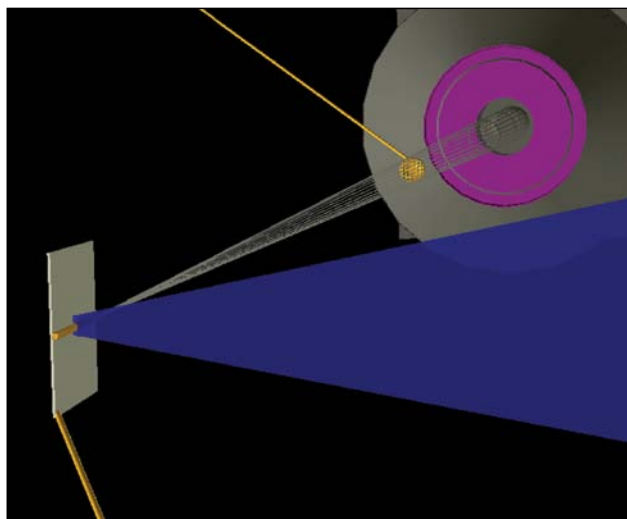
Figure 124.122 Thomson scattering from the electron-plasma wave resonance.

High-Resolution Bremsstrahlung Backlighters: The motivation of the bremsstrahlung backlighters campaign is to develop and characterize broadband x-ray sources emitting around and above 75 keV to be used in the Compton radiography of ICF targets. In FY09, Au microwire backlighters irradiated by 10-ps-long OMEGA EP pulses were characterized.

In FY10, Au microwire backlighters irradiated by 100-ps-long OMEGA EP pulses (1 ω) and OMEGA pulses (3 ω) were characterized with the primary goal of measuring the effect of longer laser pulse widths on backlighter source size.

As backlighters, 10- μ m-diam, 300- μ m-long Au wires were used on a CH substrate in a point-projection, end-on geometry. The bremsstrahlung radiation was generated by irradiating the Au wires with either the OMEGA EP short-pulse beam, delivering up to 1000 J in 100 ps (1 ω), or six OMEGA short-pulse beams, delivering a total of 250 J in 100 ps (3 ω).

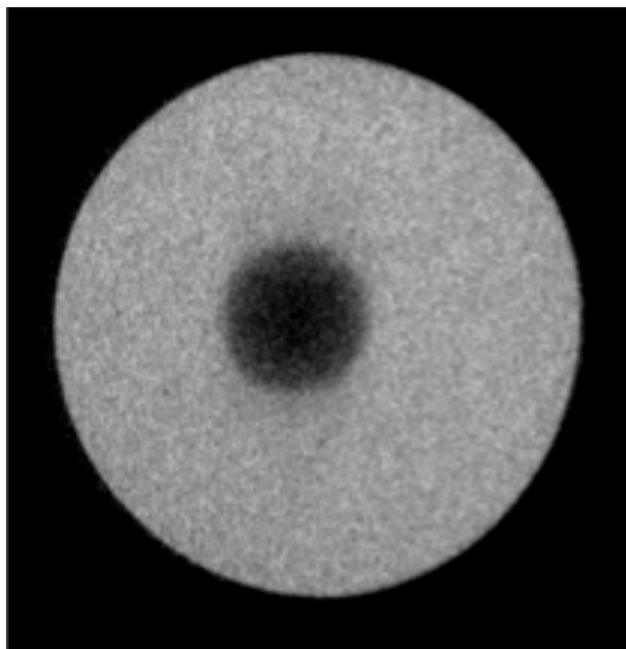
Solid W spheres with diameters of 200 μ m and 250 μ m located 10 mm from the backlighters were used as radiography samples (Figs. 124.123 and 124.124). The Compton radiography snout was used to record the radiographs and measure the backlighter spectra. A combination of high- and low-Z filters was used inside the snout to restrict the backlit photon energies to above 75 keV. A Fuji BAS imaging plate, placed at 400 mm from the backlighter, was used as a detector. An analysis of the radiographs of the W sphere allows one to reconstruct



U1166JR

Figure 124.123

Geometry used in the OMEGA EP target chamber to obtain 2-D radiographs of W spheres at photon energies above 75 keV. The short-pulse beam drives an Au microwire on a low-Z substrate.



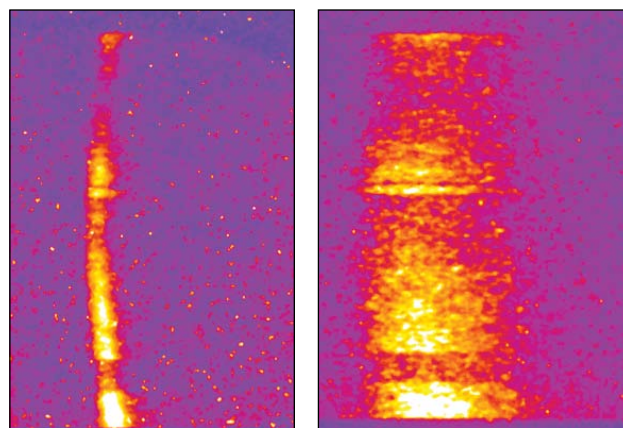
U1167JR

Figure 124.124

Point-projection radiograph of 200- μm -diam W sphere using 10- μm -diam Au microwire and six OMEGA beams (1ω , 40 J/beam/100 ps). The spatial resolution was $\sim 10\ \mu\text{m}$.

the source size of the backlights. No significant difference was found between 10-ps and 100-ps OMEGA EP-produced x-ray backlighter (1ω) and 100-ps OMEGA-produced x-ray

backlighter (3ω). In all cases, source sizes between 10 μm and 12 μm were measured. For the experiments performed in the OMEGA EP target chamber, the ultrafast x-ray streak camera was deployed, which provided durations of the soft x-ray emission from the Au microwires of ~ 12 ps and 80 ps for backlighters produced by 10-ps and 100-ps OMEGA EP pulses, respectively. First results show that the hard x-ray conversion efficiency of the lower-intensity 3ω probe is 10 to 20 \times less than the 1ω probe, as expected (Fig. 124.125). These results pave the way for the implementation of Compton radiography on the NIF, using relatively long pulses and 3ω laser irradiation for the backlighters.



U1168JR

Figure 124.125

An analysis of the streaked images shows pulse durations of the soft x-ray emission from the Au microwires of 12 ps (FWHM), when irradiated by 1 kJ/10-ps (left), and 80 ps, when irradiated by 1 kJ/100-ps (right) OMEGA EP pulses.

High-Resolution Measurements of Velocity Nonuniformities Created by Microscopic Perturbations in NIF Ablator Materials: Two FY10 CapSeed campaigns took place in January and March. The primary goals of these campaigns were to produce a survey of clean CH samples, to complete the studies of Be ablator samples, and to continue the survey of diamond samples near the melt curve, including the first 2-D velocity measurements of shock fronts propagated through single-crystal diamond samples. An upgrade to the OHRV diagnostic incorporated vacuum boxes around the interferometers to improve the noise performance of the instrument. The experimental campaigns produced preliminary data on CH, although the data collection was impeded by a pair of previously unencountered problems. During the first campaign, inadequate antireflection coatings on many of the targets degraded the data quality to an extent that required that the measurements be repeated. On the second campaign, unconverted light affected the package

more than during previous campaigns, owing to a minor design change. Better quality control on the antireflection coatings solved the first problem, and a new shield design to mitigate the unconverted light issue has already been tested successfully (on a later non-CapSeed campaign). The study of the Be ablators was completed during these campaigns, with the new data confirming results that had been achieved previously. A highlight of the CapSeed-10B campaign was the observation that the shock front of an ~ 500 -GPa shock front in a single-crystal diamond sample (below melt) was highly roughened (Fig. 124.126), equivalent to previous observations on poly-

crystalline diamond, suggesting, as a result, that the processes leading to the roughening are an intrinsic property of diamond.

Equation-of-State Measurements of Ge-doped CH: Knowledge of the EOS of NIF ablator materials is important for correctly predicting shock timing in an implosion. Plastic ablators in current NIF capsules are composed of layers of pure and Ge-doped $\text{CH}_{1.3}$. Recent shock Hugoniot measurements on both CH and CH_2 showed good agreement with models between 1 to 10 Mbar, providing confidence in the EOS for undoped plastic. In FY10, new shock Hugoniot measurements were performed on Ge-doped $\text{CH}_{1.3}$. Using impedance matching to a SiO_2 standard, the pressure and density of several samples doped with between 0.5 and 0.7 atm% Ge were measured. These data, supplemented by additional data from LLE shots, are shown in Fig. 124.127. From 1 to 6 Mbar, the data are in good agreement with LEOS 5315 (0.5% Ge) and LEOS 5315 (0.2% Ge)—models currently being used in simulations of NIF implosions—but are less compressible than these models at higher pressures (for comparison, two models for pure CH, *SESAME 7592* and LEOS 5310 are shown). Although it is unclear why there is a tendency toward stiffer behavior above 6 Mbar, the agreement in the 2- to 3-Mbar range corresponding to NIF first shocks justifies the use of these EOS tables in current simulations.

Compton Radiography: The goal of the Compton radiography campaign is to build a novel diagnostic platform for ICF to characterize the shape and density of the fuel in ICF implosions. After the successful demonstration of Compton radiography of implosions in FY09, it was applied to three kinds of implosions in FY10.

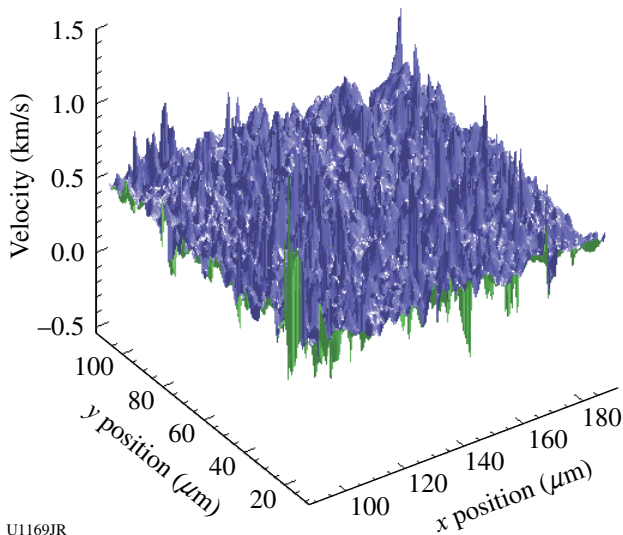


Figure 124.126
Two-dimensional velocity fluctuations over a $100 \times 100 \mu\text{m}^2$ region of a ~ 500 -GPa shock front traveling through a single-crystal diamond sample with $\langle 100 \rangle$ orientation.

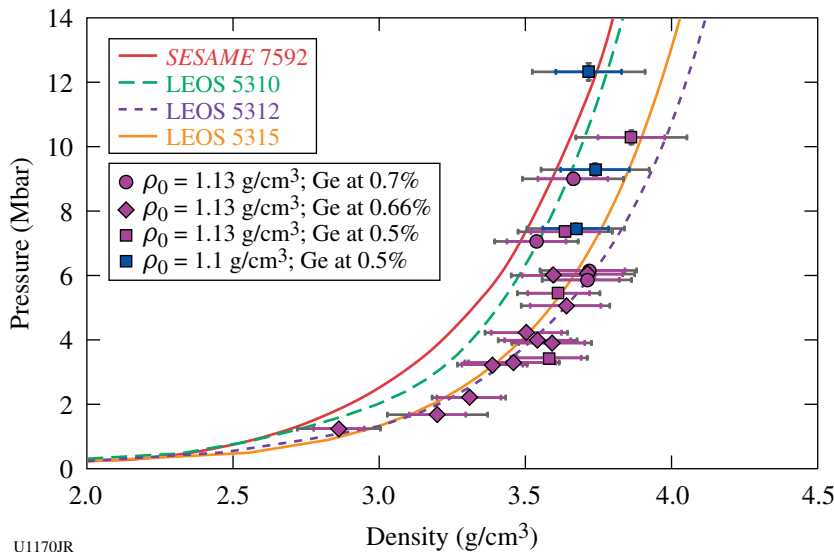
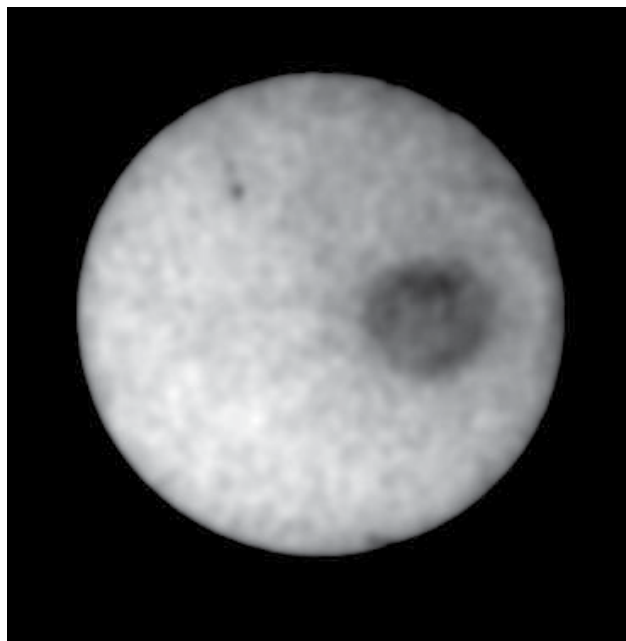


Figure 124.127
Summary of shock-Hugoniot measurements on Ge-doped $\text{CH}_{1.3}$.

In the first experiment, 60 beams of OMEGA were used to directly drive implosions of 40- μm -thick, 870- μm -diam CH capsules filled with 8 atm of D_2 gas, located at OMEGA's target chamber center. A 10- μm -diam, 300- μm -long Au wire was used as a backlighter in a point-projection, end-on geometry 10 mm from the CH shell. The backlighter was driven by the OMEGA EP short-pulse beam, delivering ~ 1 kJ at 10 ps in a 100- μm square spot size.

The time delay between the OMEGA EP short pulse and the OMEGA laser pulses was varied to bracket the peak compression time predicted by *LILAC* 1-D simulations. As an example, Fig. 124.128 shows a radiograph of the imploding CH shell, near peak compression, obtained at a photon energy of ~ 100 keV, where Compton effects dominate the fuel opacity. The radiograph, having about 10-ps and 10- μm temporal and spatial resolution, respectively, shows a limb-darkened shell of about 90- μm diameter.



U1171JR

Figure 124.128

Compton radiograph of an 870- μm -diam CH capsule filled with 8 atm of D_2 , near peak compression. The radiograph has been recorded at an effective photon energy $\langle h\nu \rangle \sim 100$ keV, where Compton effects dominate the fuel opacity. The radiograph shows an object about 90 μm in diameter inside the shadow of the Compton radiography snout collimator.

In a second experiment, at photon energies $\langle h\nu \rangle \sim 70$ keV, radiographs were successfully recorded of 54 OMEGA beam direct-drive implosions of cone-in empty CD shells and 60 OMEGA beam direct-drive implosions of empty CD shells,

without cones. Again, the Au microwire backlighters, with 10-ps and 10- μm temporal and spatial resolution, respectively, were driven by the OMEGA EP short-pulse beam, delivering ~ 750 J at 10 ps in a 100- μm square spot size. The radiographs of cone-in-shell implosions show the shell near peak compression, at a distance of 50 μm and with a diameter of about 50 μm . A third experiment was dedicated to recording Compton radiographs of cryogenic direct-drive implosions. This effort is a work in progress since the experimental setup imposes very tight tolerances on the alignment of the target and backlighter and relies on an improvement of the cryogenic-target alignment system. The CompRad campaigns fully validated a novel diagnostic technique, Compton radiography, which will be extremely useful when implemented on NIF implosions.

Conductivity of D_2 and CH: The thermal-transport properties of D_2 and CH at high densities have important implications for the stability of ICF implosions. The OMEGA laser was used to prepare off-Hugoniot states of these materials using multishock compression. Pressure, density, temperature, and optical properties of the compressed materials were determined by simultaneous VISAR and SOP measurements (Fig. 124.129). D_2 states up to 10 Mbar and 3 g/cc have been achieved at temperatures below 1 eV. CH states up to 8 Mbar and 4.5 g/cc have been achieved at temperatures near 3 eV. A Drude-like model was used to infer band-gap closure and electrical and thermal conductivities from the optical behavior at different states. Preliminary results indicate that D_2 thermal conductivity at such high-density, low-temperature states may be well below theoretical predictions.

Characterization of Hard X-Ray Sensitivity of MCP-Based Gated Imagers: An MCP-based gated x-ray imager is one of the most important diagnostics of the NIC. In FY09, the neutron-induced background of the MCP-based x-ray imagers with a CCD (Kodak KA-16801E) and a photographic-film readout (TMAX 3200) was characterized on OMEGA high-neutron-yield shots.⁴¹ In FY10, a new MCP-based x-ray framing camera, radiation hardened gated x-ray imager (hGXI) was assembled, and its x-ray sensitivity was tested at the Omega Laser Facility.

To optimize experimental setup of NIF implosion experiments, it is crucial to know the absolute sensitivity of the gated x-ray imager for 10- to 20-keV x rays. To test x-ray sensitivity in this energy region, calibration experiments were performed on OMEGA.

A Au-coated spherical target (1.015-mm diameter) was irradiated by 60 laser beams (UV, 500 J/beam, 1-ns square pulse).

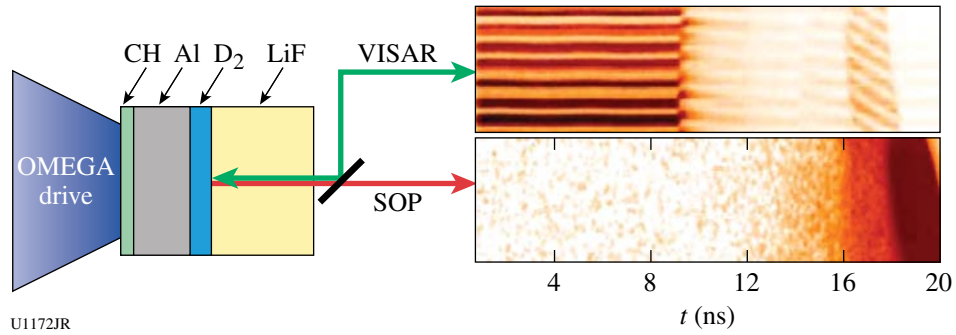


Figure 124.129

A sequence of three OMEGA laser-driven shocks was sent into a thin layer of liquid D_2 trapped between an Al pusher and a LiF window. For the states reached in this experiment, the LiF remained transparent, and the VISAR and SOP records tracked the velocity, reflectance, and optical emission of the D_2 -LiF interface. A dramatic increase in the D_2 reflectance was observed upon the arrival of the third shock at this interface (at ~ 16 ns), corresponding to a large increase in the conductivity. The three shocks coalesce in the LiF at about 18 ns, increasing the LiF temperature and ending its transparency.

The laser intensity on the sphere was 1.2×10^{15} W/cm². Absolute x-ray emission spectrum was recorded by x-ray spectrometers (HENWAY and DCS). To compare relative sensitivities, three different gated x-ray imagers (hGXI, XRFC1, XRFC3) were located 1600 mm from the target chamber center. In front of the MCP, a 2.5-mm-thick-polyimide, 0.6-mm-thick-Al filter was used to cut off a low-energy component (<7 keV) and attenuate the x-ray fluence. Figure 124.130 shows estimated x-ray production on the target and spectrum through the filters. The estimated x-ray flux on the MCP is 2.5 to 5 kW/cm². Figure 124.131 shows images obtained with this experiment. The signal intensity obtained by those cameras (hGXI: OD = 1.97, 193 merg/cm²; XRFC1: 1250 ADU/pix; XRFC3: 1750 ADU/pix) was consistent with our numerical model. Those numbers will be used to benchmark the MCP model.

Plasma Characterization of the LEH Region of Gas-Filled Hohlräume: The objective of this campaign was to characterize the plasma conditions at the laser entrance hole (LEH) of a gas-filled hohlraum using Thomson scattering. This region is of special interest for crossed-beam energy transfer, which is a process that can transfer a large percentage of laser energy between beam cones. The energy transfer is governed by the

electron temperature, plasma-flow velocity, and laser-beam wavelength. Thomson-scattering measurements from the ion feature were made for a series of hohlraums with LEH diameters of 800, 1000, and 1200 μ m (Fig. 124.132).

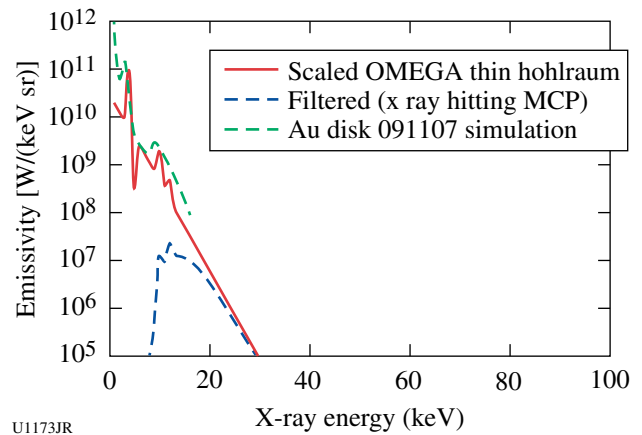


Figure 124.130

X-ray production and spectrum from the Au sphere. X-ray conversion efficiency was estimated by a radiation-hydrodynamic simulation and extrapolating x-ray spectra of previous experiments.

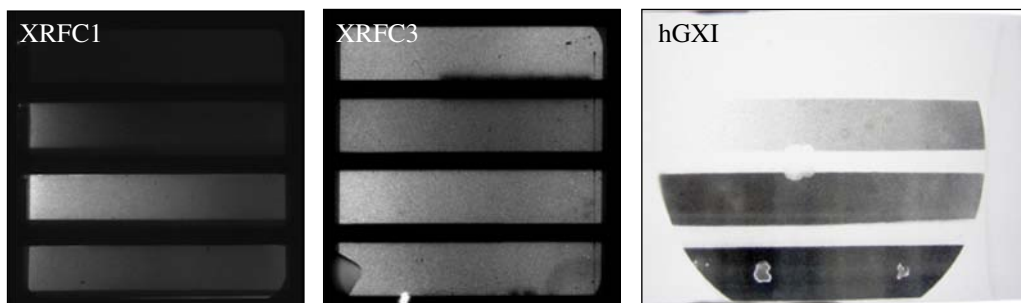


Figure 124.131

Images obtained on a flat-fielding experiment from three different x-ray imaging systems: XRFC1, XRFC3, and hGXI.

U1174JR

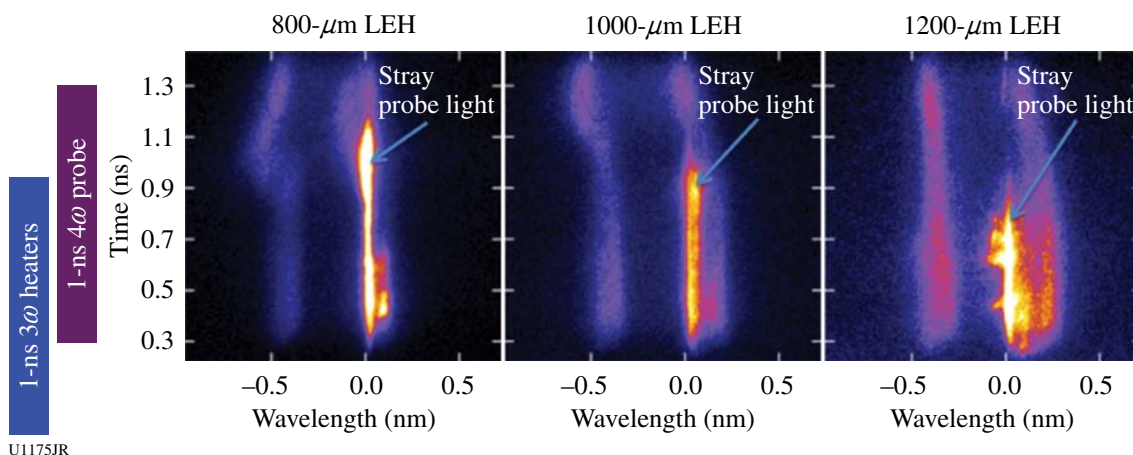


Figure 124.132
Thomson-scattering measurements of the LEH region of a gas-filled hohlraum.

The Thomson-scattering measurements are compared to hydrodynamic simulations using the code *HYDRA* in Fig. 124.133. The plasma-flow velocity is shown for three different locations along the simulation hohlraum axis. Large gradients in this region are predicted by the modeling. The measured electron temperature and flow velocity will be used to benchmark different heat-transport models.

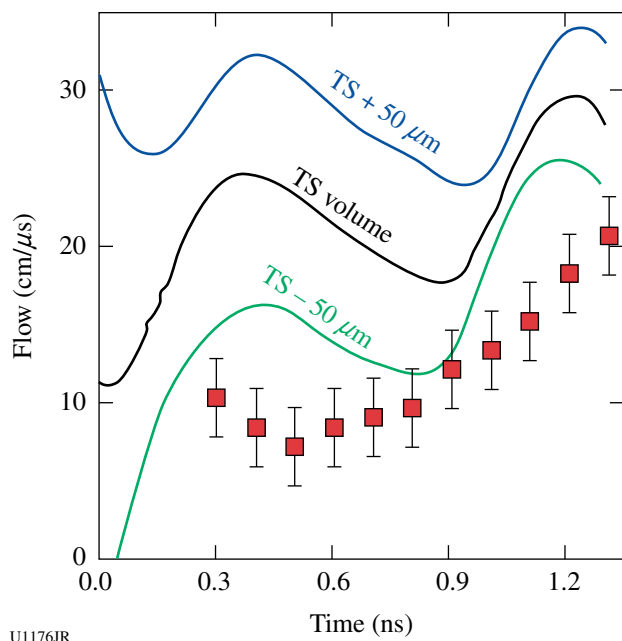


Figure 124.133
The experimental measurements (red squares) are compared to hydrodynamic simulations at different locations outside the LEH.

Validation of the Modeling of Multibeam Scattering Occurring in NIC Targets: A series of experiments was carried out to verify a critical component of the model of backscatter from the multiple NIC beams that indicates that backscatter from the interior of the hohlraum can be amplified by each of the crossing beams it encounters as it exits the laser entrance hole. The model predicts that even with a small gain exponent from each of several crossing beams, the overall gain exponent and amplification produced by all the beams can be quite significant with the additive gain exponents of linear waves. The OMEGA experiments used a 3- μm -thick CH foil target illuminated with 28 heater beams to produce plasma conditions similar to what are found in NIC ignition targets and the Mach-1 flow velocity that is necessary to produce resonant amplification of a seed with the same wavelength as the pumps, as shown in Fig. 124.134.

Experiments were performed in which the transmission of a seed beam (B46) was measured in the case of no pump beam and one and two crossing pump beams (B30, B50); the transmitted power in each case is shown in Fig. 124.135.

Note that a single pump beam produces enhanced transmission relative to the no-pump case near 1.4 ns, as expected from the simulations of the resonance conditions, and a second pump beam produces an even greater increase in the power at a somewhat later time. These results were obtained at three different seed intensities, and similar amplifications were found in each case, consistent with a linear ion-acoustic wave response. Further experiments were carried out to demonstrate the control of energy and power transfer by the relative align-

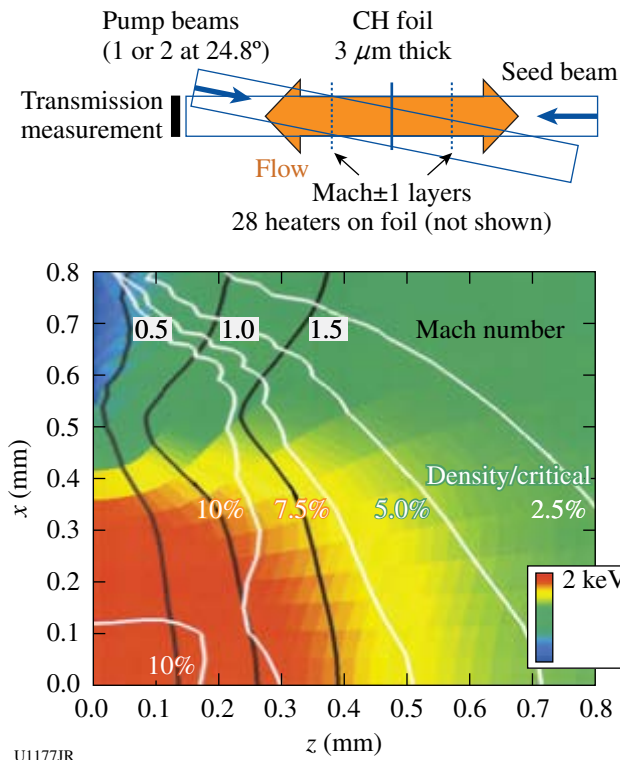


Figure 124.134 The experimental geometry of a foil target used to produce the plasma conditions and Mach-1 flow, shown at 1.4 ns, that is necessary for resonant amplification of a seed of 351-nm light representing the SBS backscatter produced in the interior of the NIC hohlraum.

ment of the polarization vectors of the pump and seed beam, as shown in Fig. 124.136.

To change the polarization, the half-wave plate, or polarization rotator, was installed in B50 and its polarization was rotated through 90° with respect to the seed-beam polarization. The experiments demonstrated greatest amplification when the polarizations were aligned, as determined from the energy-amplification factor measured in three experiments and shown in Fig. 124.136. The greatly reduced amplification when the polarization angle was near 90° demonstrates the importance of relative polarization in controlling this effect. This work has increased confidence in the modeling of multibeam scattering occurring in NIC targets.

Measurements of the Plasma Conductivity by Means of Collective X-Ray Thomson Scattering: The goal of this experiment was to measure the electron-ion collision frequency n_{ei} in isochorically heated Be from the broadening of plasmon signals measured with x-ray Thomson scattering.⁴² The n_{ei} is directly related to the conductivity, which is an important

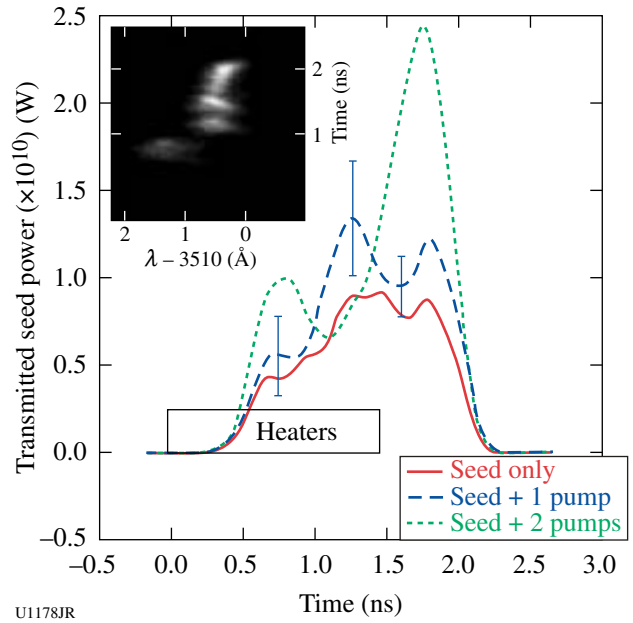


Figure 124.135 Streaked spectrum and transmitted power waveforms of the seed beam transiting the foil target plasma, for the cases of no amplifying pump and one and two amplifying pumps, showing enhancements in the seed power produced by energy transfer from the pumps to the seed beam.

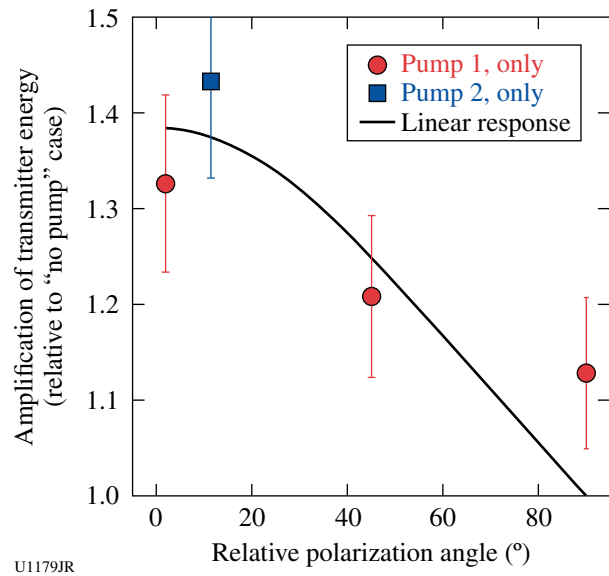


Figure 124.136 Energy-amplification factor produced by a single pump beam as a function of its polarization angle relative to the seed beam.

parameter to correctly model capsule implosions on the NIF; at the same time, it is known only with great uncertainty from theoretical predictions.

On this joint OMEGA–OMEGA EP shot day, the OMEGA EP beam (250 J in 10 ps) was used to isochorically heat a 200- μm Be cube to 35 eV, assuming 20% conversion efficiency into hot electrons ($T_{\text{hot}} \sim 200$ keV), as shown in Fig. 124.137(a). Since it is properly shielded, the Be's front surface, which gets much hotter, is not seen by the scattering experiment. The size of the gold shields was chosen such that plasma moving around the shield and still emitting line radiation would be imaged to the detector well separated from the scattering signal. This is important because gated detectors cannot be used in this short-pulse environment. Fourteen OMEGA beams at 3ω drive irradiated a 12- μm -thick Saran foil to create the Cl Ly α probe line at 2.96 keV. A pulse width of 200 ps was chosen to achieve an adequate time resolution of the scattering experiment. Radiation–hydrodynamic simulations show that at temperatures of a few 10 eV, the Be cube does not disintegrate within the first 750 ps. The scattering angle was at 30° to ensure a large collectivity parameter $\alpha \sim 1.7$, necessary to observe plasmon broadening caused by collisions.

To measure the scattering spectrum, a new high-efficiency von-Hamos geometry Bragg crystal spectrometer was developed using a cylindrical curved HOPG crystal [see Fig. 124.137(b)]. The signal was recorded on image plates. The CLVH spectrometer was successfully fielded for the first time on this shot day. For cross-calibration, and as source monitors, the Cl K-shell emission was monitored with the GTS and XRS1 spectrometers, operated with image plates, and with SSCA on the OMEGA-only shots.

A total of nine shots were taken, including three joint shots at full energy, two OMEGA EP–only shots, and four OMEGA-only shots. On the low-energy qualification shot of the OMEGA EP beam, the emission from an Au-coated CH sphere was used to measure the timing between the OMEGA and OMEGA EP lasers and to establish a 400-ps delay of the OMEGA probe beams with respect to the OMEGA EP beam. During the day, conditions used to create the x-ray probe were varied. On most of the targets, the Saran foil had a 30- μm

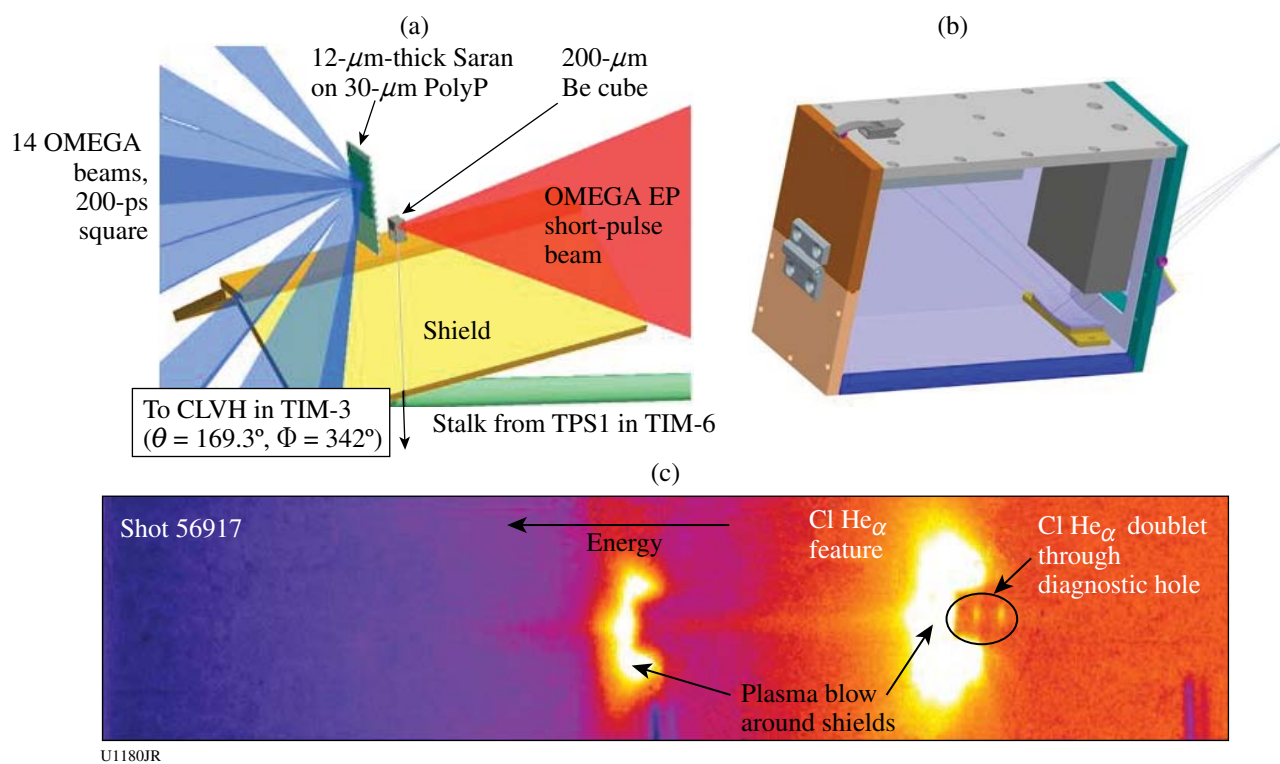


Figure 124.137

(a) Experimental setup to isochorically heat a 200- μm Be cube and characterize the plasma conditions with x-ray Thomson scattering using the Cl Ly α line at 2.96 keV. (b) The CLVH spectrometer, utilizing a cylindrically curved HOPG crystal in von-Hamos geometry to achieve high detection efficiency, was developed for this campaign and successfully fielded for the first time. (c) Data from CLVH.

polypropylene backing to prevent Cl-containing plasma from moving into the line of sight of the CLVH spectrometer above the Be cube and obscuring the scattering signal. In combination with the low backlighter drive energy (~1 kJ in 0.2 ns compared to ~7.5 kJ in 1 ns for other XRTS platforms), it was not possible to observe a scattering signal. The strongest signal was obtained for a target that had no polypropylene backing, and the OMEGA pulse length was increased to 600 ps, as shown in Fig. 124.137(c).

The most prominent features are due to Cl He α and Cl Ly α emission from plasma that was moving around the shields. In the nondispersive axis the spectrometer was imaging with M = 1, and the extension of the shields of ~±3 mm from the center axis can clearly be seen. X-ray emission from the direction of the Be cube at TCC was imaged to the central axis. Clearly, a weak bremsstrahlung signal and the He α doublet can be identified originating from that direction.

2. High-Energy-Density Experiments

Material Dynamics and Equation of State

Iron equation of state: Ramp compression of Fe to 300 GPa.

The preliminary design for a ramp-compression experiment on Fe up to 300 GPa is shown in the upper right image in Fig. 124.138, along with the ramp laser pulse shape as calculated by a radiation-hydrodynamics code (lower right). The ramped laser pulse shape for the 36 beams focused onto the inner walls of the hohlraum results in a time dependence in the radiation temperature, and subsequently a ramp-compression wave is launched into the stepped Fe sample. The raw VISAR data and the extracted free-surface velocity U_{fs} versus time profiles for 25.5/21.9/38- μ m-thick Fe samples are shown on the left in Fig. 124.138.

The $U_{fs}(t)$ profiles reveal a strong rate dependence associated with the $\alpha \rightarrow \epsilon$ structural phase transformation. The equilibrium pressure for this transformation as measured in

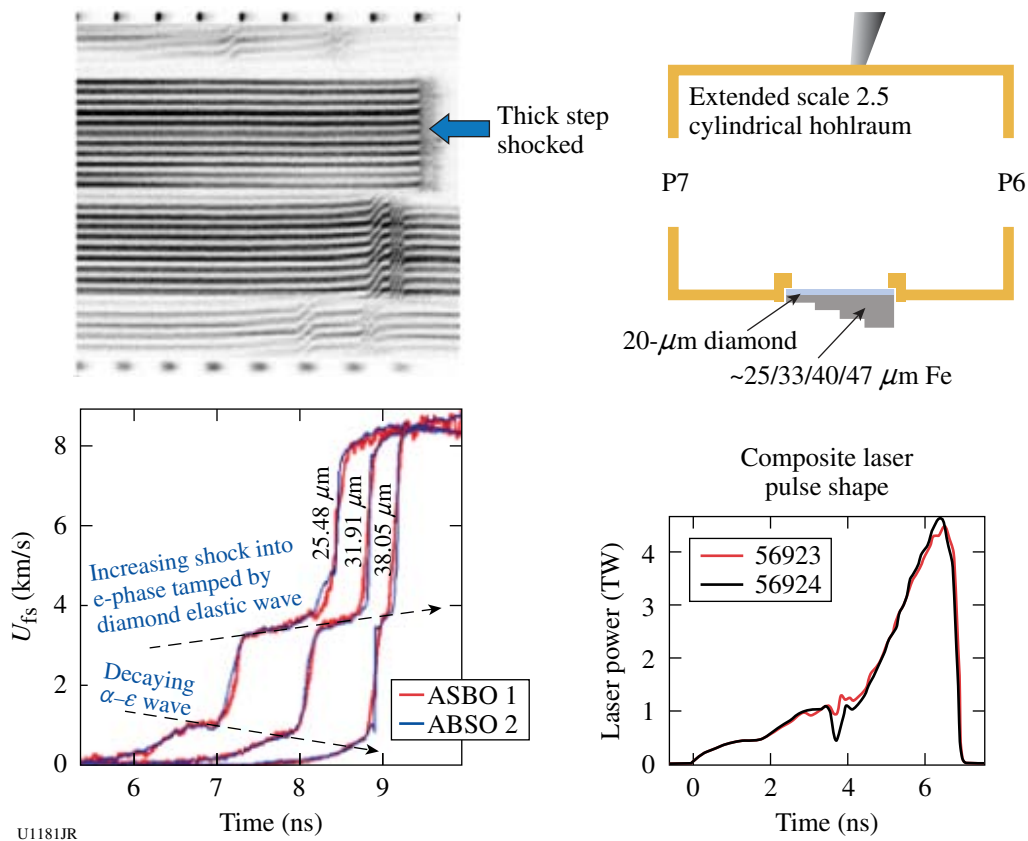


Figure 124.138

Preliminary attempts to ramp compress multisteped Fe samples to a peak stress of ~300 GPa were successful. However, strong time dependence was observed associated with compression across the $\alpha \rightarrow \epsilon$ phase boundary.

shock-compression experiments with millimeter-thick samples is 13 GPa. The measured pressure, however, for the $\alpha \rightarrow \epsilon$ phase transformation in these experiments for thin samples and high strain rates is ~ 20 GPa. This strong time dependence compromises the extraction of stress-density data using the standard ramp-compression analysis techniques. To overcome this difficulty, subsequent experiments have been designed such that a steady initial ~ 70 -GPa shock is launched into the stepped Fe sample followed by subsequent ramp compression to ~ 300 to 400 GPa. This initial shock compresses directly into the ϵ phase by overdriving the $\alpha \rightarrow \epsilon$ phase transformation and therefore avoids the complications associated with the kinetics of this transformation. With the high-pressure ramp-compression platform developed during this period, compression of solid Fe to peak stresses of 300 GPa was demonstrated, and strong time dependence in the structural phase transformations was observed.

Boron ablator for quasi-isentropic compression experiments. The purpose of this campaign was to demonstrate the performance of B as an ablator. By measuring the shock-break times of a stepped reservoir, the ablation pressure created by the ablator material was deduced. The data matched well with the LASNEX simulation with an ablation pressure of 52 Mbar, which will be sufficient to create up to 5-Mbar pressure for the quasi-isentropic drive for the material-strength Rayleigh–Taylor experiments on the NIF.

Tantalum Rayleigh–Taylor experiments. The goal of the ICETaRT experiments is to measure the dynamic properties of solid-state Ta under high pressures (>1 Mbar) and high strain rates (10^6 to 10^8 s $^{-1}$) using the Rayleigh–Taylor (RT) instability. Quasi-isentropic high-pressure conditions were achieved by using a unique plasma piston configuration where

the sample materials stay well below the melting temperature while they are plastically deformed under high pressure, as shown in Fig. 124.139. The growth of the RT instability was measured in V 43 and Ta, and these data were used to compare with predictions using different material strength models. The amount of growth was measured by face-on radiography using laser-driven x-ray backlighters. High-energy backlighter x rays of 20 to 50 keV generated by the OMEGA EP beam were used to probe high-Z materials such as Ta.

The experiment was conducted in the main OMEGA chamber in the joint OMEGA/OMEGA EP shot configuration. A series of successful radiographs were obtained from these experiments. Figure 124.140(a) shows one example of a face-on, 22-keV x-ray radiograph of a rippled sample target of Ta at 60 ns after the initial laser pulse. The driven ripples constitute the circular central part of the image, while the upper portion of the image contains calibration features (stepped filters and knife-edge resolution block) to aid in the extraction of the growth factor. The ripple amplitudes were derived from transmission contrast between the peak and valley of the ripple regions. The initial growth-factor measurements are compared to several strength models in Fig. 124.140(b), including the new Ta multiscale model, which starts with a quantum mechanical interatomic potential and is based on the motion and multiplication of dislocations, 44 and the Preston–Tonks–Wallace (PTW) strength model. 45

Experiments later in the year addressed the effect that grain size (Hall–Petch effect) had on the strength under these high-pressure and high-strain-rate conditions. While there are many measurements of the Hall–Petch effect at ambient conditions, where strength varies as (grain size) $^{-1/2}$ (Ref. 46), no previous theory or experimental measurements under high-

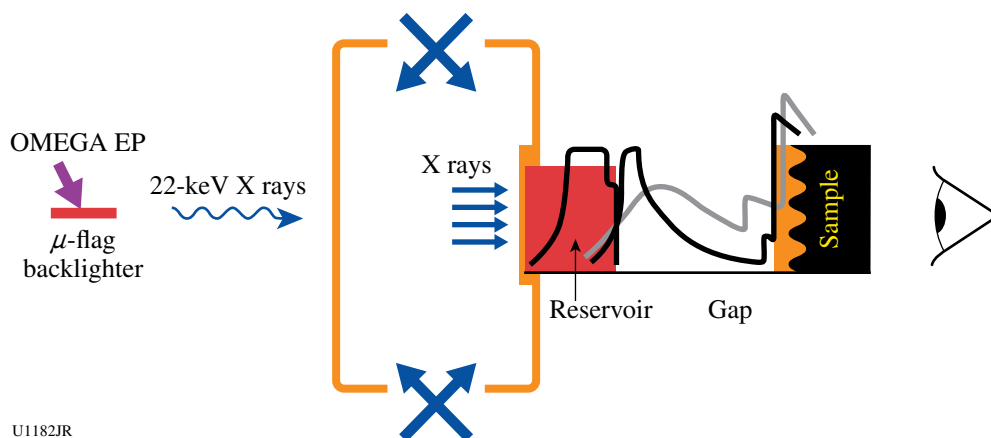


Figure 124.139
ICETaRT experiment configuration for an OMEGA/OMEGA EP joint shot.

U1182JR

pressure, high-strain-rate dynamic conditions existed. Three different types of targets were fabricated, with average grain sizes of 90, 15, and 0.25 μm , as shown in Fig. 124.141(a). The radiography data quality was very high, and useful data were obtained on all shots. The strength is inversely related to the RT growth factor, which is shown as a function of the average grain size in Fig. 124.141(b). Within the error bars of the data, no obvious Hall–Petch effect is observed. The data analysis is still in progress to understand the theoretical and physical implications of these results.

Equation of state of SiO_2 aerogel foam. The study of the EOS of low-density foams allows one to achieve states of matter with high temperatures at lower than solid density. These conditions appeal to a range of interest for high-energy-density science. Foams at different densities can be used in EOS experiments to study points along unloading isentropes, which allows one to study the material EOS of the Hugoniot. Foams also play an important role in laboratory-based astrophysical experiments like supercritical radiative shocks or simulate supernovae remnant formation. All of these uses for foams

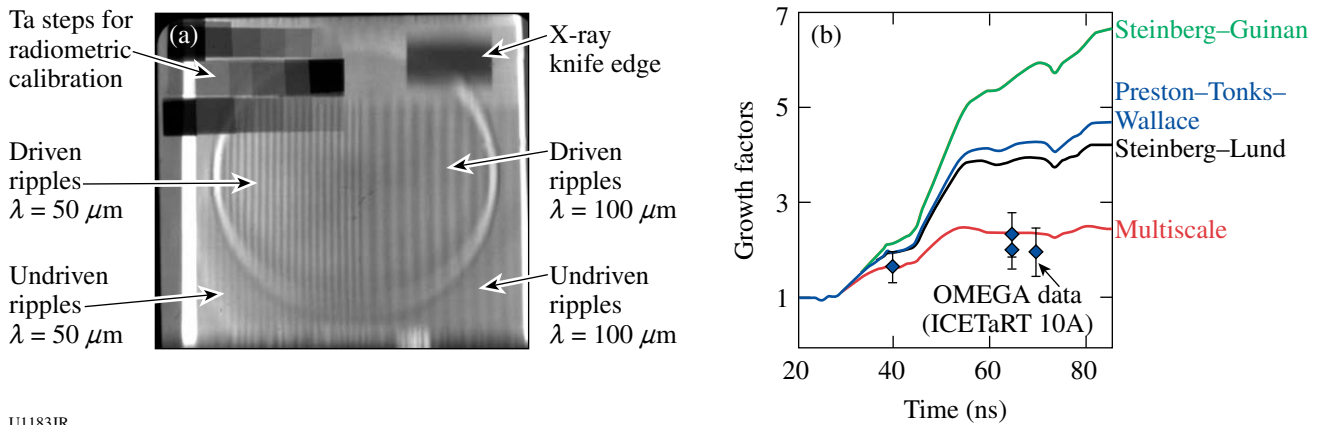


Figure 124.140

(a) Face-on 22-keV x-ray radiograph of a rippled sample target of Ta at 60 ns after the initial laser drive. The driven ripples constitute the center of the image, while the upper portion of the image contains added features (stepped filters and knife-edge resolution block) to aid in the extraction of the growth factor. The ripple amplitudes were derived from transmission contrast between the peak and valley of the ripple regions. (b) Comparison of various model predictions with growth-factor data. The data reach peak pressures between 1.2 and 1.4 Mbar and average strain rates around $2 \times 10^7 \text{ s}^{-1}$.

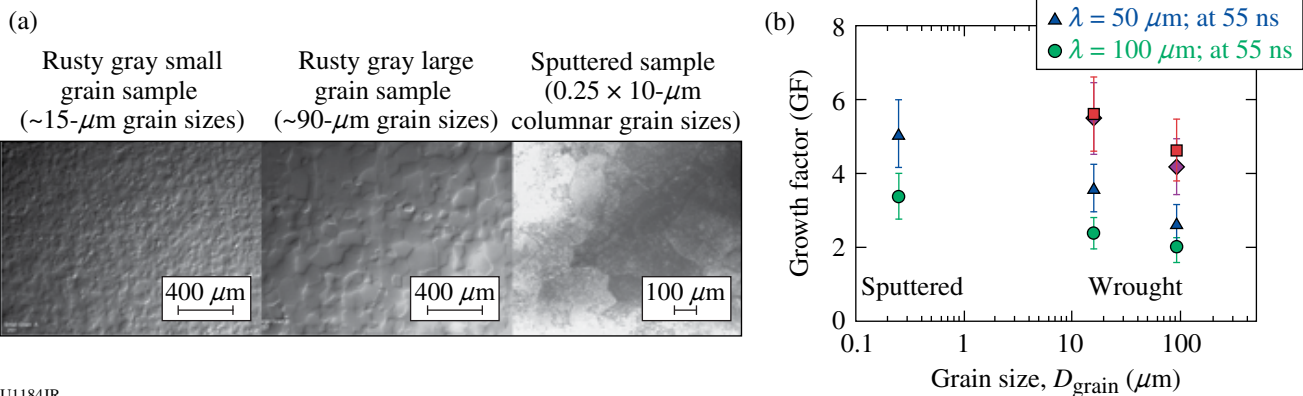


Figure 124.141

(a) SEM and TEM pictures of the different Ta grain-size samples. (b) Growth factor, which is sensitive to material strength, as a function of grain size. No obvious Hall–Petch effect is observed.

require a detailed understanding of the EOS of the foam itself. Unlike other material EOS studies, which vary pressure and temperature, the foam has an adjustable initial density that plays a key role in determining the material's behavior. In these experiments, the foam of interest, in this case 100 mg/cc of SiO₂ aerogel, was placed between two quartz plates, as shown in Fig. 124.142. A decaying shock wave was launched through one of the quartz plates, and the propagation of the reflecting shock front through the quartz and foam was followed by an optical VISAR system. In this system the known Hugoniot of the quartz was used with an impedance-matching model to determine the properties of the foam. Figure 124.143 is a plot of data taken over four shots at a single initial density. The large increase in density at low pressures was caused by the compaction of voids in the material at the higher shock pressures; the compaction of the voids causes heating and the majority of the pressure is due to thermal pressure.

CH-foam shock-breakout experiment. Understanding the behavior of foams in the presence of a strong shock is an ongoing effort at several institutions. A series of experiments were performed to investigate the material properties of a new foam material, dicyclopentadiene (C₁₀H₁₂), at a density of 40 mg/cc. The targets were configured as shown in Fig. 124.144, and were driven by 15 beams with a pulse length of 1 ns. Some targets were driven with a plastic (CH) ablator and an Al piston, while others used a Cu-foam piston (density 0.9 g/cc).

The primary diagnostic was VISAR, including the streaked optical pyrometer (SOP), which was used to measure the shock breakout. Data from these shots are shown in Fig. 124.145. The shock in the foam at full drive (5488 J) showed dramatic

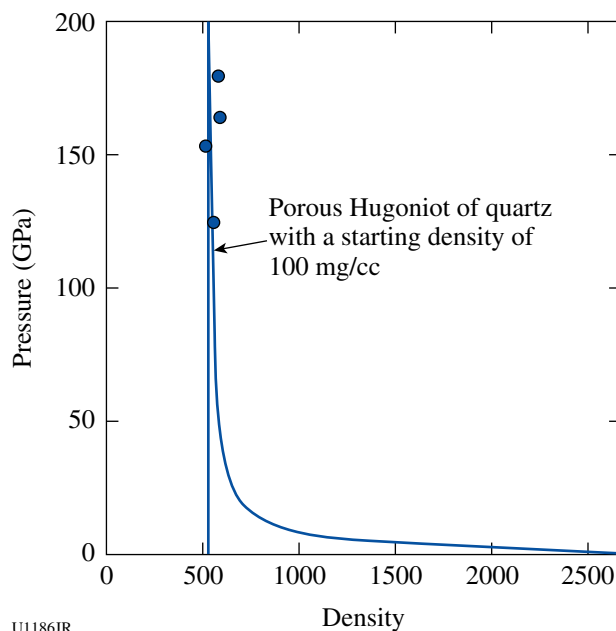


Figure 124.143
Plotting the pressure–density points compared to a model prediction of the shock Hugoniot of 100 mg/cc of SiO₂ aerogel.

evidence of preheat (presumed to be caused by drive x rays preheating the foam), although the shock in the quartz was measurable as may be seen in Fig. 124.145(a). With significantly reduced drive (3057 J), shock breakout from the foam was observed. See Fig. 124.145(b). This experimental series has been put on hold while the mechanical properties of the material for fabricating targets are being evaluated. These were the first targets fabricated from DCPD, and the material appears to have less rigidity than expected.

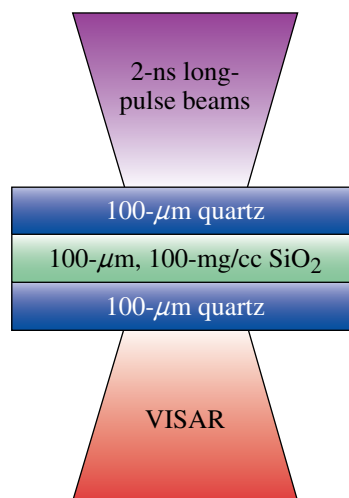
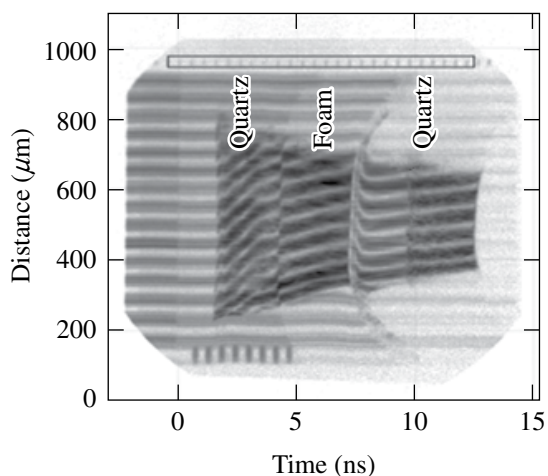


Figure 124.142
Target geometry and example data. The VISAR trace shown follows the shock wave through the quartz and 100 mg/cc of SiO₂ aerogel.

U1185JR

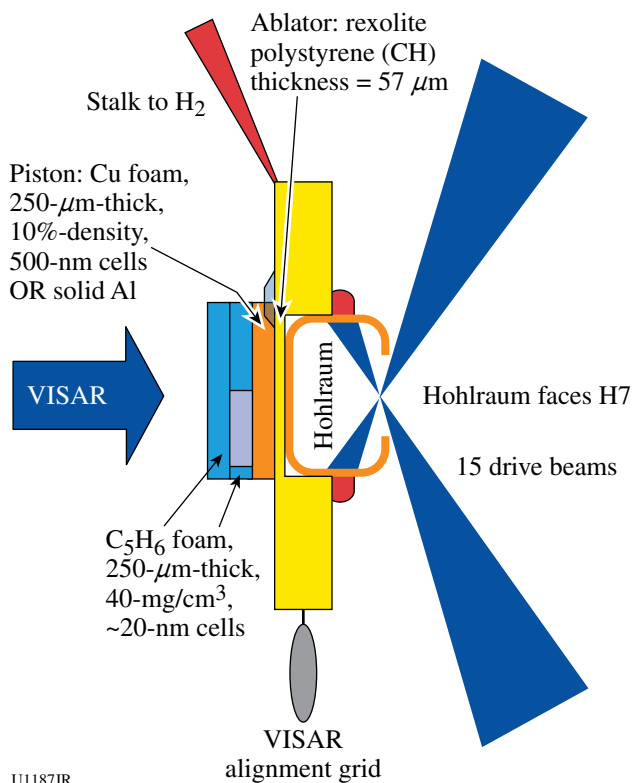


Figure 124.144 Target, laser, and diagnostic configuration for the CH-foam shock-breakout campaign.

CO₂ Hugoniot measurements to 950 GPa. CO₂ EOS, which is found in the core of giant planets, is of wide scientific interest. It is a mixture that challenges models to accurately predict. Prior experimental data were limited to below 100 GPa. Experimental measurement of the CO₂ Hugoniot was extended up to 950 GPa by launching shocks into CO₂ samples precompressed

in diamond anvil cells to ~0.5 GPa (see Fig. 124.146). VISAR and SOP measurements of the CO₂ shock front in comparison to concomitant measurements in quartz were used to infer pressure, density, reflectance, and temperature of shocked CO₂. CO₂-shock reflectance saturated at about 35% above 350 GPa, and the pressure, density, and temperature results are consistent with the theoretical LEOS table.

Melt and resolidification in Sn. This was the first set of experiments that investigated the use of velocimetry for exploring the melt line of Sn. The strategy was to develop a drive to shock-melt the tin and then ramp-compress it across the liquid-

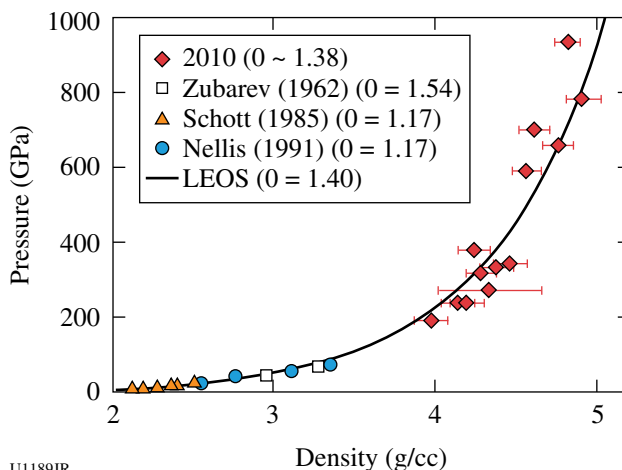


Figure 124.146 Previous experimental measurements of the CO₂ Hugoniot (open data points) reached 80 GPa. In FY10, the OMEGA laser was used to extend the range to 200 to 950 GPa (solid diamonds). The CO₂ shock pressure and density were inferred by shock-velocity measurements impedance matched to a SiO₂ standard, using the Hicks (2005) SiO₂ equation of state.⁴⁷

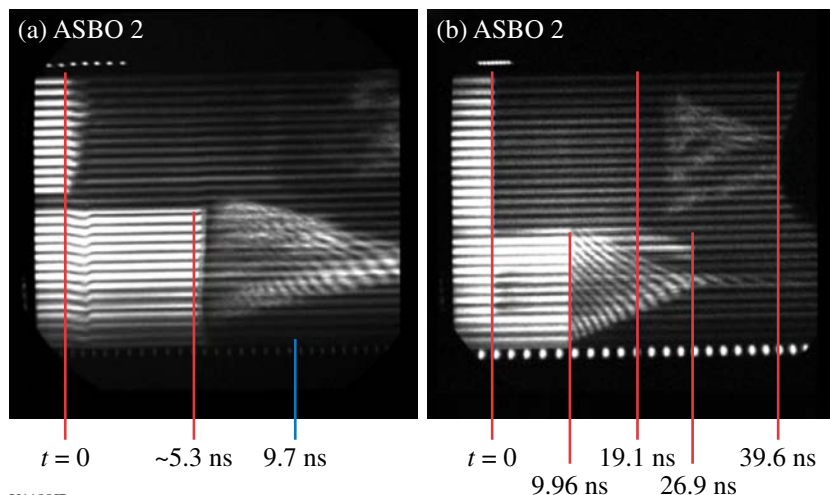
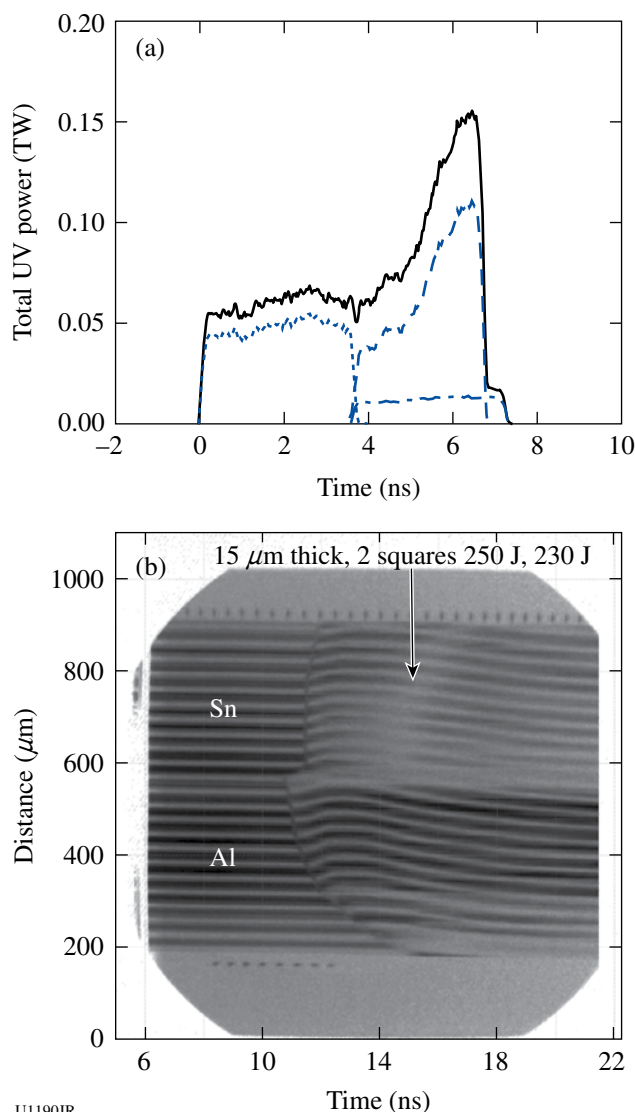


Figure 124.145 (a) VISAR signal from the target shown in Fig. 124.144, driven with 5488 J. No shock breakout is visible in the top of the image, and the reflected signal appears to come only from the back surface of the quartz anvil. (b) VISAR signal from a similar target driven with 3057 J. The shock breaks out of the C₁₀H₁₂ at about 19.1 ns and is visible in the quartz anvil before breaking out at 39.6 ns.

U1188JR

solid phase boundary. While analysis of the data is ongoing, a number of important observations were made (Fig. 124.147). It was verified that the sample design was feasible, data were produced across a wide range of shock pressures (20 to 200 GPa), and a reference material (Al) was used on each shot. Initial designs, based on extrapolation of diamond pressure-intensity measurements made at high pressures, proved to overestimate the achieved pressure. It was possible to generate the necessary data by utilizing the calibrant. This data will serve as the basis for future designs. Lastly, an interesting change in the reflectivity of the tin was observed during the apparent release portion of the loading. This remains to be explained.



U1190JR

Figure 124.147

(a) Composite shock-ramp pulse shape used to generate first attempt at compression-driven resolidification in Sn. (b) VISAR recording showing late-time reflectivity changes (arrow) that occur only in the Sn.

High-Temperature Plasma Opacity: Opacity experiments in FY10 had three main goals. The first addressed physics questions from the very successful 2009 Ti opacity shots, where the observed Ti continuum opacity did not match code predictions, although spectral absorption lines from charge states consistent with ~ 120 -eV LTE sample temperatures matched the code quite well. A modification in the configuration was made using thinner Ti samples, and new data were successfully taken on a half-day in January. A follow-up full-day experiment is scheduled for FY11.

The second goal was to better characterize the x-ray framing cameras (XRFC's) used on the experiments. NIF data from November 2009 revealed that the gain along with the gain profile of a microchannel-plate detector strip was sensitive to the relative delays between individual strips, as a result of electromagnetic crosstalk in the pulser input lines and the detector strips themselves. This effect produced $\sim 3\times$ differences in gain between strips, $\sim 2\times$ changes in the relative point-to-point gain in a single strip (compared to a synchronized-strip baseline case), and 30% to 50% changes in gain from one edge of a strip to the other (transverse to the pulse-propagation direction). The latter effect would impair the analysis of space-resolved gated absorption spectra if a similar effect occurred on the cameras used for opacity experiments. Data were taken for three framing cameras on OMEGA on 8 July, measuring these effects as a function of interstrip delay and gated detector pulse width. While the XRFC data showed $\sim 2\times$ differences in gain between strips, and significant (50% to 100%) changes in point-to-point relative gain along a strip, no significant gain variation across the strip was measured. Therefore, the performance of the camera was not a factor in the discrepancy in the Ti data.

The third goal was to compare short-pulse-heated opacity measurements with similar long-pulse conditions (Ti, $T \approx 100$ to 150 eV, density ~ 0.1 to 1.0 g/cm³). In principle, much higher temperatures are possible with short-pulse-heated materials, but questions exist as to whether LTE conditions can be maintained. In these experiments, the OMEGA EP sidelighter beam was operated at 250- to 800-J, 100-ps pulse width and broad focus to heat an opacity sample at intensities between 10^{15} to 10^{17} W/cm². The OMEGA EP backlighter beam was delayed by 100 to 500 ps and then operated at 800 to 1000 J, 10 ps to drive a broadband 3- to 6-keV backlighter. The backlighter x rays probed the hot, expanded opacity sample. A separate line of sight allows one to take space- and energy-resolved sample emission spectra in a different spectral band. The experiment used the two opacity spectrometers that were transferred to OMEGA EP from the 60-beam OMEGA chamber and fielded

with “rotating SPCA” frames and time-integrated image-plate detectors. Shots in February demonstrated an opacity-quality broadband backlighter using a Zn microdot on an Al substrate, with data shown in Fig. 124.148. (Subsequent shots using a CH substrate failed as a result of very high instrument backgrounds but may have reflected a change in the pointing or laser conditions.) Further optimization of the backlighter will take place in FY11. In parallel, space-resolved broadband emission spectra from 10 to 50 Å were obtained from a CH/Ti/CH/Al exploding-foil sample (driven by the OMEGA EP sidelighter at $\sim 10^{16}$ to 10^{17} W/cm²). Al-, C-, and O-line features have been identified from a shot at lower intensity, along with a broad

continuum (see Fig. 124.149). Bright Ti emission was seen at higher intensity. Ti absorption lines were not observed; FY11 shots will assess whether this is caused by cool Ti plasma conditions or perhaps mistiming of the OMEGA EP backlighter and sidelighter. The source of the O lines is being investigated.

Hydrodynamics

Kelvin–Helmholtz instability experiments. A Kelvin–Helmholtz (KH) growth experiment was performed using a platform successfully developed in earlier OMEGA experiments.^{48–50} The main goal of the most recent campaign was to measure turbulent mixing on an interface between CRF foam and I-doped plastic. Figure 124.150 shows a target schematic that consists of a plastic ablator and a shock tube. In the shock tube, the interface between low-density foam and high-density plastic had pre-imposed sinusoidal modulation at a wavelength of 400 μm and an amplitude of 30 μm. The central part of the plastic target contained a layer of I-doped CH to increase a contrast to 5-keV backlighter x rays. The ablator of the target was directly driven with laser light, producing a strong shock that propagated through the target. The shock produced a velocity gradient at the interface between the foam and plastic. This velocity difference between the two materials resulted in the KH growth of the surface modulations. The density of foam was varied from 50 mg/cc to 100 and 200 mg/cm³. Turbulent mixing between a foam and plastic materials was expected to grow from short-scale surface finish modulations (with rms amplitude of 100 nm) on the interface between the two materials.

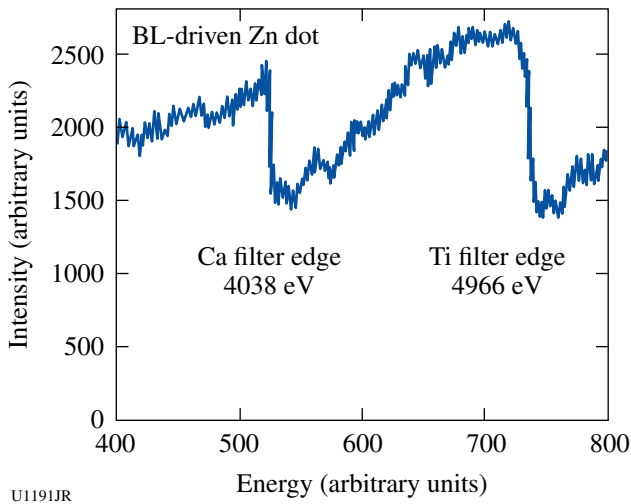


Figure 124.148
Initial Zn microdot broadband backlighter spectra from ~3- to 6-keV photon energy.

Figure 124.151 shows experimental data. The shock travelled from left to right, so the modulations on the left side of

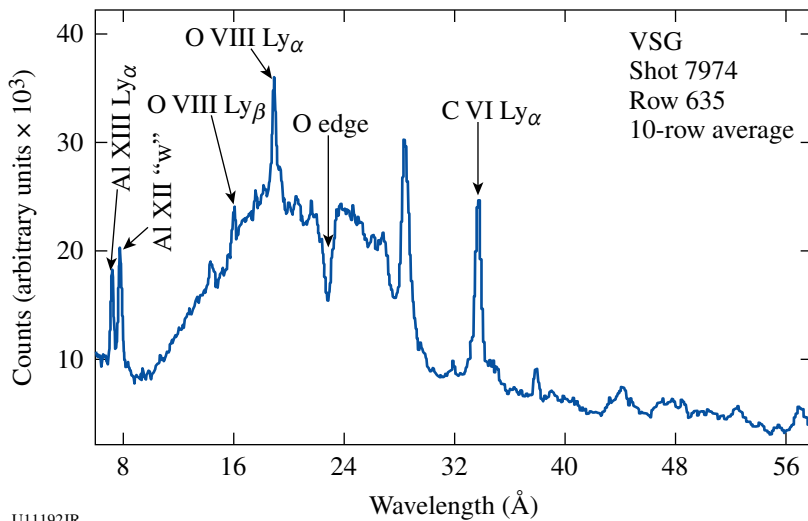
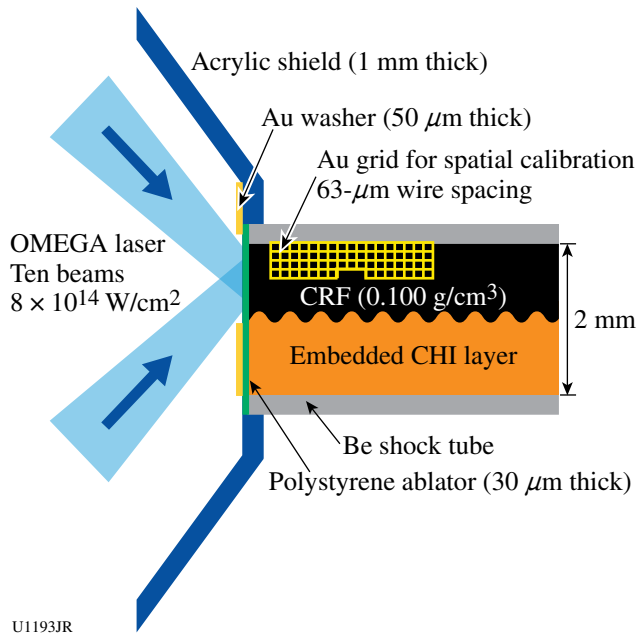
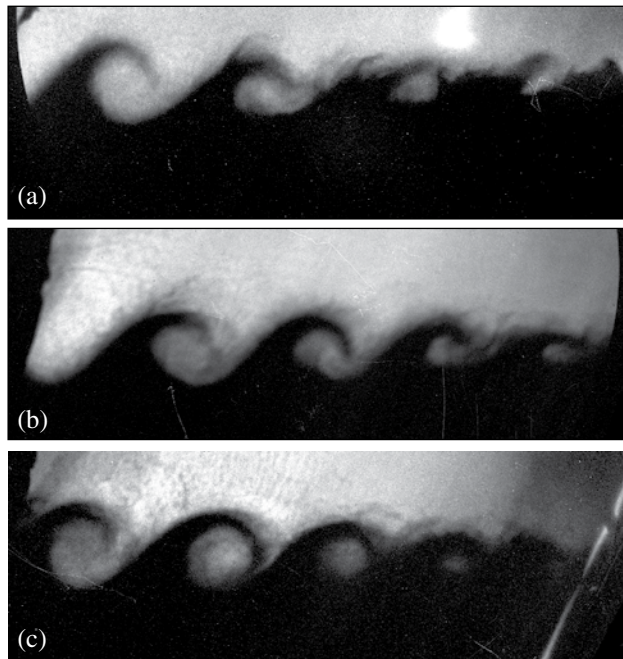


Figure 124.149
X-ray emission spectrum from the interior of the laser-driven CH/Ti/CH/Al foil, with initial line identifications.



U1193JR

Figure 124.150
Experimental configuration. The interface between lower-density CRF foam and higher-density I-doped plastic had a pre-imposed 2-D modulation with 400- μm wavelength. Three densities of CRF foam were used: 50, 100, and 200 mg/cm^3 .

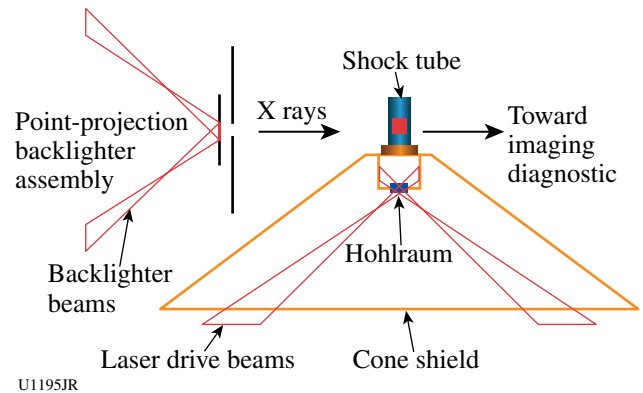


U1194JR

Figure 124.151
X-ray radiographs of KH growth were taken with (a) 50 mg/cc of CRF foam at 47 ns, (b) 100 mg/cc of CRF foam at 75 ns, and (c) 200 mg/cc of CRF foam at 117 ns. The vortices on the right-hand side of the images experienced more KH growth than those on the left-hand side. Short-scale mix can be seen as "hair-like" structures on top of the vortices from pre-imposed modulations.

the image had more time to grow than the modulations on the right side. The light color in the image corresponded to foam material, while the dark color corresponded to plastic. The initial sinusoidal 400- μm -wavelength modulation developed into the vortices. In addition, the growth of short-scale modulations caused by surface imperfections developed "hair-like" nonuniformities. These nonuniformities represent turbulent mixing of two materials, as expected since the Reynolds number was high in this experiment, $\text{Re} \sim 1 \times 10^6$. The Reynolds numbers in hydrodynamic simulations, used to model the experiments, typically do not exceed $\sim 1 \times 10^3$ because of the finite spatial resolution of spatial grids. Therefore the simulations themselves are not expected to correctly predict evolution of short-scale mixing. These experimental data are used to develop and validate mix models that are based on post-processing of hydrodynamic simulations, currently in progress.

High-Mach-number Cu-foam jet experiments. Some of the most challenging experiments to model for hydrodynamics codes are jet-evolution experiments. Several aspects of hydrodynamics-code predictions can be validated by these experiments, including physics of shocks, material flows, and equation-of-state physics. The current experiment studied evolution of a Cu-foam jet into a low-density plastic foam. Figure 124.152 shows the experimental setup. A high-Mach-number jet was generated in a shock tube, driven by x rays from a hohlraum irradiated by 12 OMEGA drive beams. A point-projection backlighter x-ray source, driven by three beams, generated $\sim 4.3\text{-keV}$ x rays that illuminated the jet at time intervals ranging from 15 to 35 ns after the beginning of



U1195JR

Figure 124.152
Experimental configuration of the high-Mach-number Cu-foam jet campaign. The jet was generated in a shock tube, driven by hohlraum x rays. X rays, generated by a point-projection backlighter, radiographed the jet at various times, from 15 to 35 ns after the beginning of the drive.

the drive. The cone shield prevented x rays generated in the hohlraum from reaching the imaging diagnostic, which would contribute to background on the data.

Figure 124.153 shows an example of a radiograph taken at 30 ns of the jet. In the image, a mushroom-like jet of Cu-foam material (darker color) penetrates the plastic foam (lighter color). The height, width, and position of the jet with respect to the grid (shown on the right side of the image) are some of the measurements used to compare with code predictions. In addition, the shock position and compression of the plastic foam will also be used to test various aspects of hydrodynamics codes. Preliminary simulations of jet evolution and shock propagation are close to experimental data, with much better agreement than in previous campaigns, primarily because of well-fabricated Cu foams.

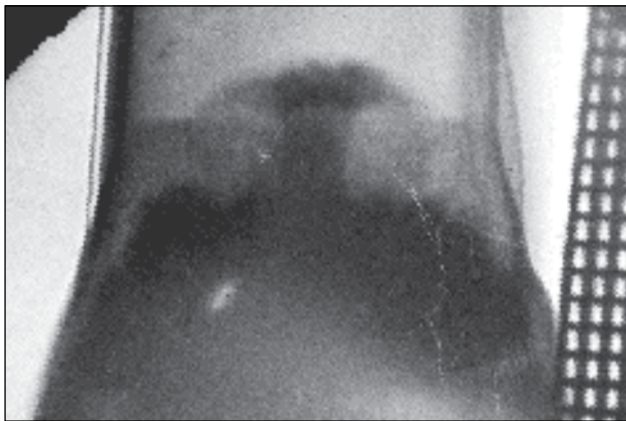


Figure 124.153
X-ray radiograph of a Cu-foam jet driven into a plastic foam with a density of 0.1 g/cc. The image was taken at ~30 ns after the beginning of the drive. The jet structure is clearly visible. The height, width, and position of the jet, as well as the shock position and compression of the plastic foam, will be used to test various aspects of hydrocodes.

X-Ray Source Development and Application: Bright, tunable x-ray sources are necessary for radiography applications, radiation-effects experiments, and use as backlighters for high-energy-density experiments. LLNL's x-ray source development campaign had one full day and two half-days of shots (22 shots total) during which two types of multi-keV x-ray sources were shot. These experiments were performed in collaboration with scientists from CEA (France). Two half-days (XRSD-10A, XRSD-10C) were used to investigate the performance of Ti foil targets confined by cylinders of ultralow-density SiO₂ aerogel material. A photo of one of the targets is shown in Fig. 124.154(a) (with bundled laser beams shown

schematically), and an x-ray image of the Ti K-shell emission (energies > 4.5 keV) from the target in shot 56933 is shown in Fig. 124.154(b). Target yields were studied as a function of the aerogel density, the aerogel volume, the foil thickness, the laser intensity, and the laser pulse length. Data are consistent with CEA predictions of an optimal aerogel density for maximal Ti K-shell radiation production.

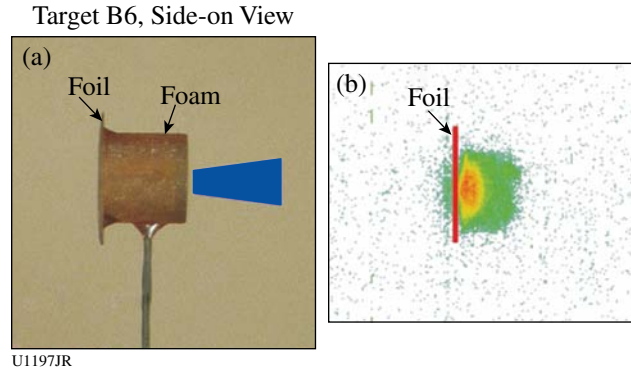


Figure 124.154
(a) A hybrid foam-foil target that was shot in the LLNL-CEA x-ray source development experiments. Five or six OMEGA laser beams entered the target's foam cylinder from the left and created x rays from the Ti foil at the right. (b) An x-ray framing camera image from shot 56933 of a hybrid foam-foil target (2 mg/cm³ of foam, 3-μm-thick foil).

Dedicated investigations of x-ray emission from noble gases were also carried out (XRSD-10B, XRSD-10C). During these experiments, the scaling of x-ray yield from gas-filled Be cans was studied as a function of gas-fill pressure and gas mixture. Pure Ar, Kr, and Xe targets were shot, as were mixed Ar:Xe targets; for all targets, fill pressures ranged from 1.0 to 1.5 atm. Figure 124.155 shows the measured spectra from five Xe-filled targets shot on the two dedicated days. During the XRSD-10B series of shots, the x-ray environments produced by the targets were also applied to investigate changes in the material properties of, and surface interactions on, sets of samples in response to x-ray loading. Samples included radiation-hardened-by-design mirrors and photovoltaic solar cells. An example of one specimen is shown in Fig. 124.155. Changes in reflectivity and surface profiles of the mirrors, and changes in the performance of the solar cells were characterized for exposures of several different fluences and spectral contents, which greatly expands the knowledge of the x-ray survivability of these materials.

Diagnostic Technique Development

Development of VISAR with a target-mounted turning mirror. It is known that measurement of the shock speed inside a quartz (Qz) window is a reliable way to understand the hohl-

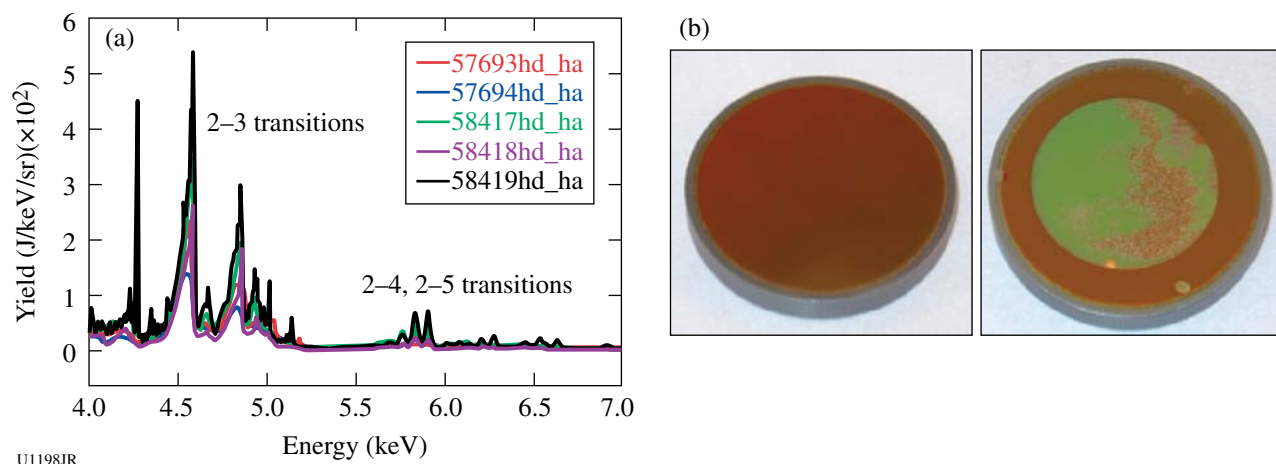


Figure 124.155

(a) The measured spectra from a series of Xe-filled targets shot during the x-ray source development and application campaigns in FY10. The x rays from the targets were used to study the response of radiation-hardened-by-design mirrors and photovoltaic solar cells. (b) Before and after images of a mirror specimen that was exposed to the unfiltered output of an Ar gas target on shot 57692.

raum drives.⁵¹ One of the NIF experiments (Rad-Transport) will apply this technique to characterize the drive inside a half-hohlraum. Because the VISAR is located along the equator on the NIF, characterization of the drive at the end of a half-hohlraum requires the use of a target-mounted turning mirror. A potential failure mode was the loss of reflectivity from the turning as a result of M-band x-ray preheat. An experiment was designed to empirically test the turning mirror's performance under an equivalent heat loading of the NIF radiation-transport experiment. A new configuration was designed that carefully followed constraints from the simulations and experiments, as shown in Fig. 124.156(a). Two types of mirrors were tested: Si and nanodiamond mirrors. The experiments were highly successful—no mirror blanking was observed in Fig. 124.156(b). One example of the VISAR image is shown in Fig. 124.156(c). From this data, the peak shock velocity was measured up to 50 km/s, or ~50-Mbar pressure in quartz. This is the highest-pressure shock measured inside quartz to date. Both mirror types worked well and delivered high-quality meaningful data. From this data, it is expected that the mirrors will survive until the thinnest ablator section burns through and that the NIF experiment will deliver meaningful measurements.

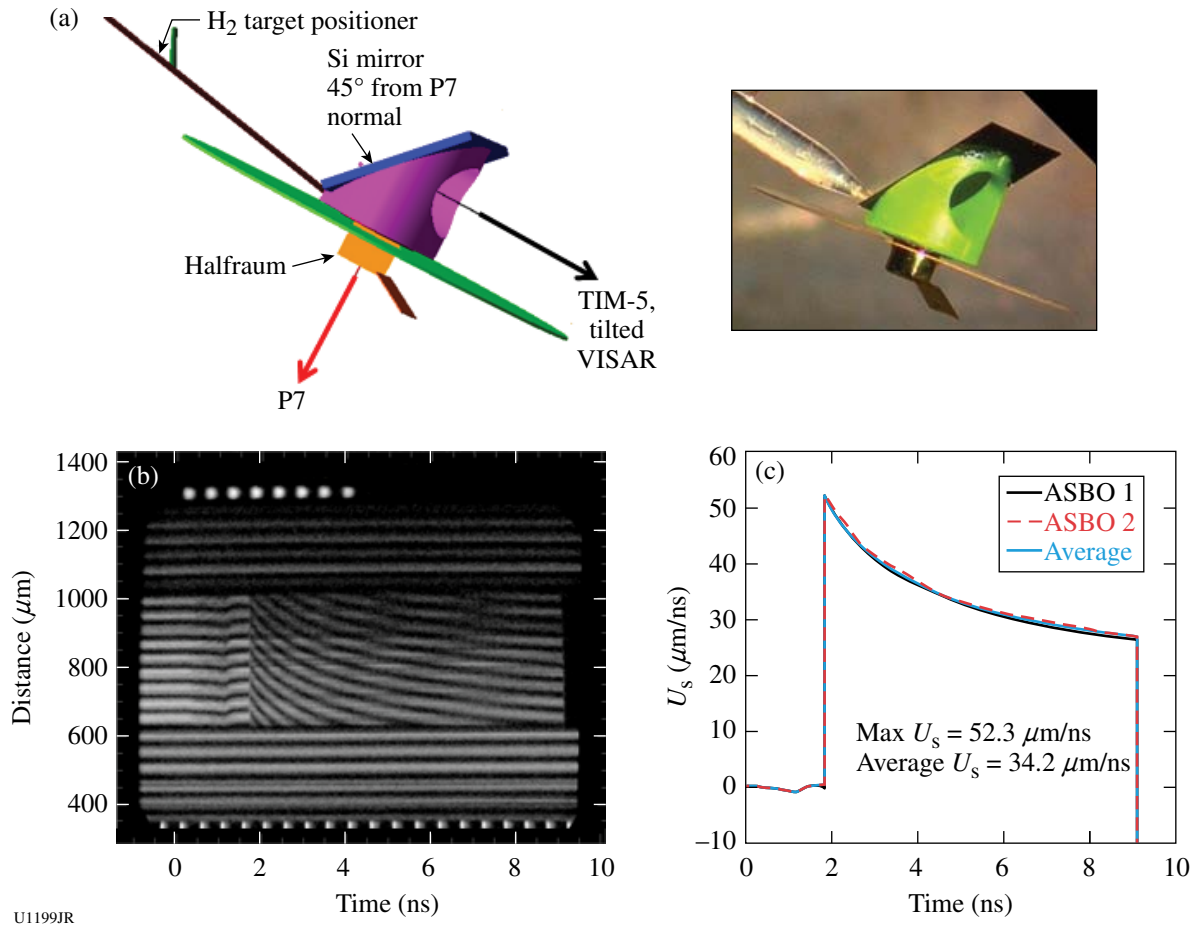
Beryllium x-ray Thomson scattering. The objective of the BeXRTS-10 campaign was to isochorically heat Be utilizing short-pulse-generated hot electrons and to measure the plasma temperature by means of noncollective x-ray Thomson scattering with high time resolution. Two OMEGA EP short-pulse beams were used with the backlighter beam heating a 250- μ m Be cube and the sidelighter beam creating a Zn K_{α} x-ray probe

at 8.6 keV. On this shot day, the sidelighter was delayed by 200 ps with an accuracy of ~25 ps, as observed by an ultrafast x-ray streak camera.

Zinc K_{α} x rays were scattered off the Be and collected by the Zinc von Hamos (ZVH) spectrometer, which uses a curved, highly efficient HOPG Bragg crystal for energy dispersion and focusing in the nondispersive direction. The spectrometer, specifically developed for the K_{α} scattering project, had to be rebuilt to meet new safety standards, and the new instrument was successfully fielded on this shot day.

A total of six shots were conducted including two low-energy activation shots. The latter ones were used to measure a high-resolution source spectrum and to record background signal levels. The facility had made a big effort to establish the beam timing, i.e., the delay between the backlighter and the sidelighter beams, on previous shot days. The single-photon-counting (SPC) camera was successfully used to observe the Zn K-shell source spectrum.

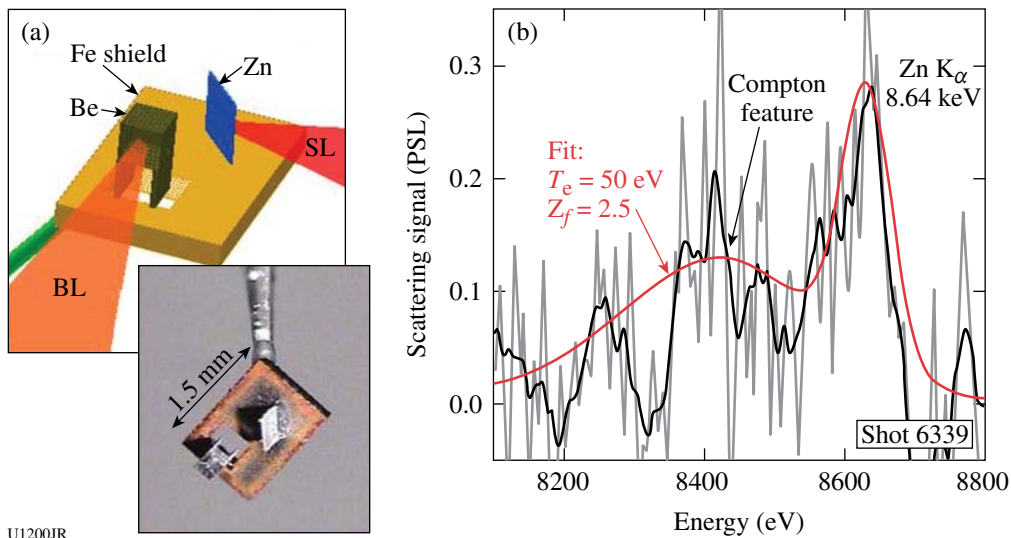
Compared to a previous shot campaign, the target size was significantly reduced and lower-Z shields were used in an effort to reduce bremsstrahlung levels. Different shield compositions were also tested. At the end of the shot day, an inelastically scattered Compton signal was successfully recorded from isochorically heated Be [cf. Fig. 124.157(b)], employing 62 J in the backlighter beam and 250 J in the sidelighter beam. These results represent significant progress compared to the previous shot campaign.



U1199JR

Figure 124.156

(a) VISAR mirror test experimental configuration. (b) An example of VISAR data measuring the shock speed in a SiO₂ window. No blanking is observed. (c) The measured shock speed is 52 μm/ns, corresponding to an ~50-Mbar ablation pressure.



U1200JR

Figure 124.157

(a) Experimental configuration and (b) x-ray Thomson-scattering spectrum from isochorically heated Be, utilizing a Zn K_α source line at 8.6 keV. The experimental data are fitted with $T_e = 50 \text{ eV}$ and ionization of $Z_f = 2.5$.

High-energy-backlighter development. The goal of this experiment was to compare the backlighter conversion efficiencies of high-Z materials driven by short- and long-pulse lasers. Short-pulse-generated x rays are believed to result from hot electrons that collide with K-shell electrons, causing K_{α} x-ray fluorescence. Long-pulse-generated x rays are believed to be created by thermal heating and ionization of the material. The goal was to perform systematic comparisons at high x-ray energies. The OMEGA EP Laser System is ideal for this type of test since both short- and long-pulse lasers are available to illuminate a target using the same diagnostics. In this set of experiments, three different types of materials were tested: Cu, Ag, and Sm. The initial analysis shows that the long pulse is much more efficient at generating the 8-keV Cu backlighter; whereas the 40-keV Sm x ray is much more efficiently generated with the short-pulse lasers. From these data, it was observed that the conversion efficiencies are approximately the same at ~ 17 keV, driven by either long- or short-pulse lasers (Fig. 124.158). At 8 keV, the long-pulse laser was more efficient by a factor of 10, whereas at 22 keV, the short-pulse laser was more efficient by a factor of 5.

Broadband x-ray Laue diffraction development. The lattice scattering campaign uses the broadband thermal x-ray emission from a direct-drive-implosion capsule to perform single-shot, *in-situ* white-light x-ray diffraction. This employs the classic Laue diffraction on a subnanosecond time scale

to investigate material behavior during shock or ramp compression. This technique will give insight into the material microstructure because lattice defects will cause nonuniform strain in the atomic structure, causing the diffraction spots to broaden and change shape. A directly driven implosion on the OMEGA laser is ideally suited for this technique, providing a short burst (~ 150 ps) of bright broadband x rays. The laser beams were pointed to five different pointing locations on the capsule to maintain implosion symmetry. Figure 124.159 shows gated framing camera images of the implosion capsule on a previous campaign that had 42 beams for the implosion, while Fig. 124.160 shows the improved symmetry by using the five different targeting locations. In principle, symmetry can be improved even further by adding more locations.

For these experiments the broadband x-ray diffraction (BBXRD) diagnostic was designed and qualified (Fig. 124.161). The diagnostic is designed with a tapered profile so that as many beams as possible can reach an implosion capsule placed 20 mm away from the single-crystal target that sits on the front plate of the BBXRD. The inside of the BBXRD has four trapezoidal image plate detectors on the tapered sides and a square piece on the back to record the transmitted diffraction. Simultaneous VISAR measurements can be made from the rear surface through a hole in the back plate. The diagnostics capability was successfully demonstrated on two campaigns

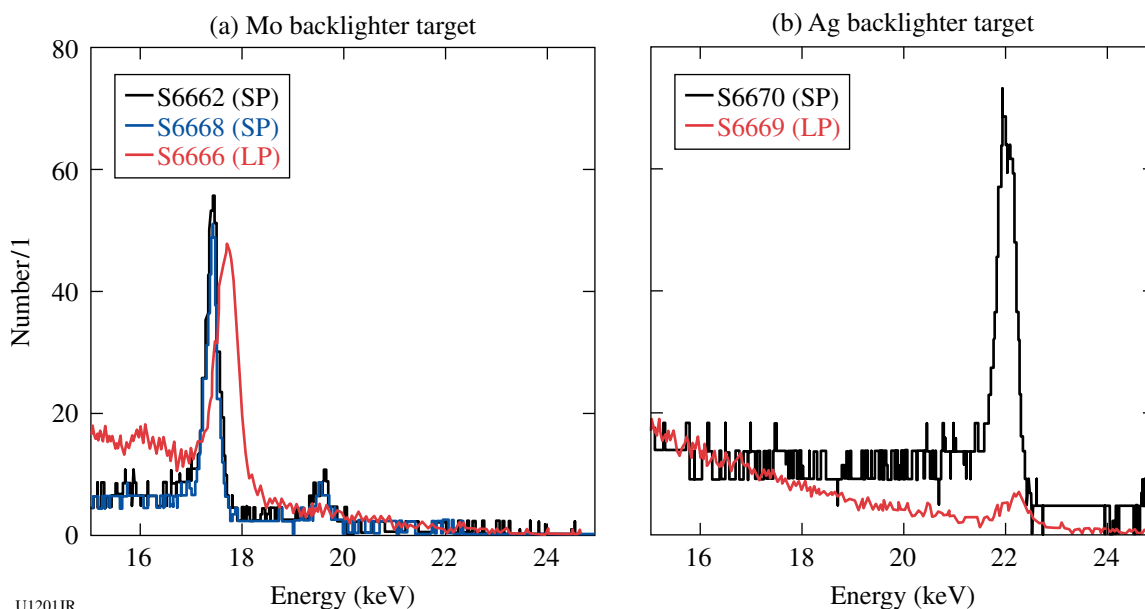


Figure 124.158

Comparison of high-energy backlighter yields driven by the 1-ns, 3ω long-pulse (LP) laser versus the 100-ps, 1ω short-pulse (SP) laser. The data were taken with the single-photon-counting camera. When normalized by the laser energies, we found that the Mo backlighter conversion efficiencies were about the same, whether driven by the short pulse or the long pulse.

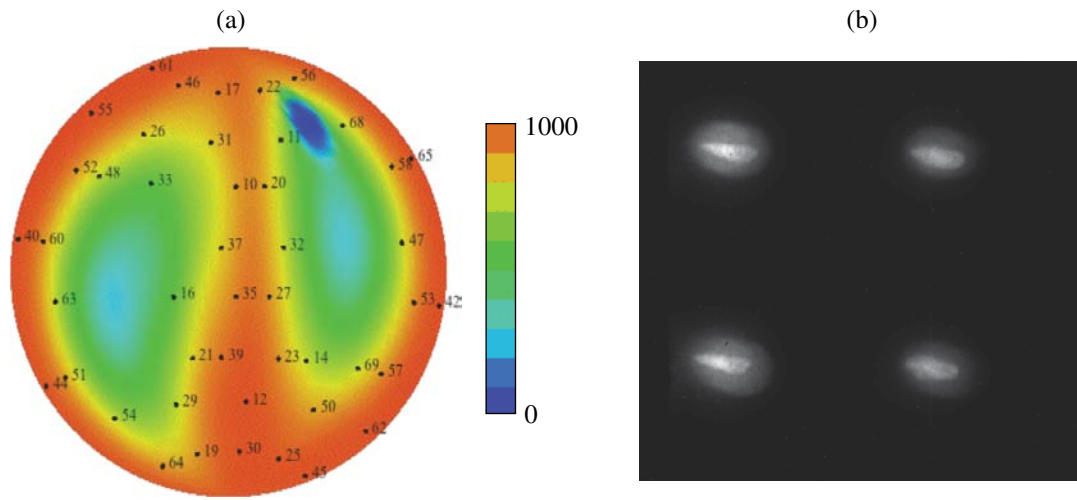
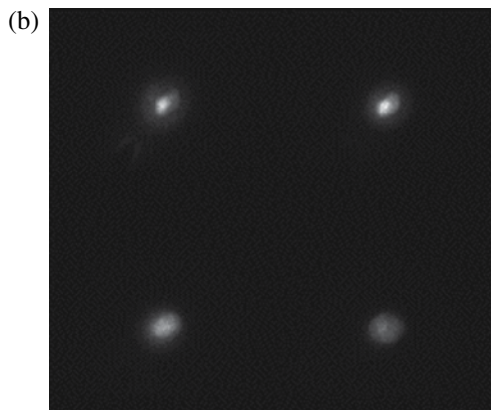
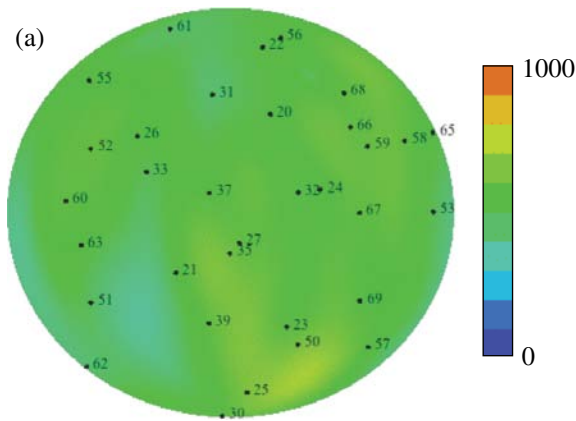


Figure 124.159

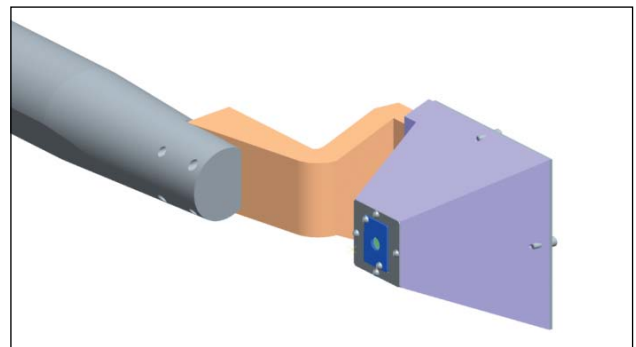
(a) The total laser power deposited and (b) gated framing camera images from the implosion capsule using 42 beams pointed to the center of the capsule.



U1203JR

Figure 124.160

(a) The total laser power deposited (TW/cm^2) and (b) gated framing camera images from the implosion capsule using 33 beams pointed to five different targeting locations on the capsule.



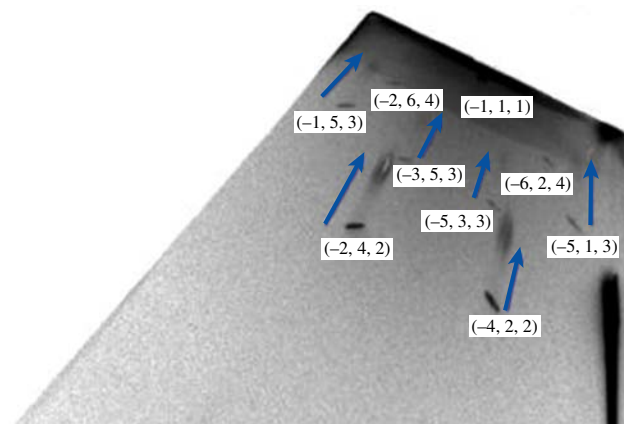
U1204JR

Figure 124.161

The BBXRD diagnostic in the VISRAD model showing the location of the implosion capsule and beams and CAD model.

of shock-compressed silicon (shown in Fig. 124.162) and copper. For the silicon images shown, it was estimated that the anisotropy in the compression by the shift in the spots was approximately 8% along the driven direction.

Powder x-ray diffraction development. The objective of this campaign is to demonstrate the use of powder x-ray diffraction



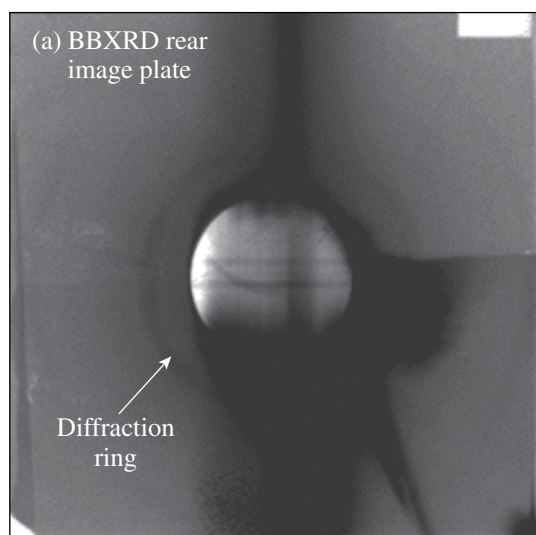
U1205JR

Figure 124.162
The tip of one of the trapezoidal image plates showing diffraction from uncompresses and shock-compressed silicon.

methods in the characterization of dynamically loaded (shocked and ramped) polycrystalline materials, particularly with a view to application on forthcoming NIF experiments. Such x-ray diffraction methods offer insight into processes occurring on the scale of the material lattice, which in turn determine the macroscopic response of the material to dynamic loads (e.g., its strength).

To date, the campaign has demonstrated x-ray diffraction from polycrystalline Ta foils using a quasi-monochromatic Mo backlighter source (see Fig. 124.163). Future campaigns will concentrate on improving the signal-to-noise ratio of the diffraction signal and will then aim to use this signal to characterize tantalum under a variety of shock and ramp-loaded conditions.

Powder x-ray diffraction measurements of solid Fe, Sn, and Ta to 500 GPa. An experimental platform was developed to measure powder x-ray diffraction on solid samples at pressures above Hugoniot melt. Fe, Sn, and Ta samples were sandwiched between a diamond pusher and window and ramp-compressed to high pressure and density using up to six OMEGA beams. VISAR velocity measurements were used to infer the pressure history in the sample, and the 8.37-keV Cu-He α x-ray source, driven by ten beams, was timed to coincide with the peak pressure. The diffraction signal was collimated through



U1206JR

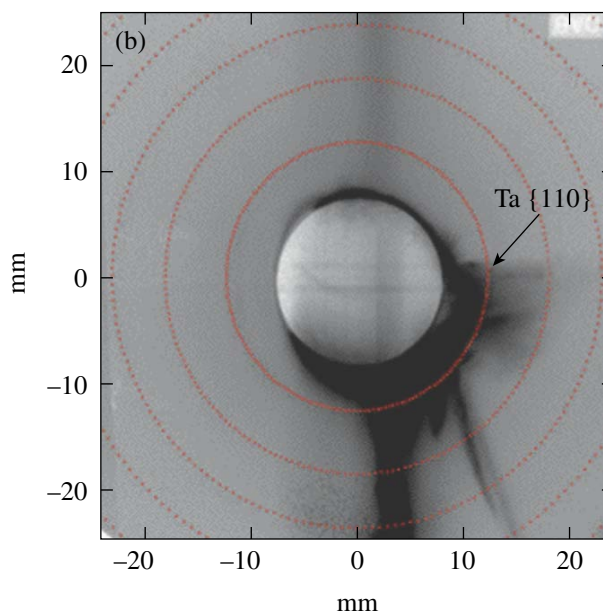


Figure 124.163
(a) Diffraction signature from polycrystalline Ta foil using a 17.5-keV x-ray source and LLNL broadband x-ray diffraction (BBXRD) diagnostics. Each crystallographic plane (hkl) generates a characteristic cone of x rays; the intersection of these cones with the image plate detectors results in a characteristic ring pattern. (b) Calculated pattern shown overlaid over data.

a 300- μm -diam aperture in a 150- μm -thick Ta substrate and captured on image-plate detectors. Density was inferred from the diffraction data by assuming a crystal structure, then verifying self-consistency with a best fit to density. Maximum diffraction pressures attained on Fe, Ta, and Sn samples were 480, 310, and 220 GPa, respectively, all above Hugoniot melt. Data from iron samples are shown in Fig. 124.164.

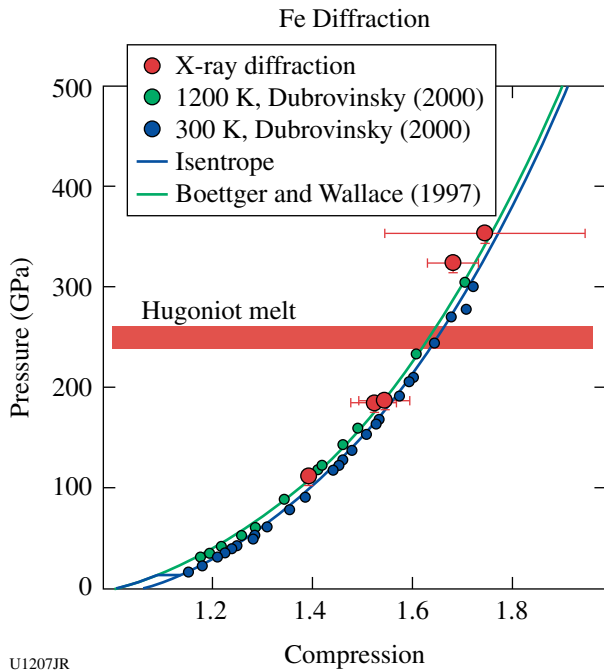


Figure 124.164
 In FY10, the OMEGA laser was used to obtain x-ray diffraction measurements of solid Fe (red circles) at pressures above the Hugoniot melt (red band at 250 GPa). The results are consistent with Fe remaining in an HCP structure up to the highest pressures observed (~480 GPa). Diffraction data from diamond anvil cells⁵² are also shown, along with a theoretical isentrope from Ref. 53.

ACKNOWLEDGMENT

This work was performed under the auspices of the U.S. Department of Energy by Lawrence Livermore National Laboratory under Contract DE-AC52-07NA27344.

FY10 LANL OMEGA Experimental Programs

In FY10, Los Alamos National Laboratory (LANL) executed 135 shots on the OMEGA Laser System and 24 shots on the OMEGA EP Laser System. LANL had three instruments qualified for use on OMEGA EP: the NIF5 spectrometer, the target-heating Verdi laser (THVL), and Thomson parabola ion energy (TPIE) diagnostic.

LANL experiments contributed to the National Ignition Campaign (NIC) in the following ways:

- Studies of the equation of state (EOS) of plastic ablaters
- New experimental methods for determining the areal density of imploded ICF capsules using 4.44-MeV $^{12}\text{C}(n,n')\gamma$ rays
- Demonstration of NIF components of the neutron imaging system

High-energy-density (HED) campaigns included

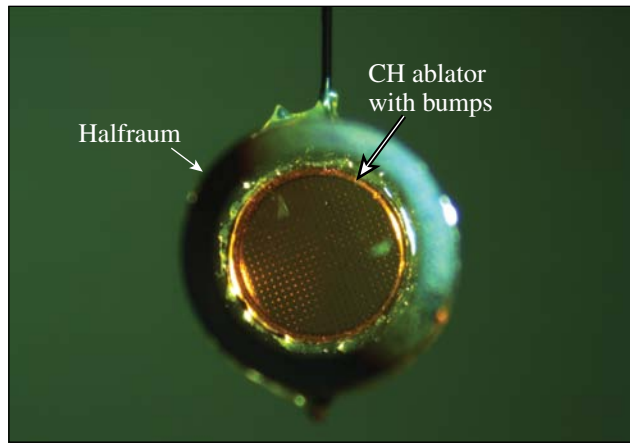
- Measurement of a supersonic radiation wave
- Measurement of capsule yield in the presence of high-Z dopants
- DT reaction product branching ratio measurements
- Energetic-ion generation from hemispherical targets
- Development of x-ray sources for phase-contrast imaging

Collaborations with AWE, LLE, LLNL, NRL, and National Security Technologies (NSTec) remain an important component of LANL's program on OMEGA.

CHaRM: Disagreement between EOS models is found in the prediction of bump evolution, which the CHaRM campaign hopes to resolve. This year a campaign began to measure the ablative Richtmyer–Meshkov (aRM) growth of isolated Gaussian-shaped bumps on plastic ablaters. The ablative Richtmyer–Meshkov instability operates at the ablation front and is important because it controls the ablation surface perturbations present at the onset of Rayleigh–Taylor growth, which initiates once the shock has broken out and begins to accelerate the capsule.

General Atomics has sputtered 25- μm FWHM bumps, which are 4 to 8 μm tall, onto 120- μm -thick planar plastic ablaters. The ablaters are placed over one side of 0.9-scale gold halfraums (see Fig. 124.165), which are driven to 65-eV radiation temperatures corresponding to NIC foot levels. On-axis x-ray radiography using Saran backlighters (2.8 keV) allows one to measure bump areal density at successive times. Experiments this year have been hampered by low contrast from the combination of small areal-density variations from which to measure, as well as unwanted high-energy x rays in the system. An example of a measured low-contrast, 5- μm bump is shown in Fig. 124.166. The center of the bump (and lineout) shows a region of higher transmission, characteristic of a bump with a dip at its peak, which agrees with predictions at this time (4 ns after the start of the laser drive). Higher-contrast experiments are planned for FY11 along with shock-speed measurements to independently measure the drive conditions.

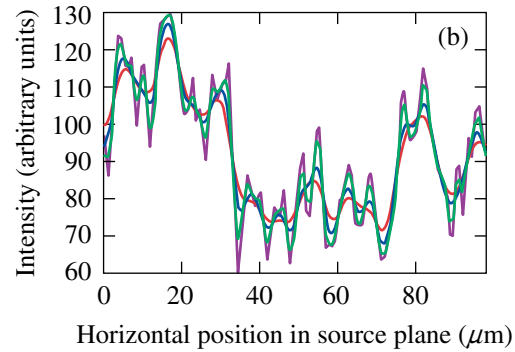
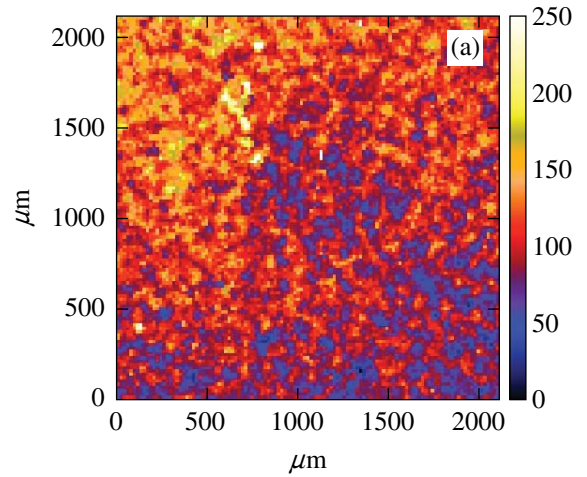
Gamma Reaction History: Gamma-ray measurements on fusion implosions were further developed for the NIC using



U1208JR

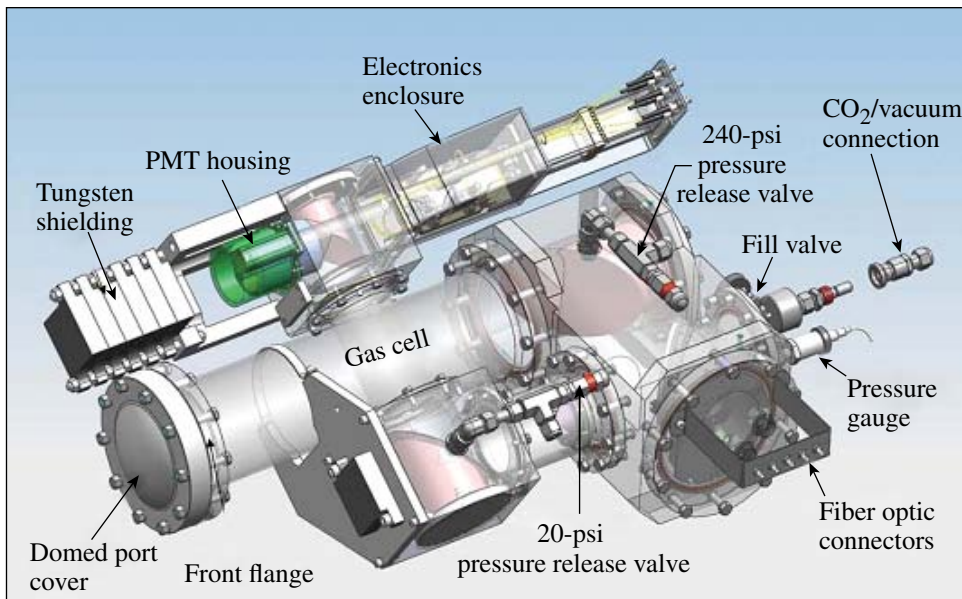
Figure 124.165
An optical image of a CHaRM target showing the perturbed plastic on the end of a 0.9-scale gold halfracum.

the gamma reaction history (GRH) diagnostic in FY10 (see Fig. 124.167). The GRH was first installed on the exterior of the OMEGA target chamber in 2009 (see Fig. 124.168). This instrument is a gas Cherenkov detector (GCD) designed for the NIF and being tested and used for nuclear studies on OMEGA. GCD's convert energetic γ rays to UV/visible Cherenkov photons for collection by fast optical recording systems. System impulse response better than 100-ps FWHM has been made possible by the combination of low-temporal-dispersion GCD's, ultrafast microchannel-plate photomultiplier tubes (PMT's),



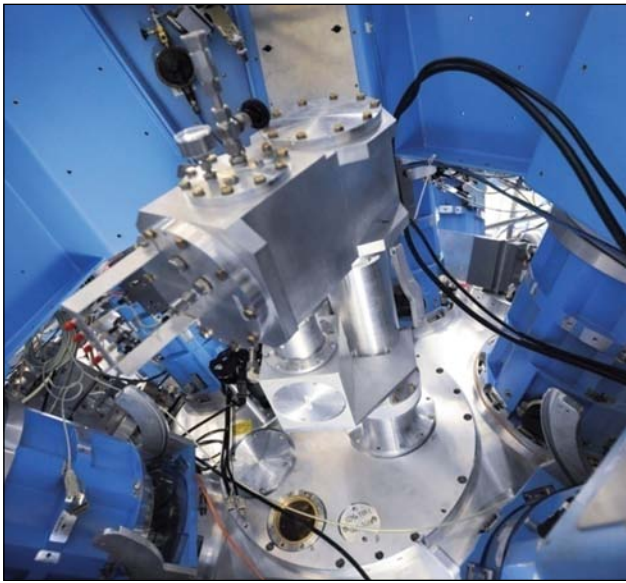
U1209JR

Figure 124.166
Image of the backlighter data obtained from radiography of a perturbed surface. The lineout indicates the presence of a bump.



U1210JR

Figure 124.167
Isometric view of the GRH diagnostic. After exiting the target chamber, energetic γ rays interact with a converter plate inside the domed port cover. The resulting relativistic electrons with energy above threshold generate UV/visible Cherenkov radiation inside the pressurized gas cell. A series of off-axis parabolic mirrors concentrate this light down to a 1-cm-diam active area of an ultrafast photomultiplier tube located inside the PMT housing. The electrical signal from the PMT is converted to infrared photons by a Mach-Zehnder modulator inside the electronics enclosure. This optical signal is then converted back to an electrical signal using high-speed photoreceivers connected directly to high-speed digitizers. The PMT is well shielded against direct-radiation effects by the tungsten shielding. Calibration and timing fiducial signals are injected into the optical path through the fiber-optic connectors.



U1211JR

Figure 124.168
Photograph of the GRH attached to the OMEGA target chamber.

and high-bandwidth Mach-Zehnder fiber-optic data links and digitizers, resulting in burnwidth measurement accuracy better than 10 ps.

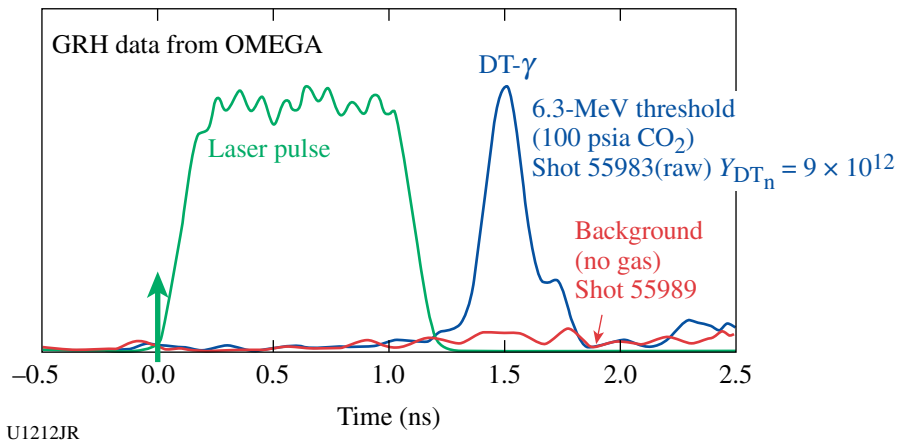
The GRH was absolutely timed using x rays from Au-ball shots on OMEGA. It has been shown that fusion bang times measured using the GCD-1 and the GRH agree to within 5 ps on average. Error budgets indicate that the GRH will be able

to meet the NIF requirement of measuring bang time to within 30 ps relative to the start of the laser pulse. Figure 124.169 shows raw GRH data placed on the laser time base along with the 1-ns laser pulse. Data with and without pressurized CO₂ demonstrate Cherenkov production and backgrounds, respectively.

Inherent variable energy-thresholding capability allows one to use GCD's as γ -ray spectrometers to explore fusion and other interesting nuclear processes. Recent GRH measurements of 4.44-MeV ¹²C(*n,n'*) γ rays produced as 14.1-MeV DT fusion neutrons pass through plastic capsules are paving the way for a new CH-ablator areal density measurement. This measurement is made possible by the use of SF₆ at high pressure (200 psia) resulting in a 3-MeV Cherenkov threshold.

The NIF GRH system consists of four individual gas cells, all essentially identical to the GRH on OMEGA. Located 6 m from target chamber center, the GRH-6m system began taking data on NIF in September 2010. OMEGA has provided an excellent platform to develop the detector technology and measurement techniques and will continue to provide a test bed for new physics investigations using GRH in the future.

The Neutron-Imaging System: In FY10, LANL successfully tested a major component of the NIF neutron-imaging system using the Omega Laser Facility. In order to record two images (14-MeV primary and 10- to 12-MeV down-scattered), a complex, multi-element lens (Fig. 124.170) must be used to view the front side of the neutron-to-light scintillator. Preliminary



U1212JR

Figure 124.169
Raw GRH data shown on the laser time base along with the 1-ns laser pulse used to drive the fusion implosion. The GRH was pressurized with 100-psia CO₂ for shot 55983, resulting in a 6.3-MeV Cherenkov threshold. DT fusion γ rays at 16.75 MeV produced the signal shown. The small peak riding on the tail of the main peak is a result of ringing in the PMT. This feature is removed, and the main peak is sharpened by deconvolving the instrument response of the system. The GRH, evacuated for shot 55989, provided a background measurement of direct radiation interaction with the PMT and demonstrated gas is necessary to generate a real signal.

data analysis indicates that the lens channel obtains a source plane resolution close to $10\ \mu\text{m}$ and comparable to the fiber-coupled channel.

Flat-field images at prompt gamma time of flight and NIF down-scattered neutron time of flight were collected for important scintillator background and temporal response studies.

NIF-5

Radiation flow. The NIF-5 project obtained invaluable data on OMEGA for the development of a future NIF diagnostic to measure the propagation of a supersonic radiation front in a low-density foam. These data were obtained using two principal diagnostics: the NIF-5 spectrometer with the GXI-T detector and an x-ray backlighter to perform absorption spectroscopy of

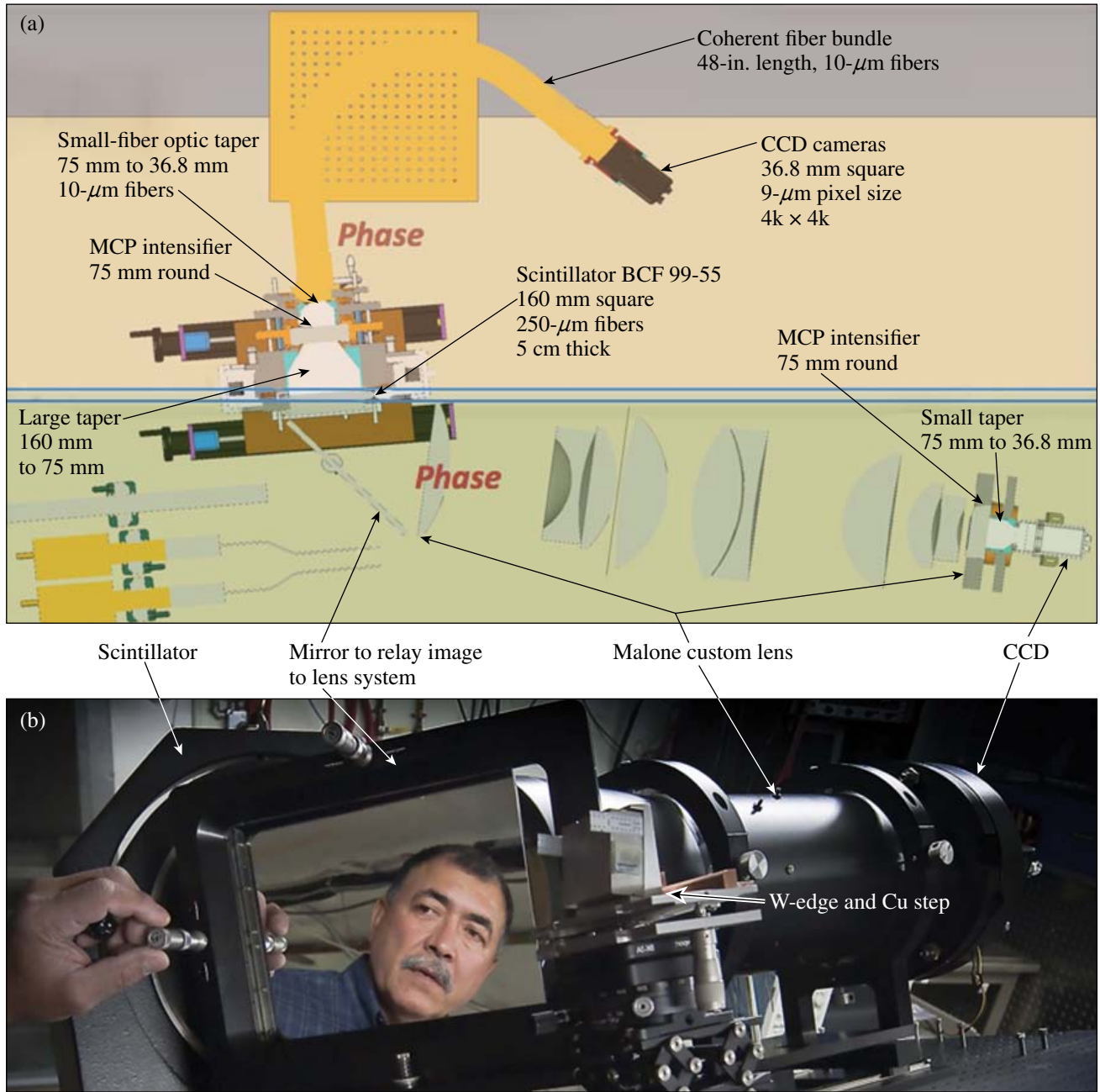


Figure 124.170
 (a) A schematic of the neutron imaging system; (b) a photograph of the neutron-imaging system while being aligned.

a tracer foil, and an x-ray framing camera and x-ray backlighter to measure the hydrodynamic expansion of the same foil. Together, these two diagnostics greatly constrain the models in an effort to better validate simulation codes.

The radiation flows from the hohlraum (top left, Fig. 124.171) and into a Be tube filled with a low-density (65-mg/cc) CH foam (bottom left, Fig. 124.171). A thin, square Ti foil (shown in blue but at an angle in the figure) is embedded in the target to diagnose the propagation of the radiation front down the tube. The hydrodynamic expansion of the foil (viewed edge-on) and the shock wave in the tube wall were imaged using an x-ray backlighter. The inset compares our data and a 2-D cylindrical RAGE simulation of the shock in the tube wall. The code is able

to qualitatively recreate the data. A more-detailed quantitative analysis is currently underway.

The absorption of CsI x rays by the foil in the orthogonal direction was also measured, providing a measurement of the charge state of the foil as a function of location along the radiation propagation direction. Figure 124.172 shows a schematic of the diagnostic: GXI-T with a Ge (111) crystal spectrometer snout. The absorption spectrum of the tracer was measured (along the detector strips) as a function of distance from the Au can bottom (orthogonal direction). Results are shown Fig. 124.173, along with a simulated Ti absorption spectrum, the latter showing the absorption lines expected given a certain foil temperature. The data show the Ti absorption lines

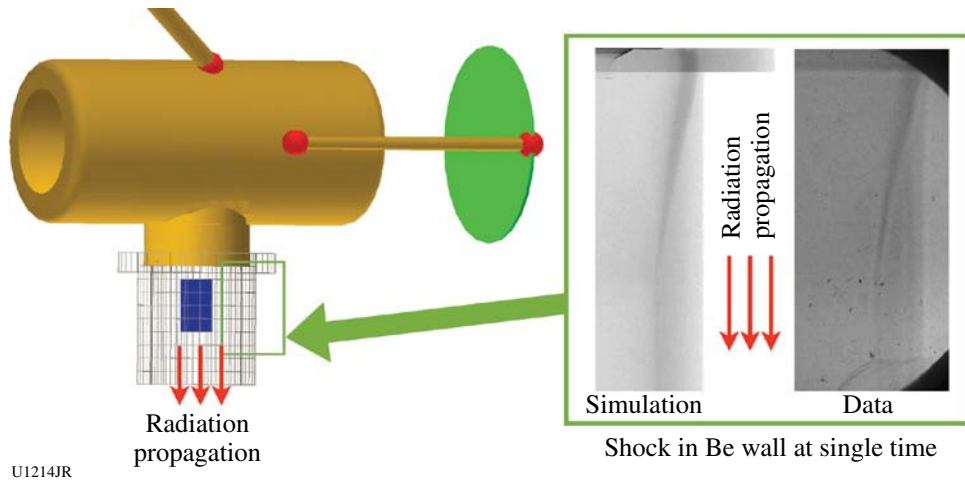


Figure 124.171
Radiation flows from the source, a hohlraum, into a foam cylinder (with an embedded tracer foil, in blue) enclosed in a Be tube (cross-hatched region). Inset: A comparison of simulation and data showing the shock in the tube wall.

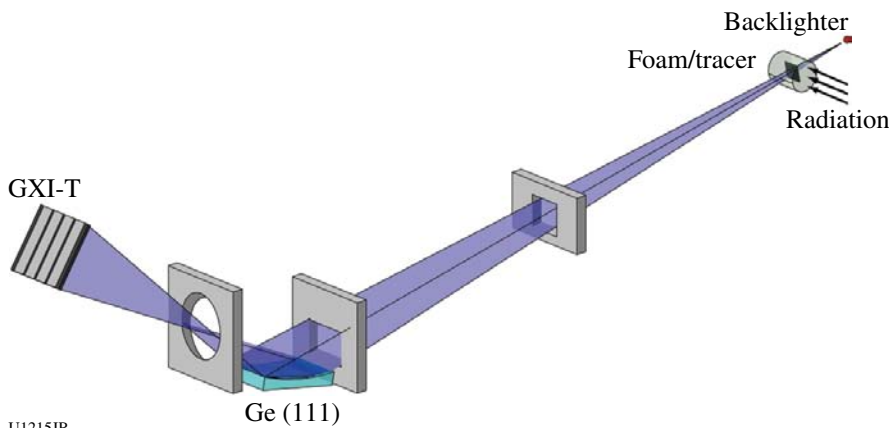
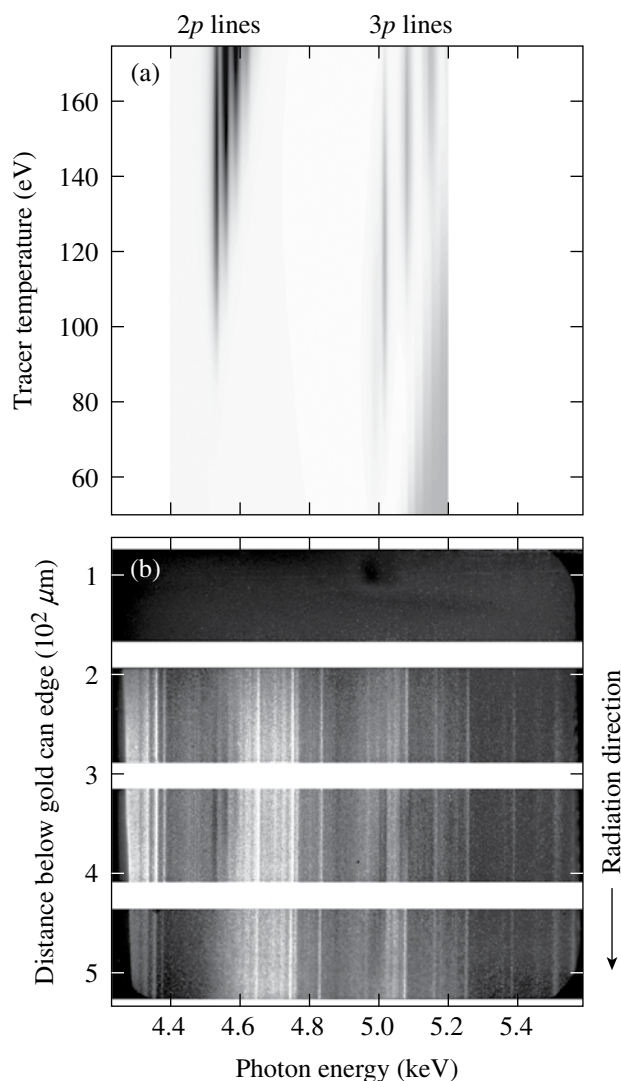


Figure 124.172
Schematic of the diagnostic foam/tracer (target not to scale). A broadband x-ray backlighter illuminates a thin foil embedded in a low-density foam cylinder as a radiation front travels across it. The image of the foil is dispersed along one axis by a curved Ge crystal. The detector is composed of four separately gated strips.

U1215JR



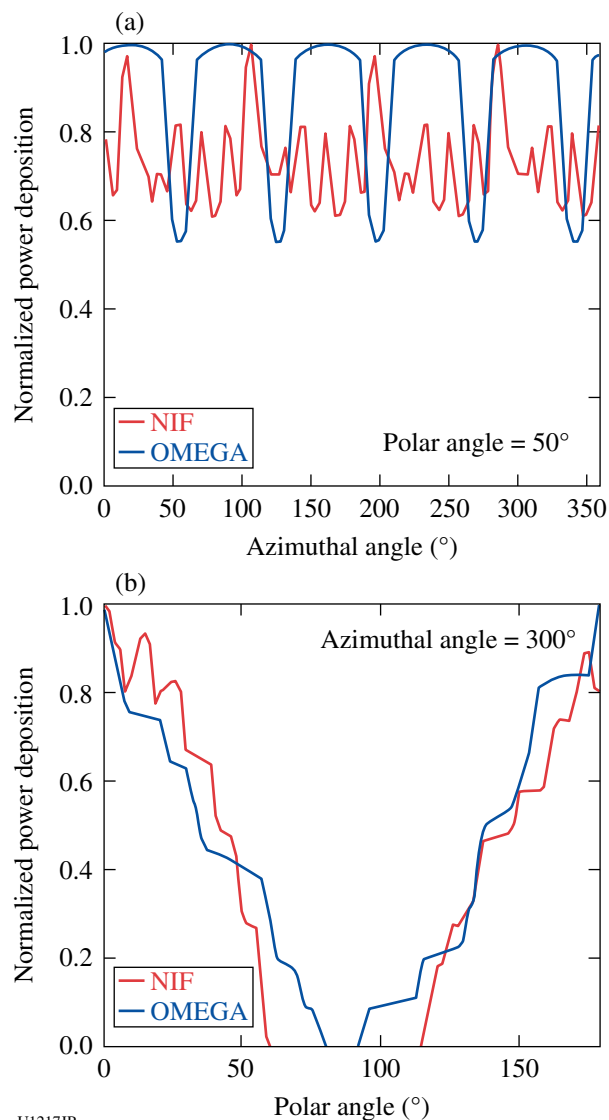
U1216JR

Figure 124.173
 (a) Simulated titanium absorption spectrum showing how the absorption lines can be used to determine the temperature of the tracer foil. (b) Data showing the titanium absorption lines overlaid onto our CsI backlighter-emission spectrum.

overlaid on the CsI backlighter emission spectrum. The initial analysis shows an ~200-mm-long radiation front with the tracer temperature ranging from ~130 eV midway down the foil to ~50 eV at the end of the foil.

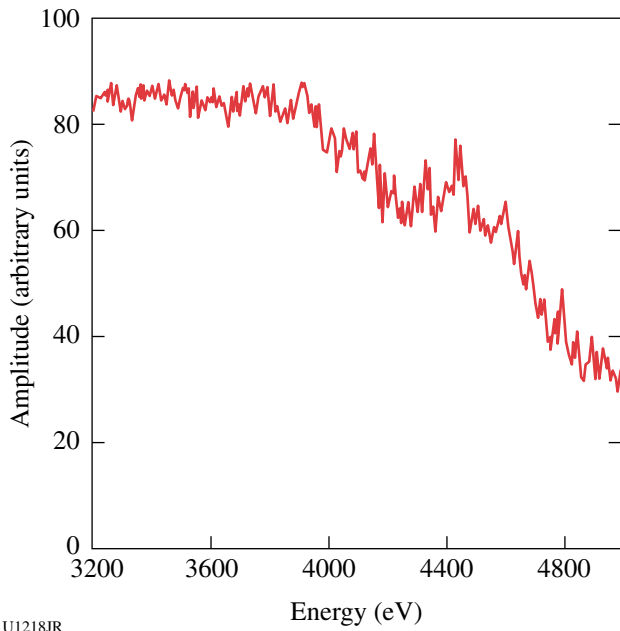
Short-duration backlighters. The NIF-5 campaign also executed a two-prong investigation into short-pulse quasi-continuum backlighters. This involved experiments on OMEGA EP using short-pulse lasers to irradiate a foil target and OMEGA experiments imploding Kr-fill capsules using a NIF-like irradiation pattern.

On the NIF, capsules must be polar driven because of the laser-beam geometry. Experiments were performed to determine what effect a polar-driven laser drive has on a capsule backlighter. Figure 124.174(a) shows the normalized laser power deposition in the azimuthal direction at the NIF and OMEGA. Although there are differences in the details, the peak-to-trough difference is nearly the same for both. Figure 124.174(b) shows the laser deposition as a function of polar angle for both the NIF and OMEGA configurations. Although there is some slight discrepancy, particularly at the equator, the profiles are very similar.



U1217JR

Figure 124.174
 Lineouts of the NIF and OMEGA laser power deposition profiles in the (a) azimuthal and (b) polar directions.



U1218JR

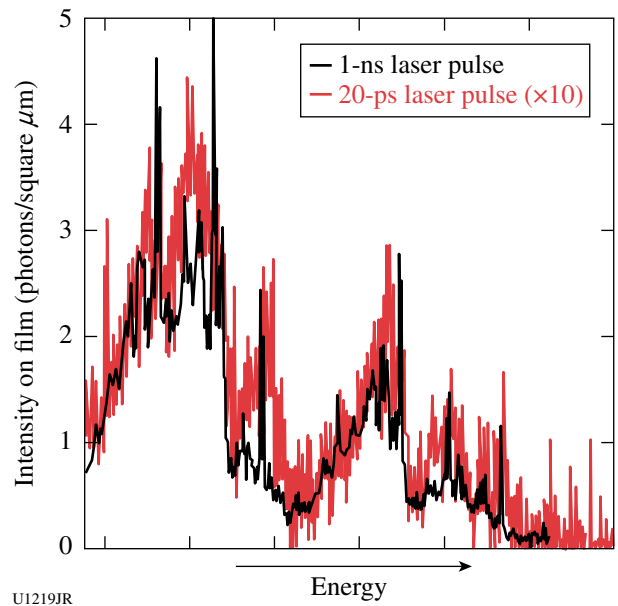
Figure 124.175
Signal amplitude versus photon energy for the bright core of a Kr capsule implosion.

Figure 124.175 shows the spectrum from a Kr capsule implosion. The spectrum is much more uniform than one would measure for a foil target, such as an L- or M-shell emitter, which is often chosen for spectroscopic measurements.

Experiments conducted on OMEGA EP studied both the K-shell and L-shell spectra of a CsI foil at three different laser pulse lengths (20 ps, 40 ps, and 1 ns). Figure 124.176 shows the L-shell spectrum of a CsI foil generated by a 1-ns and a 20-ps laser pulse. While the 1-ns spectrum has many narrow features, the 20-ps data show a broadening of the spectral lines.

The results of both of these backlighter experiments have provided invaluable data to evaluate their use for future LANL-led NIF experiments.

High-Z: The High-Z campaign had two main objectives: (1) to determine if the yield from plastic capsules would behave similarly to the yield of glass capsules when a high-Z dopant was added, and (2) to measure if the Ti x-ray emission from the Ti dopant in the shell was sufficiently high to use the multiframe monochromatic imager (MMI) in future experiments. The MMI diagnostic allows one to measure spatial and temporal profiles of the electron density and temperature in the plasma.



U1219JR

Figure 124.176
A comparison of the L-shell emission from a CsI foil resulting from irradiation from a 1-ns laser (black) and a 20-ps laser (red). The intensity of the 20-ps data has been multiplied by a factor of 10 to fit on the same scale as the 1-ns data.

To check the equivalency between plastic and glass capsules, a 900- μm -diam, 13.5- μm -thick plastic-shell target that contained 10 atm of D_2 gas was imploded and doped with varying amounts of Kr gas. The Kr gas-fill levels were designed to cover a range that produced significant degradation in the yield of the glass-shell capsules measured in previous experiments. In addition, some of the capsules contained Ti doped into the inner 1.5 μm of the plastic shell. The implosions were driven using the 60-beam OMEGA laser with full beam smoothing, resulting in a total laser energy of 23 kJ.

These experiments successfully demonstrated the equivalent behavior of the plastic capsules to the glass capsules as the Kr dopant level in the gas was increased. We also obtained Ti emission measurements from the capsule implosions. Based on these results, the second shot day was focused on enhancing the Ti emission from the capsules to improve the feasibility of using the MMI diagnostic.

Some examples of the spectrometer and imaging data are shown in Figs. 124.177 and 124.178. Figure 124.177 shows an image from the Henway time-integrated spectrometer for shot 56577. X-ray H-like and He-like Ti emission lines 2-1 transitions can be seen on channel C and 3-1 transitions on channel A. One can also see an absorption feature on channel C that comes from the colder Ti in the shell near the peak of

the implosion. The different horizontal strips in each image represent different filters that are used to provide a wavelength calibration. Figure 124.178 shows multiple images using the DDMMI spectrometer.

Good neutron data were also obtained from these shots. A comparison of the yield as a function of Kr dopant between the glass and plastic capsules is shown in Figure 124.179. The data indicate that the plastic capsules behave very similarly to the glass capsules with the yield dropping as the Kr concentration is increased, just as it did for the gas capsules. This indicates that the physics important for the observed degradation in yield

do not depend on the capsule material. In the future, we will use whichever type of capsule is appropriate for obtaining a better understanding of this physics.

The goal of additional experiments with these shots was to improve the Ti emission from the capsule implosions so that the DDMMI diagnostic could be used to measure temperature and density profiles in the gas. At present, the data for these shots are still being analyzed, and an evaluation will be made concerning the usefulness of these Ti-doped plastic capsules to enable one to measure the DDMMI of the plasma properties in the gas.

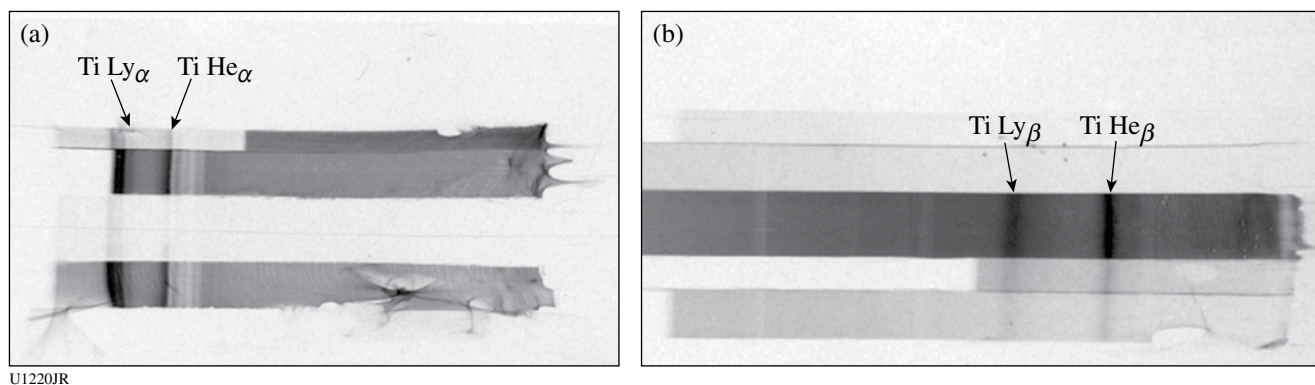


Figure 124.177 (a) Henway data showing the Ti He $_{\alpha}$ and Ti Ly $_{\alpha}$ lines; (b) Henway data showing the Ti He $_{\beta}$ and Ti Ly $_{\beta}$ lines.

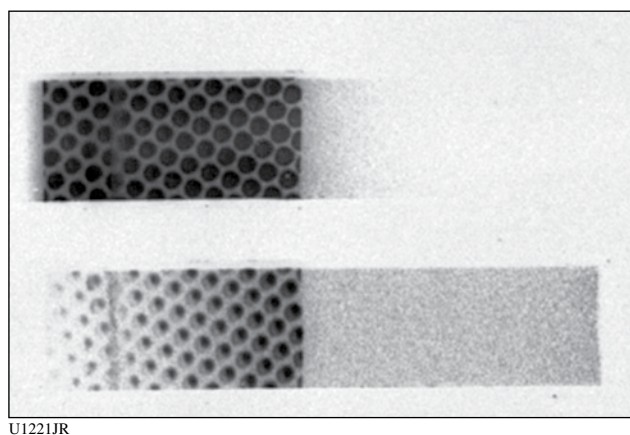


Figure 124.178 Image taken from one of the DDMMI spectrometers for shot 56568. Time goes from top to bottom for these images and the spectrum goes from lower to higher energy, right to left on each strip. The individual circles on these strips represent capsule images at a given photon energy and time. The lines that are just visible in the top strip are the He $_{\alpha}$ and Ly $_{\alpha}$ lines of Ti.

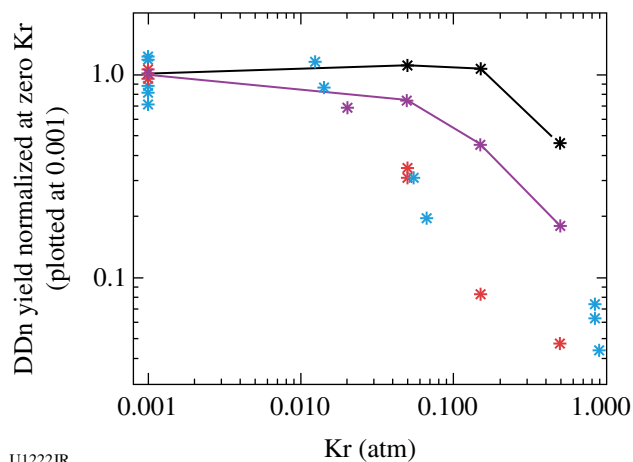


Figure 124.179 Comparison of normalized yields for glass and plastic capsules to simulations. The blue stars are data from glass-capsule implosions, while the red stars are data from the plastic-capsule shots. The purple curve represents calculations that include mix, while the black curve represents calculations without mix. The normalized yield levels for each set of capsules are 1.25×10^{11} for glass and 3.06×10^{11} for plastic, while the normalized simulation levels are 7.43×10^{11} for no mix and 2.85×10^{11} with mix.

DTRat: In addition to alphas and neutrons, the DT fusion reaction produces γ rays from the intermediate ${}^5\text{He}$ nucleus with a small branching ratio (BR) of several 10^{-5} γ/n . The excited ${}^5\text{He}$ can decay to the ground state, emitting a 16.75-MeV (width ~ 0.5 MeV) γ ray or to the broad first excited state emitting an ~ 13 -MeV (width ~ 4 MeV) γ ray. Knowledge of the BR between these two states is important to making absolutely calibrated measurements of the overall γ -ray spectrum on the NIF.

An energy-thresholding experiment was carried out for DT ICF implosions on OMEGA using a gas Cherenkov detector. After background subtraction, the fusion γ -ray Cherenkov peak was integrated for four different threshold energies (6.3, 8, 12, and 14 MeV). These integrated signals were then normalized to a specific threshold energy (for example, 12 MeV) and compared to the expected signal trends assuming a single γ -ray line at 16.75 MeV—assuming the two lines at 16.75 MeV and 13 MeV have nearly equal yield contributions (i.e., the “Hale” spectrum). Expected signal trends were calculated using the ACCEPT and Geant4 codes (Fig. 124.180).

In all of the intensity ratio graphs, a clear grouping of the experimental data around the theoretical values of the Hale spectra (double peak) was evident. This indicates that the DT reaction spectra are more like the Hale spectra and its mirror reaction D^3He than the previously assumed single-peak spectra. This study does not decisively conclude that the spectra are exactly like the Hale spectra but it confirms that there is a second peak in the spectra that has not been previously considered. This study is significant in that this is the first experimental evidence that clearly points to a double-peak spectra for D–T fusion in an ICF experiment. The refining of the exact spectra will be the subject of further studies.

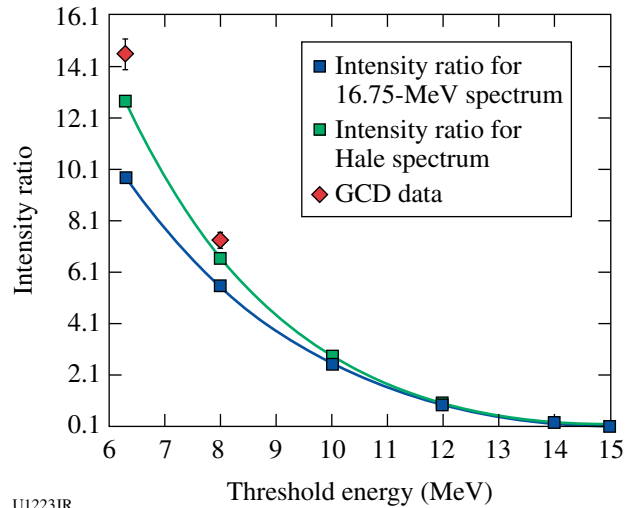


Figure 124.180

Ratio of GCD intensities as a function of threshold energy (MeV) normalized to 12-MeV threshold intensity ratio compared to Geant4 simulations. Red diamonds are experimental data. The green curve is obtained by folding the double-peak spectra⁵⁴ with a detector response of the GCD. The blue curve is assumed from a 16.75-MeV single-peak spectrum.

The DTRat campaign also performed experiments to examine the reduction of D–D yield attributable to the presence of ${}^3\text{He}$. These experiments not only measured the D^3He gamma signals but also observed D_2 gammas for the first time. This measurement provides new information to understand the nuclear reactions in an ICF capsule implosion.

OMEGA EP Ions: The LANL target-heating Verdi laser (THVL) was commissioned on OMEGA EP and was used to heat chemical-vapor-deposition (CVD) diamond hemispheres to greater than 1000 °C with the goal of producing nearly pure,

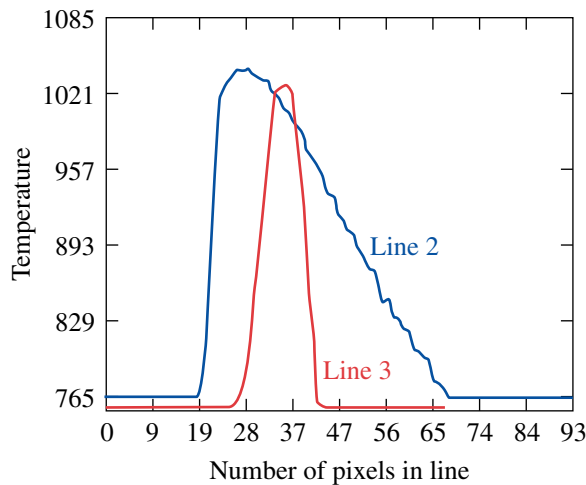
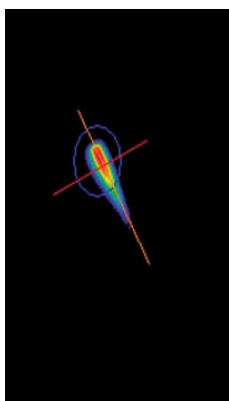


Figure 124.181

Temperature profile of a 500- μm -diam carbon rod heated at the tip by the THVL.

laser-accelerated carbon ion beams. Figure 124.181 shows a 500- μm -diam stand-in alignment target heated by the THVL to over 1000 $^{\circ}\text{C}$ as viewed through the system's pyrometer (left) and the software showing the lineout temperatures (right). Figure 124.182 shows similar data from the pyrometer, this time overlaid on a VisRAD representation of our CVD diamond Hemi target assembly for producing focused ions, showing the hemi heated to over 1000 $^{\circ}\text{C}$ in the center of the assembly.

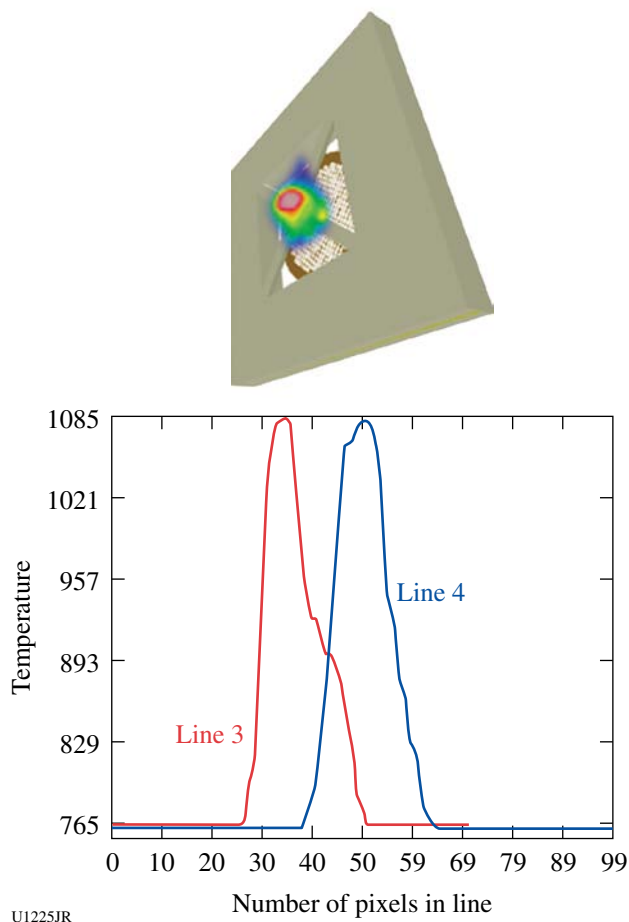


Figure 124.182
Temperature profile of a heated target overlaid with a VisRad image of target.

These heated targets were then shot using the short-pulse OMEGA EP Laser System with a 10-ps pulse at nearly a kilojoule, producing focused ion beams. The accelerated ions were diagnosed with the LANL-TPIE and LLNL-PFPII diagnostics. TPIE included a new cover plate that demonstrated an improved signal-to-noise ratio on the CR-39 solid-state nuclear track detector (SSNTD), and a LiF plate was added to the film-pack configuration to serve as a nuclear activation diagnostic of the carbon ion beam.

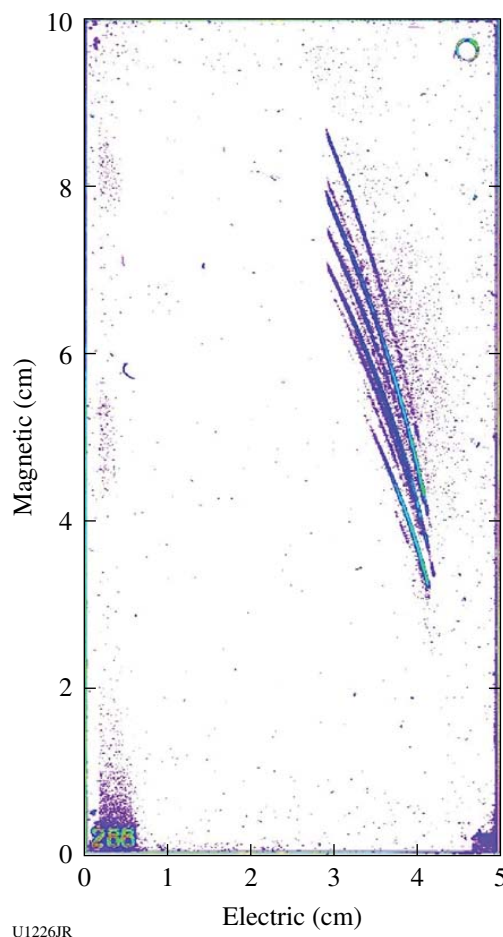


Figure 124.183
CR39 spectra from TPIE. The cutoff energies are for C5+ ~33 MeV (same as for C6+), C4+ ~28 MeV, and C3+ ~14 MeV.

TPIE recorded carbon and oxygen ions and an absence of protons on the SSNTD from the heated targets (Fig. 124.183). Energies of up to 2.75 MeV/nucleon for carbon were observed in large numbers, leading to preliminary conversion efficiencies of a few percent of laser energy into ion energy for each carbon species (depending on assumptions made about the beam size versus the solid angle of TPIE). This means that if all the carbon species could be focused to a 30- μm volume, energy densities of the order of 10^{14} J/m^2 could be achievable.

High-Energy X-Ray Generation (HEX): The high-energy x-ray campaign at LANL has shifted from x-ray production to application of high-energy x rays in phase-contrast imaging. The intent is to generate x rays of sufficient energy that the x-ray absorption is minimal through a Au-walled hohlraum. Given the correct geometric constraints, an interference pattern will be produced in the region of strong phase (or density) gradients. The relationship used to determine the optimal x-ray source to

target distance is $z = (2\lambda u^2)^{-1}$, where z is the propagation distance, λ is the x-ray wavelength, and u is the spatial frequency defined as the inverse of the x-ray source size, in this context. For example, using an x-ray energy of 17.48 keV and an x-ray source size, defined as wire diameter, of 5 μm , the optimal distance from source to target is 17.6 cm.

Experiments this year used K_{α} x-ray emission from Ag (22-keV) and Cu (8-keV) microfoils to investigate shocks produced in CH targets. As shown in Fig. 124.184, the backlighter beam drove a microfoil ($100 \times 100 \times 5 \mu\text{m}$) from the side using a 20-ps pulse at 1 kJ, and the edge was used to backlight the CH target driven by two 2-ns UV pulses with a total energy of 2 kJ.

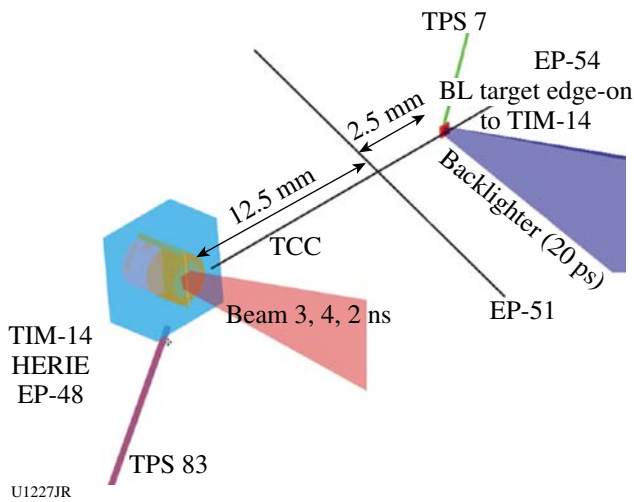


Figure 124.184 Configuration for HEX experiments on OMEGA EP. The primary diagnostic is the HERIE using image plates as the detector. A number of spectrometers were also employed including the TCS, DCS, ZVH, and DCHOPG.

Predicted shock behavior is shown in Fig. 124.185. Data were taken at 4, 6, and 8 ns. Image analysis is still ongoing. Figure 124.186 shows static data taken from gold grids illuminated by Cu emission on the left and Ag emission on the right. Both show high resolution and sufficient signal-to-noise ratio for the intended applications.

FY10 CEA Experiments on the Omega Facility

CEA-led teams conducted 62 shots on OMEGA during FY10. The experiments included ablator preheat characterization, Rayleigh–Taylor (RT) growth measurements, and rugby hohlraum characterization.

Ablator Preheat: Preheat and shock-breakout measurements were obtained in graded dopant targets on OMEGA on 14 June

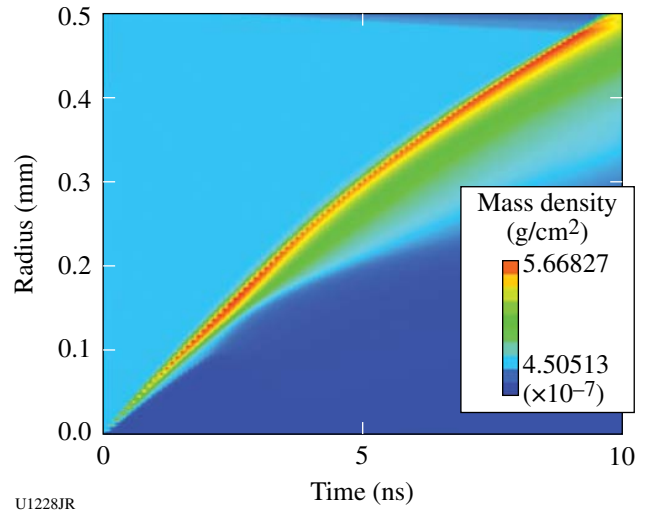


Figure 124.185 One-dimensional hydrodynamics calculation using HELIOS-CR predicting the shock structure as a function of time and position for a CH target driven by 2-kJ, 2-ns UV drive on OMEGA EP.

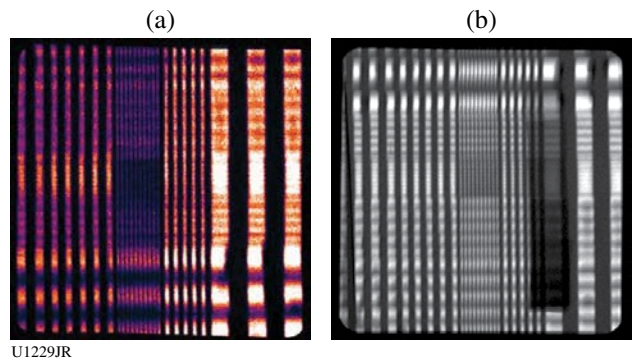


Figure 124.186 Static gold grids illuminated by Cu (left) and Ag (right) backlighters showing sufficient resolution and signal-to-noise ratio.

2010. CEA may use the graded dopant scheme for future ICF capsules. It consists of using several layers of Ge-doped plastic to protect the fuel from hard x rays; moreover, it must ensure hydrodynamic stability at the pusher/fuel interface. To this extent, the Ge-doped layers must be preheated by the M-band radiation so that the density profile across the shell will become nearly constant.

Two-dimensional transpositions of this design were shot on OMEGA. Preheat and shock breakouts were monitored using the ASBO diagnostic (Fig. 124.187). Extensive hohlraum energetics data were obtained using DMX and Dante broadband spectrometers. Detailed M-band radiation was measured using CEA μDMX and Henway spectrometers.

Rayleigh–Taylor Instability Experiments: We measured RT growths in indirectly driven rippled samples as function of Ge on OMEGA on 15 June 2010. These shots were intended to constrain physical models used in CEA hydrodynamic simulations.

These experiments will also provide us with a scaling between the length of RT spikes and corresponding optical-

depth variation measured on face-on radiography images. Differentiated behaviors as a function of dopant fraction were found, and as predicted, the highest growth factors were measured on highly doped samples (Fig. 124.188).

Additional data on face-on x-ray source characterization were obtained. For this purpose, a single Sc foil was shot in

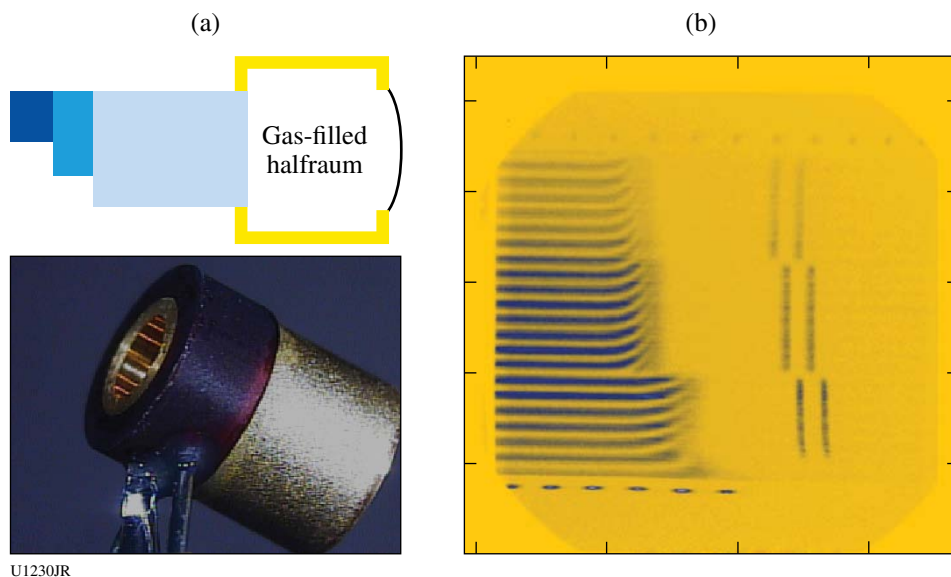


Figure 124.187
 (a) Schematic and real views of a target assembly. Samples were planar and comprised different steps of plastic doped with different atomic proportions of Ge. Steps were coated with Ta to be reflective. (b) Example of a VISAR image: fringe movement is due to preheat until the Ta coating stays reflective. Short flashes seen later in time are due to shock breakout.

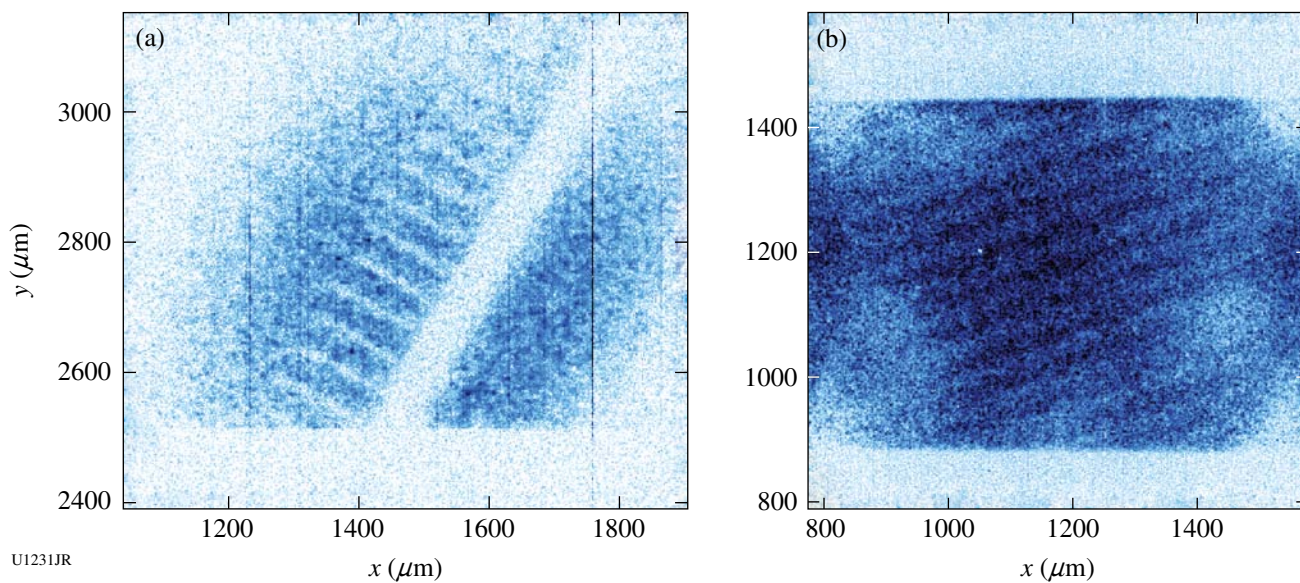


Figure 124.188
 (a) Side-on and (b) face-on radiography of a 20% atomic Ge plastic foil. Nonlinear RT growth spikes seen in (a) are approximately 200 μm long.

order to calibrate the radiography source routinely used in RT growth and in an implosion experiment. The influence of a gas-filled hohlraum plasma on the radiography signal was also studied using a Sc x-ray source placed behind a gas-filled hohlraum with no sample mounted on it (Fig. 124.189).

Implosions in Rugby Hohlräume: In the last few years, CEA has conducted extensive experimental investigations of the rugby hohlraum concept on OMEGA. Rugby hohlraums are part of an effort toward advanced, high-efficiency hohlraum designs, which could provide increased margin for ignition on LMJ and NIF and could also be suited for use in an IFE context because of their higher gains.

In 2009, in collaboration with LLNL (H. S. Park, H. F. Robey, and P. A. Amendt) and MIT (C. K. Li, F. H. Séguin, and R. D. Petrasso), a significant enhancement of x-ray drive in rugby hohlraums with respect to classical cylindrical hohlraums in a direct comparison (Fig. 124.190) was demonstrated. The improved capsule design led to the highest yields for indirect drive with noncryogenic deuterium fuel at the time, enabling researchers to use many nuclear diagnostics (neutron imaging, NTD, Fig. 124.191) for the first time in this configuration. These results were published in *Physical Review Letters* and *Science*.^{55,56} In 2010, the symmetry of implosion (Fig. 124.192) was successfully tuned with a calculated cone-balancing scheme based on the detailed simulations of a 2009

OMEGA experiment, therefore confirming the understanding of rugby hohlraum performance. The work this year was also extended to gas-filled rugby hohlraums with shaped pulses. Measurements have shown a relatively low level of backscatter (~5%), which could be further reduced by the use of polarization smoothing, and performance in good agreement with simulations. Direct comparison of gas-filled rugby and cylindrical hohlraums is planned on OMEGA at the end of 2010.

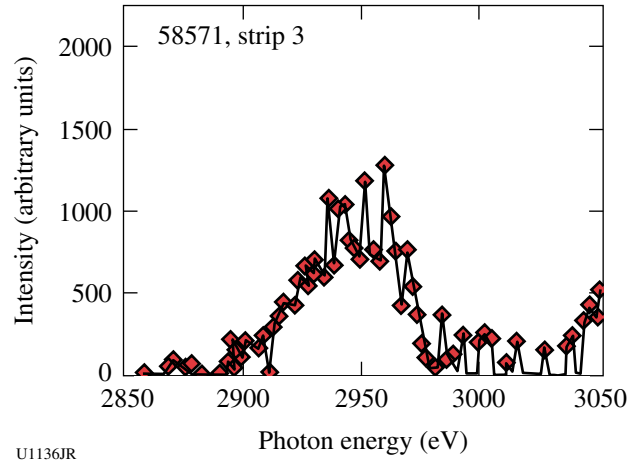


Figure 124.190
Evidence of 18% x-ray-drive enhancement with rugby hohlraums.

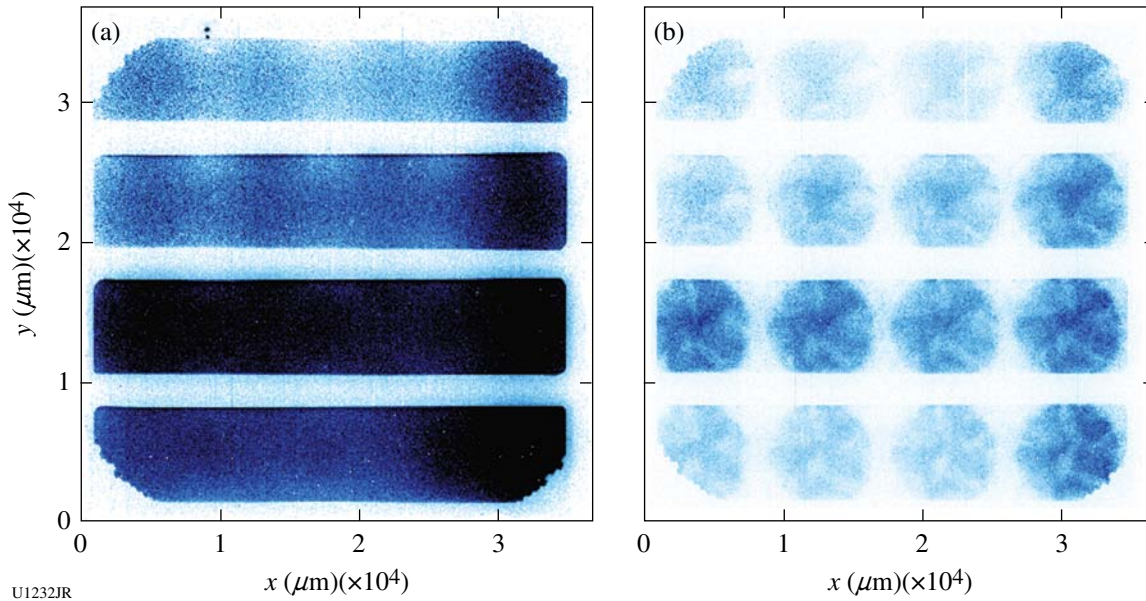
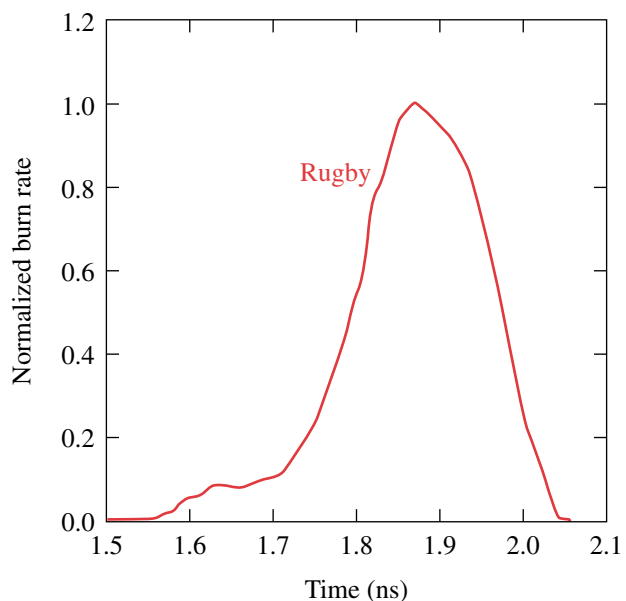
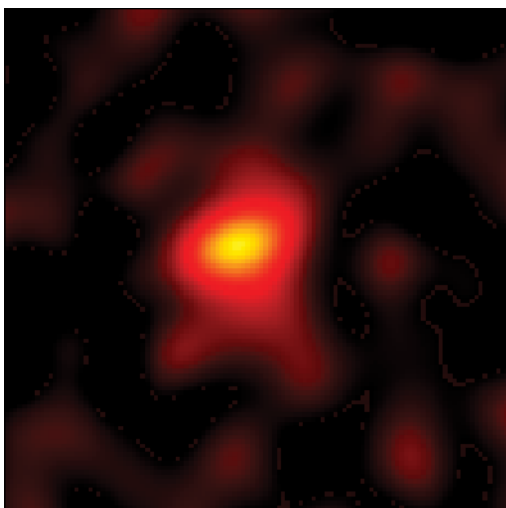
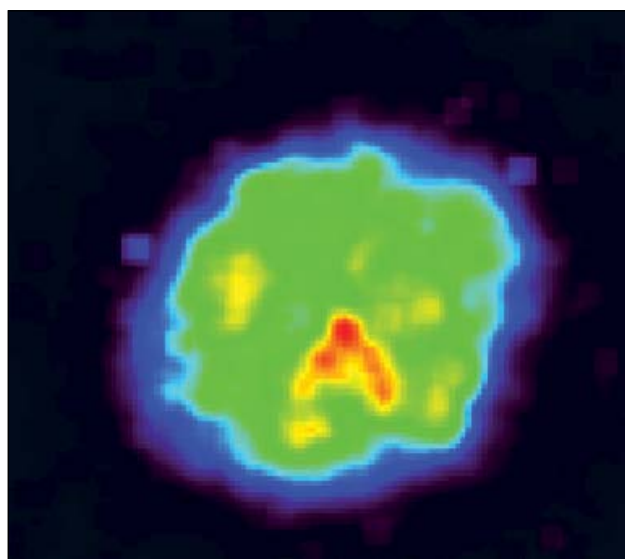


Figure 124.189
XRF images given by (a) a single Sc x-ray source and (b) a Sc source placed behind a gas-filled hohlraum with no sample mounted on it.



U1234JR

Figure 124.191
Neutron image and reaction history of deuterium-filled indirectly driven capsules.



U1235JR

Figure 124.192
Symmetric implosion obtained with calculated cone balance to compensate evaluated backscatter effects.

FY10 AWE OMEGA Experimental Programs

In FY10, AWE led three shot days on the OMEGA laser. This work encompassed an investigation of asymmetrically driven hohlraums (two days) and a Laue x-ray diffraction study of the dynamics of shocked tantalum crystals (one day).

Asymmetrically Driven Hohlraums: Work by AWE has continued to study the asymmetrically driven implosion of thin glass shells and aerogel-foam witness balls in hohlraum targets, as a sensitive test of radiation hydrodynamic modeling. Asymmetry of radiation drive is achieved by asymmetry of laser-beam energy and timing, by asymmetry of capsule position, and by introducing an annular restriction of diameter (baffle) within the hohlraum.

A 1.6-mm-diam, 2.7-mm-long hohlraum is heated by up to 30 OMEGA beams. X-ray backlighting of a thin-wall glass capsule (600- μm diameter, 3.5- μm wall thickness, 30- μm CH ablator) or silica aerogel sphere (600- μm diameter, 300- mg cm^{-3} density) provides the primary diagnostic of the angular distribution of radiation drive near the center of the hohlraum. The hydrodynamics are diagnosed by x-ray backlighting using an area-backlighting source together with a 16-image pinhole camera and a four-strip gated microchannel-plate (MCP) detector, or by point-projection x-ray backlighting together with a single-strip MCP detector. In the case of point backlighting (new to this campaign in FY10), just one single image is recorded but this is of higher spatial resolution (lower statistical “shot noise”) than in the case of multiple images, and this technique has the further advantage of potential sensitivity to refraction (phase-contrast enhancement) at the steep density gradients encountered at ablation and shock fronts within the capsule or foam witness ball.

In previous work⁵⁷ using hohlraums with end-to-end asymmetry of laser drive, a polar jet was recorded and was a particularly sensitive diagnostic of the angular distribution of early-time radiation drive. Many features of the hydrodynamics were successfully reproduced by hydrocode modeling, but modeling and experiment differed in one important respect: simulation showed a small “bump” of material at the most strongly driven pole of thin-shell capsules that was not observed in the experiment. Work during FY10 further investigated this feature of the hydrodynamics. The position of the capsule in the hohlraum was offset from hohlraum center (Fig. 124.193) to provide a further modulation of the angular distribution of the early-time drive at the hot pole. The polar bump was observed and demonstrated to be a genuine feature of the hydrodynamics (and not a near-axis artifact arising in the modeling). These

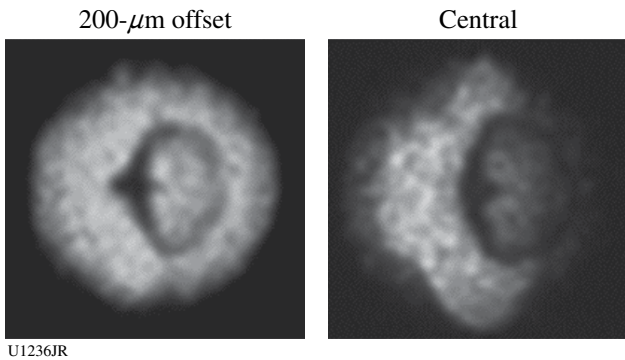
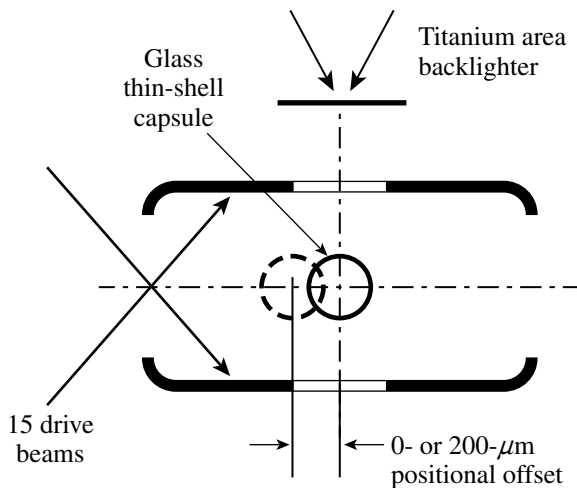


Figure 124.193 Experiment to investigate sensitivity of the polar “bump” to capsule position in an asymmetrically driven hohlraum. The hohlraum is aligned on the P6–P7 axis of the OMEGA target chamber and is driven by 15 beams of the OMEGA laser from one side only. A small displacement of position of the thin-wall glass capsule introduces a further modulation of the angular distribution of asymmetric drive, evident in the radiographs.

experimental data from OMEGA have been used to improve AWE’s hydrocode simulations, and detailed attention to pre-heat, near-axis resolution, and radiation-transport modeling has resulted in very much closer agreement with the experiment (Fig. 124.194).

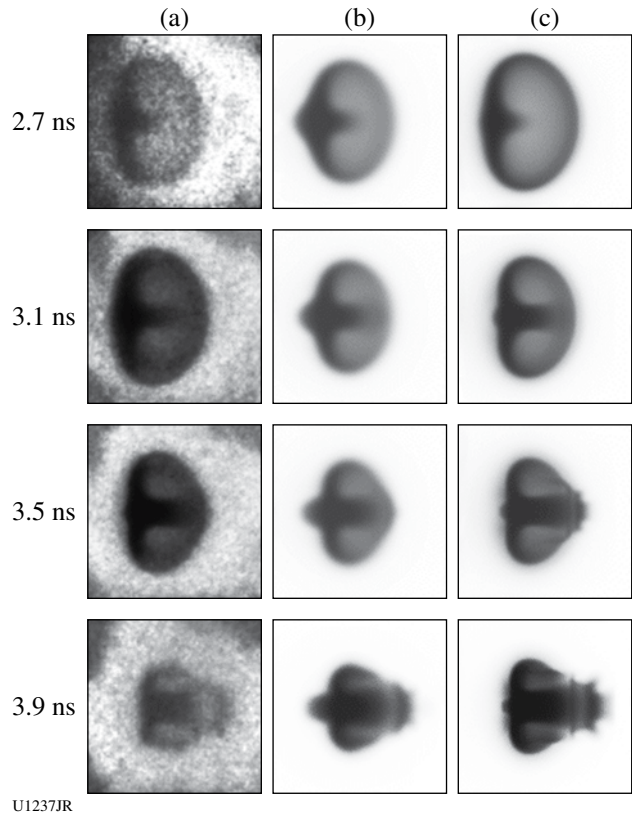
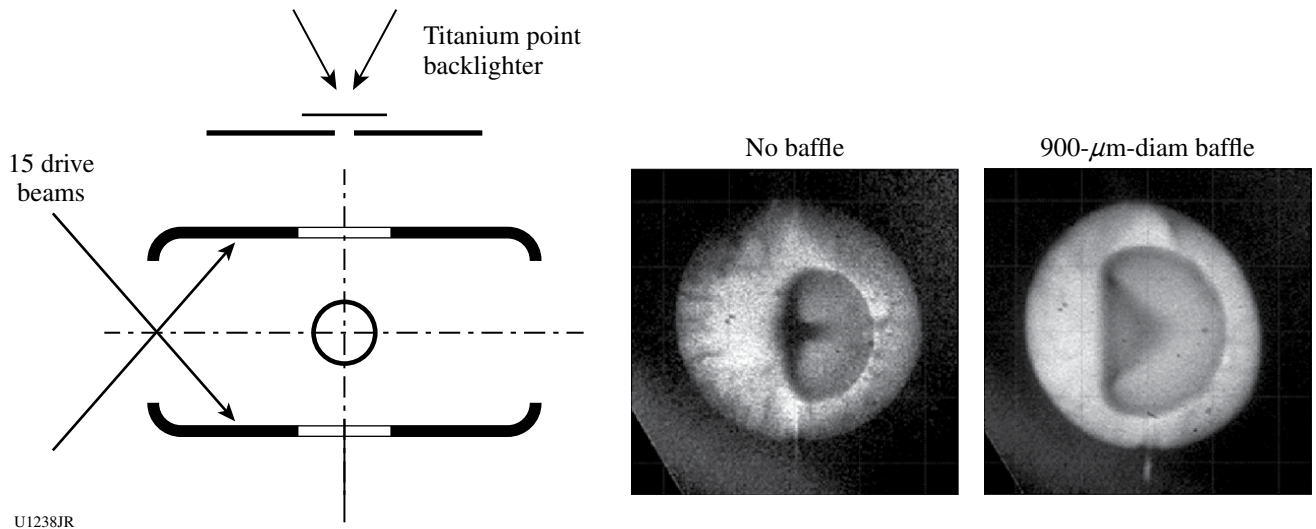


Figure 124.194 Sequence of experimental radiographs (a) of implosion of an asymmetrically driven thin-shell glass capsule compared with simulation before (b) and after (c) improvements to the modeling arising from experiments at OMEGA.

The use of internal, washer-shaped baffles (Fig. 124.195) in hohlraum targets provides a means of shielding an experimental assembly at hohlraum center from a direct view of the individual laser “hot spots” at the hohlraum wall (although at the expense of significant loss of symmetry of angular distribution of drive). X-ray backlighting measurements of capsule implosions in such targets have also been made during FY10 to provide a further benchmark test of hohlraum modeling. Figure 124.195 shows a comparison of 10- μm -resolution, point-projection-backlit images of capsule implosion in regular and baffled hohlraums. The improvement of spatial resolution in these images, in comparison with area-backlit images, is readily apparent (compare Figs. 124.193 and 124.195), as is the



U1238JR

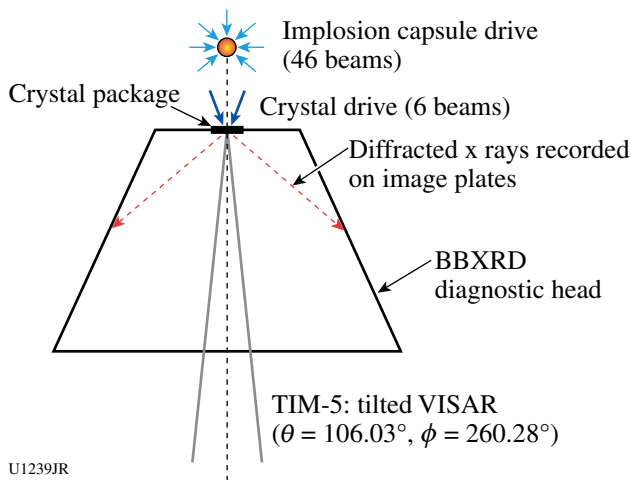
Figure 124.195
Point-backlit images of thin-shell implosions in regular and baffled hohlraums.

possible refraction-enhanced gradient of image intensity near the ablation front at the cold pole of the capsule.

Laue X-Ray Diffraction: The objective of this one-day campaign was to demonstrate the use of broadband x-ray (“white light”) Laue diffraction to probe the lattice dynamics of single-crystal tantalum under shock-loaded conditions, in conjunction with the newly commissioned LLNL BBXRD diagnostic (Fig. 124.196). This campaign complements work by

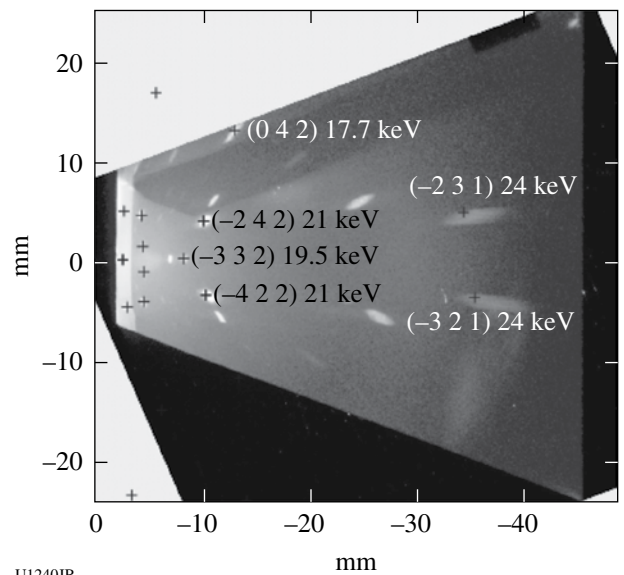
LLE and LLNL, which used the same developmental diffraction technique to investigate the lattice dynamics of shocked copper and silicon samples.

The white-light Laue technique produces a characteristic diffraction pattern (Fig. 124.197), in which each spot can be



U1239JR

Figure 124.196
Sketch of experimental setup showing an implosion capsule backlighter, a Ta crystal package mounted on BBXRD diagnostic, image plate detectors to record the diffraction pattern, and a VISAR diagnostic used to infer the state of the driven sample.

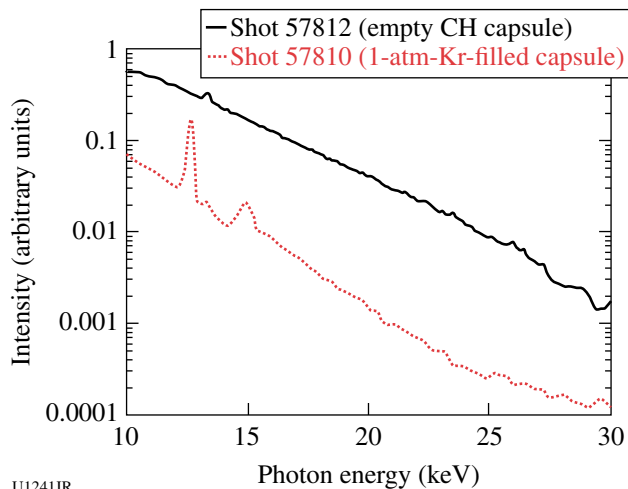


U1240JR

Figure 124.197
Diffraction pattern obtained from 5- μm -thick, single-crystal (100) Ta using an implosion capsule backlighter and LLNL broadband x-ray diffraction (BBXRD) diagnostic. Each crystallographic plane (hkl) generates a characteristic diffraction spot, some of which are labeled in the figure.

attributed to a crystallographic plane in the sample lattice. In principle, this pattern offers unique insight into changes in lattice structure generated under loaded conditions (be it ramp or shock loading), such as the formation and growth of defects and 1-D-to-3-D relaxation processes, by examining and interpreting the location and structure of the characteristic diffraction spots.

An implosion capsule backlighter (980- μm outer diameter with a 10- μm -thick CH wall) driven by 46 OMEGA beams (each beam contained 500 J in a 1-ns square pulse and was used with SG4 DPP) was employed to generate a smooth, broadband spectrum of x rays to produce the white-light diffraction pattern (Fig. 124.198). Such backlighters also have the advantage of a short temporal duration of emission, useful for probing lattice dynamics on an ~ 100 -ps time scale.



U1241JR

Figure 124.198
Time-integrated spectrum from an implosion capsule backlighter recorded using the double-crystal spectrometer (DCS).

Diffraction data were successfully recorded from both static and driven tantalum samples. Figure 124.197 illustrates the diffraction pattern from a static (i.e., undriven) Ta sample.

Several improvements will be employed in future campaigns. First, one of the most-challenging aspects of this experiment was the production of high-quality crystal samples that were flat and nominally free of crystallographic defects. Modifications will be made to the crystal package design, and improvements will be made to the assembly process in order to address this issue. Second, VISAR measurements indicated that the spatial uniformity of the drive on the crystal package should be improved in order to simplify the interpretation of the data. Changes in beam configuration are being examined to address this point.

REFERENCES

1. S. H. Glenzer *et al.*, *Phys. Rev. Lett.* **90**, 175002 (2003).
2. H. J. Lee, P. Neumayer, J. Castor, T. Döppner, R. W. Falcone, C. Fortmann, B. A. Hammel, A. L. Kritcher, O. L. Landen, R. W. Lee, D. D. Meyerhofer, D. H. Munro, R. Redmer, S. P. Regan, S. Weber, and S. H. Glenzer, *Phys. Rev. Lett.* **102**, 115001 (2009).
3. S. H. Glenzer *et al.*, *Phys. Rev. Lett.* **98**, 065002 (2007); A. L. Kritcher *et al.*, *Science* **322**, 69 (2008); A. García Saiz *et al.*, *Nat. Phys.* **4**, 940 (2008).
4. S. H. Glenzer *et al.*, *Phys. Plasmas* **10**, 2433 (2003); O. L. Landen *et al.*, *J. Quant. Spectrosc. Radiat. Transf.* **71**, 465 (2001); H. Sawada, S. P. Regan, D. D. Meyerhofer, I. V. Igumenschev, V. N. Goncharov, T. R. Boehly, R. Epstein, T. C. Sangster, V. A. Smalyuk, B. Yaakobi, G. Gregori, S. H. Glenzer, and O. L. Landen, *Phys. Plasmas* **14**, 122703 (2007).
5. L. M. Barker and R. E. Hollenbach, *J. Appl. Phys.* **43**, 4669 (1972).
6. G. W. Collins *et al.*, *Science* **281**, 1178 (1998); P. M. Celliers, D. K. Bradley, G. W. Collins, D. G. Hicks, T. R. Boehly, and W. J. Armstrong, *Rev. Sci. Instrum.* **75**, 4916 (2004); P. M. Celliers *et al.*, *J. Appl. Phys.* **98**, 113529 (2005); D. G. Hicks, T. R. Boehly, P. M. Celliers, J. H. Eggert, S. J. Moon, D. D. Meyerhofer, and G. W. Collins, *Phys. Rev. B* **79**, 014112 (2009); M. D. Knudson and M. P. Desjarlais, *Phys. Rev. Lett.* **103**, 225501 (2009).
7. J. Eggert, S. Brygoo, P. Loubeyre, R. S. McWilliams, P. M. Celliers, D. G. Hicks, T. R. Boehly, R. Jeanloz, and G. W. Collins, *Phys. Rev. Lett.* **100**, 124503 (2008).
8. Ya. B. Zel'dovich and Yu. P. Raizer, in *Physics of Shock Waves and High-Temperature Hydrodynamic Phenomena*, edited by W. D. Hayes and R. F. Probstein (Academic Press, New York, 1966), Vol. I, Chap. II, pp. 107–175.
9. R. P. Drake, *High-Energy-Density Physics: Fundamentals, Inertial Fusion, and Experimental Astrophysics*, Shock Wave and High Pressure Phenomena (Springer, Berlin, 2006).
10. J. J. Fortney *et al.*, *Phys. Plasmas* **16**, 041003 (2009).
11. B. A. Remington, R. P. Drake, and D. D. Ryutov, *Rev. Mod. Phys.* **78**, 755 (2006).
12. T. Guillot, *Science* **286**, 72 (1999).
13. W. J. Nellis, M. Ross, and N. C. Holmes, *Science* **269**, 1249 (1995).
14. W. J. Nellis, S. T. Weir, and A. C. Mitchell, *Science* **273**, 936 (1996).
15. N. Nettelmann *et al.*, *Astrophys. J.* **683**, 1217 (2008).
16. B. Militzer *et al.*, *Astrophys. J.* **688**, L45 (2008).
17. I. de Pater and J. J. Lissauer, *Planetary Sciences*, 5th ed. (Cambridge University Press, Cambridge, England, 2007), p. 544.
18. E. C. Stone and E. D. Miner, *Science* **246**, 1417 (1971).
19. S. Stanley and J. Bloxham, *Nature* **428**, 151 (2004).

20. P. Hartigan *et al.*, *Astrophys. J.* **705**, 1073 (2009).
21. J. M. Foster *et al.*, *Phys. Plasmas* **17**, 112704 (2010).
22. P. M. Celliers, P. Loubeyre, J. H. Eggert, S. Brygoo, R. S. McWilliams, D. G. Hicks, T. R. Boehly, R. Jeanloz, and G. W. Collins, *Phys. Rev. Lett.* **104**, 184503 (2010).
23. W. Lorenzen, B. Holst, and R. Redmer, *Phys. Rev. Lett.* **102**, 115701 (2009).
24. C. K. Li, F. H. Séguin, J. A. Frenje, J. R. Rygg, R. D. Petrasso, R. P. J. Town, P. A. Amendt, S. P. Hatchett, O. L. Landen, A. J. Mackinnon, P. K. Patel, V. Smalyuk, J. P. Knauer, T. C. Sangster, and C. Stoeckl, *Rev. Sci. Instrum.* **77**, 10E725 (2006).
25. T. R. Boehly, D. L. Brown, R. S. Craxton, R. L. Keck, J. P. Knauer, J. H. Kelly, T. J. Kessler, S. A. Kumpan, S. J. Loucks, S. A. Letzring, F. J. Marshall, R. L. McCrory, S. F. B. Morse, W. Seka, J. M. Soures, and C. P. Verdon, *Opt. Commun.* **133**, 495 (1997).
26. J. R. Rygg, F. H. Séguin, C. K. Li, J. A. Frenje, M. J.-E. Manuel, R. D. Petrasso, R. Betti, J. A. Delettrez, O. V. Gotchev, J. P. Knauer, D. D. Meyerhofer, F. J. Marshall, C. Stoeckl, and W. Theobald, *Science* **319**, 1223 (2008).
27. C. K. Li, F. H. Séguin, J. A. Frenje, M. Rosenberg, R. D. Petrasso, P. A. Amendt, J. A. Koch, O. L. Landen, H. S. Park, H. F. Robey, R. P. J. Town, A. Casner, F. Philippe, R. Betti, J. P. Knauer, D. D. Meyerhofer, C. A. Back, J. D. Kilkenny, and A. Nikroo, *Science* **327**, 1231 (2010).
28. C. K. Li, F. H. Séguin, J. A. Frenje, J. R. Rygg, R. D. Petrasso, R. P. J. Town, P. A. Amendt, S. P. Hatchett, O. L. Landen, A. J. Mackinnon, P. K. Patel, V. A. Smalyuk, T. C. Sangster, and J. P. Knauer, *Phys. Rev. Lett.* **97**, 135003 (2006).
29. C. K. Li, F. H. Séguin, J. A. Frenje, J. R. Rygg, R. D. Petrasso, R. P. J. Town, P. A. Amendt, S. P. Hatchett, O. L. Landen, A. J. Mackinnon, P. K. Patel, M. Tabak, J. P. Knauer, T. C. Sangster, and V. A. Smalyuk, *Phys. Rev. Lett.* **99**, 015001 (2007).
30. C. K. Li, F. H. Séguin, J. A. Frenje, J. R. Rygg, R. D. Petrasso, R. P. J. Town, O. L. Landen, J. P. Knauer, and V. A. Smalyuk, *Phys. Rev. Lett.* **99**, 055001 (2007).
31. C. K. Li, F. H. Séguin, J. R. Rygg, J. A. Frenje, M. Manuel, R. D. Petrasso, R. Betti, J. Delettrez, J. P. Knauer, F. Marshall, D. D. Meyerhofer, D. Shvarts, V. A. Smalyuk, C. Stoeckl, O. L. Landen, R. P. J. Town, C. A. Back, and J. D. Kilkenny, *Phys. Rev. Lett.* **100**, 225001 (2008).
32. C. K. Li, F. H. Séguin, J. A. Frenje, R. D. Petrasso, P. A. Amendt, R. P. J. Town, O. L. Landen, J. R. Rygg, R. Betti, J. P. Knauer, D. D. Meyerhofer, J. M. Soures, C. A. Back, J. D. Kilkenny, and A. Nikroo, *Phys. Rev. Lett.* **102**, 205001 (2009).
33. R. D. Petrasso, C. K. Li, F. H. Séguin, J. R. Rygg, J. A. Frenje, R. Betti, J. P. Knauer, D. D. Meyerhofer, P. A. Amendt, D. H. Froula, O. L. Landen, P. K. Patel, J. S. Ross, and R. P. J. Town, *Phys. Rev. Lett.* **103**, 085001 (2009).
34. O. V. Gotchev, P. Y. Chang, J. P. Knauer, D. D. Meyerhofer, O. Polomarov, J. Frenje, C. K. Li, M. J.-E. Manuel, R. D. Petrasso, J. R. Rygg, F. H. Séguin, and R. Betti, *Phys. Rev. Lett.* **103**, 215004 (2009).
35. G. Li, R. Yan, C. Ren, T.-L. Wang, J. Tonge, and W. B. Mori, *Phys. Rev. Lett.* **100**, 125002 (2008).
36. H. Chen, S. C. Wilks, D. D. Meyerhofer, J. Bonlie, C. D. Chen, S. N. Chen, C. Courtois, L. Elberson, G. Gregori, W. Kruer, O. Landoas, J. Mithen, J. Myatt, C. D. Murphy, P. Nilson, D. Price, M. Schneider, R. Shepherd, C. Stoeckl, M. Tabak, R. Tommasini, and P. Beiersdorfer, *Phys. Rev. Lett.* **105**, 015003 (2010).
37. S. H. Glenzer *et al.*, *Phys. Rev. Lett.* **88**, 235002 (2002).
38. University of Washington, Department of Physics, FEFF Project, 2004, <http://leonardo.phys.washington.edu/feff/> (24 June 2004).
39. W. Theobald, A. A. Solodov, C. Stoeckl, K. S. Anderson, R. Betti, T. R. Boehly, R. S. Craxton, J. A. Delettrez, C. Dorrer, J. A. Frenje, V. Yu. Glebov, H. Habara, K. A. Tanaka, J. P. Knauer, R. Lauck, F. J. Marshall, K. L. Marshall, D. D. Meyerhofer, P. M. Nilson, P. K. Patel, T. C. Sangster, W. Seka, N. Sinenian, T. Ma, F. N. Beg, and R. B. Stephens, *Bull. Am. Phys. Soc.* **55**, 291 (2010).
40. J. A. Halbleib *et al.*, *IEEE Trans. Nucl. Sci.* **39**, 1025 (1992).
41. N. Izumi, C. Hagmann, G. Stone, D. Hey, S. Glenn, A. Conder, A. Teruya, C. Sorce, R. Tommasini, W. Stoeffl, P. Springer, O. L. Landen, H. W. Herrmann, G. A. Kyrala, R. Bahukutumbi, V. Y. Glebov, T. C. Sangster, M. Eckart, A. J. Mackinnon, J. A. Koch, D. K. Bradley, and P. Bell, *Rev. Sci. Instrum.* **81**, 10E515 (2010).
42. T. Döppner, C. Fortmann, P. F. Davis, A. L. Kritcher, O. L. Landen, H. J. Lee, R. Redmer, S. P. Regan, and S. H. Glenzer, *J. Phys., Conf. Ser.* **244**, 032044 (2010).
43. H.-S. Park *et al.*, *Phys. Rev. Lett.* **104**, 135504 (2010); H.-S. Park *et al.*, *Phys. Plasmas* **17**, 056314 (2010).
44. N. R. Barton, private communication (2010).
45. D. L. Preston, D. L. Tonks, and D. C. Wallace, *J. Appl. Phys.* **93**, 211 (2003).
46. M. A. Meyers, A. Mishra, and D. J. Benson, *Prog. Mater. Sci.* **51**, 427 (2006).
47. D. G. Hicks, T. R. Boehly, P. M. Celliers, J. H. Eggert, E. Vianello, D. D. Meyerhofer, and G. W. Collins, *Phys. Plasmas* **12**, 082702 (2005).
48. O. A. Hurricane, *High Energy Density Phys.* **4**, 97 (2008).
49. E. C. Harding *et al.*, *Phys. Rev. Lett.* **103**, 045005 (2009).
50. O. A. Hurricane *et al.*, *Phys. Plasmas* **16**, 056305 (2009).
51. R. E. Olson *et al.*, *Rev. Sci. Instrum.* **77**, 10E523 (2006).
52. L. S. Dubrovinsky *et al.*, *Phys. Rev. Lett.* **84**, 1720 (2000).
53. J. C. Boettger and D. C. Wallace, *Phys. Rev. B* **55**, 2840 (1997).
54. G. M. Hale and D. C. Dodder, in *Nuclear Cross Sections for Technology*, edited by J. L. Fowler, C. H. Johnson, and C. D. Bowman, Natl. Bur. Stand. (U.S.), Spec. Publ. 594 (U.S. Government Printing Office, Washington, DC, 1980), pp. 650–658.

55. F. Philippe, A. Casner, T. Caillaud, O. Landoas, M. C. Monteil, S. Liberatore, H. S. Park, P. Amendt, H. Robey, C. Sorce, C. K. Li, F. Seguin, M. Rosenberg, R. Petrasso, V. Glebov, and C. Stoeckl, *Phys. Rev. Lett.* **104**, 035004 (2010).
56. C. K. Li, F. H. Séguin, J. A. Frenje, M. Rosenberg, R. D. Petrasso, P. A. Amendt, J. A. Koch, O. L. Landen, H. S. Park, H. F. Robey, R. P. J. Town, A. Casner, F. Philippe, R. Betti, J. P. Knauer, D. D. Meyerhofer, C. A. Back, J. D.ilkenny, and A. Nikroo, *Science* **327**, 1231 (2010).
57. K. Vaughn *et al.*, *Phys. Plasmas* **17**, 056316 (2010).

Publications and Conference Presentations

Publications

- S.-W. Bahk, E. Fess, B. E. Kruschwitz, and J. D. Zuegel, "A High-Resolution, Adaptive Beam-Shaping System for High-Power Lasers," *Opt. Express* **18**, 9151 (2010).
- M. A. Barrios, D. G. Hicks, T. R. Boehly, D. E. Fratanduono, J. H. Eggert, P. M. Celliers, G. W. Collins, and D. D. Meyerhofer, "High-Precision Measurements of the Equation of State of Hydrocarbons at 1–10 Mbar Using Laser-Driven Shock Waves," *Phys. Plasmas* **17**, 056307 (2010).
- Z. Bei, T. B. Jones, and D. R. Harding, "Electric Field Centering of Double-Emulsion Droplets Suspended in a Density Gradient," *Soft Matter* **6**, 2312 (2010).
- R. Betti, P. Y. Chang, B. K. Spears, K. S. Anderson, J. Edwards, M. Fatenejad, J. D. Lindl, R. L. McCrory, R. Nora, and D. Shvarts, "Thermonuclear Ignition in Inertial Confinement Fusion and Comparison with Magnetic Confinement," *Phys. Plasmas* **17**, 058102 (2010).
- T. R. Boehly, R. E. Olson, P. M. Celliers, D. H. Munro, W. Seka, O. L. Landen, G. W. Collins, L. J. Suter, T. C. Sangster, and D. D. Meyerhofer, "The Effect of Condensates and Inner Coatings on Vacuum Hohlraum Targets," *Phys. Plasmas* **17**, 032701 (2010).
- J. Bromage, C. Dorrer, and J. D. Zuegel, "Angular-Dispersion-Induced Spatiotemporal Aberrations in Noncollinear Optical Parametric Amplifiers," *Opt. Lett.* **35**, 2251 (2010).
- P. Y. Chang, R. Betti, B. K. Spears, K. S. Anderson, J. Edwards, M. Fatenejad, J. D. Lindl, R. L. McCrory, R. Nora, and D. Shvarts, "Generalized Measurable Ignition Criterion for Inertial Confinement Fusion," *Phys. Rev. Lett.* **104**, 135002 (2010).
- C. E. Clayton, J. E. Ralph, F. Albert, R. A. Fonseca, S. H. Glenzer, C. Joshi, W. Lu, K. A. Marsh, S. F. Martins, W. B. Mori, A. Pak, F. S. Tsung, B. B. Pollock, J. S. Ross, L. O. Silva, and D. H. Froula, "Self-Guided Laser Wakefield Acceleration beyond 1 GeV Using Ionization-Induced Injection," *Phys. Rev. Lett.* **105**, 105003 (2010).
- G. P. Cox, K. L. Marshall, J. C. Lambropoulos, M. Leitch, C. Fromen, and S. D. Jacobs, "Modeling the Effects of Microencapsulation on the Electro-Optic Behavior of Polymer Cholesteric Liquid Crystal Flakes," *J. Appl. Phys.* **106**, 124911 (2009).
- A. S. Cross, D. Kochanowska, M. Witkowska-Baran, A. Mycielski, M. Mikulics, D. Grützmacher, and R. Sobolewski, "Femtosecond Electro-Optic Effect in (Cd,Mn)Te Single Crystals," *J. Phys. Conf. Series* **193**, 012057 (2009).
- W. R. Donaldson, J. R. Marciante, and R. G. Roides, "An Optical Replicator for Single-Shot Measurements at 10 GHz With a Dynamic Range of 1800:1," *IEEE J. Quantum Electron.* **46**, 191 (2010).
- C. Dorrer and J. Bromage, "High-Sensitivity Optical Pulse Characterization Using Sagnac Electro-Optic Spectral Shearing Interferometry," *Opt. Lett.* **35**, 1353 (2010).
- R. Florido, R. C. Mancini, T. Nagayama, R. Tommasini, J. A. Delettrez, S. P. Regan, V. A. Smalyuk, R. Rodríguez, and J. M. Gil, "Argon K-Shell and Bound-Free Emission from OMEGA Direct-Drive Implosion Cores," *High Energy Density Phys.* **6**, 70 (2010).
- D. French, C. Dorrer, and I. Jovanovic, "Two-Beam SPIDER for Dual-Pulse Single-Shot Characterization," *Opt. Lett.* **34**, 3415 (2009).
- E. Głowacki, K. Horovitz, C. W. Tang, and K. L. Marshall, "Photoswitchable Gas Permeation Membranes Based on Liquid Crystals," *Adv. Funct. Mater.* **20**, 2778 (2010).
- E. Głowacki, K. Hunt, D. Abud, and K. L. Marshall, "Photoswitchable Gas Permeation Membranes Based on Azobenzene-Doped Liquid Crystals. II. Permeation-Switching Characteriza-

tion Under Variable Volume and Variable Pressure Conditions,” in *Liquid Crystals XIV*, edited by I. C. Khoo (SPIE, Bellingham, WA, 2010), Vol. 7775, p. 77750G (invited).

E. Glowacki, C. W. Tang, and K. L. Marshall, “Photoswitchable Gas Permeation Membranes Based on Azobenzene-Doped Liquid Crystals,” in *Liquid Crystals XIII*, edited by I. C. Khoo (SPIE, Bellingham, WA, 2009), Vol. 7414, p. 74140H (invited).

V. N. Goncharov, T. C. Sangster, T. R. Boehly, S. X. Hu, I. V. Igumenshchev, F. J. Marshall, R. L. McCrory, D. D. Meyerhofer, P. B. Radha, W. Seka, S. Skupsky, C. Stoeckl, D. T. Casey, J. A. Frenje, and R. D. Petrasso, “Demonstration of the Highest Deuterium-Tritium Areal Density Using Multiple-Picket Cryogenic Designs on OMEGA,” *Phys. Rev. Lett.* **104**, 165001 (2010).

O. V. Gotchev, P. Y. Chang, J. P. Knauer, D. D. Meyerhofer, O. Polomarov, J. Frenje, C. K. Li, M. J.-E. Manuel, R. D. Petrasso, J. R. Rygg, F. H. Séguin, and R. Betti, “Laser-Driven Magnetic-Flux Compression in High-Energy-Density Plasmas,” *Phys. Rev. Lett.* **103**, 215004 (2009).

W. Guan and J. R. Marciante, “Power Scaling of Single-Frequency Hybrid Brillouin/Ytterbium Fiber Lasers,” *IEEE J. Quantum Electron.* **46**, 674 (2010).

W. Guan and J. R. Marciante, “Single-Frequency Hybrid Brillouin/Ytterbium Fiber Laser with 1-W Output Power,” in the *2010 Conference on Optical Fiber Communication and National Fiber Optic Engineers Conference* (IEEE, New York, 2010), Paper OThQ4.

W. Guan and J. R. Marciante, “Single-Frequency 1 W Hybrid Brillouin/Ytterbium Fiber Laser,” *Opt. Lett.* **34**, 3131 (2009).

S. X. Hu, “Optimizing the FEDVR-TDCC Code for Exploring the Quantum Dynamics of Two-Electron Systems in Intense Laser Pulses,” *Phys. Rev. E* **81**, 056705 (2010).

S. X. Hu, B. Militzer, V. N. Goncharov, and S. Skupsky, “Strong Coupling and Degeneracy Effects in Inertial Confinement Fusion Implosions,” *Phys. Rev. Lett.* **104**, 235003 (2010).

S. X. Hu, P. B. Radha, J. A. Marozas, R. Betti, T. J. B. Collins, R. S. Craxton, J. A. Delettrez, D. H. Edgell, R. Epstein, V. N. Goncharov, I. V. Igumenshchev, F. J. Marshall, R. L. McCrory, D. D. Meyerhofer, S. P. Regan, T. C. Sangster, S. Skupsky, V. A. Smalyuk, Y. Elbaz, and D. Shvarts, “Neutron Yield

Study of Direct-Drive, Low-Adiabatic Cryogenic D₂ Implosions on OMEGA Laser System,” *Phys. Plasmas* **16**, 112706 (2009).

H. Irie and R. Sobolewski, “Picosecond Electric Pulse Excitation of Three-Branch Ballistic Nanodevices,” *J. Phys. Conf. Series* **193**, 012097 (2009).

H. Irie and R. Sobolewski, “Terahertz Electrical Response of Nanoscale Three-Branch Junctions,” *J. Appl. Phys.* **107**, 084315 (2010).

T. B. Jones, R. Gram, K. Kentch, and D. R. Harding, “Capillarity and Dielectrophoresis of Liquid Deuterium,” *J. Phys. D: Appl. Phys.* **42**, 225505 (2009).

A. M. Kaplan, G. P. Agrawal, and D. N. Maywar, “Optical Square-Wave Clock Generation Based on an All-Optical Flip-Flop,” *IEEE Photonics Technol. Lett.* **22**, 489 (2010).

V. Kaushal, M. Margala, Q. Yu, P. Ampadu, G. Guarino, and R. Sobolewski, “Current Transport Modeling and Experimental Study of THz Room Temperature Ballistic Deflection Transistors,” *J. Phys. Conf. Series* **193**, 012092 (2009).

J. P. Knauer, O. V. Gotchev, P. Y. Chang, D. D. Meyerhofer, O. Polomarov, R. Betti, J. A. Frenje, C. K. Li, M. J.-E. Manuel, R. D. Petrasso, J. R. Rygg, and F. H. Séguin, “Compressing Magnetic Fields with High-Energy Lasers,” *Phys. Plasmas* **17**, 056318 (2010).

J. C. Lambropoulos, C. Miao, and S. D. Jacobs, “Magnetic Field Effects on Shear and Normal Stresses in Magnetorheological Finishing,” *Opt. Express* **18**, 19,713 (2010).

J. R. Marciante, R. G. Roides, V. V. Shkunov, and D. A. Rockwell, “Near-Diffraction-Limited Operation of Step-Index Large-Mode-Area Fiber Lasers Via Gain Filtering,” *Opt. Lett.* **35**, 1828 (2010).

M. Margala, P. Ampadu, Y. Shapir, and R. Sobolewski, “Ballistic Electronics: Breaking the Barrier in Terahertz Speed Processing,” in *Terahertz Physics, Devices, and Systems IV: Advanced Applications in Industry and Defense*, edited by M. Anwar, N. K. Dhar, and T. W. Crowe (SPIE, Bellingham, WA, 2010), Vol. 7671, p. 76710I.

N. Marrocco, G. P. Pepe, A. Capretti, L. Parlato, V. Pagliarulo, G. Peluso, A. Barone, R. Cristiano, M. Ejrnaes, A. Casaburi, N. Kashiwazaki, T. Taino, H. Myoren, and R. Sobolewski, “Strong Critical Current Density Enhancement in NiCu/NbN

- Superconducting Nanostripes for Optical Detection,” *Appl. Phys. Lett.* **97**, 092504 (2010).
- R. L. McCrory, D. D. Meyerhofer, R. Betti, T. R. Boehly, R. S. Craxton, J. A. Delettrez, D. H. Edgell, V. Yu. Glebov, V. N. Goncharov, D. R. Harding, S. X. Hu, J. P. Knauer, F. J. Marshall, P. W. McKenty, P. B. Radha, S. P. Regan, T. C. Sangster, W. Seka, R. W. Short, D. Shvarts, S. Skupsky, V. A. Smalyuk, J. M. Soures, C. Stoeckl, W. Theobald, B. Yaakobi, J. A. Frenje, C. K. Li, R. D. Petrasso, F. H. Séguin, and D. T. Casey, “Progress in Cryogenic Target Implosions on OMEGA,” *J. Phys.: Conf. Ser.* **244**, 012004 (2010).
- R. L. McCrory, D. D. Meyerhofer, S. J. Loucks, S. Skupsky, R. E. Bahr, R. Betti, T. R. Boehly, R. S. Craxton, T. J. B. Collins, J. A. Delettrez, W. R. Donaldson, R. Epstein, K. A. Fletcher, C. Freeman, J. A. Frenje, V. Yu. Glebov, V. N. Goncharov, D. R. Harding, P. A. Jaanimagi, R. L. Keck, J. H. Kelly, T. J. Kessler, J. D. Kilkenny, J. P. Knauer, C. K. Li, L. D. Lund, J. A. Marozas, P. W. McKenty, F. J. Marshall, S. F. B. Morse, S. Padalino, R. D. Petrasso, P. B. Radha, S. P. Regan, S. Roberts, T. C. Sangster, F. H. Séguin, W. Seka, V. A. Smalyuk, J. M. Soures, C. Stoeckl, K. A. Thorp, B. Yaakobi, and J. D. Zuegel, “Direct-Drive Inertial Fusion Research at the University of Rochester’s Laboratory for Laser Energetics: A Review,” in *Current Trends in International Fusion Research—Proceedings of the Fifth Symposium*, edited by E. Panarella and R. Raman (NRC Press, Ottawa, Canada, 2008), pp. 267–277.
- R. L. McCrory, D. D. Meyerhofer, S. J. Loucks, S. Skupsky, R. Betti, T. R. Boehly, M. J. Bonino, R. S. Craxton, T. J. B. Collins, J. A. Delettrez, D. H. Edgell, R. Epstein, V. Yu. Glebov, V. N. Goncharov, D. R. Harding, R. L. Keck, J. H. Kelly, T. J. Kessler, J. P. Knauer, L. D. Lund, D. Jacobs-Perkins, J. R. Marciante, J. A. Marozas, F. J. Marshall, A. V. Maximov, P. W. McKenty, S. F. B. Morse, J. Myatt, S. G. Noyes, P. B. Radha, A. Rigatti, T. C. Sangster, W. Seka, V. A. Smalyuk, J. M. Soures, C. Stoeckl, K. A. Thorp, L. J. Waxer, M. D. Wittman, B. Yaakobi, J. D. Zuegel, K. A. Fletcher, C. Freeman, S. Padalino, J. A. Frenje, C. K. Li, R. D. Petrasso, and F. H. Séguin, “Direct-Drive Inertial Fusion Research at the University of Rochester’s Laboratory for Laser Energetics: A Review,” in *Current Trends in International Fusion Research—Proceedings of the Sixth Symposium*, edited by E. Panarella and R. Raman (NRC Research Press, Ottawa, Canada), pp. 155–176.
- P. W. McKenty, R. S. Craxton, F. J. Marshall, T. C. Sangster, J. A. Marozas, A. M. Cok, M. J. Bonino, D. R. Harding, D. D. Meyerhofer, R. L. McCrory, J. D. Kilkenny, A. Nikroo, J. Fooks, M. L. Hoppe, J. M. Edwards, A. J. MacKinnon, D. H. Munro, and R. J. Wallace, “Design of High-Neutron-Yield, Polar-Drive Targets for Diagnostic Activation Experiments on the NIF,” *J. Phys.: Conf. Ser.* **244**, 032054 (2010).
- D. D. Meyerhofer, J. Bromage, C. Dorrer, J. H. Kelly, B. E. Kruschwitz, S. J. Loucks, R. L. McCrory, S. F. B. Morse, J. F. Myatt, P. M. Nilson, J. Qiao, T. C. Sangster, C. Stoeckl, L. J. Waxer, and J. D. Zuegel, “Performance of and Initial Results from the OMEGA EP Laser System,” *J. Phys.: Conf. Ser.* **244**, 032010 (2010).
- C. Miao, J. C. Lambropoulos, and S. D. Jacobs, “Process Parameter Effects on Material Removal in Magnetorheological Finishing of Borosilicate Glass,” *Appl. Opt.* **49**, 1951 (2010).
- C. Miao, J. C. Lambropoulos, H. Romanofsky, S. N. Shafrir, and S. D. Jacobs, “Contributions of Nanodiamond Abrasives and Deionized Water in Magnetorheological Finishing of Aluminum Oxynitride,” in *Optical Manufacturing and Testing VIII*, edited by J. H. Burge, O. W. Föhnle, and R. Williamson (SPIE, Bellingham, WA, 2009), Vol. 7426, p. 74260D.
- C. Miao, S. N. Shafrir, J. C. Lambropoulos, and S. D. Jacobs, “Normal Force and Drag Force in Magnetorheological Finishing,” in *Optical Manufacturing and Testing VIII*, edited by J. H. Burge, O. W. Föhnle, and R. Williamson (SPIE, Bellingham, WA, 2009), Vol. 7426, p. 74260C.
- P. M. Nilson, S. P. D. Mangles, L. Willingale, M. C. Kaluza, A. G. R. Thomas, M. Tatarakis, R. J. Clarke, K. L. Lancaster, S. Karsch, J. Schreiber, Z. Najmudin, A. E. Dangor, and K. Krushelnick, “Plasma Cavitation in Ultraintense Laser Interactions with Underdense Helium Plasmas,” *New J. Phys.* **12**, 045014 (2010).
- P. M. Nilson, S. P. D. Mangles, L. Willingale, M. C. Kaluza, A. G. R. Thomas, M. Tatarakis, Z. Najmudin, R. J. Clarke, K. L. Lancaster, S. Karsch, J. Schreiber, R. G. Evans, A. E. Dangor, and K. Krushelnick, “Generation of Ultrahigh-Velocity Ionizing Shocks with Petawatt-Class Laser Pulses,” *Phys. Rev. Lett.* **103**, 255001 (2009).
- P. M. Nilson, W. Theobald, J. F. Myatt, C. Stoeckl, J. D. Zuegel, R. Betti, D. D. Meyerhofer, and T. C. Sangster, “X-Ray Spectroscopy of Solid-Density Plasmas in High-Intensity Laser Interactions,” in *Atomic Processes in Plasmas*, edited by K. B. Fournier (American Institute of Physics, New York, NY, 2009), Vol. CP1161, pp. 17–23.

- A. V. Okishev, "Optical Differentiation and Multimillijoule ~150 ps Pulse Generation in a Regenerative Amplifier with a Temperature-Tuned Intracavity Volume Bragg Grating," *Appl. Opt.* **49**, 1331 (2010).
- G. P. Pepe, L. Parlato, N. Marrocco, V. Pagliarulo, G. Peluso, A. Barone, F. Tafuri, U. Scotti di Uccio, F. Miletto, M. Radovic, D. Pan, and R. Sobolewski, "Novel Superconducting Proximized Heterostructures for Ultrafast Photodetection," *Cryogenics* **49**, 660 (2009).
- J. Qiao, A. W. Schmid, L. J. Waxer, T. Nguyen, J. Bunkenburg, C. Kinglsey, A. Kozlov, and D. Weiner, "*In Situ* Detection and Analysis of Laser-Induced Damage on a 1.5-m Multilayer-Dielectric Grating Compressor for High-Energy, Petawatt-Class Laser Systems," *Opt. Express* **18**, 10,423 (2010).
- S. P. Regan, N. B. Meezan, L. J. Suter, D. J. Strozzi, W. L. Krueer, D. Meeker, S. H. Glenzer, W. Seka, C. Stoeckl, V. Yu. Glebov, T. C. Sangster, D. D. Meyerhofer, R. L. McCrory, E. A. Williams, O. S. Jones, D. A. Callahan, M. D. Rosen, O. L. Landen, C. Sorce, and B. J. MacGowan, "Suprathermal Electrons Generated by the Two-Plasmon-Decay Instability in Gas-Filled *Hohlraums*," *Phys. Plasmas* **17**, 020703 (2010).
- S. P. Regan, P. B. Radha, T. R. Boehly, T. Doepfner, K. Falk, S. H. Glenzer, V. N. Goncharov, G. Gregori, O. L. Landen, R. L. McCrory, D. D. Meyerhofer, P. Neumayer, T. C. Sangster, and V. A. Smalyuk, "Inferring the Electron Temperature and Density of Shocked Liquid Deuterium Using Inelastic X-Ray Scattering," *J. Phys.: Conf. Ser.* **244**, 042017 (2010).
- S. P. Regan, B. Yaakobi, T. R. Boehly, R. Epstein, J. A. Delettrez, V. Yu. Glebov, V. N. Goncharov, P. A. Jaanimagi, J. P. Knauer, F. J. Marshall, R. L. McCrory, D. D. Meyerhofer, P. B. Radha, T. C. Sangster, V. A. Smalyuk, J. Soures, C. Stoeckl, R. C. Mancini, D. A. Haynes, Jr., L. Welser-Sherrill, J. A. Koch, R. Tommasini, and H. Sawada, "Applied Plasma Spectroscopy: Laser-Fusion Experiments," *High Energy Density Phys.* **5**, 234 (2009).
- H. F. Robey, T. R. Boehly, R. E. Olson, A. Nikroo, P. M. Celliers, O. L. Landen, and D. D. Meyerhofer, "Experimental Validation of a Diagnostic Technique for Tuning the Fourth Shock Timing on National Ignition Facility," *Phys. Plasmas* **17**, 012703 (2010).
- T. C. Sangster, V. N. Goncharov, R. Betti, T. R. Boehly, D. T. Casey, T. J. B. Collins, R. S. Craxton, J. A. Delettrez, D. H. Edgell, R. Epstein, K. A. Fletcher, J. A. Frenje, V. Yu. Glebov, D. R. Harding, S. X. Hu, I. V. Igumenshchev, J. P. Knauer, S. J. Loucks, C. K. Li, J. A. Marozas, F. J. Marshall, R. L. McCrory, P. W. McKenty, D. D. Meyerhofer, P. M. Nilson, S. P. Padalino, R. D. Petrasso, P. B. Radha, S. P. Regan, F. H. Seguin, W. Seka, R. W. Short, D. Shvarts, S. Skupsky, V. A. Smalyuk, J. M. Soures, C. Stoeckl, W. Theobald, and B. Yaakobi, "Shock-Tuned Cryogenic-Deuterium-Tritium Implosion Performance on Omega," *Phys. Plasmas* **17**, 056312 (2010).
- J. E. Schoenly, W. Seka, and P. Rechmann, "Investigation Into the Optimum Beam Shape and Fluence for Selective Ablation of Dental Calculus at $\lambda = 400$ nm," *Lasers Surg. Med.* **42**, 51 (2010).
- J. E. Schoenly, W. Seka, and P. Rechmann, "Selective Near-UV Ablation of Subgingival Dental Calculus: Measurement of Removal Rates," in *Lasers in Dentistry XVI*, edited by P. Rechmann and D. Fried (SPIE, Bellingham, WA, 2010), Vol. 7549, p. 754906.
- S. N. Shafir, C. D. Roll, and P. D. Funkenbusch, "Optimization of Deterministic Microgrinding (DMG) Conditions for Optical Glasses and Ceramics," in *International Optical Design Conference (IODC)/Optical Fabrication and Testing (OF&T) Technical Digest on CD-ROM* (Optical Society of America, Washington, DC, 2010), Paper OWD4.
- S. N. Shafir, H. J. Romanofsky, M. Skarlinski, M. Wang, C. Miao, S. Salzman, T. Chartier, J. Mici, J. C. Lambropoulos, R. Shen, H. Yang, and S. D. Jacobs, "Zirconia Coated Carbonyl Iron Particle-Based Magnetorheological Fluid for Polishing," in *Optical Manufacturing and Testing VIII*, edited by J. H. Burge, O. W. Föhnle, and R. Williamson (SPIE, Bellingham, WA, 2009), Vol. 7426, p. 74260B.
- S. N. Shafir, H. J. Romanofsky, M. Skarlinski, M. Wang, C. Miao, S. Salzman, T. Chartier, J. Mici, J. C. Lambropoulos, R. Shen, H. Yang, and S. D. Jacobs, "Zirconia-Coated Carbonyl-Iron-Particle-Based Magnetorheological Fluid for Polishing Optical Glasses and Ceramics," *Appl. Opt.* **48**, 6797 (2009).
- R. Shen, S. N. Shafir, C. Miao, M. Wang, J. C. Lambropoulos, S. D. Jacobs, and H. Yang, "Synthesis and Corrosion Study of Zirconia-Coated Carbonyl Iron Particles," *J. Colloid Interface Sci.* **342**, 49 (2010).
- M. D. Skarlinski and S. D. Jacobs, "Modifying the Rheological Properties of Zirconia Coated Carbonyl Iron Suspensions through Acid-Base Titration and the Addition of Di-Ammono-

- mium Citrate,” in *International Optical Design Conference (IODC)/Optical Fabrication and Testing (OF&T) Technical Digest on CD-ROM* (Optical Society of America, Washington, DC, 2010), Paper JMB.
- V. A. Smalyuk, R. Betti, J. A. Delettrez, V. Yu. Glebov, D. D. Meyerhofer, P. B. Radha, S. P. Regan, T. C. Sangster, J. Sanz, W. Seka, C. Stoeckl, B. Yaakobi, J. A. Frenje, C. K. Li, R. D. Petrasso, and F. H. Séguin, “Implosion Experiments using Glass Ablators for Direct-Drive Inertial Confinement Fusion,” *Phys. Rev. Lett.* **104**, 165002 (2010).
- V. A. Smalyuk, S. X. Hu, J. D. Hager, J. A. Delettrez, D. D. Meyerhofer, T. C. Sangster, and D. Shvarts, “Spherical Rayleigh–Taylor Growth of Three-Dimensional Broadband Perturbations on OMEGA,” *Phys. Plasmas* **16**, 112701 (2009).
- A. A. Solodov, M. Storm, J. F. Myatt, R. Betti, D. D. Meyerhofer, P. M. Nilson, W. Theobald, and C. Stoeckl, “Simulations of Electron-Beam Transport in Solid-Density Targets and the Role of Magnetic Collimation,” *J. Phys.: Conf. Ser.* **244**, 022063 (2010).
- L. Sun, S. Jiang, and J. R. Marciante, “All-Fiber Optical Faraday Mirror Using 56-wt%-Terbium-Doped Fiber,” *IEEE Photon. Technol. Lett.* **22**, 999 (2010).
- L. Sun, S. Jiang, and J. R. Marciante, “All-Fiber Optical Magnetic Field Sensor Based on Faraday Rotation,” in the *2010 Conference on Optical Fiber Communication and National Fiber Optic Engineers Conference* (IEEE, New York, 2010), Paper OWL3.
- L. Sun, S. Jiang, and J. R. Marciante, “All-Fiber Optical Magnetic-Field Sensor Based on Faraday Rotation in Highly Terbium-Doped Fiber,” *Opt. Express* **18**, 5407 (2010).
- L. Sun, S. Jiang, J. D. Zuegel, and J. R. Marciante, “All-Fiber Optical Isolator Based on Faraday Rotation in Highly Terbium-Doped Fiber,” *Opt. Lett.* **35**, 706 (2010).
- L. Sun, S. Jiang, and J. R. Marciante, “Compact All-Fiber Optical Faraday Components Using 65-wt%-Terbium-Doped Fiber with a Record Verdet Constant of $-32 \text{ rad}/(\text{Tm})$,” *Opt. Express* **18**, 12,191 (2010).
- W. Theobald, K. S. Anderson, R. Betti, R. S. Craxton, J. A. Delettrez, J. A. Frenje, V. Yu. Glebov, O. V. Gotchev, J. H. Kelly, C. K. Li, A. J. Mackinnon, F. J. Marshall, R. L. McCrory, D. D. Meyerhofer, J. F. Myatt, P. A. Norreys, P. M. Nilson, P. K. Patel, R. D. Petrasso, P. B. Radha, C. Ren, T. C. Sangster, W. Seka, V. A. Smalyuk, A. A. Solodov, R. B. Stephens, C. Stoeckl, and B. Yaakobi, “Advanced-Ignition-Concept Exploration on OMEGA,” *Plasma Phys. Control. Fusion* **51**, 124052 (2009).
- H. X. Vu, D. F. DuBois, D. A. Russell, and J. F. Myatt, “The Reduced-Description Particle-in-Cell Model for the Two Plasmon Decay Instability,” *Phys. Plasmas* **17**, 072701 (2010).
- B. Yaakobi, O. V. Gotchev, R. Betti, and C. Stoeckl, “Study of Fast-Electron Transport in Laser-Illuminated Spherical Targets,” *Phys. Plasmas* **16**, 102703 (2009).
- R. Yan, A. V. Maximov, and C. Ren, “The Linear Regime of the Two-Plasmon Decay Instability in Inhomogeneous Plasmas,” *Phys. Plasmas* **17**, 052701 (2010).
- L. Zeng, T. N. Blanton, and S. H. Chen, “Modulation of Phase Separation Between Spherical and Rodlike Molecules Using Geometric Surfactancy,” *Langmuir* **26**, 12,877 (2010).
- L. Zeng, T. Y.-H. Lee, P. B. Merkel, and S. H. Chen, “A New Class of Non-Conjugated Bipolar Hybrid Hosts for Phosphorescent Organic Light-Emitting Diodes,” *J. Mater. Chem.* **19**, 8772 (2009).
- L. Zeng, C. W. Tang, and S. H. Chen, “Effects of Active Layer Thickness and Thermal Annealing on Polythiophene: Fullerene Bulk Heterojunction Photovoltaic Devices,” *Appl. Phys. Lett.* **97**, 053305 (2010).
- J. Zhang, A. Belousov, J. Karpinski, B. Batlogg, and R. Sobolewski, “Femtosecond Optical Spectroscopy Studies of High-Pressure-Grown (Al,Ga)N Single Crystals,” *J. Phys. Conf. Series* **193**, 012058 (2009).

OMEGA External Users' Publications

- P. Amendt, O. L. Landen, H. F. Robey, C. K. Li, and R. D. Petrasso, "Plasma Barodiffusion in Inertial-Confinement-Fusion Implosions: Application to Observed Yield Anomalies in Thermonuclear Fuel Mixtures," *Phys. Rev. Lett.* **105**, 115005 (2010).
- D. J. Ampleford, C. A. Jennings, G. N. Hall, S. V. Lebedev, S. N. Bland, S. C. Bott, F. Suzuki-Vidal, J. B. A. Palmer, J. P. Chittenden, M. E. Cuneo, A. Frank, E. G. Blackman, and A. Ciardi, "Bow Shocks in Ablated Plasma Streams for Nested Wire Array Z-Pinches: A Laboratory Astrophysics Testbed for Radiatively Cooled Shocks," *Phys. Plasmas* **17**, 056315 (2010) (invited).
- J. W. Berkery, S. A. Sabbagh, R. Betti, B. Hu, R. E. Bell, S. P. Gerhardt, J. Manickam, and K. Tritz, "Resistive Wall Mode Instability at Intermediate Plasma Rotation," *Phys. Rev. Lett.* **104**, 035003 (2010).
- J. W. Berkery, S. A. Sabbagh, H. Reimerdes, R. Betti, B. Hu, R. E. Bell, S. P. Gerhardt, J. Manickam, and M. Podestà, "The Role of Kinetic Effects, Including Plasma Rotation and Energetic Particles, in Resistive Wall Mode Stability," *Phys. Plasmas* **17**, 082504 (2010) (invited).
- E. Brambrink, H. G. Wei, B. Barbrel, P. Audebert, A. Benuzzi-Mounaix, T. Boehly, T. Endo, C. D. Gregory, T. Kimura, R. Kodama, N. Ozaki, H.-S. Park, and M. Koenig, "Direct Density Measurement of Shock-Compressed Iron Using Hard X Rays Generated by a Short Laser Pulse," *Phys. Rev. E* **80**, 056407 (2009).
- A. Budde, R. P. Drake, C. C. Kuranz, M. J. Grosskopf, T. Plewa, and N. C. Hearn, "Simulation of Fabrication Variations in Supernova Hydrodynamics Experiments," *High Energy Density Phys.* **6**, 135 (2010).
- P. M. Celliers, D. J. Erskine, C. M. Sorce, D. G. Braun, O. L. Landen, and G. W. Collins, "A High-Resolution Two-Dimensional Imaging Velocimeter," *Rev. Sci. Instrum.* **81**, 035101 (2010).
- P. M. Celliers, P. Loubeyre, J. H. Eggert, S. Brygoo, R. S. McWilliams, D. G. Hicks, T. R. Boehly, R. Jeanloz, and G. W. Collins, "Insulator-to-Conducting Transition in Dense Fluid Helium," *Phys. Rev. Lett.* **104**, 184503 (2010).
- H. Chen, S. C. Wilks, J. D. Bonlie, S. N. Chen, K. V. Cone, L. N. Elberson, G. Gregori, D. D. Meyerhofer, J. Myatt, D. F. Price, M. B. Schneider, R. Shepherd, D. C. Stafford, R. Tommasini, R. Van Maren, and P. Beiersdorfer, "Making Relativistic Positrons Using Ultraintense Short Pulse Lasers," *Phys. Plasmas* **16**, 122702 (2009).
- H. Chen, S. C. Wilks, D. D. Meyerhofer, J. Bonlie, C. D. Chen, S. N. Chen, C. Courtois, L. Elberson, G. Gregori, W. Krueer, O. Landoas, J. Mithen, J. Myatt, C. D. Murphy, P. Nilson, D. Price, M. Schneider, R. Shepherd, C. Stoeckl, M. Tabak, R. Tommasini, and P. Beiersdorfer, "Relativistic Quasimonoenergetic Positron Jets from Intense Laser-Solid Interactions," *Phys. Rev. Lett.* **105**, 015003 (2010).
- J. D. Colvin, K. B. Fournier, M. J. May, and H. A. Scott, "A Computational Study of X-Ray Emission from Laser-Irradiated Ge-Doped Foams," *Phys. Plasmas* **17**, 073111 (2010).
- F. W. Doss, R. P. Drake, and C. C. Kuranz, "Repeatability in Radiative Shock Tube Experiments," *High Energy Density Phys.* **6**, 157 (2010).
- J. H. Eggert, D. G. Hicks, P. M. Celliers, D. K. Bradley, R. S. McWilliams, R. Jeanloz, J. E. Miller, T. R. Boehly, and G. W. Collins, "Melting Temperature of Diamond at Ultrahigh Pressure," *Nature Phys.* **6**, 40 (2010).
- G. Faussurier, C. Blancard, P. Cossé, and P. Renaudin, "Equation of State, Transport Coefficients, and Stopping Power of Dense Plasmas from the Average-Atom Model Self-Consistent Approach for Astrophysical and Laboratory Plasmas," *Phys. Plasmas* **17**, 052707 (2010).
- K. B. Fournier, M. J. May, J. D. Colvin, J. O. Kane, M. Schneider, E. Dewald, C. A. Thomas, S. Compton, R. E. Marrs, J. Moody, E. Bond, P. Michel, J. H. Fisher, C. D. Newlander, and J. F. Davis, "Multi-keV X-Ray Source Development Experiments on the National Ignition Facility," *Phys. Plasmas* **17**, 082701 (2010).
- J. A. Frenje, D. T. Casey, C. K. Li, F. H. Séguin, R. D. Petrasso, V. Yu. Glebov, P. B. Radha, T. C. Sangster, D. D. Meyerhofer, S. P. Hatchett, S. W. Haan, C. J. Cerjan, O. L. Landen, K. A. Fletcher, and R. J. Leeper, "Probing High Areal-Density Cryogenic Deuterium-Tritium Implosions Using Downscattered Neutron Spectra Measured by the Magnetic Recoil Spectrometer," *Phys. Plasmas* **17**, 056311 (2010) (invited).
- D. H. Froula, L. Divol, R. A. London, R. L. Berger, T. Döppner, N. B. Meezan, J. Ralph, J. S. Ross, L. J. Suter, and S. H. Glenzer,

- “Experimental Basis for Laser-Plasma Interactions in Ignition Hohlräume at the National Ignition Facility,” *Phys. Plasmas* **17**, 056302 (2010) (invited).
- B. Fryxell, C. C. Kuranz, R. P. Drake, M. J. Grosskopf, A. Budde, T. Plewa, N. Hearn, J. F. Hansen, A. R. Miles, and J. Knauer, “The Possible Effects of Magnetic Fields on Laser Experiments of Rayleigh–Taylor Instabilities,” *High Energy Density Phys.* **6**, 162 (2010).
- S. H. Glenzer, H. J. Lee, P. Davis, T. Döppner, R. W. Falcone, C. Fortmann, B. A. Hammel, A. L. Kritcher, O. L. Landen, R. W. Lee, D. H. Munro, R. Redmer, and S. Weber, “Dense Plasma X-Ray Scattering: Methods and Applications,” *High Energy Density Phys.* **6**, 1 (2010).
- P. Hartigan, J. M. Foster, B. H. Wilde, R. F. Coker, P. A. Rosen, J. F. Hansen, B. E. Blue, R. J. R. Williams, R. Carver, and A. Frank, “Laboratory Experiments, Numerical Simulations, and Astronomical Observations of Deflected Supersonic Jets: Application to HH 110,” *Astrophys. J.* **705**, 1073 (2009).
- C. M. Huntington, C. M. Krauland, C. C. Kuranz, S. H. Glenzer, and R. P. Drake, “Imaging Scattered X-Ray Radiation for Measurement of Local Electron Density in High-Energy-Density Experiments,” *High Energy Density Phys.* **6**, 194 (2010).
- A. L. Kritcher, P. Neumayer, C. R. D. Brown, P. Davis, T. Döppner, R. W. Falcone, D. O. Gericke, G. Gregori, B. Holst, O. L. Landen, H. J. Lee, E. C. Morse, A. Pelka, R. Redmer, M. Roth, J. Vorberger, K. Wünsch, and S. H. Glenzer, “Measurements of Ionic Structure in Shock Compressed Lithium Hydride from Ultrafast X-Ray Thomson Scattering,” *Phys. Rev. Lett.* **103**, 245004 (2009).
- C. C. Kuranz, F. W. Doss, R. P. Drake, M. J. Grosskopf, and H. F. Robey, “Using Wall Shocks to Measure Preheat in Laser-Irradiated, High-Energy-Density, Hydrodynamics Experiments,” *High Energy Density Phys.* **6**, 215 (2010).
- C. C. Kuranz, R. P. Drake, M. J. Grosskopf, B. Fryxell, A. Budde, J. F. Hansen, A. R. Miles, T. Plewa, N. Hearn, and J. Knauer, “Spike Morphology in Blast-Wave-Driven Instability Experiments,” *Phys. Plasmas* **17**, 052709 (2010).
- K. L. Lancaster, M. Sherlock, J. S. Green, C. D. Gregory, P. Hakel, K. U. Akli, F. N. Beg, S. N. Chen, R. R. Freeman, H. Habara, R. Heathcote, d. S. Hey, K. Highbarger, M. H. Key, R. Kodama, K. Krushelnick, H. Nakamura, M. Nakatsutsumi, J. Pasley, R. B. Stephens, M. Storm, M. Tampo, W. Theobald, L. Van Woerkom, R. L. Weber, M. S. Wei, N. C. Woolsey, T. Yabuuchi, and P. A. Norreys, “Effect of Reentrant Cone Geometry on Energy Transport in Intense Laser-Plasma Interactions,” *Phys. Rev. E* **80**, 045401 (2009).
- O. L. Landen, T. R. Boehly, D. K. Bradley, D. G. Braun, D. A. Callahan, P. M. Celliers, G. W. Collins, E. L. Dewald, L. Divol, S. H. Glenzer, A. Hamza, D. G. Hicks, N. Hoffman, N. Izumi, O. S. Jones, R. K. Kirkwood, G. A. Kyrala, P. Michel, J. Milovich, D. H. Munro, A. Nikroo, R. E. Olson, H. F. Robey, B. K. Spears, C. A. Thomas, S. V. Weber, D. C. Wilson, M. M. Marinak, L. J. Suter, B. A. Hammel, D. D. Meyerhofer, J. Atherton, J. Edwards, S. W. Haan, J. D. Lindl, B. J. MacGowan, and E. I. Moses, “Capsule Performance Optimization in the National Ignition Campaign,” *Phys. Plasmas* **17**, 056301 (2010).
- S. Le Pape, P. Neumayer, C. Fortmann, T. Döppner, P. Davis, A. Kritcher, O. Landen, and S. Glenzer, “X-Ray Radiography and Scattering Diagnosis of Dense Shock-Compressed Matter,” *Phys. Plasmas* **17**, 056309 (2010).
- C. K. Li, F. H. Séguin, J. A. Frenje, M. Rosenberg, R. D. Petrasso, P. A. Amendt, J. A. Koch, O. L. Landen, H. S. Park, H. F. Robey, R. P. J. Town, A. Casner, F. Philippe, R. Betti, J. P. Knauer, D. D. Meyerhofer, C. A. Back, J. D. Kilkenny, and A. Nikroo, “Charged-Particle Probing of X-Ray–Driven Inertial-Fusion Implosions,” *Science* **327**, 1231 (2010).
- T. Ma, M. H. Key, R. J. Mason, K. U. Akli, R. L. Daskalova, R. R. Freeman, J. S. Green, K. Highbarger, P. A. Jaanimagi, J. A. King, K. L. Lancaster, S. P. Hatchett, A. J. Mackinnon, A. G. MacPhee, P. A. Norreys, P. K. Patel, R. B. Stephens, W. Theobald, L. D. Van Woerkom, M. S. Wei, S. C. Wilks, and F. N. Beg, “Transport of Energy by Ultraintense Laser-Generated Electrons in Nail-Wire Targets,” *Phys. Plasmas* **16**, 112702 (2009).
- M. J. May, K. Widmann, C. Sorce, H.-S. Park, and M. Schneider, “Uncertainty Analysis Technique for OMEGA Dante Measurements,” *Rev. Sci. Instrum.* **81**, 10E505 (2010).
- R. G. McClarren and R. P. Drake, “Anti-Diffusive Radiation Flow in the Cooling Layer of a Radiating Shock,” *J. Quant. Spectrosc. Radiat. Transf.* **111**, 2095 (2010).
- R. G. McClarren, R. P. Drake, J. E. Morel, and J. P. Holloway, “Theory of Radiative Shocks in the Mixed, Optically Thick–Thin Case,” *Phys. Plasmas* **17**, 093301 (2010).

R. S. McWilliams, J. H. Eggert, D. G. Hicks, D. K. Bradley, P. M. Celliers, D. K. Spaulding, T. R. Boehly, G. W. Collins, and R. Jeanloz, “Strength Effects in Diamond Under Shock Compression from 0.1 to 1 TPa,” *Phys. Rev. B* **81**, 014111 (2010).

N. B. Meezan, L. J. Atherton, D. A. Callahan, E. L. Dewald, S. Dixit, E. G. Dzenitis, M. J. Edwards, C. A. Haynam, D. E. Hinkel, O. S. Jones, O. Landen, R. A. London, P. A. Michel, J. D. Moody, J. L. Milovich, M. B. Schneider, C. A. Thomas, R. P. J. Town, A. L. Warrick, S. V. Weber, K. Widmann, S. H. Glenzer, L. J. Suter, B. J. MacGowan, J. L. Kline, G. A. Kyrala, and A. Nikroo, “National Ignition Campaign Hohlraum Energetics,” *Phys. Plasmas* **17**, 056304 (2010) (invited).

M. Murakami, N. Sarukura, H. Azechi, M. Temporal, and A. J. Schmitt, “Optimization of Irradiation Configuration in Laser Fusion Utilizing Self-Organizing Electrodynamical System,” *Phys. Plasmas* **17**, 082702 (2010).

H.-S. Park, K. T. Lorenz, R. M. Cavallo, S. M. Pollaine, S. T. Prisbrey, R. E. Rudd, R. C. Becker, J. V. Bernier, and B. A. Remington, “Viscous Rayleigh-Taylor Instability Experiments at High Pressure and Strain Rate,” *Phys. Rev. Lett.* **104**, 135504 (2010).

H.-S. Park, B. A. Remington, R. C. Becker, J. V. Bernier, R. M. Cavallo, K. T. Lorenz, S. M. Pollaine, S. T. Prisbrey, R. E. Rudd, and N. R. Barton, “Strong Stabilization of the Rayleigh-Taylor Instability by Material Strength at Megabar Pressures,” *Phys. Plasmas* **17**, 056314 (2010) (invited).

F. Philippe, A. Casner, T. Caillaud, O. Landoas, M. C. Monteil, S. Liberatore, H. S. Park, P. Amendt, H. Robey, C. Sorce, C. K. Li, F. Seguin, M. Rosenberg, R. Petrasso, V. Glebov, and C. Stoeckl, “Experimental Demonstration of X-Ray Drive Enhancement with Rugby-Shaped Hohlraums,” *Phys. Rev. Lett.* **104**, 035004 (2010).

H. F. Robey, P. Amendt, H.-S. Park, R. P. J. Town, J. L. Milovich, T. Döppner, D. E. Hinkel, R. Wallace, C. Sorce, D. J. Strozzi, F. Philippe, A. Casner, T. Caillaud, O. Landoas, S. Liberatore, M.-C. Monteil, F. Séguin, M. Rosenberg, C. K. Li, R. Petrasso, V. Glebov, C. Stoeckl, A. Nikroo, and E. Giraldez, “High Performance Capsule Implosions on the OMEGA Laser Facility with Rugby Hohlraums,” *Phys. Plasmas* **17**, 056313 (2010).

H. F. Robey, T. R. Boehly, R. E. Olson, A. Nikroo, P. M. Celliers, O. L. Landen, and D. D. Meyerhofer, “Experimental

Validation of a Diagnostic Technique for Tuning the Fourth Shock Timing on National Ignition Facility,” *Phys. Plasmas* **17**, 012703 (2010).

R. Rodriguez, R. Florido, J. M. Gil, J. G. Rubiano, D. Suarez, P. Martel, E. Minguez, and R. C. Mancini, “Collisional-Radiative Calculations of Optically Thin and Thick Plasmas Using the Computational Package ABAKO/RAPCAL,” *Commun. Comput. Phys.* **8**, 185 (2010).

J. D. Sethian, D. G. Colombant, J. L. Giuliani, Jr., R. H. Lehmberg, M. C. Myers, S. P. Obenschain, A. J. Schmitt, J. Weaver, M. F. Wolford, F. Hegeler, M. Friedman, A. E. Robson, A. Bayramian, J. Caird, C. Ebberts, J. Latkowski, W. Hogan, W. R. Meier, L. J. Perkins, K. Schaffers, S. Abdel Kahlik, K. Schoonover, D. Sadowski, K. Boehm, L. Carlson, J. Pulsifer, F. Najmabadi, A. R. Raffray, M. S. Tillaack, G. Kulcinski, J. P. Blanchard, T. Heltemes, A. Ibrahim, E. Marriott, G. Moses, R. Radell, M. Sawan, J. Santarius, G. Sviatoslavsky, S. Zenobia, N. M. Ghoniem, S. Sharafat, J. El-Awady, Q. Hu, C. Duty, K. Leonard, G. Romanoski, L. L. Snead, S. J. Zinkle, C. Gentile, W. Parsells, C. Prinski, T. Kozub, T. Dodson, D. V. Rose, T. Renk, C. Olson, N. Alexander, A. Bozek, G. Flint, D. T. Goodin, J. Hund, R. Paguio, R. W. Petzoldt, D. G. Schroen, J. Sheliak, T. Bernat, D. Bittner, J. Karnes, N. Petta, J. Streit, D. Geller, J. K. Hoffer, M. W. McGeoch, S. C. Glidden, H. Sanders, D. Weidenheimer, D. Morton, I. D. Smith, M. Bobecia, D. Harding, T. Lehecka, S. B. Gilliam, S. M. Gidcumb, D. Forsythe, N. R. Parikh, S. O’Dell, and M. Gorenssek, “The Science and Technologies for Fusion Energy With Lasers and Direct-Drive Targets,” *IEEE Trans. Plasma Sci.* **38**, 690 (2010).

M. Suggit, G. Kimminau, J. Hawreliak, B. Remington, N. Park, and J. Wark, “Nanosecond X-Ray Laue Diffraction Apparatus Suitable for Laser Shock Compression Experiments,” *Rev. Sci. Instrum.* **81**, 083902 (2010).

M. Tanabe, H. Nishimura, N. Ohnishi, K. B. Fournier, S. Fujioka, A. Iwamae, S. B. Hansen, K. Nagai, F. Girard, M. Primout, B. Villette, D. Brebion, and K. Mima, “Characterization of Heat-Wave Propagation Through Laser-Driven Ti-Doped Underdense Plasma,” *High Energy Density Phys.* **6**, 89 (2010).

I. Thfoin, O. Landoas, T. Caillaud, L. Disdier, M. Vincent, J.-L. Bourgade, B. Rossé, T. C. Sangster, V. Yu. Glebov, G. Pien, and W. Armstrong, “Alignment Effects on a Neutron Imaging System Using Coded Apertures,” *Rev. Sci. Instrum.* **81**, 033503 (2010).

K. Vaughn, S. McAlpin, J. M. Foster, R. M. Stevenson, S. G. Glendinning, and C. Sorce, “Asymmetrically Driven Implosions” *Phys. Plasmas* **17**, 056316 (2010) (invited).

L. Welsch-Sherrill, D. A. Haynes, R. C. Mancini, J. H. Cooley, R. Tommasini, I. E. Golovkin, M. E. Sherrill, and S. W. Haan, “Inference of ICF Implosion Core Mix Using Experimental Data and Theoretical Mix Modeling,” *High Energy Density Phys.* **5**, 249 (2009).

B. Westover, A. MacPhee, C. Chen, D. Hey, T. Ma, B. Maddox, H.-S. Park, B. Remington, F. N. Beg, “Study of Silver $K\alpha$ and Bremsstrahlung Radiation from Short-Pulse Laser-Matter Interactions with Applications for X-Ray Radiography,” *Phys. Plasmas* **17**, 082703 (2010).

L. Willingale, P. M. Nilson, M. C. Kaluza, A. E. Dangor, R. G. Evans, P. Fernandes, M. G. Haines, C. Kamperidis, R. J. Kingham, C. P. Ridgers, M. Sherlock, A. G. R. Thomas, M. S. Wei, Z. Najmudin, K. Krushelnick, S. Bandyopadhyay, M. Notley, S. Minardi, M. Tatarakis, and W. Rozmus, “Proton Deflectometry of a Magnetic Reconnection Geometry,” *Phys. Plasmas* **17**, 043104 (2010).

L. Willingale, A. G. R. Thomas, P. M. Nilson, M. C. Kaluza, S. Bandyopadhyay, A. E. Dangor, R. G. Evans, P. Fernandes, M. G. Haines, C. Kamperidis, R. J. Kingham, S. Minardi, M. Notley, C. P. Ridgers, W. Rozmus, M. Sherlock, M. Tatarakis, M. S. Wei, Z. Najmudin, and K. Krushelnick, “Fast Advection of Magnetic Fields by Hot Electrons,” *Phys. Rev. Lett.* **105**, 095001 (2010).

Conference Presentations

The following presentations were made at Frontiers in Optics 2009, San Jose, CA, 11–15 October 2009:

W. Guan and J. R. Marciante, “Power Scaling of Single-Frequency Hybrid Brillouin/Ytterbium Fiber Lasers.”

J. R. Marciante, “Spatial-Filtering Properties of Large-Mode-Area Fibers with Confined Gain Dopants.”

L. Sun, S. Jiang, J. D. Zuegel, and J. R. Marciante, “All-Fiber Isolator Based on Faraday Rotation.”

C. Dorrer, “Signal Reconstruction Techniques for Optical Pulse Characterization,” *Signal Recovery and Synthesis*, San Jose, CA, 13–14 October 2009.

The following presentations were made at the 51st Annual Meeting of the APS Division of Plasma Physics, Atlanta, GA, 2–6 November 2009:

K. S. Anderson, R. Betti, P. Y. Chang, R. Nora, M. Fatenejad, and D. Shvarts, “Single- and Multidimensional Robustness Studies of the NIF Ignition Point Design.”

M. A. Barrios, D. G. Hicks, T. R. Boehly, D. E. Fratanduono, J. H. Eggert, P. M. Celliers, G. W. Collins, and D. D. Meyerhofer,

“High-Precision Measurements of the Equation of State (EOS) of Hydrocarbons at 1 to 10 Mbar Using Laser-Driven Shock Waves” (invited).

R. Betti, K. S. Anderson, P. Y. Chang, R. Nora, C. D. Zhou, B. Spears, J. Edwards, S. W. Haan, and J. Lindl, “ICF Ignition, the Lawson Criterion, and Comparison with MFE Ignition” (invited).

T. R. Boehly, V. N. Goncharov, W. Seka, D. E. Fratanduono, M. A. Barrios, S. X. Hu, J. A. Marozas, T. C. Sangster, D. D. Meyerhofer, D. G. Hicks, and P. M. Celliers, “Shock-Timing Measurements in Directly Driven Spherical Inertial Confinement Fusion Targets.”

P. Y. Chang, R. Betti, K. S. Anderson, R. Nora, B. Spears, M. Fatenejad, and D. Shvarts, “A Measurable Three-Dimensional Ignition Criterion for Inertial Confinement Fusion.”

T. J. B. Collins, P. W. McKenty, K. S. Anderson, M. M. Marinak, M. A. Barrios, D. G. Braun, T. R. Boehly, and P. M. Celliers, “Simulations of the Direct-Drive NIF Shock-Timing Diagnostic Commissioning Experiments.”

R. S. Craxton, W. Theobald, W. Seka, S. Ivancic, G. Li, C. Ren, and D. Weiner, “Hydrodynamic Simulations and Optical Diagnosis of a Long-Scale-Length Channeling Experiment on OMEGA EP.”

J. A. Delettrez, J. P. Knauer, V. N. Goncharov, P. B. Radha, C. Stoeckl, A. V. Maximov, J. A. Frenje, and D. Shvarts,

“Analysis of the Effect of a High-Z-Doped CH Ablator and Glass Ablators on Preheat and Hard X-Ray Radiation from Two-Plasmon Decay Electrons.”

D. H. Edgell, W. Seka, J. A. Delettrez, R. S. Craxton, V. N. Goncharov, I. V. Igumenshchev, J. F. Myatt, A. V. Maximov, R. W. Short, T. C. Sangster, and R. E. Bahr, “Cross-Beam Energy Transport in Direct-Drive-Implsion Experiments.”

R. Epstein, J. A. Delettrez, V. N. Goncharov, P. W. McKenty, F. J. Marshall, D. D. Meyerhofer, P. B. Radha, S. P. Regan, T. C. Sangster, V. A. Smalyuk, and W. Theobald, “Simulation and Analysis of Backlit Images of Cryogenic Implsions on OMEGA.”

D. E. Fratanduono, M. A. Barrios, T. R. Boehly, D. D. Meyerhofer, R. Smith, J. H. Eggert, D. G. Hicks, P. M. Celliers, G. W. Collins, and R. Rygg, “Measurements of Strain-Induced Refractive Index Changes in LiF Using Direct-Drive Ramp Compression.”

V. Yu. Glebov, C. Stoeckl, W. Theobald, T. C. Sangster, K. L. Marshall, M. Cruz, M. J. Shoup III, T. Buczek, A. Pruyne, M. Fox, T. Duffy, M. J. Moran, and R. Lauck, “Development of Scintillator Detectors for Fast-Ignition Experiments and Down-Scattered Neutron Measurements.”

V. N. Goncharov, T. C. Sangster, T. R. Boehly, R. L. McCrory, D. D. Meyerhofer, P. B. Radha, V. A. Smalyuk, S. Skupsky, J. A. Frenje, and R. D. Petrasso, “Multiple-Picket Cryogenic Target Designs and Performance for OMEGA and the National Ignition Facility.”

J. D. Hager, J. P. Knauer, S. X. Hu, D. D. Meyerhofer, T. C. Sangster, and V. A. Smalyuk, “Rayleigh–Taylor Measurements in Planar CH and SiO₂ Foils on OMEGA.”

S. X. Hu, B. Militzer, V. N. Goncharov, T. R. Boehly, P. B. Radha, and S. Skupsky, “Theoretical Investigation of Strong Coupling and Degeneracy Effects in ICF Implsions.”

I. V. Igumenshchev, D. H. Edgell, V. N. Goncharov, W. Seka, J. F. Myatt, A. V. Maximov, A. Shvydky, and J. A. Delettrez, “Modeling Crossed-Beam Energy Transfer in Implsion Experiments on OMEGA.”

J. P. Knauer, O. V. Gotchev, P. Y. Chang, D. D. Meyerhofer, A. Polomarov, R. Betti, J. A. Frenje, C. K. Li, M. J.-E. Manuel, R. D. Petrasso, J. R. Rygg, and F. H. Séguin, “Compressing Magnetic Fields with High-Energy Lasers” (invited).

J. A. Marozas, T. J. B. Collins, and J. D. Zuegel, “2-D Simulations of a 1-MJ CH-Foam Ignition Target on the NIF with 0.5 THz of 1-D Multi-FM SSD Bandwidth Using an Analytic Model.”

F. J. Marshall, R. S. Craxton, R. Epstein, V. Yu. Glebov, V. N. Goncharov, J. P. Knauer, P. W. McKenty, P. B. Radha, A. Shvydky, J. A. Frenje, C. K. Li, R. D. Petrasso, and F. H. Séguin, “Polar-Driven Implsions on OMEGA: Observations and Simulations of Low-Mode Perturbations in the Main Fuel Layer and Hot Spot.”

A. V. Maximov, J. F. Myatt, R. W. Short, W. Seka, J. A. Delettrez, and C. Stoeckl, “Growth and Saturation of Two-Plasmon-Decay Instability Driven by Crossing Laser Beams in OMEGA Plasmas.”

P. W. McKenty, R. S. Craxton, J. A. Marozas, A. M. Cok, M. J. Bonino, D. R. Harding, D. D. Meyerhofer, R. L. McCrory, J. D. Kilkenny, A. Nikroo, J. Fooks, M. L. Hoppe, M. J. Edwards, A. J. MacKinnon, D. H. Munro, and R. J. Wallace, “Design of High-Neutron-Yield, Polar-Drive Targets for Diagnostic Activation Experiments on the NIF.”

D. D. Meyerhofer, R. Betti, T. R. Boehly, J. H. Kelly, S. J. Loucks, R. L. McCrory, S. F. B. Morse, P. M. Nilson, S. P. Regan, T. C. Sangster, V. A. Smalyuk, C. Stoeckl, W. Theobald, and L. J. Waxer, “Initial Results from the OMEGA EP Laser System.”

J. F. Myatt, J. A. Delettrez, A. V. Maximov, R. W. Short, D. H. Edgell, W. Seka, D. F. DuBois, D. A. Russell, and H. X. Vu, “Extended Zakharov Modeling of Preheat Caused by the Two-Plasmon Decay Instability in Direct-Drive ICF Plasmas.”

P. M. Nilson, W. Theobald, J. F. Myatt, L. Gao, C. Stoeckl, P. A. Jaanimagi, J. A. Delettrez, B. Yaakobi, J. D. Zuegel, R. Betti, D. D. Meyerhofer, T. C. Sangster, A. J. MacKinnon, P. K. Patel, and K. Akli, “Fast-Electron Generation with Multi-kJ Pulses on OMEGA EP.”

O. Polomarov, P. Y. Chang, O. V. Gotchev, and R. Betti, “Effects of External and Self-Generated Magnetic Fields on Laser-Driven Implsions.”

P. B. Radha, C. Stoeckl, V. N. Goncharov, J. A. Delettrez, T. C. Sangster, R. Betti, R. L. McCrory, D. D. Meyerhofer, S. P. Regan, W. Seka, D. Shvarts, S. Skupsky, and V. A. Smalyuk, “Intensity Dependence of Target Performance in Low-Adiabatic, Warm Implsions on OMEGA.”

S. P. Regan, P. B. Radha, T. R. Boehly, V. N. Goncharov, R. L. McCrory, D. D. Meyerhofer, T. C. Sangster, V. A. Smalyuk, K. Falk, G. Gregori, T. Doeppner, S. H. Glenzer, and O. L. Landen, “Inferring Electron Temperature of Shocked Liquid Deuterium Using Inelastic X-Ray Scattering.”

T. C. Sangster, V. N. Goncharov, R. Betti, T. R. Boehly, D. T. Casey, T. J. B. Collins, R. S. Craxton, J. A. Delettrez, D. H. Edgell, R. Epstein, K. A. Fletcher, J. A. Frenje, V. Yu. Glebov, D. R. Harding, S. X. Hu, I. V. Igumenshchev, J. P. Knauer, S. J. Loucks, C. K. Li, J. A. Marozas, F. J. Marshall, R. L. McCrory, P. W. McKenty, D. D. Meyerhofer, P. M. Nilson, S. P. Padalino, R. D. Petrasso, P. B. Radha, S. P. Regan, F. H. Séguin, W. Seka, R. W. Short, D. Shvarts, S. Skupsky, V. A. Smalyuk, J. M. Soures, C. Stoeckl, W. Theobald, and B. Yaakobi, “Shock-Tuned Cryogenic DT-Implosion Performance on OMEGA” (invited).

W. Seka, D. H. Edgell, J. F. Myatt, A. V. Maximov, R. W. Short, R. S. Craxton, D. Russell, D. F. DuBois, and H. X. Vu, “Mitigation of Fast-Electron Production by the Two-Plasmon-Decay Instability in Directly Driven Targets.”

R. W. Short, “Anisotropy and Angular Dependence of Two-Plasmon Decay Driven by Multiple Overlapping Laser Beams in Direct-Drive Geometry.”

A. Shvydky, P. W. McKenty, J. A. Delettrez, I. V. Igumenshchev, D. H. Edgell, S. Skupsky, and R. L. McCrory, “Numerical Investigation of the Effects of Cross-Beam Energy Transfer on the Drive Uniformity of OMEGA Implosions.”

A. A. Solodov, M. Storm, J. F. Myatt, R. Betti, D. D. Meyerhofer, P. M. Nilson, W. Theobald, and C. Stoeckl, “Simulations of Electron-Beam Transport in Solid-Density Targets and the Role of Magnetic Collimation.”

C. Stoeckl, W. Theobald, R. Betti, R. S. Craxton, J. A. Delettrez, O. V. Gotchev, V. Yu. Glebov, F. J. Marshall, D. D. Meyerhofer, W. Seka, T. C. Sangster, C. D. Zhou, J. A. Frenje, and R. D. Petrasso, “Shock-Ignition Experiments on OMEGA at NIF-Relevant Intensities.”

W. Theobald, C. Stoeckl, V. Yu. Glebov, F. J. Marshall, K. L. Marshall, K. S. Anderson, R. Betti, R. S. Craxton, D. D. Meyerhofer, P. M. Nilson, T. C. Sangster, A. A. Solodov, J. A. Frenje, N. Sinenian, R. D. Petrasso, P. A. Norreys, D. Hey, M. H. Key, P. K. Patel, R. Lauck, and R. B. Stephens, “Integrated Fast-Ignition Experiments on OMEGA.”

J.-H. Yang and R. S. Craxton, “An Empirical Model for the Interaction of Ultra-Intense Laser Pulses with Fully Ionized Plasmas Including Electrostatic Effects.”

J. E. Schoenly, W. Seka, and P. Rechmann, “Selective Near-UV Ablation of Dental Calculus: Measurement of Removal Rates,” BiOS 2010, San Francisco, CA, 23–28 January 2010.

L. Sun, S. Jiang, and J. R. Marciante, “Compact All-Fiber Optical Faraday Isolator,” SPIE Photonics West–LASE, San Francisco, CA, 23–28 January 2010.

The following presentations were made at Advanced Solid-State Photonics, San Diego, CA, 31 January–3 February 2010:

J. Bromage, C. Dorrer, and J. D. Zuegel, “High-Resolution Spatio-Spectral Characterization of Noncollinear Optical Parametric Amplifiers.”

J. Bromage, C. Dorrer, and J. D. Zuegel, “Performance Trade-Offs for High-Repetition-Rate Noncollinear Optical Parametric Amplifiers.”

R. Xin and J. D. Zuegel, “Directly Chirped Laser Source for Chirped-Pulse Amplification.”

A. V. Okishev, D. Wang, D. Westerfeld, L. Shterengas, and G. Belenky, “Characterization of Highly Stable Mid-IR, GaSb-Based Laser Diodes,” Laser Applications to Chemical, Security and Environmental Analysis, San Diego, CA, 31 January–4 February 2010.

The following presentations were made at the 19th Target Fabrication Meeting, Orlando, FL, 21–26 February 2010:

Z. Bei, T. B. Jones, D. R. Harding, and A. Tucker-Schwartz, “Electric-Field Mediated Double-Emulsion Droplet Centering Using Density Gradient Suspension.”

M. J. Bonino, D. R. Harding, S. G. Noyes, J. Fooks, D. Turner, M. D. Wittman, and L. D. Lund, “Stalk-Mounted Cryogenic Targets: Rationale and Results.”

D. H. Edgell, M. D. Wittman, R. S. Craxton, D. R. Harding, B. Smith, and T. Lu, “Three-Dimensional Characterization of Cryogenic Targets Using X-Ray Phase-Contrast Imaging and Shadowgraphy at LLE.”

D. R. Harding, T. B. Jones, R. Q. Gram, Z. Bei, W. Wang, M. Moynihan, and S.-J. Scott, “Mass Fabrication of Cryogenic Targets for Inertial Fusion Energy.”

R. L. McCrory, “Inertial Confinement Fusion Research at the Laboratory for Laser Energetics.”

P. W. McKenty, R. S. Craxton, J. A. Marozas, A. M. Cok, R. Epstein, M. J. Bonino, D. R. Harding, D. D. Meyerhofer, R. L. McCrory, J. D. Kilkenny, A. Nikroo, J. Fooks, M. Hoppe, J. M. Edwards, A. J. MacKinnon, D. H. Munro, and R. J. Wallace, “Results of Recent NIF Polar-Drive Diagnostic Activation Experiments.”

M. Moynihan, D. R. Harding, and S. H. Chen, “Microfluidic T-Junctions to Mass Produce NIF and IFE Size Foam Targets.”

S.-J. Scott, D. R. Harding, and J. Fooks, “Mechanical Forces that Develop in Foam Material During Evaporative Drying.”

W. T. Shmayda, “Decontaminating Tritiated Surfaces with Humid Purge Streams.”

W. Wang, T. B. Jones, and D. R. Harding, “On-Chip Double-Emulsion Droplet Assembly Using EWOD and DEP.”

M. D. Wittman and D. R. Harding, “Development of NIF-Scale Polar-Drive Cryogenic Targets.”

The following presentations were made at OFC 2010, San Diego, CA, 21–25 March 2010:

J. R. Marciante and W. Guan, “Single-Frequency Hybrid Brillouin/Ytterbium Fiber Laser with 1-W Output Power.”

L. Sun, S. Jiang, and J. R. Marciante, “All-Fiber Optical Magnetic Field Sensor Based on Faraday Rotation.”

D. R. Harding, T. B. Jones, and D. D. Meyerhofer, “Mass Production of Targets for Inertial Fusion Energy,” 5th IAEA Technical Meeting, Vienna, Austria, 24–26 March 2010.

W. T. Shmayda and J. E. Fair, “Humidity and Temperature-Stimulated Outgassing from Contaminated Metal Surfaces,” Hydrogen and Helium Isotopes in Materials, Oak Ridge, TN, 20–21 April 2010.

J. F. Myatt, J. A. Delettrez, A. V. Maximov, D. D. Meyerhofer, R. W. Short, C. Stoeckl, M. Storm, S. C. Wilks, and H. Chen, “Optimizing Pair Production on Kilojoule-Class Lasers,” Workshop on Antimatter Using Intense Lasers, Berkeley, CA, 27–28 April 2010.

The following presentations were made at the OMEGA Laser Facility Users Workshop, Rochester, NY, 28–30 April 2010:

M. A. Barrios, D. G. Hicks, T.R. Boehly, D. E. Fratanduono, J. H. Eggert, P. M. Celliers, G. W. Collins, and D. D. Meyerhofer, “High-Precision Measurements of the Equation of State of Hydrocarbons at 1- to 10-Mbar Using Laser-Driven Shock Waves.”

C. Dorrer, D. Irwin, A. Consentino, and J. Qiao, “OMEGA EP Temporal Contrast Measurements.”

G. Fiksel, R. Jungquist, P. M. Nilson, W. Theobald, and C. Stoeckl, “Development of a Spherical Crystal X-Ray Imaging Diagnostic for OMEGA and OMEGA EP.”

D. E. Fratanduono, M. A. Barrios, T. R. Boehly, D. D. Meyerhofer, J. H. Eggert, R. Smith, D. G. Hicks, P. M. Celliers, and G. W. Collins, “Measures of Strain-Induced Refractive-Index Changes in Ramp-Compressed Lithium Fluoride.”

J. D. Hager, V. A. Smalyuk, S. X. Hu, D. D. Meyerhofer, and T. C. Sangster, “Rayleigh–Taylor Measurements in Planar CH and SiO₂ Foils on OMEGA.”

B. E. Kruschwitz, S.-W. Bahk, J. Bromage, D. Irwin, and M. Moore, “On-Shot Focal-Spot Characterization on OMEGA EP.”

S. F. B. Morse, "Facility Overview and Progress on 2009 OLUG Recommendations."

P. M. Nilson, R. Betti, J. A. Delettrez, L. Gao, P. A. Jaanimagi, J. F. Myatt, T. C. Sangster, A. A. Solodov, C. Stoeckl, W. Theobald, B. Yaakobi, J. D. Zuegel, A. J. Mackinnon, P. K. Patel, K. Akli, L. Willingale, and K. M. Krushelnick, "Intense-Energy Coupling with Multikilojoule, 10-ps Pulses on OMEGA EP."

G. Pien, "Diagnostic Qualification and Infrastructure Update."

W. Theobald, W. Seka, M. Bedzyk, R. Boni, R. Brown, R. S. Craxton, S. Ivancic, P. M. Nilson, J. Puth, A. V. Okishev, R. G. Roides, T. C. Sangster, C. Stoeckl, T. Duffy, D. Weiner, and J. Zuegel, "Fourth-Harmonic Probe Diagnostic for OMEGA EP."

K. A. Thorp, "Omega Facility Status and Performance Update."

The following presentations were made at the 18th Topical Conference on High-Temperature Plasma Diagnostics, Wildwood, NJ, 16–20 May 2010:

D. H. Edgell, W. Seka, V. N. Goncharov, I. V. Igumenshchev, R. S. Craxton, J. A. Delettrez, J. F. Myatt, A. V. Maximov, T. C. Sangster, and R. W. Short, R. E. Bahr, "Time-Resolved Scattered-Light Spectroscopy in Direct-Drive-Implsion Experiments on OMEGA."

G. Fiksel, C. Freeman, J. A. Frenje, J. C. Mileham, P. M. Nilson, N. Sinenian, C. Stoeckl, and W. Theobald, "Characterization of Composition and Energy Spectra of Laser-Produced Ions with Thomson Parabola."

V. Yu. Glebov, T. C. Sangster, C. Stoeckl, J. P. Knauer, W. Theobald, K. L. Marshall, M. J. Shoup III, T. Buczek, M. Cruz, T. Duffy, M. Romanofsky, M. Fox, A. Pruyne, M. J. Moran, R. A. Lerche, J. McNaney, J. D. Kilkenny, M. Eckart, D. Schneider, D. Munro, W. Stoeffl, R. A. Zacharias, J. J. Haslam, T. Clancy, M. Yeoman, D. Warwas, C. J. Horsfield, J.-L. Bourgade, O. Landoas, L. Disdier, G. A. Chandler, and R. J. Leeper, "The National Ignition Facility Neutron Time-of-Flight System and Its Initial Performance" (invited).

F. J. Marshall, T. DeHaas, and V. Yu. Glebov, "Charge-Injection-Device Performance in the High-Energy-Neutron Environment of Laser-Fusion Experiments."

C. Stoeckl, M. Cruz, V. Yu. Glebov, J. P. Knauer, R. Lauck, K. L. Marshall, C. Mileham, T. C. Sangster, and W. Theobald, "A Gated Liquid-Scintillator-Based Neutron Detector for Fast-Ignitor Experiments and Down-Scattered Neutron Measurements."

The following presentations were made at CLEO 2010, San Jose, CA, 16–21 May 2010:

J. Bromage, C. Dorrer, and J. D. Zuegel, "Eliminating Spatio-temporal Distortions from Angular Dispersion in Noncollinear Optical Parametric Amplifiers."

C. Dorrer, D. Irwin, A. Consentino, and J. Qiao, "Contrast Measurements of Kilojoule Laser Pulses at the Omega Laser Facility."

B. E. Kruschwitz, S.-W. Bahk, J. Bromage, D. Irwin, M. Moore, L. J. Waxer, J. D. Zuegel, and J. H. Kelly, "Improved On-Shot Focal-Spot Diagnosis on the OMEGA EP Short-Pulse Laser System."

J. Qiao, L. J. Waxer, T. Nguyen, J. Bunkenburg, C. Kingsley, J. H. Kelly, A. W. Schmid, and D. Weiner, "*In-Situ* Detection and Analysis of Laser-Induced Damage on a 1.5-m Multilayer-Dielectric Grating Compressor for High-Energy, Petawatt-Class Laser Systems."

R. C. G. Smith, A. M. Sarangan, and J. R. Marciante, "Direct Measurement of Bend-Induced Mode Deformation Using a Helical-Core Fiber."

L. Sun, S. Jiang, and J. R. Marciante, "A Compact All-Fiber Optical Faraday Mirror."

M. Vargas, Z. Zhao, K. L. Marshall, and C. Dorrer, "Optically Patterned Liquid Crystal Devices for High-Resolution Beam Shaping."

R. Xin and J. D. Zuegel, "Generation of CPA Seed Pulse by Direct Phase Modulation."

J. D. Zuegel, "Laser Fusion for Laser Jocks: Basic Principles of a Laser Application Meeting a Grand Challenge," CLEO Applications, San Jose, CA, 16–21 May 2010 (invited tutorial).

The following presentations were made at Optical Interference Coatings, Tucson, AZ, 6–11 June 2010:

K. L. Marshall, E. Glowacki, C. Sileo, L. Chockalingam, J. Lee, V. Guiliano, and A. Rigatti, “Improving the Abrasion Resistance of Organosilane-Modified Sol-Gel Coatings for High-Peak-Power Laser Applications.”

J. B. Oliver, P. Kupinski, A. L. Rigatti, A. W. Schmid, J. C. Lambropoulos, S. Papernov, A. Kozlov, and R. D. Hand “Modification of Stresses in Evaporated Hafnia Coatings for Use in Vacuum.”

J. B. Oliver, P. Kupinski, A. L. Rigatti, A. W. Schmid, J. C. Lambropoulos, S. Papernov, A. Kozlov, and R. D. Hand “Stress Compensation in Hafnia/Silica Optical Coatings by Inclusion of Alumina Layers.”

J. B. Oliver, P. Kupinski, A. L. Rigatti, A. W. Schmid, J. C. Lambropoulos, S. Papernov, A. Kozlov, J. Spaulding, D. Sadowski, Z. Chrzan, R. D. Hand, D. R. Gibson, I. Brinkley, and F. Placido, “Large-Aperture Plasma-Assisted Deposition of ICF Laser Coatings.”

A. L. Rigatti, J. B. Oliver, P. Kupinski, H. Floch, E. Lavastre, G. Ravel, and F. Geffraye, “CEA Deformable-Mirror Coating Test Results.”

J. F. Myatt, R. Betti, J. A. Delettrez, L. Gao, P. A. Jaanimagi, A. V. Maximov, D. D. Meyerhofer, T. C. Sangster, R. W. Short, C. Stoeckl, M. Storm, W. Theobald, B. Yaakobi, J. D. Zuegel, S. C. Wilks, A. J. MacKinnon, P. K. Patel, H. Chen, and K. Akli, “High-Intensity Laser-Matter Interaction Experiments on the Kilojoule-Class OMEGA EP Laser,” 2010 Canadian Association of Physicists Congress, Toronto, Canada, 7–11 June 2010.

The following presentations were made at Optical Fabrication and Testing, Jackson Hole, WY, 13–17 June 2010:

S. N. Shafir, H. J. Romanofsky, M. D. Skarlinski, M. Wang, C. Miao, S. Salzman, T. Chartier, J. Mici, J. C. Lambropoulos, R. Shen, H. Yanh, and S. D. Jacobs, “Corrosion Resistant Zirconia Coated Carbonyl Iron Particle-Based Magnetorheological Fluid.”

M. D. Skarlinski and S. D. Jacobs, “Modifying the Rheological Properties of Zirconia Coated Carbonyl Iron Suspen-

sions Through Acid-Base Titration and the Addition of Di-Ammonium Citrate.”

The following presentations were made at the 40th Annual Anomalous Absorption Conference, Snowmass Village, CO, 13–18 June 2010:

T. J. B. Collins, J. A. Marozas, S. Skupsky, P. W. McKenty, V. N. Goncharov, P. B. Radha, R. S. Craxton, F. J. Marshall, R. Epstein, D. Jacobs-Perkins, and A. Shvydky, “Preparing for Polar Drive at the National Ignition Facility.”

D. H. Edgell, J. F. Myatt, W. Seka, J. A. Delettrez, A. V. Maximov, R. W. Short, and R. E. Bahr, “Anisotropic Distribution of Hard X Rays from the Two-Plasmon-Decay Hot-Electron Distribution.”

M. G. Haines, J. A. Delettrez, J. F. Myatt, A. A. Solodov, T. J. B. Collins, and J. A. Marozas, “Electrothermally Generated Filaments in Laser–Solid Interactions.”

S. X. Hu, V. N. Goncharov, P. B. Radha, J. A. Marozas, S. Skupsky, T. R. Boehly, T. C. Sangster, D. D. Meyerhofer, and R. L. McCrory, “Two-Dimensional Radiation-Hydrodynamic Simulations of Cryogenic-DT Implosions at the Omega Laser Facility.”

A. V. Maximov, J. F. Myatt, R. W. Short, R. Yan, and W. Seka, “Modeling of Two-Plasmon-Decay Instability in the Plasmas of Direct-Drive Inertial Confinement Fusion.”

J. F. Myatt, J. A. Delettrez, W. Seka, D. H. Edgell, A. V. Maximov, R. W. Short, D. F. DuBois, D. A. Russell, and H. X. Vu, “Calculations of Preheat Caused by the Two-Plasmon-Decay Instability in Direct-Drive ICF Plasmas.”

W. Seka, D. H. Edgell, J. F. Myatt, R. S. Craxton, A. V. Maximov, and R. W. Short, “SBS, SRS, and TPD in Planar Target Experiments Relevant to Direct-Drive ICF.”

R. W. Short, “Anisotropy of Collectively Driven Two-Plasmon Decay in Direct-Drive Spherical Irradiation Geometry.”

H. X. Vu, D. F. DuBois, D. A. Russell, J. F. Myatt, and W. Seka, “Hot-Electron Generation by the Two-Plasmon-Decay Instability in Inhomogeneous Plasmas.”

P. B. Radha, R. Betti, T. R. Boehly, J. A. Delettrez, V. N. Goncharov, I. V. Igumenshchev, J. P. Knauer, J. A. Marozas, F. J. Marshall, R. L. McCrory, D. D. Meyerhofer, S. P. Regan, T. C. Sangster, W. Seka, S. Skupsky, A. A. Solodov, C. Stoeckl, W. Theobald, J. A. Frenje, D. T. Casey, C. K. Li, and R. D. Petrasso, "Inertial Confinement Fusion Using the OMEGA Laser," 37th International Conference on Plasma Science, Norfolk, VA, 20–24 June 2010.

E. Głowacki, K. Hunt, D. Abud, and K. L. Marshall, "Photo-switchable Gas Permeation Membranes Based on Azobenzene-Doped Liquid Crystals. II. Permeation-Switching Characterization Under Variable Volume and Variable Pressure Conditions," SPIE Optics and Photonics 2010, San Diego, CA, 1–5 August 2010.

The following presentations were made at ICUIL, Watkins Glen, NY, 26 September–1 October 2010:

S.-W. Bahk, "A Simple Self-Referenced Piston Measurement for Characterizing a Segmented Wavefront from Tiled Gratings."

S.-W. Bahk, E. Fess, I. A. Begishev, and J. D. Zuegel, "High-Resolution, Adaptive Beam Shaping (HRABS) in a Multi-Terawatt Laser."

J. Bromage, C. Dorrer, and J. D. Zuegel, "A 160-nm-Bandwidth Front End for Ultra-Intense OPCPA."

C. Dorrer, "Temporal Characterization Diagnostics for High-Intensity Laser Systems."

C. Dorrer, D. Irwin, A. Consentino, and J. Qiao, "Contrast Measurements of Kilojoule Laser Pulses at the OMEGA EP Laser Facility."

C. Dorrer, P. Leung, M. Vargas, J. Boule, K. Wegman, Z. Zhao, and K. L. Marshall, "Development of High-Fluence Beam Shapers."

B. E. Kruschwitz, S.-W. Bahk, J. Bromage, D. Irwin, and M. D. Moore, "Improved On-Shot Focal-Spot Measurement Using Phase-Retrieval-Assisted Wavefront Measurements."

B. E. Kruschwitz, M. J. Guardalben, J. H. Kelly, J. Qiao, I. A. Begishev, J. Bromage, S.-W. Bahk, C. Dorrer, L. Folsbee, S. D. Jacobs, R. Jungquist, T. J. Kessler, R. W. Kidder, S. J. Loucks, J. R. Marciante, R. L. McCrory, D. D. Meyerhofer, S. F. B. Morse, A. V. Okishev, J. B. Oliver, G. Pien, J. Puth, A. L. Rigatti, A. W. Schmid, M. J. Shoup III, C. Stoeckl, K. A. Thorp, and J. D. Zuegel, "Current Performance of the OMEGA EP High-Energy Short-Pulse Laser System."

J. Qiao, A. W. Schmid, L. J. Waxer, T. Nguyen, J. Bunkenburg, C. Kingsley, A. Kozlov, and D. Weiner, "Real-Time Detection of Laser-Induced Damage on a 1.5-m Tiled-Grating Compressor During a 15-ps, 2.2-kJ Energy Ramp on OMEGA EP."

S. Papernov, A. Tait, W. Bittle, A. W. Schmid, J. B. Oliver, and P. Kupinski, "Submicrometer-Resolution Mapping of Ultraweak 355-nm Absorption in HfO₂ Monolayers Using Photothermal Heterodyne Imaging," XLII Annual Symposium on Optical Materials for High Power Lasers, Boulder, CO, 27–29 September 2010.



UNIVERSITY *of*
ROCHESTER